Search for fourth generation b' quarks in same-sign dilepton final states with ATLAS

D I S S E R T A T I O N

zur Erlangung des akademischen Grades

doctor rerum naturalium
(Dr. rer. nat.)
im Fach Physik

eingereicht an der
Mathematisch-Naturwissenschaftlichen Fakultät I
Humboldt-Universität zu Berlin

von
M.Sc. Dennis Patrick Wendland

Präsident der Humboldt-Universität zu Berlin:
Prof. Dr. Jan-Hendrik Olbertz

Dekan der Mathematisch-Naturwissenschaftlichen Fakultät I:
Prof. Stefan Hecht, PhD

Gutachter:
1. Prof. Dr. Heiko Lacker
2. Prof. Dr. Thomas Lohse
3. Jun.-Prof. Dr. Arno Strässner

eingereicht am: 02.07.2013
Tag der mündlichen Prüfung: 24.10.2013

Abstract

This thesis presents a search for the production of down-type $b'\bar{b}'$ quark-antiquark pairs of a sequential fourth generation of fermions. In this search, final states with two same-sign charged leptons (e or μ), at least two jets (including at least one b-jet), missing transverse energy and a large total sum of the transverse momenta of all electrons, muons and jets were considered. Two different scenarios were assumed for the decays of these $b'\bar{b}'$ quark pairs. In the first scenario the two b' quarks were considered to decay exclusively into a t quark and a W boson. For the second scenario, variable branching fractions for the decays of the b' quarks into tW, cW and uW were allowed. The search was performed using data from pp collisions at a center-of-mass energy of $\sqrt{s} = 8\,\text{TeV}$ recorded by the ATLAS detector at the Large Hadron Collider. The used dataset corresponds to an integrated luminosity of $\mathcal{L} = 14.3\,\text{fb}^{-1}$. No significant excess of events over the background expectation was observed. Hence a lower limit on the b' mass of 0.724 TeV was set with 95% confidence level in the first scenario. In case of the second scenario with variable branching fractions, exclusion areas with 95% confidence level were derived as a function of the b' mass and its decay branching fractions. These limits are less stringent compared to the result assuming a branching fraction of 100% for $b' \to tW$.

Zusammenfassung

In dieser Dissertation wird eine Suche nach der Produktion von 'down'-artigen $b'\bar{b}'$ Quark-Antiquark-Paaren einer sequentiellen vierten Generation von Fermionen präsentiert. Für die Suche wurden Endzustände mit zwei gleich geladenen Leptonen (e oder μ), mindestens zwei Jets (davon ein b-Jet), fehlender transversaler Energie und einer großen Summe der Transversalimpulse aller Elektronen, Muonen und Jets betrachtet. Für den Zerfall dieser $b'\bar{b}'$ Quark-Antiquark-Paare wurden zwei verschiedene Szenarien untersucht. Im ersten Szenario wird angenommen, dass beide b' Quarks ausschliesslich in ein t Quark und ein W Boson zerfallen. Für das zweite Szenario werden variable Verzweigungsverhältnisse für die Zerfälle der b' Quarks nach tW, cW und uW erlaubt. Die Suche wurde mit Daten durchgeführt, die von pp Kollisionen mit einer Schwerpunktsenergie von $\sqrt{s} = 8\,\text{TeV}$ vom ATLAS Detektor am Large Hadron Collider aufgezeichnet wurden. Der benutzte Datensatz entspricht einer integrierten Luminosität von $\mathcal{L} = 14.3\,\text{fb}^{-1}$. Es wurde kein signifikanter Überschuss an Ereignissen über den erwarteten Ereignissen vom Untergrund beobachtet. Daher wurde im ersten Szenario eine untere Grenze auf die b'-Masse ($m_{b'}$) von $0.724\,\text{TeV}$ mit einem Konfidenzniveau von 95% bestimmt. Im Falle des zweiten Szenarios mit variablen Verzweigungsverhältnissen wurden Ausschlussregionen mit einem Konfidenzniveau von 95% als Funktion der Masse des b'-Quarks und seiner Verzweigungsverhältnisse bestimmt. Die erhaltenen Grenzen auf $m_{b'}$ sind schwächer verglichen mit dem Ergebnis für ein Verzweigungsverhältniss von 100% für $b' \to tW$.

Contents

1 Introduction

The construction of the Large Hadron Collider (LHC) [1, 2] at CERN marks a new era of particle physics. As a hadron machine, it collides protons with centre-of-mass energies of currently up to 8 TeV (in the future this will be extended to up to 14 TeV), allowing to probe the Standard Model of particle physics, as well as theories that go beyond, with accuracies well above those achieved at previous colliders as the *Tevatron* [3].

The Standard Model (SM) of particle physics [4–9], the summary of our current theoretical understanding of elementary particles and their interactions, has been verified with high precision in many independent experiments. However, one main ingredient of the SM is the Higgs mechanism [10–15], which is responsible for generating masses of the SM particles by electroweak symmetry breaking (EWSB) and interaction of these particles with the Higgs field. In the case of the existence of the Higgs field, there must be an additional particle, the Higgs boson, which was not discovered until recently. A milestone was achieved at the LHC in 2012, when both multi-purpose experiments, ATLAS [16] and CMS [17], claimed the discovery of a boson with a mass of about 125 GeV [18, 19] that has properties compatible with the SM Higgs boson. Further measurements in the future will show, whether the observed particle is indeed the SM Higgs boson.

Although providing an almost complete theory for particle physics, the Standard Model has some shortcomings. For instance, the SM is not able to explain the asymmetry between matter and antimatter we observe in the universe. Following the conditions written down by Sakharov [20], this asymmetry can be generated by a sufficient CP violation in nature. Nevertheless, the CP violating processes known from the SM can not produce an effect of the required size and this mechanism requires a Higgs boson with a low mass of about 70 GeV.

Another unexplained observation is the existence of dark matter, which might consist of gravitational and weakly interacting particles. The weakly interacting neutrinos in the SM do not have sufficient mass in order to be a possible candidate for dark matter.

Besides the particle content, the Standard Model describes the interactions between these particles via three different forces: the electromagnetic, the weak and the strong force. There is strong hint, that these forces were combined in a single interaction at energy scales which existed directly after the Big Bang, the creation of the universe. The idea of such unification is modelled in grand unification theories (GUTs), which are beyond the SM and hence can not be explained by the SM itself.

Until decisive tests, whether the Higgs-like boson observed at the LHC is responsible for the mass generation of the SM particles, the nature of the EWSB could still have different sources. For instance, there were theories developed, which consider that condensates of heavy quarks take place of the scalar Higgs field and are responsible for a dynamical EWSB [21, 22]. Nevertheless, the heaviest quark in the SM, the t quark, does

not have sufficient mass to form such condensates with the required properties.

The fermions that have been discovered so far and that were predicted by the SM, are grouped into three generations, each consisting of a quark doublet and a lepton doublet. However, the SM does not predict the number of existing fermion generations. An interesting model, that addresses above issues of the SM and that will be the topic of this thesis, is a sequential fourth generation. Within this theory, the three fermion generations are extended by a fourth generation, which consists of two additional fermion doublets containing two quarks and two leptons. The recent Higgs results from ATLAS and CMS exclude the model of a fourth generation, if the observed boson is indeed the SM Higgs boson. However, a fourth generation of fermions is not finally excluded, though when extending the Higgs sector.

In this thesis, I will discuss a search for the production of fourth generation down-type $b'\bar{b'}$ quark-antiquark pairs. For this search I used the data taken in proton-proton collisions by the ATLAS experiment. The data were collected for collisions with a centre-of-mass energy of $\sqrt{s} = 8\,\text{TeV}$ in the time period between April and October 2012, yielding in an integrated luminosity of $\mathcal{L} = 14.3\,\text{fb}^{-1}$.
In my analysis, the quark-antiquark pairs are assumed to be directly produced from the proton-proton collisions: $pp \to b'\bar{b'}$. For their decays, I consider two different decay scenarios. In the first scenario, I will assume that both quarks decay into tW with 100% branching fraction. Since the t quark decays nearly exclusively into bW, this decay topology results in two b quarks and four W bosons, two of which are having the same charge. For the second scenario the two quarks can decay either into tW, cW or uW. When requiring that at least one b' quark decays into tW, this scenario ends up with at least three W bosons in the final state.
In both scenarios, when two of the same-sign charged W bosons decay leptonically, this allows for selecting two same-sign charged leptons as search topology, which is rare in SM processes and hence is an optimal final state for searches for new physics beyond the SM.

In the case that there is no evidence of b' pair production in the data, I will set exclusion ranges on the parameters of this model. In the first scenario with exclusive decays into tW, I will derive upper limits on the cross-section for the pair-production, which can be translated into a lower mass limit. In the second scenario with variable decays, the analysis is performed for different assumptions on the branching fractions for $b' \to tW$, $b' \to cW$ and $b' \to uW$. Hence I will draw exclusion ranges in the plane of the branching fractions and the b' mass.

This thesis is structured as follows: in Chapter 2, I will give a brief description of the Standard Model content, which is relevant for this analysis. This is followed by the introduction of the fourth generation of fermions, where I will discuss the impact of such additional particles on the Standard Model and theories that go beyond. Furthermore, I will summarise the constraints that have been derived in previous searches. The following Chapter 3 will explain the experimental setup that was used to record the data analysed in this thesis. This incorporates a description of the Large Hadron Collider and the ATLAS detector. In searches for physics beyond the SM, it is necessary to compare the observed data to the expectations of possible background processes and the signal

model. These expectations were partly derived using Monte-Carlo simulations, which will be described in Chapter 4. In the following Chapter 5, I will describe the various reconstruction algorithms and selection criteria that were used to select the physical objects (electrons, muons, jets, jets containing b-quarks and missing transverse momentum) for this analysis. The following Chapter 6 addresses the analysis itself: I will discuss the search topology, as well as possible background processes that could contribute to the final state of two same-sign charged leptons. After selecting possible candidate events for the signal process of $b'\bar{b}'$ production in data, this is compared to the expectations of the background and signal processes, in order to derive the limits mentioned above. Finally, I will give a summary and present an outlook in Chapter 7.

In the following I will use the 'natural units' system of particle physics. That means, that the speed of light c and the reduced Planck constant $\hbar$ are both equal to one:

$$c = \hbar = 1 \ . \tag{1.1}$$

This thesis was created using the document markup language LaTeX[23]. All presented Feynman diagrams have been created using the `FeynMF` [24] package. The various histograms and plots in this thesis were created using `ROOT` [25] and the `Python` [26] extension module `PyROOT` [27].

2 Theoretical introduction and motivation

This thesis describes a search for fourth generation quarks realised as a simple extension to the Standard Model. Before describing this extension, I will give a brief introduction to the Standard Model (SM) of elementary particle physics in Section 2.1. This includes descriptions of the particle content of the SM, its interactions and the generation of masses with the Higgs mechanism. The SM section is mostly based on the references [28–30].
Afterwards, in Section 2.2, I will introduce the fourth generation extension to the SM and discuss the impact of a fourth generation on the SM and theories beyond. Furthermore, I will present constraints on the fourth generation coming from electroweak data, flavor observables and direct searches. Additionally, I will discuss the recent observation of a Higgs-like boson at the Large Hadron Collider and its implications on the viability of the fourth generation sector. Finally, I will present possible production and decay scenarios of fourth generation quarks at hadron colliders.

2.1 Standard Model

The Standard Model of elementary particle physics [4–9] is a quantum field theory (QFT) describing three of the four known fundamental interactions in nature, namely the electromagnetic, weak and strong interactions.
The gravitational interaction is not considered in the SM, because its nature has not been fully understood so far and there is no quantum theoretical description up to now. Furthermore its strength on the scale of elementary particles is much smaller compared to the other three interactions. However, there are theories under development to also describe the gravitation with a QFT (see for example references [31, 32] for further reading).

The Standard Model describes the fields of the elementary particles and their interactions by the gauge symmetries

$$SU(3)_C \otimes SU(2)_L \otimes U(1)_Y, \tag{2.1}$$

where the group $SU(3)_C$ describes the strong interactions and $SU(2)_L \otimes U(1)_Y$ denotes the combination of electromagnetic and weak interactions, which is formulated in the electroweak theory. These interactions and their symmetry groups are further described in the following sections.

The matter found predominantly in nature is formed of protons, neutrons and electrons, where the former two are built of the elementary up- and down-quarks (u and d). In addition to the electron (e), there is an electron neutrino (ν_e) which appears for

example in β-decay. Both belong to a group called leptons. All four particles (u, d, e and ν_e) form one generation of fermions and have a spin of 1/2, but differ in mass and electrical charge. Up to now we know two additional generations of fermions, where each one consists of two quarks (up- and down-type), one charged lepton and its electrically neutral partner neutrino. The fermions charm-quark (c), strange-quark (s), muon (μ) and the muon neutrino (ν_μ) form the content of the second generation, whereas the top-quark (t), bottom-quark (b), tau (τ) and tau neutrino (ν_τ) are the ingredients of the third generation. All known fermions are summarised in Figure 2.1.

The neutrinos were assumed to be massless for a long time. Recent discoveries of

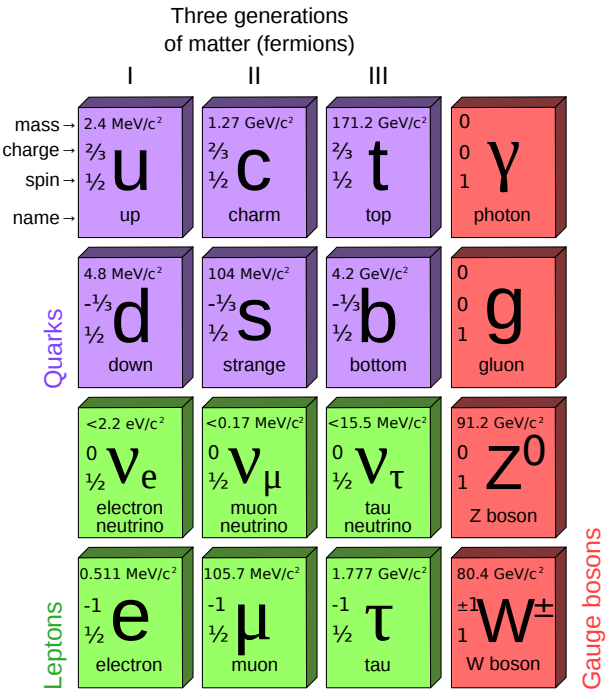

Figure 2.1: Particle content of the Standard Model [33]. The fermions of the three generations are shown together with the gauge bosons which are the mediators of the electromagnetic, weak and strong interactions. For each particle, its mass, electric charge and spin are presented. In case of the neutrinos, only mass limits have been determined so far.

neutrino oscillations proved that neutrinos have masses, but up to now only upper mass limits have been determined (see for instance references [34, 35] for further reading).

In addition to each fermion in the SM there exists an anti-particle which has opposite additive quantum numbers, but equal mass.

The forces between the particles are described by gauge bosons with spin 1. The electromagnetic interaction appears as the exchange of a massless photon γ, weak interactions are mediated by the massive $W^\pm$ and Z^0 bosons and the strong interaction

manifests as exchange of eight massless gluons g. The four mentioned force mediators are also summarised in Figure 2.1.
All above mentioned fermions appear in the weak interaction, electrically charged fermions participate in electromagnetic interactions and the strong interaction is limited to quarks.

2.1.1 Electroweak interaction

The electroweak (EW) theory (a unification of the electromagnetic and weak interactions) is described by the $SU(2)_L \otimes U(1)_Y$ part of the SM symmetry groups in Equation (2.1). Within this theory, particles are assigned the quantum numbers weak isospin I and hypercharge Y [36–38]. The third component of the weak isospin, I_3, and the hypercharge are conserved in charged-current EW interactions involving left-handed fermions. The directions of the momentum vector and the projection of the spin vector onto the momentum are opposite for such left-handed fermions, in the case that they are massless. This behaviour of the EW interaction is represented in the V-A (vector-axialvector) structure of the weak charged-current interaction.

Therefore, left-handed states of one fermion generation are grouped into weak isospin doublets with $I = 1/2$ and $I_3 = \pm 1/2$. The right-handed states, which do not couple to charged-current EW interactions, form isospin singlets with $I = 0$. As a convention, up-type quarks and neutrinos are assigned $I_3 = +1/2$, while the down-type quarks and charged leptons carry $I_3 = -1/2$. The hypercharge then depends on the weak isospin and the electrical charge Q through $Y = 2Q - 2I_3$. This means, that within one doublet the particles carry the same hypercharge ($Y = -1$ for the leptons and $Y = 1/3$ for the quarks). The SM fermions and their EW quantum numbers are summarised in Table 2.1. Flavor changing transitions within a doublet are allowed by changing the

Fields			Y	I	I_3	Q
$\begin{pmatrix} u \\ d \end{pmatrix}_L$	$\begin{pmatrix} c \\ s \end{pmatrix}_L$	$\begin{pmatrix} t \\ b \end{pmatrix}_L$	$1/3$	$1/2$	$+1/2$ $-1/2$	$+2/3$ $-1/3$
u_R	c_R	t_R	$+4/3$	0	0	$+2/3$
d_R	s_R	b_R	$-2/3$	0	0	$-1/3$
$\begin{pmatrix} \nu_e \\ e \end{pmatrix}_L$	$\begin{pmatrix} \nu_\mu \\ \mu \end{pmatrix}_L$	$\begin{pmatrix} \nu_\tau \\ \tau \end{pmatrix}_L$	-1	$1/2$	$+1/2$ $-1/2$	0 -1
ν_R^e	ν_R^μ	ν_R^τ	0	0	0	0
e_R	μ_R	τ_R	-2	0	0	-1

Table 2.1: The electroweak quantum numbers of the SM fermions. For each fermion, the hypercharge Y, weak isospin I, its third component I_3, and the electrical charge Q are presented. It can be seen, that weak isospin doublets carry $I = 1/2$, while isospin singlets have $I = 0$.

third component of the weak isospin by $|\Delta I_3| = 1$. In order to conserve this quantum number this is explained by the emission of a $W^\pm$ boson with $I = 1$ and $I_3 = \pm 1$.

Before describing the dynamics of the EW theory, I will introduce the quantum field

theory of the electromagnetic interaction, also called quantum electrodynamics (QED), which is based on the symmetry group $U(1)$.
A field theory is described by the Lagrangian density $\mathcal{L}$ which is in general a function of its fields ϕ^i and their derivatives $\partial_\mu \phi^i$. Similar to analytical mechanics, the fundamental law of motion can be derived by the Euler-Lagrange equation:

$$\partial_\mu \left(\frac{\partial \mathcal{L}}{\partial \left(\partial_\mu \phi^i \right)} \right) = \frac{\partial \mathcal{L}}{\partial \phi^i} \ . \tag{2.2}$$

In the following, the fermions are described by spinor fields ψ which are functions of the space-time coordinates x^μ. The Lagrangian density (in the following is simply called the Lagrangian) of an interaction-free particle of mass m is given by

$$\mathcal{L}_0 = i\bar{\psi}\gamma^\mu \partial_\mu \psi - m\bar{\psi}\psi, \tag{2.3}$$

where γ_μ denote the Dirac matrices. For the successful description of a particle interaction theory, it is required that the Lagrangian is invariant under local phase space transformations (here a local $U(1)$ transformation)

$$\psi(x) \to e^{i\alpha(x)}\psi(x), \tag{2.4}$$

where $\alpha(x)$ denotes a phase depending on space and time. The requirement of a global invariance follows from Noether's Theorem: invariance under symmetry transformations leads to a conservation of quantum numbers. The extension to a local invariance is required, in order to achieve a renormalisable gauge theory.
When applying the $U(1)$ transformation in Equation (2.4) to the free particle Lagrangian $\mathcal{L}_0$, one notices that $\mathcal{L}_0$ is not invariant. This can be solved by replacing ∂_μ by a covariant derivative

$$D_\mu \equiv \partial_\mu - ieA_\mu, \tag{2.5}$$

and introducing the new vector field A_μ and a coupling constant e which will turn out to be the electrical charge. The transformation of A_μ is constructed as in the following

$$A_\mu \to A_\mu + \frac{1}{e}\partial_\mu \alpha(x) \ , \tag{2.6}$$

in order to cancel unwanted terms in the non-invariant Lagrangian. After replacing the derivative in $\mathcal{L}_0$, the resulting Lagrangian is invariant under the local $U(1)$ transformation. When adding a kinetic term

$$-\frac{1}{4}F_{\mu\nu}F^{\mu\nu} \tag{2.7}$$

of the gauge field A_μ, where $F_{\mu\nu}$ denotes the field tensor $F_{\mu\nu} = \partial_\mu A_\nu - \partial_\nu A_\mu$, one obtains

the final Lagrangian of QED:

$$\mathcal{L}_{\text{QED}} = \bar{\psi}\left(i\gamma^\mu\partial_\mu - m\right)\psi + e\bar{\psi}\gamma^\mu A_\mu\psi - \frac{1}{4}F_{\mu\nu}F^{\mu\nu} \ . \tag{2.8}$$

In a similar way one can construct a theory based on the symmetry group $SU(2)_L \otimes U(1)_Y$, which unifies the electromagnetic and weak interactions. This was developed by Glashow [36], Salam [38] and Weinberg [37] and is therefore also called the GSW model. The symmetry group $SU(2)_L$ consists of the generators T^a $(a = 1, 2, 3)$ which are represented by the Pauli matrices σ_a: $T^a = \sigma^a/2$. One characteristic property is that the generators do not commute:

$$\left[T^a, T^b\right] = i\epsilon^{abc}T^c, \tag{2.9}$$

where ϵ^{abc} denotes the structure constant. The symmetry group $SU(2)_L$ is therefore non-Abelian. The phase $\alpha(x)$ introduced in the $U(1)$ transformation needs to be replaced by a 3-component vector $\vec{\alpha}(x)$. Furthermore the $U(1)_Y$ group is built from the generator Y and a phase $\beta(x)$. Finally, the local phase transformation of $SU(2)_L \otimes U(1)_Y$ acting on left- and right-handed spinors ψ_L and ψ_R, looks as follows:

$$\psi_L \to e^{ig\vec{\alpha}(x)\vec{T}+ig'\beta(x)Y}\psi_L, \tag{2.10}$$

$$\psi_R \to e^{ig'\beta(x)Y}\psi_R \ . \tag{2.11}$$

For convenience, the coupling constants g and g' have been pulled out of $\alpha(x)$ and $\beta(x)$, in order to distinguish the different strengths of the two interactions. As can be seen from above transformations, the $SU(2)_L$ part acts only on the left-handed spinors. When applying this transformation, one notices again that the Lagrangian is not invariant. Similar to the procedure for $U(1)$, a covariant derivative is built

$$D_\mu \equiv \partial_\mu + igW_\mu^a T^a + ig'\frac{1}{2}B_\mu \tag{2.12}$$

and the gauge fields $W_\mu = W_\mu^a T^a$ and B_μ are introduced for $SU(2)_L$ and $U(1)_Y$, respectively. The kinetic Lagrangian term of these fields is then given by

$$\mathcal{L}_{B,W}^{\text{kin}} = -\frac{1}{4}B_{\mu\nu}B^{\mu\nu} - \frac{1}{4}W_{\mu\nu}^a W^{\mu\nu,a}, \tag{2.13}$$

with the field tensors

$$B_{\mu\nu} = \partial_\mu B_\nu - \partial_\nu B_\mu \text{ and} \tag{2.14}$$

$$W_{\mu\nu}^a = \partial_\mu W_\nu^a - \partial_\nu W_\mu^a - g\epsilon^{abc}W_\mu^b W_\nu^c \ . \tag{2.15}$$

The third term of $W_{\mu\nu}^a$ arises from the non-Abelian character of $SU(2)_L$ and contains the structure constant ϵ^{abc}.
Inserting the above ingredients and assuming massless spinor fields, one obtains the final

invariant Lagrangian of the EW theory:

$$\mathcal{L}_{\mathrm{EW}} = \bar{\psi}_L \gamma^\mu \left[\partial_\mu + igW_\mu^a T^a + ig' \frac{Y_L}{2} B_\mu \right] \psi_L + \bar{\psi}_R \gamma^\mu \left[\partial_\mu + ig' Y_R B_\mu \right] \psi_R - \frac{1}{4} B_{\mu\nu} B^{\mu\nu} - \frac{1}{4} W_{\mu\nu}^a W^{\mu\nu,a} \ . \tag{2.16}$$

2.1.1.1 Electroweak symmetry breaking and Higgs mechanism

The EW Lagrangian in Equation (2.16) is not complete: the gauge bosons do not have mass terms, although these particles are quite heavy. Introducing mass terms again violates the invariance of the Lagrangian under $SU(2)_L \otimes U(1)_Y$ transformations. A possible solution for this problem is based on the principle of spontaneous symmetry breaking and is called the Higgs mechanism [10–15].

At first, an $SU(2)$ doublet of complex scalar fields is introduced

$$\Phi = \begin{pmatrix} \Phi_a \\ \Phi_b \end{pmatrix} = \frac{1}{\sqrt{2}} \begin{pmatrix} \Phi_1 + i\Phi_2 \\ \Phi_3 + i\Phi_4 \end{pmatrix} \tag{2.17}$$

with a Lagrangian density

$$\mathcal{L}_\Phi = (D_\mu \Phi)^\dagger \, (D^\mu \Phi) - V(\Phi^\dagger \Phi) \tag{2.18}$$

and potential

$$V(\Phi^\dagger \Phi) = \mu^2 \Phi^\dagger \Phi + \lambda (\Phi^\dagger \Phi)^2, \tag{2.19}$$

where the first term can be interpreted as mass term and the second term as self-interaction of the field Φ. When assuming $\mu^2 < 0$ and $\lambda > 0$, the minimum of the potential V appears at the vacuum state Φ_{vac} with

$$|\Phi_{\mathrm{vac}}| = \sqrt{-\frac{\mu^2}{2\lambda}}, \tag{2.20}$$

which means a non-zero vacuum expectation value. This ground state breaks the $SU(2)_L$ symmetry, which is also known as spontaneous symmetry breaking.

It is now possible to expand the field Φ around its minimum state and one chooses

$$\Phi_1 = \Phi_2 = \Phi_4 = 0 \tag{2.21}$$

$$\Phi_3^2 = -\frac{\mu^2}{\lambda} \equiv v^2 \ . \tag{2.22}$$

At first order, the field Φ consists of only one field $h(x)$ which describes the shift from

the vacuum state:

$$\Phi = \frac{1}{\sqrt{2}} \begin{pmatrix} 0 \\ v + h(x) \end{pmatrix} \ . \tag{2.23}$$

When substituting the resulting field Φ into the Lagrangian $\mathcal{L} = \mathcal{L}_{\mathrm{EW}} + \mathcal{L}_{\Phi}$, one observes one mass term for the (Higgs) field $h(x)$ and mass terms for the W^a_μ which can be identified as the longitudinal polarisations of the massive vector bosons $W^\pm$ and Z. When introducing the following complex fields,

$$W^\pm_\mu = \frac{1}{\sqrt{2}} \left(W^1_\mu \mp i W^2_\mu \right), \tag{2.24}$$

the relevant mass term in the Lagrangian $\mathcal{L}$ becomes

$$\left| \left(-igT^a W^a_\mu - ig' B_\mu Y \right) \Phi \right|^2 = \left(\frac{1}{2} vg \right)^2 W^+_\mu W^{-\mu} + \tag{2.25}$$

$$\frac{1}{8} v^2 \left(W^3_\mu, B_\mu \right) \underbrace{\begin{pmatrix} g^2 & -gg' \\ -gg' & g'^2 \end{pmatrix}}_{\text{mass matrix } G} \begin{pmatrix} W^{3\mu} \\ B^\mu \end{pmatrix}, \tag{2.26}$$

where the massive fields $W^\pm_\mu$ can be interpreted as the $W^\pm$ bosons with mass $m_W = vg/2$. One notices that the mass matrix G is not diagonal, therefore B_μ and W^3_μ are not the physical fields. After diagonalisation of G one finds that the physical fields of the massless photon A_μ and the massive Z boson Z_μ are linear combinations of B_μ and W^3_μ:

$$\begin{pmatrix} A_\mu \\ Z_\mu \end{pmatrix} = \begin{pmatrix} \cos\theta_W & \sin\theta_W \\ -\sin\theta_W & \cos\theta_W \end{pmatrix} \begin{pmatrix} B_\mu \\ W^3_\mu \end{pmatrix} \ . \tag{2.27}$$

The strength of the mixing is described by the Weinberg angle θ_W, which is connected to the coupling strengths g and g' and the elementary electrical charge by:

$$e = g \sin\theta_W = g' \cos\theta_W \ . \tag{2.28}$$

The resulting Lagrangian consists now of mass terms for the massive $W^\pm$ and Z bosons and remains invariant under $SU(2)_L \otimes U(1)_Y$ transformations.
Using the relation $m_W = vg/2$ and with the measured values for the W boson mass m_W, the Weinberg angle θ_W and the electrical charge e [39], it is possible to calculate the energy of the vacuum expectation state:

$$v = \frac{2m_W}{g} = \frac{2m_W \sin\theta_W}{e} \approx 246\,\mathrm{GeV}, \tag{2.29}$$

which marks the scale at which the electroweak symmetry breaking appears.

A similar procedure can be performed in order to generate masses for the quark and lepton spinor fields. The mass generation is done by adding so-called Yukawa couplings

[40] to the Lagrangian, which couple the fermion fields to the Higgs field h. An attractive feature of the SM is that the same Higgs doublet Φ, that has been introduced for the mass generation of the $W^{\pm}$ and Z bosons (Equation (2.17)), can be used to generate fermion masses.
In case of a lepton doublet, the Yukawa coupling term for a particular lepton with flavor $\ell = e, \mu, \tau$ would look like the following:

$$\mathcal{L}_\ell = -G_\ell \left[\left(\bar{\nu}_\ell, \bar{\ell} \right)_L \begin{pmatrix} \Phi_a \\ \Phi_b \end{pmatrix} \ell_R + \bar{\ell}_R \left(\bar{\Phi}_a, \bar{\Phi}_b \right) \begin{pmatrix} \nu_\ell \\ \ell \end{pmatrix}_L \right], \tag{2.30}$$

where the Yukawa coupling constant G_ℓ has been introduced. After spontaneous symmetry breaking (SSB) the scalar Higgs doublet obtains the same structure as in Equation (2.23):

$$\Phi = \frac{1}{\sqrt{2}} \begin{pmatrix} 0 \\ v + h(x) \end{pmatrix} . \tag{2.31}$$

When substituting Φ into the Yukawa Lagrangian term in Equation (2.30)

$$\mathcal{L}_\ell = -\frac{G_\ell}{\sqrt{2}} v \left(\bar{\ell}_L \ell_R + \bar{\ell}_R \ell_L \right) - \frac{G_\ell}{\sqrt{2}} \left(\bar{\ell}_L \ell_R + \bar{\ell}_R \ell_L \right) h, \tag{2.32}$$

one observes that it has split into an interaction term, which couples the lepton to the Higgs field, and a mass term for the charged lepton with mass

$$m_\ell = \frac{G_\ell v}{\sqrt{2}} . \tag{2.33}$$

By construction the neutrino appears to be massless, as it was assumed when this theory was developed. However, if one would consider neutrino masses, one needs to extend the procedure as it is done for the quarks explained below.
In order to introduce masses for the quarks, one can follow the same procedure. In the result for the leptons, the upper member of the lepton doublet has become massless. Since the quarks are all massive, one needs to construct a new Higgs doublet for the coupling to the upper members of the quark doublets:

$$\Phi_C = \begin{pmatrix} -\bar{\Phi}_b \\ \bar{\Phi}_a \end{pmatrix}, \tag{2.34}$$

which consists of the charge conjugates of the same complex fields as in Equation (2.17) and, after SSB, translates into a similar shifted state around the vacuum expectation value:

$$\Phi_C = \frac{1}{\sqrt{2}} \begin{pmatrix} v + h(x) \\ 0 \end{pmatrix} . \tag{2.35}$$

The Yukawa term for quark generation i looks similar to that of the leptons:

$$\mathcal{L}_{iQ} = -G_{id}\left(\bar{u}_i, \bar{d}_i\right)_L \begin{pmatrix}\Phi_a \\ \Phi_b\end{pmatrix} d_R^i - G_{iu}\left(\bar{u}_i, \bar{d}_i\right)_L \begin{pmatrix}-\bar{\Phi}_b \\ \bar{\Phi}_a\end{pmatrix} u_R^i + h.c., \tag{2.36}$$

but with different Yukawa couplings for the up- and down-type quarks. Here, *h.c.* denotes the hermitian conjugate of the former terms. When substituting Φ and Φ_C into the Lagrangian after SSB, one obtains interaction and mass terms for the quark fields. The mass terms become

$$\mathcal{L}_Q = D_L^\dagger G_d D_R + D_R^\dagger G_d^\dagger D_L + U_L^\dagger G_u U_R + U_R^\dagger G_u^\dagger U_L, \tag{2.37}$$

where

$$D_{L/R} = \begin{pmatrix}d_1 \\ d_2 \\ d_3\end{pmatrix}_{L/R} \quad \text{and } U_{L/R} = \begin{pmatrix}u_1 \\ u_2 \\ u_3\end{pmatrix}_{L/R} \tag{2.38}$$

contain the left-/right-handed weak up-/down-type quark eigenstates u_i/d_i of the i-th fermion generation. $G_{u/d}$ describes the corresponding quark mass matrices, which consist of the quark masses

$$m_{ij} = \frac{G_{ij} v}{\sqrt{2}} \tag{2.39}$$

with Yukawa coupling constants G_{ij} for quark type $j = u, d$ and fermion generation i. Similar to the mass matrix G in Equation (2.25), the $G_{u/d}$ are not diagonal, which means that u_i and d_i are not the physical fields. After diagonalisation of G_u and G_d with unitary transformations, one finds that the weak eigenstates u_i and d_i are linear combinations of the (physical) mass eigenstates u, c, t and d, s, b. As a convention, the weak and mass eigenstates of the up-type quarks are set to be equal. This results in the mixing of the down-type quarks described by the following equation:

$$\begin{pmatrix}d_1 \\ d_2 \\ d_3\end{pmatrix} = V_{\text{CKM}}^{\text{3x3}} \begin{pmatrix}d \\ s \\ b\end{pmatrix}_L, \tag{2.40}$$

where

$$V_{\text{CKM}}^{\text{3x3}} = \begin{pmatrix}V_{\text{ud}} & V_{\text{us}} & V_{\text{ub}} \\ V_{\text{cd}} & V_{\text{cs}} & V_{\text{cb}} \\ V_{\text{td}} & V_{\text{ts}} & V_{\text{tb}}\end{pmatrix} \tag{2.41}$$

denotes the so-called Cabibbo-Kobayashi-Maskawa (CKM) matrix [41–43]. Due to this mixing, quark transitions in charged-current interactions are also allowed between different fermion generations. The probability of such a transition depends on the absolute

value of the corresponding CKM matrix element.

There also exists a matrix describing the neutrino mixing which is called Pontecorvo-Maki-Nakagawa-Sakata (PMNS) or Maki-Nakagawa-Sakata (MNS) matrix [44, 45] and has a similar structure.

2.1.1.2 CKM matrix

In the case of N fermion families, V_{CKM} is described by an $N \times N$ matrix. In total, the matrix consists of $2N^2$ parameters, since in general each component has a real and imaginary part. From the unitarity of the matrix, one can construct N^2 unitary conditions

$$\sum_{k=1}^{N} |V_{ik}|^2 = 1, \text{ for rows } i = 1, \ldots, N \tag{2.42}$$

$$\sum_{n=1}^{N} |V_{nj}|^2 = 1, \text{ for columns } j = 1, \ldots, N \ . \tag{2.43}$$

One is free to modify each of the $2N$ quark fields by additional phases, because these phases are not visible in physical observables and do not change the physics. Hence, one has the freedom to redefine these phases in a way, that $2N - 1$ phases vanish and one overall phase remains. The resulting number of parameters in the $N \times N$ quark mixing matrix is then:

$$2N^2 - \underbrace{N^2}_{\text{unitarity}} - \underbrace{(2N-1)}_{\text{phase redefinition}} = N^2 - 2N + 1 \tag{2.44}$$

$$= (N-1)^2 \ . \tag{2.45}$$

The values of the $(N-1)^2$ parameters can not be predicted within the Standard Model and have to be measured by experiments. In the case of three fermion families, four parameters remain in the 3×3 CKM matrix of Equation (2.41). These consist of three real parameters and one overall phase factor describing the complex part of the matrix. A possible parametrisation for the matrix with these parameters is created by introducing three Euler angles (θ_{12}, θ_{13}, θ_{23}) to describe the mixing between the three families and a phase δ. The CKM-matrix is then of the form (see Chapter 11 in reference [39]):

$$V_{CKM} = \begin{pmatrix} c_{12}c_{13} & s_{12}c_{13} & s_{13}e^{-i\delta} \\ -s_{12}c_{23} - c_{12}s_{23}s_{13}e^{i\delta} & c_{12}c_{23} - s_{12}s_{23}s_{13}e^{i\delta} & s_{23}c_{13} \\ s_{12}s_{23} - c_{12}c_{23}s_{13}e^{i\delta} & -c_{12}s_{23} - s_{12}c_{23}s_{13}e^{i\delta} & c_{23}c_{13} \end{pmatrix} \ . \tag{2.46}$$

s_{ij} and c_{ij} describe the sine and cosine of the mixing angle θ_{ij} which represents the strength of the mixing between the i-th and j-th fermion generation:

$$s_{ij} = \sin\theta_{ij} \tag{2.47}$$

$$c_{ij} = \cos\theta_{ij} \ . \tag{2.48}$$

The complexity of the CKM matrix ($\delta \neq 0$ or $\delta \neq \pi$) is a source of CP violation (see reference [46]), e.g. a non-invariance of physical states after parity and charge transformations. Above mentioned unitarity conditions can be used to draw unitarity triangles. One common relation, that can be drawn from Equation (2.42) is

$$V_{ud}V_{ub}^* + V_{cd}V_{cb}^* + V_{td}V_{tb}^* = 0 \ . \tag{2.49}$$

When dividing this equation by the well-known scalar product $V_{cd}V_{cb}^*$ one obtains the vector triangle equation represented in Figure 2.2a. The area of this triangle is a measure

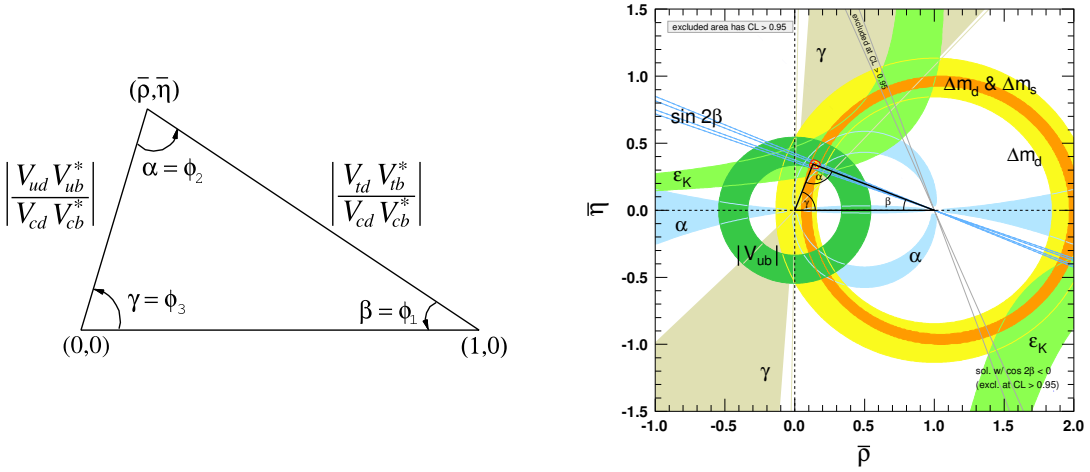

(a) Unitarity triangle

(b) Constraints in the $\bar{\rho}, \bar{\eta}$ plane

Figure 2.2: Figure (a) shows one definition of the unitarity triangle resulting from the unitarity condition in Equation (2.49) [39]. Constraints on the parameter of this triangle, resulting from a global fit to electroweak and flavor observables, are presented in (b) [39, 47].

of the CP violation and therefore its angles can be determined by measuring CP violating processes.
The definition of the upper triangle vertex, $(\bar{\rho}, \bar{\eta})$, arises from the so-called Wolfenstein parametrisation [48] of the CKM matrix, which is different from the parametrisation shown above. In this parametrisation, the CKM matrix is written in terms of the parameters

$$\lambda = s_{12} \tag{2.50}$$

$$A = \frac{s_{23}}{\lambda^2} \tag{2.51}$$

$$\rho + i\eta = \frac{s_{13}e^{i\delta}}{A\lambda^3}, \tag{2.52}$$

whereby the matrix can be written up to the third order in λ as

$$V_{CKM} = \begin{pmatrix} 1-\lambda^2/2 & \lambda & A\lambda^3(\rho - i\eta) \\ -\lambda & 1-\lambda^2/2 & A\lambda^2 \\ A\lambda^3(1-\rho-i\eta) & -A\lambda^2 & 1 \end{pmatrix} + \mathcal{O}(\lambda^4) \ . \tag{2.53}$$

Hence this parametrisation is only an expansion in few of the elements from the exact parametrisation in Equation (2.46).
The coordinates $(\bar{\rho}, \bar{\eta})$ are then given by the equation

$$\bar{\rho} + i\bar{\eta} = -\frac{V_{ud}V_{ub}^*}{V_{cd}V_{cb}^*} \ . \tag{2.54}$$

The absolute values of the matrix elements can be determined by direct measurements and a global fit to electroweak and flavor observables. Assuming the SM is valid, the most precise values result from a global fit assuming three fermion generations [39, 47]. Figure 2.2b shows the resulting constraints on the unitarity triangle in the $\bar{\rho}, \bar{\eta}$ plane, while the resulting magnitudes of the CKM matrix elements are given below [39, 47]:

$$|V_{\mathrm{CKM}}^{3\mathrm{x}3}| = \begin{pmatrix} 0.97427 \pm 0.00015 & 0.22534 \pm 0.00065 & 0.00351^{+0.00015}_{-0.00014} \\ 0.22520 \pm 0.00065 & 0.97344 \pm 0.00016 & 0.0412^{+0.0011}_{-0.0005} \\ 0.00867^{+0.00029}_{-0.00031} & 0.0404^{+0.0011}_{-0.0005} & 0.999146^{+0.000021}_{-0.000046} \end{pmatrix} \ . \tag{2.55}$$

It can be seen that the diagonal elements are close to 1, which means that the probabilities for flavor transitions within one fermion generation are significantly larger than the mixings with the other generations. As a result a transition of e.g. $t \to b$ is more probable than $t \to s$ or $t \to d$.
One also commonly says that in above case the mixing within one fermion generation is larger than the mixings with the other generations.

2.1.2 Strong interactions

The theory of strong interactions is called Quantum Chromodynamics (QCD) and bases on the gauge group $SU(3)_C$, where C denotes the colour charge. Within this theory, quarks carry a colour charge which can be either r (red), g (green) or b (blue). This colour charge can be changed in strong interactions by the emission of gluons, which carry a combination of colour and anti-colour.

The theoretical field description is very similar to $SU(2)$, therefore I will concentrate on the essential differences between these two theories.
The spinor fields ψ of a given fermion flavor are grouped into colour triplets consisting of the spinor fields belonging to the three different colour charges r, g and b:

$$\Psi = \begin{pmatrix} \psi_r \\ \psi_g \\ \psi_b \end{pmatrix} \ . \tag{2.56}$$

Similar to $SU(2)$, the Lagrangian, describing the dynamics of all quark flavors f, can be written as

$$\mathcal{L}_{\mathrm{QCD}} = \sum_f \bar{\Psi}_f \left(i\gamma^\mu D_\mu - m_f\right) \Psi_f - \frac{1}{4} G^a_{\mu\nu} G^{\mu\nu,a}, \tag{2.57}$$

where $\bar{\Psi}_f$ denotes the charge conjugate of Ψ_f and the covariant derivative is formed as

$$D_\mu = \partial_\mu + i g_s G^a_\mu T^a \ . \tag{2.58}$$

G^a_μ denotes the eight gauge fields, represented as the massless gluons, and the T^a describe the $a = 1, \ldots, 8$ generators of $SU(3)$, which are also known as Gell-Mann matrices. The field tensor $G^a_{\mu\nu}$ has the same structure as for $SU(2)$:

$$G^a_{\mu\nu} = \partial_\mu G^a_\nu - \partial_\nu G^a_\mu - g_s f^{abc} G^b_\mu G^c_\nu \ . \tag{2.59}$$

Again, the third term arises from the non-Abelian character, since

$$\left[T^a, T^b\right] = i f^{abc} T^c \ . \tag{2.60}$$

The strong coupling constant g_s is often written as $\alpha_s = g_s^2/4\pi$. However, to be precise, it is not a real constant, but rather a so-called 'running' coupling, because its strength depends on the transferred momentum Q in strong interactions: $\alpha_s = \alpha_s(Q)$. This comes from the fact that loops containing quarks or gluons can contribute in strong interactions[1]. At one-loop, the running coupling constant (after renormalisation) is given by

$$\alpha_s(Q^2) = \frac{12\pi}{(33 - 2n_f) \log\left(\frac{Q^2}{\Lambda^2}\right)} \ , \tag{2.61}$$

where n_f is the number of quark flavors contributing to the quark loops at energy scale Q. Λ is defined by

$$\Lambda^2 = \mu_r^2 \exp\left[\frac{-12\pi}{(33 - 2n_f)\, \alpha_S(\mu_r^2)}\right] \tag{2.62}$$

and constitutes the region where perturbation theory is no longer an adequate description of the observed process. Therefore, Λ is also called the 'cut-off parameter' and it lies in the range of a few hundred MeV. Here, μ_r denotes the renormalisation scale that was introduced in order to avoid divergencies at low Q^2 (for instance see reference [29] for further reading). Figure 2.3 shows the theoretical prediction and some experimental results for α_S as a function of Q. In interactions with a large momentum transfer (hard

[1] A similar 'running coupling' behaviour is also observed for the coupling constants of $SU(2)_L \otimes U(1)_Y$ due to fermion and photon loops in EW interactions. However, the behaviour of these coupling constants is not discussed here.

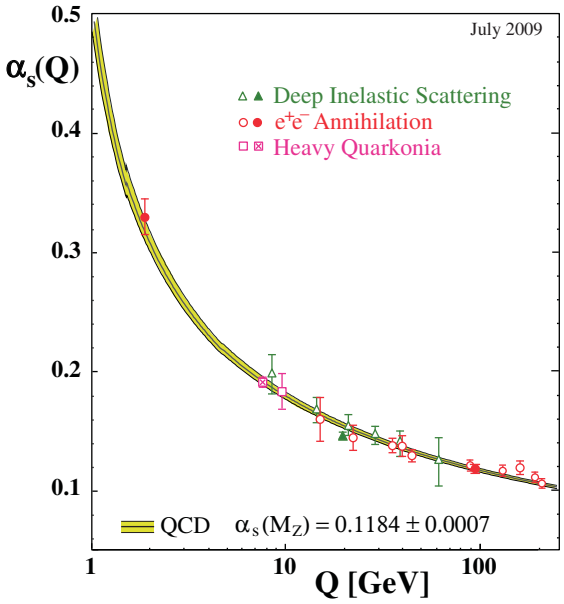

Figure 2.3: Summary of measurements of α_s as a function of the respective energy scale Q [39]. The shown band illustrates the QCD prediction based on a given scale M_Z.

processes), the coupling gets smaller and in the limit of an infinite momentum transfer α_s becomes 0: $\alpha_s(Q) \xrightarrow{Q^2 \to \infty} 0$. This behaviour is also known as asymptotic freedom. In contrast to this, the coupling becomes larger in interactions with small momentum transfer. This is known as confinement. Due to this the force between two quarks becomes stronger with increasing distance and therefore quarks can not be observed as single particles. At a specific separation distance the coupling between the two quarks 'breaks off' and a new quark anti-quark pair is produced from the vacuum. As a result, quarks produced in e.g. collisions at particle accelerators form 'particle jets' traversing the detector.

2.2 Fourth generation extension

In Equation (2.37), I introduced the mass terms of the three generation quarks:

$$\mathcal{L}_Q = D_L^\dagger G_d D_R + D_R^\dagger G_d^\dagger D_L + U_L^\dagger G_u U_R + U_R^\dagger G_u^\dagger U_L \ . \tag{2.63}$$

The choice of three generations relied on the experimentally verified fermions to date, but in general the number of fermion generations is not predicted by the SM. Therefore, a natural question is whether there can be a fourth generation of fermions. This will be addressed in the following.

In this thesis, I consider the fourth generation as a simple extension of the Standard

Model [49]. This means that the quark fields $D_{L/R}$ and $U_{L/R}$ in above Lagrangian are simply extended by two additional weak eigenstates d_4 and u_4:

$$D_{L/R} = \begin{pmatrix} d_1 \\ d_2 \\ d_3 \\ d_4 \end{pmatrix}_{L/R} \quad \text{and } U_{L/R} = \begin{pmatrix} u_1 \\ u_2 \\ u_3 \\ u_4 \end{pmatrix}_{L/R} \quad . \tag{2.64}$$

The same needs to be also done in the leptonic sector: ν_4 and ℓ_4. In the following, the mass eigenstates of the fourth generation fermions will be denoted as t' (up-type quark), b' (down-type quark), ν' (neutrino) and ℓ' (charged lepton). These new fermions adopt the quantum numbers of the other three generations. Table 2.2 shows the fermions and their electroweak quantum numbers in the context of a four generation Standard Model (SM4). The fourth generation quarks have not been experimentally verified so far, hence

Fields				Y	I	I_3	Q
$\begin{pmatrix} u \\ d \end{pmatrix}_L$	$\begin{pmatrix} c \\ s \end{pmatrix}_L$	$\begin{pmatrix} t \\ b \end{pmatrix}_L$	$\begin{pmatrix} t' \\ b' \end{pmatrix}_L$	$1/3$	$1/2$	$+1/2$ $-1/2$	$+2/3$ $-1/3$
u_R	c_R	t_R	t'_R	$+4/3$	0	0	$+2/3$
d_R	s_R	b_R	b'_R	$-2/3$	0	0	$-1/3$
$\begin{pmatrix} \nu_e \\ e \end{pmatrix}_L$	$\begin{pmatrix} \nu_\mu \\ \mu \end{pmatrix}_L$	$\begin{pmatrix} \nu_\tau \\ \tau \end{pmatrix}_L$	$\begin{pmatrix} \nu' \\ \ell' \end{pmatrix}_L$	-1	$1/2$	$+1/2$ $-1/2$	0 -1
ν_R^e	ν_R^μ	ν_R^τ	ν'_R	0	0	0	0
e_R	μ_R	τ_R	ℓ'_R	-2	0	0	-1

Table 2.2: The electroweak quantum numbers of the fermions in the four generations Standard Model. For each fermion, the hypercharge Y, weak isospin I, its third component I_3, and the electrical charge Q are presented. It can be seen, that weak isospin doublets carry $I = 1/2$, while isospin singlets have $I = 0$.

it is assumed that these particles need to be quite heavy ($m_{q'} \gtrsim m_t$, further constraints will be discussed in the following). This results in strong Yukawa couplings for the fourth generation quarks:

$$m_{ij} = \frac{G_{ij} v}{\sqrt{2}} \ . \tag{2.65}$$

Since the quarks b' and t' also participate in the mixing of the weak eigenstates, the CKM matrix needs to be extended to a 4×4 matrix:

$$V_{CKM}^{4x4} = \begin{pmatrix} V_{ud} & V_{us} & V_{ub} & V_{ub'} \\ V_{cd} & V_{cs} & V_{cb} & V_{cb'} \\ V_{td} & V_{ts} & V_{tb} & V_{tb'} \\ V_{t'd} & V_{t's} & V_{t'b} & V_{t'b'} \end{pmatrix} \ . \tag{2.66}$$

As discussed in Section 2.1.1.2, such a CKM matrix is described by $(4-1)^2 = 9$ parameters, including six real mixing angles $\Theta_{12}, \Theta_{13}, \Theta_{23}, \Theta_{14}, \Theta_{24}, \Theta_{34}$ (denoting the mixings between the four generations) and three phases $\delta_1, \delta_2, \delta_3$. In this parametrisation, the 4×4 CKM matrix can be constructed by extending the 3×3 CKM matrix and multiplying by three matrices accounting for the additional mixings:

$$V_{CKM}^{4x4} = \begin{pmatrix} & & & 0 \\ & V_{CKM}^{3x3} & & 0 \\ & & & 0 \\ 0 & 0 & 0 & 1 \end{pmatrix} \times \begin{pmatrix} 1 & 0 & 0 & 0 \\ 0 & 1 & 0 & 0 \\ 0 & 0 & c_{34} & s_{34} \\ 0 & 0 & -s_{34} & c_{34} \end{pmatrix} \times$$
$$\times \begin{pmatrix} 1 & 0 & 0 & 0 \\ 0 & c_{24} & 0 & s_{24}e^{-i\delta_2} \\ 0 & 0 & 1 & 0 \\ 0 & -s_{24}e^{i\delta_2} & 0 & c_{24} \end{pmatrix} \times \begin{pmatrix} c_{14} & 0 & 0 & s_{14}e^{-i\delta_3} \\ 0 & 1 & 0 & 0 \\ 0 & 0 & 1 & 0 \\ -s_{14}e^{i\delta_3} & 0 & 0 & c_{14} \end{pmatrix} . \quad (2.67)$$

In the following I will address several aspects of a fourth generation of fermions: implications on the SM and theories that go beyond, constraints on masses and mixing angles, and also implications of the recent discovery of a Higgs-like boson at the LHC. Finally, I will discuss the production and decay of fourth generation quarks at hadron colliders.

2.2.1 Impact of a fourth generation on the Standard Model and beyond

As mentioned before, the fourth generation quarks are assumed to be quite heavy, which results in strong Yukawa couplings. Obviously a fourth generation must have effects on the electroweak symmetry breaking (EWSB) sector.
In reference [50] a possible effect of fourth generation quarks q' on the EWSB is discussed. Due to a new strong interaction, these quarks could form condensates $\langle \bar{q}' q' \rangle$ which take the place of the scalar (Higgs) field and are responsible for a dynamical EWSB. This is similar to Technicolor theories as discussed in e.g. reference [21]. In low-scale Technicolor theories ($m_{q'} \lesssim 2\,\text{TeV}$) additional fermions are required [22] and a sequential fourth generation is an interesting candidate. A phenomenological description is given by the Nambu-Jona-Lasinio model (see e.g. reference [51, 52]), where the new dynamics are described by a 4-fermion interaction

$$\frac{g^2}{\Lambda^2} \left(\bar{q'}_L q'_R \right) \left(\bar{q'}_R q'_L \right) . \quad (2.68)$$

Λ represents a cutoff parameter which marks a softening of this interaction, and g has to be above a critical value g_c that marks the scale above which the condensation occurs. The EWSB scale v is then given by the Pagels-Stokar formula [53] at one-loop approximation:

$$v^2 = (246\,\text{GeV})^2 \approx \frac{3m_{q'}^2}{4\pi^2} \ln \frac{\Lambda^2}{m_{q'}^2} \quad (2.69)$$

Hence, a heavy quark with $m_{q'} \approx 750\,\text{GeV}$ and $\Lambda \approx 2 \times m_{q'}$ would result in a suitable v from this theory.

Another interesting effect due to a fourth generation could appear in grand unification theories (GUTs). These describe the unification of the electromagnetic (α), weak (α_w) and strong (α_s) couplings at a specific scale. The minimal model is described by an $SU(5)$ symmetry group [54], which involves a single coupling strength representing one fundamental interaction. All known forces are supposed to be different manifestations of this single interaction.
Such unification can not be generated with the ingredients of the SM, but there exist several models beyond the SM which contain the necessary ingredients (for instance supersymmetric models, but these introduce a large number of additional parameters to the SM).

One model that affects the gauge couplings evolution is the fourth generation of fermions. Its effect on the GUT is discussed in reference [55] and will be briefly presented in the following.
Previously, I discussed that α_s is a running coupling constant, meaning that its strength depends on the energy scale. The same applies to the electromagnetic and weak couplings[2]. Measurements of the coupling-strengths dependence on the energy scale indicate that the couplings do not converge at some point, if they evolve according to the three generation Standard Model. A calculation of the evolution of the gauge couplings with increasing energy scale in the three generation SM is shown in Figure 2.4a. Here, the α_i are connected to the gauge couplings g_i of the $SU(3) \times SU(2) \times U(1)$ gauge group by $\alpha_1 = \frac{5}{3}\frac{g'^2}{4\pi}$, $\alpha_2 = \frac{g^2}{4\pi}$ and $\alpha_3 = \frac{g_s^2}{4\pi}$. As can be seen the couplings do not converge at some point. In the calculation of the gauge couplings, the Yukawa couplings enter in the

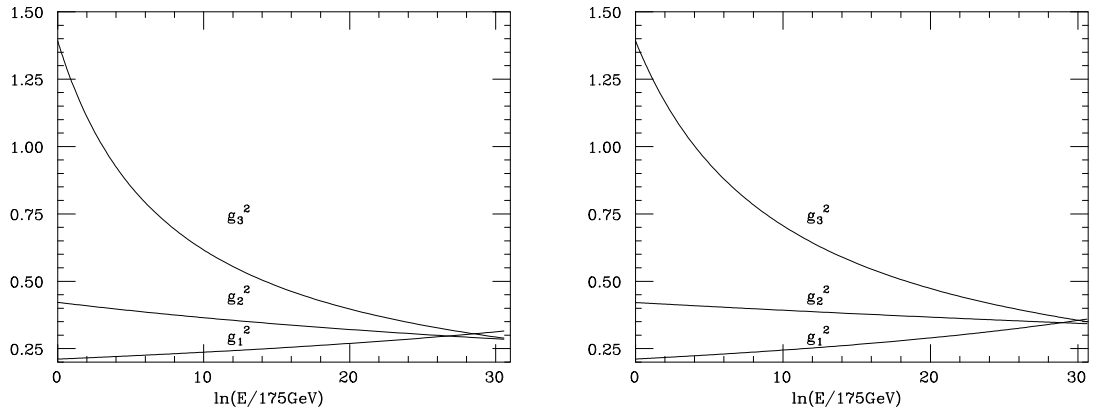

(a) Evolution of gauge couplings in the SM

(b) Evolution of gauge couplings in the SM4

Figure 2.4: Evolution of the three gauge couplings resulting from calculations for the SM assuming three (a) and four (b) generations of fermions [55].

[2]Note that their scale dependence is similar due to the connection via the Weinberg angle, but different to the one in α_s due to the different coupling behaviour of gluons and W, Z, γ.

two-loop β-functions (see e.g. reference [56]). Due to the strong Yukawa couplings of the fourth generation quarks, these would have a significant effect to the gauge couplings evolution. The analysers in reference [55] have calculated the contribution of the fourth generation, assuming the following masses:

- b' and t' quark: $m_{b'} = m_{t'} = 151\,\text{GeV}$,
- ℓ' and ν' lepton: $m_{\ell'} = m_{\nu'} = 95.3\,\text{GeV}$,
- t quark: $m_t = 175\,\text{GeV}$ and
- Higgs boson: $m_H = 188\,\text{GeV}$.

The resulting gauge coupling evolution is presented in Figure 2.4b. The curves nearly converge with a difference below 4%, which is a good indication for a possible unification due to the fourth generation. In reference [55] it is discussed that further changes on the parameters of the gauge couplings allow a unification within the SM4 at a scale of about 10^{15}GeV. However, one should note that the fourth generation particle masses assumed in this study have been already excluded in the latest direct search results, which will be presented in Section 2.2.3.1. There was no updated study with higher masses, but in reference [57] it is stated that a heavy fourth generation of fermions, if generating the dynamical EWSB as discussed before, could also allow for a possible unification of the gauge couplings.

One of the still unsolved problems in the Standard Model is the origin of the matter-antimatter asymmetry, also called baryon asymmetry of the universe (BAU). At the big bang it is assumed that matter and antimatter were created equally, but to date the world only consists of matter, whereas antimatter does not appear naturally. This is a very fundamental problem, because one would expect that the equally created matter and antimatter would have completely annihilated into photons. These photons are expected to be the source of the cosmic microwave background radiation. The group of the Wilkinson Microwave Anisotropy Probe (WMAP) [58] has measured the baryon-to-photon ratio to be

$$\frac{n_{\mathcal{B}}}{n_\gamma} = (5.1^{+0.3}_{-0.2}) \times 10^{-10}, \tag{2.70}$$

which means that for every baryon in the universe there are 2×10^9 photons in the cosmic microwave background.
There are three conditions, written down by Sakharov in 1967 [20], that are required to dynamically generate the BAU:

1. violation of baryon numbers,
2. C and CP violation and
3. a deviation from thermal equilibrium.

In reference [59] it is shown that the SM is able to satisfy the first and the third Sakharov conditions (in the case of a low Higgs boson mass of about 70 GeV), hence I will focus on the second one: the CP violation.
In general, CP violation exists when there are phases in the couplings of a Lagrangian, which can not be removed by field redefinitions, and which therefore cause a non-invariance of the Lagrangian under CP transformations (see reference [59]). One source of such phases is the CKM matrix introduced in Section 2.1.1.2, which contains (in the case of three fermion generations) one unique weak phase. One measure of the CP violation arising from the CKM matrix is the Jarlskog invariant [60]

$$J = \Im \det \left[M_u M_u^\dagger, M_d M_d^\dagger \right] \tag{2.71}$$

$$= (m_t^2 - m_u^2)(m_t^2 - m_c^2)(m_c^2 - m_u^2)(m_b^2 - m_d^2)(m_b^2 - m_s^2)(m_s^2 - m_d^2) \cdot A, \tag{2.72}$$

where $M_{u/d}$ denote the quark mass matrices, m_i are the masses of the quarks and A is twice the area of the unitarity triangle constructed from the unitarity condition in Equation (2.49). One clearly sees that in the case where the unitarity triangle has zero area or there are degenerate quark pairs, J vanishes and there is no CP violation coming from the CKM matrix. When normalising J to the electroweak phase transition temperature (see reference [61]) $T_{\mathrm{EW}} \sim 100\,\mathrm{GeV}$ and using the measured value of $A \simeq 3.1 \cdot 10^{-5}$ [39], one obtains (for a measure of CP violation) a value of

$$\frac{J}{T_{\mathrm{EW}}^{12}} \sim 10^{-20} \tag{2.73}$$

which is by ten orders of magnitude smaller than the measured value from WMAP.
In the fourth generation case the CKM matrix is extended to having three weak phases. The resulting impact to the CP violation is discussed in reference [62, 63]. There are two effects on the Jarlskog invariant: the unitarity triangle becomes a quadrangle with sizeable area, and the additional heavy quark masses appear in the mass matrices. Assuming fourth generation quark masses in the range of $m_{q'} \sim 300 - 600$ GeV, one obtains an increase of the measure of the CP violation J/T_{EW}^{12} of about $10^{13} - 10^{15}$ and hence a fourth generation of fermions could produce the required CP violation for the BAU.

As mentioned in the beginning of this thesis, one shortcoming of the SM is the explanation of the existence of dark matter. The neutrinos in the three generation SM do not have sufficient mass in order to be a possible candidate. However, in references [64–66] it is shown that a heavy ($m_{\nu'} \gtrsim 200\,\mathrm{GeV}$), stable fourth generation neutrino could contribute to a small fraction of the relic density of dark matter, but does not provide a full explanation.

Other interesting effects of a fourth generation can be observed in flavor physics, especially in meson mixing and CP violating meson decays.
Meson mixing can be described by box diagrams, like those shown in Figure 2.5 for $B_{s/d}$ mixing. As can be seen a fourth generation with heavy fermions would have significant contributions to the inner loop and therefore influence the corresponding amplitudes.
Meson decays with flavor changing neutral currents (FCNC) contain contributions from

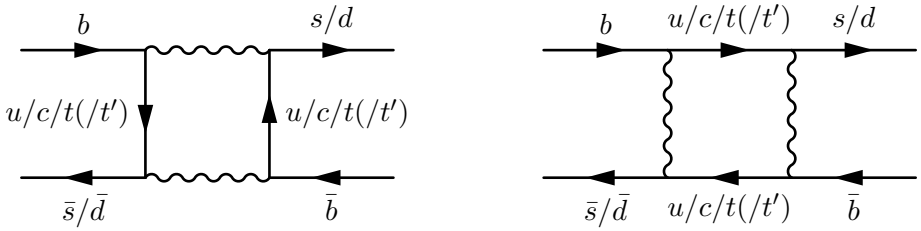

Figure 2.5: Box diagrams representing the mixing of a B_d or B_s meson. It can be seen that a fourth generation t' quark would contribute to such diagrams and therefore would influence the corresponding amplitudes.

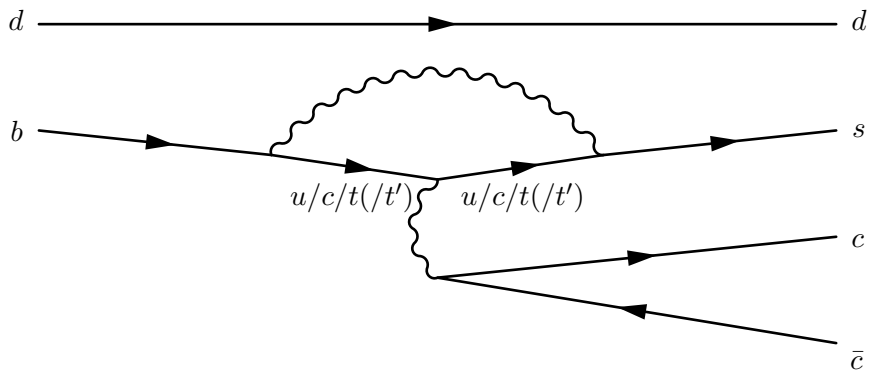

Figure 2.6: $B_d \to J/\Psi K_s$ decay containing a penguin diagram. A fourth generation t' quark would give additional contributions to this flavor changing neutral current.

penguin diagrams as shown in Figure 2.6 for the $B_d \to J/\Psi K_s$ decay. Here too, a fourth generation quark would contribute to the inner loop due to the heavy masses of the new particles. However, the effect is expected to be small [67].
There are several meson processes that would be affected by the existence of a fourth generation. A detailed description is beyond the scope of this thesis, but can be looked up in the references [67–73]. I only want to mention that in reference [74] it is shown that a fourth generation of fermions could explain the CP violation in $D^0 \to h^+h^-$ ($h = \pi, K$) decays observed at the LHCb experiment [75, 76].

2.2.2 Constraints from electroweak data and flavor observables on the parameters of a fourth generation

The parameters of a fourth generation of fermions (such as the masses and mixing angles) can be constrained by measurements of electroweak observables, e.g. the Z boson mass or decay width. These observables have been precisely measured in reference [77] at LEP [78], an electron-positron collider with the capability of operating with a centre-of-mass energy at the Z resonance.
A common parametrisation of the electroweak precision observables (EWPOs) is the STU formalism, also called the Peskin-Takeuchi parameters [79, 80]. In this formalism the parameters S, T and U denote parametrisations of vacuum polarisation functions, which are mainly made up of the self-energy diagrams of the photon, Z boson and W boson. Contributions from new physics result in shifts of these parameters, if one assumes that the scale of the new physics is well above the EW scale. With fits to the experimentally measured EWPOs and their uncertainties it is possible to derive allowed regions in the STU parameter space, which constrain such new physics. This is demonstrated in Figure 2.7, where the 95% confidence level (C.L.) ellipses are drawn in the ST space at several fixed U values. The reference point $(S, T, U) = (0, 0, 0)$ is plotted

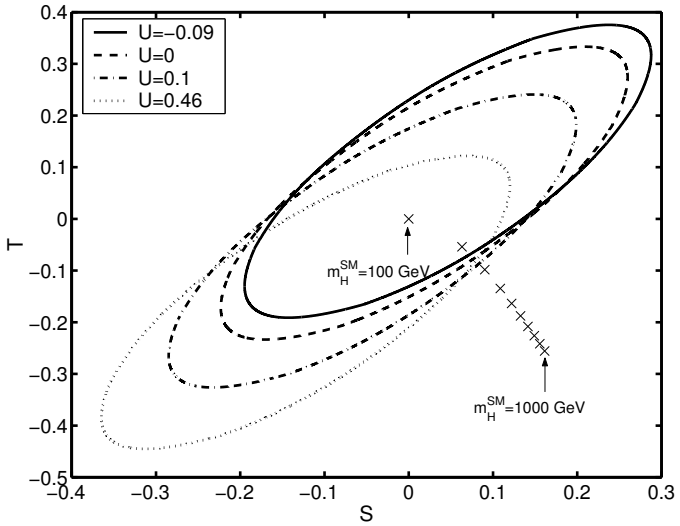

Figure 2.7: The 95% C.L. contours for S and T for fixed values of U at a reference point with $m_H = 100\,\text{GeV}$ [81]. The 'x' symbols depict the shifts in S and T due to higher Higgs masses in the range $m_H \in [100, 1000]$ GeV.

for a chosen Higgs mass of $m_H = 100\,\text{GeV}$ whilst the '$\times$' symbols depict the shift in S and T due to increased Higgs masses.
The addition of a fourth generation of fermions (quarks and leptons) would result in

shifts of S and T as shown below [81, 82]:

$$\Delta S = \frac{N_c}{6\pi}\left(1 - 2Y\left[\ln\frac{m_{u'}^2}{m_{d'}^2}\right]\right) \tag{2.74}$$

$$\Delta T = \frac{N_c}{12\pi s_W^2 c_W^2}\left[\left(\frac{m_{u'}^2 - m_{d'}^2}{m_Z}\right)^2\right], \tag{2.75}$$

where N_C denotes the colour factor, Y is the weak hypercharge, m_Z the Z boson mass and s_W and c_W represent the sine and cosine of the Weinberg angle. $m_{u'}$ and $m_{d'}$ denote the masses of the upper (u) and lower (d) fourth generation fermion in the weak isospin doublets (t' and b' or ν' and ℓ'). It can be seen that the shift in the S parameter depends logarithmically on the mass ratios, whereas T is shifted by the size of the mass splittings. The U parameter is typically very small ($\lesssim 0.02$) in many calculations and is therefore usually neglected [82].
It should be noted that above equations only hold if one neglects the mixing due to the CKM matrix. Allowing this mixing would result in more complex formulae ΔS and ΔT.

By scanning over the fourth generation mass range it is possible to check which mass combinations result in shifts that still lie within the ST ellipses and are therefore allowed by the EWPOs given a specific confidence level (C.L.). This has been performed in reference [82] (when neglecting the CKM mixing) and the result is presented in Figure 2.8. The reference point $(S, T) = (0, 0)$ is defined with $m_H = 115\,\text{GeV}$ and $m_t = 170.9\,\text{GeV}$. The red curve depicts the shifts due to higher Higgs masses, whilst the blue lines represent the shifts due to the addition of fourth generation fermions for selected parameter sets (Table 2.3). It can be seen that the total shifts in S and T for these parameter sets lie

Parameter set	$m_{t'}$ [GeV]	$m_{b'}$ [GeV]	m_H [GeV]	ΔS	ΔT
(a)	310	260	115	0.15	0.19
(b)	320	260	200	0.19	0.20
(f)	400	325	300	0.21	0.25

Table 2.3: Parameter sets demonstrating allowed shifts in the ST plane (Figure 2.8) [82]. The lepton masses are fixed to $m_{\nu'} = 100\,\text{GeV}$ and $m_{\ell'} = 115\,\text{GeV}$. All shifts lie within the 68% C.L. ellipse.

within the 68% C.L. ellipse and are therefore compatible with the electroweak precision data. Additionally, it should be mentioned that the fourth generation compensates for the shifts due to higher Higgs masses and hence would allow for a higher Higgs mass than in the three generation SM.
In summary, the analysers in reference [82] have derived mass differences which are in agreement with all experimental constraints and are favoured by the electroweak

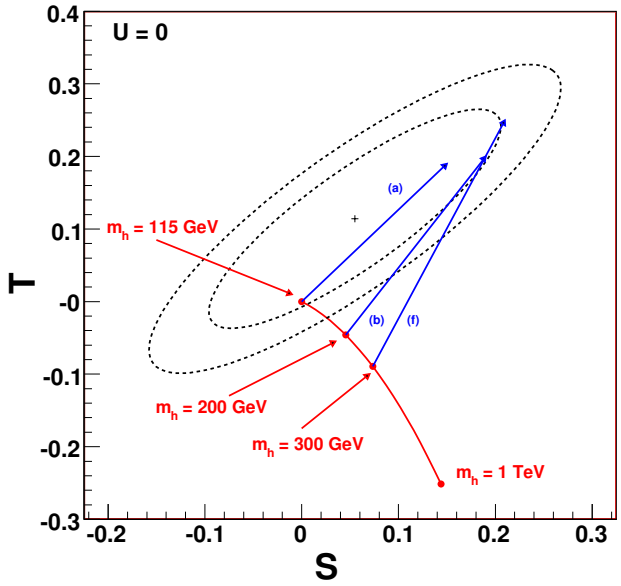

Figure 2.8: The 95% and 68% C.L. constraints on the S and T parameters [82, 83]. The reference point $(S, T) = (0, 0)$ is defined with $m_H = 115\,\text{GeV}$ and $m_t = 170.9\,\text{GeV}$. The red curve depicts the shifts due to higher Higgs masses, whereas the blue curves represent the shifts due to the fourth generation fermions for selected parameter sets (when neglecting the CKM mixing). The selected parameter sets represent mass combinations of the fourth generation particles which are compatible with the electroweak precision data and are summarised in Table 2.3.

observables:

$$m_{t'} - m_{b'} \simeq \left(1 + \frac{1}{5} \ln \frac{m_H}{115\,\text{GeV}}\right) \times 50\,\text{GeV} \tag{2.76}$$

$$m_{\ell'} - m_{\nu'} \simeq 30 - 60\text{GeV}\ . \tag{2.77}$$

This means that the EWPOs favour the scenarios $m_{t'} > m_{b'}$ and $m_{\ell'} > m_{\nu'}$. Assuming a Higgs mass of $m_H \approx 125\,\text{GeV}$ this would give an allowed mass difference for the fourth generation quarks of $m_{t'} - m_{b'} \lesssim 50\,\text{GeV}$.
However, when including the CKM mixing one finds slightly different results, which will be discussed at the end of this section.

The EWPOs can also be used to constrain the mixing angle Θ_{34} between the third and fourth fermion generation. In the results presented above the CKM parameters have been neglected, although the shifts in S and T also depend on the mixing angles Θ_{ij}. In references [84, 85] the analyser has performed a χ^2 fit to the EWPOs by considering the S and T shifts due to a fourth generation when also including the CKM mixing between the

third and fourth generation. The mass differences are assumed to be $m_{t'} - m_{b'} = 16\,\text{GeV}$, $m_{\ell'} - m_{\nu'} = 91\,\text{GeV}$ and the neutrino mass is set to $m_{\nu'} = 101\,\text{GeV}$. These assumptions are motivated by the best-fit results obtained in reference [86], where a similar χ^2 fit was performed, but when neglecting the CKM mixing. When considering the CKM mixing, in references [84, 85] it was found that the best-fit value is obtained for $\Theta_{34} = 0$, but a mixing of the size $\Theta_{34} \lesssim 0.17$ is allowed with 95% C.L. assuming a heavy quark mass at the order of $m_{q'} \approx 500\,\text{GeV}$.

Further studies on the mixing angles have been performed by additionally considering constraints from measured flavor observables, specifically including the mixings within the D, K and B meson systems and the flavor changing neutral current (FCNC) decay $b \to s\gamma$ (see references [69, 71–73, 87]). The expected changes in these flavor observables due to the fourth generation have been calculated and a scan through the parameter space was performed for several sets of fourth generation fermion masses. In summary, it is found that small mixings between the fourth and the other three generations are allowed, but no direct constraints on the mixing angles and CKM matrix elements could be derived.

Another approach to constrain the CKM matrix elements is to perform a global fit to electroweak and flavor observables and from this to derive possible values of the 4x4 CKM matrix elements that fulfil all constraints. This also allows to test new physics models with scales, which are not well above the EW scale, as it is required when using the STU formalism. Such an analysis was presented in reference [88] where the global fit was performed using the `CKMfitter` package [47]. The analyser considered the experimental constraints coming from the directly measured CKM matrix elements, electroweak observables formalised using the STU parameters and several flavor observables (e.g. $B_s \to \mu^+\mu^-$ and $b \to s\gamma$ decays). The obtained central values and the corresponding 1σ standard deviations are given below:

$$|V_{CKM}^{4x4}| = \begin{pmatrix} 0.97378^{+0.00026}_{-0.00023} & 0.22349^{+0.00099}_{-0.00100} & (4.3788^{+0.0890}_{-0.2860}) \cdot 10^{-3} & 0.0318^{+0.0080}_{-0.0072} \\ 0.2232^{+0.0010}_{-0.0024} & 0.973115^{+0.000770}_{-0.002001} & 0.04028^{+0.00148}_{-0.00038} & 0.029^{+0.035}_{-0.029} \\ 0.01159^{+0.00096}_{-0.00158} & 0.0421^{+0.0034}_{-0.0019} & 0.9921^{+0.0047}_{-0.0040} & 0.0898^{+0.0377}_{-0.0407} \\ 0.0264^{+0.0127}_{-0.0117} & 0.062^{+0.033}_{-0.041} & 0.092^{+0.037}_{-0.041} & 0.9876^{+0.0058}_{-0.0019} \end{pmatrix} . \tag{2.78}$$

One should note that these values only represent the mean and standard deviations of the obtained numbers, that laid within the allowed regions. Hence, the given ranges should not be misinterpreted as confidence levels, but rather give an idea of which values are preferred by the fit. Although there is a strong preference for a large mixing within the fourth generation, mixings with the other three generations are not excluded and

the preference follows the order:

$$|V_{t'b'}| \gg |V_{t'b}|, |V_{tb'}| > |V_{cb'}|, |V_{t's}| \sim |V_{ub'}|, |V_{t'd}| \ . \tag{2.79}$$

The same global fit also allows to constrain the allowed mass difference between the two fourth generation quarks. This has been performed for the scenarios when assuming no CKM mixing and when including the mixing. The results have been presented in reference [88] and are shown in Figure 2.9. Both plots depict the resulting p-values of the

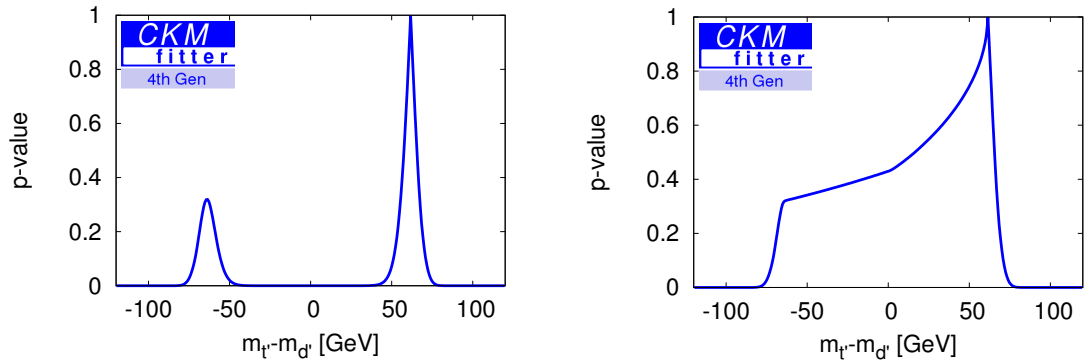

(a) Without CKM mixing

(b) With CKM mixing

Figure 2.9: Fourth generation quarks mass difference resulting from a global fit to EW precision observables [88]. The fourth generation b' quark is denoted as d' here.
Figure (a) presents the p-values resulting from the fit when neglecting the quark mixing due to the CKM matrix. The same is shown in (b) when including the CKM mixing and one can see that there is a small preference for a heavier t' quark.

fit as a function of the mass difference. A large p-value would give hint for a preference of the assumed mass difference.
Without the CKM mixing (Figure 2.9a) one notices a preference for $m_{t'} > m_{b'}$ with a mass difference of about $m_{t'} - m_{b'} \gtrsim 50\,\text{GeV}$, as it was also shown in the beginning of this section using the simple parameter scan in reference [82]. When including the CKM mixing (Figure 2.9b), the preference for a heavier t' quark persists, but all mass differences in the range $\simeq [+80, -80]$ GeV would be allowed by the global fit.
The preference of a heavier t' quark can be seen from the shift in the S parameter in Equation (2.74), which logarithmically depends on the ratio of the masses of t' and b'. For a heavier t' quark the shift becomes negative, which can be compensated by a higher Higgs mass. If the b' is heavier, the shift is positive and the (S, T) point moves out of the ellipse.

2.2.3 Direct constraints on the masses of fourth generation fermions

One well-known measurement affecting the fourth generation has been performed at the LEP experiment [77], where electrons and positrons have been collided with centre-of-mass energies ($\sqrt{s}$) near to the Z boson mass. In general the cross section for the fermion-antifermion $f\bar{f}$ production via $e^+e^- \to Z \to f\bar{f}$, depending on the centre-of-mass energy, is given by [77]

$$\sigma_{f\bar{f}}(s) = \sigma_{f\bar{f}}^{\text{peak}} \frac{s\Gamma_Z^2}{(s-m_Z)^2 + \frac{s^2\Gamma_Z^2}{m_Z^2}}, \tag{2.80}$$

where Γ_Z denotes the total decay width of the Z boson and m_Z is the Z boson mass. $\sigma_{f\bar{f}}^{\text{peak}}$ represents the peak cross-section at $\sqrt{s} = m_Z$:

$$\sigma_{f\bar{f}}^{\text{peak}} = \frac{12\pi}{m_Z^2} \frac{\Gamma_{ee}\Gamma_{f\bar{f}}}{\Gamma_Z^2} \tag{2.81}$$

and depends on the partial Z decay widths Γ_{ee} and $\Gamma_{f\bar{f}}$ for the initial and final state, respectively. The total decay width can be split into the partial widths for decays into e^+e^-, $\mu^+\mu^-$, $\tau^+\tau^-$, hadrons and invisible neutrinos:

$$\Gamma_Z = \Gamma_{ee} + \Gamma_{\mu\mu} + \Gamma_{\tau\tau} + \Gamma_{\text{had}} + \Gamma_{\text{inv}}, \tag{2.82}$$

where the invisible decay width can be written as the product of the number of light neutrino families N_ν and the partial decay width into $\nu\nu$ final states: $\Gamma_{\text{inv}} = N_\nu \cdot \Gamma_{\nu\nu}$. With these ingredients it can be clearly seen that the cross section for any final state depends on the number of light neutrino families. A measurement of the hadronic production cross section as a function of $E_{\text{cm}} = \sqrt{s}$ is presented in Figure 2.10. The curves indicate the predicted cross-section for two, three and four light neutrino families. The result shows that the measured data points are compatible with the scenario of $N_\nu = 3$. However, this result does not exclude a fourth generation neutrino, but rather sets a lower limit on its mass of $m_{\nu'} > m_Z/2$, because higher neutrino masses were not accessible at centre-of-mass energies near to the Z boson mass.

An upper limit on the masses can be obtained by requiring that the fourth generation Standard Model remains unitary. There are several studies (see e.g. references [89–91]) that have shown that the Yukawa interactions become non-perturbative at masses of about $m_{q'} \sim 500\,\text{GeV}$. However, this limit should not be viewed too strictly, as these estimates are mostly based on tree level expressions. In reference [92] the strong Yukawa couplings have been simulated successfully on the lattice with a fourth generation t' quark of mass $m_{t'} \approx 700\,\text{GeV}$.

2.2.3.1 Direct searches

Searches for fourth generation fermions have been performed at ATLAS and other experiments. The most stringent mass limits resulting from these searches are summarised

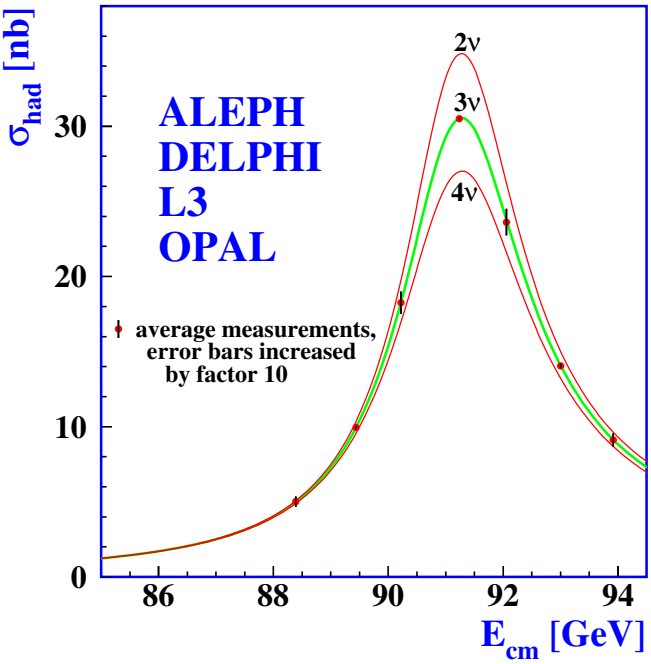

Figure 2.10: Measurements of the hadronic production cross-section around the Z resonance, performed at LEP [77]. The curves indicate the theoretical Standard Model description for the cases of two, three and four light neutrino families.

in the following.

In the ATLAS analysis [93] $t'\bar{t}'$ production with the decay hypothesis $t' \to qW$ was searched for, where q denotes any light quark u, d, c, s, b. In the dataset taken from pp collisions at $\sqrt{s} = 7\,\text{TeV}$, which corresponds to an integrated luminosity of $\mathcal{L} = 1.04\,\text{fb}^{-1}$, events with two leptons of opposite charge, a large missing transverse momentum[3] E_T^{miss} and at least two jets have been selected. A mass reconstruction has been performed on the selected events in order to distinguish signal and background events. No excess has been observed and therefore masses below $m_{t'} < 350\,\text{GeV}$ have been excluded at 95% C.L.

Another ATLAS search with the same dataset has been performed in reference [94], looking for $t'\bar{t}'$ production decaying with an assumed 100% branching fraction (BF) into $t' \to bW$. Events with single leptons (electron or muon) having high transverse momentum, high E_T^{miss} and at least three jets have been selected. The observed data events were compatible with the background prediction and hence a lower mass limit of $m_{t'} \geq 404\,\text{GeV}$ has been set.

A similar search has been done in the CMS analysis [95]. In the dataset taken at $\sqrt{s} = 7\,\text{TeV}$ and corresponding to $\mathcal{L} = 5.0\,\text{fb}^{-1}$, $t' \to bW$ processes were searched for in events with two leptons, high E_T^{miss} and two b-jets. No evidence of $t'\bar{t}'$ production has

[3]The E_T^{miss} represents the momentum imbalance in the event and is also commonly referred to as missing transverse energy.

been found and a mass limit of $m_{t'} \geq 557\,\text{GeV}$ was presented.

An ATLAS analysis searching for $b'\bar{b}'$ production is given in reference [96], where a dataset corresponding to $\mathcal{L} = 1.04\,\text{fb}^{-1}$ taken at $\sqrt{s} = 7\,\text{TeV}$ has been analysed. This analysis assumed the decay $b' \to tW$ with 100% BF and selected events with one lepton, large E_T^{miss} and at least six jets. W bosons with high transverse momentum were identified by the invariant mass of nearby jets. No excess was observed and masses below $m_{b'} < 480\,\text{GeV}$ were excluded.

The same $b'\bar{b}'$ production and decay topology $b' \to tW$ has been used in the CMS analysis [97]. In a dataset of $\mathcal{L} = 4.9\,\text{fb}^{-1}$ taken at $\sqrt{s} = 7\,\text{TeV}$, events with two same-sign charged or three leptons and at least one b-jet were looked for. The observed events are compatible with the Standard Model background prediction and a lower mass limit of $m_{b'} \geq 611\,\text{GeV}$ was set.

In the ATLAS analysis [98] (which was the predecessor of the analysis results presented in this thesis) the same final state of two same-sign leptons was used. Additional requirements were a high E_T^{miss}, at least two jets, at least one b-jet and a large overall transverse momentum. A dataset taken at $\sqrt{s} = 7\,\text{TeV}$ corresponding to $\mathcal{L} = 4.7\,\text{fb}^{-1}$ was used. There was no evidence of $b'\bar{b}'$ production and hence a lower mass limit of $m_{b'} \geq 670\,\text{GeV}$ was set.

All above analyses assumed 100% branching fraction for the decays. A more model independent approach was followed in the CMS analysis [99]. Here, it was searched for $t'b$, $t'\bar{t}'$, $b't$, $b't'$ and $b'\bar{b}'$ production in a dataset corresponding to $\mathcal{L} = 5.0\,\text{fb}^{-1}$ taken at $\sqrt{s} = 7\,\text{TeV}$. The fourth generation quarks b' and t' were assumed to have degenerate masses ($m_{b'} = m_{t'} = m_{q'}$) and only decays $b' \to tW$ and $t' \to bW$ were allowed with variable branching fractions. Depending on the production channel, different final states were selected, consisting of single lepton, same-sign dilepton and trilepton events. No deviation from the background expectation was observed and limits on the fourth generation quark mass $m_{q'}$ were derived as a function of the mixing between the fourth and third generation. Assuming a minimal mixing, masses below $m_{q'} < 685\,\text{GeV}$ were excluded.

A summary of all mentioned fourth generation quarks mass limits is given in Table 2.4. One should note that all these analyses have assumed short-lived particles and 100% branching fractions (besides the CMS analysis with model independent approach) for the considered decay channels. If these decays have smaller branching fractions, this would result in smaller rates of these processes and hence relaxed mass limits. Moreover it is possible that the particles have traversed the detector and escaped the detection if they have long lifetimes (see e.g. reference [100]).

Searches for the heavy leptons of a fourth generation have been performed by the L3 experiment [101] at LEP.
In the search for the heavy charged lepton ℓ' [102] it was distinguished between the pair-production of short-lived and long-lived leptons via the decays of a Z boson or photon. In the case of a short-living lepton, the particle is assumed to decay into a W boson and any neutrino, whereas for the long-lifetime scenario the pair-produced ℓ' are assumed to traverse the detector without decay resulting in two back-to-back tracks. For each scenario, no excess due to the signal was observed and mass limits of 102.6 GeV

Production	Decay	Final state	$\mathcal{L}$ [fb^{-1}]	$m_{q'}$ [GeV]	Reference (exp.)
$pp \to t'\bar{t'}$	$t' \to qW$	$\ell^+\ell^-$+jets	1.04	≥ 350	[93] (ATLAS)
$pp \to t'\bar{t'}$	$t' \to bW$	$\ell^\pm$+jets	1.04	≥ 404	[94] (ATLAS)
$pp \to t'\bar{t'}$	$t' \to bW$	$\ell^+\ell^-$+2 b-jets	5.0	≥ 557	[95] (CMS)
$pp \to b'\bar{b'}$	$b' \to tW$	$\ell^\pm$+jets	1.04	≥ 480	[96] (ATLAS)
$pp \to b'\bar{b'}$	$b' \to tW$	$\ell^\pm\ell^\pm$+jets	4.9	≥ 611	[97] (CMS)
$pp \to b'\bar{b'}$	$b' \to tW$	$\ell^\pm\ell^\pm$+jets	4.7	≥ 670	[98] (ATLAS)
Various	$b'/t' \to t/bW$	Various	5.0	≥ 685	[99] (CMS)

Table 2.4: A summary of mass limit results ($m_{q'}$) for fourth generation quarks obtained from direct searches performed at ATLAS and CMS. Each line represents a specific decay topology assumed in the analyses. $\mathcal{L}$ denotes the integrated luminosity of the analysed dataset. All listed analyses used data taken from pp collisions at a centre-of-mass energy of $\sqrt{s} = 7\,\text{TeV}$.
In case of the CMS analysis using a model independent approach (last line), several production channels and final states were considered (see text).

and 100.8 GeV were set for the cases of a long-lived and short-lived charged lepton, respectively.

The search for the heavy fourth generation neutrino ν' in reference [102] was performed under the assumptions of a Dirac and a Majorana neutrino[4]. The search was restricted to the pair-production of neutrinos with a decay length smaller than 1 cm. This was done in order to avoid decays far away from the interaction point and to ensure high detection and reconstruction efficiencies. Each of the neutrinos was considered to decay into an electron, muon or tau and associated with a W boson. No excess over the background expectation has been observed and mass limits of 90.3 GeV and 80.5 GeV have been set for the case of a Dirac and Majorana neutrino, respectively. However, the limit for the Majorana neutrino was made under the assumption of a left-handed only fermion. Since the fourth generation neutrino must be much heavier than the neutrinos of the first three generations, there must be also a right-handed ν'. Therefore the L3 results have been revisited in reference [103] taking into account the existence of left- and right-handed fourth generation neutrinos and the analysers found a lower mass limit for the Majorana neutrino of only 62.1 GeV.

All mentioned fourth generation leptons mass limits are summarised in Table 2.5.

2.2.4 Implications from Higgs searches

One of the goals of the Large Hadron Collider is the discovery of the Higgs boson. At this proton-proton collider, the dominant Higgs production mechanisms [104] are gluon-gluon fusion (ggH), vector boson fusion (VVH with $V = W, Z$), and associated production with vector bosons (VH) and heavy fermions (dominantly $t\bar{t}H$ due to the strong Yukawa coupling of the t quark). The Feynman diagrams representing these

[4] A Majorana particle is identical for the particle and anti-particle

Particle	Assumption	$\mathcal{L}$ [pb^{-1}]	Mass limit [GeV]	References
ℓ'	Long-lived	450	102.6	[102] (L3)
ℓ'	Short-lived	450	100.8	[102] (L3)
ν'	Dirac	450	90.3	[102] (L3)
ν'	Majorana	450	62.1	[102] (L3), [103]

Table 2.5: The table summarises the mass limits on fourth generation leptons obtained from direct searches performed at L3. In the analysis of the charged lepton ℓ' it was assumed that the particle is either short-lived and decays within the detector, or that it is long-lived (quasi-stable) and traverses the detector without decaying. In the case of the ν' the analysis was performed under the assumption of a short-lived Dirac or Majorana neutrino. $\mathcal{L}$ denotes the integrated luminosity of the analysed dataset. The listed analyses used data taken from e^+e^- collisions at a centre-of-mass energy of $\sqrt{s} \simeq 200\,\text{GeV}$.

production mechanisms are summarised in Figure 2.11. In the searches for the Higgs boson, there are several Higgs decay channels [104] of interest: $H \to \gamma\gamma$, $H \to VV$ ($V = W, Z$), $H \to b\bar{b}$ and $H \to \tau^+\tau^-$. The Higgs can also decay into lighter fermions, but these decays are suppressed due to the weaker Yukawa couplings. All decay channels differ by their branching fractions which are shown in Figure 2.12 together with some example Feynman graphs.

2.2.4.1 Discovery of a Higgs-like boson at the LHC

In summer 2012, both the ATLAS and CMS experiments at the Large Hadron Collider claimed the discovery of a boson with a mass of about 125 GeV which is compatible with the SM Higgs boson.

The ATLAS search [18] combined the analyses using data taken at $\sqrt{s} = 8\,\text{TeV}$ in the channels $H \to ZZ \to 4\ell$, $H \to \gamma\gamma$ and $H \to WW$ with analyses using 7 TeV data in the channels $H \to ZZ$, WW, $b\bar{b}$, $\tau^+\tau^-$ and $\gamma\gamma$. A clear excess of events above the expected background is seen in the channels $H \to ZZ \to 4l$ and $H \to \gamma\gamma$. Figure 2.13a presents the local p-values from the combination of all channels as a function of the Higgs boson mass. The largest local significance appears at $m_H = 126.5\,\text{GeV}$ with a value of 5.9σ when considering all systematic uncertainties. When calculating the global significance for this excess in the mass range $m_H \in [100, 600]$ GeV the ATLAS collaboration obtains a value of 5.1σ. The observed mass of the boson is obtained by performing a Likelihood fit for the channels $H \to ZZ \to 4l$ and $H \to \gamma\gamma$ and gives a value of $m_H = 126.0 \pm 0.4(\text{stat.}) \pm 0.4(\text{syst.})$ GeV.

In the CMS analysis [19] the searches in the channels $H \to \gamma\gamma$, ZZ, WW, $\tau^+\tau^-$ and $b\bar{b}$ with separate datasets at $\sqrt{s} = 7$ and 8 TeV have been combined. Similar to the ATLAS result, the CMS analysers observe a significant excess in the channels $H \to ZZ \to 4l$ and $H \to \gamma\gamma$. The local p-values depending on the Higgs mass are shown in Figure 2.13b, where the combination of all results gives a significance of 5σ at a mass of 125.5 GeV. Calculating the global p-value in the mass range $m_H \in [110, 145]$ GeV gives a significance

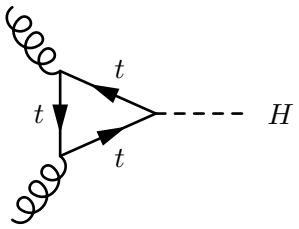

(a) Gluon fusion

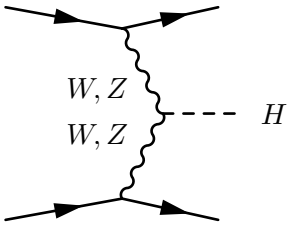

(b) Vector boson fusion

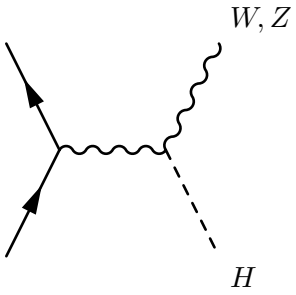

(c) Associated production with W, Z

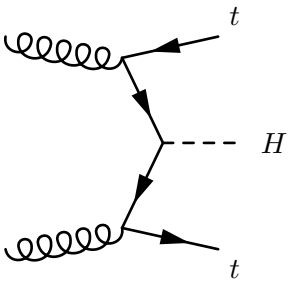

(d) Associated production with t

Figure 2.11: Feynman diagrams of dominant Higgs production mechanisms. Figure (a) shows gluon-gluon fusion, Figure (b) displays vector boson fusion, and the associated production with vector bosons and top quarks is presented in (c) and (d), respectively.

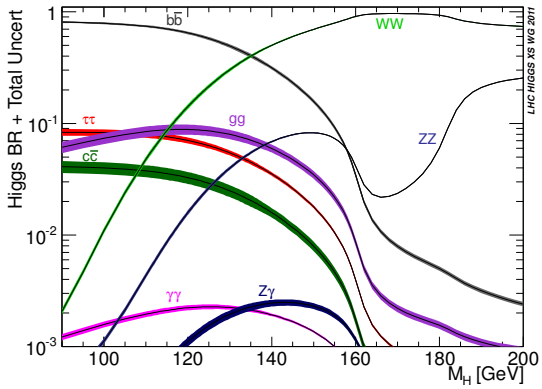

(a) Higgs decay branching ratios

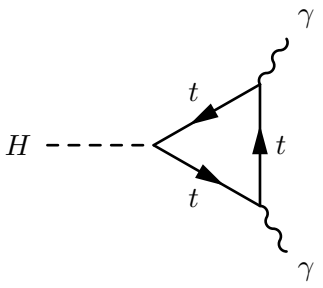

(b) $H \to \gamma\gamma$

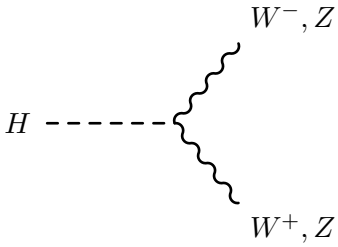

(c) $H \to VV$

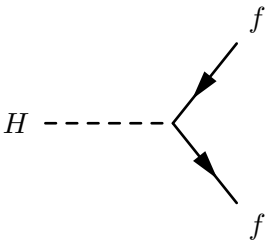

(d) $H \to ff$

Figure 2.12: Several Higgs decay channels are presented. Figure (a) shows the branching fractions depending on the Higgs boson mass [104] when assuming a three generations SM, while Figures (b)-(d) provide example Feynman diagrams for some decay channels. The $H \to \gamma\gamma$ decay in (b) can also be formed by a loop of the heavy W bosons instead of the top quark.

of 4.5σ for the local excess. A fit has been performed for the $H \to ZZ \to 4l$ and $H \to \gamma\gamma$ channels yielding a mass of $m_H = 125.3 \pm 0.4(\text{stat.}) \pm 0.5(\text{syst.})$ GeV.

2.2.4.2 Implications on the fourth generation sector

In the loop diagrams for $gg \to H$ production (Figure 2.11a) and $H \to \gamma\gamma$ decay (Figure 2.12b), it can be clearly seen that any fourth generation fermions contributing to these loops would have a significant impact to the Higgs production and decays due to their strong Yukawa couplings.

In references [105–107] it has been shown that the $gg \to H$ production cross-section experiences an increase compared to the three-generation Standard Model (SM3) expectation, when adding a fourth generation of fermions. Figure 2.14a presents the SM4 production cross-section, normalised to the SM3 value, as a function of the Higgs boson mass. At $m_H = 125\,\text{GeV}$, the enhancement yields a factor of ~ 9. However, the total rates in the Higgs decay channels are not expected to be increased in general, because the branching fractions (BFs) of several channels are changed compared to the SM ex-

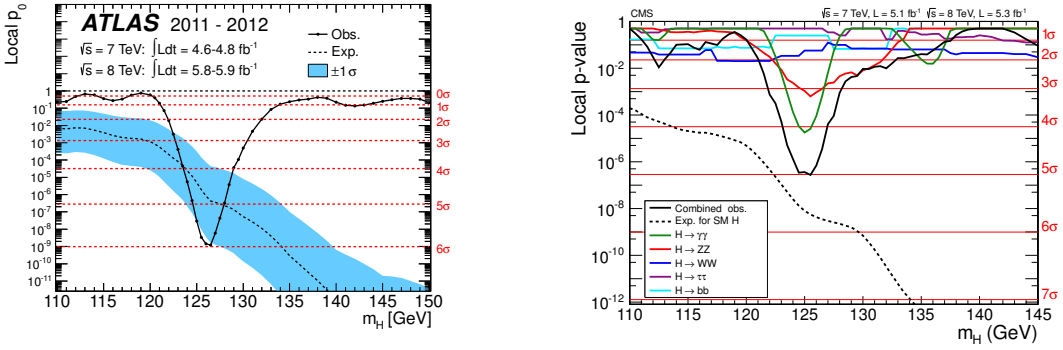

(a) ATLAS (b) CMS

Figure 2.13: The expected and observed local p-values as a function of the Higgs boson mass m_H in the Higgs searches at ATLAS [18] and CMS [19] are presented. The ATLAS result (a) shows the expected local p-value as a combination of all search channels. In the CMS plot (a) the separate results for each channel are shown together with their combination. Both experiments claim a local significance of $\geq 5\sigma$ at a mass of $\approx 125\,\text{GeV}$.

pectation. A detailed study of the fourth generation implications on the Higgs decay branching fractions has been performed in reference [108] and is summarised in the following. Figure 2.14b presents the decay branching ratios in SM4, normalised to the SM3 values, as a function of the fourth generation neutrino mass $m_{\nu'}$. In this plot a Higgs boson mass of 125 GeV has been assumed and the masses of the fourth generation quarks and leptons have been set to $m_{b'} = m_{t'} + 50\,\text{GeV} = 600\,\text{GeV}$ and $m_{\ell'} = m_{\nu'} + 50\,\text{GeV}$ (these assumptions are based on the studies of the EWPOs when neglecting the CKM mixing, see Section 2.2.2) where the neutrino mass is required to be $m_{\nu'} \geq m_Z/2$. The branching fractions, which have been calculated using `HDECAY` [109], are shown for the decay channels $H \to gg$, $b\bar{b}$, VV $(V = W, Z)$ and $\gamma\gamma$. The corrections to the Higgs decays due to the addition of a fourth generation have been implemented according to the results of the studies in references [110, 111]. They show that the HVV and $H\gamma\gamma$ couplings experience a decrease compared to their SM3 values when considering higher-order loops in addition to the tree-level processes [108].

For neutrino masses below $m_H/2$ it can be seen that all branching fractions experience a large drop. This is due to the additional allowed Higgs decay channel $H \to \nu'\bar{\nu}'$, which enhances the total Higgs decay width. In the $H \to \gamma\gamma$ channel the reduction is stronger than the factor ~ 9 increase in the Higgs production cross-section, which results in a lower expected rate in this channel. Since the Higgs discovery results in the channel $\gamma\gamma$ are compatible with the three generation SM expectation, such a reduction is disfavoured.

For neutrino masses above $m_H/2$ the $H \to gg$ BF is enhanced, whereas all other BFs are reduced compared to their SM3 expectations. The enhancement of the $H \to gg$ BF is analogue to the increase in the $gg \to H$ production cross-section. However, for

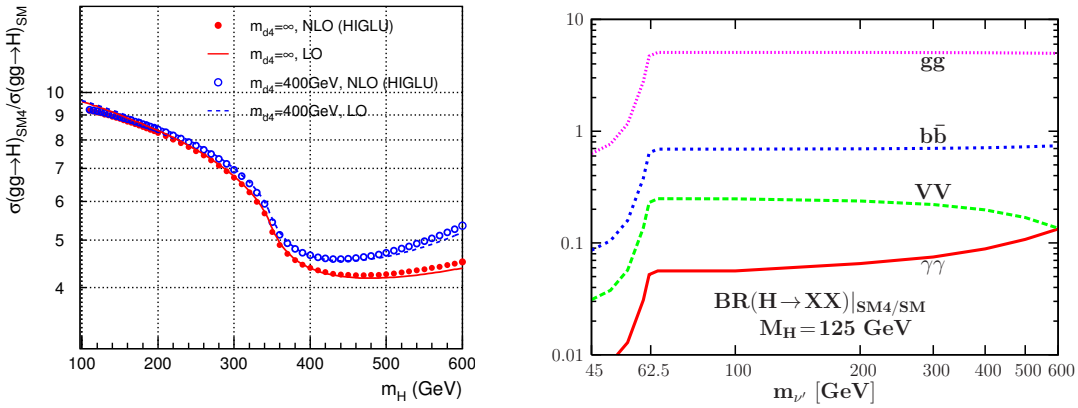

(a) Higgs production (b) Higgs decay

Figure 2.14: The Figures show the enhancement of the Higgs production cross-section and the change in the decay branching fractions in SM4. In (a), the Higgs production cross-section in SM4, normalised to the SM3 expectation, is presented as a function of the Higgs boson mass [107]. The curves indicate the behaviour of the cross-section enhancement factor for two different mass scenarios (400 GeV and infinite b' mass) and at different precisions (leading-order and next-to-leading order). At $m_H = 125\,\text{GeV}$, all curves show an enhancement by a factor of ~ 9.
In (b), the Higgs decay branching fractions in SM4, normalised to the SM3 expectation, are shown as a function of the heavy neutrino mass $m_{\nu'}$ [108]. In the calculation, a Higgs mass of $m_H = 125\,\text{GeV}$ was assumed. Besides the $H \to gg$ channel, all branching fractions are lowered compared to the SM3 value for heavy neutrino masses above $m_H/2$. Taking into account the production cross-section increase by a factor of ~ 9, only the $H \to \gamma\gamma$ channel (if $m_{\nu'} \geq m_H/2$) can compensate the cross-section enhancement, whereas the other channels will experience an increase in the total rates.

$m_{\nu'} \lesssim 500\,\text{GeV}$ only the $H \to \gamma\gamma$ channel can compensate the cross-section enhancement of ~ 9, whereas the other channels will experience an increase in the total rates, since their reduction in the BF is less than $1/9$. At $m_{\nu'} \approx 600\,\text{GeV}$ the reductions in the BFs of $\gamma\gamma$ and VV are equal with a value of about $\sim 1/7.5$. Taking into account the factor ~ 9 increase in the production cross-section, this would give an increase in the rates of these channels of about $\sim 20\%$ for SM4 compared to SM3.

When combining the discussed implications of a fourth generation on the Higgs sector with the recent Higgs results at ATLAS and CMS, it is possible to check whether the fourth generation is compatible with the observed results assuming a Higgs boson sector equal to that of the SM. This has been performed in references [112–114] and is presented in the following. Using the `CKMfitter` package [47], a global fit to EWPOs and the Higgs

signal strengths has been done. These signal strengths are defined as

$$\hat{\mu} = \frac{\sigma(X \to H)\mathcal{B}(H \to Y)|_{\text{exp}}}{\sigma(X \to H)\mathcal{B}(H \to Y)|_{\text{theory}}}, \tag{2.83}$$

where $\sigma(X \to H)$ denotes the production cross-section for any initial state X and $\mathcal{B}(H \to Y)$ represents the branching fraction for the Higgs decay into the final state Y. The denominator stands for the $\sigma \times \mathcal{B}$ predicted by theory assuming SM3 or SM4, whereas the numerator indicates the experimental result. In the analysis, branching fractions are calculated using `HDECAY` [109] and the SM4 production cross-section is approximated by

$$\sigma(X \to H)_{\text{SM4}}\mathcal{B}(H \to Y)_{\text{SM4}} = \sigma(X \to H)_{\text{SM3}} \cdot \frac{\Gamma(H \to X)_{\text{SM4}}}{\Gamma(H \to X)_{\text{SM3}}} \cdot \mathcal{B}(H \to Y)_{\text{SM4}} \tag{2.84}$$

with $\Gamma(H \to X)$ being the Higgs decay width for $H \to X$. In the fit, the heavy quark masses have been constrained to $m_{q'} \geq 400\,\text{GeV}$, while the leptons are required to be $m_{\ell'} \geq 100\,\text{GeV}$ and $m_{\nu'} \geq m_Z/2$. For the experimental signal strengths, the results from ATLAS [18], CMS [19] and also Tevatron [115] were used as input. These experimental signal strengths are then compared to the SM3 and SM4 theory expectation. The deviations (pulls) in the signal strengths for the different channels resulting from the fit are shown in Figure 2.15, where these deviations are defined as

$$\frac{\hat{\mu}_{\text{exp}} - \hat{\mu}_{\text{fit}}}{\Delta\hat{\mu}} \ . \tag{2.85}$$

$\hat{\mu}_{\text{exp}}$ and $\Delta\hat{\mu}$ denote the signal strengths and errors, respectively, taken directly from the experimental results. For deriving $\hat{\mu}_{\text{fit}}$, the signal strengths are fitted using the experimental input and considering the relationships between all decay channels. The best-fit results are then taken as $\hat{\mu}_{\text{fit}}$, which denotes the prediction coming from the underlying theory SM3 or SM4.

The plot shows the deviations assuming a three generation SM in blue, whilst the results assuming SM4 are shown in green (with experimental data input before the Higgs-like boson discovery presented at ICHEP'12) and red (with the addition of the experimental input of this discovery). When including the ICHEP'12 results, the deviation in the $H \to \gamma\gamma$ exceeds 4σ when comparing to the SM4 expectation[5]. Moreover, the $p\bar{p} \to H \to b\bar{b}$ results from Tevatron show an incompatibility of the SM4 with more than 2σ.

The fluctuations in the different channels assuming SM3 are in all cases below 2σ, which gives a hint that the SM4 fit results are not compatible with the Higgs search experimental data, especially in the channels $H \to \gamma\gamma$ and $H \to b\bar{b}$. Therefore the analysers in reference [114] computed the statistical significance for excluding a fourth generation using the `myFitter` package [116]. This is done by performing a likelihood ratio test with all experimental inputs. The analysers find that the fourth generation extension is

[5] This should not be interpreted as statistical significance, but rather denotes the size of the pull.

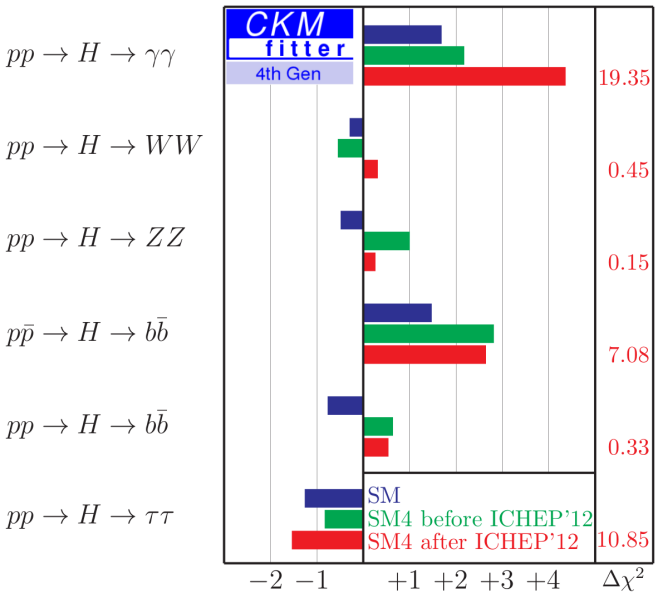

Figure 2.15: Deviations of the Higgs signal strengths (as defined in Equation (2.85)) for the three (blue) and four generation SM (green and red) assumptions [114]. In the green results, the experimental results prior to the publication of the Higgs-like boson discovery in summer 2012 (ICHEP'12) have been used, whilst the red bars represent the fit results after the discovery results (presented at ICHEP'12) have been included. The right column shows the change in the minimum χ^2 of the SM4 fit, when the corresponding signal strength is not used in the fit.

excluded at 5.3σ.

Above presented results rule out a fourth generation of fermions under one assumption: the boson observed at ATLAS and CMS is indeed the Standard Model Higgs boson. However, a fourth generation of fermions could be still in accordance with the experimental constraints if one extends the Higgs sector. A possible scenario is the existence of two Higgs doublets (instead of just one doublet as shown in Section 2.1.1.1), which are predicted by theories beyond the Standard Model, e.g. supersymmetry. In reference [117] such a scenario is studied and the analysers find that the fourth generation would be still realisable under this assumption.

2.2.5 Pair production of fourth generation quarks at hadron colliders

The production of particles at hadron colliders occurs through interaction of quarks, antiquarks and gluons, the constituents of the hadrons. In the case of proton-proton collisions, like those at the Large Hadron Collider, the interacting particles can be the valence quarks *uud* of the proton or it's sea quarks and gluons. These proton ingredients are also called partons.

When a high energetic proton is moving with a longitudinal momentum P, each parton carries some fraction x of this total momentum (the transverse momentum is neglected, as it is small compared to the longitudinal component). Therefore, the parton longitudinal momentum $p = x \cdot P$, and the usually much smaller transverse momentum define the kinematics of the interaction. The distribution function for x can not be described by perturbative QCD, because the soft interactions inside the proton occur at low momentum transfers Q which correspond to large strong couplings $\alpha_s(Q)$. Hence, the longitudinal parton momentum structure is described by parton distribution functions (PDFs), which can not be predicted by theory and need to be measured by experiment. The PDFs are measured at deep inelastic lepton-nucleon scattering experiments, like electron-proton colliders (e.g. HERA [118]) or fixed target experiments.
There are several groups analysing this data, e.g. MSTW [119] or CTEQ/CT [120, 121], and they provide the PDFs together with error sets that describe the theoretical and experimental uncertainties. An example is shown from the MSTW group in Figure 2.16. Here, the PDFs $f_i(x)$, multiplied by the momentum fraction x for two different momen-

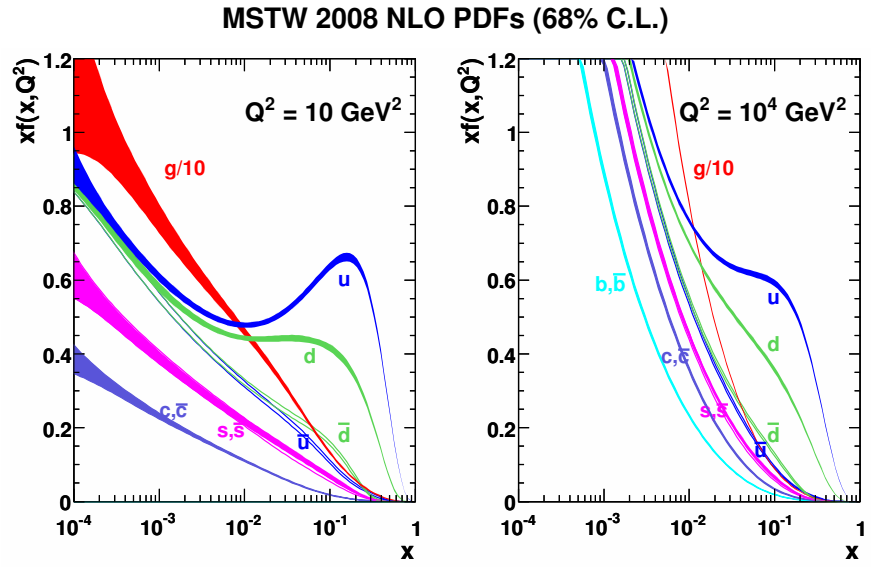

Figure 2.16: Parton distribution functions $f_i(x)$ and their 68% confidence intervals, multiplied by the momentum fraction x, for two different scales Q^2. The plots are provided by the MSTW group and show the PDFs for different partons at next-to-leading order [119].

tum transfer squared Q^2 and for the different parton types are presented together with their 68% confidence intervals. The function f_i represents the probability density of finding a parton with momentum fraction x inside the proton. It can be seen that the gluons carry most momentum for $x \lesssim 0.1$, whereas the quarks contribute significantly at higher values of x.

At tree-level there are two dominant production mechanisms for heavy-quark pair

production at a proton-(anti)proton collider: gluon-gluon fusion and quark-antiquark annihilation. The corresponding Feynman diagrams are shown in Figure 2.17. Which of

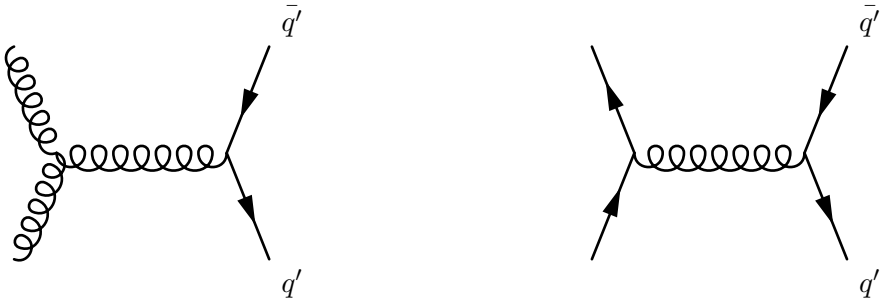

(a) Gluon-gluon fusion (b) $q\bar{q}$ annihilation

Figure 2.17: The dominant tree-level amplitudes of heavy quark $q'\bar{q}'$ production at a proton-proton collider are shown: gluon-gluon fusion (a) and quark-antiquark annihilation (b).

the two processes dominates depends on the collider type (pp or $p\bar{p}$) and the mass $m_{q'}$ of the heavy quark, which constitutes the required momentum fraction x that provides sufficient energy for the creation of the $q'\bar{q}'$ pair.

In order to calculate the total production cross section σ_{tot} for heavy-quark $q'\bar{q}'$ production in proton-proton collisions, one needs to consider all partonic cross-sections $\hat{\sigma}_{ij}$. Each $\hat{\sigma}_{ij}$ represents the cross-section for the interaction of incoming partons i and j, which can be either gluons or any quark and antiquark inside the proton.
When also considering additional gluon radiations of the partons, one needs to modify the cross-section calculation. The emissions of gluons with low momenta (soft-gluons) can not be described by perturbative QCD. Therefore, one defines a factorisation scale μ_f, below which the interaction terms are factored into the PDF. This becomes relevant for processes beyond leading order.
The total cross section is then obtained by the convolution of the factorised partonic cross sections [30]:

$$\sigma_{\text{tot}} = \sum_{i,j} \int \mathrm{d}x_i \mathrm{d}x_j f_i\left(x_i, \mu_f\right) f_j\left(x_j, \mu_f\right) \hat{\sigma}_{ij}\left(x_i, x_j, S, m_{q'}, \alpha_s(\mu_r), \mu_f\right), \tag{2.86}$$

where S denotes the hadronic centre-of-mass energy squared ($S = \sqrt{s}^2$) and $f_{i/j}$ are the PDFs for parton i/j with momentum fraction $x_{i/j}$. The centre-of-mass energy of the parton-parton system is then given by $\hat{s} = x_i x_j S$ and the integration over x_i and x_j is performed in a way, that $\hat{s}$ is above the minimum energy required for the heavy quark pair production ($(2m_{q'})^2$). μ_r denotes the renormalisation scale, which was introduced in Section 2.1.2 and defines the scale at which α_s is expanded.
In the perturbative regime of QCD the partonic cross-section $\hat{\sigma}_{ij}$ can be expanded in the QCD coupling constant α_s. The expansion up to next-to-next-to-leading-order (NNLO)

is then given by [122]

$$\hat{\sigma}_{ij} = \left(\frac{\alpha_s}{\pi}\right)^2 \hat{\sigma}_{ij}^{(0)}(\hat{s}, m_{q'}) + \left(\frac{\alpha_s}{\pi}\right)^3 \hat{\sigma}_{ij}^{(1)}(\hat{s}, m_{q'}, \mu_r, \mu_f) \tag{2.87}$$

$$+ \left(\frac{\alpha_s}{\pi}\right)^4 \hat{\sigma}_{ij}^{(2)}(\hat{s}, m_{q'}, \mu_r, \mu_f) + \mathcal{O}(\alpha_s^5), \tag{2.88}$$

where the $\hat{\sigma}_{ij}^{(k)}$ describe the partonic cross-sections at the k-th loop level.

A program that calculates the heavy quark pair production cross-section using the described ansatz is `HATHOR` [122]. It allows the calculation of the cross-section up to approximate NNLO precision (in the sense that some of the NNLO terms in the partonic cross-section $\hat{\sigma}_{ij}^{(2)}$ are calculated in an approximate way).
The approx. NNLO heavy quark pair production cross-sections have been calculated for different masses (here denoted as m_Q instead of $m_{q'}$) and centre-of-mass energies in proton-proton collisions and are displayed in Figure 2.18. In this calculation the

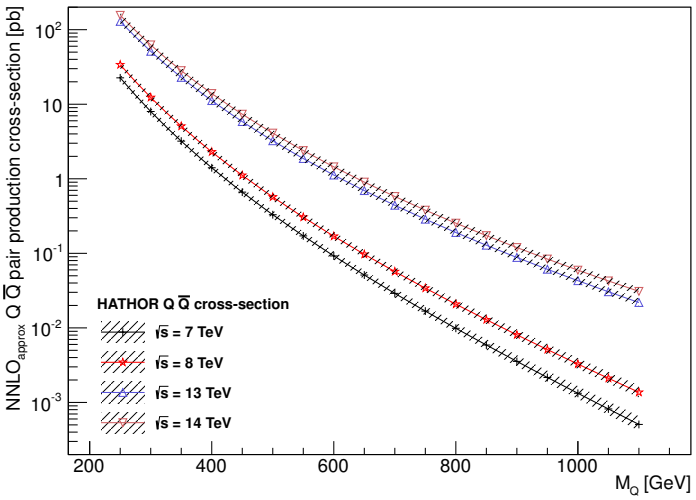

Figure 2.18: Heavy quark pair production cross-sections with approx. NNLO precision, calculated with `HATHOR` [122]. The cross-sections are presented for different mass points and centre-of-mass energies in proton-proton collisions. The error bands show the combination of scale and α_s+PDF uncertainties.

renormalisation and factorisation scale have been set to $\mu_r = \mu_f = m_Q$ and the PDF `MSTW2008 NNLO` with 90% C.L. [119] has been used via the `LHAPDF` interface [123]. Each point is assigned a combined error consisting of scale and α_s plus PDF uncertainty.
The scale uncertainty is derived by varying μ_r and μ_f independently by factors of 1/2 and 2 and using the envelope of the resulting four cross-sections as uncertainty.
In order to estimate the uncertainties from α_s and the PDF error sets, one could calculate the cross-sections separately for different values of α_s and for different PDFs from the

error sets before then taking the envelopes as uncertainties. However, for each value of α_s there is a central PDF set together with its PDF error sets. Therefore, I followed a better approach, which is suggested in reference [124]: the uncertainties are evaluated for specific PDF sets that represent the -1σ, $-1/2\sigma$,$+1/2\sigma$ and $+1\sigma$ changes to the value of α_s. For each of the five α_s PDF sets ($\pm 1/2\sigma$, $\pm 1\sigma$ and central value) the central cross-section and the PDF uncertainty is derived from the PDF error sets. In the end one takes the envelope of all derived values as the total α_s+PDF uncertainty.

2.2.6 Decay scenarios of fourth generation quarks

In the following I will discuss possible decay scenarios of fourth generation quarks, considering the constraints on the masses and mixings discussed in Sections 2.2.2 and 2.2.3.

Studies of the electroweak observables revealed that the scenario of $m_{t'} > m_{b'}$ is favoured. This means that in this case the decay $b' \to t' + W$ is kinematically not allowed and therefore the b' will decay into the quarks of the other three SM generations. This requires that there is a non-zero mixing between the fourth and the other three generations. Although the studies of the mixing angles and CKM matrix elements revealed that large mixings within the fourth generation are favoured, a mixing with the other generations was not excluded.
One can differ now between two different scenarios:

- $|\mathbf{V_{ub'}}|, |\mathbf{V_{cb'}}| > |\mathbf{V_{tb'}}|$: In this case the decay $b' \to u/c + W$ will be dominant. The resulting decay topology is depicted in Figure 2.19. In the final state two

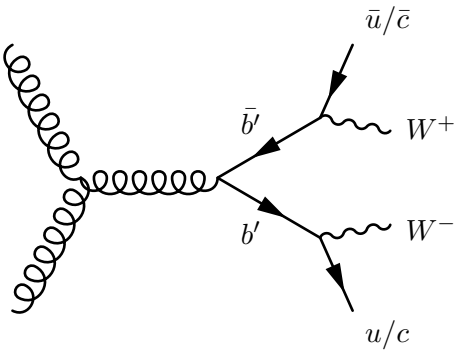

Figure 2.19: $b' \to u/c + W$ decay topology

  u or c quarks appear which will form 'light jets' (in the sense that these quarks are very light compared to the b or t quark) along with two oppositely-charged W bosons. Depending on the decay scenarios of these W it is possible to select either single lepton or opposite-sign dilepton events. This is a similar topology as in $t\bar{t}$ production and subsequent $t/\bar{t}$ decays. The scenario where both W decay hadronically is usually not searched for in analyses at hadron colliders, because it is difficult to distinguish such a signature from the hadronic background.

- $|\mathbf{V_{ub'}}|, |\mathbf{V_{cb'}}| < |\mathbf{V_{tb'}}|$: This scenario is favoured by the global fits to EWPOs and

flavor observables and results in the dominant decay being $b' \to t + W$. For two-body decays this requires that $m_{b'} > m_W + m_t \approx 255\,\text{GeV}$. Smaller b' masses are already excluded from direct searches. Such a decay topology is depicted in Figure 2.20. The top quark has a very short lifetime and decays dominantly as

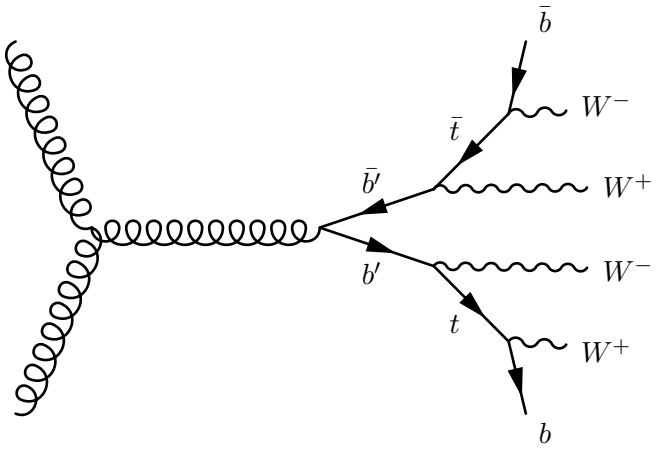

Figure 2.20: $b' \to t + W$ decay topology

$t \to Wb$, because $|V_{tb}|$ is expected to be close to 1 (this is supported by single-top measurements e.g. presented in references [125–127], see also reference [128] for a discussion about V_{tb} measurements assuming a four-generations SM). Then the final state consists of a b quark, $\bar{b}$ quark and four W bosons with charges $W^+W^+W^-W^-$. These four W bosons allow the selection of several different final states with up to four leptons. An interesting scenario, which will be also used in this thesis, is to require that two same-sign charged W bosons decay leptonically, whilst the other two W bosons decay hadronically. This results in a signature of two same-sign charged leptons and a high jet multiplicity, which is rare in the SM and therefore well suited to searches for new physics. A further discussion of this decay topology follows in the analysis section of this thesis (Section 6.1).

In the scenario $m_{t'} > m_{b'}$, decays of $t' \to b' + W$ could also appear which result in a similar topology as the previously discussed scenario $b' \to t + W$. This decay is also favoured by the large mixing within the fourth generation. However, the mass difference between t' and b' is favoured to be $m_{t'} - m_{b'} < m_W$, which means that such a decay could only occur via three-body decays with virtual off-shell W bosons: $t' \to b' + W^*$.

Another scenario would be $m_{t'} < m_{b'}$. Although it is disfavoured by the EWPOs, it has not been excluded. Depending on the mass difference, there are two different scenarios:

- $\mathbf{m_{b'} - m_{t'} < m_W}$: The two-body decay $b' \to t' + W$ is not allowed. Besides the three-body decay the b' will then decay into quarks of the other three generations, as discussed above through $b' \to u/c + W$ and $b' \to t + W$. However, for (quasi) degenerate b' and t' masses, the decay products of the W boson produced in the

decay $b' \to t' + W$ will have small momenta and hence might not pass the selection criteria of the analysis.

- $\mathbf{m_{b'} - m_{t'} > m_W}$: In this case the decay $b' \to t' + W$ is allowed. For a large $|V_{t'b}|$ the resulting final state $b' \to t' + W^- \to b + W^+ + W^-$ is equal to the scenario for $m_{t'} > m_{b'}$ and $|V_{ub'}|, |V_{cb'}| < |V_{tb'}|$. If there is a larger mixing with the first or second generation, $|V_{t'd}|, |V_{t's}| > |V_{t'b}|$, the final state of the decay chain $b' \to t' + W^- \to d/s + W^+ + W^-$ contains the same multiplicity of W bosons, but 'light jets' instead of b-jets.

3 The ATLAS experiment

This thesis aims for the search of fourth generation quarks in data collected at the ATLAS detector, which is one of the two multi-purpose detectors at the Large Hadron Collider (LHC).

In the following I will present the structure of the LHC accelerator complex (Section 3.1), followed by a description of the ATLAS detector including the performance that has been reached so far (Section 3.2).

3.1 The Large Hadron Collider

The Large Hadron Collider is a particle accelerator located near Geneva (Switzerland) and belongs to the European Organization for Nuclear Research (CERN). It has been installed in the former Large Electron Positron collider (LEP) tunnel, and is designed to collide protons or heavy ions with very high centre-of-mass energies of up to 14 TeV. Since this thesis deals with data taken from proton-proton collisions, in the following I will focus on the LHC setup when running such collisions.
The following information are mostly taken from references [1, 2], which also allow for further reading, and represent the design parameters of the LHC. The actual running conditions in 2011 and 2012 will be presented in Section 3.2.8.

The main LHC ring has a circumference of 26.7 km and is located 100 m under the surface of Switzerland and France. Before being injected into the main ring, the protons traverse several pre-accelerators where they subsequently gain higher energies. Figure 3.1 gives an overview of the CERN accelerator complex including these pre-accelerators.
In the beginning, hydrogen gas is ionised inside a duoplasmatron (see for example reference [130] for further reading) using an electron beam. After extracting the obtained protons, these are passed to the Radio Frequency Quadrupole (RFQ). The RFQ is a linear accelerator providing the focusing and separation of the protons into particle bunches. From the RFQ the proton bunches are passed to the linear accelerator LINAC2 with an energy of about 750 keV, where they then reach an energy of up to 50 MeV. The next step is a ring accelerator: the Proton Synchrotron Booster (PSB), which accelerates the protons up to an energy of 1.4 GeV. After leaving the PSB the protons enter the Proton Synchrotron (PS). Here the six bunches coming from the PSB are separated into 72 bunches with a spacing of 25 ns. In the PS the proton bunches reach an energy of 25 GeV and are then passed to the last pre-accelerator, the Super Proton Synchrotron (SPS). Here the bunches are accelerated to 450 GeV, split into two transfer lines and then transferred to the two LHC rings: one beam going in clockwise direction, the other one in the opposite direction. The LHC ring then allows to accelerate the proton bunches up to energies of 7 TeV using super-conducting radio frequency (RF) cavities.

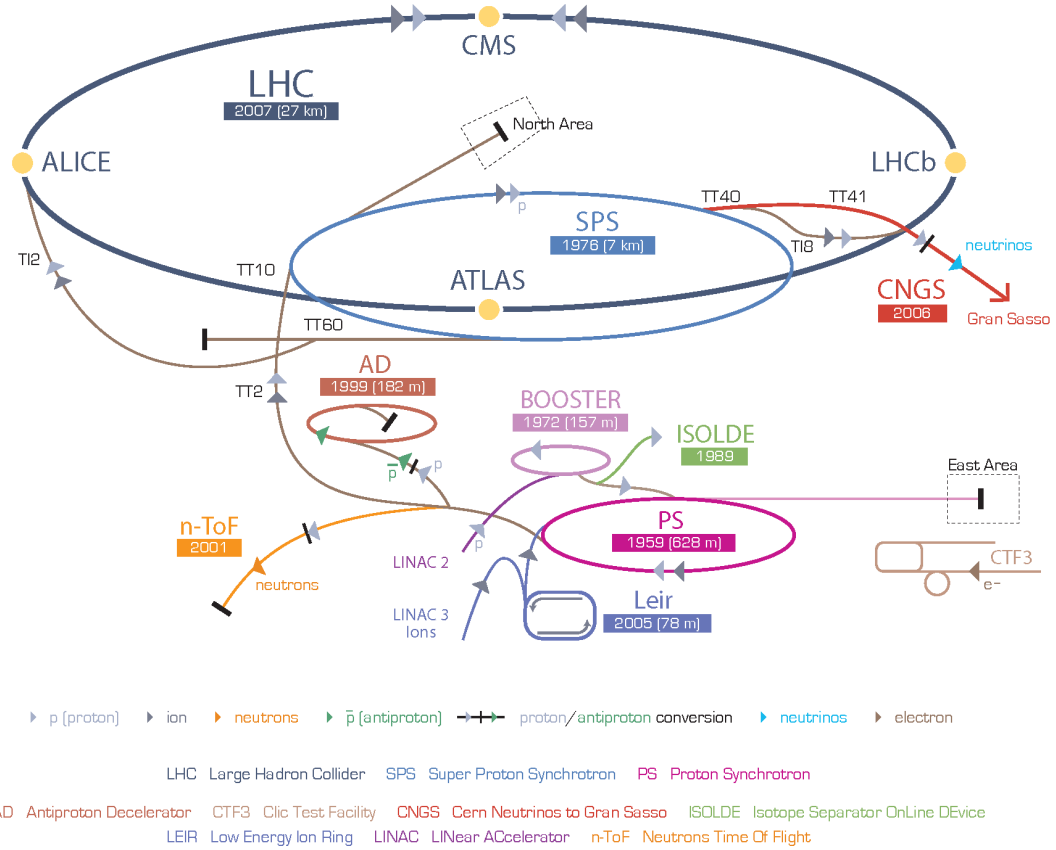

Figure 3.1: CERN accelerator complex [129].

In order to hold the protons on the circular path at such high energies, dipole magnets with very high field strengths of more than 8 T are required, which can currently only be realised using super-conducting magnets. The LHC ring consists of 1232 dipoles with a length of 15 m each, which are responsible for the bending of the proton tracks, and 392 quadrupole magnets performing the focusing of the beams. To achieve the super-conducting phase inside the magnets, these are cooled down to a temperature of 1.9 °K using super-fluid helium.
At the moment, the LHC is not running with the maximum design centre-of-mass energy of $\sqrt{s} = 14\,\text{TeV}$. This is due to an incident which occurred a few days after the LHC start-up in September 2008 [131]. In order to already collect physics data while running with safe operations, it was decided to limit the beam energy to 3.5 TeV in 2011 and 4 TeV in 2012, resulting in centre-of-mass energies of $\sqrt{s} = 7\,\text{TeV}$ and $\sqrt{s} = 8\,\text{TeV}$ in 2011 and 2012, respectively.

The rate R at which physical processes occur is proportional to the corresponding cross-section σ of the process: $R = L{\cdot}\sigma$. The constant of proportionality is the luminosity

L which can be calculated from

$$L = f \cdot \frac{n_1 n_2}{4\pi\sigma_x\sigma_y}, \tag{3.1}$$

where f denotes the collision frequency, $n_{1/2}$ the number of protons in the two colliding bunches and $\sigma_{x/y}$ the beam widths in x and y direction. A commonly used variable is the integrated luminosity $\mathcal{L}$, which is obtained by integrating the luminosity over the time period in which the LHC was running:

$$\mathcal{L} = \int L\mathrm{d}t \ . \tag{3.2}$$

When running with design parameters, the LHC reaches a luminosity of $L \approx 10^{34}\mathrm{cm}^{-2}\mathrm{s}^{-1}$. This is achieved by a maximum of 2808 bunches with $\sim 10^{11}$ protons each and a bunch spacing of 25 ns. This bunch spacing corresponds to a bunch crossing rate of 40 MHz, which needs to be handled by the detectors that record the event information from the collisions. The small bunch spacing and the high luminosity cause that several proton-proton interactions are measured during each bunch crossing and from successive bunch crossings. These additional interactions are commonly referred to as so-called 'pile-up' events.

At the LHC, there are four main detectors in operation and located at the beam crossing interaction points. Two of them, ATLAS [16] and CMS [17], are multi-purpose experiments covering a wide field of physical topics. The LHCb detector [75] aims on measuring the production and decays of b-hadrons and hence investigating e.g. the CP violation. The fourth experiment, ALICE [132], is designed for the LHC running mode with heavy ions, in particular lead ions. The aim is to measure the properties of the produced quark-gluon plasma and to study the QCD phase diagram.
The locations of these detectors are also illustrated in Figure 3.1.

3.2 The ATLAS detector

The ATLAS detector [16] (A Toroidal Lhc ApparatuS) is located at point 1, the southern interaction point of the LHC main ring next to the CERN site. The multi-purpose detector has a nearly 4π coverage, which means that it covers almost the entire solid angle. With a length of 45 m and a height of 22 m, it is the largest detector at the LHC. But with a mass of 7000 t it is only the second heaviest detector, lighter than the CMS detector [17] having a mass of 12 000 t. It is built in a cylindrical symmetry, with a barrel part around the interaction point and end-caps at each end of the beam pipe. A cut-away view of the detector is illustrated in Figure 3.2. The following information are mainly taken from reference [16].

Its main task is the reconstruction of the primary interactions in the proton-proton collisions. In order to detect the different particle types created at these collisions, a mixture of several sub-detectors is required which are able to measure the different properties of the particles.

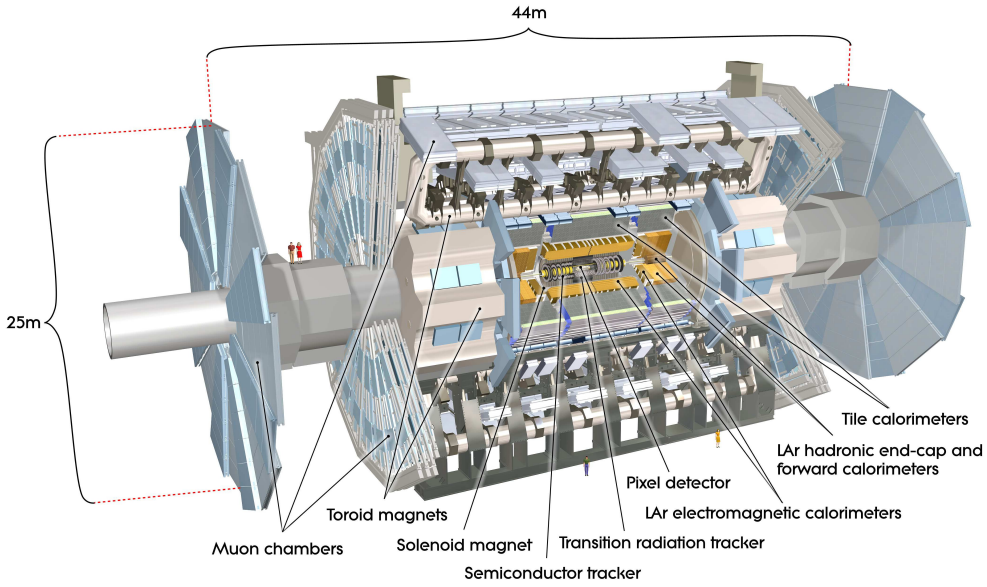

Figure 3.2: Cut-away view of the ATLAS detector [16].

The sub-detectors of ATLAS are assembled in an onion shell structure. Next to the beam pipe reside the high resolution tracking detectors, capable of measuring the momenta, charges and directions of charged particles, and also to reconstruct the primary and secondary vertices of the interactions (Section 3.2.3). The tracking device is followed by the calorimeter system, which measures the energy of almost all particles by completely absorbing them (Section 3.2.4). The outermost layer is the muon tracking system (described in Section 3.2.5) measuring the momenta of the muons, which are the only particles that traverse the whole detector while retaining nearly their whole energy due to their highly penetrating behaviour. ATLAS is equipped with two different magnet systems (Section 3.2.2): a solenoid providing the magnetic field with up to 2 T for the inner tracking detector and a toroid generating a magnetic field with up to 1 T for the muon tracker.

3.2.1 Coordinate system

Due to the cylindrical symmetry, it is common to use a cylindrical coordinate system in the description of positions and directions of particles at ATLAS. The z coordinate describes the position along the beam pipe, whereas a positive z value represents points in the clockwise direction of the LHC ring. ϕ describes the azimuthal angle in the x-y plane and Θ denotes the polar angle between the beam pipe and the particle direction. Particles created in the proton-proton collisions can have large boosts along the z-axis, whilst the angle Θ is not invariant under boosts in this direction. Therefore one commonly uses

the pseudorapidity

$$\eta = -\ln\left(\tan\frac{\Theta}{2}\right), \tag{3.3}$$

which, in the massless limit, is equal to the rapidity y defined as

$$y = \frac{1}{2}\ln\frac{E+p_z}{E-p_z}\ . \tag{3.4}$$

E and p_z denote the particles energy and longitudinal component of the momentum, respectively. In contrast to the polar angle Θ, differences in the rapidity y are invariant under Lorentz boosts. This can be seen by first rearranging the rapidity formula to

$$y = \ln\left(\frac{\sqrt{E+p_z}}{\sqrt{E-p_z}}\right) = \ln\left(\frac{E+p_z}{E^2-p_z^2}\right) = \ln\left(\frac{E+p_z}{\sqrt{p_T^2+m^2}}\right)\ . \tag{3.5}$$

The last equality derives from splitting the momentum $\vec{p}$ in $E^2 = \vec{p}^2 + m^2$ into its longitudinal (p_z) and transverse (p_T) part. When introducing a Lorentz boost with velocity $v = \beta c$ along the z axis, E and p_z transform as:

$$E \to \gamma(E + \beta p_z) \tag{3.6}$$

$$p_z \to \gamma(p_z + \beta E), \tag{3.7}$$

with $\gamma = (1-\beta^2)^{-1/2}$. The insertion of these expressions yields in the boosted rapidity

$$y' = \ln\left(\frac{\gamma(E+p_z)(\beta+1)}{\sqrt{p_T^2+m^2}}\right) = y + \ln\left[\gamma(\beta+1)\right]\ , \tag{3.8}$$

which denotes the sum of the original rapidity y and an additional constant. The difference in the rapidity of two particles is therefore independent of Lorentz boosts along the z axis.
An example of pseudorapidity values for some given polar angles Θ is illustrated in Figure 3.3.

Another common quantity is ΔR which describes the difference of two particle tracks in the η-ϕ space:

$$\Delta R = \sqrt{(\Delta\phi)^2 + (\Delta\eta)^2} \tag{3.9}$$

and which is invariant under Lorentz boosts along the z-axis in case of massless particles, as has been shown above.

Due to the unknown longitudinal momenta of the interacting partons, the particle's

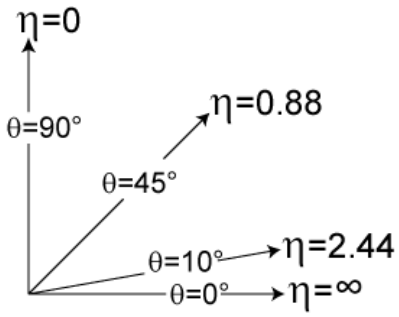

Figure 3.3: Pseudorapidity η for several polar angles Θ [133].

energy E and momenta p are mostly described by their transverse components:

$$p_T = p_x^2 + p_y^2 \tag{3.10}$$

and

$$E_T = E \cdot \sin\Theta \tag{3.11}$$

$$= E \cdot \frac{2\tan\frac{\Theta}{2}}{1+\tan^2\frac{\Theta}{2}} = \frac{2E}{\frac{1}{\tan\frac{\Theta}{2}} + \tan\frac{\Theta}{2}} \tag{3.12}$$

$$= \frac{2E}{e^{-\ln(\tan\Theta/2)} + e^{\ln(\tan\Theta/2)}} = \frac{2E}{e^{\eta} + e^{-\eta}} \tag{3.13}$$

$$= \frac{E}{\cosh\eta} \ . \tag{3.14}$$

The last derivation will be later used in the analysis to calculate the transverse energy of electrons (Section 5.3).

3.2.2 Magnet system

The ATLAS detector features two separate strong magnet systems which are required to bend the tracks of charged particles due to the Lorentz force:

$$\vec{F} = q\left(\vec{v} \times \vec{B}\right) \ . \tag{3.15}$$

Here, q and $\vec{v}$ denote the charge and the velocity of the particle, respectively, and $\vec{B}$ represents the magnetic field vector. By reconstructing the radius and the direction of the curvature it is then possible to determine the charge and momentum of the particle.

The two fields of the ATLAS magnet system are formed of a hybrid system of four super-conducting Al-stabilised NbTi magnets. The whole system has a length of 26 m and a diameter of 22 m and in operation it stores a total energy of 1.6 GJ.

At a distance of ~ 2.5 m to the beam pipe resides the solenoid, which is aligned along the beam axis. It provides a 2 T axial magnetic field for the enclosed inner tracking

detector. In order that particles do not loose too much energy when traversing the solenoid and hence influence the calorimeter performance, a low material thickness of only 0.66 radiation lengths X_0 has been chosen for the solenoid material. The radiation length X_0 describes the mean distance over which an electron loses $1/e$ of its energy by Bremsstrahlung processes when interacting with the detector/magnet material.
The solenoid, with an inner diameter of 2.46 m and an axial length of 5.8 m, consists of a coil mass of 5.4 t and stores 40 MJ energy. Within one day the solenoid material can be cooled down to the operation temperature of 4.5 °K.

The magnetic field for the track measurements in the muon systems is generated by the toroid system, consisting of a barrel toroid and two end-cap toroids, which provides a toroidal magnetic field with strengths of 0.5 T and 1 T in the central and end-cap regions, respectively. In the barrel region, the toroid magnet consists of eight coils encased in individual racetrack-shaped, stainless-steel vacuum vessels with a total length of 25.3 m and inner and outer diameters of 9.4 m and 20.1 m, respectively. The conductor bases on pure Al-stabilised NbTiCu conductors winded into pancake-shaped coils. A total energy of 1.1 GJ is stored in the whole toroid magnet system which weighs about 830 t. For the cooling down to the operation temperature of 4.6 °K it takes up to five weeks.
The toroids in the end-cap regions have a similar shape and optimise the bending power for the muon system end-caps. Each toroid end-cap consists of eight flat, square coil units and eight keystone wedges, and weighs 240 t.
The geometry of the magnet windings is illustrated in Figure 3.4.

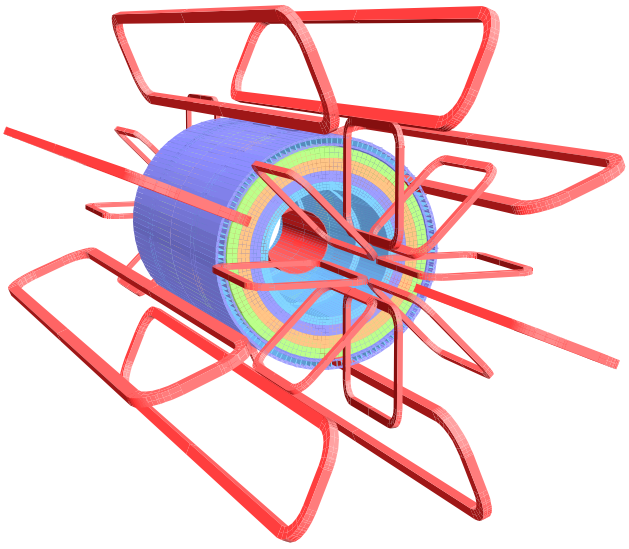

Figure 3.4: Geometry of magnet windings [16]. Visible are the eight barrel toroid coils, together with the end-cap coils. The solenoid winding lies inside the calorimeter volume.

The cooling of the ATLAS magnet system is provided by a complex cryogenics system. A control dewar with a capacity of 250 l stores the liquid helium for the solenoid, which

is cooled by a direct Joule-Thomson flow (see for example reference [134] for further reading).
For the toroids, a forced flow of boiling helium is used for the cooling, whereas the liquid helium is stored in a storage dewar with capacity of 11 000 l.

3.2.3 Inner detector

There are $\sim$ 1000 particles emerging from the collision point every 25 ns (at LHC design parameters), which results in a very large track density in the detector. In order to reconstruct the momenta and vertices with high resolution, the inner tracking detector (ID), illustrated in Figure 3.5, provides high precision measurements with a very fine granularity. In total, the ID has a length of 5.3 m and a diameter of 2.5 m and covers

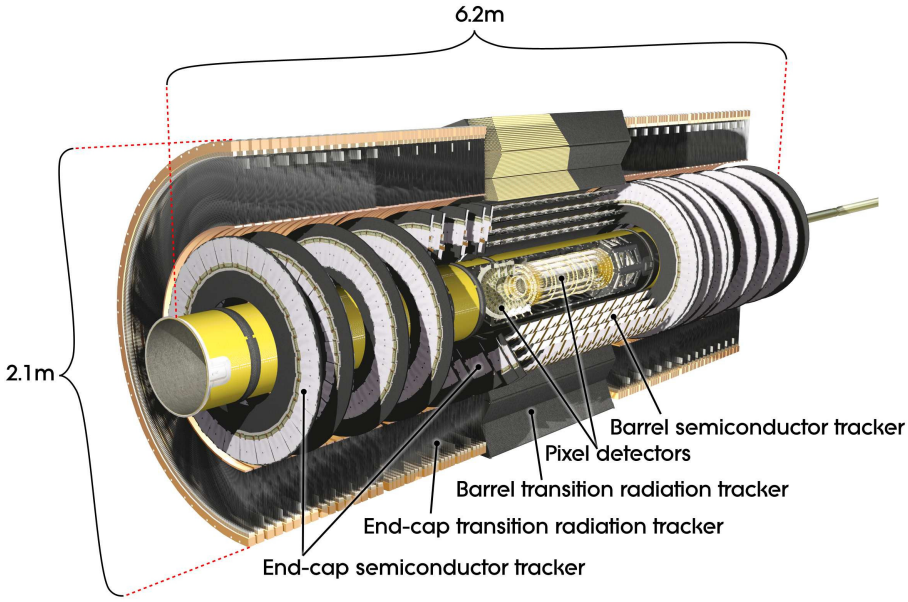

Figure 3.5: Cut-away view of the ATLAS inner detector [16].

a pseudorapidity range of $|\eta| < 2.5$. Its task is the reconstruction of the momenta and charges of the particles and to determine the location of primary and secondary vertices. For this purpose, three sub-detectors are collaborating, the pixel detector, the Semiconductor Tracker (SCT) and the Transition Radiation Tracker (TRT), whereas the latter one also provides the capability of the identification of particles due to the transition radiation.

In reference [135] the momentum resolution of the inner detector has been determined using a simulation of muons traversing the ID. Muons have been chosen, because these particles are a good representation of the ideal case, that there are no interactions other than multiple scattering. The $1/p_T$ resolution was expressed by a simple parametrisation

and has the form

$$\sigma\left(\frac{1}{p_T}\right)[\mathrm{TeV}^{-1}] = 0.36 \oplus \frac{13}{p_T[\mathrm{GeV}]\sqrt{\sin\Theta}}, \tag{3.16}$$

where the coefficients (0.36 and 13) were determined from tracks in the barrel with transverse momenta of 1 GeV and 1 TeV.

Figure 3.6 illustrates two charged tracks traversing a quarter part of the ATLAS inner detector. In the barrel region, only the parts of the pixel and SCT are shown. In the following further details of the three sub-detectors are presented.

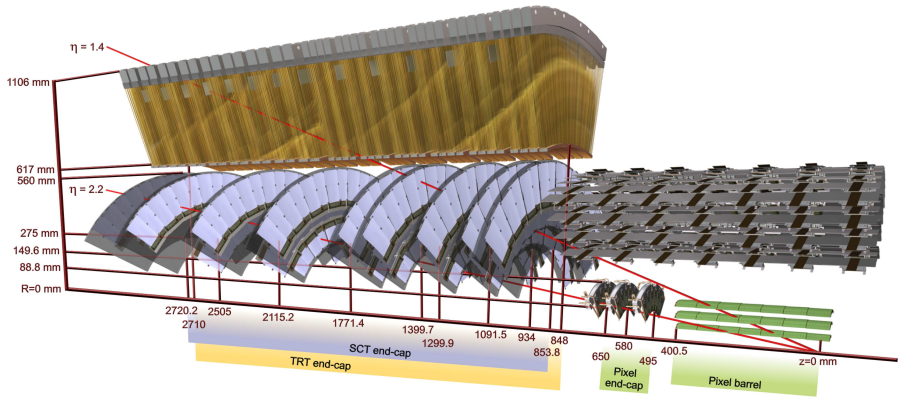

Figure 3.6: A view of a quarter of the ATLAS inner detector is shown [16]. The figure presents quarter views of the pixel and SCT barrel parts and the end-cap disks of pixel, SCT and TRT.

3.2.3.1 Pixel detector

The pixel detector, illustrated in Figure 3.7a, denotes the inner-most part of the ATLAS inner tracking system. Its main target is the reconstruction of primary and secondary vertices, which is essential for the identification of jets arising from b-hadron decays (b-jets). For this purpose, a spatial resolution of only $\sim 10\,\mu\mathrm{m}$ is required.

The main component of the pixel detector is the 'sensor', which is a 250 µm thick, oxygenated n-type wafer, designed to meet the requirements in radiation hardness and resolution. Each sensor, with an area of $63.4 \times 24.4\mathrm{mm}^2$, consists of 47232 semi-conducting silicon pixels each with a size of $50 \times 400\mu\mathrm{m}^2$. The silicon pixels are operated at a bias voltage between 150 V and 600 V, depending on the received radiation.
Each sensor constitutes the main part of a pixel module, which is shown in Figure 3.7b. On each module the pixels are bump-bonded using solder (PbSn) and indium (In) technologies to elements of the integrated circuits in the front-end (FE) chips, where 16 FE chips are connected to one pixel module. In addition, each module is equipped with a Module Control Chip (MCC), that reads out the 2880 channels of each FE chip, resulting in $16 \times 2800 = 46080$ readout channels per module. In total there are 1744 pixel

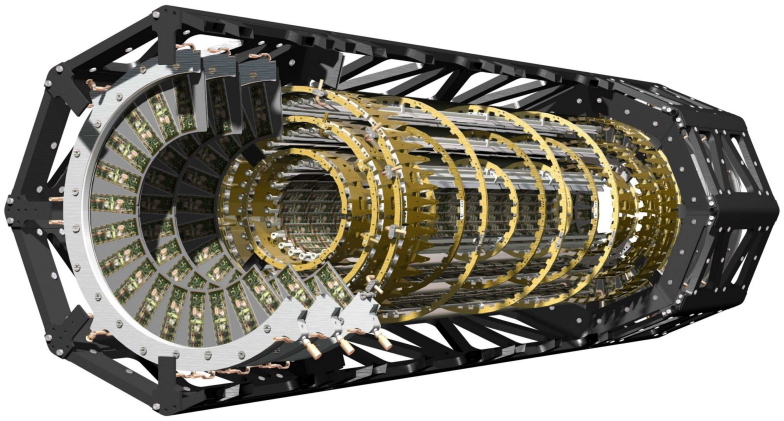

(a) ATLAS pixel detector

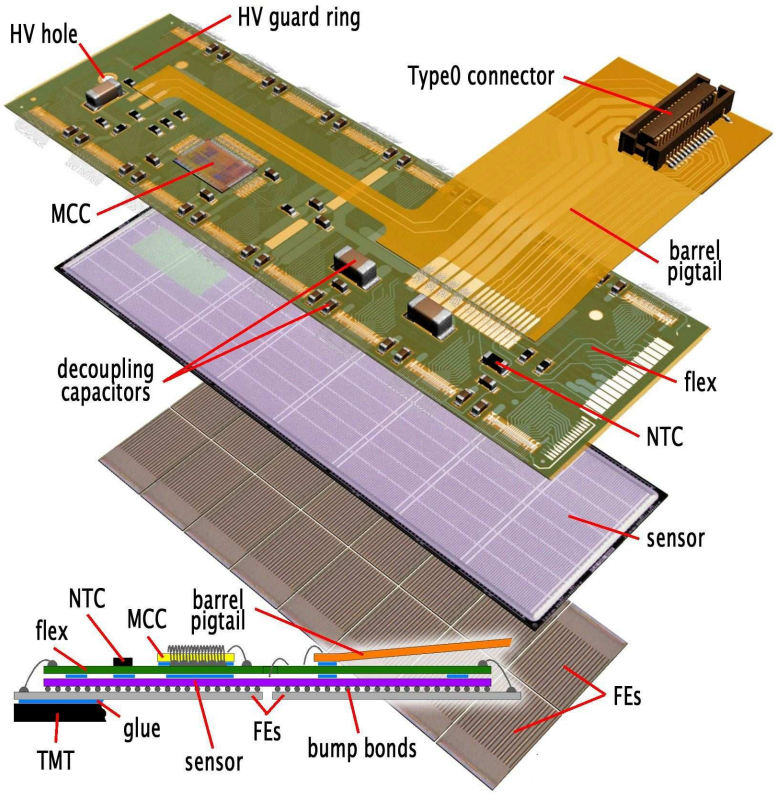

(b) ATLAS pixel module

Figure 3.7: A cut-away view of the ATLAS pixel detector is presented in (a), whereas (b) shows a pixel module [16].

modules arranged in three barrel layers and two end-caps, whereas each end-cap consists of three disk layers. Combining all pixels of the detector results in a total of 80.4 million readout channels.

Using a test beam, the spatial resolution of an individual pixel module has been determined in reference [136] to be between 12 µm and 6 µm for incidence angles between 0° and 15°, respectively. The reason for a better resolution at non-zero incidence angle can be explained by the fact, that the traversing particle hits more than one pixel. For the track reconstruction all pixels with a signal height above a given threshold are combined to pixel clusters. The information of each individual pixel can be used to determine the cluster centre with a higher precision, than in the case of a single pixel hit which mainly occurs at normal incidence.

The three barrel layers are made of 112 staves, each having a total length of $\approx 80\,\text{cm}$ and holding 13 modules in a row, and are located at radial distances of 50.5 mm, 88.5 mm and 122.5 mm to the beam pipe. The layer closest to the beam pipe is also referred to as 'b-layer', because it provides the critical information for the identification of b-jets. In order to provide an optimal incidence angle for a high spatial resolution and having a full coverage in the ϕ space, the staves are tilted by an angle of $-20\,^\circ$ defined via the tangent of the cylinder surface perpendicular to the cylinder axis.
Each of the end-cap disks, having an area of $\approx 29\,\text{cm}^2$, consists of eight sectors, whereas each is composed of six pixel modules. The end-cap disks on each side have the following distances to the interaction point: 49.5 cm, 58.0 cm and 65.0 cm.

With the three barrel layers and the three disks on each side, a particle traversing the pixel detector creates at least three hits in the pixel system, which can be used to reconstruct the primary and secondary vertices.

3.2.3.2 Semiconductor Tracker

Starting from the beam pipe, the pixel detector is followed by the semiconductor tracker (SCT). Its main component, the 15912 SCT sensors, each consist of 770 semiconducting silicon micro-strips with a length of 6 cm and a strip pitch of 80 µm. The 285 µm thick sensors are operated with bias voltages between 150 V and 350 V.

An SCT module, as shown in Figure 3.8, is made of four sensors, two each glued on the top and bottom side of the thermal pyrolitic graphite (TPG) base board. The top and bottom sensors are daisy-chained together and rotated by an angle of 40 mrad, as it can be seen in Figure 3.8b. With an orientation along the beam pipe, the rotated sensors allow to measure both coordinates in the $r-\phi$ plane. Using a test beam, the spatial resolution at normal incidence has been determined to be 17 µm in the lateral $r-\phi$ plane and 580 µm in the longitudinal z direction.

In total, the SCT consists of 4088 modules resulting in 6.3 million readout channels, whereas 2112 modules are arranged on the four cylindrical barrel layers and 1976 modules are distributed over the two end-caps with 9 disks each. This setup allows to measure at least four space-points (in eight strip layers) of a charged particle traversing the SCT. The SCT barrel layers reside at radial distances between 284 mm and 498 mm.

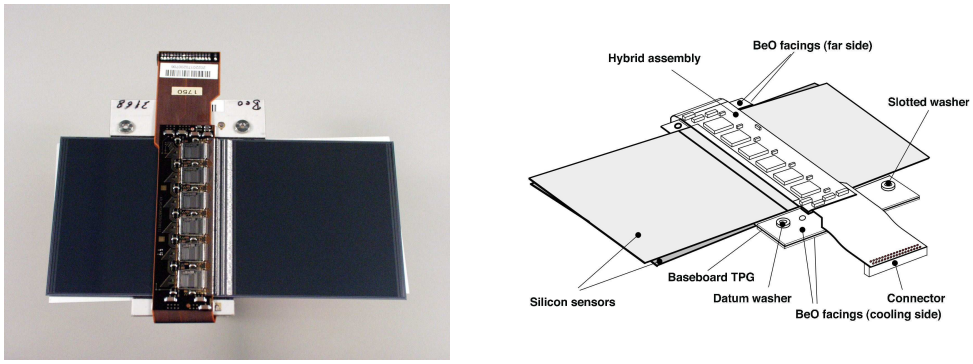

(a) (b)

Figure 3.8: ATLAS semiconductor tracker module [16].

3.2.3.3 Transition Radiation Tracker

The outer-most part of the inner detector is the Transition Radiation Tracker (TRT), which is a multi-wire proportional chamber with a total of 298304 drift tubes (also called straws). Each drift tube, with 4 mm of diameter and a length of 144 cm in the barrel and 37 cm in the end-caps, contains a 31 µm diameter tungsten anode wire and is operated at 1530 V. The straws, with a hit resolution of 130 µm per straw, are filled with a mixture of xenon (70%), carbon dioxide (27%) and oxygen (3%).

The straws are arranged in 73 barrel layers and 160 end-cap planes, whilst the drift tubes are interleaved with fibres and foils in the barrel and end-cap, respectively, in which traversing particles will create transition radiation. In addition to the drift tube measurement, the gas mixture allows to measure this transition radiation and, depending on the signal height, to identify the particle type.

In the barrel, between 329 and 793 straws are arranged on a TRT module, whereas an end-cap module is made of 6144 straws. These modules consist of a carbon-fibre laminate shell, where the straws are embedded in an uniform axial array with a mean spacing of ~ 7 mm.
The TRT barrel is composed of three rings, each with 32 modules, whilst the drift tubes are oriented parallel to the beam axis. All barrel rings cover radial distances between 563 mm and 1066 mm.
In the end-cap, there are two sets of independent wheels. The first set, closest to the interaction point, is made of 12 wheels each with eight drift tube layers and a spacing of 8 mm. Eight wheels with each eight drift tube layers form the outer wheel set, whilst each layer is composed of 766 radially oriented straws.

In total, the TRT provides 351000 readout channels. It covers an η range of $|\eta| < 2.0$ and a charged particle will produce typically 36 TRT hits, which can be used to reconstruct the particles track.

3.2.4 Calorimeters

In the previous section, I presented the inner tracking system, which allows to measure the interaction vertices and tracks of charged particles. The ATLAS calorimeter system measures the energies of the particles and also allows to detect uncharged particles like photons or neutrons.

At ATLAS it has been chosen to use sampling calorimeters. This calorimeter type is made of alternating layers of absorber and active material.

The ATLAS calorimeter system, as shown in Figure 3.9, covers a range of $|\eta| < 4.9$ and encloses the inner detector and solenoid magnet. It consists of two calorimeters: an electromagnetic calorimeter with fine granularity, optimised for measuring electrons and photons, and a hadronic calorimeter with coarser granularity which is sufficient for measuring hadronic particle jets.

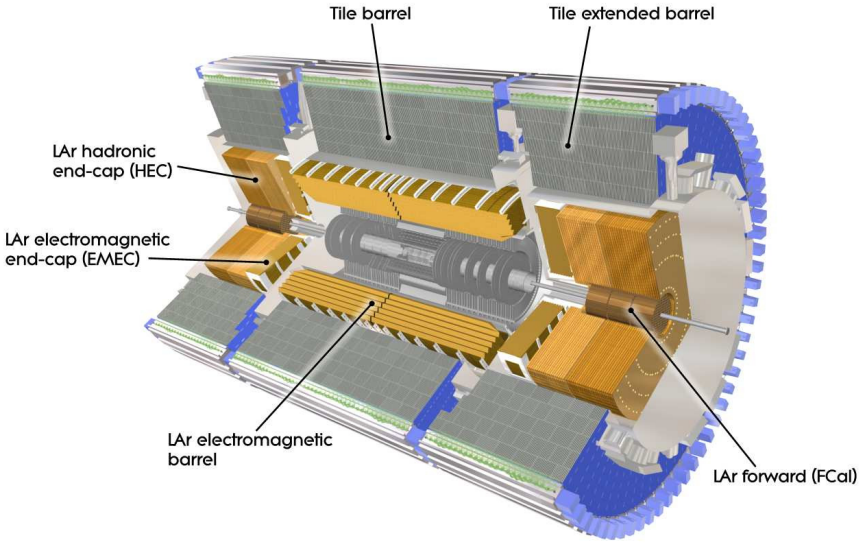

Figure 3.9: Cut-away view of the ATLAS calorimeter system [16].

3.2.4.1 Electromagnetic calorimeter

The ATLAS electromagnetic calorimeter (ECAL), optimised for the energy measurement of electrons and photons, is made of lead as absorber and liquid argon (LAr) as active detection material. Its alternating layers of absorber and Kapton electrodes, each enclosing a $\sim 2.1\,\text{mm}$ gap filled with LAr, are arranged in an accordion shape in order to provide a full coverage in the ϕ space without any gaps.

The ECAL is composed of a barrel part, covering the range $|\eta| < 1.475$, and two end-caps in the range $1.375 < |\eta| < 3.2$, whilst each part is placed in an own cryostat. Its thickness has been chosen to achieve radiation lengths X_0 of $> 22\ X_0$ and $> 24\ X_0$ in the barrel and end-cap, respectively.

The barrel is divided into two half-barrels with a small gap of 4 mm in between at $\eta \approx 0$. Each of the half-barrels contains 1024 lead absorber plates and has a length of 3.2 m and inner and outer diameters of 2.8 m and 4 m, respectively.
The end-caps are each divided into two coaxial wheels, which cover the η ranges $1.375 < |\eta| < 2.5$ and $2.5 < |\eta| < 3.2$. Between the barrel and the end-caps, at $1.37 < |\eta| < 1.52$, there is a gap which is used as service area for cables. In this region, also called 'crack region', traversing particles can produce a large amount of secondary particles, which influence the particle reconstruction. Hence electrons traversing this 'crack-region' are not considered in many ATLAS analyses.

In the region of $|\eta| < 2.5$, the ECAL surrounds the inner detector, which allows for precise reconstruction algorithms that combine the measured information of ECAL and ID. In this region the ECAL is segmented into three sections/layers, where the granularity is getting coarser with increasing radial distance. A sketch of the calorimeter cells in such a barrel ECAL calorimeter module is presented in Figure 3.10. The first

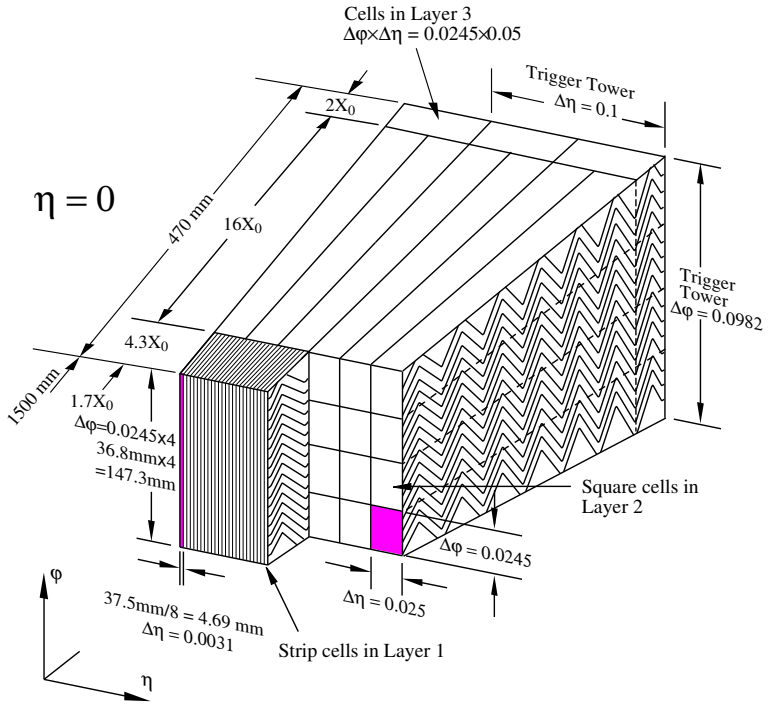

Figure 3.10: Sketch of an ATLAS LAr electromagnetic calorimeter module, showing the granularity in η and ϕ for the three barrel layers [16].

layer is used as preshower detector to separate photons from electrons and has a very fine segmentation. Most cells are formed as strips with cell sizes in η and ϕ of $\Delta\eta = 0.025/8$ and $\Delta\phi = 0.1$. At the edges of barrel and end-caps, the cells appear with coarser granularities of up to $\Delta\eta \times \Delta\phi = 0.05 \times 0.1$. In the second layer, all cells have an equal square size of $\Delta\eta \times \Delta\phi = 0.025 \times 0.025$ and nearly cover the full range of $|\eta| < 2.5$. This layer is supposed to collect the largest fraction of the energy of the

electromagnetic calorimeter. The cells in the third layer have the coarsest granularity of $\Delta\eta \times \Delta\phi = 0.05 \times 0.025$.
Between the solenoid and the first layer, the ECAL is extended by a presampler detector in the region $|\eta| < 1.8$. The presampler consists of no lead absorbers and only of one LAr layer with a thickness of 1.1 cm and 0.5 cm in the barrel and end-cap region, respectively. Its purpose is to correct for the energy loss of electrons and photons in the inner detector and the solenoid magnet.

In reference [137], the energy resolution of the ECAL has been measured using a test beam on a prototype of the calorimeter. For electrons with $\eta = 0.28$, the parametrised resolution was obtained to be

$$\frac{\sigma_E}{E} = \frac{9.99\%}{\sqrt{E[\text{GeV}]}} \oplus \frac{28.2\%}{E[\text{GeV}]} \oplus 0.35\%, \tag{3.17}$$

where the first term describes the statistical fluctuations in the development of the shower, the second term includes the uncertainties due to electronic noise and the last term describes the constant systematics, like inhomogeneities in the calorimeter response.

3.2.4.2 Hadronic calorimeter

The hadronic calorimeter (HCAL) of ATLAS is split into three parts: a tile barrel, LAr hadronic end-caps (HEC) and LAr forward calorimeters (FCal), and is responsible for measuring the energies of hadronic particle jets. Its material thickness has been chosen to achieve hadronic interaction lengths λ_{hadr} of 9.7 λ_{hadr} and 10 λ_{hadr} in the barrel and end-cap parts, respectively.

The tile barrel is divided into a central barrel with a length of 5.8 m and two extended barrels, each having a length of 2.6 m. All three tile barrels have an inner and outer radius of 2.28 m and 4.25 m, respectively. The tile barrels are placed directly outside the ECAL and cover the η range of $|\eta| < 1.0$ for the central barrel and $0.8 < |\eta| < 1.7$ for the extended barrels. Each barrel, made of a sampling calorimeter using steel as absorber and scintillating plastic tiles as active material, is subdivided into three layers with different cell sizes. The former two layers have a granularity of $\Delta\eta \times \Delta\phi = 0.1 \times 0.1$, whereas the third layer has a coarser granularity of 0.2×0.1.

The LAr hadronic end-cap (HEC) covers the range $1.5 < |\eta| < 3.2$ and is composed of two wheels per end-cap, directly placed behind the ECAL end-caps. There is an overlap with the tile barrel and the forward calorimeter (described below), which is supposed to increase the material density in this region.
Each HEC wheel is composed of 32 wedge-shaped calorimeter modules arranged in two layers. In total there are four layers per end-cap with granularities of $\Delta\eta \times \Delta\phi = 0.1 \times 0.1$ and 0.2×0.2. The wheels closest to the interaction point are made of sampling calorimeter modules with 25 mm thick copper plates interleaved with 8.5 mm LAr gaps, whereas the wheels further away have copper plates with a thickness of 50 mm.

The farthermost part of the HCAL is the LAr forward calorimeter (FCal), which covers the range $3.1 < |\eta| < 4.9$. Its two end-caps are each composed of three modules with LAr as active material but different absorbers. Each module is composed of concentric

rods and tubes parallel to the beam axis, where the LAr is filled in the gaps in between. The first module contains copper plates as absorber with cell sizes in x and y of $\Delta x \times \Delta y = 3.0 \times 2.6$ cm^2 and is optimised for electromagnetic measurements. The latter two modules are formed of tungsten absorbers and are optimised for measuring the energies of hadronic interactions. The cells of the second and third module have sizes of $\Delta x \times \Delta y = 3.3 \times 4.2$ cm^2 and 5.4×4.7 cm^2, respectively.

The energy resolution of the HCAL has been measured in reference [138] using a test beam with pions on a HCAL prototype (consisting of tile and LAr modules) and is expressed in the same parametrisation as in Equation (3.17):

$$\frac{\sigma_E}{E} = \frac{38.3\%}{\sqrt{E[\text{GeV}]}} \oplus \frac{3.06}{E[\text{GeV}]} \oplus 1.62\% \ . \tag{3.18}$$

3.2.5 Muon spectrometer

In the previous section, I described the ATLAS calorimeter system. The ECAL and HCAL measure the energies of electrons, photons and hadrons by completely absorbing them. However, high energetic muons traverse the whole ATLAS detector while loosing only a small amount of energy and therefore can pass the ATLAS calorimeters. One source of energy loss is ionisation, which can be described by the Bethe-Bloch formula [139] plotted in Figure 3.11. The curve shows the stopping power $\langle -dE/dx \rangle$, which

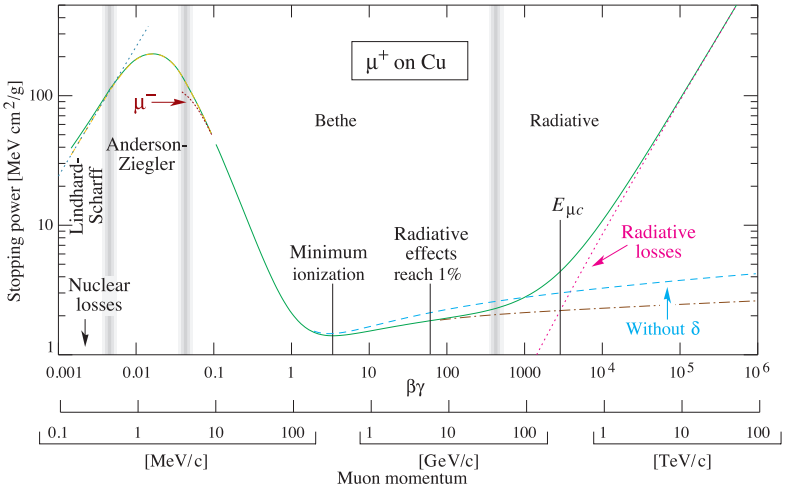

Figure 3.11: Stopping power $\langle -dE/dx \rangle$ for positive muons in copper as a function of the muon momentum [39]. The solid curve indicates the total stopping power.

in general describes the energy loss dE via ionisation when traversing a distance dx in a specific material. Here, the plot shows the behaviour of the stopping power for positive muons in copper as a function of the muon momentum. It can be seen that in the momentum range of 1 GeV to 100 GeV, the muon stopping power runs through a minimum which means that muons loose only a small amount of energy.

In order to detect the muons that have traversed the whole detector, ATLAS is equipped with a large muon spectrometer (MS) system surrounding the calorimeters and inner tracking detector. The MS, which is shown in Figure 3.12, allows to measure

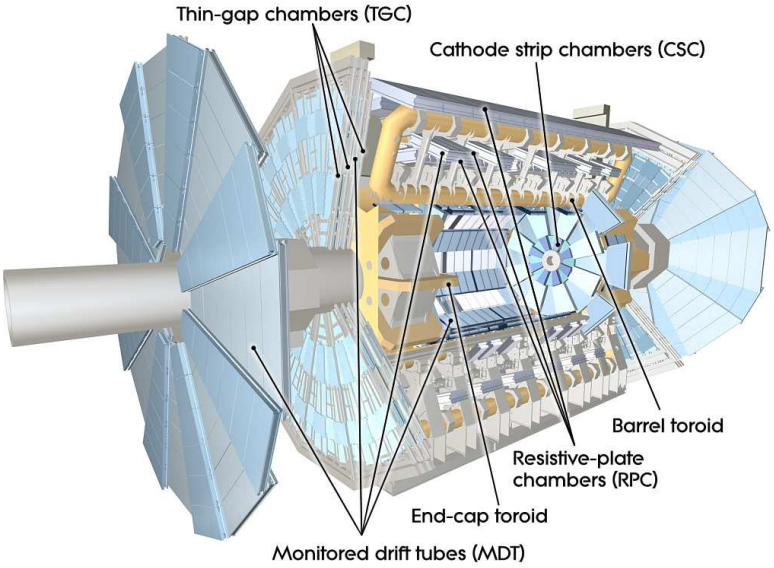

Figure 3.12: Cut-away view of the ATLAS muon system [16].

the tracks and momenta of muons. Similar to the tracks in the inner detector, the muons are deflected by the toroid magnet (see Section 3.2.2), which results in a bending of the muon tracks in the η direction. In addition to the tracking, the MS also provides information for the trigger, which will be explained in Section 3.2.6.

The MS is divided into a barrel and two end-caps. In the barrel, muon tracks are measured in tracking chambers, which are arranged in three cylindrical layers around the beam axis. In each end-cap the chambers are arranged in three layers of planes perpendicular to the beam axis. The ATLAS muon spectrometer is equipped with four different muon chambers, as shown in Figure 3.13, which will be explained in the following.

The high precision muon momentum measurement is performed in the monitored drift tubes (MDT), which cover the entire muon spectrometer range of $|\eta| < 2.7$. The aluminium drift tubes are arranged in three to eight layers, distributed over a total of 1088 chambers, whilst each chamber has a spatial resolution of $\sim 35\,\mu\text{m}$ when measuring the bending in η and the radial coordinate. The tubes, which are oriented along the ϕ direction, each have a diameter of 29.97 mm and are filled with a gas mixture of argon (93%) and carbon dioxide (7%). Between the cathode and the tungsten-rhenium wire anode, a voltage of 3080 V is applied.

The MDT are limited to counting rates of $\sim 150\,\text{Hz/cm}^2$, because of the long drift time of about 700 ns. Higher counting rates would lead to a distortion of the electric field inside the tube and therefore reduce the spatial resolution. The counting rate of

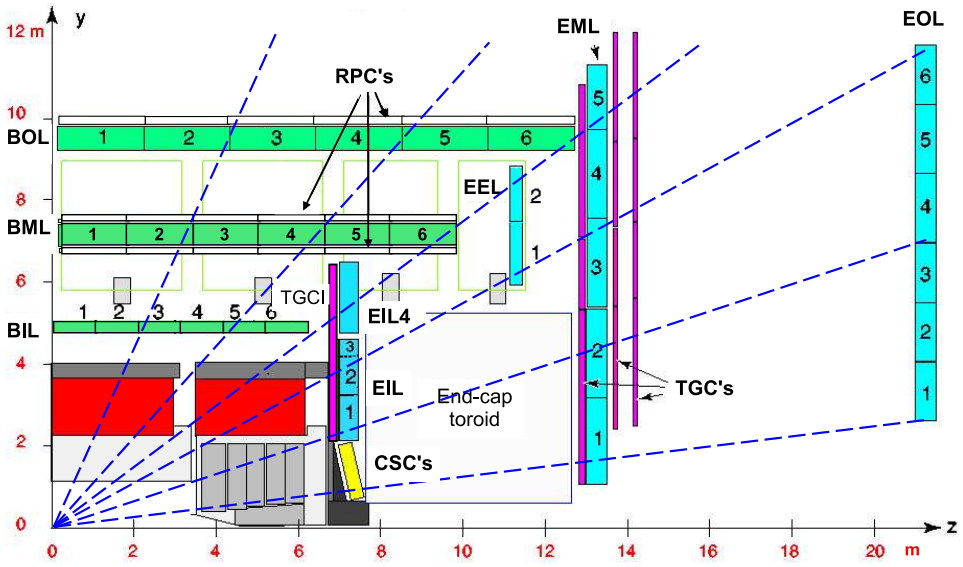

Figure 3.13: Cross-section of the ATLAS muon system in the bending plane along the z-axis [16]. The dashed lines indicate the trajectories of muons with infinite momentum, which typically traverse three muon stations.
BIL, BML, BOL, EIL, EML and EOL denote the inner, middle and outer (I,M,O) MDT chambers in the barrel and end-cap (B,E), respectively.

$\sim 150\,\mathrm{Hz/cm^2}$ is expected to be exceeded in the range $2.0 < |\eta| < 2.7$. Therefore, the first layer of the MDT in this region is replaced by the cathode strip chambers (CSC), which allow counting rates up to $1000\,\mathrm{Hz/cm^2}$. The CSC consist of multi-wire proportional chambers, where the cathode planes are segmented into strips with orthogonal directions. This allows to measure both coordinates η and ϕ. Compared to the MDT, the CSC have a higher time resolution, but a lower spatial resolution of $40\,\mu\mathrm{m}$ per chamber. This is due to the higher granularity, which has been chosen to deal with the larger radiation exposure for $|\eta| > 2.0$.
The CSC are distributed over two disks with eight chambers each. These chambers each contain four CSC planes.

As previously mentioned, the muon spectrometer has a dedicated trigger system. In addition to the tracking chambers, the muon spectrometer is equipped with trigger chambers, which deliver the muon track information in just a few nano-seconds. The MDT and CSC are not capable of triggering, because their drift times are too long. Hence, the MDT and CSC are complemented by two different chamber types. These additional chambers also provide the measurement of the azimuthal ϕ coordinate which is missing in the MDT tracking.

In the region of $|\eta| < 1.05$ the triggering is performed by the resistive plate chambers (RPC). In the barrel, the RPC consist of three concentric cylindrical layers of gaseous

parallel electrode plates around the beam pipe. The three layers are placed at radial distances of 7, 7.5 and 10 m, where the inner two layers are optimised for triggering muons with low transverse momenta (p_T) of $6 - 9$ GeV and the outer layer focuses on the triggering of high p_T muons with momenta of $9 - 35$ GeV.
The RPC each are composed of two parallel resistive plates at a distance of 2 mm, which are made of phenolic-melaminic plastic laminate. Between the two plates, a potential of 4.9 kV/mm is applied and the gap is filled with a gas mixture of $C_2H_2F_4$ (94.7%), iso-C_4H_{10} (5%) and SF_6 (0.3%).

In the higher η range of $1.05 < |\eta| < 2.7$, the RPC is complemented by the thin gap chambers (TGC). The TGC are composed of multi-wire proportional chambers with a wire-wire spacing of 1.8 mm and a cathode-wire distance of 1.4 mm. Each chamber consists of graphite cathode planes and tungsten-gold wires with a potential of 2900 V. The volume between the plates is filled with a gas mixture of carbon dioxide and n-C_5H_{12} (n-pentane).

The muon momentum resolution has been measured using cosmic ray data taken in the years 2008 and 2009 in reference [140]. The resolution function was fitted to the measured data and found to be

$$\frac{\sigma_{p_T}}{p_T} = \frac{0.29}{p_T[\text{GeV}]} \oplus 4.3\% \oplus (4.1 \times 10^{-4})\ \text{GeV}^{-1} \times p_T, \tag{3.19}$$

where the first term denotes the energy loss correction, the second term considers the multiple scattering and the third term stands for the intrinsic resolution.

3.2.6 Trigger system and data acquisition

As previously mentioned, the LHC delivers a bunch crossing rate at the collision points of 40 MHz at its design luminosity of $L \approx 10^{34}\ \text{cm}^{-2}\text{s}^{-1}$. Given the large number of readout channels of all sub-detectors and the maximum rate of writing events on disk of about $200 - 400$ Hz, it is obvious that a pre-selection of events is required. This is performed by the trigger system. An optimal solution is a system separated in several trigger stages, where each stage refines the decisions made at the previous stage and therefore successively reduces the event rate. At ATLAS, a three-level trigger system was chosen, which is composed of the level 1 trigger (L1), the level 2 trigger (L2) and the event filter (EF), as shown in Figure 3.14. The first level L1 bases on a hardware trigger, whereas the latter two levels, L2 and EF, form the software based high level trigger (HLT).
Processes with very high cross-sections, e.g. QCD jet production, appear with very high event rates, although such events are not of interest for most physics analyses at ATLAS. Therefore, the trigger system filters the 'non-interesting' events and reduces the event rates to a level which can be handled by the readout system. This is depicted in Figure 3.15. After each trigger level the event rate is reduced, which also provides more processing time for the following trigger level and allows to run more complex analysis routines. The three different trigger levels will be explained in further detail in the following.

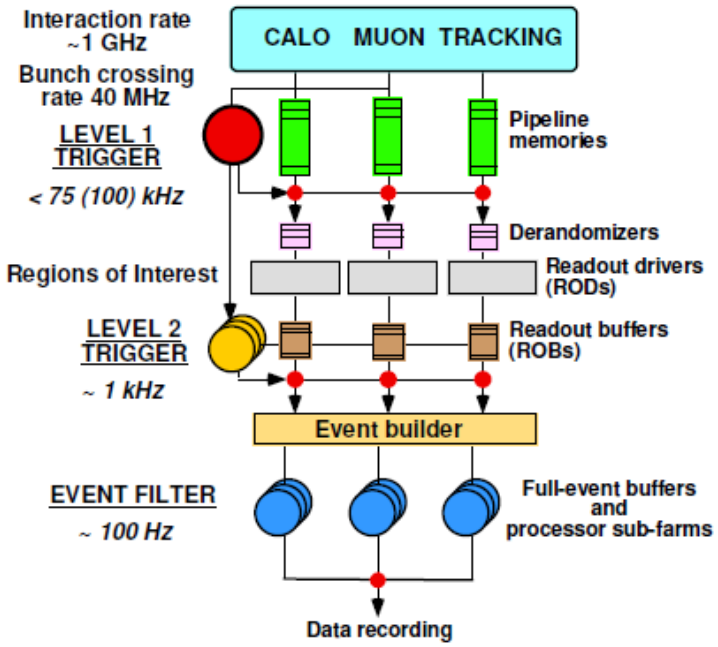

Figure 3.14: Overview of the three-level ATLAS trigger system [141].

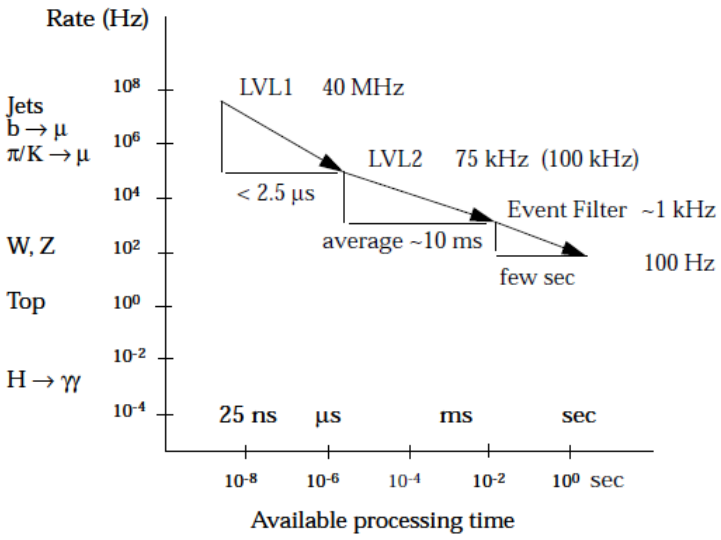

Figure 3.15: Event rates versus event processing time [135].

The first trigger level, the L1 trigger shown in Figure 3.16, analyses all events at the bunch crossing rate of 40 MHz. It bases on a hardware trigger and only uses the information of the muon trigger chambers, RPC and TGC, and the calorimeter subsystems. Hence, the L1 trigger only searches for muons with high momenta and objects that deposit energy in the calorimeters, namely electrons, photons, taus and jets. Using

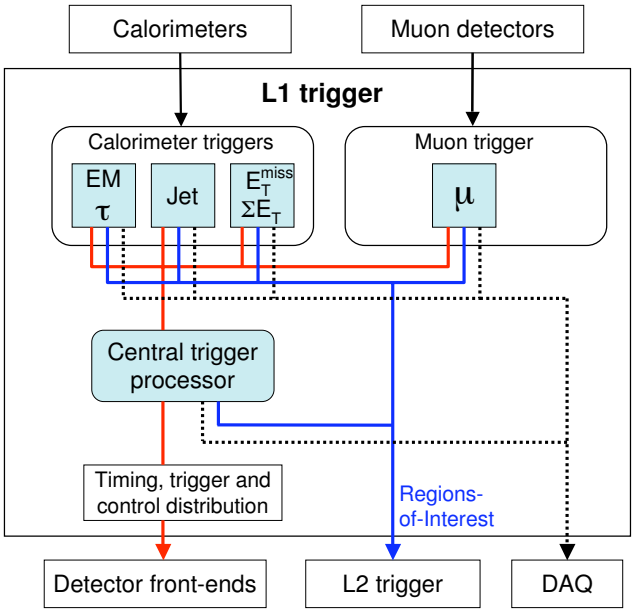

Figure 3.16: Block diagram of the ATLAS level 1 trigger [16].

the overall calorimeter information, the L1 also allows to trigger events with missing transverse energy E_T^{miss} and large total transverse energy sums. Finally, the L1 also allows to trigger on isolated electrons, photons and taus by requiring a minimal angular separation of the significant energy deposits in the electromagnetic calorimeter.
In the L1 trigger, the accept decision is made by the central trigger processor (CTP) with a rate of up to 75 kHz (this is upgradeable to 100 kHz when the LHC is running with higher luminosity in the future), which is the maximum that the whole detector readout system can handle. The decision is then distributed to the detector readouts and front-ends via the 'timing, trigger and control distribution' system (TTC). Furthermore, the geometric location of the triggered objects is provided to the L2 trigger as so-called regions of interest (RoI) and the event data is temporarily buffered in the data acquisition system (DAQ). There, the event data first passes the readout drivers (ROD) and is then transferred to the 1574 readout buffers (ROB), where the event information is then accessible by the subsequent trigger stages. In total, the L1 trigger works with a latency for the decision of less than 2.5 µs.

When accepted by the L1 trigger, the selected regions of interest seed the L2 trigger. It has access to the full granularity and precision of all sub-detectors (ID, calorimeters and MS), but only analyses the event information in the specific regions. The L2 reduces

the event rate to less than 3.5 kHz and works with a latency of $10 - 40$ ms.

If an event has passed the L2 trigger, it is processed in the event builder and then passed to the event filter. The EF has access to the full event information over the whole detector acceptance region. With a latency of few seconds it can already run complex offline analysis routines for a further event selection. After the EF, the event rate is reduced to $\lesssim 200$ Hz, which is recordable on disk.

3.2.7 Luminosity measurement

An accurate luminosity determination is very important in ATLAS physics analyses. Not only precision SM measurements require a precise luminosity measurement, but also searches for new physics rely on it in order to evaluate the background rates and determine the sensitivity.

The luminosity measurement method at ATLAS, which is explained in reference [142], is based on determining the interaction rate of inelastic scatterings with independent detectors and calibrating the luminosity scale with so-called van der Meer (vdM) scans [143].

In general, the luminosity can be written as [142]

$$L = \frac{\mu_{\text{vis}} n_b f_r}{\sigma_{\text{vis}}}, \tag{3.20}$$

where μ_{vis} denotes the observed interaction rate per bunch crossing by a specific detector, n_b is the number of colliding bunch pairs, f_r the revolution frequency and σ_{vis} defines the visible cross-section, which depends on the total inelastic cross-section σ_{inel} and the particular detector efficiency ϵ: $\sigma_{\text{vis}} = \epsilon \cdot \sigma_{\text{inel}}$.

The only unknown quantity is the visible cross-section, whose determination is explained in the following.
The delivered luminosity of the accelerator can be written as

$$L = f_r \cdot \frac{n_b n_1 n_2}{4\pi \sigma_x \sigma_y}, \tag{3.21}$$

where $\sigma_{x/y}$ denote the beam widths in the x and y direction. These can be determined with the vdM scan, in which the beams are separated by steps of known distance. The bunch populations n_1 and n_2 are measured externally. During the vdM scan, the peak interaction rate $\mu_{\text{vis}}^{\text{max}}$ is measured by the independent detectors. Combining above ingredients allows to determine the visible cross-section:

$$\sigma_{\text{vis}} = \mu_{\text{vis}}^{\text{max}} \cdot \frac{2\pi \sigma_x \sigma_y}{n_1 n_2}, \tag{3.22}$$

which can then be used to determine the luminosity for the unseparated beams in Equation (3.20).

For the determination of the interaction rates μ_{vis}, ATLAS currently uses two independent detectors, which measure the rates bunch-by-bunch: LUCID [144] and BCM

[145].
LUCID (LUminosity measurement using a Cherenkov Integrating Detector) is a Cherenkov detector placed with a distance of 17 m on each side of the interaction point. It consists of 16 aluminium tubes filled with a gas mixture of C_4F_{10}. The tubes surround the beam pipe and are oriented along the z axis, whereby LUCID covers the region $5.6 < |\eta| < 6.0$. Charged particles, traversing the gas mixture, create Cherenkov photons, which are then collected using photo multipliers (PMT).
The second detector used is BCM (Beam Conditions Monitor), which consists of four diamond sensors on each side of the interaction point. Its main purpose is to monitor the beam conditions and to issue a beam-abort request in case of a possible damage to the ATLAS detector. However, it also allows to measure the bunch-by-bunch interaction rates at a specific pseudorapidity of $|\eta| = 4.2$.
In addition to LUCID and BCM, there are also measurements from the Tile and forward hadronic calorimeter used for cross-checking the results from the former two detectors.

Another luminosity detector, which is still not fully commissioned yet, is ALFA (Absolute Luminosity For Atlas) [146], which allows an absolute luminosity measurement and is supposed to replace the vdM scan in the near future. It is located at a distance of 240 m on both sides of the interaction point and allows to measure the elastic scattering rates at very small angles ($\sim 3\,\mu$rad) in special calibration runs. With the precisely known cross-sections of these elastic scattering processes, it is then possible to directly determine the luminosity using the optical theorem (see for example reference [147] for further reading).
At ALFA, a Roman-Pot technique is being used, which means that the detector volume (the pot) is separated from the accelerator vacuum, but can be moved very close to the beam pipe (~ 1 mm). For the detection, a scintillating-fibre tracker is used inside the pot.

3.2.8 Performance of the LHC and ATLAS

After the previously mentioned incident, few days after the LHC start in 2008, it took more than one year to repair the machine and install additional protection systems. Then, in 2009, the LHC restarted with first proton-proton collisions, in the beginning with a centre-of-mass energy of $\sqrt{s} = 1.8$ TeV which then was subsequently increased to $\sqrt{s} = 2.1$ TeV and $\sqrt{s} = 2.36$ TeV.

Finally, in 2010, the LHC delivered the first proton-proton collisions at $\sqrt{s} = 7$ TeV, which should be used to perform the first physics analyses. In total, the LHC delivered an integrated luminosity of $\mathcal{L} = 45\,\text{pb}^{-1}$.

The data taking continued in 2011 with the same centre-of-mass energy. Over the year, further improvements have been achieved to the beam parameters, resulting in a maximum number of colliding bunch pairs of 1380 and a bunch spacing of 50 ns. Each bunch had a proton population of 1.49×10^{11} and a length of 1.25 ns. After the 2011 run, the total delivered integrated luminosity amounted to $\mathcal{L} = 5.25\,\text{fb}^{-1}$, whereas the LHC reached a peak luminosity of $L = 3.65 \times 10^{33}\ \text{cm}^{-2}\text{s}^{-1}$.

For the LHC run in 2012, the centre-of-mass energy was increased to $\sqrt{s} = 8$ TeV,

while staying with a maximum number of 1380 bunches and a spacing of 50 ns. In total, the LHC reached a peak luminosity of $L = 7.73 \times 10^{33}$ cm^{-2}s^{-1} and delivered a total integrated luminosity of $\mathcal{L} = 23.3\,\text{fb}^{-1}$. In the end of 2012, the bunch spacing was halved to 25 ns and the LHC reached a new record of 2748 bunches per beam, but only running with the injection energy of 450 GeV and without collisions.

The instantaneous and the delivered integrated luminosity, as a function of the day in the years 2010, 2011 and 2012, are presented in Figure 3.17.

After the successful runs up to the beginning of the year 2013, the machine is shutdown for about two years. In this time, the LHC is prepared to run with design parameters afterwards.

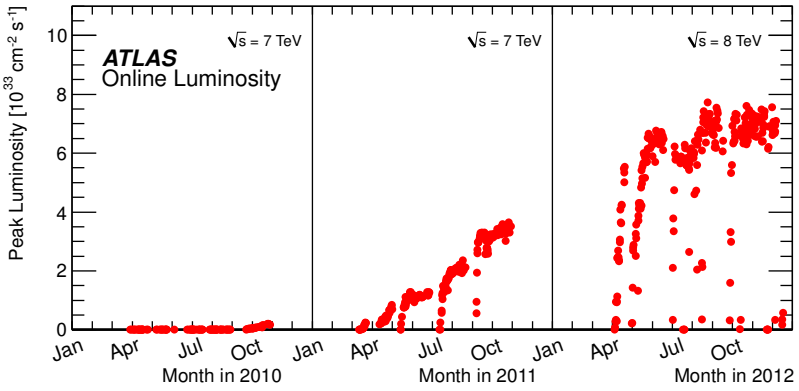

(a) Peak instantaneous luminosity

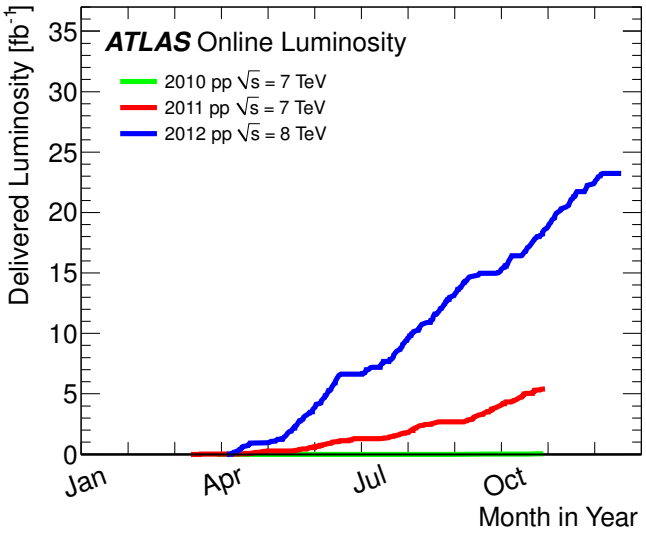

(b) Integrated luminosity

Figure 3.17: Peak instantaneous [148] and integrated luminosity [149] as a function of the day in the years 2010, 2011 and 2012.

4 Event simulation at ATLAS

In order to quantify the amount of background events and to determine the contribution of signal events to selected data events, it is necessary to simulate these signal and background processes. This is performed in two steps: first, the process is simulated using Monte-Carlo (MC) event generators, described in Section 4.1. The section includes a summary of the MC generators relevant for this analysis. A detailed discussion of the simulated signal and background processes will be given in Section 6.2. Secondly, the generated event information is passed to the detector simulation, which simulates the interactions of the produced particles with the detector material and also the detector response of the sub-detectors and the trigger and DAQ system (Section 4.2).
The output of the detector simulation is then similar to the recorded real data and passed to the physical object reconstruction, described in Chapter 5.

4.1 Event generators

4.1.1 Event generation

In a collision event at the LHC several hundreds of particles appear, which need to be simulated in the event generation. Besides the particles produced in the hard process there is a large amount of additional particles produced by gluon and photon radiations from the initial and final state partons, and also the proton remnants not participating in the hard process. For each of these additional processes it is impossible to calculate the transition amplitudes at arbitrary orders, but the factorisation theorem allows to separate the treatment of the different processes into different regimes of energy scales. While the high scale process amplitudes can be calculated using perturbative QCD, the soft scale regime ($\lesssim 1\,\text{GeV}$) needs to be simulated by phenomenological models. These models rely on several free parameters, which need to be determined from data (also called 'tuning').
Hence the generation of a typical event, as depicted in Figure 4.1, is separated into several steps, each covering different energy scale regimes.
In the beginning, the hard subprocess (Section 4.1.1.1) is generated by considering the longitudinal momentum distributions of the incoming partons, which are given by the parton distribution functions (PDFs, see Section 2.2.5). For the transverse momentum of the incoming partons, the so-called 'primordial k_T' model (for instance see reference [151] for further reading) is used, which randomly takes the value of the transverse momentum from a one-sided Gaussian with width $\sim 2\,\text{GeV}$. The generation of the hard subprocess is followed by the simulation of the parton shower (Section 4.1.1.2), which results from the previously mentioned gluon radiations. After showering, colour singlet hadrons are

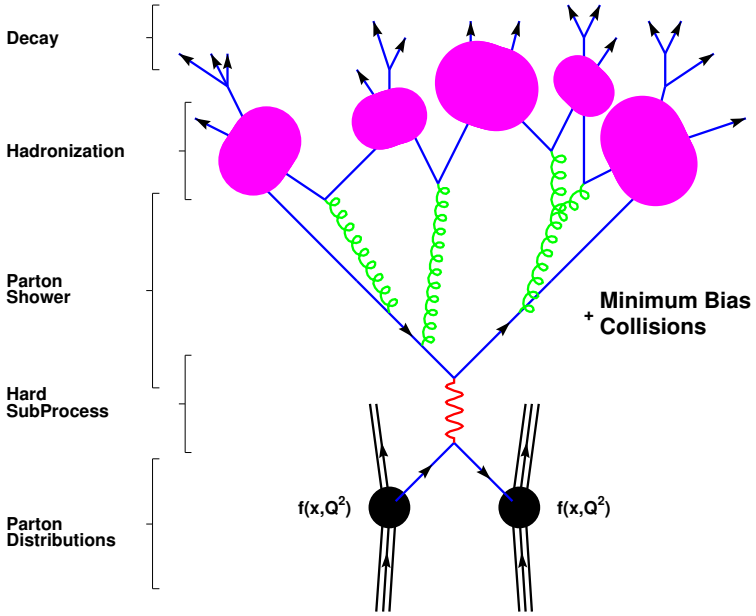

Figure 4.1: Structure of Monte-Carlo event generation [150]. The incoming partons at the bottom, modelled by the parton distribution functions, interact in the hard subprocess. Afterwards the parton shower simulates parton cascades, both for initial-(not shown) and final-state radiation partons. This step includes the simulation of the parton showers arising from interactions of the proton remnants and additional soft parton-parton scatterings, which are also called 'underlying event' (in this picture denoted as 'Minimum Bias Collisions'). At the end of the showering, which is determined by yet another tuning parameter, the final partons are combined into colourless hadrons (hadronisation), followed by the simulation of decays into stable particles.

formed from the final partons in the hadronisation step (Section 4.1.1.3). This is followed by further decays of unstable particles until they reach stable states (at ATLAS a stable particle is defined to have a lifetime of $c\tau > 10\,\text{mm}$ [152]).
A pictorial representation of a full event is presented in Figure 4.2. The information presented in the following are mostly taken from reference [154].

4.1.1.1 Hard subprocess

The LHC collisions, especially those producing heavy particles or high energetic jets, involve large momentum transfers of the incoming partons. At these large scales the strong coupling α_s becomes small enough in order to calculate the cross-sections of such processes using perturbative QCD. Monte-Carlo event generators make use of the factorisation ansatz, previously introduced in Section 2.2.5. The factorised cross-section in Equation (2.86) can be rewritten for the production of a final state with n par-

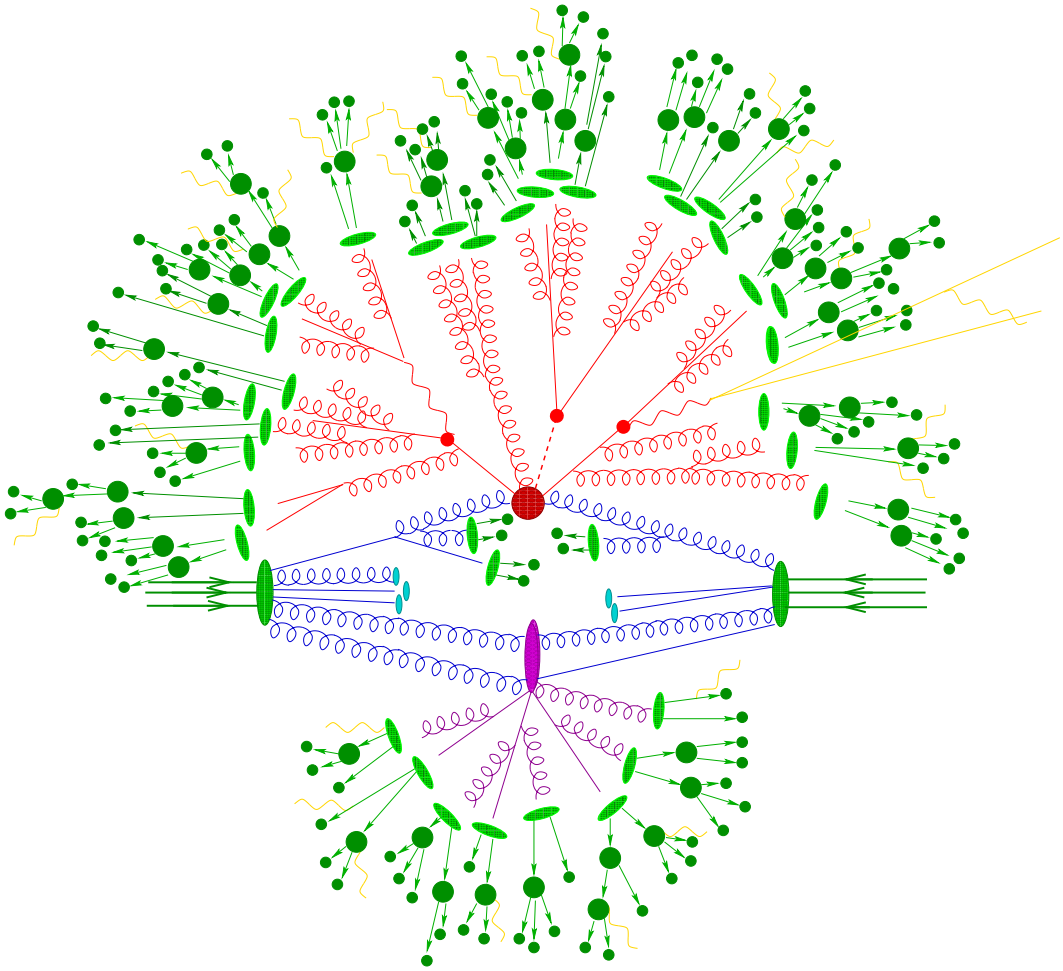

Figure 4.2: Pictorial representation of a fully simulated event (here: $pp \to t\bar{t}H$) [153]. The hard subprocess (big red blob) is followed by the decay (small red blobs) of both top quarks (solid red lines) and the Higgs boson (dashed red line). The parton shower arises from the gluon radiations of the initial state gluons (blue), the final state partons (red) and secondary proton remnant interactions (one is represented by the purple blob). At the end of the parton showers (red, blue and purple), hadronisation takes place (light green blobs), followed by hadron decays (dark green blobs). At any stage of the event generation process, photon radiations by charged particles can occur (yellow).

ticles/partons [154]:

$$\begin{aligned}\sigma &= \sum_{a,b} \int_0^1 \mathrm{d}x_a \mathrm{d}x_b \int \mathrm{d}\Phi_n f_a^{h1}(x_a,\mu_f) f_b^{h2}(x_b,\mu_f) \hat{\sigma}_{ab\to n}(\mu_f,\mu_r,\Phi_n) \\ &= \sum_{a,b} \int_0^1 \mathrm{d}x_a \mathrm{d}x_b \int \mathrm{d}\Phi_n f_a^{h1}(x_a,\mu_f) f_b^{h2}(x_b,\mu_f) \times \frac{1}{2\hat{s}} |\mathcal{M}_{ab\to n}(\Phi_n,\mu_f,\mu_r)|^2, \end{aligned} \tag{4.1}$$

where the sum runs over initial partons a and b. $f_{a/b}$ denote the previously introduced PDFs, describing the parton distributions of hadrons $h1$ and $h2$ at specific factorisation scales μ_f and parton momentum fractions $x_{a/b}$. The partonic cross-section $\hat{\sigma}$ is split into a parton flux $1/(2\hat{s})$ ($\hat{s} = x_a x_b s$, s=hadronic centre-of-mass energy), a matrix element (ME) $\mathcal{M}$ and a differential phase space element Φ_n for final state n.

- The ME $\mathcal{M}_{ab\to n}$ is the invariant amplitude for a process $ab \to n$ and contains the physics of the interaction. It is derived from the corresponding Lagrangian describing the respective process (see Section 2.1). In general, the ME is calculable by perturbation theory and can be written as a sum of the Feynman diagrams $\mathcal{F}$

$$\mathcal{M}_{ab\to n} = \sum_i \mathcal{F}^{(i)}_{ab\to n}, \tag{4.2}$$

  representing the processes with the same initial and final state. Such matrix elements can be calculated in different ways and at different orders of the strong coupling constant α_s. Most multi-purpose leading-order (LO) MC generators, as used in this analysis, provide lists of matrix elements for most $2 \to 1$, $2 \to 2$ and $2 \to 3$ (the numbers represent the particle multiplicity in the initial and final state) processes of the Standard Model and also some new physics models. For final states with higher final state multiplicities there exist dedicated generators, like `AlpGen` [155], `Amegic++` [156], `COMIX` [157] or `MadGraph/MadEvent` [158]. These generators make use of different methods, e.g. helicity method or recursive relations, and are limited by computing resources because the number of (tree-level) diagrams for n final state particles is proportional to $n!$.

- The differential phase space element $\mathrm{d}\Phi_n$ and the parton flux, together contribute the kinematics of the process to the total cross-section. $\mathrm{d}\Phi_n$ can be factorised into the phase space factors of the particular final state particles:

$$\mathrm{d}\Phi_n = \prod_{i=1}^{n} \frac{\mathrm{d}^3 p_i}{(2\pi)^3 2E_i} \cdot (2\pi)^4 \delta^{(4)} \left(p_a + p_b - \sum_{i=1}^{n} p_i \right), \tag{4.3}$$

  with the differential momentum $\mathrm{d}p_i$ and energy E_i of final state particle i, and δ-functions ensuring the momentum conservation of initial parton momenta p_a, p_b and final state momenta p_i.

Using the described cross-section formula, MC generators then produce hypothetical events by sampling over the phase space and defining particular events with random numbers filling the variables of the phase space.

Leading-order MC generators are mostly used to model the shapes of the final state particle's kinematic distributions. However, higher order matrix elements provide additional contributions to the total cross-section of the processes and hence the absolute normalisation is not well described by LO generators. There exist several NLO MC generators, like `MC@NLO` [159] or `Powheg Box` [160] (which implements the `Powheg` method [161]), that allow to generate events and calculate cross-sections with NLO precision.

A common procedure is to generate the events with a LO generator and then to normalise the distributions using a so-called k-factor, derived from the ratio of NLO and LO cross-sections:

$$k = \frac{\sigma^{\mathrm{NLO}}}{\sigma^{\mathrm{LO}}} \ . \tag{4.4}$$

A typical NLO partonic cross section has the form [154]

$$\mathrm{d}\hat{\sigma}^{\mathrm{NLO}} = \mathrm{d}\tilde{\Phi}_n \left[\mathcal{B}(\tilde{\Phi}_n) + \alpha_s \mathcal{V}(\tilde{\Phi}_n)\right] + \mathrm{d}\tilde{\Phi}_{n+1} \alpha_s \mathcal{R}(\tilde{\Phi}_{n+1}), \tag{4.5}$$

where $\tilde{\Phi}_n$ denotes the integral over the n-particle phase space elements including the parton flux, and $\mathcal{B}$, $\mathcal{V}$ and $\mathcal{R}$ represent the leading-order (or Born), virtual and real-emission part of the matrix elements, respectively.

4.1.1.2 Parton shower

The particles entering and leaving the hard subprocess (typically QCD partons) can radiate gluons at any stage of the process. These gluons can either radiate further gluons or produce $q\bar{q}$-pairs, which then can radiate further gluons as well. This results in showers of outgoing partons, that would be represented by matrix elements at very high orders. However, it is nearly impossible to calculate all these MEs. Furthermore, at the end the showering process reaches low scales which can not be described by perturbative QCD anymore. Therefore, MC generators make use of algorithms that simulate the parton showers, starting from high scales (hard subprocess) down to low scales of the order of $\sim 1\,\mathrm{GeV}$. These algorithms simulate the showering in separate steps using a so-called Markov-chain [162].

For the parton shower simulation there exist two common approaches, which are quite similar:

- The approach of the 'collinear final state evolution' is based on the treatment of a produced $q\bar{q}$-pair, where one of the quarks radiates off a gluon. The corresponding differential cross section can be expressed as [154]

$$\frac{\mathrm{d}\sigma_{q\bar{q}g}}{\mathrm{d}\cos\theta dz} \approx \sigma_{q\bar{q}} \cdot C_F \cdot \frac{\alpha_s}{2\pi} \cdot \frac{2}{\sin^2\theta} \cdot \frac{1+(1-z)^2}{z} \tag{4.6}$$

  and is (at LO) proportional to the cross-section of the $q\bar{q}$ production $\sigma_{q\bar{q}}$. Here, $C_F = (N_c^2 - 1)/(2N_c)$ represents the colour factor for N_c colour charges, θ denotes the angle between the gluon and the quark, which radiated the gluon, and z stands for the gluon energy fraction (which is defined by the ratio of the gluon energy and the energy of the originating quark). One can see that the cross section is divergent for collinear gluon radiations and vanishing energy fractions. Hence, the emission pattern is dominated by collinear and low energetic radiations. The divergence is solved by introducing a cutoff scale parameter Q_0, below which a collinear parton pair can not be distinguished from a single parton with same total momentum and

quantum numbers. The size of the cutoff scale is a free parameter and is tuned to data.

Above cross-section formula can be generalised to an expression for a hard process producing n partons i (with cross section σ_0), accompanied by an additional parton j [154]:

$$\mathrm{d}\sigma \approx \sigma_0 \sum_{\text{parton } i}^{n} \frac{\alpha_s}{2\pi} \cdot \frac{\mathrm{d}\theta^2}{\theta^2} \cdot P_{ji}(z,\phi)\mathrm{d}z\mathrm{d}\phi, \tag{4.7}$$

where P_{ji} denotes a universal (scale independent), flavor and spin dependent function, which describes the cross-section dependence on the energy fraction z and the azimuthal angle ϕ (defined around the axis of parton i) between partons i and j.

The cross-section expression in Equation (4.7) can be used to derive the Sudakov form factor [163], which represents the probability that a gluon is not radiated. In the shower generation this form factor is used in an iterative procedure (Markov-chain), starting from the hard process. At each step it is probabilistically chosen whether a gluon is radiated off or not. The resulting final state of the collinear splitting is then treated as 'hard process' and a new splitting is evaluated. This is performed until either all probabilities are zero or the relative transverse momenta of the partons have reached the cutoff scale Q_0. Therefore, this Markov-chain results in the evolution of the transverse momenta (p_T) of the radiated gluons, starting from the highest p_T.

It should be mentioned that instead of performing an angular ordering ($d\theta^2/\theta^2$), it is also possible to parametrise the phase space by the transferred momentum q or the transverse momentum p_T, which in the collinear limit give mathematically the same results. This is possible, because both q and p_T are proportional to θ^2 and the following holds:

$$\frac{d\theta^2}{\theta^2} = \frac{dq^2}{q^2} = \frac{dp_T^2}{p_T^2} \ . \tag{4.8}$$

However, this does not hold in the non-collinear extrapolation and basically each parametrisation could give slightly different results.

- A similar strategy is performed in the 'dipole approach', where the parton shower is formulated as an emission of sets of colour dipoles. One makes use of the 'large-N_c' limit, which means one assumes an infinite number of colour charges (instead of three). In this limit, it is possible to decompose a complicated parton system as a 'colour flow', meaning that the colour structure of a Feynman diagram is represented by a set of δ-functions which can be depicted by colour lines connecting ingoing and outgoing partons (see Figure 4.3). Each of these colour lines then forms a colour-anticolour dipole.

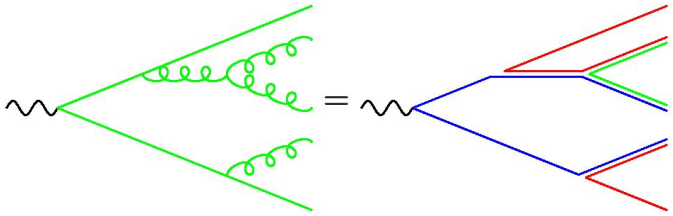

Figure 4.3: Pictorial representation of the 'colour flow' model [154].

Starting from the hard process, the gluon emission is generated for each colour line independently. For this, the classical radiation pattern is used as introduced for the 'collinear approach'. Each gluon is then represented by colour lines of two dipoles. In an iterative procedure the event is evolved globally, starting from the highest energetic emission. This results in a momentum ordered and therefore also angular ordered (due to Equation (4.8)) outgoing parton shower.

In each event there also occur interactions of particles, which are not associated to the primary hard process. This is observed as the so-called 'underlying event' (UE). There is strong evidence, that these secondary processes arise from interactions of the other constituent partons in the protons, which did not participate in the hard process [164]. While the harder secondary interactions can be formulated by perturbative QCD, the soft part needs to be simulated by a phenomenological model. Commonly used is the 'multiple parton interactions' (MPI) model, which relies on free parameters to be tuned to data.
The simulation of the UE and also its gluon radiations is performed during the 'parton shower' step of the MC generator.

4.1.1.3 Hadronisation

In nature coloured partons do not appear as observable particles. Therefore, the final partons after the parton shower process need to be combined into colour singlet hadrons. The parton showering ends at a low scale and hence the transition from the partonic final state to a complete hadronic final state is simulated using phenomenological hadronisation models with tunable parameters.

Currently there are two main model classes in use which will be described in the following.

- In the 'string model', which is the standard hadronisation implementation in the `Pythia` [165] generator, $q\bar{q}$-pairs are connected by massless colour-strings. This is justified by the linear behaviour of the confinement at large distances. As the partons of the $q\bar{q}$-pair move apart, a colour flux tube is stretched between them (see Figure 4.4 (a)). The tube is uniform along its length, representing the linearly rising potential $V(r) = \kappa r$, where the constant κ denotes the energy per length stored in the strings. With rising distance r, the potential energy stored in the string increases. At some specific maximum potential (which is a tuning parameter)

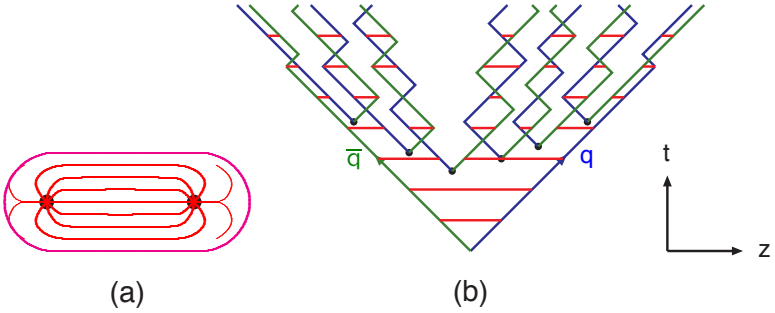

Figure 4.4: String hadronisation model [154]. Figure (a) presents a colour flux tube spanned between two partons. The motion and breakup of a string system is shown in Figure (b).

the string breaks and produces a new $q'\bar{q}'$-pair, resulting in two colour singlets $q\bar{q}'$ and $q'\bar{q}$.

The hadronisation of a $q\bar{q}$-pair is simulated in an iterative procedure, forming new quark-antiquark-pairs out of the string connections (see Figure 4.4 (b)). This is performed until the string tensions are below a specific cut-off value (which is a tuning parameter as well) and then ordinary hadrons are formed from the remaining quark pairs. There are further tuning parameters used in the hadronisation, that steer the probabilities of the formation of hadrons with spin 0 or spin 1 and hadrons containing strange or heavy flavors.

- The 'cluster model', incorporated in the generators `Sherpa` [153] and `Herwig` [166], is based on the so-called preconfinement property of parton showers [167]. This means that at any evolution scale Q_0 of the parton shower, colour singlet parton (cluster) combinations can be formed with an asymptotically ($Q \gg Q_0$) universal (independent of scale Q and underlying process) invariant mass distribution. In the limit of $Q_0 \gg \Lambda$ (Λ being the QCD scale in the running α_s coupling, which is also tuned to data), the mass distribution can be computed perturbatively.

  The preconfinement mechanism also makes use of the 'large-N_c' limit, where the gluons in the shower can be represented by colour line pairs (Figure 4.3). Hence, at the 'low scale' end of the parton shower, each colour line is connected to an adjacent partner colour line. The preconfinement mechanism then enforces splittings into light $q\bar{q}$-pairs of all gluons and allows adjacent colour lines to form colour singlets (clusters), whereas non-adjacent pairs have ~ 0 probability for hadron formation. The multiplicities of flavors of the produced mesons and baryons are determined by the universal invariant mass distribution mentioned above. Hence, massive clusters decay into lighter clusters until reaching stable 'light' states with no further decays.

Summarising both models, it can be said [154] that the 'cluster model' provides a fairly good overall description of high energy collider data. Compared to the 'string model',

the 'cluster model' describes the data slightly worse, but on the other hand it deals with less parameters which need to be tuned to data.

At the end of the hadronisation, the decays of the particles into stable states are simulated under consideration of the known branching fractions, usually taken from reference [39].

4.1.2 Event and matrix element generators used in this analysis

In the following, I will give a brief overview on the MC generators used in this analysis. A detailed description of the simulated signal and background processes will follow in Section 6.2.

4.1.2.1 Pythia 8

`Pythia8` [168] is a multi-purpose LO MC event generator and the successor of `Pythia6` [165]. While `Pythia6` was completely written in the programming language `Fortran`, `Pythia8` marks the final transition to `C++`, written from a clean start. It is able to generate complete events, meaning it is capable to generate hard processes and to simulate parton shower and hadronisation.

For the hard subprocess, `Pythia` contains a list of over 200 hard coded matrix elements. These processes cover the main SM and Beyond-the-Standard-Model (BSM) $2 \to 1$, $2 \to 2$ and some $2 \to 3$ transitions. It is also used for the generation of the heavy fourth generation quark pair production, required in this analysis.

The parton showering in `Pythia` is based on a dipole-type approach, resulting in showers ordered in the transverse momentum of the outgoing partons. For describing the parton shower coming from the initial state partons, `Pythia` uses a backwards evolution. For this it starts from the hard subprocess and dresses it with additional radiation using the parton shower evolution. Therefore at each step of the showering the probability for a parton coming from another parton with higher momentum fraction is evaluated.

The hadronisation model in `Pythia` is based on the Lund string fragmentation framework [169, 170], which incorporates the 'string model'.

4.1.2.2 Sherpa

`Sherpa` [153] is a multi-purpose MC event generator written in `C++`, which is capable of generating events at LO and NLO, and also allows for higher parton multiplicities $2 \to n$ in the final state. It is built in a modular structure, having several physics modules covering the different steps of the event generation.
In this analysis, `Sherpa` is used to model the diboson background, accompanied by additional partons.

For the hard subprocess, `Sherpa` provides two different matrix element generators, `AMEGIC++` [156] and `COMIX` [157], which can be chosen by the user. Both have the possibility to automatically generate tree-level matrix elements for a given set of initial and final state particles.
The `COMIX` generator is especially suited for producing final states with high parton

multiplicities and is based on an extension of the Berends-Giele recursive relations [171]. AMEGIC++ in addition also allows to generate parton-level events with NLO precision.

For the parton showering, Sherpa uses per default a factorised formalism of the dipole approach, developed by Catani and Seymour [172, 173]. In this formalism a dipole is formed of the actual parton, which is supposed to split, and a spectator parton which is colour-connected to the emitter.

The hadronisation part of the event generation in Sherpa is performed by the module AHADIC++, which is based on a modified cluster hadronisation model [174]. It allows to combine all possible flavors (including diquark-pairs) into clusters and provides a flavor-dependent dynamic separation of the regimes of clusters and hadrons.

4.1.2.3 MadGraph 5 and MadEvent

MadGraph5 [175], the successor of MadGraph4 [158], is a matrix element generator written in Python. This means that the parton shower and the hadronisation need to be performed by separate generators.

MadGraph5 allows to generate matrix elements for user-defined processes with arbitrary parton multiplicities in the final state ($2 \to n$). For this MadGraph evaluates helicity wave functions and amplitudes, as firstly implemented in the HELAS [176] package. MadGraph produces computer code for the calculation of the matrix elements for all Feynman diagrams contributing to the specified process. The code is then used within the MadEvent package for the event generation, where the $2 \to n$ Feynman diagrams are read in and the kinematics of the final state is generated.
In this analysis, MadGraph5 is used to simulate the background coming from $t\bar{t}$ processes accompanied with additional vector bosons and partons, and processes with two same-sign charged W bosons.

For parton showering and hadronisation, MadGraph is commonly complemented with the Pythia8 generator.

4.2 Detector simulations

After the events have been generated by the different MC generators up to the hadron level, they are passed to the ATLAS detector simulation framework before entering the object reconstruction. The simulation is split into two parts: at first, the event is processed by the detector simulation, which simulates the interactions of the particles with the detector material and decays of unstable particles like hadrons (π, K, Λ) and muons. This can be performed by a full (time-intensive) simulation (Section 4.2.1) or a fast simulation (Section 4.2.2) in which the interactions with some sub-detector parts are estimated by parametrisation. This analysis makes use of both simulation types.
Afterwards follows the 'digitisation' step (Section 4.2.3), in which the response of the sub-detectors and electronics to the particle interactions is simulated. At the same step the events are mixed up with so-called pile-up events (obtained from simulations using Pythia8 with the Minimum Bias AM2 tune [177]), which account for the additional proton-proton interactions occurring in each bunch crossing.

The following description of the ATLAS detector simulation framework is mainly taken from reference [152].

All steps in the event simulation, event generation, detector simulation and digitisation, are embedded in the ATLAS software framework `Athena` [178]. Figure 4.5 presents the data flow within the ATLAS simulation software.

Rounded boxes represent data formats coming out from the different algorithms (depicted by square-cornered boxes). The generator produces the output in the `HepMC` format, which is then forwarded to the detector simulation. Simulated energy depositions in the detector are then stored in so-called `Hits` files, which can be used by the digitisation. In addition, the pile-up contributions (dashed boxes) can be added at this step and will be merged into the `Hits` files. The digitisation produces `Digit` files, which contain the detector response (voltages, currents, etc.) to the detector hits. In addition, the MC truth information (original information of the generated particles) is merged into Simulated Data Objects (`SDOs`) during the digitisation. A readout driver (ROD) emulation follows the digitisation, whose output is stored as Raw Data Objects (RDOs). This is the final output format, which enters the object reconstruction.

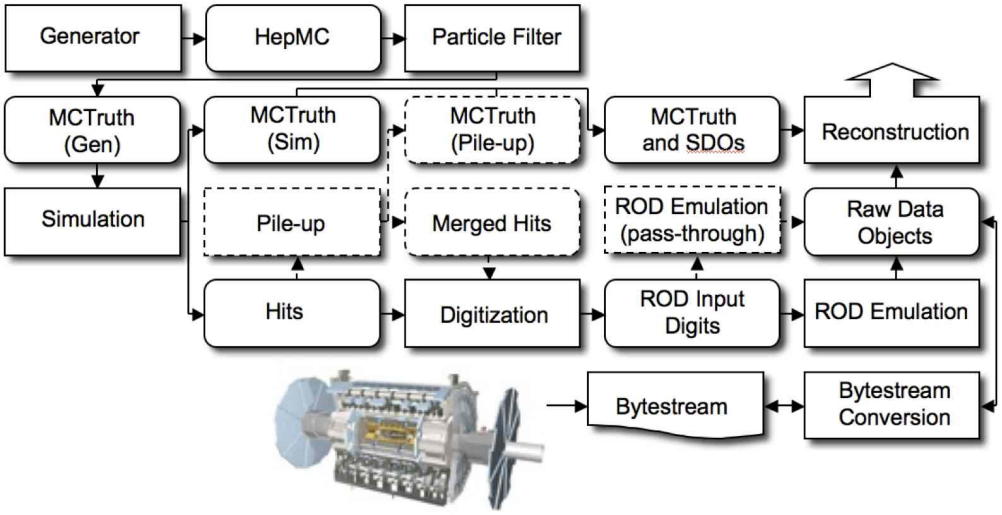

Figure 4.5: Overview of data flow in ATLAS event generation and detector simulation [152]. Rounded boxes represent data formats coming out from the different simulation algorithms (depicted by square-cornered boxes). The optional addition of pile-up events is represented by dashed boxes.

4.2.1 Full detector simulation

The events leaving the event generation, shower generation and hadronisation are forwarded to the ATLAS detector simulation, which is based on the `GEANT4` simulation toolkit [179]. This step requires a precise description of the detector's geometry and its conditions, that are stored in two databases:

- The *ATLAS Geometry Database* stores the geometric structure of the detector. It is based on the `GeoModel` library [180], in which the structure is built in terms of so-called solids. Solids describe the basic shapes of detector components without position and property definitions. Logical volumes are formed by a set of solids with applied properties (e.g. material). Finally, physical volumes describe the placements of the logical volumes within the detector geometry.

- The *ATLAS Conditions Database* allows to apply modifications to the geometric structure due to the running conditions of the ATLAS detector. This includes detector misalignments (e.g. geometric shifts of sub-detector parts or envelopes), dead channels in the readout electronics or the temperatures of the detector components. During the detector simulation step, one can select the conditions from a specific run.

Given the geometric structure and the detector conditions, `GEANT4` then simulates all kinds of physics processes occurring due to the interactions of the generated particles with the detector material. This includes bremsstrahlung processes and further decays of particles produced in the interactions with the detector. In addition, `GEANT4` also simulates the decays of particles, which resulted from the event generator and decay inside the detector.

However, the full detector simulation using `GEANT4` is very time-consuming and hence fast detector simulations have been developed, which will be explained in the following section.

4.2.2 Fast detector simulation

Due to the complicated detector geometry and the detailed physics description in `GEANT4`, a full detector simulation is very time-consuming. Especially the simulation of particles traversing the large calorimeter volume takes up to 80% of the computing time. 75% is spent on the simulation of electromagnetic particle interactions. Hence several fast detector simulation programs have been developed with the aim to complement `GEANT4`. The ones most commonly used are `Fast G4 Simulation` [181], `ATLFAST-I` [182] and `ATLFAST-II` [183]. Since in this analysis only the `ATLFAST-II` simulation has been used, I will focus on a brief description of this program. All fast simulations rely on substituting the full simulation of some detector parts by parametrisations.

In general, `ATLFAST-II` is based on replacing the full simulation of the ATLAS calorimeters by the `Fast Calorimeter Simulation` (FastCaloSim [184]). In addition, `ATLFAST-II` allows to replace the simulation of the inner detector and the muon spectrometer by the `Fast ATLAS Tracking simulation` (Fatras [185]), but this is not used by default.

Fatras denotes a complete simulation developed within the ATLAS track reconstruction framework. It relies on a simplified description of the full detector geometry, while keeping the accuracy for sensitive parts. The interactions are simulated using different methods: multiple Coulomb scatterings are approximated by a Gaussian mixture model (due to the central limit theorem the small multiple deflections can be described by a Gaussian probability density function, therefore this is not a good approximation for

wide angle scattering), whereas ionisation and radiative energy losses are modelled using the Bethe-Bloch [139] and Bethe-Heitler [186] descriptions.
FastCaloSim relies on parametrisation of the longitudinal and lateral profiles of the energy deposited by particle showers in the calorimeters. It is restricted to parametrisation for only three particle types: electrons, photons and charged pions, where the latter is used for the simulation of all types of hadrons. The parametrisations of FastCaloSim have been derived from single particle events simulated with `GEANT4`. For the total energy deposition and the longitudinal shower development, the parametrisation is based on a function of the longitudinal shower depth. The lateral energy distribution is described by a radial symmetric function (3rd order polynomial spline function).

There have been several performance and validation studies for `ATLFAST-II`. A comparison between full and fast detector simulations of some distributions of kinematic variables is presented in Figure 4.6. In general, the simulated distributions using `ATLFAST-II` show a good agreement with the full detector simulation (Full G4). Only the distribution of the resolution of the jet transverse momentum reveals a deviation of 10-20% to the full simulation. This is due to the fact that all individual hadrons are treated as pions in the fast simulation. More validation studies can be looked up for example in references [152, 183, 187–189]. Finally, a validation study performed for the fast simulated fourth generation signal samples used in this analysis will be presented in the analysis chapter in Section 6.8.1.1.
A study of the performance showed that the time improvement when using FastCaloSim is only by a factor of ~ 10, whereas the combination of FastCaloSim and Fatras (`ATLFAST-IIF`) gives an improvement of ~ 100.

4.2.3 Digitisation and pile-up

The digitisation process converts the particle hits in the detector into a response of the detector readout systems. These responses (also called 'digits') are represented by voltages or currents at the particular readout channels. In addition, special properties (like cross-talk or electronic noise) are modelled during the digitisation and dead channels and noise rates are taken from the *ATLAS Conditions Database*.

A simulation of the detector readout for single hard scatterings is very unrealistic, because the main proton-proton collision is overlaid by additional interactions. Hence, the ATLAS digitisation step allows to mix the main process with the hits from these additional interactions. These types of events are referred to as 'pile-up'.
One source of such processes are additional proton-proton interactions during the same bunch crossing. At the design luminosity of the LHC it is expected to have in mean 23 interactions per bunch crossing. For the data taking in 2011 and 2012, Figure 4.7 presents the amount of data (recorded luminosity) as a function of the mean number of interactions per bunch crossing. In 2011 only an average of 9.1 interactions appeared per bunch crossing, whereas this number was increased to 20.1 with the running conditions in 2012. This source of additional interactions is also referred to as 'in-time pile-up'.
Besides the 'in-time pile-up', there also appears 'out-of-time pile-up', which refers to events from successive bunch crossings. These result from the fact that the read-out

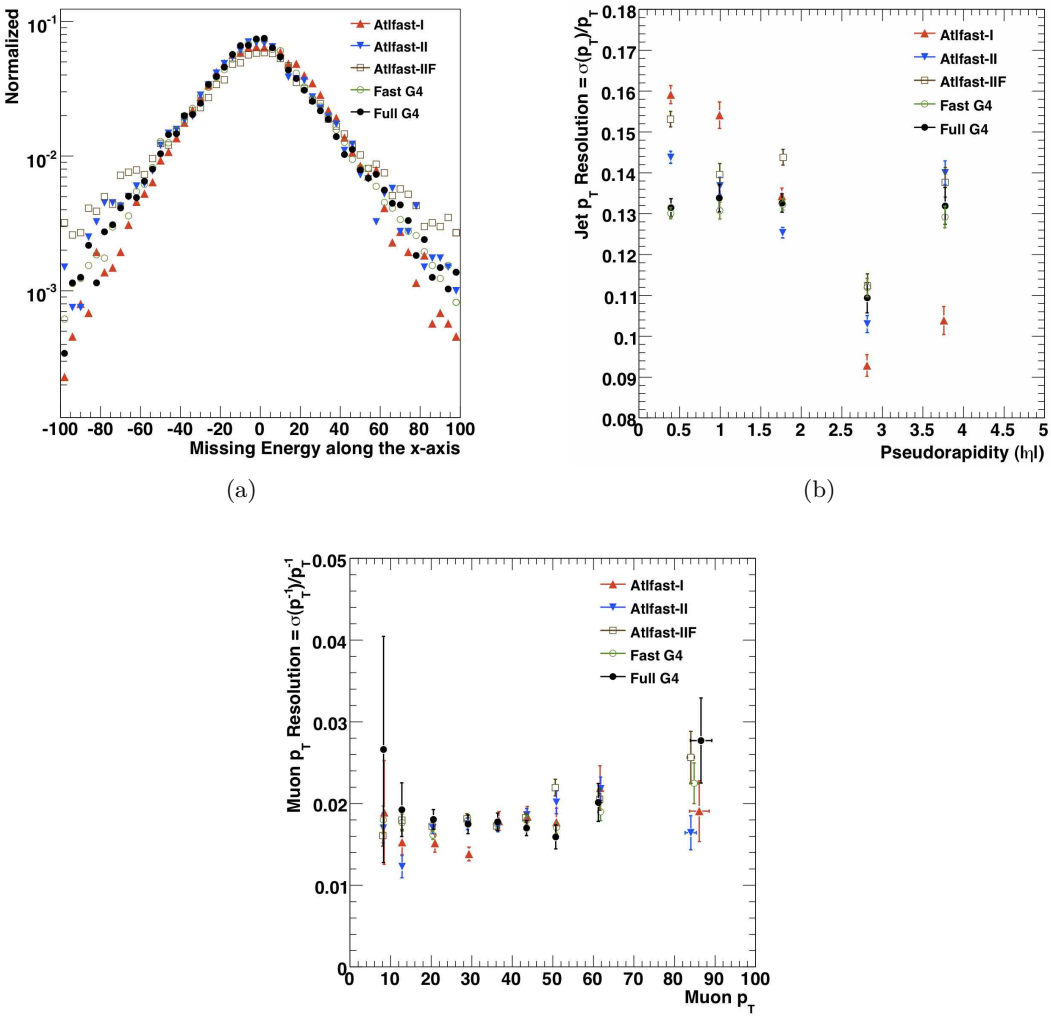

(a) (b)

(c)

Figure 4.6: Comparison between ATLAS fast simulations and full simulation of some kinematic distributions [152]. Figure (a) presents the missing transverse energy along the x-axis in di-jet events. A comparison of the jet transverse momentum (p_T) resolution as a function of the jet pseudorapidity is given in (b). In (c) the muon p_T resolution is shown as a function of the muon p_T.

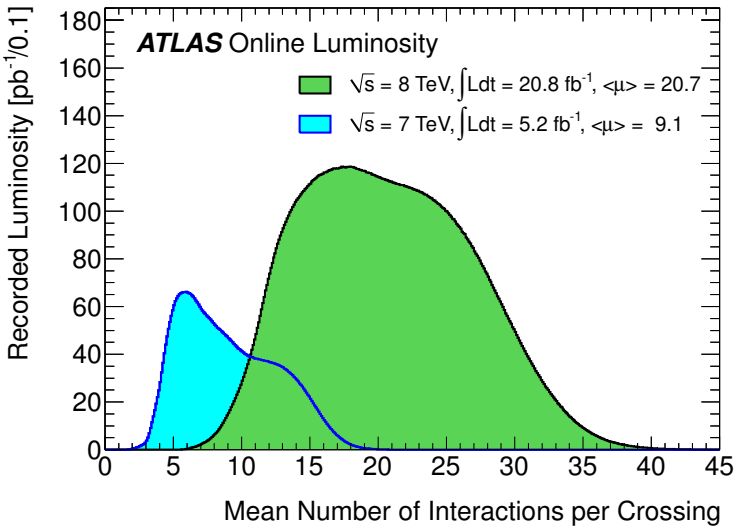

Figure 4.7: Mean number of interactions per bunch crossing ($= \mu$) for data taken in 2011 and 2012 (until November 26th) [190]. An average of $\langle\mu\rangle = 9.1$ interactions appeared per bunch crossing in the 2011 data-taking, whereas this number is increased to $\langle\mu\rangle = 20.1$ with the running conditions in 2012.

time of some of the ATLAS sub-detectors (in particular the LAr calorimeter) is longer than the bunch spacing of 50 ns and hence these sub-detectors also detect particles arising from these successive bunch crossings.
Another source of additional interactions occurs from the cavern background, which mainly consists of thermalised slow neutrons and long-lived Kaons traversing the detector cavern.
Finally, there is a contribution of beam-gas events and beam halo: the beam halo background results from interactions between the proton beam and the upstream accelerator elements, whereas the beam-gas events consist of interactions of residual hydrogen, oxygen and carbon gases in the ATLAS beam pipe.
The pile-up contributions to the main hard process can be taken from simulations or measured on real data using special 'zero-bias trigger'. In this analysis, the pile-up events were generated with `Pythia8` using the Minimum Bias tune `AM2` [177].

5 Event reconstruction at ATLAS

For the search of fourth generation quarks it is not possible to directly measure these new particles. In the case that they have a short life-time, the quarks would decay before traversing the detector. On the other hand, if they are long-lived, the quarks would form hadrons and build particle jets. For short-living quarks, it is therefore required to reconstruct their decay products. This analysis makes use of electrons (Section 5.3), muons (Section 5.4), jets (Section 5.5) and missing transverse momentum (Section 5.7), whose reconstruction algorithms and selection criteria will be explained in the following. Furthermore, the corrections to the physical objects and events, which are required to account for several physical and detector related effects, will be discussed in the corresponding subsections.

All algorithms for the reconstruction and calibration of the physical objects are embedded in the ATLAS software framework `Athena` [178]. The application of the selection criteria, additional energy and momentum corrections, and efficiency scale factors is performed in the analysis.

5.1 Tag and probe method

In the following sections, several selection efficiencies will be shown, that have been determined by a so-called Tag & Probe (T&P) method, which will be briefly explained in the following.

In general, one would define a selection efficiency as

$$\epsilon = \frac{N_{\text{sel}}}{N_{\text{total}}}, \tag{5.1}$$

where N_{sel} denotes the amount of selected events/particles and N_{total} represents the total number before the selection. In MC simulations, one could access the total number by the true event information, but this information is not accessible when measuring the efficiencies on data.

Hence, a common approach, the T&P method, allows to select events from a tagged sample and from this to calculate the efficiencies. Therefore, the method can be applied to both, data and MC, and hence allows to compare the obtained efficiencies.
In a typical example the method is performed on events with two leptons (e^+e^- or $\mu^+\mu^-$) stemming from a Z boson decay, because such a signature provides a clean lepton sample. The main idea of the T&P method is to 'tag' a clean sample of events using one of the leptons. The 'tag' lepton usually needs to fulfil tight selection criteria, which ensure the selection with a low background contamination. Then the efficiency under study

is measured using the second lepton (candidate), which is called 'probe' lepton. The 'probe' lepton candidate is selected by looser selection requirements than for the 'tag' selection and does not need to fulfil the selection criteria for the efficiency under study. Depending on the considered efficiency (and the lepton flavor), this could be for instance just a reconstructed track from the inner detector or a measured energy deposit in the calorimeter system.

The number of events that have a 'tag' and 'probe' lepton pair with an invariant mass close to the Z boson mass, are counted as N_{total}. If a 'probe' lepton in addition fulfils the selection criteria for the selection efficiency under study, the event is counted for N_{sel}. The selection efficiency is then given by the ratio presented above.

The determined efficiencies in simulated MC samples and real data are not necessarily equal. For instance, the electron identification relies on identifying particular shapes of the electromagnetic showers in the calorimeter. Here, the simulation can only provide a good approximation of the physics occurring in real data. Therefore, if there are significant differences between the efficiencies in MC and data, these differences need to be corrected for each event in the analysis. This is performed by applying so-called 'scale factors' (SFs) as weights to each event (for instance when filling histograms or counting event yields). These are given by the ratio of the efficiencies determined in data and MC:

$$SF = \frac{\epsilon_{\text{data}}}{\epsilon_{\text{MC}}} \, . \tag{5.2}$$

Usually these scale factors are parametrised as a function of kinematic variables of the objects.

5.2 Data quality and good run lists

As mentioned above, this analysis uses electrons, muons, jets and missing transverse energy. The reconstruction of all these objects requires to make use of all ATLAS sub-detectors. Hence it is necessary that the whole detector was functional during the data taking.

The data recorded by the ATLAS detector is split into separate runs, that mostly correspond to one proton fill of the LHC. As soon as the beam intensity reaches a too low value or the beam gets unstable, it is kicked out of the accelerator (beam dump). Afterwards the LHC starts with a new proton fill and new collisions, and the ATLAS DAQ starts a new run.
Each run is separated into luminosity blocks (LBs), which define time periods of mostly two minutes in which the detector, the trigger system and the LHC can be treated as being in a constant state. In case there is a change in the detector state or in the trigger, the current LB is interrupted and a new LB is started.

The state of the ATLAS sub-detectors is used to build so-called Good Run Lists (GRLs). These lists define the runs and LBs, in which all detector components were in a sufficient good state. Such lists are then used in the analysis to pre-select the data, so

that only events with a good detector condition are analysed.
The good run list used in this analysis corresponds to a reduced dataset of the data taken in 2012 (up to October 8th), which was available for analyses when the results in this thesis have been prepared. The run numbers of this reduced dataset range from 200803 up to 212272 and are arranged within the run periods A-G. Only the runs and LBs listed in the used GRL are considered for the calculation of the total integrated luminosity, which amounts to $14.324\,\mathrm{fb}^{-1}$.

5.3 Electrons

The W bosons produced in the decay chains of the fourth generation quarks decay with a probability of $\sim 11\%$ into electrons and electron-neutrinos. However, there is the possibility that jets arising from QCD background processes are reconstructed as electrons, since they also deposit energy in the ECAL. These deposits are used to seed the electron reconstruction algorithm, described in the following section. The production cross-section of such QCD processes with high jet multiplicities is high compared to the one for the fourth generation quarks. In the p_T range of $20 - 50$GeV, the ratio of the number of electrons arising from prompt W decays and QCD jets is expected to be $\sim 10^{-5}$ [191]. Therefore, in order to distinguish the signal electrons from these jets, an excellent electron reconstruction and identification with optimal jet rejection rate is required.
The algorithms and selection criteria for the electron reconstruction, which are presented in the following, have been developed and optimised by the *ATLAS ElectronGamma* performance group.

5.3.1 Electron identification, reconstruction and efficiencies

The ATLAS electron reconstruction features two main algorithms:

- a standard, cluster-based algorithm and
- a track-based algorithm preferred for low energetic electrons.

The latter algorithm is not used in this analysis and hence is not further discussed here. The standard algorithm is seeded from energy deposits (clusters) in the electromagnetic calorimeter (ECAL), where the conversion from the raw detector signal of each ECAL cell into energy deposits is performed using the method described in reference [135]. Clusters are reconstructed from longitudinal energy deposits in the calorimeter cells (see Figure 3.10), called longitudinal towers, with a minimum total transverse energy of 3 GeV. These towers are searched for using a so-called 'sliding-window' algorithm [191, 192], which forms rectangular clusters and positions them for a maximum amount of energy within the cluster. The window of the algorithm has a size of 3×5 in units of 0.025×0.025 ($\Delta\eta \times \Delta\phi$) of the ECAL middle layer granularity. Having found a suitable cluster, it is then searched for a matching track in the inner detector (ID) within a window of 0.05×0.10 ($\Delta\eta \times \Delta\phi$). The track momentum p has to be compatible with the

cluster energy E ($E/p < 10$) and the track is required not to belong to a an electron-positron pair from photon conversion in the detector material [191].
Finally, the total (cluster) energy of the electron candidate is calculated from the sum of the measured energy deposit in the cluster, the estimated energy deposit in front of the ECAL and the estimated energy deposits outside the cluster (longitudinal and lateral leakage). The transverse energy is calculated as (see Equation (3.11))

$$E_T = \frac{E_{\text{cluster}}}{\cosh \eta_{\text{track}}}, \tag{5.3}$$

where E_{cluster} denotes the above mentioned total cluster energy and η_{track} represents the pseudorapidity of the ID track. In this analysis, electrons are required to have $E_T \geq 25\,\text{GeV}$ and $|\eta_{\text{cluster}}| < 2.47$ (η_{cluster} = pseudorapidity of the cluster position), whereby the 'crack-region' $1.37 < |\eta_{\text{cluster}}| < 1.52$ is excluded. The cut value on the transverse energy is chosen slightly above the trigger threshold (see Section 5.3.4), whilst the pseudorapidity range marks the acceptance region of the inner detector.

The electrons passing the inner detector loose energy due to bremsstrahlung and hence a track re-fit needs to be performed after the reconstruction in order to estimate these material effects.
In the electron reconstruction algorithms used for the analysis of 2010 and 2011 data, a simple track re-fitting using a linear least-squares fit has been performed, assuming a pion hypothesis. However, the electron energy loss is dominated by bremsstrahlung processes and therefore this assumption is not a good approximation. Furthermore, the bremsstrahlung radiation results in alterations of the track curvature and it is possible, that the electron was not reconstructed before the track re-fitting procedure. Hence, the track re-fitting procedure has been improved for 2012 analyses, where the track parameters of electron candidates are corrected by a bremsstrahlung re-fit using the Gaussian Sum Filter (GSF) method [193] prior to the electron reconstruction. This fit is based on a generalisation of the Kalman Filter [194] and has been developed in reference [195]. With this method, the GSF accounts for the radiative loss in the ID and allows to perform a bremsstrahlung recovery at the initial step of the electron trajectory formation.
The performance of the GSF method on the track parameters has been studied in reference [193] for electrons coming from simulated $Z \to e^+e^-$ events. Figures 5.1a and 5.1b present the resolution width of the transverse track parameter d_0 as a function of the true pseudorapidity η^{truth} and true transverse momentum p_T^{truth}, respectively. d_0 is defined as the distance of closest approach between the track and the beam pipe. The resolution is then given by d_0/σ_{d_0}, where σ_{d_0} denotes the uncertainty from the track fitting procedure. The plots show the distributions for the old method (Standard) and with the usage of the GSF method (GSF). Another important parameter is the track inverse momentum multiplied by the charge q/p. Its mean relative bias as a function of η^{truth} and p_T^{truth} is presented in Figures 5.1c and 5.1d, respectively. All plots show a significant improvement in the resolution of the track parameters. Further distributions can be looked up in reference [193].

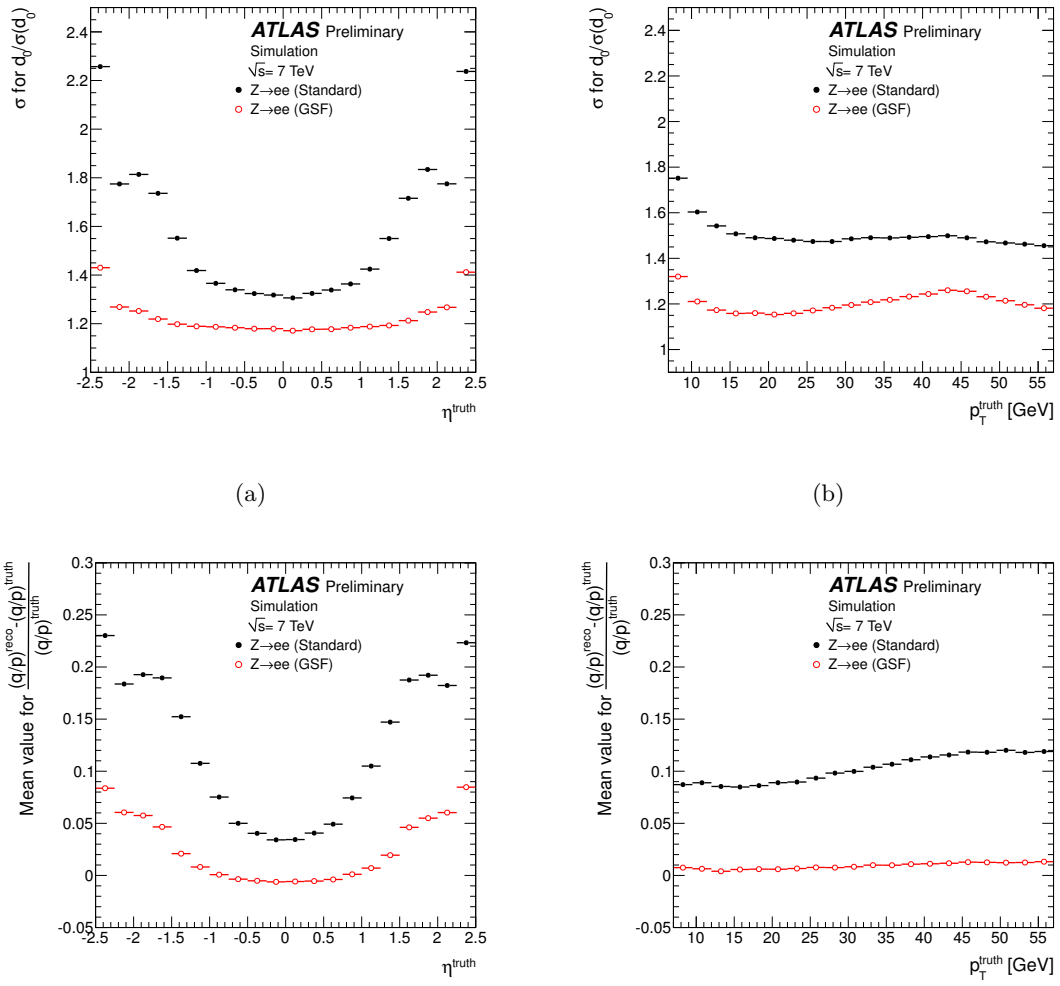

(a) (b)

(c) (d)

Figure 5.1: Performance of the Gaussian Sum Filter-based model [193]. Shown are the width of the transverse impact parameter significance d_0/σ_{d_0} and the mean relative bias of the track inverse momentum multiplied by the charge q/p, both as a function of the true η and p_T.

The procedure for the measurement of the electron reconstruction and track-cluster matching efficiency is described in reference [192] and is based on the T&P method in $Z \rightarrow e^+e^-$ events. The obtained results for 2011 and 2012 data were presented in reference [196]. Tag electrons were selected after the final electron reconstruction and were required to fulfil tight selection criteria. For the reconstruction efficiency measurement, a probe electron candidate was selected from a calorimeter cluster coming out of the 'sliding-window' algorithm. Then it was tested whether this cluster also fulfils the requirements of the electron reconstruction. In case of the measurement of the track-cluster matching efficiency, probe candidates were selected from ID tracks and then tested for fulfilling the cluster matching requirements. Both types of electron probes were required to have together with the tag electron an invariant mass close to the Z boson mass. The obtained reconstruction efficiencies presented in Figure 5.2 have been measured on MC and in 2011 and 2012 data. One notices a higher efficiency

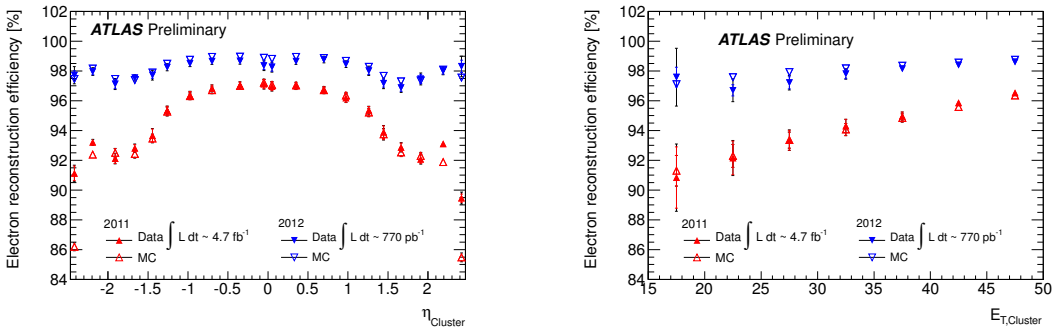

(a) (b)

Figure 5.2: Electron reconstruction efficiencies in 2011 and 2012 data as a function of cluster η (a) and cluster E_T (b) [196].

in 2012, which is due to the improved electron reconstruction with the GSF method. The differences in the efficiencies between data and MC are corrected by applying scale factors, which are parametrised in the η of the electron's cluster.

The above presented electron reconstruction selects all electron candidates in the event, but there is no rejection of 'background' electrons, like electrons not stemming from the hard scatter process (e.g. electrons from heavy flavor hadron decays) or hadron jets faking an electron signature. Hence, several sets of independent cuts are provided in the standard electron identification menu, which provide a separation between signal and background electrons. The standard menu, summarised in Table 5.1, provides three sets of cuts with increasing background rejection powers: `loose`, `medium` and `tight`.
In the `loose` electron selection, the cuts are limited to information from the electromagnetic and hadronic calorimeters (ECAL and HCAL). This incorporates cuts on variables describing the hadronic leakage and shower shapes in ECAL and HCAL. In total, the `loose` selection provides an excellent electron identification efficiency (close to 100%) [191], but low background rejection.

Type	Description	Name
Loose selection		
Acceptance	$\|\eta\| < 2.47$	
Hadronic leakage	Ratio of E_T in the first layer of the hadronic calorimeter to E_T of the EM cluster (used over the range $\|\eta\| < 0.8$ and $\|\eta\| > 1.37$)	R_{had1}
	Ratio of E_T in the hadronic calorimeter to E_T of the EM cluster (used over the range $\|\eta\| > 0.8$ and $\|\eta\| < 1.37$)	R_{had}
Middle layer of EM calorimeter	Ratio of the energy in 3×7 cells over the energy in 7×7 cells centred at the electron cluster position	R_η
	Lateral shower width, $\sqrt{(\Sigma E_i \eta_i^2)/(\Sigma E_i) - ((\Sigma E_i \eta_i)/(\Sigma E_i))^2}$, where E_i is the energy and η_i is the pseudorapidity of cell i and the sum is calculated within a window of 3×5 cells	$w_{\eta 2}$
Medium selection (includes loose)		
Strip layer of EM calorimeter	Shower width, $\sqrt{(\Sigma E_i (i - i_{\text{max}})^2)(\Sigma E_i)}$, where i runs over all strips in a window of $\Delta\eta \times \Delta\phi \approx 0.0625 \times 0.2$, corresponding typically to 20 strips in η, and i_{max} is the index of the highest-energy strip	w_{stot}
	Ratio of the energy difference between the largest and second largest energy deposits in the cluster over the sum of these energies	E_{ratio}
Track quality	Number of hits in the pixel detector (≥ 1)	n_{pixel}
	Number of total hits in the pixel and SCT detectors (≥ 7)	n_{Si}
	Transverse impact parameter ($\|d_0\|$ <5 mm)	d_0
Track–cluster matching	$\Delta\eta$ between the cluster position in the strip layer and the extrapolated track ($\|\Delta\eta\| < 0.01$)	$\Delta\eta$
Tight selection (includes medium)		
Track–cluster matching	$\Delta\phi$ between the cluster position in the middle layer and the extrapolated track ($\|\Delta\phi\| < 0.02$)	$\Delta\phi$
	Ratio of the cluster energy to the track momentum	E/p
	Tighter $\Delta\eta$ requirement ($\|\Delta\eta\| < 0.005$)	$\Delta\eta$
Track quality	Tighter transverse impact parameter requirement ($\|d_0\|$ <1 mm)	d_0
TRT	Total number of hits in the TRT	n_{TRT}
	Ratio of the number of high-threshold hits to the total number of hits in the TRT	f_{HT}
Conversions	Number of hits in the b-layer (≥ 1)	n_{BL}
	Veto electron candidates matched to reconstructed photon conversions	

Table 5.1: Definition of variables used for `loose`, `medium` and `tight` electron identification cuts for the central region of the detector with $|\eta| < 2.47$ [192]. Distributions of the variables can be found in reference [197].

In the `medium` cut set, which includes the whole `loose` selection, the shower-shape cuts are extended by the information of the strip cells in the first ECAL layer. Furthermore, the `medium` selection includes cuts on variables from the electron track. By applying the `medium` cuts, the electron identification efficiency is reduced by about 10%, whereas the background rejection increases by a factor of about $\sim 3 - 4$ compared to the `loose` selection [191].
The `tight` cut set makes use of all available particle identification tools and incorporates the `loose` and `medium` cuts. Additional requirements are on the matching of tracks and clusters and the track quality using information from the TRT. Furthermore, electrons

from photon conversions are rejected by requiring a hit in the first pixel layer (if expected). Using the `tight` selection, the initial goal of a background rejection of 10^5 is achieved with an overall identification efficiency of about 64% [191].

The performance of the identification criteria has been studied in reference [192] using the T&P method on a sample of $Z \to e^+e^-$ decays measured in 2010 data ($\mathcal{L} = 40\,\text{pb}^{-1}$, $\sqrt{s} = 7\,\text{TeV}$) and MC. The tag electron was selected from a sample of electrons passing the identification requirements. For the probe electron, all electrons passing the electron reconstruction algorithm (before the identification criteria) were considered, that have together with the tag electron an invariant mass close to the Z boson mass and opposite charges. In Figure 5.3, the efficiencies are shown for the `medium` and `tight` identification criteria as a function of the electron E_T. It can be seen that the efficiency for the `medium`

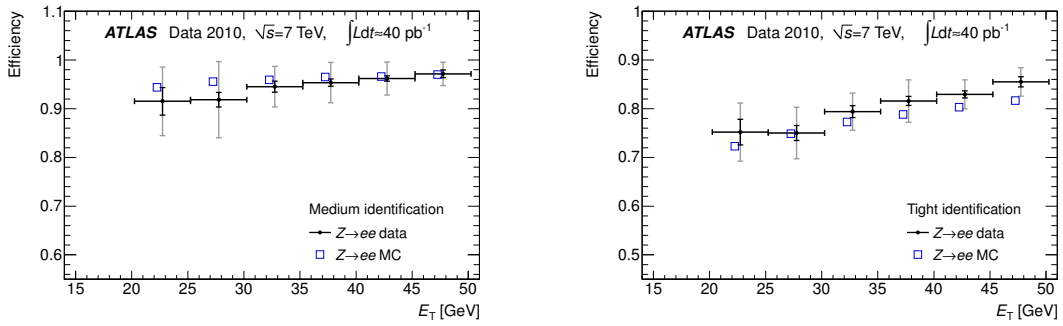

(a) (b)

Figure 5.3: Electron identification efficiencies with the standard menu [192]. The plots show the efficiencies for `medium` (a) and `tight` (b) identification criteria in $Z \to e^+e^-$ events in 2010 data and MC simulations.

selection is well above 90%, whereas it is reduced to $70 - 90\%$ for the `tight` selection[1]. More distributions can be found in reference [192].

With the increased instantaneous luminosity and the higher pile-up contributions in the 2012 data taking runs, an improved electron identification was required, in order to achieve comparable efficiencies and background rejection rates. Therefore, the electron `PlusPlus` identification menu was introduced.
In general, it incorporates the cuts of the standard menu, but the cut values on pile-up sensitive variables like R_{had} and R_η have been loosened in order to be more pile-up robust. Furthermore, additional cuts have been introduced. The changes compared to the standard menu are listed below.

- **`Loose++`:** This cut set applies additional loose cuts on the variables E_{ratio} and w_{stot}, which have been also used in the standard medium set. Additional cuts

[1] One should note that expected efficiency of about 64% in reference [191] is based on preliminary MC studies. For the final `loose`, `medium` and `tight` identification criteria, also used in the measurement of reference [192], the cuts have been optimised for achieving higher efficiencies.

refer to the track quality: the sum of the number of pixel hits and pixel outliers has to be at least one (outliers are hits, that belong to tracks with unresolvable ambiguities in the track reconstruction), whilst the number of SCT hits and SCT outliers has to be larger than six. Finally, a loose track-cluster match is required: $|\Delta\eta| < 0.015$.

- **`Medium++`:** The `medium++` cut set requires tighter cuts on the shower-shape variables than in `loose++`. The requirement on the sum of pixel hits and pixel outliers has been increased to at least 2. Additionally, there is a requirement on the sum of b-layer hits and b-layer outliers (for $|\eta| < 2.37$), which has to be at least 1. Finally, a cut on the variable $f3$ is introduced, which denotes the fraction of energy deposited in the third ECAL layer (see Section 3.2.4.1).
- **`Tight++`:** For `tight++` the cuts on the variables E/p and $\Delta\phi$ have been changed in comparison to the standard `tight` selection. The requirement on the b-layer hits and outliers has been extended to the full η region.

The identification efficiencies for the `PlusPlus` menu, which are presented in Figure 5.4, have been measured on MC and 2012 data ($\mathcal{L} = 770\,\text{pb}^{-1}$, $\sqrt{s} = 8\,\text{TeV}$) using the same T&P method as discussed for the efficiencies obtained for the standard menu measured on 2010 data. The identification criteria achieve efficiencies of $\gtrsim 95\%$ (`loose++`), $\sim 90\%$ (`medium++`) and $\sim 80\%$ (`tight++`).

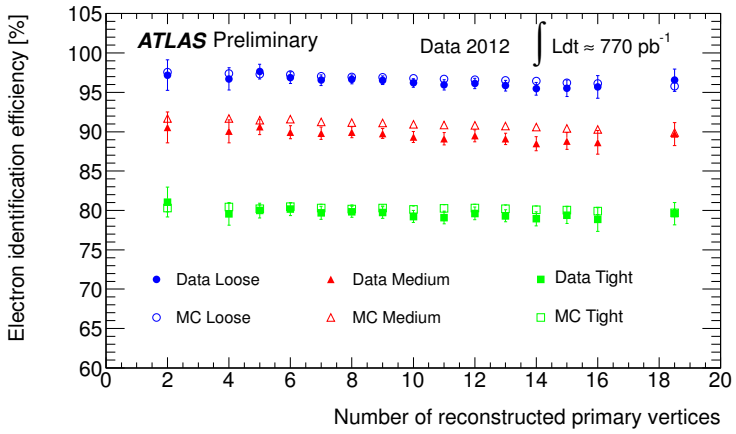

Figure 5.4: Electron identification efficiency in 2012 data as a function of the number of reconstructed primary vertices [196]. In this plot, Loose, Medium and Tight represent the identification criteria from the `PlusPlus` menu: `Loose++`, `Medium++` and `Tight++`.

The analysis in this thesis uses `tight++` electrons for the signal electron selection. In case of the estimation of mis-reconstructed leptons, a loosened selection using `medium++` is chosen (see Section 6.2.4).

In addition to the identification criteria, further cuts are applied in order to improve the electron selection:

- The magnitude of the longitudinal impact parameter $|z_0|$, which is defined by the position on the z-axis of the point of closest approach between the track and the beam pipe, has to be less than 2 mm.

- Several issues can cause hardware problems in the ECAL: for instance regions with no or too low nominal high voltage, dead front-end-boards (FEBs) or dead optical links. The *ElectronGamma* performance group provides object quality (OQ) maps, which mark the affected regions. Reconstructed electrons, that have traversed the problematic ECAL areas, are rejected in the analysis.

- Dramatic detector problems in the ECAL, in particular so-called noise bursts and data integrity errors, affect the calorimeter performance. Hence, events which are flagged with a so-called 'LArError' are rejected in the analysis.

5.3.2 Electron energy scale and resolution

As previously discussed, the electron energy is reconstructed from the energy deposits in the ECAL. This energy needs to be calibrated in order to recover the energy loss in front of the ECAL and due to the longitudinal and lateral leakage behind the ECAL and outside the clusters, respectively. There are several calibration coefficients applied to the cluster energies, which are obtained using the 'calibration hits' technique [198]. The estimation of these coefficients is based on special simulated MC samples with single electrons traversing the detector. For the detector simulation, a special ATLAS setup for `GEANT4` is used, in which the energy deposits in all detector materials is recorded (including the inactive material). The calibration coefficients are finally obtained by a parametrisation of the reconstructed energy inside the clusters, the estimated energy outside the clusters (but within the ECAL active material), the estimated energy leakage behind the ECAL and the estimated energy in front of the ECAL (as a function of the energy deposit in the presampler).
On top of the calibration, the electron energy in data is corrected by a factor α, which is obtained by comparing the invariant mass shape of $Z \to e^+e^-$ events in data and MC. The factor α, as shown in Figure 5.5a, was measured as a function of the electron pseudorapidity in 2011 and 2012 data. By applying a factor $(1+\alpha)^{-1}$ to the electron energy, this results in a match of the $Z \to e^+e^-$ shapes in data and MC. The uncertainty on this correction factor has been determined to be $1-2\%$ (based on internal ATLAS information, no published result was available).

The energy resolution

$$\frac{\sigma_E}{E} = \frac{a}{\sqrt{E[\text{GeV}]}} \oplus \frac{b}{E[\text{GeV}]} \oplus c, \tag{5.4}$$

with the coefficients defined in Equation (3.17), was measured by exploiting the invariant mass shape of $Z \to e^+e^-$ events in data and MC, in order to estimate the parameters a, b and c. For a and b the values are determined directly from MC, whereas the constant

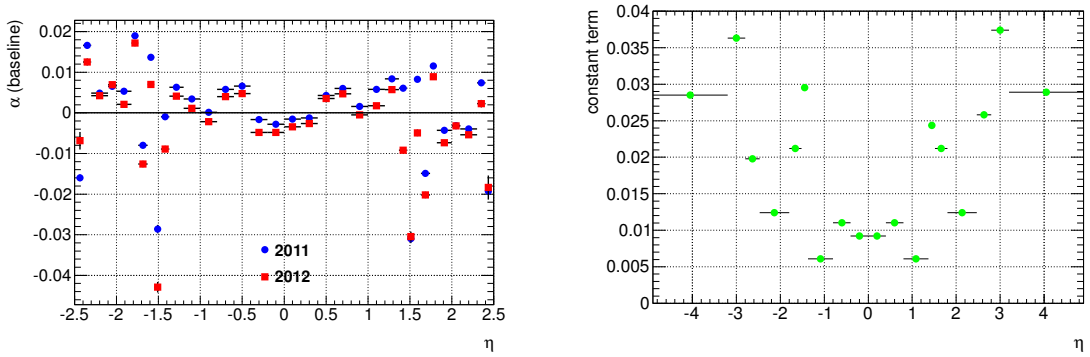

(a) (b)

Figure 5.5: The electron intercalibration coefficients α, which are presented in Figure (a), have been measured by comparing the invariant mass shapes of $Z \to e^+e^-$ events in MC and data collected in 2011 (blue) and 2012 (red) [199].
The constant term of the electron energy resolution is shown in Figure (b) [199] and has been obtained from 2012 data and MC using Equation (5.5).

term is determined from both, data and MC, with the formula [192]

$$c = \sqrt{2 \cdot \left[\left(\frac{\sigma}{m_Z} \right)^2_{\text{data}} - \left(\frac{\sigma}{m_Z} \right)^2_{\text{MC}} \right] + c^2_{\text{MC}}}, \tag{5.5}$$

where m_Z denotes the precisely measured Z boson mass [77], c_{MC} is the constant term obtained directly from MC ($\sim 0.5\%$ [192]) and the two σ represent the Gaussian widths of the experimental resolution. This resolution is obtained from fits to the invariant mass distributions in data and MC using a Breit-Wigner convolved with a Crystal Ball function [200], where the Breit-Wigner width is fixed to the measured Z width [77] and the experimental resolution is described by the Crystal Ball function. The constant resolution term c, obtained by applying above method on 2012 data and MC, is presented in Figure 5.5b and has been found to be between 0.5% and 4% depending on the electron η [192].

In the analysis, the energy of the electrons in MC events is randomly smeared in order to match the energy resolution in data. For the smearing a Gaussian with width σ_E is used describing the total energy resolution width.

5.3.3 Electron isolation

The electron identification criteria already provide a good background rejection rate, especially for electrons coming from hadron decays in jets. However, in order to further suppress the mis-identification of narrow jets or leptonic hadron decays, additional isolation criteria have been introduced. These are based on an energy and track isolation of the electron, presented in the following.

The energy isolation is performed by collecting the energy deposited in the calorimeters in a cone of size ΔR around the considered electron. This energy sum is usually called E_T^{Cone20} or E_T^{Cone30}, which corresponds to cone sizes of 0.2 and 0.3, respectively. In the centre of the cone a grid with a size of 5×7 (in units of $\Delta\eta \times \Delta\phi = 0.025 \times 0.025$) is excluded, in order to remove the energy of the electron itself.
Although most of the electron energy is included in the 5×7 cluster, the electron energy is leaking outside of this cluster with increasing energy. Therefore, a correction to the energy collected in the cone is applied, which is supposed to remove the amount of leakage energy (leakage correction). This correction term was determined in dedicated MC studies within ATLAS. An additional correction is applied to account for the energy deposits of pile-up and underlying event in the electron isolation cone, using the technique described in references [201, 202].

The track isolation is performed similar to the energy isolation. Tracks from the inner detector within a cone radius $\Delta R = 0.3$ around the electron are summed up and form the variable P_T^{Cone30}. The tracks have to fulfil the following requirements:

- $p_T > 0.4\,\text{GeV}$.
- $|d_0| < 1.5\,\text{mm}$ and $|z_0| < 1.0\,\text{mm}$.
- At least one hit in the pixel b-layer (if expected).
- At least 9 hits in the pixel and SCT.

Due to the cuts on the transverse and longitudinal impact parameters d_0 and z_0, the P_T^{Cone} variable is already pile-up robust and hence no further corrections need to be applied.

For 2012 analyses in general and in the analysis of this thesis, the variables E_T^{Cone20} and P_T^{Cone30} (with cone sizes $\Delta R = 0.2$ and $\Delta R = 0.3$, respectively) are used to improve the electron isolation. In order to achieve a uniform isolation efficiency distribution, there are no constant cuts on the isolation variables. Instead an efficiency map has been measured using the T&P method in $Z \to e^+e^-$ events. Then cut values on the isolation variables, which depend on the η and E_T of the electron, were evaluated separately for E_T^{Cone20} and P_T^{Cone30} in order to achieve an isolation efficiency of 90% in each case. The resulting cut values are presented in Figure 5.6 and range between 0.65 GeV and 3 GeV.

The resulting isolation efficiencies, when applying the cuts on both isolation variables E_T^{Cone20} and P_T^{Cone30} are shown in Figure 5.7 and have been also measured using the T&P method in $Z \to e^+e^-$ events on 2012 data and MC. It can be seen that both, the η and E_T dependence of the isolation efficiency, show a mostly uniform behaviour (besides a small efficiency loss directly behind the 'crack-region') and range between $\sim 80\%$ and $\sim 85\%$. In order to achieve a matching of the MC isolation efficiencies to the data efficiencies, the scale factors shown at the bottom of the plots (obtained by the ratio of data over MC efficiencies) are applied on the MC events when performing the analysis.

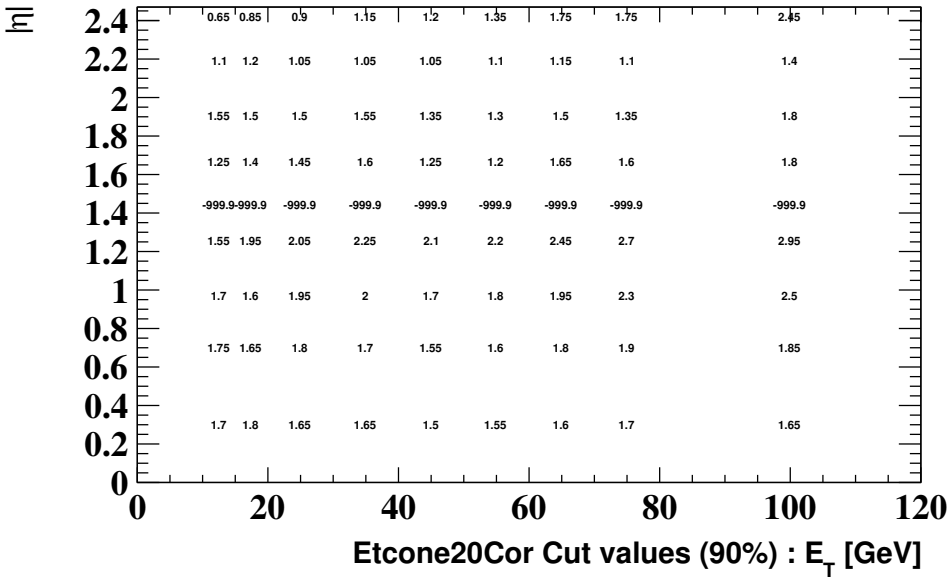

(a)

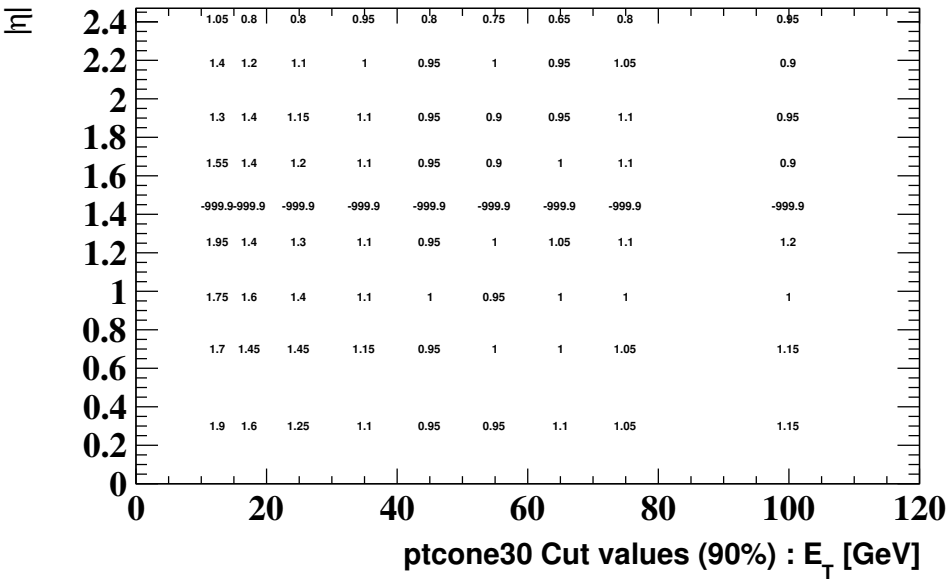

(b)

Figure 5.6: Electron isolation cut values in GeV on the variables E_T^{Cone20} (a) and P_T^{Cone30} (b) for achieving an isolation efficiency of 90%, taken from reference [203]. The cut values of -999.9 denote the 'crack-region', where no electrons are considered.

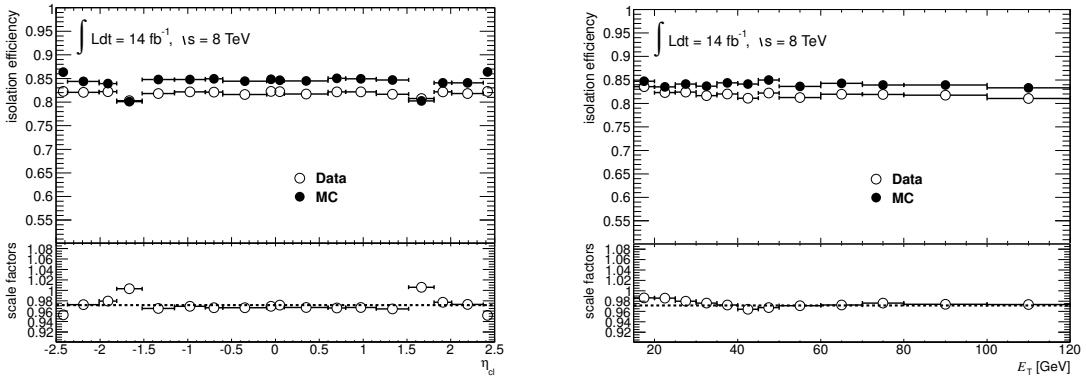

(a) (b)

Figure 5.7: Electron isolation efficiencies for cuts with 90% efficiency on E_T^{Cone20} and P_T^{Cone30}, taken from reference [203].

5.3.4 Electron trigger

The ATLAS trigger system is used for a pre-selection of events, in order to reduce the amount of data stored on disk (see Section 3.2.6). This analysis makes use of electron and muon triggers, where the former ones will be explained in this section and the latter ones in Section 5.4.4.

Events that are stored for further analysis need to pass a so-called trigger chain. Such trigger chains are combinations of trigger items for the L1, L2 and EF trigger level. Each trigger item represents a set of cuts, which need to be fulfilled by a particle object at the corresponding trigger level. As already mentioned in Section 3.2.6, the L1 hardware trigger is limited to certain sub-detectors for achieving a fast processing time. The HLT trigger, L2 and EF, are then capable of running more complex algorithms, whose implementations are close to the offline reconstruction and identification algorithms.

For the analysis in this thesis, the lowest unprescaled single electron triggers are used. Prescaled triggers had too high trigger rates during data taking and hence events are randomly rejected before writing to disk (this is performed by a random reset of passed trigger chains or items to 'false'). A single lepton trigger requires that at least one object in the event fulfils the trigger requirements (one also says the object has 'fired' the trigger), before the event is accepted and written to disk.

Events in this analysis are required to pass one of two different trigger chains L1 $\rightarrow$ L2 $\rightarrow$ EF. The first one is named `L1_EM18VH` $\rightarrow$ `L2_e24vh_medium1` $\rightarrow$ `EF_e24vhi_medium1` and hence consists of the L1 trigger item `L1_EM18VH`, the L2 item `L2_e24vh_medium1` and the final event filter item `EF_e24vhi_medium1`.
The `18` in the L1 item represents an E_T threshold of 18 GeV for the energy deposit in the ECAL. `V` stands for 'varied threshold' and means that a correction for coarse dead material in the ECAL has been applied to the trigger threshold. The `H` represents a hadronic core isolation at the L1 trigger level, which denotes a veto on the HCAL activity by requiring only a small fraction of deposited energy in the HCAL. In the L2

item the small capitals `v` and `h` appear, which only represent that the L2 item is seeded from a L1 item with varied threshold and hadronic core isolation. In contrast to the strict threshold of 18 GeV at the L1 trigger, the minimum transverse energy requirement for the L2 and EF item is below the 24 GeV value encoded in the trigger item name. It rather represents the E_T value, above which the trigger efficiency reaches a plateau with efficiencies close to 1. The `medium1` in the L2 and EF items stands for the `medium++` criteria, that are mirrored from the offline identification. Hence, the same variables and cut values are used here as in the offline selection. The additional `i` in the EF item stands for a loose track isolation, similar to the offline isolation presented in the previous Section 5.3.3. The electrons at the EF trigger level are required to have a $P_T^{\text{Cone20}}/E_T < 0.1$, where the same track criteria are applied as in the offline isolation, besides that the track momentum has to fulfil $p_T > 1\,\text{GeV}$ (instead of 0.4 GeV in the offline isolation).

The hadronic core isolation in the L1 item leads to inefficiencies for electrons with $E_T \gg 200\,\text{GeV}$. Therefore, the electrons are allowed to pass a second trigger chain, with significantly higher p_T thresholds but without the hadronic core isolation: `L1_EM30` → `L2_e60_medium1` → `EF_e60_medium1`. Furthermore, this chain contains no varied threshold (`V/v`) and isolation (`i`).

The performance of the combinations of these two electron triggers has been studied using the T&P method in $Z \to e^+e^-$ events. The trigger efficiencies for MC and a subset of the 2012 data (D4+ $\widehat{=}$ runs 208179-212272 corresponding to $\sim 40\%$ of the $14.324\,\text{fb}^{-1}$) are presented in Figure 5.8. As for the reconstruction and isolation efficiencies, scale

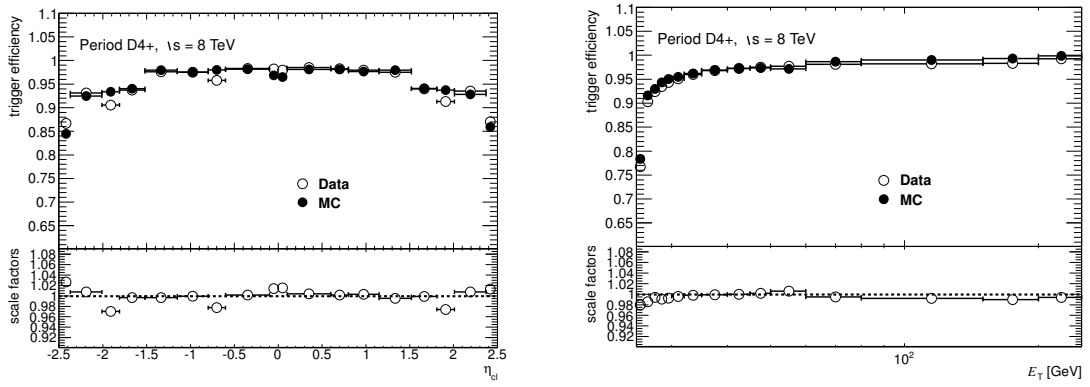

(a) (b)

Figure 5.8: Electron trigger efficiencies for electrons passing the `EF_e24vhi_medium1` or `EF_e60_medium1` trigger chains as a function of the cluster η (a) and transverse energy (b), taken from reference [203].

factors are derived from the measured efficiencies in data and MC and applied on MC events when performing the analysis, so that the MC trigger efficiencies match the ones from data.

5.4 Muons

As for the electrons, the W bosons produced in the fourth generation event topology decay also with a probability of $\sim$ 11% into muons and muon-neutrinos. Although muons give a much cleaner signature in the detector due to their penetrating behaviour, the muons need to be distinguished from leptonic hadron decays in jets. The different muon reconstruction algorithms and selection criteria presented in the following, have been developed and optimised by the *ATLAS Muon Combined* performance group.

5.4.1 Muon identification, reconstruction and efficiencies

The main detector part for the muon reconstruction are the three layers of MDT and CSC chambers (see Section 3.2.5), and there is also the possibility to reconstruct muons from the information of the inner detector. In general, at ATLAS there exist four different strategies for the reconstruction of muons:

- standalone (based on the information of the muon chambers only),
- combined (based on the information of the muon chambers and the inner detector),
- tagged (based on the information from the inner detector) and
- calorimeter tagged (combines inner detector and calorimeter information).

Two main muon reconstruction families have been developed in ATLAS, which both incorporate algorithms for each strategy. The analysis of this thesis uses muons reconstructed by the algorithms of the `Muid` family [204]. The other family, `STACO` [191], is not used and hence not further discussed here.

An explanation of the four strategies is given in the following:

- **Standalone:** This strategy is based on the information of the muon chambers and its implementation in `Muid` is called `Moore` [205]. In order to select muon candidates, the algorithm searches for track segments in the different layers of the muon chambers. This is performed by using a specific procedure for detecting tracks which is called 'Hough transformation' [206]. Then the detected segments are combined in a fit, which also takes into account the energy loss of the muons that have traversed the calorimeter system. The correction for the material effects is based on parametrisations for the crossed material and the measured energy deposits in the calorimeters [207]. The resulting track from the fit is finally extrapolated to the beam pipe and then called a 'standalone track'.
- **Combined:** A problem of the standalone track reconstruction is that it also detects muons coming from e.g. pion or kaon decays inside jets, which are commonly called fake or background muons. A possible procedure for rejecting such muons is to combine the standalone track reconstruction with tracks from the inner detector (ID). The track reconstruction algorithm, described in reference [208], starts with the identification of space points in the pixel and SCT. These space points are then

connected to track seeds within the first four layers of the ID. Finally, these track seeds are extended with measurements of the outer layers to form the whole ID tracks.
In the end, the tracks from the muon spectrometer (MS) and ID are combined and the combined track parameters are determined by minimising the χ^2_{match} given by [191]

$$\chi^2_{\text{match}} = (\mathbf{T}_{\text{MS}} - \mathbf{T}_{\text{ID}})^T (\mathbf{C}_{\text{ID}} + \mathbf{C}_{\text{MS}})^{-1} (\mathbf{T}_{\text{MS}} - \mathbf{T}_{\text{ID}}) , \tag{5.6}$$

where $\mathbf{T}_{\text{MS}}$ and $\mathbf{T}_{\text{ID}}$ denote vectors of the track parameters coming from the MS and ID, respectively, and $\mathbf{C}_{\text{MS}}$ and $\mathbf{C}_{\text{ID}}$ are the corresponding covariance matrices with the uncertainties of the measurements. Furthermore, the matching χ^2_{match} also provides a measure of the quality of the track match.

- **Tagged:** Another approach for muon reconstruction starts with tracks from the inner detector. These tracks, which are reconstructed with the same algorithm mentioned above, are then propagated to the first layer of muon chambers, where it is then searched for nearby track segments. If such track segments are found, there are two different spectrometer tagging algorithms used: `MuTag` [208] calculates a tagging χ^2 from the difference of the extrapolated track to the MS segments. In `MuGirl` [209] an artificial neural network is used to define a discriminant for the tagging decision. If the track fulfils the tagging requirements, it is tagged as 'corresponding to a muon' [191]. Both algorithms allow to use the MS measurements for a combined track re-fit afterwards.

- **Calorimeter tagged:** The calorimeter tagging combines the information of tagged tracks and the information of energy deposits in the calorimeters, but is not used in this analysis.

Depending on with which algorithms a muon has been reconstructed, there are different muon quality labels:

- All tagged muons that have hits in the pixel or SCT are marked as **`loose`**.

- Muons with standalone tracks are labelled as **`medium`**.

- All combined muons and those resulting from the `MuGirl` algorithm followed by a combined fit are marked as **`tight`**.

Muons in the analysis of this thesis are required to carry the `tight` quality. Further requirements are on the muon transverse momentum $p_T > 25\,\text{GeV}$ (due to the trigger threshold, see Section 5.4.4) and the pseudorapidity $|\eta| < 2.5$ (due to the acceptance region of the ID). Furthermore, there is the same cut on the longitudinal impact parameter of $|z_0| < 2\,\text{mm}$ as for the electrons. In addition, several requirements on the hits in the ID of the associated tracks are applied for improving the track quality:

- at least one b-layer hit (if expected),

- $N_{\text{Hits}}^{\text{Pix}} + N_{\text{CDS}}^{\text{Pix}} > 0$, where $N_{\text{Hits}}^{\text{Pix}}$ denotes the number of hits in the pixel and $N_{\text{CDS}}^{\text{Pix}}$ represents the number of crossed dead pixel sensors (in order to account for the detector conditions),
- $N_{\text{Hits}}^{\text{SCT}} + N_{\text{CDS}}^{\text{SCT}} \geq 5$, where $N_{\text{Hits}}^{\text{SCT}}$ denotes the number of hits in the SCT and $N_{\text{CDS}}^{\text{SCT}}$ represents the number of crossed dead SCT sensors,
- $N_{\text{Holes}}^{\text{Pix}} + N_{\text{Holes}}^{\text{SCT}} < 3$, where $N_{\text{Holes}}^{\text{Pix/SCT}}$ denotes the number of layers in the pixel and the SCT without a hit produced by the track
- and there are two η dependent criteria on the hits and outliers (similar to the pixel these are TRT hits, that belong to tracks with unresolvable ambiguities in the track reconstruction) of the TRT.
  - For $0.1 < |\eta| < 1.9$, the variable $n = N_{\text{Hits}}^{\text{TRT}} + N_{\text{Outliers}}^{\text{TRT}}$ has to be larger than 5 and $N_{\text{Outliers}}^{\text{TRT}}/n$ must be smaller than 0.9.
  - Outside this region ($|\eta| \leq 0.1$ or $|\eta| \geq 1.9$) it is also required that $N_{\text{Outliers}}^{\text{TRT}}/n$ is smaller than 0.9, but only if $n > 5$.

Finally, there is a so-called 'cosmic-rejection', which is supposed to remove events where two muons have been identified but were originating from cosmic rays. A 'cosmic muon' enters the detector at some point and leaves it on the opposite side. Since the muon reconstruction does not consider any timing information, it will reconstruct in such an event two back-to-back muon candidates, originating from the point of closest approach (PCA) to the beam line. In order to reject such cosmic muons, an event is rejected if there is a muon pair fulfilling all of the following requirements:

- Their transverse impact parameters d_0^{beam} (here it is defined as the distance of the PCA to the beam line or rather the z-axis) are required to have opposite signs. The sign is defined as follows

$$\text{sign}(d_0^{\text{beam}}) = \text{sign}\left(\vec{e_z} \cdot (\vec{X_T} \times \vec{P_T})\right), \tag{5.7}$$

  where $\vec{e_z}$ denotes a unit vector along the z-axis, $\vec{P_T}$ represents the direction of the muon track at the PCA and $\vec{X_T}$ is a vector pointing from the detector origin to the PCA. The vector product $\vec{X_T} \times \vec{P_T}$ can also be interpreted as angular momentum of the muon around the beam pipe. In general, above scalar triple product is defined positive, if the three vectors form a right-handed system. Hence, the transverse impact parameters of two muons, whose points of closest approach lie in the same hemisphere of the detector and whose angular momenta point into opposite directions, will have opposite signs. This is the case for cosmic muons, because they originate from the same vertex and point into opposite directions.
- Cosmic muons can enter the detector at any point. Due to the large size of the detector, only in rare cases the muon tracks will be very close to the beam pipe. Hence, a large part of events with a cosmic muon is rejected by requiring $|d_0^{\text{beam}}| > 0.5\,\text{mm}$.

- As previously mentioned, the two tracks from a cosmic muon will be back-to-back. Therefore, cosmic muons are selected if $\Delta\phi > 3.1$, where $\Delta\phi$ denotes the angular difference of the two tracks in the ϕ space.

The performance of the muon reconstruction has been studied in reference [210] using the T&P method in $Z \to \mu^+\mu^-$ events, where the tag object is a combined muon and the probe is an ID track fulfilling the track quality criteria. The resulting reconstruction efficiencies and scale factors, that have been measured in 2012 data ($\mathcal{L} = 2.264\,\text{fb}^{-1}$, $\sqrt{s} = 8\,\text{TeV}$) and MC, are presented in Figure 5.9 as a function of the muon pseudorapidity. The scale factors, which are below 1%, are applied to MC events in the analysis, so that there is a match between the data and MC reconstruction efficiencies.

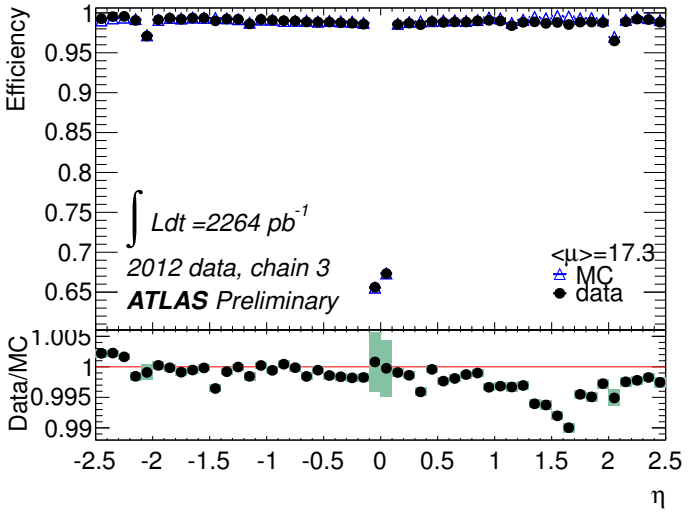

Figure 5.9: Muon reconstruction efficiency measured in 2012 data and MC as a function of the muon pseudorapidity [210]. Here, 'chain 3' refers to a muon reconstruction algorithm family, that will be used in future analyses. Basically, this is a unification of the `Muid` and the `STACO` family. However, a plot showing the efficiencies for the `Muid` family only was not provided by the *ATLAS Muon Combined* performance group, but the corresponding efficiencies are similar.

5.4.2 Muon momentum scale and resolution

The measurement of the muon momentum scale and resolution, as described in reference [211], is performed by selecting opposite-sign dimuon events with invariant masses close to the Z boson mass. The position and the width of the invariant mass distribution is sensitive to the transverse momentum scale and resolution. Using a template fit to the invariant mass distribution, the overall scale and resolution parameters (as defined in Equation (3.19)) are determined. Figure 5.10 presents the muon momentum resolution

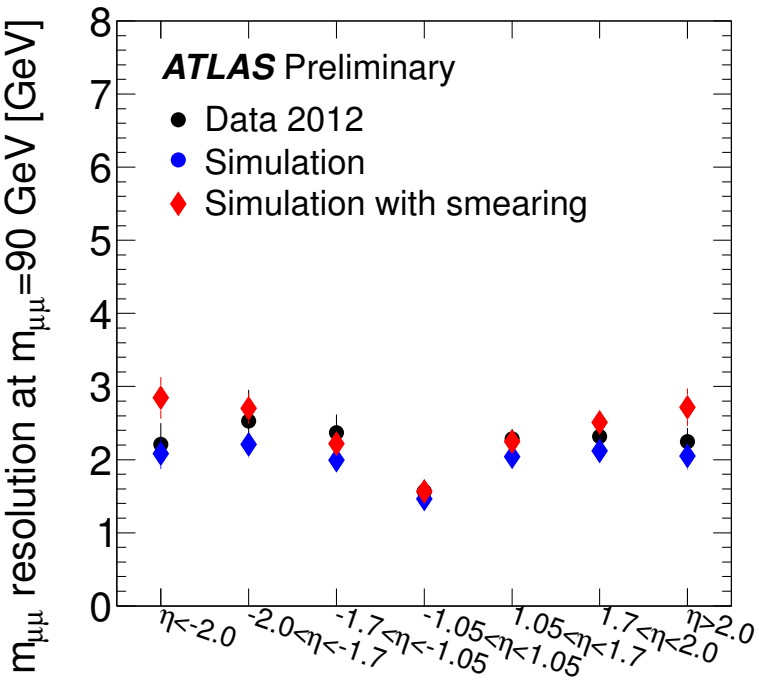

Figure 5.10: Muon momentum resolution measured in 2012 data ($\mathcal{L} = 824\,\mathrm{pb}^{-1}$, $\sqrt{s} = 8\,\mathrm{TeV}$) and MC as a function of the muon pseudorapidity [210]. The resolution is the width of a Gaussian which is convoluted with the dimuon mass resolution. In the red points a smearing correction has been applied to the muon momenta for matching the resolution in data.

obtained from 2012 data ($\mathcal{L} = 824\,\mathrm{pb}^{-1}$, $\sqrt{s} = 8\,\mathrm{TeV}$) and MC. In the red points, an additional smearing of the muon momenta has been applied in order to match the resolution in data.

Figure 5.11 shows the dimuon invariant mass distributions before applying any corrections to the muon momenta and after applying a scaling and smearing correction, obtained from 2012 data ($\mathcal{L} = 5.8\,\mathrm{fb}^{-1}$, $\sqrt{s} = 8\,\mathrm{TeV}$) and MC using the fitting procedure mentioned above. After the corrections, data and MC show a better agreement in average. Hence, in the analysis, for the muons in MC events such a scaling and smearing correction is applied.

5.4.3 Muon isolation

As previously mentioned, muons can appear in leptonic decays of hadrons inside jets. Such muons can be rejected, if there is a large track density around the muon in the inner detector. Instead of requiring a similar isolation as for the electrons with fixed cone sizes, another approach has been initially proposed in reference [213] and is called

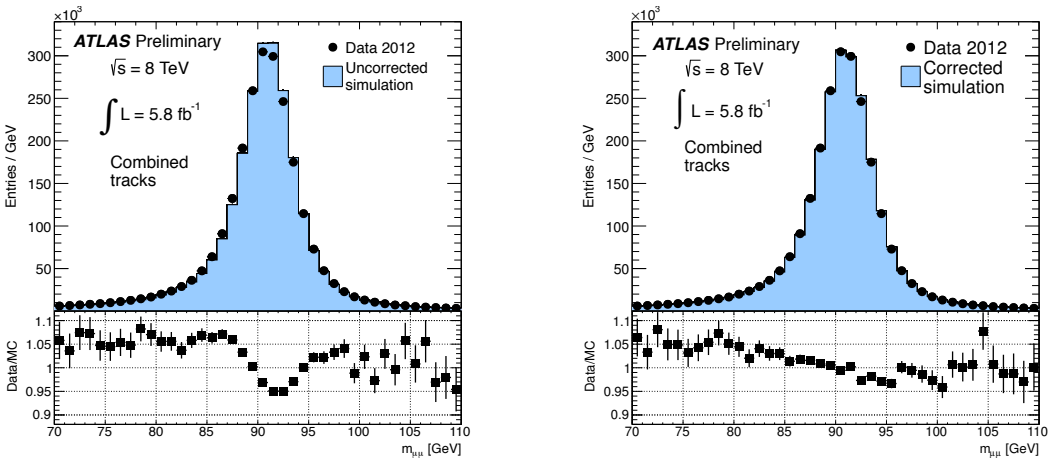

(a) (b)

Figure 5.11: Dimuon invariant mass performance plots [212] in 2012 data ($\mathcal{L} = 5.8\,\text{fb}^{-1}$, $\sqrt{s} = 8\,\text{TeV}$) and MC before applying any corrections to the muon momenta (a) and after applying a scaling and smearing correction (b). There remains a small discrepancy of up to 5% due to technical problems, that occurred in the modelling of multiple scatterings in the `GEANT4` detector simulation.

'Mini-Isolation' (MI). The idea is that instead of summing the track transverse momenta in a fixed cone around the muon, the isolation cone size is varied depending on the muon p_T. It has been shown in reference [213] that such an isolation has a high performance in analyses with boosted fermions, which arise in the decay topology of heavy particles (also called 'boosted topologies').

The isolation variable is defined as

$$I_{\text{mini}} = \sum_{\text{tracks}} \frac{p_T^{\text{track}}}{p_T^{\mu}}, \tag{5.8}$$

where the sum runs over all tracks with $p_T^{\text{track}} > 1\,\text{GeV}$ and a maximum distance to the muon of $\Delta R < K_T/p_T^{\mu}$. Here, p_T^{μ} denotes the muon transverse momentum and K_T is an arbitrary scale parameter. Due to the distance requirement, the cone size becomes smaller for increasing muon momenta. Further requirements on the summed tracks are $|d_0| < 10\,\text{mm}$, $|z_0 \cdot \sin\theta_{\text{track}}| < 10\,\text{mm}$ and $N_{\text{Hits}}^{\text{Pix(SCT)}} + N_{\text{CDS}}^{\text{Pix(SCT)}} \geq 4$, where the latter equation denotes the total sum of all hits and crossed dead sensors in the pixel (SCT) associated to the tracks.

In reference [213] it has been found that $K_T = 10\,\text{GeV}$ and $I_{\text{mini}} < 0.05$ achieves an optimal isolation performance. Therefore, these isolation criteria are also required for the muons in this analysis.

The performance of the muon isolation has been studied using the T&P method in $Z \to \mu^+\mu^-$ events of 2012 data ($\mathcal{L} = 14\,\text{fb}^{-1}$, $\sqrt{s} = 8\,\text{TeV}$) and MC. The resulting

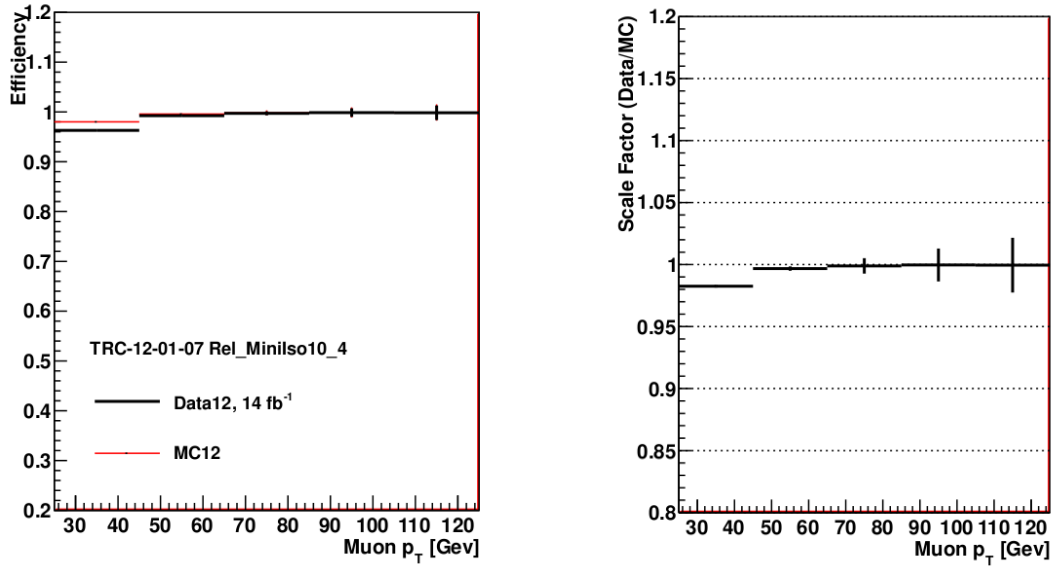

(a) (b)

Figure 5.12: Efficiencies (a) and scale factors (b) for the muon mini-isolation [203]. The efficiencies have been determined from 2012 data ($\mathcal{L} = 14\,\text{fb}^{-1}$, $\sqrt{s} = 8\,\text{TeV}$) and MC.

efficiencies and scale factors are presented in Figure 5.12. The scale factors are close to 1 over the whole p_T range. Hence, there is no isolation scale factor applied in the analysis. The small difference in the first p_T bin is taken into account as a systematic uncertainty later in the analysis.

5.4.4 Muon trigger

In addition to the single electron triggers, the events in this analysis can also pass one of the single muon trigger chains explained below.

The muon triggering starts in the muon system RPC and TGC chambers (see Section 3.2.5), where the L1 trigger level algorithm searches for hit coincidences within the different chamber layers. If such coincidence is found, the corresponding region-of-interest (RoI) is selected and passed to the L2 trigger level.
The main algorithm of the L2 trigger is called `muFast` [191] and analyses the data with full granularity within the RoI. `muFast` performs a pattern recognition using the trigger hits and then selects MDT regions within the RoI that have been crossed by the muon track. Then a track fit is performed using the selected MDT information. Finally, at the end of the L2 trigger stage, the algorithm `muComb` [191] allows to combine the tracks from the muon spectrometer with corresponding inner detector tracks.
If the event has passed the L2 trigger, it is passed to the EF trigger level, which analyses the full event with full granularity. The EF uses the algorithms from the offline muon

reconstruction, interfaced by a wrapper called `TrigMuonEF`. The procedure is similar to the one from L2: first, tracks are reconstructed in the MS and a full track fitting is performed. Then the muon tracks are extrapolated to the beam pipe. Finally, the MS track is combined with reconstructed tracks from the ID.

In this analysis, two different single muon trigger chains are used. As for the electrons, a muon only needs to pass at least one of them. The first trigger `EF_mu24i_tight` corresponds to the chain `L1_MU15` $\rightarrow$ `L2_mu24_tight` $\rightarrow$ `EF_mu24i_tight`, whereas the second trigger `EF_mu36_tight` correlates to the chain `L1_MU15` $\rightarrow$ `L2_mu36_tight` $\rightarrow$ `EF_mu36_tight`. Both triggers represent unprescaled trigger items with the lowest p_T thresholds during the whole 2012 data taking.
The isolation in the former trigger item was introduced, in order to obtain a trigger item where the plateau region starts below $p_T = 25\,\text{GeV}$. The trigger isolation applied at the EF level requires $P_T^{\text{Cone20}}/p_T > 0.12$, for tracks with $p_T^{\text{track}} > 1\,\text{GeV}$ and a difference of the longitudinal impact parameters of muon and track of $|z_0^{\mu} - z_0^{\text{track}}| < 6\,\text{mm}$.
The `tight` label in the L2 and EF items represents the same quality criteria as for the offline muon reconstruction.

The trigger efficiencies have been measured using the T&P method in $Z \rightarrow \mu^+\mu^-$ events, as explained in reference [214]. The tag sample uses combined muons, whereas ID tracks are used as probe. Only ID tracks are selected, that have together with the tag object an invariant mass $m_{\mu^+\mu^-}$ close to the Z boson mass. The measured trigger efficiencies in 2012 data ($\mathcal{L} = 5.56\,\text{fb}^{-1}$, $\sqrt{s} = 8\,\text{TeV}$) for the `EF_mu24i_tight` trigger are presented in Figure 5.13 as a function of the muon pseudorapidity. The same measurement has been performed for the `EF_mu36_tight` item and also on simulated MC events (not shown here). The variations between the data and MC trigger efficiencies

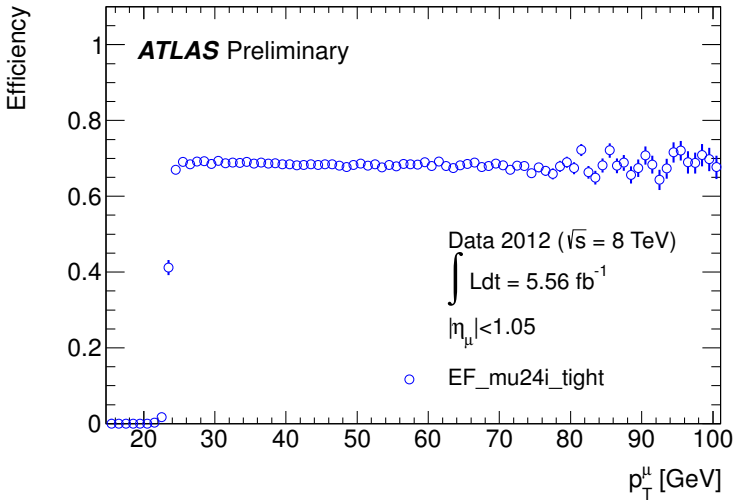

Figure 5.13: Muon trigger efficiency in 2012 data ($\mathcal{L} = 5.56\,\text{fb}^{-1}$, $\sqrt{s} = 8\,\text{TeV}$) as a function of the muon pseudorapidity [215]. Shown is the efficiency for the trigger item `EF_mu24i_tight`.

are corrected in the analysis by applying scale factors to the MC events. These scale factors were derived as a function of the muon η and ϕ and range between 0.9 and 1.1.

5.5 Jets

For the fourth generation quark decays it is expected that several partons are produced. Further partons can also result from the underlying event. As previously discussed, these partons form parton showers which finally hadronise and appear as particle bundles (jets) in the detector.
Jets are reconstructed from the energy deposits in the calorimeters. The challenge for the jet reconstruction algorithms is to form jets from the energy clusters and relate the jet kinematic properties to those of the parton shower. It should be said that in contrast to the electron and muon reconstruction algorithms, which are supposed to reconstruct real existing particles, jets do not exist in the sense of a physical object. They are rather defined by the jet algorithms and hence different algorithms will provide different results for the reconstructed jet multiplicities and kinematics.

The development and optimisation of the jet reconstruction and selection criteria has been performed by the *ATLAS Jet and EtMiss* performance group.

5.5.1 Jet reconstruction and efficiencies

In general, there exist two main categories of jet algorithms: cone jet algorithms, which make use of ordering relations in the position space, and recombination algorithms that order in the momentum space. There are two important criteria in physics analyses that should be fulfilled by the jet algorithms. They need to be

- infrared safe, which means that there are no fluctuations in the output when adding soft (low-p_T) particles (e.g. coming from additional radiations), and
- collinear safe, that means that collinear splittings of the incoming partons do not affect the resulting jet output from the algorithm.

The former cone jet algorithm is not infrared safe and, as a consequence, in ATLAS the recombination algorithm, which is both infrared and collinear safe, is used per default for the jet reconstruction.

This jet reconstruction algorithm belongs to the family of cluster algorithms and is based on a pair-wise clustering of the initial constituents [191]. It creates a list of all detected clusters in the calorimeters and then recombines them in an iterative procedure. At each step, for each object (cluster) i the two quantities

$$d_{ij} = \min\left(k_{T,i}^{2p}, k_{T,j}^{2p}\right) \frac{(\Delta R)^2}{R^2} \tag{5.9}$$

and

$$d_{iB} = k_{T,i}^{2p} \tag{5.10}$$

are evaluated [191], where j are all other clusters besides i, $k_{T,i(j)}^{2p}$ denotes the transverse momentum with respect to the beam axis belonging to the four-momentum of cluster i (j), ΔR is the distance between cluster i and j in the η-ϕ space and p and R are parameters which define the algorithm (and will be explained later). d_{ij} can be interpreted as the distance between i and j in momentum space and d_{iB} represents the squared transverse momentum of cluster i with respect to the beam-pipe. After creating the full list of the d_{ij} and d_{iB} values, the minimum $d_{\min}$ is selected.

- If the $d_{\min}$ is one of the d_{ij}, then the clusters i and j are combined and the list is re-made.
- If the $d_{\min}$ is one of the d_{iB}, then the object i is considered as final, that is, a complete jet and it is removed from the list of clusters.

This iterative procedure is performed until there are no remaining clusters on the list.
In the distance measure d_{ij} two parameters appear: R and p. The parameter R sets the resolution at which jets are resolved. Larger values of R result in smaller distance values d_{ij} and hence more clusters are combined before a jet is considered as complete. This analysis uses an R value of $R = 0.4$.
Depending on the p parameter, the k_T algorithm can be divided into three different classes:

- $\mathbf{p = 1}$: In this case (commonly known as the original k_T algorithm [216]), soft objects with low transverse momenta are merged first and the final merge combines the hardest clusters. This mimics and reverts the splitting within the parton showering and results in a strong ordering in the transverse momentum. However, very soft objects with $d_{iB} < d_{ij}$ for all clusters j will be not merged with other objects and hence left alone as single low energetic jets.
- $\mathbf{p = 0}$: In this class, also called the Cambridge/Aachen algorithm [217], the clustering is independent of the transverse momenta of the objects. Therefore, objects that are close in the η-ϕ space are merged first and the final merge combines the objects with the largest distances.
- $\mathbf{p = -1}$: This case is called the anti-k_T algorithm [218] and is the default choice in ATLAS (and also in the analysis presented in this thesis). Soft objects within $\Delta R < R$ to a hard object are merged first. Hence jet boundaries are not affected by soft radiations which makes this algorithm infrared safe. If there are two comparable hard objects within $R < \Delta R < 2R$, the surrounding softer clusters are merged with one of the two hard objects depending on the d_{ij} values. When a hard object has been merged with the surrounding softer clusters, the remaining hard objects within $\Delta R < R$ form single high energetic jets.

An implementation of the k_T algorithm, which is also used for the jet reconstruction at ATLAS, can be found in the `FastJet` package [219].

As previously mentioned, jets can be formed from partons resulting from the underlying event. These jets usually occur with low momenta. Therefore, in order to suppress

such jets, each jet is required to have a minimum transverse momentum of $p_T > 25\,\text{GeV}$. Furthermore, jets need to lie within the region $|\eta| < 2.5$, which is required to perform the overlap-removals with the leptons as explained in Section 5.6. Both cuts are applied after performing the jet calibration discussed in the following Section 5.5.2.

The jet reconstruction efficiency has been measured on 2010 data ($\mathcal{L} = 6\,\text{nb}^{-1}$, $\sqrt{s} = 7\,\text{TeV}$) and simulated MC events using the T&P method in di-jet events, as explained in reference [220]. The tag sample was derived by selecting so-called track jets. Such track jets are built using inner detector tracks as input to the jet reconstruction algorithm instead of the calorimeter clusters. The probe sample is then selected with track jets that are back-to-back ($\Delta\phi > 2.8$) with the tagged jet. Furthermore the probe track jets are required to have a match within $\Delta R < 0.4$ with a jet reconstructed from the calorimeter clusters. The resulting efficiencies of the T&P method are presented in Figure 5.14. The jet reconstruction is fully efficient for $p_T > 30\,\text{GeV}$ for both, data and

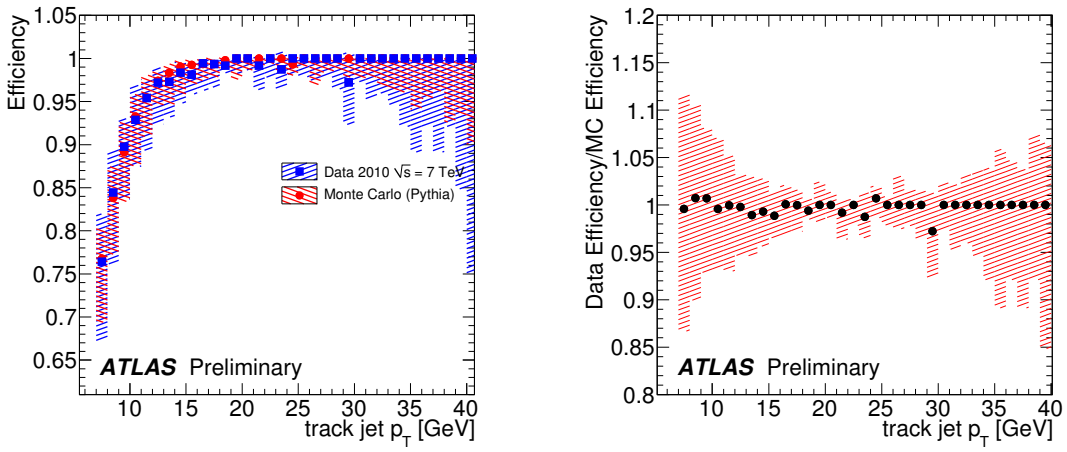

(a) (b)

Figure 5.14: Jet reconstruction efficiency measured in 2010 data ($\mathcal{L} = 6\,\text{nb}^{-1}$, $\sqrt{s} = 7\,\text{TeV}$) and MC using the Tag&Probe method [220]. The efficiency is plotted in (a) as a function of the probe track jet p_T. The shaded areas denote the combination of statistical and systematic uncertainties. Figure (b) depicts the ratio of data and MC efficiencies.

MC. The small differences between data and MC for jets with $25\,\text{GeV} < p_T < 30\,\text{GeV}$ are considered later in the analysis as systematic uncertainty on the jet reconstruction efficiency. Hence, no scale factor is applied during the analysis, as for the electron and muon efficiencies.

5.5.2 Jet energy scale and resolution

The ATLAS hadronic calorimeter system has a non-compensating nature. This means that electromagnetic and hadronic showers which have the same incident energy are

not producing the same signal. This is due to the fact that hadronic showers have an electromagnetic (EM) component, mostly initiated by π^0 decays, and a non-EM component, for instance nucleons and charged pions or kaons. While the EM component is fully measured, the latter non-EM part can (partly) escape the detection. Furthermore, the nuclear binding energy needed to release the nucleons is lost for detection (see also for instance references [221, 222] for further reading on this topic). Hence, for hadronic jets, less energy is reconstructed than it has been deposited (typically 15-55% [223]). This energy loss needs to be corrected for, which is subject to the jet calibration.

In this analysis, jets are used that have been calibrated with the 'Local Cell Weighting' (LCW) scheme [224]. This calibration scheme starts from the measured calorimeter energy at the EM energy scale (which means that this energy was calibrated by the energy deposits of electromagnetically interacting particles, as described in reference [225]). The idea of the LCW scheme is to correct locally the measured energy deposits in topological calorimeter clusters prior to the jet finding algorithm. Topological (topo) clusters are groups of clusters with neighbouring calorimeter cells that have significant energy deposits compared to the expected noise [226]. Locally means that a correction is applied to each topo cluster separately depending on a classification scheme. This classification scheme categorises each topo cluster as either electromagnetic or hadronic, depending on the longitudinal and lateral shape of the deposited energy distribution.

In general, there are three different corrections applied to the topo clusters:

- A pile-up correction is supposed to account for the energy deposits by objects from pile-up events. Hence, an average of such additional energy is subtracted from the topo cluster measurement. This average energy is determined in *in-situ* measurements (see reference [224]) and depends on the number of primary vertices and the mean number of interactions per bunch crossing. A further correction is applied to account for variations in the jet areas due to the pile-up effects.

- After the reconstruction algorithm, jets are defined to originate from the geometrical centre of the detector. In order to get the jets originating from the primary vertex, a so-called vertex correction is applied which alternates the jet direction.

- Finally, the jet energy is calibrated to the hadronic scale, which means that the previously mentioned energy loss of hadronic showers is recovered. This correction is also referred to as jet energy scale (JES) correction. The correction factors are determined by comparing kinematic observables of true and reconstructed jets in simulated QCD jet events. Figure 5.15 presents the energy response determined from such simulated events in different bins of the calibrated jet energy and as a function of the detector pseudorapidity. Here, the jet energy response is the inverse of the average JES correction factor.

Jets corrected for the pile-up, vertex and the JES are referred to as 'LCW+JES calibrated'.

After above described JES calibration, the jet p_T is corrected for differences between data and MC. These differences were measured using the *in-situ* techniques described in

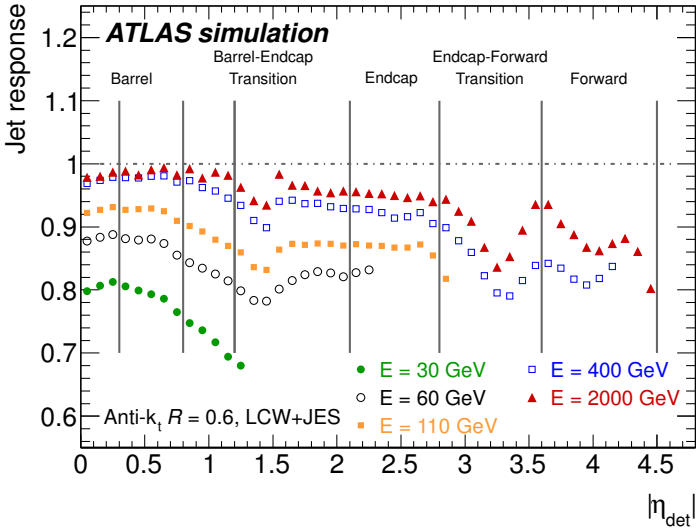

Figure 5.15: Average simulated jet energy response at the LCW scale in bins of the calibrated jet energy and as a function of the detector pseudorapidity [224].

reference [227], where the jet p_T in data is compared to the one in MC. These techniques exploit the p_T balance between the jet p_T (p_T^{jet}) and the p_T of a reference object (p_T^{ref}), which is given by [227]

$$\frac{\langle p_T^{\text{jet}} / p_T^{\text{ref}} \rangle_{\text{data}}}{\langle p_T^{\text{jet}} / p_T^{\text{ref}} \rangle_{\text{MC}}} \,. \tag{5.11}$$

In ATLAS, three different methods are used to derive the p_T balance [227]:

- **Direct $\mathbf{p_T}$ balance between a Z boson and a jet**: This method uses events with a Z boson and a recoiling jet for comparing the jet p_T with the Z boson p_T and is referred to as Z+jet method.
- **$\mathbf{p_T}$ balance between a photon and the hadronic recoil**: Here, events with a photon and jets are used (γ+jets). The photon p_T is compared to the full hadronic recoil in the event, determined by the projection of the missing transverse energy projected onto the photon direction.
- **Balance of multijets**: In this method events with several jets are used (multijets). Jets with high p_T are balanced against the recoil system of the low p_T jets.

The combination of the p_T balances obtained from 2012 data ($\sqrt{s} = 8\,\text{TeV}$) and MC for all three methods, as shown in Figure 5.16a, is finally applied as correction to the jet momenta in the analysis.

In order to determine the systematic uncertainty of the JES, 54 different sources of uncertainties need to be considered. These sources include the *in-situ* methods them-

selves and also uncertainties coming from close-by jets (these are jets which are nearby within a certain distance in the $\eta - \phi$ space, see also reference [228]) and the jet flavor composition [229]. A detailed description of the sources, as well as the methods to derive the uncertainty components are presented in reference [227]. The results obtained

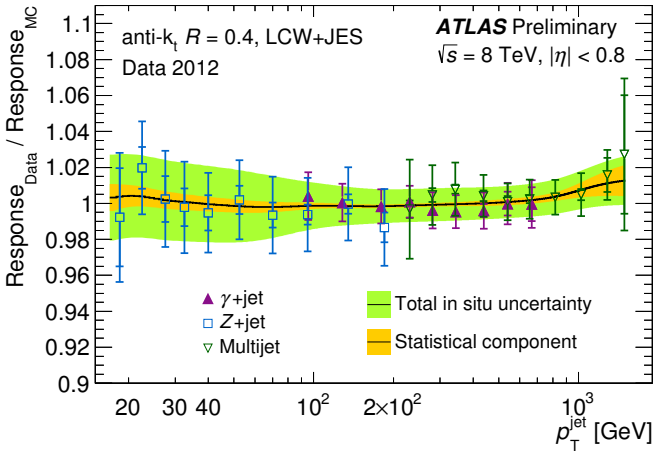

(a)

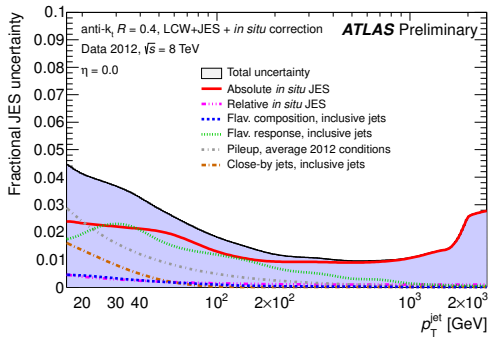

(b)

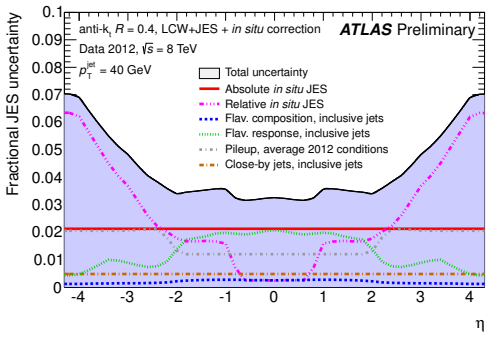

(c)

Figure 5.16: In (a) the jet response ratio for 2012 data over MC is presented as a function of the jet p_T [230]. The plot shows the combination of three different in-situ techniques (Z+jet, γ+jet and multijet) and the error bars represent the statistical and systematic uncertainties of the measurements.
In (b) and (c) the fractional jet energy scale uncertainty components are presented as a function of the jet p_T (with $\eta = 0$) and η (with $p_T = 40\,\text{GeV}$), respectively [230]. The filled blue region denotes the total systematic uncertainty of the jet energy scale.

for 2012 data ($\sqrt{s} = 8\,\text{TeV}$) are presented in Figures 5.16b and 5.16c and show JES uncertainties between 1% and 7%, depending on the jet p_T and η.

The determination of the jet energy resolution (JER) is divided into two parts: estimating a truth resolution, denoting the difference between true and reconstructed jet

energy, and measuring an *in-situ* resolution, used for comparing the resolutions between data and MC.
The truth resolution is obtained from determining the width of a Gaussian fit to the distribution of $p_T^{\text{reco}}/p_T^{\text{part}}$, where p_T^{reco} denotes the jet transverse momentum after reconstruction and p_T^{part} is the jet p_T reconstructed from stable true particles. When analysing dijet MC simulations with $\sqrt{s} = 8\,\text{TeV}$, the relative resolution (width/mean) was determined to be 10.7% for jets with $85\,\text{GeV} < p_T^{\text{reco}} < 100\,\text{GeV}$ and $|y| < 0.8$ (no public result was available).
For the measurement of the *in-situ* resolution, a so-called bisector technique is used, which is described in reference [223]. It is based on a transverse balance vector, defined as the vector sum of the momenta of the two leading jets (the two jets with highest p_T) in dijet events: $\vec{P}_T = \vec{P}_T^{j1} + \vec{P}_T^{j2}$ [223]. The balance vector is then projected onto an orthogonal coordinate system (ψ, η), in which the direction of η is chosen such that the η-axis divides the angle $\Delta\phi_{12}$ between the two jets into two sectors of equal size (see Figure 5.17). Hence the balance vector consists of two components $\vec{P}_{T,\eta}$ and $\vec{P}_{T,\psi}$. A perfectly balanced dijet event yields $\vec{P}_T = 0$ and hence any fluctuations will result

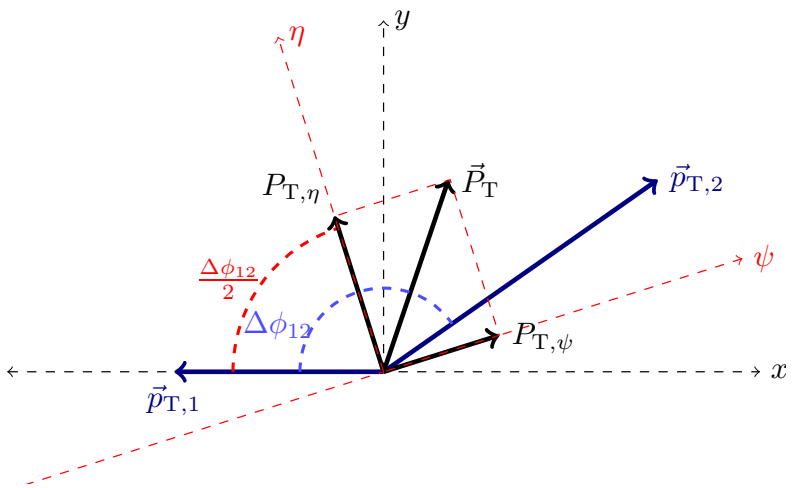

Figure 5.17: Variables used in the bisector method for measuring the jet energy resolution [223].

in non-zero variances of the η and ψ components, which are denoted as σ_η^2 and σ_ψ^2, respectively. After measuring the variances using Gaussian fits to the $\vec{P}_{T,\eta}$ and $\vec{P}_{T,\psi}$ distributions, the resulting fractional jet energy resolution can be calculated from [223]

$$\frac{\sigma(p_T)}{\langle p_T \rangle} = \frac{\sqrt{\sigma_\psi^2 - \sigma_\eta^2}}{\langle p_T \rangle \sqrt{2|\cos\Delta\phi_{12}|}}, \tag{5.12}$$

where $\langle p_T \rangle$ denotes the average p_T of both jets. In Figure 5.18, the jet energy resolution measured in reference [231] on 2011 data ($\mathcal{L} = 950\,\text{pb}^{-1}$, $\sqrt{s} = 7\,\text{TeV}$) with the bisector technique is presented. Furthermore, the relative difference to the resolution obtained

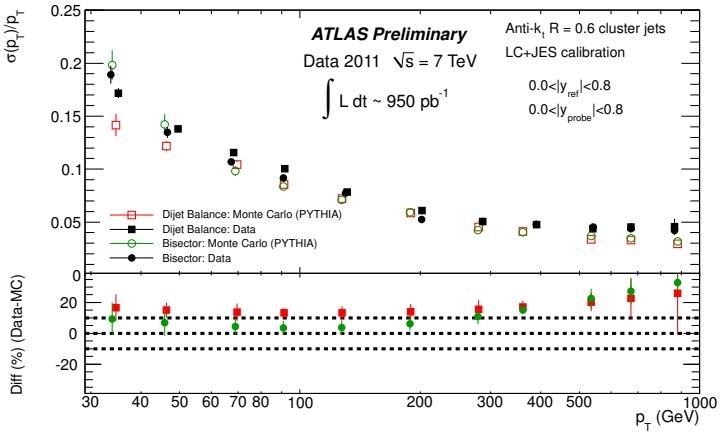

Figure 5.18: Fractional jet p_T resolution as a function of the jet p_T for anti-k_T jets with $R = 0.6$ [231]. The resolutions have been measured in 2011 data ($\mathcal{L} = 950\,\mathrm{pb}^{-1}$, $\sqrt{s} = 7\,\mathrm{TeV}$) and MC. Besides the measurement with the bisector technique, the resolutions are also shown for the dijet balance method (not discussed here). The upper plot depicts the fractional resolutions measured on data, whereas at the bottom the relative difference of the resolutions between data and MC is presented. The dotted lines indicate a relative difference of ±10%

from MC simulated dijet events is shown at the bottom of the plot.
Finally, the total jet energy resolution is obtained by the linear sum of the truth resolution and the difference of the *in-situ* measurements on data and MC.

5.5.3 Jet vertex fraction and jet quality

There are several quality criteria applied to jets, which are supposed to reject so-called 'bad jets' which were not produced by in-time real energy deposits stemming from the hard proton-proton interaction. Such reconstructed jets can be caused by e.g. hardware problems in the calorimeters, LHC beam-gas interactions or cosmic-ray induced showers. Details about these quality criteria can be found in reference [232]. If such jets are identified during the reconstruction they are labelled as 'bad jet'. In the analysis, the whole event is rejected, if a 'bad jet' is found.

Jets can also be produced in pile-up events, which results in jets not stemming from the primary vertex (PV) of the interaction. Such jets are rejected by a cut on the jet vertex fraction (JVF) that is a measure for the probability that a jet originates from the PV and is defined as

$$JVF = \frac{\sum_{\text{tracks}} p_T^{\text{PV}}}{\sum_{\text{tracks}} p_T} \,. \tag{5.13}$$

Here, the sum in the numerator runs over the transverse momenta of all tracks associated

with a jet (the association is performed by a simple ΔR matching in the $\eta - \phi$ plane) which stem from the PV, whereas the sum in the denominator runs over the p_T of all tracks associated with a jet. In case that the sums are equal to zero, a value of -1 is assigned as JVF. An optimal working point for the cut was found to be $|JVF| > 0.5$ and is required for each jet in the analysis.
The performance of the JVF cut was studied by measuring the selection efficiencies of hard scatter jets (ϵ_{HS}), which originate from the hard scatter interaction, and the pile-up jet rejection rates (ϵ_{PU}) in $Z \to e^+e^-$ and $Z \to \mu^+\mu^-$ events using a procedure based on the T&P method, which is explained in reference [203]. From the two efficiencies ϵ_{HS} and ϵ_{PU} it is possible to directly calculate the mistag probabilities I_{HS} and I_{PU} via $I_{HS} = 1 - \epsilon_{HS}$ and $I_{PU} = 1 - \epsilon_{PU}$, respectively. In the T&P method, the events are selected by requiring two leptons (e^+e^- or $\mu^+\mu^-$) with opposite charges and invariant masses close to the Z boson mass.
For the measurement of ϵ_{HS}, hard scatter events are selected by requiring a Z boson with large reconstructed transverse momentum ($p_T^Z > 30\,\text{GeV}$) and a leading jet which is back-to-back to the Z boson ($\Delta\phi > 2.9$). The selection efficiency is then defined as the fraction of events with such back-to-back jet that fulfils the $|JVF| > 0.5$ cut.
The pile-up enriched region for measuring ϵ_{PU} is selected by requiring a Z boson with low $p_T < 10\,\text{GeV}$, produced in association with exactly one jet with $p_T^{\text{jet}} > 20\,\text{GeV}$. ϵ_{PU} is then defined as the fraction of events where the single jet has $|JVF| < 0.5$.
The results of the measurements of ϵ_{HS} and ϵ_{PU} in 2012 data ($\mathcal{L} = 13.9\,\text{fb}^{-1}$, $\sqrt{s} = 8\,\text{TeV}$) and Z+jets simulated MC events are presented in Figure 5.19. It can be seen that the hard scatter jet selection efficiency ϵ_{HS} increases and achieves a better agreement between data and MC with higher jet transverse momenta. The pile-up jet rejection efficiencies of the MC are getting close to 1 for jets with $p_T \gtrsim 50\,\text{GeV}$, whereas the agreement between data and MC becomes worse in this p_T region. In reference [203], it is stated that a reason for the bad agreement is the low data statistics in the region of higher jet p_T.
In order to correct for the efficiency/rejection rate differences between data and MC, scale factors are derived from the ratios between data and MC efficiency. In the analysis, these scale factors are applied to the events when running over MC. Figure 5.20 presents the scale factors derived from the hard scatter jet selection efficiencies (ϵ_{HS}) and inefficiencies (I_{HS}).

5.5.4 Identification of b-jets

As discussed in Section 2.2.6, the b' quark decays preferably into a t quark and W boson in the scenario $|V_{u/cb'}| < |V_{tb'}|$. Due to the large size of the element $|V_{tb}|$, the t quark then decays nearly exclusively into a b quark and a W boson. Compared to the t quark, b quarks have a relatively long lifetime and hadronise into b-hadrons before decaying. These hadrons have special properties that allow to identify jets (so called b-jets) containing them. For instance, b-hadrons are quite heavy ($m > 5\,\text{GeV}$) and hence the decay products have large transverse momenta. Additionally, the fragmentation process of the b quarks is hard and hence the b-hadron retains about 70% of the original

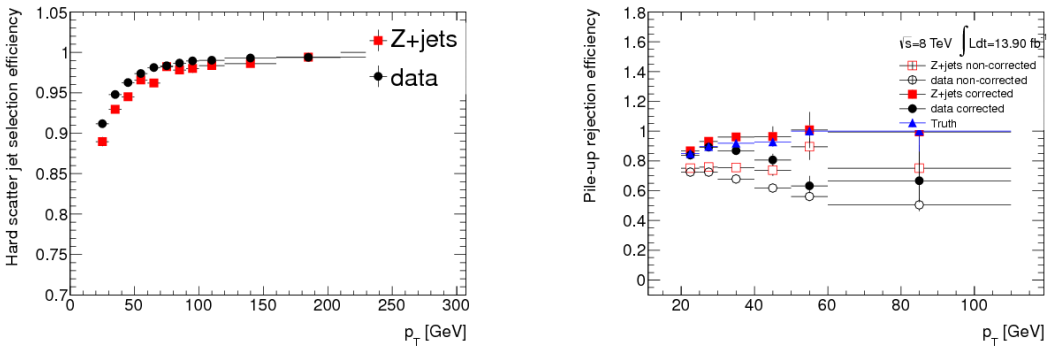

(a) (b)

Figure 5.19: Efficiencies of the $|JVF| > 0.5$ cut as a function of the jet p_T for the selection of hard scatter jets (a) and the rejection of pile-up jets (a), taken from reference [203]. The efficiencies have been measured on 2012 data ($\mathcal{L} = 13.9\,\text{fb}^{-1}$, $\sqrt{s} = 8\,\text{TeV}$) and Z+jets MC.
In case of the pile-up rejection rates, the contamination of hard scatter jets in the pile-up enriched region has been corrected by subtracting the corresponding contribution (filled rectangles and circles). In addition to the rejection efficiencies from data and (reconstructed) MC, there are also the rejection rates presented, which were obtained from the true MC information (triangles).

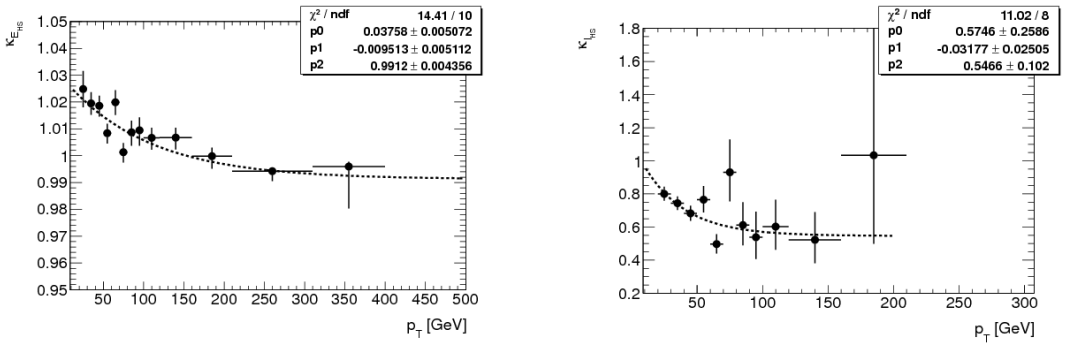

(a) (b)

Figure 5.20: Scale factors as a function of the jet p_T derived from the hard scatter jet selection efficiency (a) and inefficiency (b) for the $|JVF| > 0.5$ cut, taken from reference [203].

b-quark momentum. Furthermore, the b-hadrons traverse a distance of $\sim \mathcal{O}(3\,\text{mm})$ (in the case of a transverse momentum of about 50 GeV) due to their long lifetime of about 1.5 ps before their decay. This results in displaced secondary vertices and large impact parameters, as shown in Figure 5.21. Therefore, the impact parameters of charged

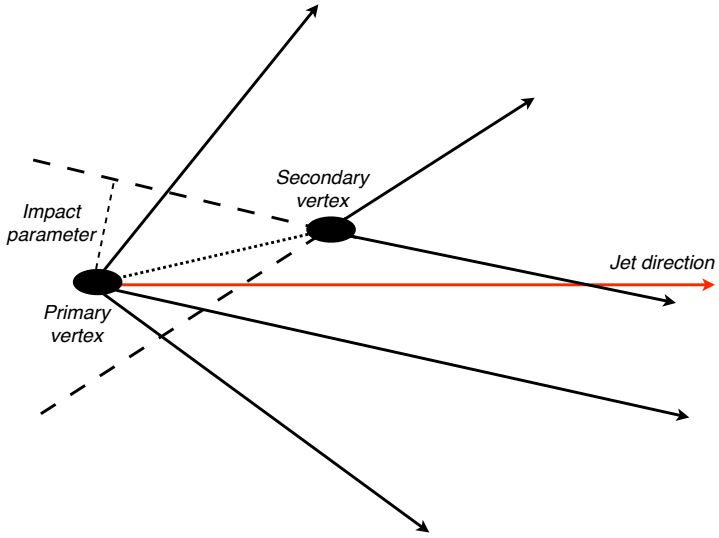

Figure 5.21: Schematic sketch of a displaced vertex coming from a b-jet [233]. The movement of the b-hadron is represented by the dotted line. The two tracks arising from the b-hadron decay point back to a secondary vertex and have large impact parameters.

tracks and the properties of secondary vertices are used as discriminant variables in many different algorithms for the identification of b-jets. Such identification procedure is also referred to as 'b-tagging'.

In ATLAS, there are several b-tagging algorithms in use which can be categorised into two main classes:

- **Impact parameter based:** Algorithms based on the impact parameter rely on measuring the sign of d_0 and z_0 (both defined with respect to the primary vertex). Here, the sign of the transverse impact parameter d_0 is defined slightly different compared to the sign of d_0^{beam} used in the cosmic muon rejection [191]:

$$\text{sign}(d_0) = \text{sign}\left[\left(\vec{P}_j \times \vec{P}_t\right) \cdot \left(\vec{P}_t \times (\vec{X}_{PV} - \vec{X}_t)\right)\right], \tag{5.14}$$

  where $\vec{P}_j$ denotes the direction of the considered jet, $\vec{P}_t$ is the direction of the track at the point of closest approach (PCA) to the primary vertex (PV), $\vec{X}_t$ represents a vector defining the position of the PCA and the position of the PV is given by the vector $\vec{X}_{PV}$. Hence, the vector resulting from $\vec{X}_{PV} - \vec{X}_t$ points from the PCA to the PV. This definition is also referred to as 'lifetime-signed' d_0, because tracks

are assigned a positive d_0, if the secondary vertex lies in the same hemisphere as the jet with respect to the PV. Hence, tracks arising at the secondary vertex from b-hadron decays, which occurs after the interaction at the PV, will most likely have a positive d_0. On the other hand, tracks from c-jets or light-jets (light = u, d, s) will originate from a point close to the PV[2], but due to the limited detector resolution, they will be assigned both signs at random. This can be also seen in Figure 5.22a, where the distributions of the signed d_0 are shown for the tracks from

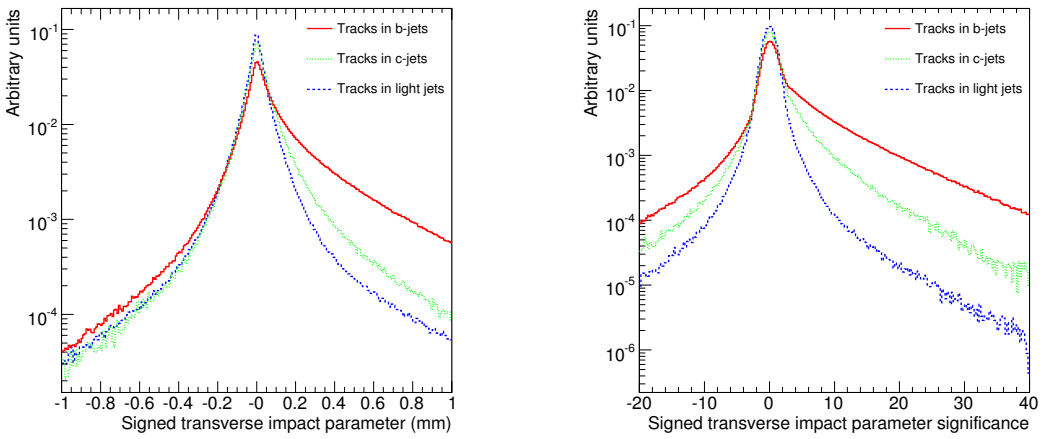

(a) (b)

Figure 5.22: Distributions of the transverse impact parameter (a) and its significance (b) for tracks from b-jets, c-jets and light-jets [191]. These distributions were obtained from simulated $t\bar{t}$ events at $\sqrt{s} = 14\,\text{TeV}$.

b-jets, c-jets and light-jets.
The sign of the longitudinal impact parameter is calculated from [191]

$$\text{sign}(z_0) = \text{sign}\left((\eta_j - \eta_t) \times z_0\right), \tag{5.15}$$

with η_j and η_t being the pseudorapidities of the jet and the track closest to the PV, respectively.

One algorithm based on the impact parameter is `IP3D` [191, 234], which takes the measurements of the distributions of the signed d_0 and z_0 significances as input. These are defined as the ratio between the impact parameters d_0 and z_0 and their resolutions $\sigma(d_0)$ and $\sigma(z_0)$ (these were determined in reference [191] by simulations and amount to $\sigma(d_0) \approx 10 - 12$ µm and $\sigma(z_0) \approx 71 - 91$ µm). The signed d_0 significance is presented in Figure 5.22b, which constitutes the better discrimination power compared to the transverse impact parameter alone. The `IP3D` algorithm then uses a Likelihood ratio technique for comparing the measured

[2] In case of c hadrons this point will be also slightly displaced, since their lifetime is of the order of 1 ps.

distributions to pre-defined ones for both a b-jet and a c-jet hypothesis, which are obtained from MC simulations. The output of the Likelihood ratio technique can then be used as discriminant for identifying b-jets.

- **Secondary vertex based:** Another approach for b-tagging is based on the measurements of the secondary vertices and is implemented in algorithms like `SV0` [235, 236] or `SV1` [191, 234]. Both algorithms use a list of all tracks associated to a jet as input. From this list, two-track pairs are built that form secondary vertices not overlapping with the PV. In an iterative procedure, the two-track vertices are merged into a common secondary vertex, where tracks giving a large χ^2 contribution are rejected. The ratio $L/\sigma(L)$, where L denotes the distance between the PV and the secondary vertex and $\sigma(L)$ represents its significance, is then used by the `SV0` tagger to identify b-jets.
  The `SV1` tagger follows a slightly different approach. Starting from the constructed secondary vertex (SV), as described above, it calculates three different vertex properties, which are then used as input to a Likelihood ratio. These are namely the invariant mass of all tracks associated to the SV, the ratio of the sum of the energies of the tracks associated to the vertex to the sum of the energies of all tracks in the jet, and the number of two-track vertices [191]. As for the impact parameter based tagger `IP3D`, the output of the Likelihood ratio is then used as discriminant for the b-jet identification.

  Another method based on secondary vertices is implemented in the algorithm `JetFitter` [237]. In addition to the variables used by `SV1`, it determines also the distances of the secondary vertices to the PV using a Kalman filter [194]. It also allows to distinguish between b-, c- and light-jets (light=u, d, s) by considering the differences in the flight paths of corresponding mesons.

The above mentioned tagger `IP3D`, `SV1` and `JetFitter` all rely on a Likelihood ratio method. By comparing the measured values S_i of the different discriminant variables to the pre-defined normalised distributions for the b-jet and light-jet (for simplicity called u-jet now) hypotheses, it is possible to determine the probabilities of these hypotheses $b(S_i)$ and $u(S_i)$, respectively. The sum of the logarithms of the ratios of $b(S_i)$ and $u(S_i)$ then defines a weight W_{jet} which can be used as cut variable for the identification of b-jets [191]:

$$W_{\text{jet}} = \sum_{i=1}^{N_t} \ln W_i = \sum_{i=1}^{N_t} \ln \frac{b(S_i)}{u(S_i)}, \tag{5.16}$$

where the sums run over the N_t determined tracks/vertices, depending on the tagging method.
Since the track/vertex weights W_i are treated separately, this also allows to combine the different taggers. A common combination at ATLAS is `JetFitter+IP3D`, which is based on an artificial neural network with MC simulated training samples [234]. In the analysis of this thesis, the so-called `MV1` tagger is used for the b-jet identification. It is

also based on a neural network and uses the output weights of `JetFitter+IP3D`, `IP3D` alone and `SV1` to determine an overall weight for each jet.

Depending on the cut value on the jet weight W_{jet}, one obtains different efficiencies for the b-jet selection. Furthermore, the increase of the b-tag efficiencies usually results in an enhancement of the mistag rate (wrongly tagged b-jets). The determination of optimal working points (cut values on W_{jet} corresponding to particular b-tag efficiencies) which are suitable for physics analyses is called 'b-tagging calibration'.
In this analysis, the calibrated b-tagging working points which were obtained from $t\bar{t}$ events are used [238]. This allows to study the b-tagging efficiencies for a broader range of the jets p_T than in the calibration based on a sample of jets containing muons, as described in reference [239]. For the measurement of the efficiencies in $t\bar{t}$ events, three different methods are performed in semi-leptonic and dilepton final states [238]:

- **Tag counting method**: This method makes use of the fact that in $t\bar{t}$ events one expects exactly two b-jets (due to the branching fraction of $t \to bW$ being close to unity). Hence, the number of events with two b-tagged jets is $\epsilon_b^2 \cdot N_{\text{sig}}$, where ϵ_b denotes the b-tagging efficiency and N_{sig} the number of $t\bar{t}$ events. The b-tagging efficiencies are then extracted by performing a Likelihood fit of the expected event rates to the observed ones. Contributions from c- and light jets (light $= u, d, s$) to the b-tagged jets are considered by evaluating the fractions of such jets which pass the event selection in MC simulated events.

- **Kinematic selection method**: This method makes use of the knowledge of the expected flavor composition in $t\bar{t}$ events. The b-tagging efficiency is extracted by measuring the fraction of b-tagged jets in data, which is given by

$$f_{b\text{-tag}} = \epsilon_b f_{b\text{-jets}} + \epsilon_c f_{c\text{-jets}} + \epsilon_l f_{l\text{-jets}} + \epsilon_{\text{fake}} f_{\text{fake}}, \tag{5.17}$$

  where $f_{b\text{-jets}}$, $f_{c\text{-jets}}$ and $f_{l\text{-jets}}$ are the expected fractions of b-, c- and light flavor jets in $t\bar{t}$ events (estimated from MC simulated events) and ϵ_c and ϵ_l denote the mistag efficiencies for c- and light-jets (also taken from MC simulation). ϵ_{fake} and f_{fake} denote the b-tag efficiency and fraction of jets coming from the fake lepton background (jets that have been mis-reconstructed as leptons), where both are measured in specific fake enriched control samples on data. The b-tag efficiency ϵ_b is finally determined by solving Equation (5.17) for ϵ_b and inserting the measured values of the different ϵ_i and f_i.

- **Kinematic fit method**: The third method is only performed on semi-leptonic $t\bar{t}$ events and is based on a kinematic fit [240–242] of the $t\bar{t}$ event topology. The masses of the two t quarks and the W bosons are exploited as constraints in the fit of the reconstructed jets and the single lepton in the event. All permutations of the six jets with highest p_T are fitted separately and the permutation resulting in the lowest χ^2 of the fit is retained. By cutting on the χ^2 of the fit, shown in Figure 5.23a, a very clean sample of b-jets can be selected. A further purification of the sample is obtained by performing a subtraction of possible backgrounds. The

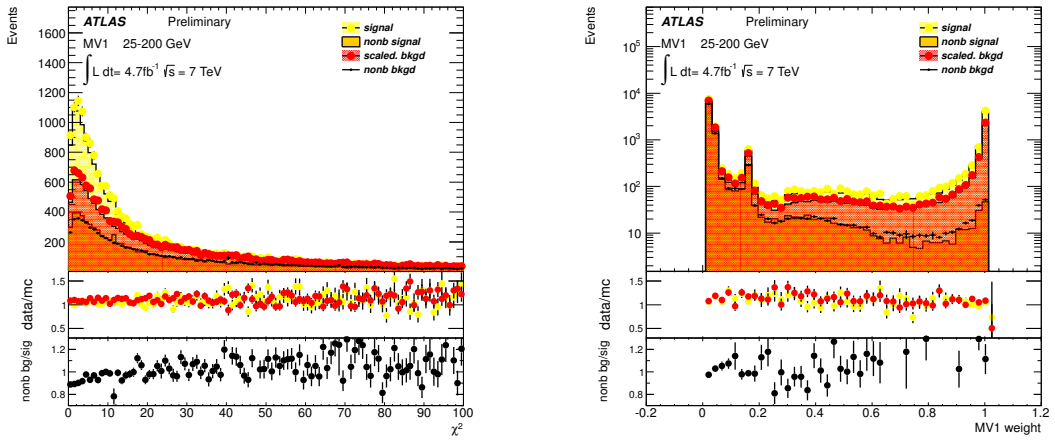

(a) (b)

Figure 5.23: Distributions of the χ^2 (a) and the MV1 weight (b) after the kinematic fit and background subtraction in 2011 data ($\mathcal{L} = 4.7\,\text{fb}^{-1}$, $\sqrt{s} = 7\,\text{TeV}$) and MC [238].

b-tagging efficiency can then be extracted by integrating the distribution of the tagger weight $T(w)$ (shown in Figure 5.23b) after the kinematic fit and background subtraction:

$$\epsilon_b = \int_{w_{\text{cut}}}^{\infty} T(w)dw \ . \tag{5.18}$$

Here, w_{cut} denotes the cut value on the tagger weight.

The efficiencies have been measured on 2011 data ($\mathcal{L} = 4.7\,\text{fb}^{-1}$, $\sqrt{s} = 7\,\text{TeV}$) and MC in reference [238] using above mentioned methods. In the analysis of this thesis, a b-tagging working point of 70% has been chosen, which corresponds to a MV1 weight of 0.772. From the differences between the efficiencies in data and MC, the scale factors presented in Figure 5.24 have been derived and are applied in the analysis of MC events in order to match the efficiencies in data. Additional scale factors are applied to also correct for the differences in the mistag rates [243] and the efficiency differences of b-tagged c-jets [244].

5.6 Overlap removals

In addition to the discussed selection criteria of electrons, muons and jets, there are several so-called overlap removals applied to the objects. These overlap removals are supposed to reject objects that are too close in the η and ϕ space, which could cause that these objects are reconstructed more than once by the different algorithms.

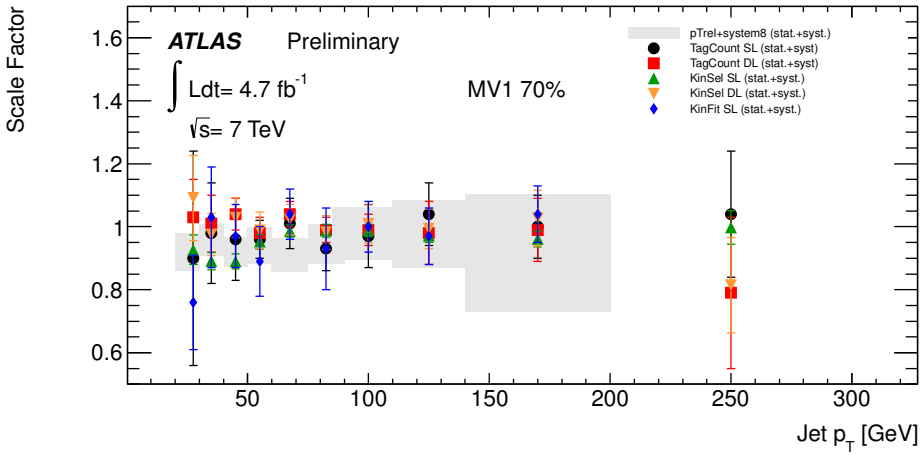

Figure 5.24: Comparison of $t\bar{t}$ based scale factors for b-tagging efficiencies obtained from 2011 data ($\mathcal{L} = 4.7\,\text{fb}^{-1}$, $\sqrt{s} = 7\,\text{TeV}$) and MC [238]. The efficiencies are presented for the three different methods Tag counting (TagCount), Kinematic selection (KinSel) and Kinematic fit (KinFit) in single lepton (SL) and dilepton (DL) final states. For comparison also the efficiencies from dijet events with muons, obtained in reference [239], are shown which have been measured using the p_T^{rel} and System8 methods. The scale factors from the different methods all agree within the statistical and systematic uncertainties and hence an average is applied in the analysis.

5.6.1 Electron muon overlap removal

The electron-muon overlap removal is supposed to reject events where muons have been wrongly reconstructed as electrons. For each combination of electrons and muons in the event, it is checked whether both objects share the same track in the inner detector. If the differences in the η and ϕ values of the electron and muon track are both smaller than 0.005, the lepton pair is flagged as overlapping. In case there is at least one such pair, the whole event is rejected during the analysis.

5.6.2 Electron jet overlap removal

The jet reconstruction algorithm is seeded by the energy deposits in both ECAL and HCAL. Therefore, there is the possibility that electrons are also reconstructed as jets. In the analysis, the closest jet to an electron fulfilling the selection criteria from Section 5.3 is rejected, if their ΔR is smaller than 0.2.

5.6.3 Jet electron overlap removal

The electron scale factors applied in the analysis are only valid if there is no jet within $\Delta R < 0.4$ to the electron. Therefore, after the previously mentioned electron-jet overlap

removal, a selected electron is rejected if there is a jet within $\Delta R < 0.4$.

5.6.4 Jet muon overlap removal

The muon selection criteria are already supposed to reject muons coming from hadron decays within jets. However, there is still a non-negligible fraction of such muons, which are hence removed by the jet-muon overlap removal. If there is a jet within $\Delta R < 0.4$ to a selected muon, this muon is rejected during the analysis.

5.7 Missing transverse momentum

The missing transverse momentum, often also referred to as missing transverse energy, is an important characteristic for events where particles traversed the detector without detection. In case of the b' decay chain this occurs in the leptonic $W \to \ell\nu$ decays, because neutrinos can not be detected by the ATLAS detector and hence carry a specific amount of energy out of the detector. In ATLAS, the missing transverse energy is commonly noted as E_T^{miss}.

Due to momentum conservation, an event where all particles have been detected should result in zero E_T^{miss}. Therefore, in the case of non-detected particles, like neutrinos, this results in a momentum imbalance in the transverse plane. The x and y components of the missing energy can be calculated by summing up the energy deposits in the calorimeter cells i

$$E_x^{\text{miss}} = -\sum_i E_i \sin\theta_i \cos\phi_i \tag{5.19}$$

$$E_y^{\text{miss}} = -\sum_i E_i \sin\theta_i \sin\phi_i, \tag{5.20}$$

when also considering the cell positions in θ and ϕ. The missing transverse energy is then given by

$$E_T^{\text{miss}} = \sqrt{(E_x^{\text{miss}})^2 + \left(E_y^{\text{miss}}\right)^2}\,. \tag{5.21}$$

5.7.1 Calibration of missing transverse energy

The x and y components of the missing energy are split into several terms, corresponding to different reconstructed objects:

$$E_{x,y}^{\text{miss}} = E_{x,y}^{\text{RefEle}} + E_{x,y}^{\text{RefPhoton}} + E_{x,y}^{\text{RefJet}} + E_{x,y}^{\text{RefSoftJet}} + E_{x,y}^{\text{RefMuon}} + E_{x,y}^{\text{CellOut}}, \tag{5.22}$$

where $E_{x,y}^{\text{RefEle}}$, $E_{x,y}^{\text{RefPhoton}}$ and $E_{x,y}^{\text{RefJet}}$ denote the energy deposits of reconstructed high-p_T ($\gtrsim 10\,\text{GeV}$) electrons, photons and jets, respectively[3]. Before the summation the initial cell energies, taken from topological clusters at the electromagnetic energy scale

[3]The term 'Ref' stands for 'refined'

(EM scale), are replaced with the refined calibrated energies according to the associated, identified physics object. This means that in the case of electrons and photons, the energy clusters are used after applying the EM scale corrections (leakage corrections and energy loss in front of the ECAL), whereas for jets the cells after the calibration with the LCW+JES scheme are used. The $E_{x,y}^{\mathrm{RefMuon}}$ term is built from the momenta of reconstructed isolated muons (here muon momenta of the standalone muon spectrometer reconstruction are used, in order to avoid double counting of the energy loss in the calorimeter). For muons that are within $\Delta R < 0.3$ of a reconstructed jet (non-isolated muons), their energy deposits in the calorimeters enter in the *RefJet* term, otherwise they are added to the muon term. All low-p_T jets ($10\,\mathrm{GeV} < p_T < 20\,\mathrm{GeV}$) are grouped into the $E_{x,y}^{\mathrm{RefSoftJet}}$ term and each cell not belonging to any high-p_T object is combined in the $E_{x,y}^{\mathrm{CellOut}}$ term. The finally obtained calibrated (refined) E_T^{miss} is then referred to as 'MET RefFinal'.

The reconstructed E_T^{miss} is also corrected for so-called 'dead material'. This mainly corrects for the energy loss of jets in the cryostat between the ECAL and HCAL. The energy loss is estimated from parametrisations and applied for each reconstructed jet.
In the analysis, there are several corrections applied to the electrons, muons and jets (mainly energy scalings and smearings). This is taken into account in the analysis by applying corrections to the E_T^{miss} depending on the changed momenta and energies of the electrons, muons and jets.

The resolution of the missing transverse energy has been studied in $Z \to \mu^+\mu^-$ events, where no E_T^{miss} is expected. This study is based on the method described in reference [245] and was performed as a function of the total transverse energy sum, which is given by

$$\sum E_T = \sum E_T^e + \sum E_T^\gamma + \sum E_T^\mu + \sum E_T^{\mathrm{jets}} + \sum E_T^{\mathrm{SoftJets}} + \sum E_T^{\mathrm{CellOut}} \ . \qquad (5.23)$$

Here, each sum runs over the transverse energies of the reconstructed objects entering the E_T^{miss} calculation. The measured values of E_x^{miss} and E_y^{miss} are plotted in bins of the $\sum E_T$ and the resolution is then obtained from the width of Gaussians fitted to these distributions. The resulting resolutions as a function of $\sum E_T$ obtained from 2012 data ($\mathcal{L} = 1.7\,\mathrm{fb}^{-1}$, $\sqrt{s} = 8\,\mathrm{TeV}$) and MC are presented in Figure 5.25 (red points). A fit to the behaviour of the E_T^{miss} resolution with the function $\sigma = k \cdot \sqrt{\sum E_T}$ was also performed and resulted in a value for the k parameter of $k = 0.73$ and $k = 0.75$ in data and MC, respectively.

5.8 Vertices and pile-up

5.8.1 Vertices

With the high peak luminosity of $L = 7.73 \times 10^{33}\mathrm{cm}^{-2}\mathrm{s}^{-1}$ in the 2012 data taking, a large number of ~ 20 interactions occurred due to pile-up events besides the hard interaction. In order to distinguish the primary vertex of the hard interaction from the various pile-up vertices, an efficient vertex reconstruction is required, which is described

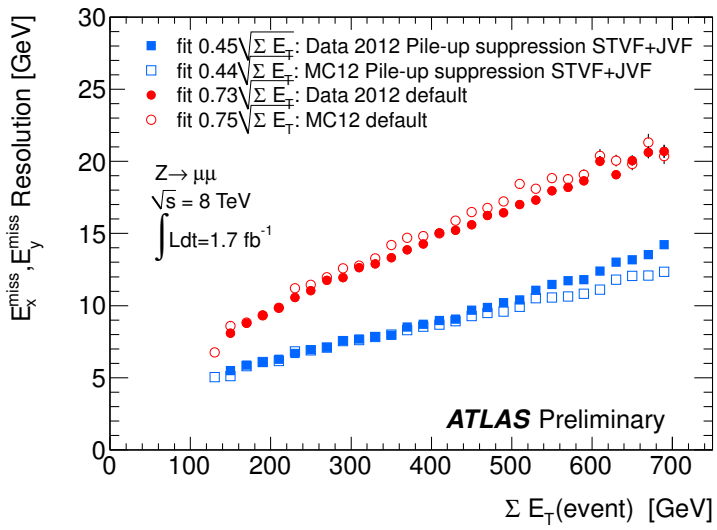

Figure 5.25: Resolution of the missing energy x and y components in 2012 data ($\mathcal{L} = 1.7\,\mathrm{fb}^{-1}$, $\sqrt{s} = 8\,\mathrm{TeV}$) and $Z \to \mu^+\mu^-$ MC as a function of the scalar sum of the transverse energies $\sum E_T$ [246]. In addition to the default E_T^{miss}, which is also used in the analysis of this thesis, there is also the resolution shown after applying a pile-up suppression using a track-based Softterm Vertex Fraction (STVF) method (see reference [245] for further information). However, this pile-up suppression was not in place when the results in this thesis were produced.

in reference [247].

Vertices are reconstructed using an iterative vertex finding algorithm explained in reference [248]. The z position at the beamline of reconstructed inner detector tracks is used as seed for the vertices. Then a χ^2 fit is performed on the seed and the neighbouring tracks, from which one obtains weights associated to each track measuring the compatibility with the fitted vertex. All tracks displaced by more than 7σ are then disassociated from the vertex and used for a new seed. The procedure is repeated until there are no vertices left.

The hard scatter process is expected to be the interaction with the highest momentum transfer. Therefore, the reconstructed vertex with the highest sum of transverse momenta $\sum p_T$ of the associated tracks is defined as the primary vertex associated with the hard interaction. In the analysis, this primary vertex is required to have more than four associated tracks (with $p_T > 400\,\mathrm{MeV}$), in order to reject non-collision backgrounds like beam halo events.

5.8.2 Pile-up reweighting

The MC samples used in this analysis have been produced during the data-taking in 2012. Therefore, only an estimate of the data pile-up conditions was used, when the pile-up events were mixed into the MC samples during the digitisation step (see Section 4.2.3). Thus, in the analysis of the MC samples, the events are reweighted in order to match the pile-up conditions from the analysed dataset.

The pile-up reweighting is performed by using the variable μ, which is the average number of proton-proton collisions in one event. This number is obtained for each luminosity block, in which it is averaged over all bunch crossings. Figure 5.26a presents the amount of data (recorded luminosity) as a function of μ in the reduced 2012 dataset ($\mathcal{L} = 14.324\,\text{fb}^{-1}$) used in this analysis. The μ distribution for the pile-up events, that have been mixed into the events during the MC sample generation, is shown in Figure 5.26b. It can be clearly seen that the distributions for data and MC are different and hence the reweighting needs to be applied to correct for the variations.

In the analysis of the MC samples, each event is categorised into one of the six data-taking run periods presented in Table 5.2. These periods contain runs with similar instantaneous luminosities and hence reflect run intervals with approximately constant pile-up conditions. For the MC samples, the categorisation is performed randomly, taking into account the luminosity fractions of the periods. Then the μ value of the MC

Period i	Run numbers	$\mathcal{L}_i/\mathcal{L}$
A - B3	200803 - 203227	7.2%
B4 - B14	203228 - 206247	33.5%
C1 - C5	206248 - 206954	2.0%
C6 - D3	206955 - 208178	19.0%
D4 - E	208179 - 210183	27.2%
F - G	210184 - 212272	11.1%

Table 5.2: Luminosity fractions $\mathcal{L}_i/\mathcal{L}$ per data taking period i used for the pile-up reweighting on MC. The fractions refer to a total integrated luminosity in periods A-G of $\mathcal{L} = 14.324\,\text{fb}^{-1}$.

events is extracted and a period weight and a pile-up (PU) weight are calculated and applied to the MC event. These weights are given by

$$w = w_{\text{period}} \times w_{\text{PU}} = \frac{\mathcal{L}_i/\mathcal{L}}{N_i/N} \times \frac{\mathcal{L}_{i,\mu}/\mathcal{L}_i}{N_{i,\mu}/N_i}, \tag{5.24}$$

where $\mathcal{L}_{i,\mu}$ denotes the fraction of the luminosity in period i that has the same μ as in the considered MC event, $N_{i,\mu}$ represents the number of events in the MC sample with the value of μ and period i, $\mathcal{L}_i$ is the associated luminosity of period i, N_i stands for the number of events in the MC sample that were assigned to period i and N represents the total number of MC events.

An example of the μ distribution after applying the pile-up reweighting is presented

in Figure 5.26c. In the MC sample used, the pair-production of b' quarks with mass $m = 800\,\text{GeV}$ and exclusive decays $b' \to tW$ was simulated (100000 events). It can be seen that there is a reasonable agreement of the shape compared to the distribution in data of Figure 5.26a.

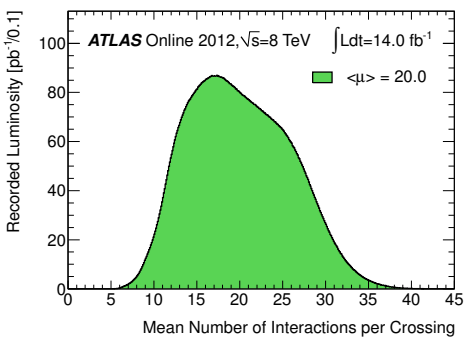

(a) Data

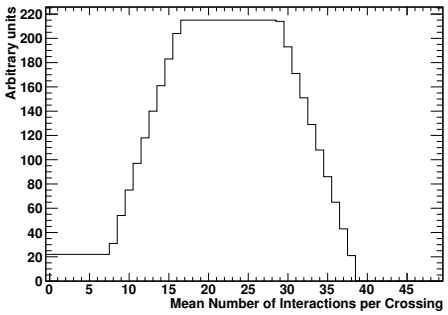

(b) MC

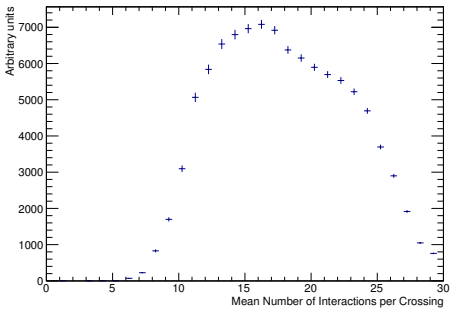

(c) MC (reweighted)

Figure 5.26: All plots present the mean number of interactions per bunch crossing μ.
Figure (a) depicts the luminosity-weighted distribution in the reduced 2012 dataset ($\mathcal{L} = 14.324\,\text{fb}^{-1}$) taken up to September 17th [249]. In average there were 20.0 pile-up collisions per bunch crossing.
In (b), the distribution is shown which represents the pile-up conditions that have been used in the generation of the MC samples.
The plot in (c) denotes the μ distribution after applying the pile-up reweighting in an MC sample, in which the pair-production of b' quarks with mass $m = 800\,\text{GeV}$ and exclusive decays $b' \to tW$ were simulated.

6 Analysis strategy and results

In this chapter, I will present the strategy of my analysis and the results I obtained. My analysis, with the search for production of fourth generation $b'\bar{b}'$ quark-antiquark pairs in final states with same-sign charged dileptons (see next section for a description of the search topology), was part of the ATLAS conference note [250]. In this note, it was looked for several exotic processes (in the sense that all these processes are based on models beyond the Standard Model), which can yield the same final state of same-sign dileptons. Therefore, the work on estimating the various background contributions to this final state was shared among the various institutes that contributed to this note, namely the Humboldt University of Berlin [251] (in the following Berlin), the University of Arizona [252] (in the following Arizona), and the University Blaise Pascal in Clermont-Ferrand [253] (in the following Clermont-Ferrand). Apart from the b' search (performed by Berlin), we looked for the production of four tops $t\bar{t}t\bar{t}$ (performed by Clermont-Ferrand), same-sign tops tt (performed by Clermont-Ferrand) and vector like quarks (VLQs, performed by Arizona). A description of these signal models is beyond the scope of this thesis, but can be looked up in the note.

In the following, I will first present the search topology for the b' quarks (Section 6.1), followed by a description of the analysed dataset and the considered signal and background processes (Section 6.2). Then, I will briefly discuss the analysis framework I used for producing my results (Section 6.3) and present the statistical methods I used at several parts of my analysis (Section 6.4). Next, I will summarise the various criteria for the selection of the physical objects (Section 6.5), as it was explicitly explained in Chapter 5. This is followed by a description of the various systematic uncertainties, which I considered in the interpretation of my results (Section 6.6). Then, I will describe the event selection criteria in Section 6.7 and how I optimised this selection for a maximum sensitivity. Afterwards, I will present the obtained estimates for the signal and background processes, after applying the optimised event selection, together with a validation of the background estimates (Section 6.8). Furthermore, this section includes the values for the systematic uncertainties, obtained with the previously introduced methods. Finally, I will show my statistical interpretation of the observed data events (Section 6.9).

6.1 Search topology

In Section 2.2.6, I already discussed the possible decay scenarios of a fourth generation b' quark. Depending on the mixings of the fourth generation with the other three generations, the b' will decay dominantly into either $t + W$ or $u/c + W$.

The first decay topology studied in this thesis arises from the assumption of $|V_{u/cb'}| < |V_{tb'}|$ and $m_{b'} < m_{t'}$ and hence the dominant decay chain is $b' \to t + W$. For this

topology, it was chosen that the b' quark decays exclusively into $t + W$. As I showed in Section 2.2.6, the final state of this decay topology consists of four W bosons (each two with the same charge) and a b quark and $\bar{b}$ quark (due to the dominant decay $t \to b+W$). Depending on the decays of these W bosons, one can select events with either one, two, three or four charged leptons. The remaining W bosons are then supposed to decay hadronically. In Figure 6.1 the corresponding branching fractions (BFs) of these decay scenarios are summarised. The largest BFs of 40.04% and 24.59% are achieved by the

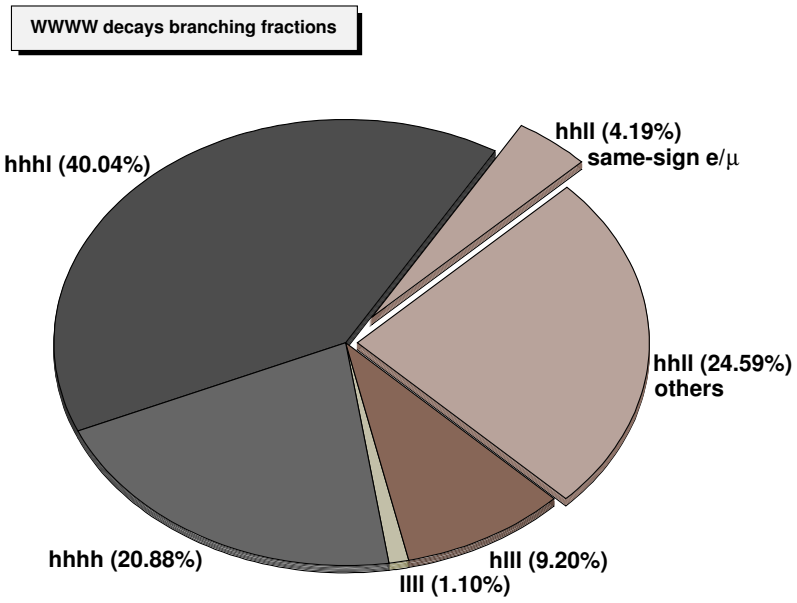

Figure 6.1: Presented are the branching fractions for the different decay scenarios of four W bosons [98]. l represents a charged lepton (e or μ) and h denotes quarks coming from hadronic W decays.

decays into one lepton and two opposite-sign charged leptons, respectively. However, these final states also contain contributions from many SM processes like W+jets, Z+jets or $t\bar{t}$+jets production. The decay scenario without leptons in the final state is also not an interesting candidate for this analysis, because it is difficult to distinguish such a signature from the hadronic background.
An interesting scenario, which has been chosen for the event selection in this analysis, is the final state of two same-sign charged leptons, as depicted in Figure 6.2. This final state is rare in the SM and only processes with very low cross sections can contribute (see Section 6.2).
As it has been discussed in Section 2.2.6, such final state can also be achieved in the scenario of $m_{b'} > m_{t'}$ with non-degenerate masses. Therefore, the search presented in this thesis is basically independent from the mass relation between the t' and b' quark (as long as they are non-degenerate) and only depends on the choice for the sizes of the quark-mixing elements between the different generations.

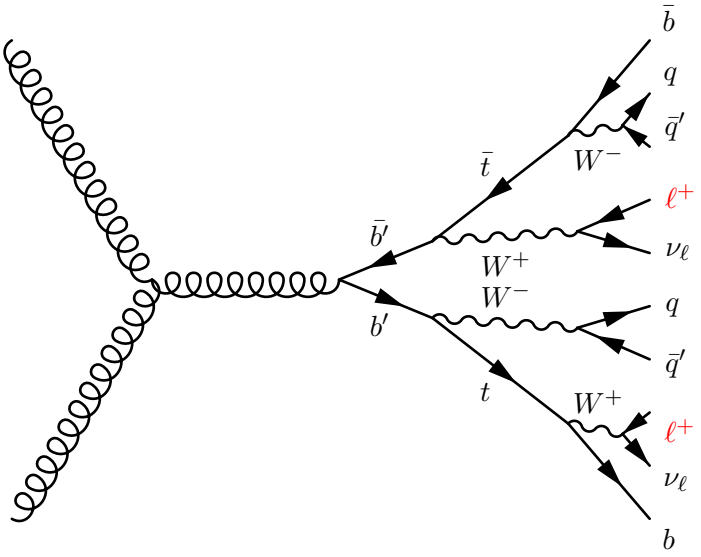

Figure 6.2: $b' \to tW$ decay topology with a final state of two same-sign charged leptons.

The second topology studied in this thesis assumes comparable sizes for the CKM matrix elements $|V_{ub'}|$, $|V_{cb'}|$ and $|V_{tb'}|$ and defines an approach which is more independent from the choice of the quark mixings. In this scenario, the b' quark is supposed to decay into either a u, c or t quark associated with a W boson. When requiring that at least one b' decays into $t + W$, one obtains at least three W bosons which still allows to select the same-sign dilepton final state, as it is shown in Figure 6.3.

6.2 Data, signal and background processes

In this section, the 2012 dataset used in the analysis will be presented, as well as the considered signal and background processes. Standard Model processes which give a real same-sign dilepton signature in the final state are called irreducible backgrounds (Section 6.2.3) and are estimated using MC samples. Some processes do not contain such a signature, but can contribute to the search signature due to lepton mis-reconstruction (Section 6.2.4) or charge mis-identification (Section 6.2.5). Both background contributions are estimated using data-driven techniques.

The MC samples (b' signal and irreducible backgrounds) were each produced with a specific amount of events N_{MC}. Given the cross section σ_{MC} for a particular process, one can calculate the corresponding integrated luminosity $\mathcal{L}_{\mathrm{MC}}$ of the MC sample, which does not have to agree necessarily with the integrated luminosity $\mathcal{L}_{\mathrm{Data}}$ of the taken dataset. In order to compare the expectations (e.g. distributions or event yields) taken from MC with the measured ones in data, one needs to apply a so-called luminosity reweighting,

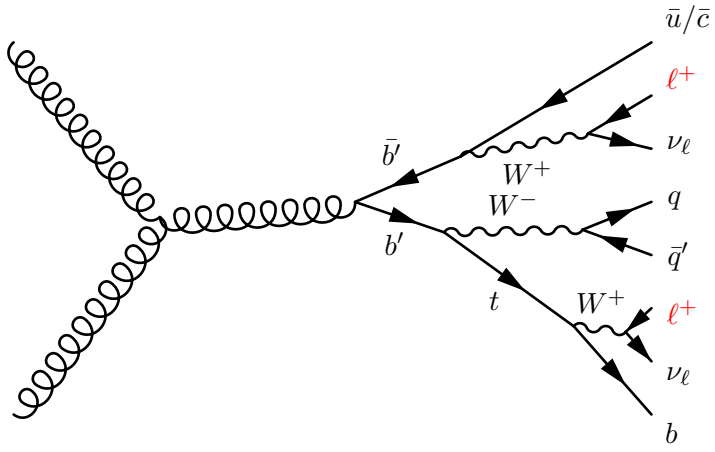

Figure 6.3: $b' \to qW$ decay topology with a final state of two same-sign charged leptons. Here it is assumed that one b' decays into $t + W$, whereas the other b' quark decays into $u + W$ or $c + W$.

which rescales the MC to the data luminosity. This weight is given by

$$w = \frac{\mathcal{L}_{\text{Data}}}{\mathcal{L}_{\text{MC}}} = \frac{\mathcal{L}_{\text{Data}} \times \sigma_{\text{MC}}}{N_{\text{MC}}} \ . \tag{6.1}$$

When selecting N events, the statistical uncertainty on this value is given by $\sigma_N = \sqrt{N}$ according to Poisson statistics. In case of the selected events in MC samples, this uncertainty needs to be multiplied by the luminosity weight and is hence given by

$$\sigma_N = w \times \sqrt{N} \ . \tag{6.2}$$

If there are zero events selected, an upper limit on this value is set with 68% confidence using Poisson statistics. Given the Poisson distribution function

$$\text{Poi}(b, d) = \frac{e^{-b} b^d}{d!}, \tag{6.3}$$

one can calculate the probability for observing d events if b events are expected. For setting an upper limit on zero observed events, one needs to solve $f(b, 0)$ for the value of b that gives a probability of $1 - 0.68 = 0.32$:

$$\text{Poi}(b, 0) = \frac{e^{-b} b^0}{0!} = 0.32 \tag{6.4}$$

$$\to b = -\ln(0.32) = 1.14, \tag{6.5}$$

and hence the upper limit on zero events amounts to 1.14.

6.2.1 Dataset

As I already mentioned in Section 5.2, only a reduced amount of the data taken in 2012 was used in the analysis, because the remaining data was not available when the analysis has been performed. The data used in the analysis is taken from two different 'streams', `Egamma` and `Muons`: if an event was fired by one of the electron triggers it is stored in the `Egamma` stream and in the case of a muon triggered event it is stored in the `Muons` stream. The analysis has been run separately on the `Egamma` and `Muons` stream.
There can be events where both electron and muon triggers have fired. In order to remove the overlap between the two streams when analysing the `Muons` stream, events were rejected if they have been also fired by the electron trigger. In total, there were 4.85×10^8 events analysed, which were reduced to 3.09×10^8 events after the trigger selection, as it is also summarised in Table 6.1. In total, the analysed data corresponds to an integrated luminosity of $\mathcal{L} = 14.3\,\text{fb}^{-1}$.

Stream	$N_{\text{events}}[\times 10^8]$	$N_{\text{events}}^{\text{trigger}}[\times 10^8]$
`Egamma`	2.11	1.56
`Muons`	2.74	1.53
`Egamma`+`Muons`	4.85	3.09

Table 6.1: The table presents the number of analysed data events N_{events} and the number of events after the trigger selection $N_{\text{events}}^{\text{trigger}}$ in both the `Egamma` and `Muons` stream. In case of the number of triggered events in the `Muons` stream, the electron triggered events were removed. The last row presents the combination of both streams and corresponds to an integrated luminosity of $\mathcal{L} = 14.3\,\text{fb}^{-1}$.

6.2.2 Signal samples

The $b'\bar{b}'$ pair-production signal samples used in this analysis were produced with `Pythia8` and the `MSTW2008` PDF, followed by the fast detector simulation `ATLFAST-II`. For each mass point in the range $[400, 1000]$ GeV (in steps of 50 GeV), there were two different samples produced: one with the exclusive decay $b' \to tW$ and one with the mixed decays $b' \to qW$ $(q = u, c, t)$. In the latter case, an equal branching ratio of 1/3 for the three decay modes was assumed. For the mass points of 500 GeV and 800 GeV, there were also samples produced with the full detector simulation using `GEANT4`, which have been used for validation of the fast detector simulation (see Section 6.8.1.1).

In the event generation using `Pythia8`, a so-called generator filter has been applied in order to increase the statistics of the MC samples. In general, a generator filter rejects events that do not fulfil specific requirements during the event generation. In case of the b' sample generation, the filter required at least one lepton (electron or muon) in the final state with $|\eta| < 2.7$ and $p_T \geq 10\,\text{GeV}$. The ratio of the number of events after and before the filter then gives the filter efficiency ϵ_f.
In the calculation of the MC luminosity for the luminosity weight given in Equation (6.1),

the filter efficiency needs to be taken into account in order to obtain the correct luminosity. Therefore the cross section needs to be multiplied by the filter efficiency: $\sigma \times \epsilon_f$.

A summary of the pair production cross-sections, filter efficiencies and integrated MC luminosities for each mass point and decay scenario is presented in Table 6.2. The b' pair

$pp \to b'\bar{b}'$		$b' \to tW$			$b' \to qW$		
Mass [GeV]	σ [pb]	ϵ_f	$\sigma \times \epsilon_f$ [pb]	$\mathcal{L}$ [fb^{-1}]	ϵ_f	$\sigma \times \epsilon_f$ [pb]	$\mathcal{L}$ [fb^{-1}]
400	2.296	0.778	1.785	56.01	0.590	1.354	73.87
450	1.113	0.786	0.875	114.3	0.600	0.668	149.8
500	0.5702	0.791	0.451	221.6	0.614	0.350	271.4
550	0.30545	0.798	0.244	410.5	0.627	0.191	522.4
600	0.1696	0.805	0.137	732.3	0.636	0.108	927.1
650	0.09707	0.812	0.0788	1256.0	0.644	0.0625	1599.0
700	0.05694	0.816	0.0465	1937.0	0.649	0.0370	2677.0
750	0.03411	0.821	0.0280	3573.0	0.656	0.0224	4470.0
800	0.02080	0.825	0.0172	5830.0	0.661	0.0137	7278.0
850	0.01287	0.830	0.0107	9270.0	0.668	0.00860	11630.0
900	0.008069	0.833	0.00672	14730.0	0.671	0.00541	18480.0
950	0.005114	0.838	0.00429	23330.0	0.674	0.00345	29010.0
1000	0.003271	0.840	0.00275	36390.0	0.678	0.00222	45080.0

Table 6.2: Approximate NNLO production cross-sections σ for the b' quark pair-production obtained using `HATHOR`, as also presented in Figure 2.18. Separate samples were produced for each mass point with the decay topologies $b' \to tW$ and $b' \to qW$ $(q = u, c, t)$, which resulted in different generator filter efficiencies ϵ_f. Each sample was generated with a total of $N = 100000$ events (after the generator filter), from which the corresponding integrated luminosities $\mathcal{L}$ are calculated by $\mathcal{L} = N/(\epsilon_f \times \sigma)$.

production signal samples with exclusive decays into tW will be referred to as $b' \to tW$ in the following, whereas the signal samples with the mixed decays into tW, cW and uW will be referred to as $b' \to qW$.

6.2.3 Irreducible backgrounds

As previously discussed, two same-sign charged leptons in the final state is very rare in the Standard Model processes. These processes are modelled using MC samples and are presented below.

All generators used in this analysis operate at leading-order (LO). For some processes, there exist generators which can calculate the cross sections at NLO. Hence, the ratio between the NLO and the LO cross-section is used in order to derive a so-called k-factor. Although NLO effects on the event kinematics are not considered, the multiplication of the LO cross-section by the k-factor allows a more reliable normalisation in the calculation of the luminosity weight.

- $\mathbf{t\bar{t} + W^+W^-}$: $t\bar{t}$ production can not result in in same-sign dilepton final states. However, $t\bar{t}$ production can be associated with two oppositely charged W bosons, as shown in Figure 6.4a. Due to the dominant decay $t \to bW$ one obtains four W bosons ($W^+W^+W^-W^-$) in the final state, which can result in same-sign charged dilepton final states. Such processes were produced with `MadGraph+Pythia`, the `MSTW2008` PDF and the fast detector simulation. The cross section listed in Table 6.3 was taken from the generator.

- $\mathbf{t\bar{t} + W^{\pm}(+jets)}$: In addition to the $t\bar{t} + W^+W^-$ process, the $t\bar{t}$ quark pair can also be produced in association with only one W boson, resulting in a total of three W bosons and hence also allowing for same-sign dilepton final states. Three separate samples have been produced with `MadGraph+Pythia`, with 0, 1 and 2 additional partons generated at the matrix-element level. In the following, these samples will be combined and referred to as $t\bar{t} + W$+jets. Figure 6.4b depicts the production without additional partons. `CTEQ6L1` was used as PDF and the samples were generated with the full detector simulation. The LO cross-section listed in Table 6.3 was obtained from the generator and is multiplied by a k-factor of 1.18 obtained from NLO cross-section calculations presented in reference [254], where the MC program `MCFM` [255] was used.

- $\mathbf{t\bar{t} + Z(+jets)}$: Pair production of t quarks can also be associated by a Z boson, which results in a final state containing W^+W^-Z and hence also allows for same-sign charged dileptons. As for the $t\bar{t} + W$+jets samples, this process is generated using `MadGraph+Pythia` with 0, 1 and 2 additional partons and using the `CTEQ6L1` PDF and the full detector simulation. These samples will be referred to as $t\bar{t} + Z$+jets. The NLO cross-section for the calculation of the k-factor was estimated in reference [256] using the MC program `PowHel`, which relies on the `POWHEG-BOX` framework [160]. The resulting k-factor, also presented in Table 6.3, is 1.34.

- $\mathbf{W^{\pm}W^{\pm}}$**+jets**: Another source of two same-sign charged leptons from the SM are processes, in which two same-sign charged W bosons are produced, as depicted in Figure 6.4d. Due to charge conservation these W bosons need to be produced in association with two partons. For the generation of this process, the `MadGraph+Pythia` generators were used, together with the `MSTW2008` PDF and the fast detector simulation. The cross section listed in Table 6.3 was taken from the generator.

- $\mathbf{W^{\pm}Z(+jets)}$: Another diboson process yielding in same-sign dileptons is the production of a W and a Z boson, which is shown in Figure 6.4e in association with one parton. The processes were generated with up to three additional partons using `Sherpa` with the `CT10` PDF. Both bosons decay exclusively into leptons. The k-factor of 1.06 was obtained in reference [257] by comparing the cross-section reported by `Sherpa` to one obtained at NLO using `MCFM`. This background will be referred to as WZ+jets.

- **ZZ $\to 4\ell$(+jets)**: Pair production of Z bosons with exclusive leptonic decay results in four leptons and hence allows for the selection of same-sign dileptons. As for the WZ sample, this process was generated with up to three additional partons using `Sherpa` and `CT10` as PDF. The NLO cross-section calculation with `MCFM` in reference [257] results in a k-factor of 1.11. This background will be also referred to as ZZ+jets.

In some of the following tables and histograms, I will combine some of these samples in order to improve the visibility. WZ/ZZ+jets will refer to the combination of WZ+jets and ZZ+jets, whereas $t\bar{t}+W/Z/WW$+jets denotes the combination of $t\bar{t}+W$+jets, $t\bar{t}+Z$+jets and $t\bar{t}+WW$.
Selected Feynman graphs for the irreducible backgrounds are presented in Figure 6.4 and a summary of the MC samples used in the analysis, together with the generator, PDF, cross section, k factor and corresponding integrated luminosity is given in Table 6.3.

Process	Generator	PDF	σ [pb]	k	$\mathcal{L}$ [fb^{-1}]	Simulation
$t\bar{t}+WW$	Madgraph+Pythia	MSTW2008	0.0022	1.00	91730	AF2
$t\bar{t}+W$	Madgraph+Pythia	CTEQ6L1	0.104	1.18	3270	G4
$t\bar{t}+W$+j	Madgraph+Pythia	CTEQ6L1	0.053	1.18	7493	G4
$t\bar{t}+W$+jj	Madgraph+Pythia	CTEQ6L1	0.041	1.18	9638	G4
$t\bar{t}+Z$	Madgraph+Pythia	CTEQ6L1	0.068	1.34	4409	G4
$t\bar{t}+Z$+j	Madgraph+Pythia	CTEQ6L1	0.045	1.34	8819	G4
$t\bar{t}+Z$+jj	Madgraph+Pythia	CTEQ6L1	0.040	1.34	10050	G4
$W^{\pm}W^{\pm}$+jj	Madgraph+Pythia	MSTW2008	0.369	1.00	528	AF2
WZ+jets	Sherpa	CT10	9.75	1.06	261	G4
$ZZ \to 4\ell$+jets	Sherpa	CT10	8.73	1.11	186	G4

Table 6.3: A summary of the irreducible same-sign dilepton backgrounds taken from MC simulations. Presented are the different generated processes, used generator and PDF, LO cross section σ reported from the generator and NLO k-factor k and also the used detector simulation (G4 = full simulation, AF2 = fast simulation). The samples $t\bar{t}+W$ and $t\bar{t}+Z$ were generated with one (+j) and two (+jj) additional partons produced at the matrix-element level. In the diboson samples WZ and ZZ, up to three additional partons were generated.

6.2.4 Lepton mis-reconstruction

Basically any jet in an event can 'fake' a lepton signature (this is usually called a 'fake', in the sense that there was no real lepton or that the reconstructed lepton is not stemming from the hard process). Apart from the background contributions from real same-sign

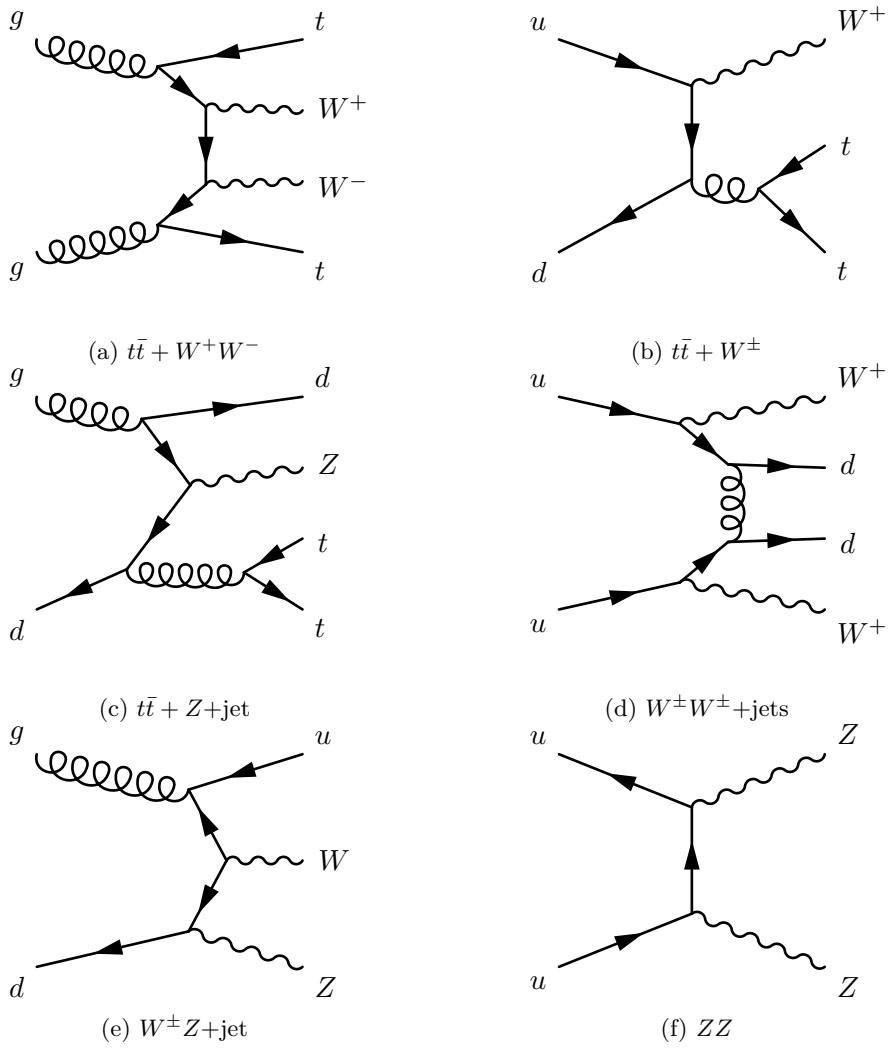

Figure 6.4: Selected Feynman diagrams of irreducible background processes, which can result in final states with two same-sign charged leptons. In the MC generation for the processes $t\bar{t} + W$, $t\bar{t} + Z$, WZ and ZZ also events with more or less additional partons in the final state than shown in above diagrams have been produced.

dilepton events, as discussed in the previous section, every process containing jets therefore could also contribute to the search signature of two same-sign charged leptons. Lepton fakes can arise from jets misidentified as leptons. In the case of electrons this can occur due to heavy flavor hadron decays, reconstruction of a π^0 shower as an electron, and from the conversion of photons or direct photons. The dominant mechanism for creating fake isolated muons is the semi-muonic decay of heavy flavor hadrons. Although the isolation criteria applied to electrons and muons (see Sections 5.3.3 and 5.4.3) are supposed to reject such 'fake' leptons, there is a non-negligible probability that these 'fake' leptons pass the isolation criteria.

The misidentification of leptons strongly depends on detector effects, the object reconstruction and the isolation requirements. Therefore, a MC based modelling of this background contribution is not sufficient and a data-driven technique was used. In general, there are several methods for estimating the lepton fakes contribution. For our dileptonic final state, we chose to use the so-called *Matrix Method*, which allows to measure the fake contribution directly from data.

The *Matrix Method* relies on defining a 'loose' lepton selection, which is supposed to select a large amount of fake leptons, and a 'tight' lepton selection, which is identical to the selection used in the analysis and which is a subset of the 'loose' selection. In specific 'loose' and 'tight' control samples, enriched with fake and real leptons (where real means prompt leptons from $W \to \ell\nu$ or $Z \to \ell\ell$ decays), respectively, the efficiencies for real (ϵ_r) and fake (ϵ_f) 'loose' leptons to pass the 'tight' selection were measured:

$$\epsilon_r = \frac{N_{\text{real}}^{\text{tight}}}{N_{\text{real}}^{\text{loose}}} \;\&\; \epsilon_f = \frac{N_{\text{fake}}^{\text{tight}}}{N_{\text{fake}}^{\text{loose}}}, \tag{6.6}$$

where $N_{\text{real}}^{\text{tight/loose}}$ and $N_{\text{fake}}^{\text{tight/loose}}$ denote the number of events with 'tight'/'loose' leptons in the real and fake control sample, respectively. The measurements of the efficiencies, which are also used in this analysis, will be explained later in this section.

Using the measured real and fake efficiencies, it is then possible to apply the *Matrix Method* in order to obtain the lepton fake background. The general idea is to construct a matrix using the efficiencies, which maps the number of events with real or fake leptons to the number of events with tight or loose leptons. In the dileptonic case, there are four possible combinations of real and fake leptons: real-real (N_{rr}), real-fake (N_{rf}), fake-real (N_{fr}) and fake-fake (N_{ff}). Now the matrix $\mathbf{M}$ translates these event numbers into the number of tight-tight (N_{TT}), tight-loose (N_{TL}), loose-tight (N_{LT}) and loose-loose (N_{LL}) events:

$$\begin{pmatrix} N_{\text{TT}} \\ N_{\text{TL}} \\ N_{\text{LT}} \\ N_{\text{LL}} \end{pmatrix} = \mathbf{M} \begin{pmatrix} N_{\text{rr}} \\ N_{\text{rf}} \\ N_{\text{fr}} \\ N_{\text{ff}} \end{pmatrix}, \tag{6.7}$$

with

$$\mathbf{M} = \begin{pmatrix} \epsilon_r^1\epsilon_r^2 & \epsilon_r^1\epsilon_f^2 & \epsilon_f^1\epsilon_r^2 & \epsilon_f^1\epsilon_f^2 \\ \epsilon_r^1(1-\epsilon_r^2) & \epsilon_r^1(1-\epsilon_f^2) & \epsilon_f^1(1-\epsilon_r^2) & \epsilon_f^1(1-\epsilon_f^2) \\ (1-\epsilon_r^1)\epsilon_r^2 & (1-\epsilon_r^1)\epsilon_f^2 & (1-\epsilon_f^1)\epsilon_r^2 & (1-\epsilon_f^1)\epsilon_f^2 \\ (1-\epsilon_r^1)(1-\epsilon_r^2) & (1-\epsilon_r^1)(1-\epsilon_f^2) & (1-\epsilon_f^1)(1-\epsilon_r^2) & (1-\epsilon_f^1)(1-\epsilon_f^2) \end{pmatrix}, \quad (6.8)$$

where $\epsilon_{r/f}^1$ and $\epsilon_{r/f}^2$ denote the real/fake efficiencies of the first and second lepton in the event.
In the analysis, we can not access the information, whether there was a real or fake lepton. Hence, the matrix $\mathbf{M}$ needs to be inverted, in order to obtain this information by using the accessible information for the number of loose and tight leptons. Above values N_{rr}, N_{rf}, N_{fr} and N_{ff} denoted the number of events in the loose selection. We are interested in the number of real-fake, fake-real and fake-fake events passing our tight selection. The sum of the fake contributions to the tight event selection $N_{\mathrm{fake}}^{\mathrm{TT}}$ is then given by [203]

$$\begin{aligned} N_{\mathrm{fake}}^{\mathrm{TT}} &= N_{\mathrm{rf}}^{TT} + N_{\mathrm{fr}}^{\mathrm{TT}} + N_{\mathrm{ff}}^{\mathrm{TT}} \\ &= \epsilon_r^1\epsilon_f^2 N_{\mathrm{rf}} + \epsilon_f^1\epsilon_r^2 N_{\mathrm{fr}} + \epsilon_f^1\epsilon_f^2 N_{\mathrm{ff}} \\ &= \alpha\epsilon_r^1\epsilon_f^2\left[(\epsilon_f^1-1)(1-\epsilon_r^2)N_{\mathrm{TT}} + (1-\epsilon_f^1)\epsilon_r^2 N_{\mathrm{TL}} + \epsilon_f^1(1-\epsilon_r^2)N_{\mathrm{LT}} - \epsilon_f^1\epsilon_r^2 N_{\mathrm{LL}}\right] \\ &\quad + \alpha\epsilon_f^1\epsilon_r^2\left[(\epsilon_r^1-1)(1-\epsilon_f^2)N_{\mathrm{TT}} + (1-\epsilon_r^1)\epsilon_f^2 N_{\mathrm{TL}} + \epsilon_r^1(1-\epsilon_f^2)N_{\mathrm{LT}} - \epsilon_r^1\epsilon_f^2 N_{\mathrm{LL}}\right] \\ &\quad + \alpha\epsilon_f^1\epsilon_f^1\left[(1-\epsilon_r^1)(1-\epsilon_r^2)N_{\mathrm{TT}} + (\epsilon_r^1-1)\epsilon_r^2 N_{\mathrm{TL}} + \epsilon_r^1(\epsilon_r^2-1)N_{\mathrm{LT}} + \epsilon_r^1\epsilon_r^2 N_{\mathrm{LL}}\right], \end{aligned} \quad (6.9)$$

where

$$\alpha = \frac{1}{(\epsilon_r^1-\epsilon_f^1)(\epsilon_r^2-\epsilon_f^2)}\ . \quad (6.10)$$

Hence, when counting the number of tight-tight, tight-loose, loose-tight and loose-loose events, one can directly evaluate the number of fake events using the measured efficiencies for the electrons and muons.
It is also possible to apply this procedure on an event-by-event base: the variables N_{TT}, N_{TL}, N_{LT} and N_{LL} are used as booleans, which mark the type of event. The obtained number for $N_{\mathrm{fake}}^{\mathrm{TT}}$ can then directly be used as an event weight which is applied when filling histograms or counting event yields.

In the following, I will briefly explain the measurements of the real and fake efficiencies, which were performed in reference [203] by the *ATLAS TopFakes* group.
The real electron efficiencies ϵ_r have been measured in events with single electrons, at least two reconstructed jets and the requirement of a trigger match[1] to one of the electron triggers described in Section 5.3.4. Furthermore, a large missing transverse

[1] A trigger matched lepton is defined to be within $\Delta R < 0.15$ of an object that has fired the trigger.

energy of $E_T^{\text{miss}} \geq 150\,\text{GeV}$ is required for the real lepton sample, because fake lepton events are expected to have lower E_T^{miss} values (this is due to the fact that one does not expect such high energetic neutrinos in hadron jets compared to those resulting from e.g. prompt W boson decays). For the measurement of the fake efficiencies ϵ_f, a similar selection as for the real sample was applied, but additionally using the transverse mass of a W boson $m_T(W)$ for the selection[2]. Instead of requiring a large E_T^{miss}, events are selected that have $E_T^{\text{miss}} < 20\,\text{GeV}$ or $m_T(W) + E_T^{\text{miss}} < 60\,\text{GeV}$, in order to obtain a fake lepton enriched control sample. 'Tight' electrons are defined with the criteria as used in the analysis (see Section 5.3.1). 'Loose' electrons need to fulfil the same criteria, but with the isolation criteria removed and passing the `medium++` cut set. The efficiencies presented in Figure 6.5 were parametrised in the E_T^{miss}, electron η, electron p_T, $\Delta\phi(E_T^{\text{miss}}, e)$, $\min \Delta R(e\text{-jet})$ (the ΔR value of the electron to the closest jet) and the total transverse energy sum $\sum E_T$. One notices only a moderate dependence of the efficiencies as a function of the different parametrisation variables. For a given electron in an event with a certain E_T^{miss} and $\sum E_T$, the total real and fake efficiencies are then obtained by the product of the different parametrised efficiencies (assuming that the parameters are uncorrelated), each normalised to the mean value of the efficiencies. In the case of $E_T^{\text{miss}} \geq 56\,\text{GeV}$, the fake efficiency in the bin $E_T^{\text{miss}} = 56\,\text{GeV}$ is used, because there was no sufficient statistics for higher E_T^{miss} values.

The real and fake muon efficiencies (ϵ_r and ϵ_f) have been measured in events with single muons and at least two reconstructed jets. 'Tight' muons need to fulfil the same criteria as in the analysis (see Section 5.4.1), whereas for 'loose' muons the mini-isolation criterion (Section 5.4.3) is removed.
Events with a high value for $m_T(W)$ ($\gtrsim m_W$) are likely to be real muons stemming from a prompt $W \to \mu\nu$ decay. The efficiency of 'loose' muons to be selected as 'tight' muons is presented in Figure 6.6a and reveals a high efficiency for large $m_T(W)$ values. Above a $m_T(W)$ value of 100 GeV the efficiency reaches a plateau and hence this $m_T(W)$ region is used for the definition of the 'real' control sample.
The dominant source of 'fake' muons are heavy flavor hadron decays. Such muons are expected to have a large significance of the transverse impact parameter d_0, which is defined as

$$\text{sig}(d_0) = \frac{d_0}{\sigma(d_0)}, \tag{6.11}$$

where $\sigma(d_0)$ denotes the resolution of the transverse impact parameter d_0. Figure 6.6b presents the efficiencies for 'loose' muons to be selected as 'tight' as a function of $\text{sig}(d_0)$ and one can see that for significances higher than five the efficiency becomes flat at small values, which indicates that the contribution of 'real' muons is small in this region. Therefore, events that contain muons with $\text{sig}(d_0) > 5$ were used as 'real' control sample

[2]The transverse mass of a W boson is defined as $m_T(W) = \sqrt{2E_T^{\text{miss}} p_T^{\ell} \left(1 - \cos(\Delta\phi(E_T^{\text{miss}}, \ell))\right)}$, where p_T^{ℓ} denotes the transverse momentum of the reconstructed lepton and $\Delta\phi(E_T^{\text{miss}}, \ell)$ is the angular difference between the direction of the missing transverse energy and the lepton. For low values of $m_T(W)$ it is likely that these lepton candidates do not originate from a $W \to \ell\nu$ decay.

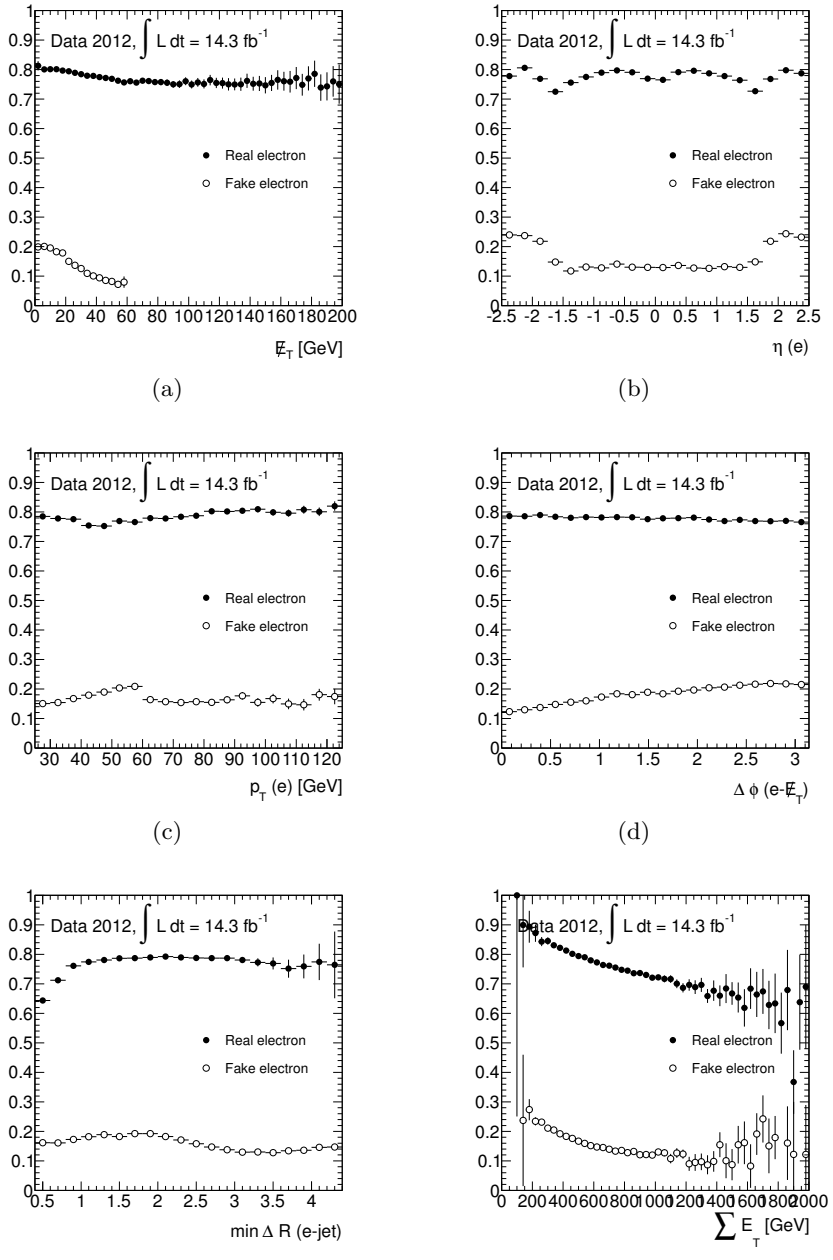

Figure 6.5: Measured real efficiency and fake efficiency for electrons as a function of E_T^{miss} (a), pseudorapidity η of the electron (b), p_T of the electron (c), $\Delta\phi$ between the electron and E_T^{miss} vector (d), ΔR between the electron and the nearest jet (e), and the $\sum E_T$ of the event (f) [203]. The electrons were required to have a match to the `EF_e24vhi_medium1` or `EF_e60_medium1` trigger.

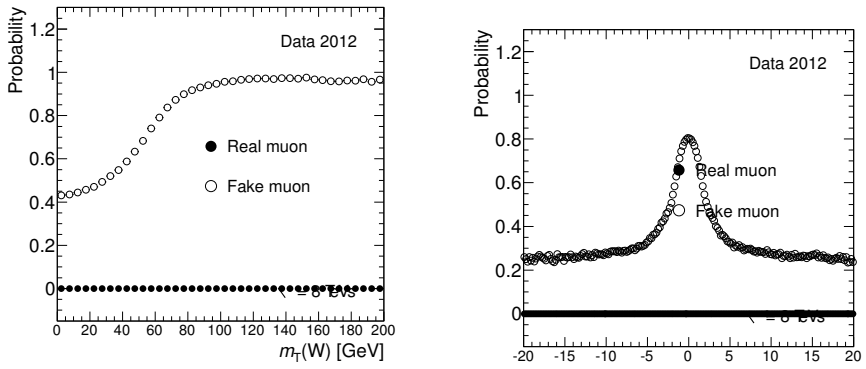

(a) $m_T(W)$ (b) sig(d_0)

Figure 6.6: Efficiencies for 'loose' muons to be selected as 'tight' muons as a function of $m_T(W)$ (a) and sig(d_0) (b) [203], denoted with the label 'Fake Muon'. 'Real muon' is not used here and the efficiencies are set to zero. The muons were required to have a match to the `EF_mu24i_tight` trigger.

for the efficiency measurement.

The real and fake efficiencies have been measured in reference [203] as a function of the muon η and p_T, the number of reconstructed jets and the number of b-tagged jets, and of the ΔR of the muon and the closest jet. The obtained efficiencies are presented in Figure 6.7 for muons matching the `EF_mu24i_tight` trigger and in Figure 6.8 for muons matching the `EF_mu36_tight` trigger. One notices a clear difference of about 20% between the fake efficiencies for `EF_mu24i_tight` and `EF_mu36_tight`. The reason is that the trigger isolation requirement already rejects a certain amount of 'fake' muons. Therefore, the efficiencies are provided separately for the two triggers. For muons with $p_T \geq 37\,\text{GeV}$ (which is slightly above the `mu36_tight` trigger threshold and marks the plateau region of the trigger efficiency) one should use the efficiencies estimated for the `mu36_tight` trigger, whereas the `mu24i_tight` efficiencies should be used for muons with smaller p_T.

Due to the observed differences, and the fact that the efficiencies have been measured separately for the two single lepton triggers, one needs to make sure that one selects the correct efficiencies for the muons in a dilepton analysis. The discussion in the following presents the outcome of several studies performed by me in collaboration with the Arizona group.

In an analysis selecting single lepton events, one would select the efficiencies depending on the matched trigger and the p_T of the muon. For muons with a match to the `mu36_tight` trigger and a $p_T \geq 37\,\text{GeV}$, one would select the efficiencies obtained with the `mu36_tight` trigger in the analysis. In contrast one would use the `mu24i_tight` efficiencies for muons with a match to the `mu24i_tight` trigger and a $p_T < 37\,\text{GeV}$.

In our dilepton analysis, we require only at least one trigger match for one of the two leptons (see also the description of the event selection in Section 6.7). When simply selecting the efficiencies depending on the p_T of the muon and then estimating the lep-

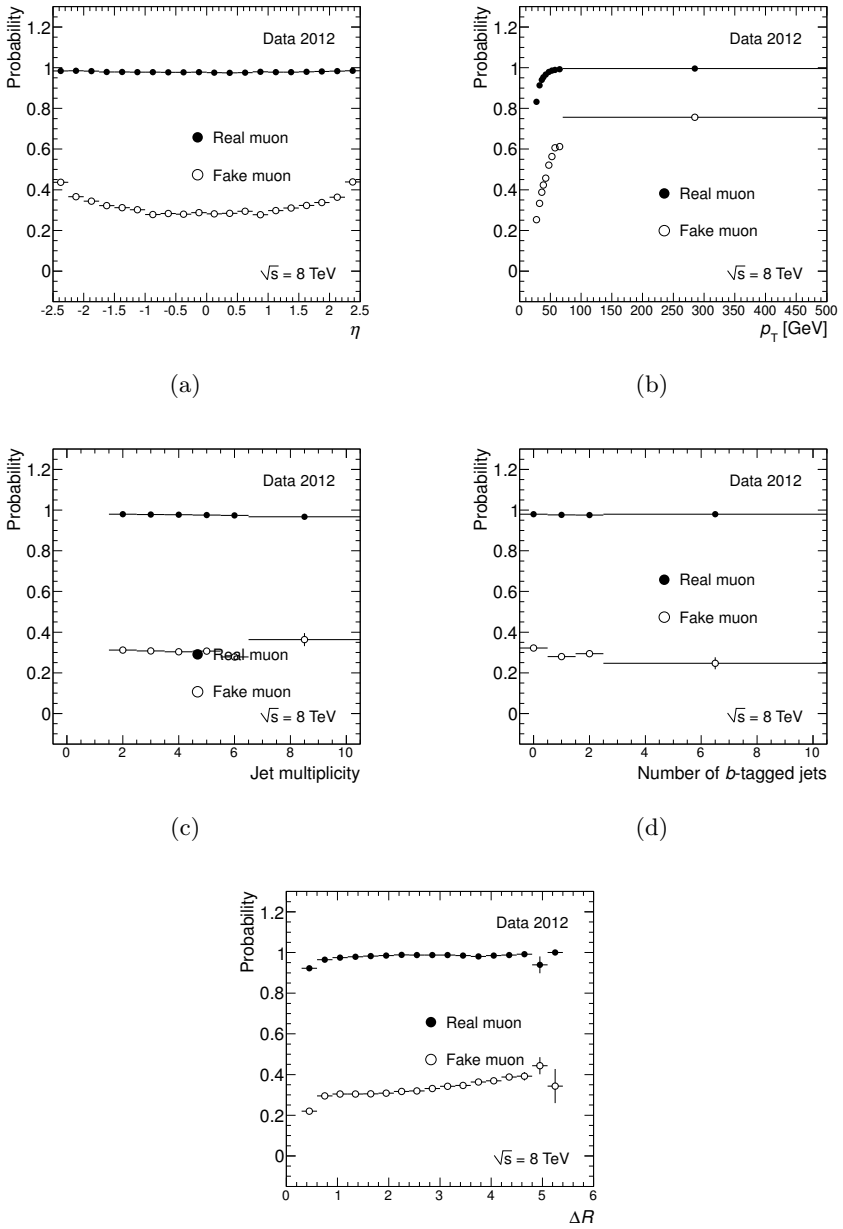

Figure 6.7: Fake and real muon efficiencies for events triggered with 24 GeV transverse momentum threshold and built-in isolation (`EF_mu24i_tight`) as a function of muon η (a), muon p_T (b), number of jets (c), number of b-tagged jets (d) and ΔR between the muon and the closest jet (e) [203].

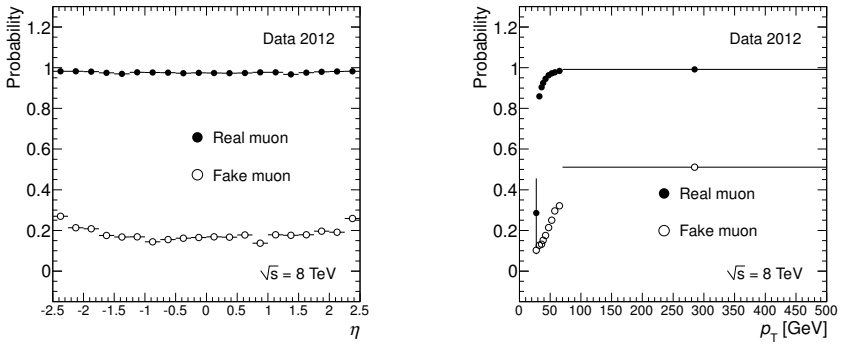

(a) (b)

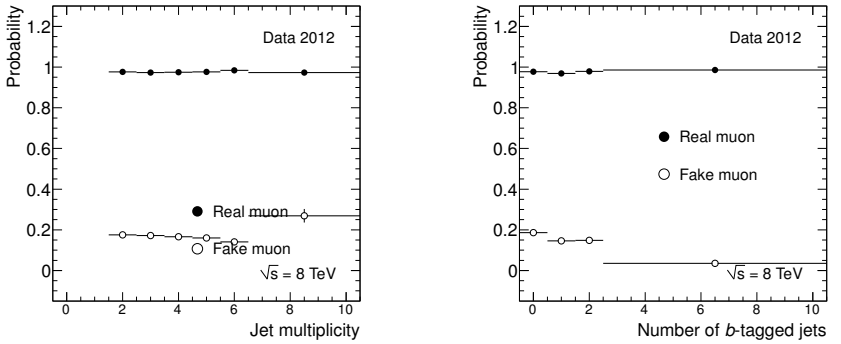

(c) (d)

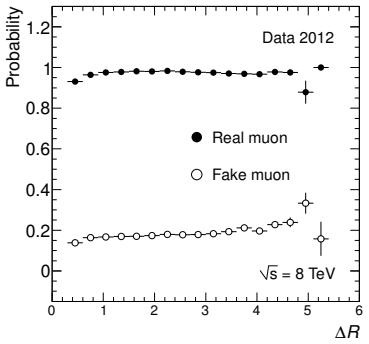

(e)

Figure 6.8: Fake and real muon efficiencies for events triggered with 36 GeV transverse momentum threshold and no isolation (`EF_mu36_tight`) as a function of muon η (a), muon p_T (b), number of jets (c), number of b-tagged jets (d) and ΔR between the muon and the closest jet (e) [203].

ton fakes contribution for one of our control regions (control regions are used for the validation of the background estimates and have orthogonal selections compared to the signal region selection, see also Section 6.8.2.1 for further discussion), we observed a large over-estimate of the lepton fake background in the di-muon ($\mu\mu$) channel, as it is presented in Figure 6.9. Shown are the number of jets distributions in the same-sign $e\mu$

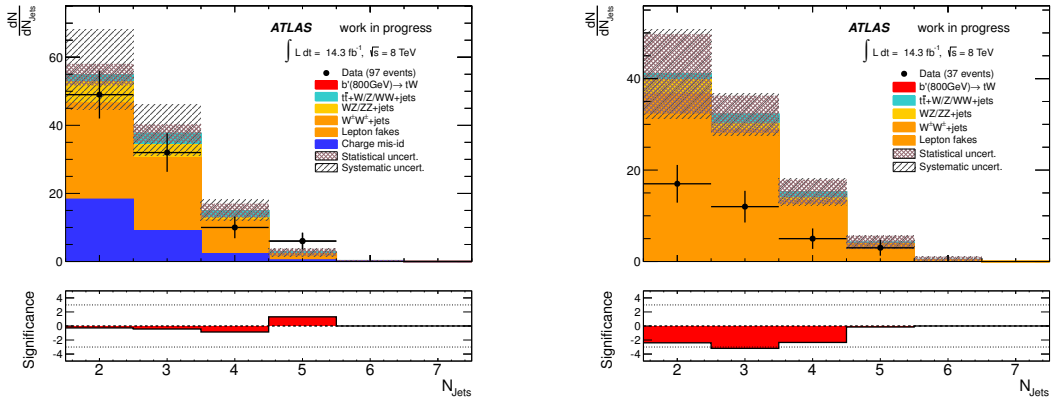

(a) $e\mu$ (b) $\mu\mu$

Figure 6.9: Number of jets distributions in the same-sign $e\mu$ (a) and same-sign $\mu\mu$ (b) channel in one of our control regions. This control region is defined as $100\,\text{GeV} < H_T < 400\,\text{GeV}$, no E_T^{miss} cut and the other cuts as for the signal region selection described in Section 6.7. The muon real and fake efficiencies have been simply selected according to the muon p_T and one clearly notices a large over-estimate of the background in the $\mu\mu$ channel.

and same-sign $\mu\mu$ channel. More distributions can also be looked up in Appendix C.1. This over-estimate is caused by two problems when selecting the muon efficiencies: first, the loose muon selection requires to remove the isolation requirement. However, in the measurement of the real and fake efficiencies for `EF_mu24i_tight` triggered events, a trigger match is required and hence an implicit isolation criterion is applied in the loose sample[3]. In case of our dilepton analysis, both muons do not have necessarily a match to the `mu24i_tight` trigger. Hence, if we select muons with a low $p_T < 37\,\text{GeV}$ that have no trigger match to `mu24i_tight`, there is no isolation applied, although we are applying efficiencies that have been measured for loose muons with isolation.
The second problem arises from the different fake efficiencies for the two triggers and that we did not select the correct efficiencies for each muon. Basically, the p_T-dependent efficiency selection, as we tried it in the beginning, is only valid for events without isolation bias, meaning only events where there was a trigger match to the `mu36_tight` trigger. In the case that there was no trigger match to `mu36_tight`, one should apply the `mu24i_tight` efficiencies only to the muon that has matched the trigger.
In order to solve the above problems, we took two steps: in order to simulate the trigger

[3]For the `mu24i_tight` trigger the isolation requirement is $P_T^{\text{Cone20}}/p_T^{\mu} < 0.12$, see also Section 5.4.3.

isolation in the case of muons with $p_T < 37\,\text{GeV}$, we required in the loose selection $P_T^{\text{Cone20}}/p_T^{\mu} < 0.12$ for such muons. This criterion is looser than the mini-isolation we apply in the tight selection and hence the tight sample is still a subset of the loose sample, as it is required by the matrix method. Then in deciding which efficiency values to apply, we used the following logic: if an $e\mu$ or $\mu\mu$ event enters into our loose sample without isolation bias, then we apply the p_T-dependent efficiencies to all muons. If an event enters the loose sample due to an isolation-biased selection for one muon, we apply the `mu24i_tight` efficiency to that muon and `mu36_tight` efficiency to the second muon, if there is one. Finally, if a $\mu\mu$ event enters the loose sample due to an isolation-biased selection for both muons, we apply the `mu24i_tight` efficiencies to both muons. The set of efficiencies applied to each muon in the $e\mu$ and $\mu\mu$ channels are listed in Tables 6.4 and 6.5, respectively. When applying this scheme for the selection of the muon real and

Electron	Muon		
Matches either electron trigger?	Matches `mu36_tight`?	Matches `mu24i_tight`?	Eff. applied
Yes	Yes or no	Yes or no	p_T-dep
No	Yes	Yes or no	p_T-dep
No	No	Yes	`mu24i_tight`

Table 6.4: Efficiencies applied to the muon in the $e\mu$ channel, depending on the characteristics of both leptons in the event. Here p_T-dep means that `mu36_tight` efficiencies are applied if the muon p_T is $\geq 37\,\text{GeV}$, and `mu24i_tight` efficiencies are applied otherwise.

Leading p_T muon			Second leading p_T muon		
Matches `mu36_tight`?	Matches `mu24i_tight`?	Eff. applied	Matches `mu36_tight`?	Matches `mu24i_tight`?	Eff. applied
Yes	Yes or no	p_T-dep	Yes	Yes or no	p_T-dep
Yes	Yes or no	p_T-dep	No	Yes	p_T-dep
No	Yes	p_T-dep	Yes	Yes or no	p_T-dep
Yes	Yes or no	p_T-dep	No	No	p_T-dep
No	No	p_T-dep	Yes	Yes or no	p_T-dep
No	Yes	`mu24i_tight`	No	Yes	p_T-dep
No	Yes	`mu24i_tight`	No	No	p_T-dep
No	No	p_T-dep	No	Yes	`mu24i_tight`

Table 6.5: Efficiencies applied to each muon in the $\mu\mu$ channel, depending on the characteristics of both muons in the event. Here p_T-dep means that `mu36_tight` efficiencies are applied if the muon p_T is $\geq 37\,\text{GeV}$, and `mu24i_tight` efficiencies are applied otherwise.

fake efficiencies, and when introducing the trigger isolation cut for low p_T muons, we achieved a much better agreement between the data and our background expectations,

as it will be shown in Section 6.8.2.1.

6.2.5 Charge mis-reconstruction

Another source of same-sign dilepton background are true opposite-sign events produced by Standard Model processes that are reconstructed as same-sign events due to one electron charge being mis-identified. Such processes will be referred to as charge mis-reconstruction or charge mis-identification (charge mis-id) in the following.
There are two main sources causing the charge mis-id background:

- Electrons interacting with the detector material can produce hard bremsstrahlung. With the further photon conversion into an electron-positron pair, as it is shown in Figure 6.10, one obtains trident electrons in the final state ($e^{\pm} \to e^{\pm}\gamma \to e^{\pm}e^{+}e^{-}$). Due to the boosted topology of the photon conversion, the p_T spectrum of the

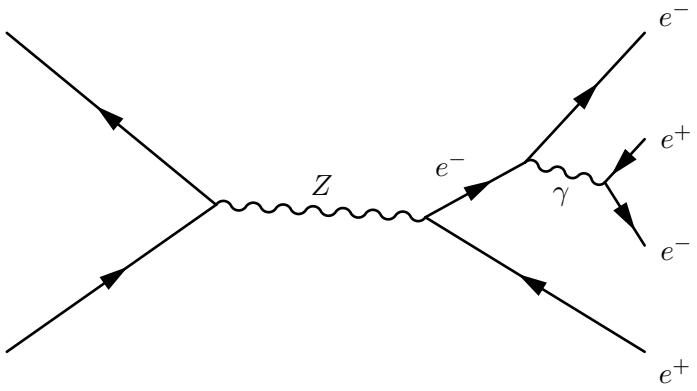

Figure 6.10: Feynman graph of trident electrons coming from a $Z \to e^{+}e^{-}$ decay, which is a source of the charge mis-identification background.

  outcoming electron and positron is not necessarily symmetric, and hence there is the chance that only one of the two particles is above the detection threshold, resulting in a possible same-sign di-electron final state. Since the production of the hard bremsstrahlung depends on the traversed detector material, this source of charge mis-id is expected to increase at higher $|\eta|$ values of the electron.

- The tracks of electrons with very high p_T have only a tiny curvature and hence can cause a measurement error of the electron charge (which is extracted from the direction of the track bending). This effect is expected to be dominant at high p_T.

Above discussed sources for charge mis-id are dominant effects for electrons. Muons do not produce such a hard bremsstrahlung (due to the higher mass), and their curvature measurement is improved due to the combination of the inner detector and muon spectrometer tracks. Therefore, charge mis-id effects from muons are neglected in the following and the charge mis-id background is only estimated for electrons in the ee and $e\mu$ same-sign dilepton channels.

For these channels, the dominant Standard Model processes are Z+jets and $t\bar{t}$+jets production, both with fully leptonic decays. While Z+jets will have a high contribution in the ee channel (the $Z \to e\mu$ decay is forbidden at tree-level in the SM), the $e\mu$ channel will be dominated by the $t\bar{t}$+jets background.
Having a true opposite-sign electron-positron event, it can be reconstructed as

- e^+e^- without any charge mis-id, with probability $(1-\epsilon)^2$,
- e^-e^+ with both electrons having a charge flip, with probability ϵ^2
- $e^\pm e^\pm$ with a mis-identified charge of only one electron, with probability $2\epsilon(1-\epsilon)$,

where ϵ denotes the probability of charge mis-identification of a single electron, which will be also called 'charge mis-id rate' in the following. The factor of 2 in the last case is due to the combinatorics of the two electrons. A description of the charge mis-id rate measurements we (Clermont-Ferrand) performed will be given later in Section 6.2.5.1.
When considering that the charge mis-id rates depend on the η and/or the p_T of the electron, both electrons need to be treated separately with the rates ϵ_i and ϵ_j. With above probabilities, it is then possible to derive the expected number of opposite-sign and same-sign events. Hence, if there are N true opposite-sign events, we expect to observe

- $N_{\mathrm{OS}} = (1 - \epsilon_i - \epsilon_j + 2\epsilon_i\epsilon_j)N$ opposite-sign events and
- $N_{\mathrm{SS}} = [\epsilon_i(1-\epsilon_j) + \epsilon_j(1-\epsilon_i)]\, N$ same-sign events

after reconstruction. When combining above two equations, it is possible to derive the expected number of same-sign events N_{SS} as a function of the number of opposite-sign events N_{OS} and the charge mis-id rates ϵ_i and ϵ_j of the two different electrons i and j in the ee channel

$$N_{\mathrm{SS}} = \frac{\epsilon_i + \epsilon_j - 2\epsilon_i\epsilon_j}{1 - \epsilon_i - \epsilon_j + 2\epsilon_i\epsilon_j} N_{\mathrm{OS}} \tag{6.12}$$

and the $e\mu$ channel

$$N_{\mathrm{SS}} = \frac{\epsilon_i}{1-\epsilon_i} N_{\mathrm{OS}}, \tag{6.13}$$

respectively. Above equations can be divided by N_{OS}, in order to obtain the event weights

$$w_{ee} = \frac{\epsilon_i + \epsilon_j - 2\epsilon_i\epsilon_j}{1 - \epsilon_i - \epsilon_j + 2\epsilon_i\epsilon_j}, \tag{6.14}$$

$$w_{e\mu} = \frac{\epsilon_i}{1-\epsilon_i}\ . \tag{6.15}$$

for the ee and $e\mu$ channel, respectively. In the analysis, we select opposite-sign events from data passing our selection criteria, apply above listed event weights and then consider the events as having a same-sign signature.

6.2.5.1 Estimation of the charge mis-identification rates

The estimation of the charge mis-identification rate ϵ requires a clean sample of opposite-sign charged di-electron events. Therefore, the rate is measured in $Z \to ee$ events, by comparing the number of opposite-sign N_{OS} and same-sign events N_{SS}. The electrons are selected according to the criteria discussed in Section 5.3.

In order to obtain e^+e^- pairs coming from Z decays, only electrons are selected that have an invariant mass close to the Z boson mass. However, even within this region there are background events not arising from a Z decay, which need to be subtracted before counting N_{OS} and N_{SS}. This is performed by a simple side-band method: two regions A and C are defined next to the Z peak region B. The number of events N_A and N_C in the A and C region, respectively, are counted. Then the average of the two regions is subtracted from the number of events in the B region:

$$N_{\mathrm{SS/OS}} = N_B - \frac{N_A + N_C}{2} \ . \tag{6.16}$$

One should note, that this method is only valid, if one assumes that the background has only a linear dependence on the invariant mass m_{ee}. The distribution of the invariant mass of opposite-sign and same-sign di-electrons measured on data, together with the definition of the A, B and C regions, is presented in Figure 6.11. In the same-sign distribution one notices a small shift and broadening of the Z peak compared to the opposite-sign distribution. This is due to the fact, that the electrons with a mis-identified charge coming from a hard bremsstrahlung process have a looser p_T than the original electron. Therefore the A, B and C regions are defined slightly differently in the opposite-sign and same-sign distribution.

The determination of the charge mis-id rates is performed by a minimisation of a log-Likelihood. This procedure allows to extract the rate and its dependence on η for both electrons in the same event.
For small charge mis-id rates the number of same-sign events in Equation (6.12) can be approximated by

$$N_{\mathrm{SS}}^{ij} \simeq (\epsilon_i + \epsilon_j) N_{\mathrm{OS}}^{ij}, \tag{6.17}$$

where i and j denote the two electrons in the ith and jth $|\eta|$ bin and N_{OS}^{ij} is the number of opposite-sign events in this η configuration. Since N_{SS}^{ij} is generally Poisson distributed, the probability to observe N_{SS}^{ij} same-sign events, when $(\epsilon_i + \epsilon_j)N_{\mathrm{OS}}^{ij}$ events are expected for particular ϵ_i and ϵ_j, is given by

$$\mathcal{P}(N_{\mathrm{SS}}^{ij} | \epsilon_i, \epsilon_j, N_{\mathrm{OS}}^{ij}) = \frac{\left[(\epsilon_i + \epsilon_j) N_{\mathrm{OS}}^{ij}\right]^{N_{\mathrm{SS}}^{ij}} e^{-(\epsilon_i + \epsilon_j) N_{\mathrm{OS}}^{ij}}}{N_{\mathrm{SS}}^{ij}!} \ . \tag{6.18}$$

The charge mis-id rates ϵ_i and ϵ_j need to be determined from data. This is performed by a minimisation of the log-Likelihood, where it is summed over all possible $\eta_{i/j}$ combinations

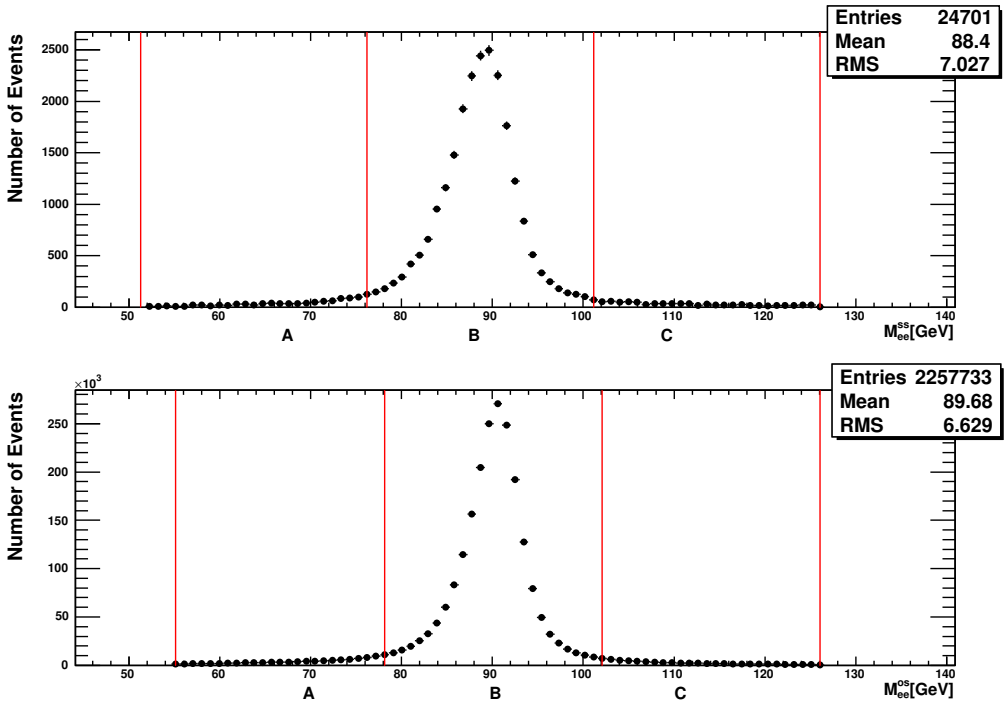

Figure 6.11: Dilepton mass spectrum for opposite-sign (bottom) and same-sign (top) electron pairs measured on data [258]. The vertical lines define the A, B and C regions used for the background subtraction.

among the two electrons:

$$-\ln\left[L(\epsilon_i,\epsilon_j|N^{ij}_{\mathrm{SS}},N^{ij}_{\mathrm{OS}})\right]=\sum_{i,j}\ln\left[(\epsilon_i+\epsilon_j)N^{ij}_{\mathrm{OS}}\right]N^{ij}_{\mathrm{SS}}-(\epsilon_i+\epsilon_j)N^{ij}_{\mathrm{OS}}\ . \tag{6.19}$$

Here, all terms have been removed that do not depend on η. The minimisation of above log-Likelihood was performed using the minimisation programs `MINUIT` [259] and `MINOS` [260] in order to extract the charge mis-id rates ϵ.

Before using the extracted charge mis-id rates in the analysis, there are two corrections which need to be applied to the rates, and will be discussed in the following.
As previously discussed, the rates are measured in $Z\to e^+e^-$ events. However, a significant contribution to the charge mis-id background in the analysis is expected to come from fully leptonic $t\bar{t}$ events decaying into $e^\pm e^\mp$ or $e^\pm\mu^\mp$ pairs. Due to the higher mass of the t quark and the different event topology, the p_T spectrum of the outcoming electrons is expected to be different compared to the one from the Z decays. Therefore, we (Clermont-ferrand) studied the difference in the rates between Z and $t\bar{t}$ events, by measuring the charge mis-id rates in MC simulated $Z\to e^+e^-$ and $t\bar{t}$ events[4]. In this

[4]These MC samples have been generated using the generators `Alpgen`+`Pythia` [155, 168] for the $Z\to e^+e^-$ events and `MC@NLO`+`Herwig` [159, 166] for the $t\bar{t}$ events.

study, the charge mis-id rates have been extracted by comparing the charges of the reconstructed electrons to the charges of the true electrons found via a so-called truth matching[5]. The obtained charge mis-id rates as a function of the electron's $|\eta|$ and in

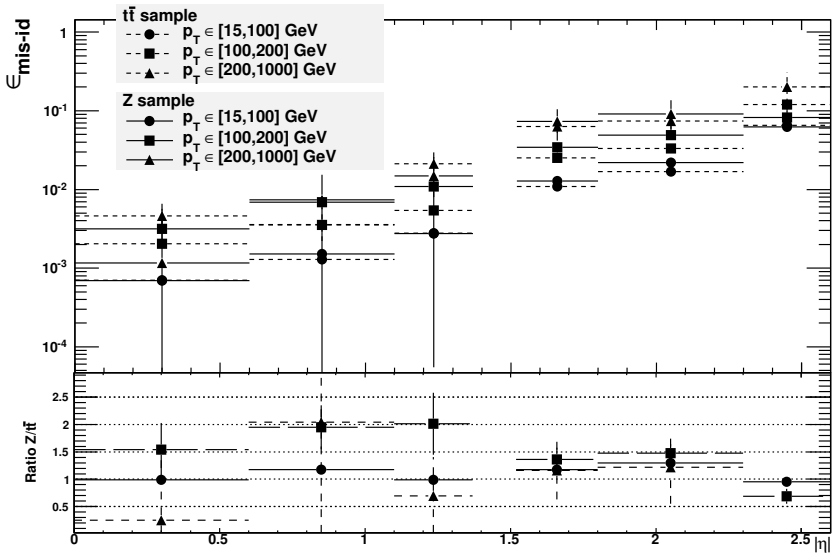

Figure 6.12: Comparison of true charge mis-id rates between Z and $t\bar{t}$ events, as a function of the $|\eta|$ of the electron in different bins of the p_T of the electron [258]. The ratio of the rates obtained from Z and $t\bar{t}$ events is presented at the bottom of the plot. For each point, the statistical uncertainties are shown.

several bins of the electron's p_T are presented in Figure 6.12. It can be seen that the rates are compatible within the statistical uncertainties for the same (η, p_T) configurations.
However, the rates measured in the $Z \to ee$ events will be dominated by the low p_T region. This can also be seen in Figure 6.13a, where the distribution of the ratio $\epsilon(\eta, p_T)/\epsilon(\eta)$ as a function of $|\eta|$ and in different bins of p_T is presented. Here, $\epsilon(\eta, p_T)$ denotes the charge mis-id rate obtained from the $Z \to e^+e^-$ MC events via truth matching and $\epsilon(\eta)$ represents the average over all p_T bins. For the region of low $p_T < 100\,\text{GeV}$ the ratio is compatible with 1. For higher p_T, the ratio fluctuates to higher values with large statistical uncertainties, which indicates that in this p_T region only low statistics is available for measuring the charge mis-id rates.
This is problematic, because for the charge mis-id background coming from $t\bar{t}$ events we expect higher p_T values of the electrons and hence we need statistically well measured rates for this region. Since such rates can not be provided by the measurements on data, the obtained rates at low p_T with sufficient statistics are complemented by the

[5]Here, a truth matching is performed by looking for a true particle in the event information from the generator (before the various reconstruction algorithms), that is within $\Delta R < 0.2$ of the reconstructed particle.

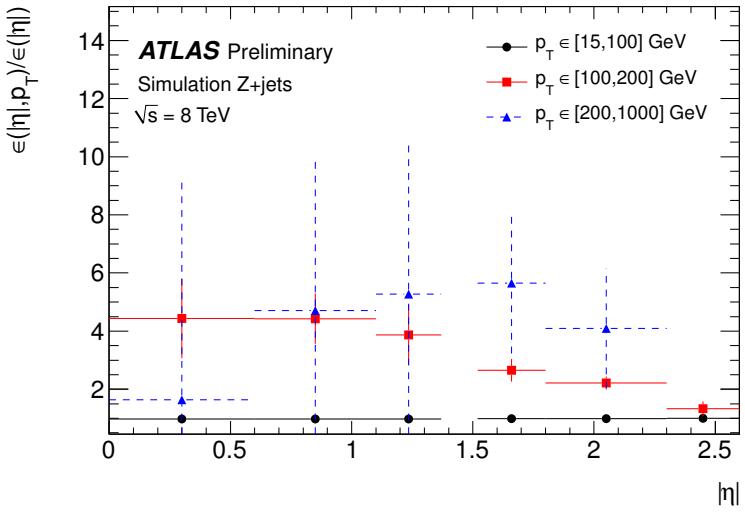

(a)

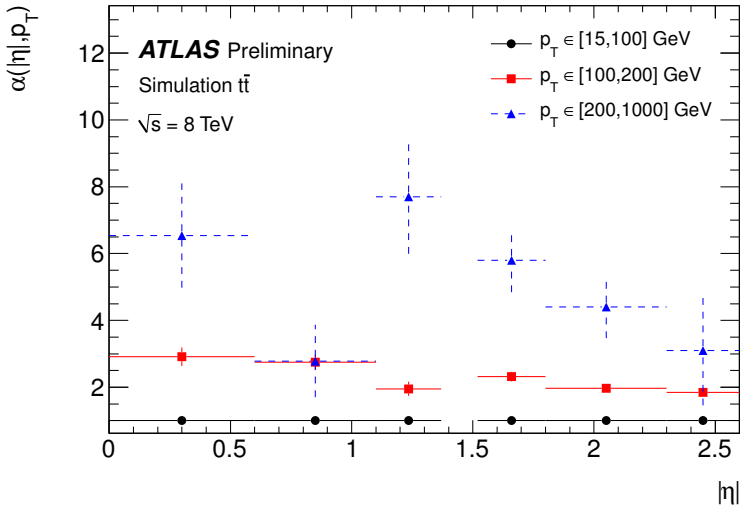

(b)

Figure 6.13: Figure (a) presents the distribution of the ratio $\epsilon(\eta, p_T)/\epsilon(\eta)$ of charge mis-id rates obtained from Z events via truth matching, where $\epsilon(\eta, p_T)$ denotes the rate for a given η and p_T bin and $\epsilon(\eta)$ represents the average rate for all p_T values [250]. The distribution is shown as a function of $|\eta|$ and in different p_T bins. The error bars represent the statistical uncertainties on the ratio.
Figure (b) shows the distribution of the correction factor $\alpha(\eta, p_T)$ as a function of $|\eta|$ and in different bins of p_T [250]. By definition, the correction factor is equal to 1 in the first p_T bin. The error bars represent the statistical uncertainties on the correction factor.

information from the $t\bar{t}$ MC sample. The idea is to correct the rates measured for the low p_T in $Z \to e^+e^-$ events by a p_T-dependent correction factor α, extracted from the MC simulated $t\bar{t}$ events. This factor is given by

$$\alpha(\eta, p_T) = \frac{\epsilon(\eta, p_T)}{\epsilon(\eta, p_T < 100\,\text{GeV})}, \tag{6.20}$$

where the rates are extracted from the truth matching method. Generally, the correction factor represents the charge mis-id rate $\epsilon(\eta, p_T)$ for particular values of η and p_T, which is then normalised to the average rate for $p_T < 100\,\text{GeV}$ at this η bin.
Finally, the charge mis-identification rate is defined as

$$\epsilon(\eta, p_T) = \epsilon_Z(\eta) \times \alpha(\eta, p_T), \tag{6.21}$$

where $\epsilon_Z(\eta)$ denotes the η-dependent rate measured in $Z \to ee$ data events for electrons with $p_T < 100\,\text{GeV}$ and $\alpha(\eta, p_T)$ is the correction factor obtained from $t\bar{t}$ MC events. Since the rates measured on data are modified by a factor determined from MC, one needs to assume that the charge mis-id processes are well modelled in the $t\bar{t}$ MC and provide a good representation of the processes in data.
The charge mis-id rates we finally obtained from data, after applying the correction factor α, as a function of $|\eta|$ and in different bins of p_T are presented in Figure 6.14.

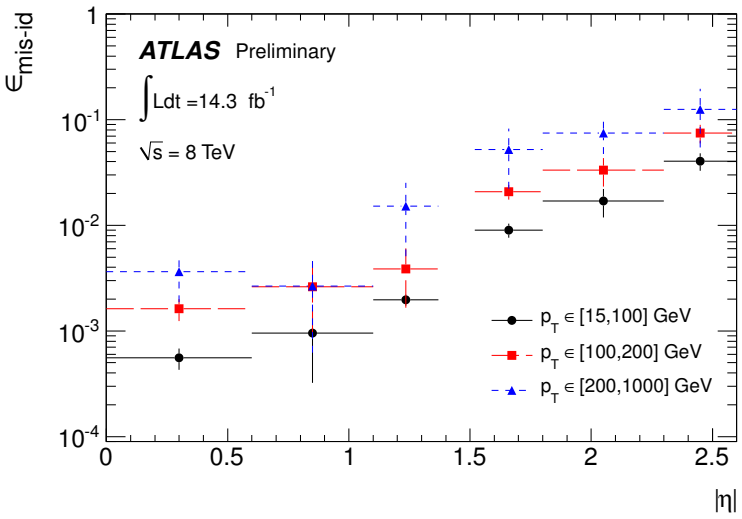

Figure 6.14: Final charge mis-identification rates measured in $Z \to ee$ events on 2012 data after applying the p_T dependent correction factor α obtained from simulated $t\bar{t}$ events [250]. The rates are presented as a function of $|\eta|$ and in different p_T bins.

The second correction, which needs to be applied to the charge mis-id rates, arises from the fact that there is an overlap between the background estimated from lepton mis-reconstruction (lepton fakes) and the charge mis-id. The reason is that the trident

electrons have a smaller probability to pass the tight selection compared to the prompt electrons, and thus are partially captured by the matrix method previously presented in Section 6.2.4. This means that such events can be counted twice (in the estimation of the charge mis-id and of the lepton fakes background) and hence we need to remove this overlap. The size of this overlap can be read off from Figure 6.15a, where the invariant mass distribution of the $Z \to ee$ data events is presented for the estimated charge mis-id background (using tight electrons) and for fake electrons captured by the matrix method. In order to remove the overlap, we (Berlin) decided to remove the fakes in the estimation

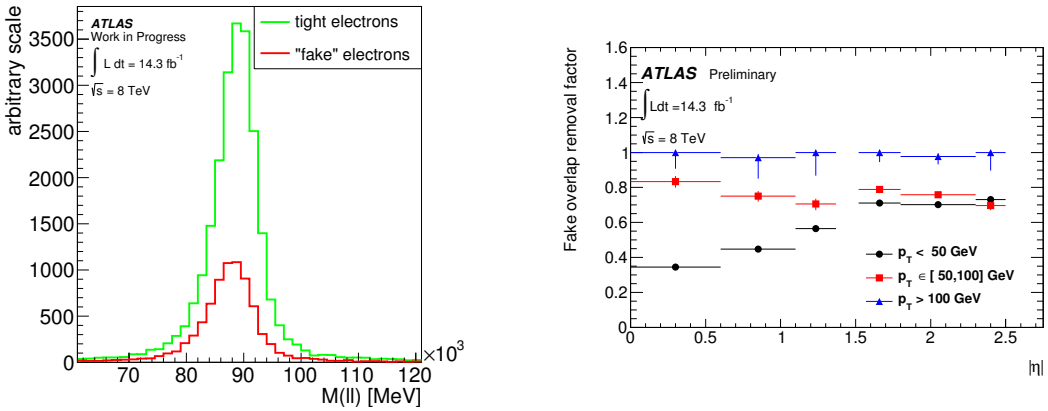

(a) (b)

Figure 6.15: Figure (a) presents the invariant mass distributions for selected $Z \to ee$ events in data for the estimated same-sign charge mis-id background with tight electrons (green) and fake electrons captured by the matrix method (red) [258].
In Figure (b) the correction factors are presented, which are applied to the charge mis-id rates in order to remove the overlap with the events from lepton mis-reconstruction (fakes) [250]. The overlap removal factor is presented as a function of $|\eta|$ and for different bins in p_T and the error bars represent the statistical uncertainties.

of the charge mis-id. The procedure is to produce the charge mis-id rates twice. First, the charge mis-id rates are extracted using all events passing our tight electron selection, called ϵ_{norm}. Afterwards, we extract the charge mis-id rates again, but this time from the difference of all events which pass the tight selection minus the number of same-sign fake events estimated by the matrix method. This gives the charge mis-id rate with removed fakes overlap ϵ_{FOR}. Finally, the ratio $\epsilon_{\text{norm}}/\epsilon_{\text{FOR}}$, shown in Figure 6.15b, will be applied to the charge mis-id rates in the analysis, in order to correct for the fakes overlap. It can be seen that there is a significant overlap correction applied to the rates for electrons with $p_T < 100\,\text{GeV}$, whereas the overlap is negligible for high p_T electrons.

6.2.5.2 Validation of the charge mis-identification estimates

We (Clermont-Ferrand) performed several studies in order to validate the estimates and extracted rates for the charge mis-identification background, which will be presented in the following.

The first study was to validate the extraction of the charge mis-id rates using the minimisation of the log-Likelihood. In the simulated $Z \to e^+e^-$ events, the rates obtained from the Likelihood method were compared to the rates extracted via truth matching. These charge mis-id rates are presented in Figure 6.16 as a function of $|\eta|$. One notices a good agreement of the rates within the statistical uncertainties.

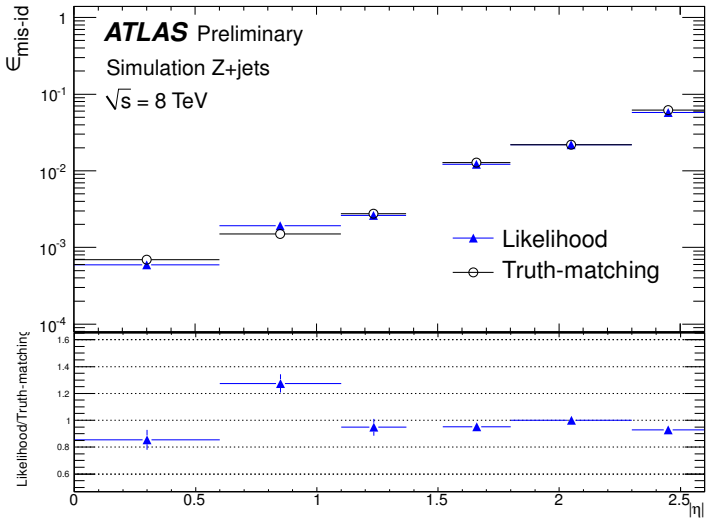

Figure 6.16: Presented are the charge mis-id rates obtained in simulated $Z \to e^+e^-$ events using the minimisation of the log-Likelihood (blue) and the truth matching method (black) [250]. At the bottom, the ratio of the rates is shown and one notices a good agreement within the presented statistical uncertainties.

Another study was to perform a closure test, where the number of directly measured same-sign events was compared to the number obtained by reweighting the opposite-sign events with the computed charge mis-id weights (Equation (6.14)). This comparison was performed on simulated $Z \to e^+e^-$ events and on data, and is presented in Figure 6.17. Presented are the obtained invariant mass distributions and one notices a good agreement between the real same-sign events and the charge mis-id estimate. The small differences in the position of the Z peaks is due to the fact, that the electrons in trident events lost a certain amount of energy due to the photon radiation.

Finally, we wanted to validate our charge mis-id estimates for $t\bar{t}$ events. For this, the distribution of the leading lepton p_T (the lepton with highest p_T) in measured same-sign events was compared to opposite-sign events reweighted by the charge mis-id weights. This was performed on simulated $t\bar{t}$ events and is presented in Figure 6.18. The rates in

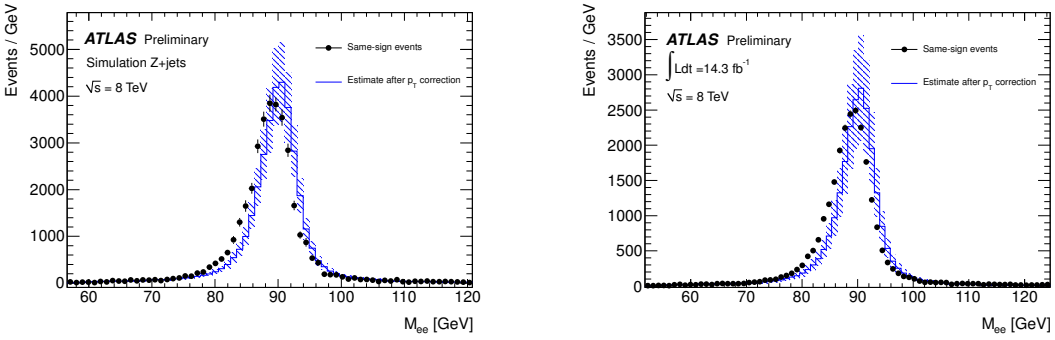

(a) (b)

Figure 6.17: A comparison of the invariant mass distributions of measured same-sign events (black) and opposite-sign events reweighted by the charge mis-id weight (red), performed on simulated $Z \to e^+e^-$ events (a) and on data (b) [250]. The distributions are not expected to overlay exactly, because of the loss of energy of the electrons in trident events.

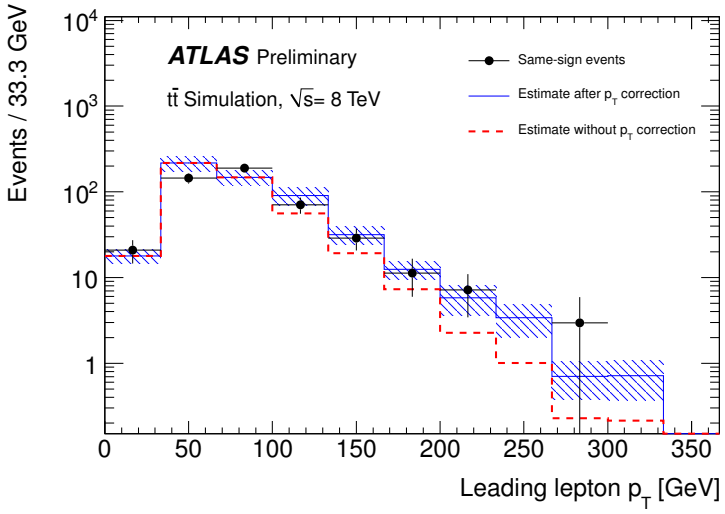

Figure 6.18: Comparison of the leading lepton p_T distribution for same-sign ee events (blue) and opposite-sign ee events reweighted by the charge mis-id weights (black) [250]. The p_T-dependent correction factor α was applied to the charge mis-id rates before calculating the charge mis-id event weights.

the calculation of the charge mis-id weights were corrected by the p_T-dependent factor α. In the leading lepton p_T distributions one notices a good agreement between the real same-sign events and the charge mis-id estimate.

6.3 Analysis framework

The event information after the various reconstruction algorithms are stored in different output formats for both, data and MC:

- **Event Summary Data (ESD):** This format contains detailed output of the reconstruction algorithms and is directly produced from the raw data. Besides particle identification, the content of ESDs allows to e.g. perform a track-refitting or change the jet calibration. The stored event size from the raw data ($\sim 1.6\,\text{MB/event}$) is reduced to $\sim 1\,\text{MB/event}$.

- **Analysis Object Data (AOD):** AODs contain a summary of the reconstructed events. The information are sufficient for common analyses. AODs can be produced from the ESD and the event size is $\sim 100\,\text{kB/event}$.

However, both formats still contain a large amount of information which are not necessary for most physics analyses and therefore provide unacceptable processing times for the analysis.
Therefore, the AODs are converted into a serialised binary file-format ('flat ntuple') by different physics analysis groups in ATLAS. This format in ATLAS is also called `D3PD` and consists of the event information (particle kinematics, event related quantities, etc.) in form of branches. In the analysis of this thesis, the `D3PDs` produced from the *ATLAS Top Physics* group are used (also called `TopD3PDs`), which contain all necessary information for top-quark physics analysis and also related analyses, as it is performed in this thesis.

The typical analysis consists of an event loop running over all events in a sample (data or MC). For each event in this loop, object and event selection criteria are applied and histograms of various variables are filled after the selection. In this analysis, I used the `DESY ATLAS Framework` [261] which is developed by the *DESY ATLAS* group [262] in collaboration with the *Berlin ATLAS* group [251].
The `DESY ATLAS Framework` is based on the `SFrame` framework [263], which is written in the programming language `C++` and makes use of the `ROOT` [25] libraries for analysing particle physics data. For this, `SFrame` provides the event loop and is responsible for making the different branches from the samples available within the user's analysis code. Furthermore, `SFrame` provides several functions for the book-keeping of histograms and allows to write out user-defined ntuples.
The `DESY ATLAS Framework` is built on top of `SFrame` and incorporates the different methods for the object selection and various corrections (e.g. energy scalings/smearings and scale factors) provided by the different performance groups, as it has been discussed in Chapter 5.

6.4 Statistical methods used in the analysis

In my analysis, I used different statistical methods for the interpretation of my results and the calculation of uncertainties and significances, which are explained in the following.

6.4.1 Limits on selection efficiencies using a Frequentist approach

In the following sections, I will present various efficiencies for the selection of events. If one selects n events out of a larger sample containing N events, n is then binomial distributed and $p = n/N$ is an estimator for the probability for an event to pass the selection. For the event selection, n would represent the number of events after a particular cut (or a set of cuts), and N is the number of events before this cut. Hence, $p = n/N$ would denote the estimate $p = \epsilon$ for the efficiency of this cut.

The standard deviation for the binomial distribution is given by

$$\sigma_\epsilon = \sqrt{\frac{1}{N}\epsilon(1-\epsilon)} \tag{6.22}$$

and can be used as estimator for the uncertainty on the efficiency, when inserting the estimator $\epsilon = n/N$. One notices that this calculation yields in symmetric error intervals, which is a sufficient approximation for efficiencies not too close to 0% and 100%. In cases where the efficiencies are getting very close to 0% or 100%, this is problematic, since one would expect asymmetric uncertainties. This due to the fact that efficiencies below 0% or above 100% are not possible. In order to get a reliable calculation of the uncertainties for such values of efficiencies, I use a calculation based on a frequentist approach for binomially distributed values, as it is explained in Section 36.3.2.5 of reference [39]. There, the upper (ϵ_{up}) and lower (ϵ_{lo}) limits on the selection efficiency ϵ are given by

$$\epsilon_{lo} = \frac{nF_F^{-1}[\alpha_{lo}; 2n, 2(N-n+1)]}{N-n+1+nF_F^{-1}[\alpha_{lo}; 2n, 2(N-n+1)]} \tag{6.23}$$

$$\epsilon_{up} = \frac{(n+1)F_F^{-1}[1-\alpha_{up}; 2(n+1), 2(N-n)]}{(N-n)+(n+1)F_F^{-1}[1-\alpha_{up}; 2(n+1), 2(N-n)]}\ , \tag{6.24}$$

where F_F^{-1} is the quantile of the Fisher-Snedecor distribution and $(1-\alpha_{lo})$ and $(1-\alpha_{up})$ are the confidence levels for the lower and upper limit on the efficiencies. In the following $\alpha_{lo} = \alpha_{up} = 0.16$ is used, which corresponds to a 68% confidence interval.

6.4.2 Significance calculation for differences between data and expectation

I will show several distributions of variables, where I will compare the observed data with the expectations of my background estimates coming from the MC simulations and data-driven techniques (as discussed in Section 6.2). These estimates are only known within certain statistical and systematic uncertainties, and hence one needs to quantify the

significance of an excess or a deficit in a particular bin. For plotting these significances, I will use the method explained in reference [264], which will be discussed in the following.

The main idea for defining a statistical significance, is to calculate the probability of finding a deviation at least as big as the one observed in data, under the assumption that the chosen theoretical model describes the system [264]. This probability is commonly referred to as 'p-value'. For convenience the 'p-value' can be translated into a so-called 'z-value', which is the deviation at the right of the mean of a Gaussian distribution, expressed in units of standard deviations, corresponding to the same p-value. The z-value is then connected to the p-value by the following integration over a Gaussian

$$p\text{-value} = \int_z^\infty \frac{1}{\sqrt{2\pi}} e^{-\frac{x^2}{2}}\, \mathrm{d}x \tag{6.25}$$

and the relationship between both variables is presented in Figure 6.19. One sees that

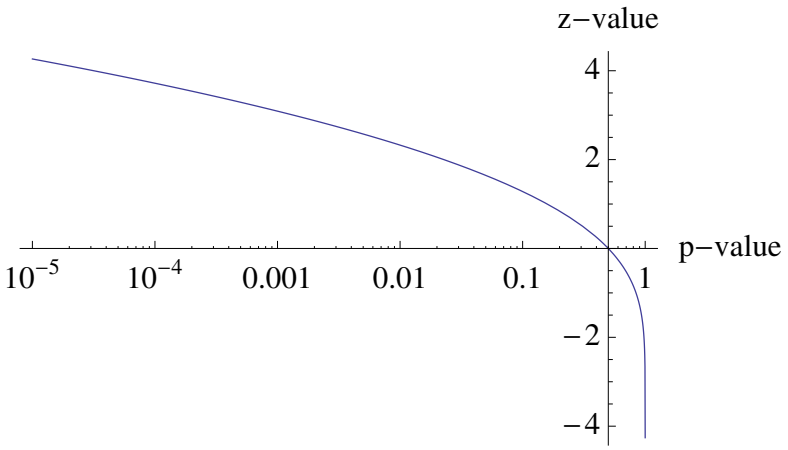

Figure 6.19: Relationship between p-value and z-value [264].

positive z-values correspond to p-values below 0.5, whereas negative z-values correspond to p-values > 0.5. A p-value of 2.87×10^{-7}, which is the 5σ deviation required in high energy physics for claiming a discovery, corresponds to a z-value of 5. On the other hand z-values below $\sim 2-3$ are usually interpreted as statistical fluctuations (although higher z-values could still result from statistical fluctuations, but with very low probability).

When plotting the event counts in each bin of a distribution, the number of events in each bin generally follows a Poisson distribution. Hence, if b events are expected, the probability of observing d events is given by

$$\mathrm{Poi}(d|b) = \frac{b^d}{d!} e^{-b} \,. \tag{6.26}$$

The p-value is then given by

$$p\text{-value} = \begin{cases} \sum_{n=d}^{\infty} \frac{b^n}{n!} e^{-b} & , d > b \\ \sum_{n=0}^{d} \frac{b^n}{n!} e^{-b} & , d \leq b \end{cases} . \tag{6.27}$$

Above calculation only considers the statistical fluctuations in each bin. However, the background and signal estimates may suffer from systematic uncertainties (e.g. due to uncertainties on the cross-sections for the MC luminosity reweighting or uncertainties on the data-driven techniques). In order to take this into account in the significance calculation, the Poisson model mentioned above is extended by uncertain parameters. One possible approach is to model the uncertainties with a Gaussian distribution (truncated at zero in order to avoid negative values), which is convoluted with the Poisson distribution. However, the resulting integral for the p-value can not be solved analytically. Therefore, one would need to generate pseudo-experiments in order to derive the probability density function (such an approach is followed for the limit determination, explained in the following section). This is very time-consuming and hence technically too expensive, if performed for each bin in a histogram.
Another approach, which was chosen in reference [264], is to model the uncertainty on the Poisson parameter b with the *Gamma* density (not to be confused with the *Gamma* function). This density can be written as [264]

$$\mathrm{Ga}(x|A,B) = \frac{B^A}{\Gamma(A)} x^{A-1} e^{-Bx}, \tag{6.28}$$

where Γ denotes the *Gamma* function and the *Gamma* density parameters A and B are connected to the expectation value b and variance $V = S^2$ (which represents the square of the systematic uncertainty) by

$$b = \frac{A}{B} \;\&\; V = \frac{A}{B^2} . \tag{6.29}$$

Hence, these parameters are given by

$$A = \frac{b^2}{S^2} \;\&\; B = \frac{b}{S^2} . \tag{6.30}$$

The advantage of using the *Gamma* density (instead of the Gaussian) is, that the resulting integral of the convolution of Poisson distribution and *Gamma* density can be solved analytically and hence results in a faster calculation of the p-values in each bin of a histogram.
For small expectations b, the *Gamma* density is asymmetric. On the other hand, it becomes a symmetric Gaussian for high b and small variances V, because in this case the *Gamma* density is equivalent to the probability density of the χ^2 distribution. This

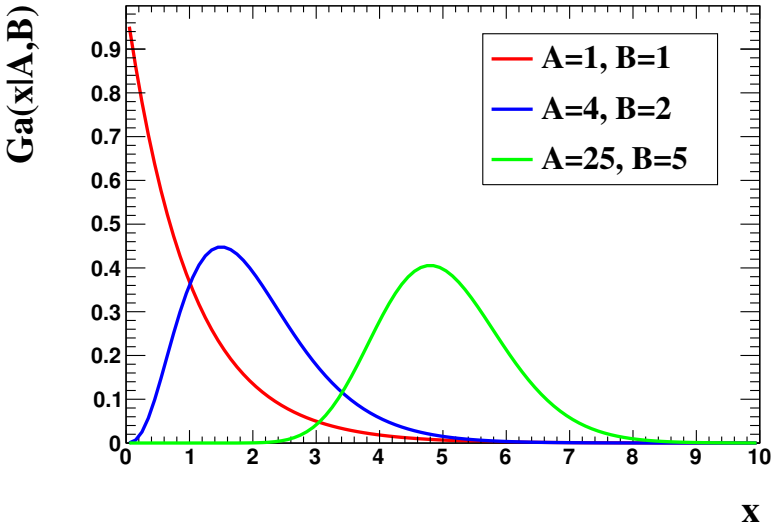

Figure 6.20: Distribution of the Gamma density as defined in Equation (6.28). The distribution is plotted for three scenarios: $A = B = 1$ (red), $(A, B) = (4, 2)$ (blue) and $(A, B) = (25, 5)$ (green). When setting $V = S^2 = 1$, then A and B only depend on the expectation value b: $(A, B) = (b^2, b)$.

can be also seen in Figure 6.20, where different scenarios for A and B were assumed. As mentioned above, the probability of observing n events can be evaluated when constructing the convolution of the Poisson and Gamma densities [264]

$$P(n|A,B) = \int_0^\infty \mathrm{Poi}(n|Y)\mathrm{Ga}(Y|A,B)\,\mathrm{d}Y = \frac{B^A}{\Gamma(A)}\frac{\Gamma(n+A)}{n!(1+B)^{n+A}}, \tag{6.31}$$

whereby the Poisson-Gamma mixture of Equation (6.31) is also known as *negative binomial*. Finally, the p-value can be obtained by summing over above probability density, as it was done over the Poisson distribution before:

$$p\text{-value} = \begin{cases} \sum_{n=d}^{\infty} P(d|A,B) & , d > b \\ \sum_{n=0}^{d} P(d|A,B) & , d \leq b \end{cases}. \tag{6.32}$$

As it was shown before, significant excesses or deficits will result in small p-values below 0.5, which correspond to positive z-values in each case. When plotting the z-value as significance for a bin which contains an excess of data, this will give the correct impression of an excess. On the other hand, if a bin contains a significant deficit, plotting the corresponding positive z-value could give the impression of an excess in this bin. Hence, the idea is to assign a negative z-value for bins that contain a deficit. This

means that for bins with a p-value > 0.5 (which corresponds to negative z-values), the significance will not be shown. This is justified, because in these cases the bins agree with the expectation and hence such deviations are not of interest.

In all following plots, in which I will compare the data with the background and/or signal expectations, there will be a plot below presenting the significance as discussed above.

6.4.3 Limit determination with the CL_s method

In the following, I will describe the statistical method, that will be used in the case of an absent signal in the observed data, in order to derive limits and exclusion ranges on the signal parameters (for instance the signal cross-section). The method is called the CL_s method and is based on the references [265–269].

In general, the statistical method is based on the principle of frequentist hypothesis tests. In case of a signal search in particle physics, one defines two hypotheses: the null hypothesis H_0 assuming the absence of the signal and hence also called the background-only hypothesis, and the alternate hypothesis H_1 assuming the existence of the signal. The formal definition of the procedure for quantifying the degree of favouring or excluding these hypotheses by the experimental observation is then given as follows: first, the observables are identified that define the amount of observed and expected events. In this analysis it is simply the number of events satisfying specific event selection criteria. Secondly, a test statistic X is defined, which is a function of the observables and that ranks the experimental outcome from least to most signal-like. In this analysis, this is a ratio of Likelihoods, as described below. Finally, one needs to define rules for claiming an exclusion or discovery of the signal model under study. In particular, this means to define a value range for the test-statistic, in which one would accept or reject one of the hypotheses. In case of an exclusion, this range is commonly defined in such a way, that the decision can be made with a confidence level (CL) of 95%.

Under the assumption of H_0 or H_1, the test-statistic X has different probability density distributions, which represent the probability to measure a value within an interval ΔX around X, given one of the hypotheses. An example is depicted in Figure 6.21 (a), where an increasing X becomes more signal-like. At this stage, one has to define the 'critical region' w, for which one would accept H_1 if $X \in w$. However, it is possible that one accepts H_1, although H_0 is true. This is known as an error of the first kind, which appears with the probability

$$\alpha = \int_{X \in w} f_0(X)\,\mathrm{d}X, \tag{6.33}$$

where f_0 denotes the probability density function for X given that the H_0 hypothesis is true. The value α is also referred to as the significance level of the test.
On the other hand, it is also possible that one rejects H_1, although it is true. This is

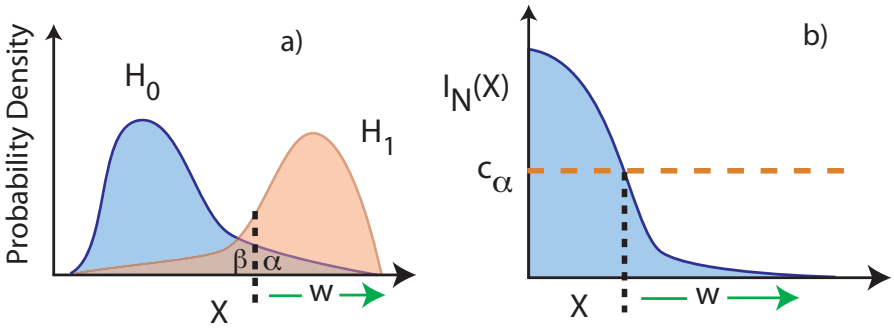

Figure 6.21: Figure (a) shows the probability densities for the test-statistic X under the two hypotheses H_0 and H_1 [267]. Figure (b) illustrates the use of the Neyman-Pearson Theorem, where the ratio I_N of the two probability densities is presented as a function of X [267].

referred to as an error of the second kind and appears with the probability

$$\beta = \int_{X \notin w} f_1(X)\,\mathrm{d}X, \tag{6.34}$$

where f_1 denotes the probability density function for X given that the H_1 hypothesis is true. The value of $1-\beta$ is also referred to as the power of the test.
In conclusion, α represents the ability to avoid errors of the first kind, whereas $1-\beta$ denotes the ability to avoid errors of the second kind. Hence, the optimal definition of the region w is given when α and β are minimal.

An optimal region can be found using the Neyman-Pearson Theorem [270]. For a given significance level α, the region w is defined such that β becomes minimal. This is constructed using the ratio

$$I_N(X) = \frac{f_0(X)}{f_1(X)}, \tag{6.35}$$

which is depicted in Figure 6.21 (b). The optimal region w is found over which I_N is maximal. Hence, one needs to find the value c_α with $w = \{X | I_N < c_\alpha\}$, such that the probability of observing $X \in w$ is equal to the significance α.
As a result, the optimal test statistic for the discrimination between signal-like and background-like events is found to be the ratio of the corresponding Likelihoods. If there are n independent channels (this can be different bins of a histogram or results of different analyses), the test statistic is then given by the product of the Likelihood ratios of each channel i:

$$X = \prod_{i=1}^{n} \frac{\mathcal{L}_0(X_i)}{\mathcal{L}_1(X_i)}, \tag{6.36}$$

where $\mathcal{L}_{0/1}(X_i)$ denotes the Likelihood assuming the H_0 or H_1 hypothesis, respectively.

In order to simplify the calculations, one commonly uses the Log-Likelihood ratio LLR, defined by

$$LLR = -2 \ln X \ . \tag{6.37}$$

Therefore, the test statistic will be described by the logarithmic sum of the different Likelihood ratios:

$$LLR = -2 \sum_{i=1}^{n} \left[\ln \mathcal{L}_0(X_i) - \ln \mathcal{L}_1(X_i) \right] \ . \tag{6.38}$$

Due to the negative sign in this definition, lower LLR values will refer to more signal-like observations. Assuming that the expected number of signal (s_i) and background (b_i) events are Poisson distributed, the LLR is then given as follows

$$LLR = -2 \sum_{i=1}^{n} \left[\ln \left(\frac{e^{-(s_i+b_i)}(s_i+b_i)^{d_i}}{d_i!} \right) - \ln \left(\frac{e^{-b_i} b_i^{d_i}}{d_i!} \right) \right], \tag{6.39}$$

where d_i denotes the number of observed events in channel i.
An example of the distributions of such LLR values under the 'signal+background' and 'background-only' hypotheses is depicted in Figure 6.22a[6], where the two distributions are well separated. Therefore, such an analysis would have a high sensitivity to the signal. This example is taken from the results of this thesis in Section 6.9.1.

After performing the measurement, one obtains an observed value LLR_{obs} for the test statistic. In the example of Figure 6.22a, a hypothetical value of $LLR_{\text{obs}} = -50.0$ is assumed. With the knowledge of the probability densities of the two hypotheses H_0 and H_1, one can then calculate the p-values for the two hypotheses, which quantify the degree of confidence that the underlying hypothesis is true. In case of the signal hypothesis H_1, the p-value is referred to as CL_{s+b} (here $s+b$ denotes the 'signal+background' H_1 hypothesis) and is given by the probability to measure an LLR value that is less signal-like than the observed one. In the current example of decreasing LLR being more signal-like, it would be given by the integral

$$CL_{s+b} = \int_{LLR_{\text{obs}}}^{\infty} f_1(LLR) \, \mathrm{d}LLR \ . \tag{6.40}$$

Therefore, a small value of CL_{s+b} would represent a poor compatibility with the H_1 hypothesis.
On the other hand, the p-value for the H_0 hypothesis, denoted as $1 - CL_b$, is calculated as the probability to measure an LLR value, which is more signal-like than the observed

[6] These distributions present the outcome of the different pseudo-experiments, which will be explained in the following. Dividing them by the number of generated pseudo-experiments (here 100000), N_{PE}, yields in the probability densities discussed in the text.

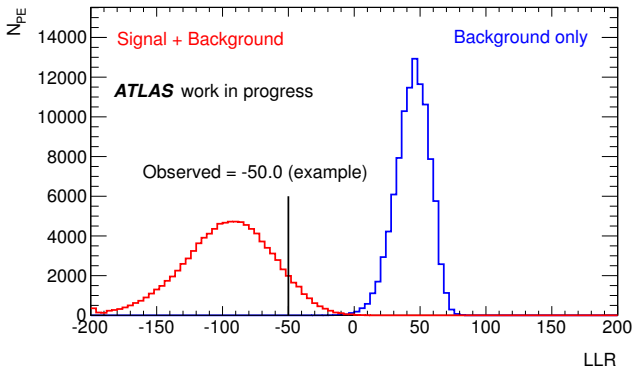

(a) High signal sensitivity

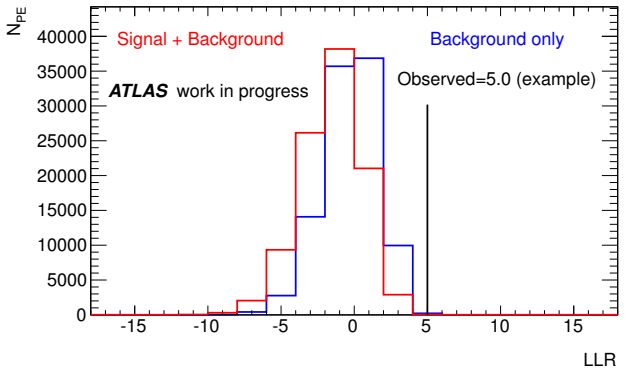

(b) Low signal sensitivity

Figure 6.22: Presented are two distributions of the Log-Likelihood ratios (LLR) with high (a) and low (b) sensitivity for the signal. These distributions were taken as an example from the results presented in Section 6.9.1.
The red curve represents the distribution under the 'signal+background' hypothesis, whereas the blue curve denotes the 'background-only' hypothesis. Several pseudo-experiments have been generated for producing these distributions and hence the y-axis denotes the number of pseudo-experiments as a function of the obtained LLR values. Dividing by the number of generated pseudo-experiments (here 100000), N_{PE}, would give the probability density distributions.
In both examples an additional (hypothetically) observed LLR value is shown, in order to illustrate the idea of the CL_s method.

one. In this example it is given by

$$1 - CL_b = \int_{-\infty}^{LLR_{\text{obs}}} f_0(LLR)\,\mathrm{d}LLR\ . \tag{6.41}$$

In the search for a particular signal model, using standard frequentist statistics one would claim an exclusion with 95% CL, if the obtained CL_{s+b} value is below $1 - 0.95 = 0.05$, whereas one accepts the signal hypothesis for values in the range $[0.05, 1.0]$. This means, that one has constructed a confidence interval, that covers the true value with 95% probability.

However, the standard frequentist technique can be problematic in the case that the analysis has only a low sensitivity to the signal model, as it is depicted in the example of Figure 6.22b. In this case, the two probability density functions for H_0 and H_1 mostly overlap. Although one can not distinguish whether one observed a LLR value compatible with the H_0 or H_1 hypothesis, the CL_{s+b} test could reject the signal hypothesis without having any sensitivity to it. For instance, consider the example of Figure 6.22b with a hypothetically observed value of $LLR_{\text{obs}} = 5.0$. This would be the case if there was a sufficient downward fluctuation of the data compared to the background expectation. The hypothesis test based on CL_{s+b} could yield in the result that the signal hypothesis is rejected, although one should clearly take the 'background-only' hypothesis into question as well. In the case of the absence of the signal, one often wants to derive limits on some parameters of the signal model (for instance the cross section). If there is a low signal sensitivity, one therefore would like that the probability for the exclusion becomes 0. This is achieved by the CL_s method, which is based on the ratio

$$CL_s = \frac{CL_{s+b}}{CL_b}, \tag{6.42}$$

where the value of CL_{s+b} is effectively penalised by the denominator CL_b. In case of H_0 and H_1 being well separated and having a signal-like observation, CL_b will be close to one (as in Figure 6.22a) and hence $CL_s \simeq CL_{s+b}$. On the other hand, if there is low sensitivity to the signal, the two probability densities overlap. When assuming that there is a less signal-like observation, then it is clear that this will be also less background-like. Therefore, the denominator CL_b becomes small, which results in an increasing CL_s value and hence prevents from excluding the signal model.
Similar to the CL_{s+b} (standard frequentist) method, one would reject the signal hypothesis, if one finds $CL_s < 0.05$. Since $CL_b < 1$, the CL_s value is always greater than CL_{s+b}, which results in an over-coverage of the desired confidence interval. Thus the CL_s method is also referred to as 'modified frequentist', but only in the region of low sensitivity for the signal.

The calculation of the CL_s value for a particular measurement relies on the knowledge of the probability density distributions for the 'signal+background' and the 'background-only' hypothesis. Assuming that the signal and background expectations follow Poisson distributions, this could be simply calculated. However, the estimation of the signal and background expectations relies on specific modellings, which are only known within

particular systematic uncertainties. Therefore, it is usually not possible to derive the underlying probability density functions analytically. The approach used in this analysis for computing the CL_s values is based on the generation of so-called pseudo-experiments (PE's) and will be explained in the following.

The presented method will allow to derive exclusion intervals on the signal cross-sections. The lower border of this interval will be referred to as 'upper limit' and denotes the cross-section above which the signal is excluded. The procedure for deriving this limit is based on the observed data events, also referred to as 'observed limit', is as follows:

1. Using the observed data events d_i in each analysis channel i, and using the signal and background expectations s_i and b_i (their determination is based on MC and data-driven techniques and will be explained later in this chapter), the observed value of the test-statistic LLR_{obs} is calculated.

2. Then the probability density functions f_1 and f_0 for the signal+background and background-only hypotheses are derived using separate pseudo-experiments. This means that pseudo events d_i' are randomly generated, based on the expectations for signal+background $s_i + b_i$ or for background-only b_i. The underlying probability distribution for the pseudo-data generation results from the product of a Poisson distribution with mean $s_i + b_i$ (or only b_i in the determination of f_0) and several Gaussian distributions representing the different systematic uncertainties on the signal and background estimates. These Gaussians have a mean of one and a width representing the size of the uncertainty. Furthermore, the Gaussians are truncated at zero in order to avoid results with negative events.
   For each pseudo-experiment outcome, the resulting value for d_i' is used to calculate the value of the test-statistic LLR_{PSE}.

3. In total, there are $n(s + b)$ and $n(b)$ pseudo-experiments generated for the signal+background and background-only hypothesis, respectively. If $n(s{+}b|LLR_{\text{PSE}} > LLR_{\text{obs}})$ and $n(b|LLR_{\text{PSE}} > LLR_{\text{obs}})$ denote the number of pseudo-events in which the test-statistic LLR_{PSE} was larger than the observed one LLR_{obs} (hence being less signal-like), then the values for CL_{s+b} and CL_b are approximately given by

$$CL_{s+b} = \frac{n(s + b|LLR_{\text{PSE}} > LLR_{\text{obs}})}{n(s + b)} \tag{6.43}$$

$$CL_b = \frac{n(b|LLR_{\text{PSE}} > LLR_{\text{obs}})}{n(b)} \ . \tag{6.44}$$

   As previously mentioned, the CL_s value is then calculated by the ratio of CL_{s+b} and CL_b and the model is considered as excluded if $CL_s < 0.05$.

4. In addition, one also would like to define a confidence interval on some parameter of the signal model. This is performed iteratively by varying the signal expectation s_i until one finds the desired CL_s value of 0.05. This defines the upper limit on the signal expectation s_i^{up} and one can calculate the signal scale factor $SF = s_i^{\text{up}}/s_i$, which needs to be multiplied by the theoretical cross-section prediction in order

to derive the upper cross-section limit with 95% CL. Hence a scale factor within $[0, 1]$ denotes the range where the signal can be excluded.

In addition to the observed limit, one also determines the limit, which one would have expected in case that the signal does not exist. This is supposed to validate the calculation of the observed limit. For instance, the analyser could have underestimated certain systematic uncertainties, which would result in too strong limits. The calculation of the expected limit is similar to the one for the observed one and is as follows:

1. Pseudo-experiments are generated for the background-only hypothesis taking into account all systematic uncertainties. The procedure is similar to the one used to derive the LLR probability density distribution for the background-only hypothesis in the calculation of the observed limit.

2. Each PE outcome gives a pseudo-data value of d_i^p. This value is used as 'observed data' and the procedure for the observed limit as explained above is repeated.

3. The outcome is a signal scale factor SF for each of the background-only pseudo-experiments. From the distribution of these scale factors, one can derive the median expected limit, as well as the $\pm 1\sigma/\pm 2\sigma$ intervals, which are defined as the regions in which 68%/95% of the scale factors lie.

In the case that there was no significant signal contribution to the observed events, the observed limit will lie in 95% of the cases within the expected $\pm 2\sigma$ interval. If, for instance, there was a significant data excess above the background expectation, this will result in the observed limit being well above the expected $+2\sigma$ limit.

The described procedure is implemented in the `mclimit` program [269]. In my analysis I used the `mclimitCode` framework [271], which is based on `mclimit` and provides a user-friendly interface for providing the observed data, the signal and background estimates and the different systematic uncertainties to the program.

6.5 Object identification

This section summarises the object selection criteria used in the analysis, which where already discussed in detail in Chapter 5, but a summary of all cuts, corrections and scale factors will be given here.

The electron selection was discussed in Section 5.3 and is summarised in Table 6.6. Electrons reconstructed from the standard cluster-based algorithm need to have passed the `tight++` quality criteria and are required to have $p_T \geq 25\,\text{GeV}$ and $|\eta| < 2.47$, whereas electrons within the crack-region are rejected. Furthermore, electrons need to have a 'good' quality and need to have passed the energy and momentum isolation criteria corresponding to an isolation efficiency of 90% (measured in $Z \to e^+e^-$ events). Finally, the longitudinal impact parameter $|z_0|$ must be $\leq 2\,\text{mm}$.
When analysing data, the electron energy scale is corrected, whereas a resolution correction is applied when analysing MC samples. In MC, events are reweighted using the scale factors on the identification, reconstruction, isolation and trigger efficiencies.

Selection	Description	Cut
Algorithm	Standard cluster-based	—
ID menu	Identification menu	`tight++`
E_T	Transverse energy	$\geq 25\,\text{GeV}$
$\lvert\eta\rvert$	Pseudorapidity	≤ 2.47 excl. $[1.37, 1.52]$
$\lvert z_0\rvert$	Longitudinal impact parameter	$\leq 2\,\text{mm}$
OQ	Object quality	Good
E_T^{Cone20}, P_T^{Cone30}	Isolation cuts for achieving specific efficiency	90%
Trigger	Trigger items (EF)	`EF_e24vhi_medium1` or `EF_e60_medium1`
Corrections		**Data/MC**
Energy scale		Data
Energy resolution		MC
Scale factors		**Data/MC**
Identification		MC
Reconstruction		MC
Isolation		MC
Trigger		MC

Table 6.6: Summary of electron selection criteria, applied corrections and scale factors. For the corrections and scale factors it is shown whether this applies for data and/or MC. Further descriptions on the listed entries can be found in Section 5.3.

The muon selection was presented in Section 5.4 and is summarised in Table 6.7. Muons are reconstructed using combined tracks coming from the inner detector and the muon spectrometer and need to have passed the `tight` quality criteria. They need to have $p_T \geq 25\,\text{GeV}$ and $|\eta| < 2.5$ and need to fulfil several track quality criteria, which are summarised in Table 6.7 as well. Furthermore, muons need to fulfil the p_T dependent mini-isolation with a value of ≥ 0.5 and have a longitudinal impact parameter $|z_0|$ of $\leq 2\,\text{mm}$.
When analysing MC samples, the muon energy scale and resolution are corrected. Furthermore, scale factors are applied as event weights, to account for the identification, reconstruction, isolation and trigger efficiency differences between data and MC.

The jet selection criteria were explained in Section 5.5 and are summarised in Table 6.8. Jets are reconstructed using the anti-k_T algorithm with cone size $R = 0.4$. They need to have a transverse momentum of $p_T \geq 25\,\text{GeV}$ and a pseudorapidity of $|\eta| < 2.5$. Furthermore, they are required to have a jet vertex fraction (JVF) of ≥ 0.5. In case of b-tagged jets, a `MV1` weight of ≥ 0.772 is required.
Corrections to the jet energy scale (JES) are applied when analysing data and MC. The corrections for the jet energy resolution and jet reconstruction efficiency are only considered as systematic uncertainties for the MC samples (see Section 6.6.3). Scale

Selection	Description	Cut
Algorithm	Combined	—
Quality	Muon quality	`tight`
P_T	Transverse momentum	$\geq 25\,\text{GeV}$
$\lvert\eta\rvert$	Pseudorapidity	≤ 2.5
$\lvert z_0\rvert$	Longitudinal impact parameter	$\leq 2\,\text{mm}$
Track quality	b-layer hits (if expected)	≥ 1
	$N^{\text{Pix}}_{\text{Hits}} + N^{\text{Pix}}_{\text{CDS}}$	≥ 1
	$N^{\text{SCT}}_{\text{Hits}} + N^{\text{SCT}}_{\text{CDS}}$	≥ 5
	$N^{\text{Pix}}_{\text{Holes}} + N^{\text{SCT}}_{\text{Holes}}$	< 3
	$n = N^{\text{TRT}}_{\text{Hits}} + N^{\text{TRT}}_{\text{Outliers}}$	
	· if $0.1 < \lvert\eta\rvert < 1.9$:	
	n	≥ 6
	$N^{\text{TRT}}_{\text{Outliers}}/n$	< 0.9
	· if $\lvert\eta\rvert \leq 0.1$ or $\lvert\eta\rvert \geq 1.9$ and if $n \geq 6$:	
	$N^{\text{TRT}}_{\text{Outliers}}/n$	< 0.9
I_{mini}	Mini-isolation for muons	< 0.05
Trigger	Trigger items (EF)	`EF_mu24i_tight` or `EF_mu36_tight`
Corrections		**Data/MC**
Energy scale		MC
Energy resolution		MC
Scale factors		**Data/MC**
Identification		MC
Reconstruction		MC
Isolation		MC
Trigger		MC

Table 6.7: Summary of muon selection criteria, applied corrections and scale factors. For the corrections and scale factors it is shown whether this applies for data and/or MC. Further descriptions on the listed entries can be found in Section 5.4.

Selection	Description	Cut
Algorithm	Anti-k_T	$R = 0.4$
p_T	Transverse momentum	$\geq 25\,\text{GeV}$
$\lvert\eta\rvert$	Pseudorapidity	≤ 2.5
|JVF|	Jet vertex fraction	≥ 0.5
b-tag weight	`MV1` weight for 70% efficiency	≥ 0.772
Corrections		Data/MC
Energy scale		Data and MC
Energy resolution		MC (only syst.)
Reconstruction efficiency		MC (only syst.)
Scale factors		Data/MC
JVF		MC
b-tagging		MC

Table 6.8: Summary of jet selection criteria, applied corrections and scale factors. For the corrections and scale factors it is shown whether this applies for data and/or MC. Some corrections are only considered as systematic uncertainty (only syst.). Further descriptions on the listed entries can be found in Section 5.5.

factors are applied when analysing MC samples to account for the JVF and b-tagging efficiencies.

6.6 Determination of systematic uncertainties

In the following, I will present, how the various systematic uncertainties (shortly also known as 'systematics') considered in the analysis have been determined. The estimation of the systematic uncertainties has been performed twice: once for the optimisation of the event selection presented in Section 6.7.1 and once for the final interpretation of the observed results in Section 6.8.4. Therefore, the obtained values for the systematics will be presented in the corresponding sections.

In general, one needs to distinguish between different types of systematics in the analysis:

- Variations of the object energy scales and resolutions in MC: these systematics affect the four momenta of the objects (electrons, muons, jets and E_T^{miss}). The energies or momenta are varied within the measured uncertainties on the parameters for the different calibrations. This results in changes to the shapes of the kinematic distributions of the objects. Therefore, it is possible that more or less objects pass the object selection criteria, which can also give changes to the expected event yields from the background and signal MC samples.

- Variations of scale factors in MC: the reconstruction, identification and trigger scale factors are varied within the measured uncertainties. This results in changed

event weights for each event and hence affects the expected event yields from the background and signal MC samples.

- Luminosity and cross-section uncertainties: the luminosity and cross-sections are required for reweighting the MC yields and distributions to the collected data luminosity. Hence these uncertainties affect the normalisation of the distributions and the expected event yields. The MC cross-sections are a theoretical input to the analysis, and hence their uncertainties can be also denoted as 'theory uncertainties'.

- Parton distribution functions and parton shower: the chosen PDF and the modelling of the parton shower affect the generation of the MC samples. Different PDFs and parton shower tuning parameters will result in different kinematic distributions of the outgoing particles in the final state, as well as of the particles coming from the parton shower. The systematic uncertainties due to the PDF and parton shower were studied for the $b' \to tW$ MC signal sample only.

- Uncertainties on data-driven techniques: these uncertainties give a handle on the data-driven background estimations. In case of the charge mis-id we are varying the charge mis-id rates within several uncertainties, which results in changed charge mis-id weights for each event and hence affects the expected event yields. For the lepton fakes we measured the difference between data and background expectation in specific control regions and derive uncertainties from these differences. Hence, this affects the final expected yield of the lepton fakes estimate.

In the statistical interpretation of the results, I will only use the final expected and observed event yields (also referred to as 'cut&count'). Hence, all above mentioned variations will only affect the final expected yields. The uncertainties on the energy scales, energy resolutions and efficiency scale factors will be also referred to as 'object systematics', as they affect the different physical objects (electrons, muons, jets and missing transverse energy).

For the determination of the systematics, the obtained event yields after the systematic variation (n_Δ) are compared to the yields obtained from running the 'nominal' analysis (n). This means running the analysis with the default scale corrections, smearings and scale factors. Hence, the relative uncertainty is obtained from $(|n - n_\Delta|)/n$, whereby the direction of the uncertainty (up/down) depends on whether there was some variation in the upward or downward direction (for e.g. energy scale corrections or scale factors). The uncertainties related to electrons (Section 6.6.1), muons (Section 6.6.2), jets (Section 6.6.3) and the missing transverse energy (Section 6.6.4) are only studied on the different MC samples (signal and irreducible backgrounds). The uncertainties on the luminosity (Section 6.6.5) and production cross-sections (Section 6.6.6) affect the luminosity reweighting of the MC yields. Finally, there are uncertainties derived for the data-driven backgrounds (charge mis-id and lepton fakes), which are determined when analysing the data (Section 6.6.8).

6.6.1 Electron systematics

The considered systematics for the electrons affect the energy scale and resolution, and the scale factors for reconstruction, identification and the electron triggers. For the determination, I followed the recommendations of the *ATLAS ElectronGamma* performance group.

In the nominal analysis, the electron energy scale is corrected when analysing the real data sample. The estimation of the systematic uncertainty on the electron energy scale is only performed for the MC samples (signal and background). For each electron, an energy scale factor $(1 + \Delta\alpha)$ is determined, where $\Delta\alpha$ represents various systematic variations. These consist of

- Z scale: the electron energy scale is calibrated by comparing the invariant mass shape of $Z \to e^+e^-$ events in MC and data (see Section 5.3.2) and deriving a correction factor α. Hence the systematic variation $\Delta\alpha$ contains variations on α due to statistical uncertainties and also from the choice of the generator for the $Z \to e^+e^-$ MC.

- Furthermore, there are additional uncertainties considered, which reflect the scale uncertainty from the ECAL presampler and electron interactions with the detector material.

The parameter $\Delta\alpha$ was determined by the ATLAS *ElectronGamma* performance group as a function of the electron energy and pseudorapidity. The analysis has to run twice over all MC samples, with variations of $\Delta\alpha$ in the positive and negative direction, resulting in higher or lower electron energies. Hence, these variations are referred to as 'electron energy scale up' and 'electron energy scale down'. The total upper and lower uncertainty due to the electron energy scale will be determined by comparing the expected event yields after the up/down variation to the nominal yields and will be referred to as `EES`.

The electron energy in MC is smeared in the nominal analysis (see Section 5.3.2), in order that the energy resolution in MC matches the one in data. These smearing factors are obtained randomly from a Gaussian, whose width represents the measured energy resolution, which was performed by the ATLAS *ElectronGamma* group. The procedure for estimating the uncertainty on the resolution correction is to run the analysis twice, while varying the smearing factor in the upper/lower direction of the measured uncertainty. For this, the mean value of the Gaussian used to generate the random smearing factors is shifted by one standard deviation. The final uncertainty is obtained from the difference in the yields with varied smearing factors to the nominal yield. It will be referred to as `EER`.

For the systematics on the scale factors of electron reconstruction, identification and trigger efficiency, the scale factors are simply varied into the up or down direction within the 1σ uncertainties of the measurements, as shown in Figures 5.2, 5.4 and 5.8. The difference in the yields compared to the analysis using the nominal scale factors is then used as uncertainty. For the reconstruction and the identification efficiency scale factor, the up or down variation is performed simultaneously, and the corresponding uncertainty will be referred to as `ESFRecID`. The trigger efficiency scale factor uncertainty

determination is performed separately and the corresponding value will be denoted as `ESFTrig`.

6.6.2 Muon systematics

For the muons, I studied the systematic uncertainties coming from the muon energy scale and resolution, and also from the reconstruction and trigger scale factors. The procedures for their determination were recommended by the *ATLAS Muon Combined* performance group.

For the muon energy scale, there were no uncertainties on the parameter available, which was used for rescaling the muon momentum. Hence, the recommendation was to study the systematic on this parameter by running the analysis once with applying the energy scale correction (nominal) and once without applying this correction. The uncertainty is then obtained by symmetrising the difference in the expected yields Δn obtained for each case, which means to obtain a symmetric uncertainty by $\Delta n/2$. This uncertainty will be referred to as `MES`.
However, this procedure gives only an estimate for the effect of the muon energy scale correction. In future analyses, when the uncertainties on the parameter for the rescaling are available within ATLAS, a better approach will be applied. As for the electrons, the scaling parameter will be varied within the measured uncertainties.

In the nominal analysis, the muon momentum in MC is smeared, in order to match the resolution of the Z peak observed in data. For the smearing factor, there are the measurement uncertainties provided by the *ATLAS Muon Combined* performance group. The procedure for estimating the systematic uncertainty due to this factor, is to run the analysis twice by varying this smearing factor up and down according to the quoted uncertainty, and then compare the obtained event yields to the one from the nominal analysis. This is performed separately for the uncertainties coming from the momentum measurements of the inner detector and the muon spectrometer. The final uncertainty is obtained by taking the envelope of the largest yield deviations in the upper and lower direction, and then to symmetrise the uncertainty, as it is done for the scale systematic. This systematic will be denoted as `MER`.

The scale factors for the muon reconstruction efficiency and trigger efficiency, as shown in Figures 5.9 and 5.13, have been measured with ± 1 σ uncertainties. The uncertainty due to these scale factors is studied by varying the scale factors within the 1σ range into the upward and downward direction. The isolation efficiency scale factors are close to 1 within 2%, as it was shown in Figure 5.12. Hence, an additional uncertainty of 2% per muon is applied when varying the muon reconstruction efficiency scale factors. The final uncertainty is obtained by taking the yield differences for the upward and downward deviation with respect to the nominal yields. These uncertainties will be referred to as `MuSFRecId` and `MuSFTrig` for the reconstruction and trigger scale factors, respectively.

6.6.3 Jet systematics

In case of the jets, I studied the systematic uncertainties on the jet energy scale and resolution, the jet reconstruction efficiency, the jet vertex fraction (JVF) scale factor and the scale factors for the b-jet identification (b-tagging SF). For their determination, I followed the recommendations of the *ATLAS Jet and EtMiss* performance group.

As mentioned in Section 5.5.2, there are several sources of uncertainties on the jet energy scale (JES). These include uncertainties from the *in-situ* methods applied for obtaining the jet energy scale parameters, from close-by jets and the jet flavor composition. The total uncertainty on the JES was presented in Figure 5.16 and is used for varying the JES correction into the upward and downward direction of the uncertainty. By calculating the difference in the yields to the nominal case, one can obtain the uncertainty due to the JES in the analysis, which will be referred to as `JES`.

In the nominal analysis, there is no correction applied for the jet-energy resolution in the MC (JER), because the measurements of the JER in data and MC showed a good agreement (see Section 5.5.2). However, for studying the systematic from the JER, a smearing factor is applied to the momentum of each jet in the MC. This smearing factor is obtained from the quadratic difference between the truth resolution plus the measured resolution uncertainty ($\sigma_{\text{truth}} + \Delta\sigma$), and the truth resolution: $\text{SmearingFactor} = \sqrt{(\sigma_{\text{truth}} + \Delta\sigma)^2 - \sigma_{\text{truth}}^2}$. The measured uncertainty is obtained from the errors in the Gaussian fits applied in the bisector technique (see Section 5.5.2). Then the factor to be applied to the jet momentum is obtained randomly from a Gaussian with mean 1 and a width equal to the smearing factor. The difference between the yield obtained with the jet smearing applied and the nominal yield is symmetrised and taken as systematic uncertainty, which will be denoted as `JER`.

The measurements of the jet reconstruction efficiencies in data and MC revealed a good agreement (see Section 5.5.1), especially for jets with $p_T \geq 30\,\text{GeV}$. For jets with $p_T < 30\,\text{GeV}$, the small differences between the data and MC efficiencies are considered for the systematic uncertainty coming from the jet reconstruction efficiency. This is performed by randomly rejecting jets in the analysis, depending on the measured efficiency for the particular jet p_T. For each jet, a uniform random number between 0 and 1 is generated. If this number is larger than the reconstruction efficiency[7] at the particular jet p_T, the jet gets rejected from the analysis. By comparing the final event yield when doing this jet rejection to the nominal yield and symmetrising the difference, the systematic uncertainty due to the jet reconstruction efficiency is obtained. This will be denoted as `JRE`.

In the nominal analysis, scale factors are applied as event weights to account for the differences in the efficiencies between data and MC for the hard scatter jet selection and pile-up jet rejection, due to the cut on the jet vertex fraction (JVF). The systematic coming from these scale factors is studied by varying the scale factors in the upward and downward direction within the measured uncertainties (see Figure 5.20). The difference

[7] Being precise there are only two jet p_T bins considered for the jet reconstruction efficiency. For jets with $15\,\text{GeV} \geq p_T < 20\,\text{GeV}$ (such jets are not selected in the analysis) the efficiency is 97.4%, while for jets with $20\,\text{GeV} \geq p_T < 30\,\text{GeV}$ it is 99.77%.

in the yields between varied JVF scale factors and nominal scale factors is used as systematic uncertainty, which will be referred to as `JVFSF`.

As discussed in Section 5.5.4, scale factors were derived to account for the differences in the b-tagging efficiencies between data and MC. Furthermore, there are scale factors applied to correct for the differences in the mistag rates and c-jet selection efficiencies. For studying the systematic uncertainty, these scale factors are varied separately into the upward and downward direction within the measured uncertainties. The differences between the yields with varied scale factors and the nominal yields are taken as systematic uncertainty. For the three scale factors, the systematics will be denoted as `BTagSFb`, `BTagSFc` and `BTagSFmistag` for the b-jet efficiencies, c-jet efficiencies and mistag rates, respectively.

6.6.4 Systematics on missing transverse energy

The systematic effects of electrons, muons and jets to the missing transverse energy are directly considered when varying the energy scales and resolutions of these objects. This is performed by re-calculating the E_T^{miss}, taking into account the changed energies and momenta of the particular objects. For instance, when varying the JES this will also influence the E_T^{miss} value of each event.

The E_T^{miss} calculation contains a *SoftJet* term, covering all low-p_T jets with $10\,\text{GeV} < p_T < 20\,\text{GeV}$ (see Section 5.7.1). The scale and resolution uncertainty on this term is studied similar to the procedure for the JES and JER. Hence, the E_T^{miss} is calculated with soft jets that have been varied in the upward and downward direction according to their scale and resolution uncertainties. This is performed separately for the scale and resolution uncertainty. Then the differences between the varied yields and the nominal yields are obtained and added quadratically, yielding in the total uncertainty on the *SoftJet* E_T^{miss}, which will be referred to as `MET`. This procedure was recommended by the *ATLAS Jet and EtMiss* performance group.

6.6.5 Luminosity

The luminosity measurement at ATLAS was described in Section 3.2.7. The uncertainty on the measured integrated luminosity is $\pm 3.6\%$. It is derived, following the same methodology as detailed in reference [142], from a preliminary calibration of the luminosity scale derived from beam-separation scans performed in April 2012.

As the luminosity information is only used for reweighting the MC yields and distributions to the data luminosity, this uncertainty only affects the MC normalisation.

6.6.6 Production cross-sections

The cross sections used for the normalisation of the MC b' signal samples were derived using the NNLO cross-section calculator program `HATHOR`. For the various irreducible backgrounds, modelled with LO MC simulations, the cross sections were taken from the generator, but applying NLO k-factors if available.

The determination of the uncertainties on the HATHOR heavy-quark pair production cross-sections was described in Section 2.2.5, where the scale (with independent variations of μ_r and μ_f) and α_s+PDF uncertainties have been considered. The uncertainties on the cross-sections were presented in Figure 2.18 and are summarised in Table 6.9. It

Mass [GeV]	σ [pb]	$\Delta\sigma_{\text{Scale}}$ [pb]	$\Delta\sigma_{\text{PDF}+\alpha_s}$ [pb]	$\Delta\sigma_{\text{Total}}$ [pb]	$\delta\sigma_{\text{Total}}$ [%]
400	2.30	$^{+0.07}_{-0.13}$	$^{+0.27}_{-0.22}$	$^{+0.28}_{-0.26}$	$+12.1/-11.2$
450	1.11	$^{+0.03}_{-0.06}$	$^{+0.14}_{-0.11}$	$^{+0.14}_{-0.12}$	$+12.6/-11.2$
500	0.570	$^{+0.018}_{-0.033}$	$^{+0.072}_{-0.055}$	$^{+0.075}_{-0.064}$	$+13.1/-11.2$
550	0.306	$^{+0.010}_{-0.018}$	$^{+0.040}_{-0.029}$	$^{+0.041}_{-0.034}$	$+13.6/-11.1$
600	0.170	$^{+0.006}_{-0.009}$	$^{+0.024}_{-0.016}$	$^{+0.024}_{-0.019}$	$+14.0/-11.1$
650	0.0971	$^{+0.0036}_{-0.0057}$	$^{+0.0136}_{-0.0094}$	$^{+0.0141}_{-0.0110}$	$+14.5/-11.3$
700	0.0570	$^{+0.0022}_{-0.0034}$	$^{+0.0083}_{-0.0056}$	$^{+0.0086}_{-0.0065}$	$+15.0/-11.5$
750	0.0341	$^{+0.0014}_{-0.0021}$	$^{+0.0051}_{-0.0034}$	$^{+0.0053}_{-0.0040}$	$+15.5/-11.7$
800	0.0208	$^{+0.0008}_{-0.0013}$	$^{+0.0033}_{-0.0022}$	$^{+0.0034}_{-0.0025}$	$+16.4/-12.0$
850	0.0129	$^{+0.0005}_{-0.0008}$	$^{+0.0022}_{-0.0014}$	$^{+0.0022}_{-0.0016}$	$+17.3/-12.4$
900	0.00807	$^{+0.00035}_{-0.00050}$	$^{+0.00143}_{-0.00090}$	$^{+0.00148}_{-0.00103}$	$+18.3/-12.8$
950	0.00512	$^{+0.00023}_{-0.00032}$	$^{+0.00097}_{-0.00060}$	$^{+0.00099}_{-0.00068}$	$+19.4/-13.3$
1000	0.00327	$^{+0.00015}_{-0.00021}$	$^{+0.00066}_{-0.00040}$	$^{+0.00068}_{-0.00045}$	$+20.6/-13.9$

Table 6.9: Heavy quark pair production approx. NNLO cross-sections. For each mass point, the cross-section σ is presented together with the derived scale $\Delta\sigma_{\text{Scale}}$ and α_s+PDF $\Delta\sigma_{\text{PDF}+\alpha_s}$ uncertainties, using the procedure described in Section 2.2.5. $\Delta\sigma_{\text{Total}}$ denotes the total cross-section uncertainty, which is the quadratic sum of scale and α_s+PDF uncertainty, whereas $\delta\sigma_{\text{Total}}$ represents the relative total cross-section uncertainty in percent derived from $\delta\sigma_{\text{Total}} = \Delta\sigma_{\text{Total}}/\sigma$.

can be seen, that the total uncertainties on the signal cross-sections vary, depending on $m_{b'}$, between 11% and 20%.

For the irreducible background processes $t\bar{t} + WW$ and $W^{\pm}W^{\pm}$+jj, which are estimated from MC, we (Berlin) derived the cross-section uncertainties by running the generator MadGraph twice, each time with varied values for the renormalisation and factorisation scale. When running the generator for the cross-section uncertainty determination, we multiply these scales by a factor of 2 (1/2), in order to obtain the variation in the upper (lower) direction. The difference to the cross-section obtained for the default sample is then used as uncertainty. This is a common practise for estimating cross-section uncertainties based on the MC generators. In our case, we obtained relative uncertainties of $+36\%/-26\%$ and $+25\%/-25\%$ for the processes $t\bar{t} + WW$ and

$W^{\pm}W^{\pm}$+jj[8], respectively.

The uncertainties on the cross-sections of the $t\bar{t}+W$(+j/+jj) and $t\bar{t}+Z$(+j/+jj) background processes have been determined in references [254] and [256]. In the first reference, they determined the scale uncertainty for $t\bar{t}+W$ by varying the factorisation and normalisation scale in the range $[m_t/4, 4m_t]$ (here m_t denotes the top-quark mass) with nominal scale m_t. Furthermore, they studied the uncertainty due to the PDF and α_s using the same method, which I described in Section 2.2.5, where I calculated the uncertainties on the signal cross-sections using `HATHOR`. In the second reference, they only studied the scale uncertainties, but for $t\bar{t}+W$ and $t\bar{t}+Z$, by varying the scales in the region $[1/2\cdot(m_t+m_V/2), 2\cdot(m_t+m_V/2)]$ ($V=W,Z$) with nominal scale $m_t+m_V/2$. No additional PDF and α_s uncertainty was determined.
The scale uncertainties in both references lie in the range of $[9, 21]$%, whereas the PDF+α_s uncertainties from reference [254] yield to $[6, 8]$%. The final quoted uncertainties in reference [254] for $t\bar{t}+W$ result from larger (conservative) scale variations and also contain a consistent PDF variation. Hence, the envelope of these results is added in quadrature, which gives the total uncertainty of ± 22% to be used for both $t\bar{t}+W$ and $t\bar{t}+Z$. However, since there is another uncertain parameter, the NLO k-factor, we chose to apply a conservative value for the cross-section uncertainty on $t\bar{t}+W$ and $t\bar{t}+Z$ of ± 30%.

For the diboson backgrounds WZ/ZZ+jets we assumed an overall relative normalisation uncertainty of $\Delta\sigma_0/\sigma_0 = 5\%$ on the diboson production cross-section without additional jets (σ_0), as it is suggested in reference [272] for both, WZ and ZZ production. Furthermore, the ratio of the production cross-sections of $R = W$+$(n$+1)jets/W+(n)jets was determined in reference [273] to be constant for all n within $n = [0, 4]$, with relative uncertainties of $\Delta R/R = 24\%$. Hence, it was recommended by the *ATLAS Top Physics* group to apply an additional uncertainty of 24% per each additional jet that is required in the analysis, and then add these uncertainties in quadrature. The usage of the R ratio is justified, because the gluon radiation in single W production appears at comparable scales as for diboson production. Since we select events with at least two jets (see following Section 6.7), this procedure gives a total relative uncertainty on the diboson production cross-section with two additonal jets (σ_2) of

$$\frac{\Delta\sigma_2}{\sigma_2} = \pm\sqrt{\left(\frac{\Delta\sigma_0}{\sigma_0}\right)^2 + 2\left(\frac{\Delta R}{R}\right)^2} = \pm\sqrt{0.05^2 + 2\cdot 0.24^2} = \pm 34\% \ . \tag{6.45}$$

However, above procedure only gives a rough estimate of the diboson cross-section uncertainty when considering additional partons. A better calculation would result from the ansatz, that the diboson production cross-section with e.g. two additional jets can be written as

$$\sigma_2 = \sigma_1 \cdot R = \sigma_0 \cdot R^2, \tag{6.46}$$

[8] Actually we obtained relative uncertainties of $+23\%/-17\%$. However, in the estimation of the uncertainty we used a different PDF (CTEQ6L1 instead of MSTW2008) than used for the sample generation. Hence we chose to apply a conservative uncertainty of $\pm 25\%$.

where σ_n denotes the diboson production cross-section with n additional jets. When using simple error propagation, the relative uncertainty on σ_2 would be then given by

$$\frac{\Delta\sigma_2}{\sigma_2} = \pm\sqrt{\left(\frac{\Delta\sigma_0}{\sigma_0}\right)^2 + 4\left(\frac{\Delta R}{R}\right)^2} = \pm\sqrt{0.05^2 + 4\cdot 0.24^2} = \pm 48\%, \tag{6.47}$$

resulting in a higher uncertainty as for the recommended approach used in the analysis. When running the analysis, this uncertainty would be needed to be determined for each event, depending on the jet multiplicity. However, it will be seen later, that the diboson background only has a small contribution to the final event selection used for the signal extraction (see Section 6.7) compared to the other backgrounds. Hence, the effect of this uncertainty difference to the final results of this analysis can be neglected.

All cross-section uncertainties for the irreducible backgrounds estimated from MC are summarised in Table 6.10.

Process	σ [pb]	$\Delta\sigma/\sigma$ [%]
$t\bar{t}+WW$	0.0022	$+38.0/-26.0$
$t\bar{t}+W$	0.123	$+30.0/-30.0$
$t\bar{t}+W$+j	0.0625	$+30.0/-30.0$
$t\bar{t}+W$+jj	0.0484	$+30.0/-30.0$
$t\bar{t}+Z$	0.0911	$+30.0/-30.0$
$t\bar{t}+Z$+j	0.0603	$+30.0/-30.0$
$t\bar{t}+Z$+jj	0.0536	$+30.0/-30.0$
$W^{\pm}W^{\pm}$+jj	0.369	$+25.0/-25.0$
WZ+jets	10.335	$+34.0/-34.0$
ZZ+jets	9.690	$+34.0/-34.0$

Table 6.10: Cross-section uncertainties from MC background samples. For each sample, the cross section times k-factor σ is presented (see also Table 6.3), together with the relative cross-section uncertainties $\Delta\sigma/\sigma$ in percent.

6.6.7 Parton distribution function and parton shower

As previously mentioned, the systematic uncertainties due to the PDF and the parton shower were determined for the $b' \to tW$ signal sample only. Moreover, the estimation was performed in the analysis of reference [98], which was done using data collected at $\sqrt{s} = 7\,\text{TeV}$. For the current analysis at $\sqrt{s} = 8\,\text{TeV}$, the determination was technically not possible. However, the derived values for these systematic uncertainties were negligible compared to the other uncertainties, and hence we decided to apply the same relative uncertainties in this analysis as quantified for $\sqrt{s} = 7\,\text{TeV}$.

In the MC event generation, the PDF is used to model the longitudinal momenta of the incoming partons. When choosing a different PDF, the kinematic distributions of the incoming partons, and hence also the whole event topology, will change. In order to derive the systematic uncertainty for the choice of the PDF, we (Berlin) applied a

method, which is called 'PDF reweighting' [274] and will be explained in the following. In the analysis of reference [98], the $b' \to tW$ signal samples have been generated with `Pythia6` [165] and the `MRST LO**` PDF [275, 276]. The idea of the PDF reweighting is to simulate the effect of a different PDF by applying an event weight to each generated event i as follows

$$w_i = \frac{f^1(f_a, x_a, Q^2)}{f^0(f_a, x_a, Q^2)} \times \frac{f^1(f_b, x_b, Q^2)}{f^0(f_b, x_b, Q^2)}, \tag{6.48}$$

where f^0 and f^1 denote the initial PDF (which was used to generate the MC sample) and the new PDF under study, respectively, $f_{a/b}$ and $x_{a/b}$ are the flavor and the momentum fraction of the incoming partons a and b, and Q^2 is the transferred four-momentum squared in the hard interaction. This event weight can be interpreted as the probability that a particular event i would have been generated, assuming the new PDF f^1 and that the incoming partons a and b have the same flavors and momentum fractions as in the case of the MC sample generated using the default PDF f^0.
The sum of all event weights gives the number of generated events N^1_{tot} assuming the new PDF f^1. When summing up the event weights for those events that passed the final event selection, one obtains the selected number of events N^1_{sel} assuming the new PDF f^1. Hence, the total event selection efficiency is given by

$$\epsilon_{\text{tot}} = \frac{N^1_{\text{sel}}}{N^1_{\text{tot}}} \ . \tag{6.49}$$

The selection efficiency obtained for the signal sample with $m_{b'} = 500\,\text{GeV}$ (this study was not performed for other masses and hence the results are applied to all b' samples) then was compared to the efficiencies obtained after applying the reweighting method with different PDFs, which were namely `CTEQ6L1` [120], `MSTW2008LO` [119], `MRSTLO*` [275] and `CT09MC2` [277]. Finally, the envelope of the maximum deviations of the efficiencies to the one obtained for the default PDF was taken as systematic PDF uncertainty and was determined to be $+1.4\%/-1.1\%$.
When using different PDFs, then also the modelling of the underlying event (UE) changes, since this relies on the choice of the PDF. This effect is not considered in the 'PDF reweighting' method and hence the presented results are only a rough estimate of the PDF uncertainty. In order to perform a complete study of the systematic uncertainty for the choice of the PDF, one would need to re-produce the same process several times with different PDFs. This was performed in internal studies within the Berlin group, and the results showed uncertainties at the same order of magnitude as for the 'PDF reweighting' method. Since the different re-generations of the signal samples with different PDFs are technically very expensive, we chose to obtain the final PDF uncertainties using the 'PDF reweighting' method. However, one should keep in mind, that these studies were only performed for this particular analysis and hence the assumption of comparable results for both methods does not hold for every analysis.

Initial and final state radiation (ISR and FSR) produces additional partons (and hence jets) through the emission of gluons from the initial and final state partons. This is also

called parton shower (PS) and was discussed in Section 4.1.1.2. In `Pythia`, which was used to generate the $b' \to tW$ signal samples in the analysis of reference [98], the amount of parton showers is steered by several tuning parameters. Hence, the variation of these parameters results in an increasing or decreasing amount of parton showering, which will affect the jet multiplicity in the final state of each event. In order to study the systematic effect of the parton showers, dedicated MC samples were generated, where the particular tuning parameters were varied in order to obtain less and more parton shower (less PS and more PS). These parameters, which were used to generate the $b' \to tW$ signal samples with $m_{b'} = 500\,\text{GeV}$ (other masses were not chosen, since this would have been technically too expensive), are summarised in Table 6.11. The varied parameters were

Parameter	Less PS	More PS	Description
`PARP(67)`	0.70	1.75	Multiplicative factor on momentum scale squared for ISR shower evolution starting scale
`PARP(64)`	3.60	0.60	Multiplicative factor of the momentum scale squared in running of α_s, used in ISR
`PARP(72)`	0.215	0.645	Value of the Λ cut-off parameter in GeV in running of α_s, used in FSR resulting from ISR
`PARJ(82)`	1.66	0.50	FSR low p_T cut-off

Table 6.11: `Pythia` parameters changed to produce samples with more and less parton shower (PS).

determined in dedicated studies and chosen in a way, such that the MC (these were dedicated QCD samples) agrees within the uncertainties with data (corrected to particle level) from the jet gap fraction analysis in reference [278], which is sensitive to the parton showering.
The analysis in reference [98] was performed with the two signal samples with more and less PS and the number of selected events were counted. Finally, the relative differences of these event yields to those obtained for the signal sample with default parton shower parameters was taken as systematic uncertainty and amounted to $\pm 6\%$.

The uncertainties on the choice of the PDF and the parton shower tuning parameters, which are also summarised in Table 6.12, are applied in the following for the $b' \to tW$ and $b' \to qW$ signal samples. However, one should keep in mind that these uncertainties

Systematic	Uncertainty [%]
PDF	$+1.4/-1.1$
Parton shower	$+6.0/-6.0$

Table 6.12: Parton distribution function and parton shower systematic uncertainties applied for the $b' \to tW$ and $b' \to qW$ signal samples.

were determined using different MC samples and at a different centre-of-mass energy of $\sqrt{s} = 7\,\text{TeV}$. Furthermore one would basically need to perform the same studies for the various background processes modelled with MC. However, these uncertainties are

considered as negligible compared to the other sources of systematic uncertainties (for instance the uncertainties on the cross-sections), and therefore a determination was not performed in this analysis.

6.6.8 Uncertainties on data-driven backgrounds

In this section, I will describe the methods, which have been used to determine the uncertainties on the data-driven background estimates, namely the charge mis-id and the lepton fakes. The estimation of these uncertainties was performed after applying several event selection criteria, which will be discussed in more detail in the following Sections 6.7 and 6.8.2.1.

6.6.8.1 Charge mis-reconstruction

The charge mis-id background is estimated, by selecting opposite-sign events from data, and applying event weights calculated from the electron charge mis-id rates ϵ. For the determination of the uncertainty on the charge mis-id background, we (Clermont-Ferrand) estimated the uncertainties on the rates Δ_ϵ and then ran the analysis twice, where the $\epsilon \pm \Delta_\epsilon$ variation of these rates was used. This will result in variations of the number of selected events, where the difference to the yields obtained with the nominal rates was taken as systematic uncertainty on this background estimate.

The rate uncertainty is the quadratic sum of six different contributions:

- The statistical uncertainty from the rate extraction using the likelihood method $\sigma_\epsilon^{\text{likelihood}}(\eta) \times \Delta\alpha(\eta, p_T)$.
- The statistical uncertainty on the obtained correction factor $\epsilon^{\text{likelihood}}(\eta) \times \sigma_\alpha(\eta, p_T)$.
- The difference between the rate measured with the likelihood method on simulated Z events (including the correction factor from $t\bar{t}$ events) and the true rate measured in simulated $t\bar{t}$ events (see Figure 6.12).
- The difference on the correction factor using different simulated $t\bar{t}$ samples. The nominal correction factor α was derived using a $t\bar{t}$ MC sample generated with `MC@NLO+Herwig`, whereas the samples used for comparison where generated with `Powheg+Pythia` and `Powheg+Herwig`. A comparison of the obtained correction factors is presented in Figure 6.23.
- The variation of the rates due to the variation of the Z peak region definition. In Figure 6.11 the definition of the region for the extraction of the nominal rates was presented. The variation is computed by shifting the widths of these regions by $\pm 6\,\text{GeV}$.
- The statistical uncertainty on the overlap removal correction factor, as presented in Figure 6.15.

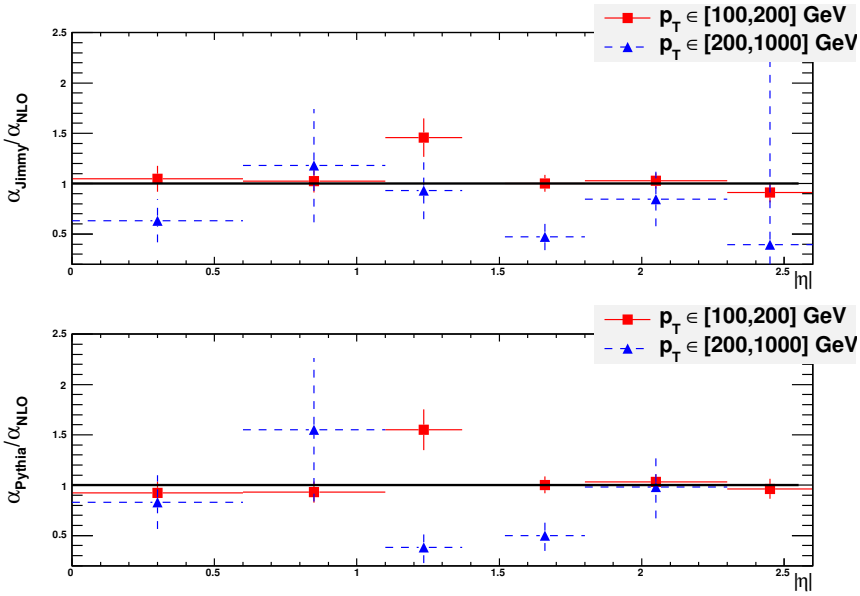

Figure 6.23: Comparison of charge mis-id correction factors obtained from $t\bar{t}$ samples generated with different generators [258]. The upper plot presents the $|\eta|$ dependence of the ratio of the correction factor α obtained from the `Powheg+Herwig` sample and the default `MC@NLO` sample. In the lower plot, the ratio compares the factor obtained from the `Powheg+Pythia` sample to the factor from the `MC@NLO` sample. These ratios are taken as one source of uncertainty on the charge mis-id rates ϵ.

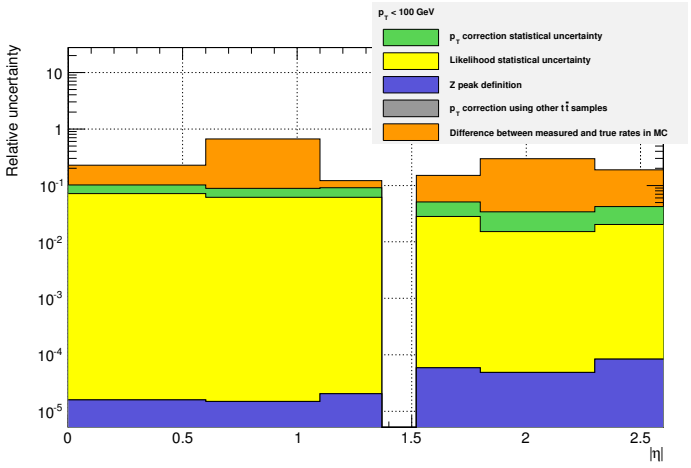

(a) $p_T \leq 100\,\text{GeV}$

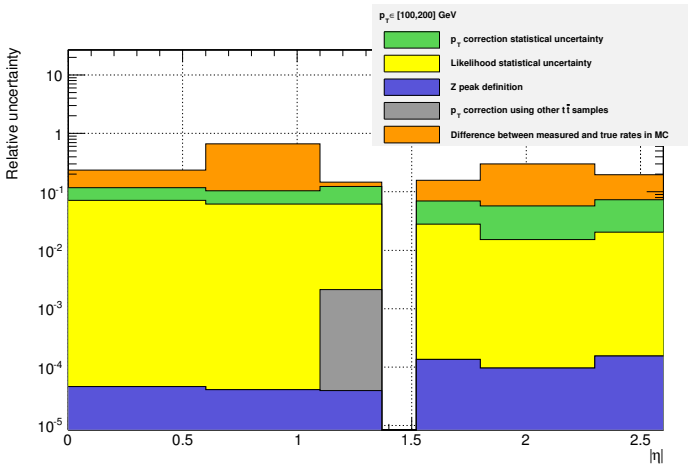

(b) $100\,\text{GeV} < p_T < 200\,\text{GeV}$

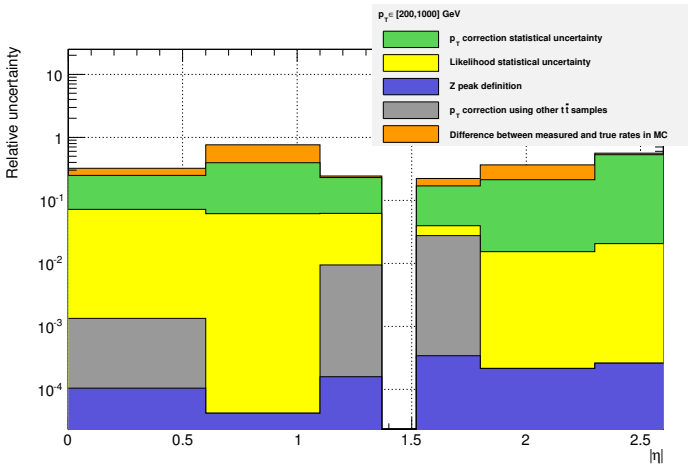

(c) $p_T \geq 200\,\text{GeV}$

Figure 6.24: Relative systematic uncertainty contributions on the charge mis-id rates, for different bins in $|\eta|$ and p_T [258].

The relative contributions of above listed sources of uncertainties are presented in Figure 6.24 as a function of $|\eta|$ and for different p_T bins. We observed that the largest contributions come from the statistical uncertainties of the likelihood method and the correction factor α.

The differences in the final event yields between the cases of using the nominal and varied charge mis-id rates were then used as systematic uncertainty. Table 6.13 presents the obtained yields after applying the final event selection (as explained in Section 6.7.1). As can be seen, the relative uncertainties on the charge mis-id estimates lie in the range of 34% to 39%.

Channel	ϵ	$\epsilon + \Delta_\epsilon$	$\epsilon - \Delta_\epsilon$	$\Delta n/n$ [%]
ee	0.61 ± 0.12	0.85 ± 0.18	0.38 ± 0.08	$+38.8/-38.0$
$e\mu$	0.90 ± 0.12	1.21 ± 0.17	0.59 ± 0.08	$+35.2/-34.7$

Table 6.13: Charge mis-id yields obtained using the nominal (ϵ) and varied charge mis-id rates ($\epsilon \pm \Delta_\epsilon$). The yields were obtained for the two channels ee and $e\mu$, for the estimation of the charge mis-id contribution to same-sign dilepton events. The events were required to pass the basic event selection and to have at least two jets, at least one b-tagged jet, $E_T^{\text{miss}} \geq 40\,\text{GeV}$ and $H_T \geq 650\,\text{GeV}$ (H_T is defined as the sum of the transverse momenta of all electrons, muons and jets in the event) (see Section 6.7 for further information). The last column presents the relative uncertainty $\Delta n/n$, derived from the differences between the yields obtained using the up/down varied rates ($\pm\Delta n$) and the yields obtained using the nominal rates (n). For each yield, also the statistical uncertainty is presented, which does not enter in the systematic uncertainty. The statistical uncertainty on the nominal yield will be considered in the further analysis.

6.6.8.2 Lepton mis-reconstruction

The optimal procedure for determining the uncertainty on the lepton fakes background would be to perform a similar strategy as for the charge mis-id: one would perform the fakes estimation by varying the real and fake rates within their uncertainties. However, the uncertainties on these rates were not provided by the *ATLAS TopFakes* group, who measured the real and fake rates, and hence we (Arizona) performed a different method for estimating the uncertainty on the fakes background.

The basic idea is to compare the background expectation to the observed data events in control regions which are orthogonal to the final event selection and which have only a tiny contamination of the signal. This means that one would expect a perfect agreement between data and the expectation, in case of a perfect background estimation. Furthermore, the lepton fakes background should have a significant controbution to these control regions, in order to obtain a reliable determination of the systematic uncertainty. Three different control regions were used, which will be further explained in Section 6.8.2.1.

All three regions are based on the basic selection described in Section 6.7 and apply further cuts:

- Low-H_T: this control regions requires a lower H_T than for the final event selection of $100\,\text{GeV} < H_T < 400\,\text{GeV}$ (in the final selection we require $H_T \geq 650\,\text{GeV}$). In addition, events are selected that have at least two jets and one b-tagged jet.
- Low-E_T^{miss}: in this control region the cut on E_T^{miss} is inverted, which means it is required that $E_T^{\text{miss}} < 40\,\text{GeV}$. Furthermore, events are required to contain at least two jets and one b-tagged jet.
- Zero b-tag: for this control region, only events are selected that contain no b-tagged jet, but at least two non-tagged jets.

As will be seen later, the low-H_T and low-E_T^{miss} control regions are dominated by the leptons fakes and the charge mis-id background. The Zero b-tag control region is mostly dominated by the lepton fakes and the diboson background. Therefore, these three control regions are well suited for the estimation of the systematic uncertainty on the lepton fakes background, since it provides a significant contribution to all three control regions.
The comparison of the observed data with the background expectation in the three control regions was performed using a so-called 'Poisson likelihood fit', which is based on maximising the likelihood of the observation given a Poisson probability. In general, the likelihood can be written as

$$\mathcal{L}(\Theta_i|x_i) = \prod_{i=1}^{n} f(x_i|\Theta_i), \tag{6.50}$$

where the product runs over the probability density function f with measured values x_i and free parameters Θ_i, which are supposed to be estimated by the fit.
For the probability density function, the Poisson distribution was chosen, defined by

$$f(b,d) = \frac{b^d e^{-b}}{d!}, \tag{6.51}$$

which gives the probability to observe d events, if b events are expected. In this case, b is the sum of the yields of all backgrounds selected in the control regions. For the fakes yields, the estimator is multiplied by a scale factor s_F which will be determined by the fit. Hence, the expected number of events are given by

$$b = \sum_{j \neq \text{fakes}}^{N} b_j + s_F \times b_{\text{fakes}}, \tag{6.52}$$

where the sum runs over all backgrounds besides the lepton fakes. By maximising the likelihood (this was performed numerically) it is possible to determine the best-fit parameters for s_F, which denote the scale factors that need to be applied to the lepton fakes yields in order to have an optimal agreement between data and expectation.

This procedure was performed separately for the three same-sign dilepton channels ee, $e\mu$ and $\mu\mu$ and for the three control region definitions. In a second run, all three control regions were combined, which is simply performed by the product of the probability density functions. The obtained best-fit values for the s_F are presented in Table 6.14. The final systematic uncertainty is derived from summing in quadrature $|s_F - 1|$ and

	ee		$e\mu$		$\mu\mu$	
Control region	s_F	δ_{tot}	s_F	δ_{tot}	s_F	δ_{tot}
Low H_T	0.84 ± 0.21		0.64 ± 0.13		0.82 ± 0.18	
Low E_T^{miss}	0.75 ± 0.24		0.56 ± 0.18		0.49 ± 0.27	
Zero b-tag	1.67 ± 0.21		0.97 ± 0.18		1.37 ± 0.42	
All	1.19 ± 0.13	23%	0.71 ± 0.10	30%	0.81 ± 0.10	24%

Table 6.14: Best-fit scale factors s_F to be applied to the fake yield to match the observed yield in each control region and same-sign dilepton channel ee, $e\mu$ and $\mu\mu$. For each scale factor also the uncertainty on the factor is presented, which was obtained from the fit. The last line presents the best-fit values when performing the procedure on the combination of all three control regions. The total systematic uncertainty δ_{tot} is derived by adding the deviation of the scale factor from unity and the uncertainty on s_F in quadrature.

the uncertainty on s_F. It can be seen, that the 'Zero b-tag' control region yields in larger scale factors than the other two control regions. Since this method is only a rough estimate of the magnitude of the uncertainty, it was chosen to use a conservative value of 30% for the uncertainty on the lepton fakes background in all channels ee, $e\mu$ and $\mu\mu$.

One should note that this fit was only performed to extract the scale factors s_F for the estimation of the uncertainty on the lepton fakes background. The systematic uncertainties on the other backgrounds have not been considered here, and the obtained results are not used for rescaling the background later in the analysis (e.g. in the control region distributions shown in Section 6.8.2.1).

6.7 Event selection

In this section, I present the criteria for the event selection, which were partly discussed in Chapter 5 and basically follow the recommendations of the *ATLAS Top Working Group* for dilepton analyses. This was chosen, because the event topology of my analysis is similar to fully leptonic $t\bar{t}$ decays, and allows to make use of several tools in the analysis, which were developed by this group. The event selection criteria are split into a *basic selection*, which is common for the final event selection and the different control regions selections, and a few additional criteria that will be optimised to obtain an optimal sensitivity for the signal search. These optimised criteria represent the *final selection*, which has been used in the analysis. Furthermore, the selected events are separated into three lepton categories, namely ee, $e\mu$ and $\mu\mu$, that represent the flavors of the two required same-sign charged leptons.

The *basic selection* consists of the following requirements:

- Events are required to pass at least one of the electron and muon triggers as discussed in Sections 5.3.4 and 5.4.4. Depending on the channel (ee, $e\mu$, $\mu\mu$), the events have to pass at least one of the electron triggers (ee), at least one of the muon triggers ($\mu\mu$) or at least one of either the electron or muon triggers ($e\mu$).
  When analysing the data, the events need to additionally pass the Good Run List (GRL), as discussed in Section 5.2.

- The primary vertex must have at least five associated tracks, as discussed in Section 5.8.1.

- Events with 'bad jets' (Section 5.5.3) or flagged as having detector problems in the ECAL (Section 5.3.1) are rejected.

- A cosmic rejection is applied in order to reject muons coming from cosmic rays (Section 5.4.1). An event with two muon tracks having opposite-sign d_0^{beam}, $|d_0^{\text{beam}}| > 0.5\,\text{mm}$ and $\Delta\Phi > 3.1$, is rejected.

- If there are overlapping electrons and muons (Section 5.6.1), the event is rejected.

- Each event must contain exactly two leptons (electrons or muons), which have the same electrical charge.

- The invariant mass m_{inv} of the two leptons (only in ee and $\mu\mu$ events) must be larger than 15 GeV, in order to suppress background coming from heavy quarkonium states (although the contribution from $\mu\mu$ charge mis-id events is expected to be negligible and hence it is also not considered in the data-driven charge mis-id estimate).
  Furthermore, the background coming from Z boson decays is suppressed by requiring $|m_{\text{inv}} - m_Z| > 10\,\text{GeV}$, where m_Z denotes the Z boson mass.

The basic selection criteria are also summarised in Table 6.15.

As a start for our analysis, we decided to adopt the event selection criteria we used for the analysis based on data taken in 2011, which was presented in reference [98]. This set of selection criteria will be referred to as 'default selection' in the following. In the default selection, the same basic selection was chosen as discussed above, and additional criteria were required:

- The events must contain at least two selected jets ($N_{\text{Jets}} \geq 2$). This cut is motivated by the fact that in the $b'\bar{b}'$ decay chain one expects a high jet multiplicity.

- At least one of the jets must be b-tagged ($N_{\text{bJets}} \geq 1$). If the branching fraction for the decay $b' \to tW$ has a sufficient size, one expects at least one b-jet. In the $b' \to tW$ scenario, both pair-produced b' quarks decay into t quarks, which both further decay into bW. Hence, this gives two b-jets in the event.
  For the $b' \to qW$ scenario, the pair-produced b' quarks can decay into tW, cW

Selection	Criterion
GRL	Good conditions (only data)
Trigger	Electron and muon triggers depending on channel
Primary vertex	≥ 5 associated tracks
Jet quality	no 'bad jets'
ECAL	no 'LAr error'
Cosmic rejection	Reject events with opposite-sign d_0^{beam}, $\lvert d_0^{\text{beam}}\rvert > 0.5\,\text{mm}$ and $\Delta\Phi > 3.1$
Lepton overlap	Reject overlapping electrons and muons
Number of leptons	$N_{\text{Leptons}} = 2$ (ee, $e\mu$ or $\mu\mu$)
Quarkonium veto	$m_{\text{inv}} \geq 15\,\text{GeV}$
Z-veto	$\lvert m_{\text{inv}} - m_Z\rvert > 10\,\text{GeV}$ (only ee and $\mu\mu$)

Table 6.15: Summary of the basic event selection criteria.

or uW. Hence, the number of decays into tW also gives the number of expected b-jets in the event. However, to achieve a same-sign dilepton signature, at least one of the two b' quarks has to decay into tW (as it was discussed in Section 6.1), and therefore one expects at least one b-jet in this scenario.

- The missing transverse energy must be $E_T^{\text{miss}} \geq 40\,\text{GeV}$. This cut further rejects background coming from Z boson production. In the leptonic Z decays, there appear no neutrinos and hence the E_T^{miss} is expected to be small.
  Furthermore, this cut also rejects QCD background coming from mis-reconstructed leptons, as these are mostly 'faked' by jets (see Section 6.2.4). Such events contain no high-energetic neutrinos.

- The decay products of the heavy b' quarks carry large transverse momenta. Therefore, the transverse momentum sum of all electrons, muons and jets in the event is defined as

$$H_T = \sum_e p_T^e + \sum_\mu p_T^\mu + \sum_{\text{jet}} p_T^{\text{jet}}, \tag{6.53}$$

  which has to be larger than 550 GeV for the default event selection.

The distributions of these four variables after applying the basic selection are presented in Figure 6.25. These distributions show the combination of the dilepton channels ee, $e\mu$ and $\mu\mu$. The same plots separated for the channels can be looked up in Appendix B.1.1. It can be clearly seen that without applying cuts one these variables, there is no sensitivity to the signal, because the distributions are totally dominated by the various backgrounds. Especially the charge mis-id and lepton fakes backgrounds give large contributions. The signal entries are populated at high H_T values above 800 GeV, as expected. For lower b' masses, the signal H_T distribution would shift to lower H_T values. The same distributions are shown in Figure 6.26, but after applying the default event

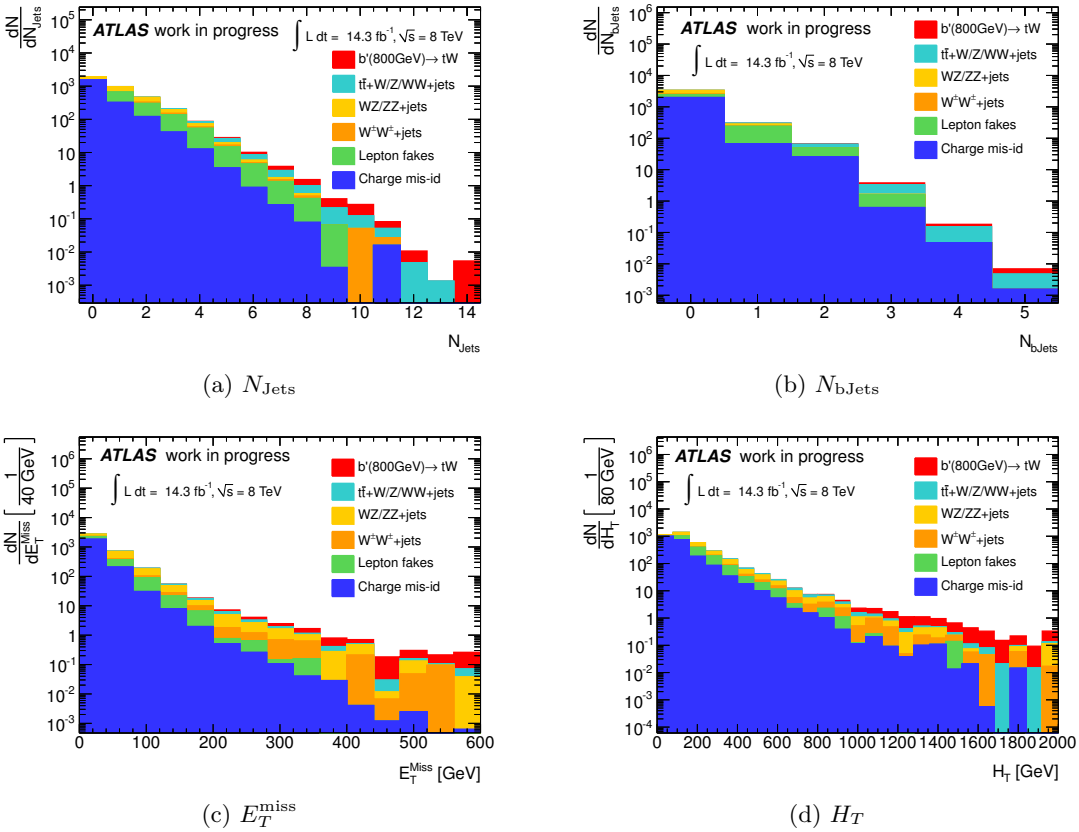

(a) N_{Jets} (b) N_{bJets}

(c) E_T^{miss} (d) H_T

Figure 6.25: Distributions of the discriminant variables N_{Jets} (a), N_{bJets} (b), E_T^{miss} (c) and H_T (d) for the various backgrounds and the $b' \to tW$ ($m_{b'} = 800\,\mathrm{GeV}$) sample after the basic event selection (Table 6.15). The plots show the combination of the channels ee, $e\mu$ and $\mu\mu$.

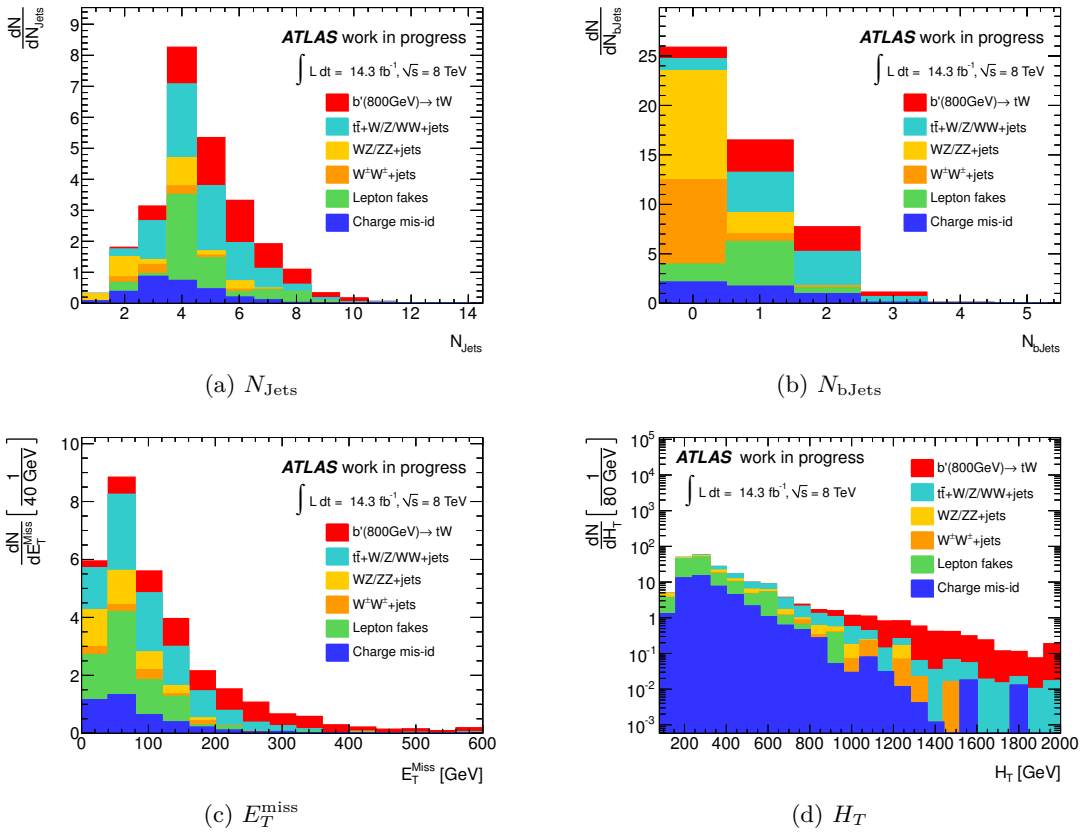

(a) N_{Jets} (b) N_{bJets}

(c) E_T^{miss} (d) H_T

Figure 6.26: Distributions of the discriminant variables N_{Jets} (a), N_{bJets} (b), E_T^{miss} (c) and H_T (d) for the various backgrounds and the $b' \to tW$ ($m_{b'} = 800\,\mathrm{GeV}$) sample after the default event selection (Table 6.19). The plots show the combination of the channels ee, $e\mu$ and $\mu\mu$. In each plot, the cut on the corresponding variable has been removed.

selection criteria. In each plot, the cut on the corresponding variable has been removed. All background contributions are heavily suppressed and the signal contribution can be better separated from the background expectation. This is required, in order to draw final conclusions when comparing to the observed events.

When comparing the H_T distribution in Figure 6.26d (where the cut on H_T was removed) with the other three distributions, one notices that most of the background suppression results from the H_T cut. This can be also seen when looking at the selection efficiencies for the four discriminant variables N_{Jets}, N_{bJets}, E_T^{miss} and H_T in Tables 6.16, 6.17 and 6.18 for the ee, $e\mu$ and $\mu\mu$ channel, respectively. The various backgrounds are reduced by more than a factor of 2 due to the H_T cut. One also notices that the requirement of at least one b-tagged jet has a strong impact on the diboson backgrounds (WZ/ZZ+jets and $W^{\pm}W^{\pm}$+jets). This is due to the fact, that these backgrounds were not modelled with additional heavy flavor partons (since such processes are expected to

Process	Basic selection	$N_{\text{Jets}} \geq 2$	$N_{\text{bJets}} \geq 1$	$E_T^{\text{miss}} \geq 40\,\text{GeV}$	$H_T \geq 550\,\text{GeV}$
$b'(800\,\text{GeV}) \to tW$	1.40 ± 0.08	1	$0.82^{+0.02}_{-0.02}$	$0.975^{+0.007}_{-0.009}$	$0.988^{+0.005}_{-0.008}$
$t\bar{t}+W$+jets	5.03 ± 0.17	$0.964^{+0.004}_{-0.005}$	$0.82^{+0.01}_{-0.01}$	$0.85^{+0.01}_{-0.01}$	$0.3524^{+0.014}_{-0.014}$
$t\bar{t}+Z$+jets	1.75 ± 0.09	$0.972^{+0.006}_{-0.008}$	$0.84^{+0.01}_{-0.02}$	$0.74^{+0.02}_{-0.02}$	$0.3291^{+0.024}_{-0.023}$
$t\bar{t}+WW$	0.089 ± 0.005	$0.993^{+0.003}_{-0.006}$	$0.77^{+0.02}_{-0.02}$	$0.90^{+0.01}_{-0.02}$	$0.5137^{+0.026}_{-0.026}$
WZ/ZZ+jets	158.20 ± 4.03	$0.286^{+0.009}_{-0.009}$	$0.11^{+0.01}_{-0.01}$	$0.54^{+0.06}_{-0.06}$	$0.1245^{+0.068}_{-0.049}$
$W^{\pm}W^{\pm}$+jets	8.70 ± 0.64	$0.77^{+0.02}_{-0.03}$	$0.10^{+0.02}_{-0.02}$	$0.87^{+0.07}_{-0.10}$	$0.3^{+0.1}_{-0.1}$
Lepton fakes	311.72 ± 14.80	$0.37^{+0.03}_{-0.03}$	$0.35^{+0.05}_{-0.05}$	$0.46^{+0.09}_{-0.09}$	$0.09^{+0.12}_{-0.06}$
Charge mis-id	1952.20 ± 6.52	$0.067^{+0.006}_{-0.006}$	$0.24^{+0.04}_{-0.04}$	$0.58^{+0.1}_{-0.1}$	$0.07^{+0.12}_{-0.05}$

Table 6.16: Cut efficiencies for the default event selection in the ee channel. Presented are the expected number of events (and their statistical uncertainties) after the basic selection, and the cut efficiencies on the following cuts on N_{Jets}, N_{bJets}, E_T^{miss} and H_T. These efficiencies are defined as $\epsilon_i = n_i/n_{i-1}$, where n_i and n_{i-1} denote the number of events after and before the cut, respectively. Upper and lower limits on the efficiencies have been calculated with the method described in Section 6.4.1. The results are shown for the $b' \to tW$ ($m_{b'} = 800\,\text{GeV}$) sample and the various backgrounds.

Process	Basic	$N_{\text{Jets}} \geq 2$	$N_{\text{bJets}} \geq 1$	$E_T^{\text{miss}} \geq 40\,\text{GeV}$	$H_T \geq 550\,\text{GeV}$
$b'(800\,\text{GeV}) \to tW$	3.95 ± 0.13	1	$0.866^{+0.009}_{-0.009}$	$0.963^{+0.005}_{-0.006}$	$0.979^{+0.004}_{-0.005}$
$t\bar{t}+W$+jets	17.38 ± 0.32	$0.967^{+0.002}_{-0.002}$	$0.823^{+0.005}_{-0.005}$	$0.825^{+0.005}_{-0.006}$	$0.340^{+0.008}_{-0.008}$
$t\bar{t}+Z$+jets	5.43 ± 0.16	$0.977^{+0.003}_{-0.004}$	$0.815^{+0.008}_{-0.009}$	$0.78^{+0.01}_{-0.01}$	$0.36^{+0.01}_{-0.01}$
$t\bar{t}+WW$	0.297 ± 0.009	$0.995^{+0.002}_{-0.002}$	$0.823^{+0.009}_{-0.009}$	$0.862^{+0.009}_{-0.009}$	$0.52^{+0.01}_{-0.01}$
WZ/ZZ+jets	453.66 ± 6.84	$0.235^{+0.005}_{-0.005}$	$0.145^{+0.009}_{-0.008}$	$0.54^{+0.03}_{-0.03}$	$0.13^{+0.03}_{-0.03}$
$W^{\pm}W^{\pm}$+jets	32.92 ± 1.28	$0.73^{+0.01}_{-0.01}$	$0.09^{+0.01}_{-0.01}$	$0.67^{+0.06}_{-0.06}$	$0.32^{+0.08}_{-0.07}$
Lepton fakes	277.74 ± 12.35	$0.57^{+0.03}_{-0.03}$	$0.51^{+0.04}_{-0.04}$	$0.58^{+0.06}_{-0.06}$	$0.04^{+0.05}_{-0.03}$
Charge mis-id	116.87 ± 1.32	$0.42^{+0.05}_{-0.05}$	$0.76^{+0.07}_{-0.08}$	$0.75^{+0.08}_{-0.09}$	$0.05^{+0.08}_{-0.04}$

Table 6.17: Cut efficiencies for the default event selection in the $e\mu$ channel. Presented are the expected number of events (and their statistical uncertainties) after the basic selection, and the cut efficiencies on the following cuts on N_{Jets}, N_{bJets}, E_T^{miss} and H_T. These efficiencies are defined as $\epsilon_i = n_i/n_{i-1}$, where n_i and n_{i-1} denote the number of events after and before the cut, respectively. Upper and lower limits on the efficiencies have been calculated with the method described in Section 6.4.1. The results are shown for the $b' \to tW$ ($m_{b'} = 800\,\text{GeV}$) sample and the various backgrounds.

Process	Basic	$N_{\text{Jets}} \geq 2$	$N_{\text{bJets}} \geq 1$	$E_T^{\text{miss}} \geq 40\,\text{GeV}$	$H_T \geq 550\,\text{GeV}$
$b'(800\,\text{GeV}) \to tW$	2.56 ± 0.11	1	$0.81^{+0.01}_{-0.01}$	$0.958^{+0.007}_{-0.008}$	$0.984^{+0.004}_{-0.006}$
$t\bar{t} + W$+jets	11.69 ± 0.27	$0.965^{+0.003}_{-0.003}$	$0.820^{+0.006}_{-0.006}$	$0.831^{+0.007}_{-0.007}$	$0.334^{+0.009}_{-0.009}$
$t\bar{t} + Z$+jets	2.7103 ± 0.1163	$0.972^{+0.005}_{-0.006}$	$0.82^{+0.01}_{-0.01}$	$0.75^{+0.02}_{-0.02}$	$0.35^{+0.02}_{-0.02}$
$t\bar{t} + WW$	0.205 ± 0.008	$0.989^{+0.003}_{-0.004}$	$0.81^{+0.01}_{-0.01}$	$0.87^{+0.01}_{-0.01}$	$0.53^{+0.02}_{-0.02}$
WZ/ZZ+jets	235.05 ± 5.03	$0.189^{+0.006}_{-0.006}$	$0.17^{+0.01}_{-0.01}$	$0.68^{+0.04}_{-0.05}$	$0.18^{+0.05}_{-0.04}$
$W^{\pm}W^{\pm}$+jets	19.58 ± 0.97	$0.69^{+0.02}_{-0.02}$	$0.10^{+0.02}_{-0.01}$	$0.73^{+0.07}_{-0.08}$	$0.28^{+0.09}_{-0.08}$
Lepton fakes	80.92 ± 10.69	$0.73^{+0.05}_{-0.06}$	$0.65^{+0.07}_{-0.07}$	$0.67^{+0.08}_{-0.09}$	$0.07^{+0.09}_{-0.05}$

Table 6.18: Cut efficiencies for the default event selection in the $\mu\mu$ channel. Presented are the expected number of events (and their statistical uncertainties) after the basic selection, and the cut efficiencies on the following cuts on N_{Jets}, N_{bJets}, E_T^{miss} and H_T. These efficiencies are defined as $\epsilon_i = n_i/n_{i-1}$, where n_i and n_{i-1} denote the number of events after and before the cut, respectively. Upper and lower limits on the efficiencies have been calculated with the method described in Section 6.4.1. The results are shown for the $b' \to tW$ ($m_{b'} = 800\,\text{GeV}$) sample and the various backgrounds.

be negligible), and therefore there are no b-quarks expected. The signal is only sparsely affected by the cuts, as the efficiencies are well above 80% for every cut.

The default event selection criteria, as they are also summarised in Table 6.19, were

Selection	Criterion
Basic	Table 6.15
N_{Jets}	≥ 2
N_{bJets}	≥ 1
E_T^{miss}	$\geq 40\,\text{GeV}$
H_T	$\geq 550\,\text{GeV}$

Table 6.19: Summary of the default event selection criteria.

based on optimisations performed for the $\sqrt{s} = 7\,\text{TeV}$ analysis in reference [98]. These default criteria will be used as starting point for the event selection optimisation described in the following section.

6.7.1 Event selection optimisation

The idea of the event selection optimisation is to improve the selection criteria for an optimal background rejection, while retaining the sensitivity to the signal.
In case of the absence of the signal contribution in the observed data, I will derive limits on the cross-sections for each b' mass point, which can be translated into a lower limit on the b' mass assuming a branching fraction for $b' \to tW$ with 100%. Hence, the optimisation is performed by varying particular event selection criteria and then

checking which set of cuts gives the highest mass limit.

For deriving the expected mass limits, I used the CL_s method as described in Section 6.4.3. The optimisation is based on the expected limits only, that are derived under the assumption of the background-only hypothesis. For each mass point, the signal scale factors are obtained, which are applied to the signal cross-section predictions to receive the upper limits with 95% CL. When plotting the upper cross-section limits as a function of the b' mass, together with the theoretical cross-section prediction (Figure 2.18), one can derive the lower mass limit from the intersection of these two curves.

This procedure is performed for several sets of cuts. In each limit calculation all the systematic uncertainties enter as they were described in Section 6.6. However, the object scale, resolution and efficiency scale factor uncertainties need to be determined for a particular event selection. Deriving these uncertainties separately for each set of cuts would have been technically too expensive. Therefore, I chose to derive these uncertainties only for the default event selection, as summarised in Table 6.19, and then to apply the obtained relative uncertainties on the yields for each set of cuts. This is justified, because it will be shown later that the systematic uncertainties only have a small impact on the limit calculation and that this analysis is hence mostly limited by the statistical uncertainties. Therefore, variations of the systematic uncertainties by few percents are not expected to change the expected limit calculation for the event-selection optimisation.

The input to the limit calculation is a simple cut&count method. This means, that for each background and signal process the selected number of events are counted. The counting is performed separately for the three dilepton channels ee, $e\mu$ and $\mu\mu$ and hence three bins containing the amount of selected events are provided to the limit setting calculation. The obtained expected event yields for the different background processes after applying the default event selection are presented in Table 6.20. Each yield is shown

Process	ee	$e\mu$	$\mu\mu$
$t\bar{t}+W$+jets	$0.97 \pm 0.07^{+0.33}_{-0.31}$	$3.11 \pm 0.13^{+0.99}_{-1.02}$	$2.07 \pm 0.10^{+0.67}_{-0.68}$
$t\bar{t}+Z$+jets	$0.32 \pm 0.04^{+0.11}_{-0.10}$	$1.09 \pm 0.07^{+0.36}_{-0.35}$	$0.50 \pm 0.05^{+0.17}_{-0.17}$
$t\bar{t}+WW$	$0.031 \pm 0.003^{+0.013}_{-0.009}$	$0.110 \pm 0.006^{+0.043}_{-0.031}$	$0.076 \pm 0.005^{+0.030}_{-0.021}$
WZ/ZZ+jets	$0.32 \pm 0.21^{+0.12}_{-0.12}$	$0.99 \pm 0.34^{+0.44}_{-0.38}$	$0.86 \pm 0.31^{+0.35}_{-0.39}$
$W^{\pm}W^{\pm}$+jets	$0.17 \pm 0.09^{+0.06}_{-0.05}$	$0.45 \pm 0.17^{+0.15}_{-0.14}$	$0.28 \pm 0.12^{+0.09}_{-0.09}$
Lepton fakes	$1.61 \pm 0.55^{+0.48}_{-0.48}$	$1.74 \pm 0.63^{+0.52}_{-0.52}$	$1.72 \pm 1.23^{+0.52}_{-0.52}$
Charge mis-id	$1.25 \pm 0.17^{+0.47}_{-0.47}$	$1.52 \pm 0.14^{+0.51}_{-0.50}$	—

Table 6.20: Expected number of events for the different background processes after applying the default event selection. The yields are presented separately for the three channels of same-sign charged ee, $e\mu$ and $\mu\mu$ pairs. For each yield the statistical (first term) and total upward and downward systematic uncertainty variations are shown.

together with the statistical and the total upward and downward systematic uncertainty variations, where the systematic uncertainties are the quadratic sum of all considered systematics. The derived relative uncertainties for each systematic for the background processes estimated from MC are summarised in Appendix B.2.1 in Tables B.2, B.3 and B.4 for the ee, $e\mu$ and $\mu\mu$ channel, respectively. A summary of the systematics on the data-driven backgrounds (lepton fakes and charge mis-id) is given in Table B.1. All presented numbers have been derived for the default event selection.

For the event selection optimisation, only the $b' \to tW$ signal samples were considered. In the analysis of the $b' \to qW$ samples with variable branching fractions, one would basically need to perform the optimisation for each set of branching fractions of the decays into tW, cW and uW. However, the optimisation for the $b' \to qW$ scenario therefore would have been technically too expensive and hence the optimised event selection obtained for the $b' \to tW$ samples will be also used for the analysis of the $b' \to qW$ samples. Therefore this is not an optimal selection for $b' \to u/c + W$.
The counted event yields for the $b' \to tW$ signal samples for different mass points are presented in Table 6.21 together with the statistical and systematic uncertainties. The relative uncertainties due to each systematic are presented in Tables B.5, B.6 and B.7 for the ee, $e\mu$ and $\mu\mu$ channels, respectively.

Now, starting from the default event selection, the cuts on N_{Jets}, N_{bJets}, E_T^{miss} and

Process	ee	$e\mu$	$\mu\mu$
$b'(400\,\text{GeV}) \to tW$	$48.91 \pm 4.75^{+7.73}_{-8.27}$	$192.9 \pm 9.5^{+30.6}_{-30.4}$	$116.7 \pm 7.6^{+19.9}_{-19.1}$
$b'(450\,\text{GeV}) \to tW$	$36.98 \pm 2.98^{+6.15}_{-5.42}$	$114.7 \pm 5.3^{+17.8}_{-16.4}$	$68.62 \pm 4.06^{+11.91}_{-11.69}$
$b'(500\,\text{GeV}) \to tW$	$26.00 \pm 1.80^{+4.23}_{-4.20}$	$72.41 \pm 3.03^{+11.38}_{-10.62}$	$38.56 \pm 2.20^{+6.59}_{-6.01}$
$b'(550\,\text{GeV}) \to tW$	$12.72 \pm 0.88^{+2.16}_{-1.86}$	$42.10 \pm 1.68^{+6.75}_{-5.99}$	$25.30 \pm 1.34^{+4.36}_{-3.82}$
$b'(600\,\text{GeV}) \to tW$	$7.86 \pm 0.52^{+1.29}_{-1.09}$	$21.93 \pm 0.89^{+3.56}_{-3.05}$	$14.79 \pm 0.75^{+2.60}_{-2.29}$
$b'(650\,\text{GeV}) \to tW$	$5.09 \pm 0.32^{+0.89}_{-0.75}$	$14.64 \pm 0.57^{+2.45}_{-2.10}$	$8.96 \pm 0.45^{+1.61}_{-1.39}$
$b'(700\,\text{GeV}) \to tW$	$2.87 \pm 0.21^{+0.50}_{-0.41}$	$8.69 \pm 0.34^{+1.49}_{-1.26}$	$5.03 \pm 0.27^{+0.93}_{-0.78}$
$b'(750\,\text{GeV}) \to tW$	$2.11 \pm 0.12^{+0.38}_{-0.32}$	$5.42 \pm 0.20^{+0.95}_{-0.79}$	$3.38 \pm 0.16^{+0.64}_{-0.54}$
$b'(800\,\text{GeV}) \to tW$	$1.11 \pm 0.07^{+0.21}_{-0.16}$	$3.22 \pm 0.12^{+0.59}_{-0.47}$	$1.95 \pm 0.10^{+0.38}_{-0.31}$
$b'(850\,\text{GeV}) \to tW$	$0.70 \pm 0.04^{+0.14}_{-0.11}$	$1.95 \pm 0.07^{+0.37}_{-0.30}$	$1.23 \pm 0.06^{+0.26}_{-0.21}$
$b'(900\,\text{GeV}) \to tW$	$0.50 \pm 0.03^{+0.10}_{-0.08}$	$1.25 \pm 0.05^{+0.25}_{-0.20}$	$0.75 \pm 0.04^{+0.16}_{-0.13}$
$b'(950\,\text{GeV}) \to tW$	$0.27 \pm 0.02^{+0.06}_{-0.04}$	$0.79 \pm 0.03^{+0.17}_{-0.13}$	$0.49 \pm 0.02^{+0.11}_{-0.08}$
$b'(1000\,\text{GeV}) \to tW$	$0.16 \pm 0.01^{+0.04}_{-0.03}$	$0.53 \pm 0.02^{+0.12}_{-0.09}$	$0.30 \pm 0.01^{+0.07}_{-0.05}$

Table 6.21: Expected number of events for the $b' \to tW$ signal process after applying the default event selection. The yields are presented separately for each mass point and the three channels of same-sign charged ee, $e\mu$ and $\mu\mu$ pairs. For each yield the statistical (first term) and total upward and downward systematic uncertainty variations are shown.

H_T have been varied and the expected signal and background yields have been derived. Together with the relative systematic uncertainties determined with the default event selection, these numbers are inserted into the limit setting procedure. For each set of cuts on the variables N_{Jets}, N_{bJets}, E_T^{miss} and H_T, a lower mass limit is obtained.

First, the cuts on E_T^{miss} and N_{bJets} were fixed to $E_T^{\text{miss}} \geq 40\,\text{GeV}$ and $N_{\text{bJets}} \geq 1$ and the cuts on H_T and N_{Jets} were varied in the ranges $H_T \in [350, 800]$ GeV and $N_{\text{Jets}} \in [2, 5]$. The obtained lower limits on the b' mass are presented in Table 6.22. For

H_T [GeV] \ N_{Jets}	≥ 2	≥ 3	≥ 4	≥ 5
≥ 350	—	—	0.693	0.718
≥ 400	0.690	0.696	0.705	0.730
≥ 450	0.706	0.713	0.721	0.738
≥ 500	0.726	0.730	0.734	—
≥ 550	0.741	0.744	0.746	—
≥ 600	0.757	0.761	0.763	—
≥ 650	0.767	0.773	0.772	—
≥ 700	0.778	—	—	—
≥ 750	0.785	—	—	—
≥ 800	0.783	—	—	—

Table 6.22: Expected lower b' mass limits in TeV assuming $b' \to tW$ for several combinations of cuts on N_{Jets} and H_T. Besides the basic selection summarised in Table 6.15, the cuts on E_T^{miss} and N_{bJets} were fixed to $E_T^{\text{miss}} \geq 40\,\text{GeV}$ and $N_{\text{bJets}} \geq 1$.
The result for the basic selection is presented in blue, whereas the red number shows the expected limit for the final event selection.

the basic selection, that was also used in the analysis of the 2011 data ($\mathcal{L} = 4.7\,\text{fb}^{-1}$, $\sqrt{s} = 7\,\text{TeV}$) presented in reference [98], where a mass limit of $m_{b'} \geq 0.67\,\text{TeV}$ (expected $m_{b'} \geq 0.64\,\text{TeV}$) has been set, an expected mass limit of $m_{b'} \geq 0.74\,\text{TeV}$ is obtained here. Hence, the improvement would be only about $\sim 70\,\text{GeV}$. For lower cut values on H_T the expected mass limits drop down. Even when increasing the cut on N_{Jets} there is no improvement for lower cuts on H_T.
In general one can see, that by increasing the cut value on N_{Jets}, the mass limit only slightly improves, whereas there are significant enhancements of the mass limits when raising the cut value on H_T.
Finally, it was decided (also as selection for the other considered signal processes in reference [250]) to choose the cuts of $H_T \geq 650\,\text{GeV}$ and $N_{\text{Jets}} \geq 2$ with an expected limit of $m_{b'} \geq 0.767\,\text{TeV}$. Although higher cut values for H_T and N_{Jets} result in higher mass limits, the background expectations become too low in order to give a trustable estimate in the end. Furthermore, this selection revealed optimal results among all considered signal processes in reference [250]. The total expected background and signal ($b' \to tW$ with $m_{b'} = 800\,\text{GeV}$) events for some of the cut combinations are presented in Table 6.23.

Cuts	ee	$e\mu$	$\mu\mu$
$H_T \geq 550\,\text{GeV}$, $N_{\text{Jets}} \geq 2$			
• Total background	$4.67 \pm 0.63^{+0.78}_{-0.77}$	$9.03 \pm 0.76^{+1.82}_{-1.42}$	$5.50 \pm 1.71^{+0.93}_{-0.93}$
• Signal $b'(800\,\text{GeV}) \to tW$	$1.11 \pm 0.07^{+0.21}_{-0.16}$	$3.22 \pm 0.12^{+0.59}_{-0.47}$	$1.95 \pm 0.10^{+0.38}_{-0.31}$
$H_T \geq 650\,\text{GeV}$, $N_{\text{Jets}} \geq 2$			
• Total background	$2.65 \pm 0.47^{+0.41}_{-0.41}$	$4.36 \pm 0.48^{+0.84}_{-0.75}$	$2.25 \pm 1.63^{+0.46}_{-0.46}$
• Signal $b'(800\,\text{GeV}) \to tW$	$1.09 \pm 0.07^{+0.20}_{-0.16}$	$3.08 \pm 0.12^{+0.56}_{-0.45}$	$1.89 \pm 0.09^{+0.37}_{-0.30}$
$H_T \geq 700\,\text{GeV}$, $N_{\text{Jets}} \geq 2$			
• Total background	$1.65 \pm 0.33^{+0.26}_{-0.26}$	$3.28 \pm 0.43^{+0.60}_{-0.56}$	$1.86 \pm 1.63^{+0.37}_{-0.37}$
• Signal $b'(800\,\text{GeV}) \to tW$	$1.06 \pm 0.07^{+0.20}_{-0.16}$	$3.03 \pm 0.12^{+0.55}_{-0.44}$	$1.86 \pm 0.09^{+0.36}_{-0.30}$
$H_T \geq 750\,\text{GeV}$, $N_{\text{Jets}} \geq 2$			
• Total background	$1.17 \pm 0.30^{+0.21}_{-0.20}$	$2.83 \pm 0.38^{+0.49}_{-0.44}$	$1.39 \pm 1.63^{+0.27}_{-0.27}$
• Signal $b'(800\,\text{GeV}) \to tW$	$1.03 \pm 0.07^{+0.19}_{-0.15}$	$2.95 \pm 0.11^{+0.54}_{-0.43}$	$1.82 \pm 0.09^{+0.36}_{-0.29}$
$H_T \geq 650\,\text{GeV}$, $N_{\text{Jets}} \geq 3$			
• Total background	$2.39 \pm 0.44^{+0.39}_{-0.38}$	$3.93 \pm 0.45^{+0.71}_{-0.69}$	$2.09 \pm 1.63^{+0.44}_{-0.44}$
• Signal $b'(800\,\text{GeV}) \to tW$	$1.08 \pm 0.07^{+0.20}_{-0.16}$	$3.06 \pm 0.12^{+0.56}_{-0.45}$	$1.88 \pm 0.09^{+0.37}_{-0.30}$

Table 6.23: Expected number of events for specific sets of cuts, that yield in optimal b' mass limits. The presented numbers are shown for the $b' \to tW$ sample with $m_{b'} = 800\,\text{GeV}$ and the total sum of the various backgrounds.

In addition to above presented variations of the cuts on H_T and N_{Jets}, it was also tried to vary the cuts on the variables N_{bJets} and E_T^{miss}. The corresponding results, which are summarised in Appendix B.2.2, revealed no improvement in the mass limit. It should be noted, that if one would optimise the selection for the $b' \to qW$ scenario, removing the cut on N_{bJets} should reveal a significant effect, because there are no b-jets expected in the topology of the decay $b' \to u/c + W$.

In summary, the optimal cut combination was found to be $H_T \geq 650\,\text{GeV}$, $E_T^{\text{miss}} \geq 40\,\text{GeV}$, $N_{\text{Jets}} \geq 2$ and $N_{\text{bJets}} \geq 1$, which is also summarised in Table 6.24 and will be referred to as 'final event selection' and 'signal region' in the following. Compared to the default selection, where the selection efficiencies have been shown in Tables 6.16, 6.17 and 6.18, only the cut on H_T has changed from 550 GeV to 650 GeV. Therefore, for comparison, the resulting selection efficiencies for the H_T cut in the default and final event selections are listed in Tables 6.25, 6.26 and 6.27 for the ee, $e\mu$ and $\mu\mu$ channel, respectively. In addition, the total selection efficiency, given by the number of selected events after applying all cuts of the final event selection divided by the number of generated events (in case of the backgrounds estimated on data it is given with respect to the number of analysed data events) is presented. Only a small impact on the signal ($b' \to tW$ with $m_{b'} = 800\,\text{GeV}$) can be seen, where the selection efficiencies are reduced

Selection	Criterion
Basic	Table 6.15
N_{Jets}	≥ 2
N_{bJets}	≥ 1
E_T^{miss}	$\geq 40\,\text{GeV}$
H_T	$\geq 650\,\text{GeV}$

Table 6.24: Summary of the final event selection criteria.

	Default selection		Final selection	
Process	$H_T \geq 550\,\text{GeV}$	ϵ_{tot}	$H_T \geq 650\,\text{GeV}$	ϵ_{tot}
$b'(800\,\text{GeV}) \to tW$	$0.988^{+0.005}_{-0.008}$	$0.0037^{+0.0002}_{-0.0002}$	$0.972^{+0.008}_{-0.010}$	$0.0037^{+0.0002}_{-0.0002}$
$t\bar{t}+W$+jets	$0.35^{+0.01}_{-0.01}$	$\left(34.4^{+1.8}_{-1.7}\right)\cdot 10^{-5}$	$0.22^{+0.01}_{-0.01}$	$\left(21.0^{+1.4}_{-1.3}\right)\cdot 10^{-5}$
$t\bar{t}+Z$+jets	$0.33^{+0.02}_{-0.02}$	$\left(116.7^{+11.0}_{-9.8}\right)\cdot 10^{-6}$	$0.19^{+0.02}_{-0.02}$	$\left(66.5^{+8.3}_{-7.4}\right)\cdot 10^{-6}$
$t\bar{t}+WW$	$0.51^{+0.03}_{-0.03}$	$\left(100.1^{+7.5}_{-7.0}\right)\cdot 10^{-5}$	$0.39^{+0.03}_{-0.03}$	$\left(76.0^{+6.6}_{-6.1}\right)\cdot 10^{-5}$
WZ/ZZ+jets	$0.12^{+0.07}_{-0.05}$	$\left(13.0^{+7.9}_{-5.2}\right)\cdot 10^{-7}$	$0.11^{+0.07}_{-0.05}$	$\left(11.6^{+7.6}_{-4.9}\right)\cdot 10^{-7}$
$W^{\pm}W^{\pm}$+jets	$0.3^{+0.1}_{-0.1}$	$\left(3.2^{+1.8}_{-1.2}\right)\cdot 10^{-5}$	$0.3^{+0.1}_{-0.1}$	$\left(3.2^{+1.8}_{-1.2}\right)\cdot 10^{-5}$
Lepton fakes	$0.09^{+0.12}_{-0.06}$	$\left(3.3^{+5.2}_{-2.3}\right)\cdot 10^{-9}$	$0.05^{+0.11}_{-0.04}$	$\left(1.7^{+4.6}_{-1.5}\right)\cdot 10^{-9}$
Charge mis-id	$0.07^{+0.12}_{-0.05}$	$\left(2.6^{+4.9}_{-2.0}\right)\cdot 10^{-9}$	$0.03^{+0.11}_{-0.03}$	$\left(1.4^{+4.8}_{-1.3}\right)\cdot 10^{-9}$

Table 6.25: Comparison of the cut efficiencies for the default (Table 6.19) and final (Table 6.24) event selection in the *ee* channel. Presented are the efficiencies for the cut on H_T ($H_T \geq 550\,\text{GeV}$ and $H_T \geq 550\,\text{GeV}$), which are defined as $\epsilon_i = n_i/n_{i-1}$, where n_i and n_{i-1} denote the number of events after and before the cut, respectively. Upper and lower limits at 68% confidence on the efficiencies have been calculated with the method described in Section 6.4.1. In addition, the total selection efficiency (ϵ_{tot}) is shown, which is given with respect to the total number of generated events (in case of the lepton fakes and charge mis-id with respect to the number of analysed data events). The results are shown for the $b' \to tW$ ($m_{b'} = 800\,\text{GeV}$) sample and the various backgrounds.

	Default selection		Final selection	
Process	$H_T \geq 550\,\text{GeV}$	ϵ_{tot}	$H_T \geq 650\,\text{GeV}$	ϵ_{tot}
$b'(800\,\text{GeV}) \to tW$	$0.979^{+0.004}_{-0.005}$	$0.0108^{+0.0003}_{-0.0003}$	$0.935^{+0.007}_{-0.007}$	$0.0103^{+0.0003}_{-0.0003}$
$t\bar{t} + W$+jets	$0.340^{+0.008}_{-0.008}$	$\left(113.9^{+3.1}_{-3.1}\right) \cdot 10^{-5}$	$0.212^{+0.007}_{-0.007}$	$\left(70.9^{+2.5}_{-2.4}\right) \cdot 10^{-5}$
$t\bar{t} + Z$+jets	$0.36^{+0.01}_{-0.01}$	$\left(41.4^{+1.9}_{-1.8}\right) \cdot 10^{-5}$	$0.22^{+0.01}_{-0.01}$	$\left(25.7^{+1.5}_{-1.5}\right) \cdot 10^{-5}$
$t\bar{t} + WW$	$0.52^{+0.01}_{-0.01}$	$0.0035^{+0.0001}_{-0.0001}$	$0.35^{+0.01}_{-0.01}$	$0.0023^{+0.0001}_{-0.0001}$
WZ/ZZ+jets	$0.13^{+0.03}_{-0.03}$	$\left(4.0^{+1.2}_{-0.9}\right) \cdot 10^{-6}$	$0.04^{+0.02}_{-0.02}$	$\left(13.9^{+8.0}_{-5.4}\right) \cdot 10^{-7}$
$W^{\pm}W^{\pm}$+jets	$0.32^{+0.08}_{-0.07}$	$\left(8.6^{+2.6}_{-2.1}\right) \cdot 10^{-5}$	$0.22^{+0.07}_{-0.06}$	$\left(5.9^{+2.3}_{-1.7}\right) \cdot 10^{-5}$
Lepton fakes	$0.04^{+0.05}_{-0.03}$	$\left(3.6^{+5.3}_{-2.4}\right) \cdot 10^{-9}$	$0.005^{+0.041}_{-0.005}$	$\left(4.4^{+40.0}_{-4.4}\right) \cdot 10^{-10}$
Charge mis-id	$0.05^{+0.08}_{-0.04}$	$\left(3.1^{+5.1}_{-2.2}\right) \cdot 10^{-9}$	$0.03^{+0.08}_{-0.03}$	$\left(2.0^{+5.1}_{-1.7}\right) \cdot 10^{-9}$

Table 6.26: Comparison of the cut efficiencies for the default (Table 6.19) and final (Table 6.24) event selection in the $e\mu$ channel. Presented are the efficiencies for the cut on H_T ($H_T \geq 550\,\text{GeV}$ and $H_T \geq 550\,\text{GeV}$), which are defined as $\epsilon_i = n_i/n_{i-1}$, where n_i and n_{i-1} denote the number of events after and before the cut, respectively. Upper and lower limits at 68% confidence on the efficiencies have been calculated with the method described in Section 6.4.1. In addition, the total selection efficiency (ϵ_{tot}) is shown, which is given with respect to the total number of generated events (in case of the lepton fakes and charge mis-id with respect to the number of analysed data events). The results are shown for the $b' \to tW$ ($m_{b'} = 800\,\text{GeV}$) sample and the various backgrounds.

	Default selection		Final selection	
Process	$H_T \geq 550\,\text{GeV}$	ϵ_{tot}	$H_T \geq 650\,\text{GeV}$	ϵ_{tot}
$b'(800\,\text{GeV}) \to tW$	$0.984^{+0.004}_{-0.006}$	$0.0066^{+0.0002}_{-0.0002}$	$0.954^{+0.007}_{-0.009}$	$0.0064^{+0.0002}_{-0.0002}$
$t\bar{t} + W$+jets	$0.334^{+0.009}_{-0.009}$	$\left(75.2^{+2.6}_{-2.5}\right) \cdot 10^{-5}$	$0.213^{+0.008}_{-0.008}$	$\left(47.9^{+2.1}_{-2.0}\right) \cdot 10^{-5}$
$t\bar{t} + Z$+jets	$0.35^{+0.02}_{-0.02}$	$\left(18.9^{+1.3}_{-1.2}\right) \cdot 10^{-5}$	$0.22^{+0.02}_{-0.02}$	$\left(12.0^{+1.1}_{-0.9}\right) \cdot 10^{-5}$
$t\bar{t} + WW$	$0.53^{+0.02}_{-0.02}$	$0.0024^{+0.0001}_{-0.0001}$	$0.39^{+0.02}_{-0.02}$	$\left(176.5^{+9.8}_{-9.3}\right) \cdot 10^{-5}$
WZ/ZZ+jets	$0.18^{+0.05}_{-0.04}$	$\left(3.5^{+1.1}_{-0.9}\right) \cdot 10^{-6}$	$0.08^{+0.04}_{-0.03}$	$\left(16.0^{+8.4}_{-5.8}\right) \cdot 10^{-7}$
$W^{\pm}W^{\pm}$+jets	$0.28^{+0.09}_{-0.08}$	$\left(5.3^{+2.2}_{-1.6}\right) \cdot 10^{-5}$	$0.23^{+0.09}_{-0.07}$	$\left(4.4^{+2.1}_{-1.5}\right) \cdot 10^{-5}$
Lepton fakes	$0.07^{+0.09}_{-0.05}$	$\left(3.5^{+5.2}_{-2.4}\right) \cdot 10^{-9}$	0	0

Table 6.27: Comparison of the cut efficiencies for the default (Table 6.19) and final (Table 6.24) event selection in the $\mu\mu$ channel. Presented are the efficiencies for the cut on H_T ($H_T \geq 550\,\text{GeV}$ and $H_T \geq 550\,\text{GeV}$), which are defined as $\epsilon_i = n_i/n_{i-1}$, where n_i and n_{i-1} denote the number of events after and before the cut, respectively. Upper and lower limits at 68% confidence on the efficiencies have been calculated with the method described in Section 6.4.1. In addition, the total selection efficiency (ϵ_{tot}) is shown, which is given with respect to the total number of generated events (in case of the lepton fakes and charge mis-id with respect to the number of analysed data events). The results are shown for the $b' \to tW$ ($m_{b'} = 800\,\text{GeV}$) sample and the various backgrounds.

by absolute values between −2% and −4%. The $t\bar{t}$ backgrounds with associated vector boson production experience a larger reduction by values of −12% to −17%. The change on the selection efficiencies for the diboson, lepton fakes and charge mis-id backgrounds lies between −2% and −10%.

The obtained distributions of the upper cross-section limits as a function of the b' mass are depicted in Figure 6.27 for the default selection used in the analysis of reference [98] and the final selection of this analysis. As already mentioned, the intersection between the curves of the cross-section limit and the theoretical cross-section prediction yields in the obtained lower limit on the b' mass.

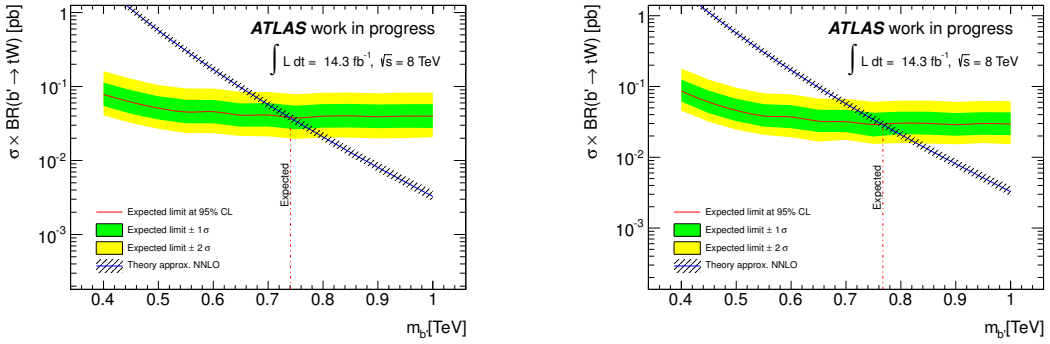

(a) $m_{b'} \geq 741\,\text{GeV}$ (b) $m_{b'} \geq 767\,\text{GeV}$

Figure 6.27: Expected cross-section limits as a function of the b' mass assuming a branching fraction of 100% for $b' \to tW$. Figure (a) depicts the expected limits for the default selection with $H_T \geq 550\,\text{GeV}$, whereas the expected limits for the final selection with $H_T \geq 650\,\text{GeV}$ are presented in Figure (b). In both cases the basic selection was applied (Table 6.15), together with the requirements $N_{\text{Jets}} \geq 2$, $N_{\text{bJets}} \geq 1$ and $E_T^{\text{miss}} \geq 40\,\text{GeV}$.

6.8 Observed data and estimates for the signal and background processes

In the following, I will present the observed data and the expectations for signal and background, which were obtained for the final event selection summarised in Table 6.24. Furthermore, I will present studies for the validation of the fast simulation of the signal samples (Section 6.8.1.1) and the various background estimates (Section 6.8.2.1). Finally, I will summarise the estimated systematic uncertainties on the object scales, resolutions and efficiency scale factors for the final event selection (Section 6.8.4).
The statistical interpretation of the observed data will then be presented in Section 6.9.

6.8.1 Signal estimates

The expected signal event yields obtained separately for the ee, $e\mu$ and $\mu\mu$ channel after the final selection (Table 6.24) are presented in Tables 6.28 and 6.29 for the $b' \to tW$ and $b' \to qW$ samples, respectively. For increasing masses the event yields decrease

Process	ee	$e\mu$	$\mu\mu$
$b'(400\,\text{GeV}) \to tW$	$37.06 \pm 4.22^{+6.20}_{-6.47}$	$126.7 \pm 7.6^{+21.0}_{-20.8}$	$81.07 \pm 6.32^{+13.98}_{-15.34}$
$b'(450\,\text{GeV}) \to tW$	$28.64 \pm 2.63^{+5.21}_{-5.01}$	$86.76 \pm 4.62^{+14.64}_{-13.22}$	$53.38 \pm 3.55^{+9.64}_{-9.56}$
$b'(500\,\text{GeV}) \to tW$	$19.49 \pm 1.56^{+3.28}_{-3.14}$	$61.09 \pm 2.80^{+9.75}_{-9.72}$	$32.07 \pm 2.03^{+5.66}_{-5.34}$
$b'(550\,\text{GeV}) \to tW$	$11.35 \pm 0.84^{+2.06}_{-1.74}$	$36.72 \pm 1.58^{+6.00}_{-5.45}$	$22.09 \pm 1.24^{+3.89}_{-3.37}$
$b'(600\,\text{GeV}) \to tW$	$7.21 \pm 0.50^{+1.20}_{-1.01}$	$20.00 \pm 0.85^{+3.29}_{-2.81}$	$12.92 \pm 0.69^{+2.29}_{-1.99}$
$b'(650\,\text{GeV}) \to tW$	$4.81 \pm 0.31^{+0.86}_{-0.74}$	$13.73 \pm 0.55^{+2.31}_{-2.00}$	$8.15 \pm 0.42^{+1.47}_{-1.26}$
$b'(700\,\text{GeV}) \to tW$	$2.77 \pm 0.20^{+0.49}_{-0.39}$	$8.28 \pm 0.34^{+1.42}_{-1.21}$	$4.72 \pm 0.26^{+0.87}_{-0.74}$
$b'(750\,\text{GeV}) \to tW$	$1.99 \pm 0.12^{+0.36}_{-0.30}$	$5.19 \pm 0.20^{+0.91}_{-0.76}$	$3.27 \pm 0.16^{+0.62}_{-0.52}$
$b'(800\,\text{GeV}) \to tW$	$1.09 \pm 0.07^{+0.20}_{-0.16}$	$3.08 \pm 0.12^{+0.56}_{-0.45}$	$1.89 \pm 0.09^{+0.37}_{-0.30}$
$b'(850\,\text{GeV}) \to tW$	$0.68 \pm 0.04^{+0.13}_{-0.11}$	$1.90 \pm 0.07^{+0.37}_{-0.29}$	$1.19 \pm 0.06^{+0.25}_{-0.20}$
$b'(900\,\text{GeV}) \to tW$	$0.49 \pm 0.03^{+0.10}_{-0.08}$	$1.23 \pm 0.05^{+0.25}_{-0.19}$	$0.74 \pm 0.04^{+0.16}_{-0.13}$
$b'(950\,\text{GeV}) \to tW$	$0.27 \pm 0.02^{+0.06}_{-0.04}$	$0.77 \pm 0.03^{+0.16}_{-0.12}$	$0.48 \pm 0.02^{+0.11}_{-0.08}$
$b'(1000\,\text{GeV}) \to tW$	$0.16 \pm 0.01^{+0.04}_{-0.03}$	$0.52 \pm 0.02^{+0.12}_{-0.08}$	$0.29 \pm 0.01^{+0.07}_{-0.05}$

Table 6.28: Expected number of signal events for the $b' \to tW$ samples after the final event selection. For each event yield, the statistical (first) and total upward and downward systematic uncertainties (second) are presented. A detailed summary of the estimated systematics is given in Section 6.8.4.

due to the lower cross sections. Overall, the $b' \to tW$ yields are higher compared to the $b' \to qW$ yields. This comes from the fact that the $b' \to qW$ samples were generated with equal branching fractions of 1/3 for the decay modes into uW, cW and tW. From the pair produced b' quarks at least one must decay into $b' \to tW$ in order to achieve a same-sign dilepton signature (neglecting the non-isolated leptons coming from hadron decays formed of the c or u quark) and the requirement of $N_{\text{bJets}} \geq 1$ suppresses events with the decay $b' \to u/c + W$. Therefore, the yields are smaller in case of the $b' \to qW$ samples.

When dividing the number of selected events by the number of generated events, one obtains the total selection efficiencies as presented in Tables 6.30 and 6.31 for the $b' \to tW$ and $b' \to qW$ samples, respectively. With increasing b' mass the selection efficiencies become larger. This comes from the fact that the decay products of the b' quarks (leptons and jets) carry larger momenta and hence have a higher probability to pass the object and event selection criteria. Overall, the selection efficiencies are at maximum of the order of 1%.

Process	ee	$e\mu$	$\mu\mu$
$b'(400\,\text{GeV}) \to qW$	$7.83 \pm 1.63^{+1.40}_{-1.26}$	$27.12 \pm 3.32^{+5.99}_{-4.20}$	$19.85 \pm 2.73^{+3.53}_{-3.19}$
$b'(450\,\text{GeV}) \to qW$	$4.74 \pm 0.79^{+0.97}_{-0.80}$	$21.95 \pm 2.20^{+3.51}_{-3.29}$	$13.11 \pm 1.50^{+2.56}_{-2.34}$
$b'(500\,\text{GeV}) \to qW$	$4.11 \pm 0.57^{+1.12}_{-0.80}$	$14.86 \pm 1.24^{+2.64}_{-2.50}$	$10.15 \pm 1.14^{+1.81}_{-1.69}$
$b'(550\,\text{GeV}) \to qW$	$3.05 \pm 0.41^{+0.53}_{-0.48}$	$10.19 \pm 0.71^{+1.74}_{-1.65}$	$5.97 \pm 0.54^{+1.12}_{-1.00}$
$b'(600\,\text{GeV}) \to qW$	$2.24 \pm 0.26^{+0.40}_{-0.34}$	$6.07 \pm 0.42^{+1.02}_{-0.88}$	$3.46 \pm 0.32^{+0.65}_{-0.60}$
$b'(650\,\text{GeV}) \to qW$	$1.21 \pm 0.14^{+0.22}_{-0.20}$	$3.58 \pm 0.24^{+0.63}_{-0.57}$	$2.43 \pm 0.20^{+0.47}_{-0.43}$
$b'(700\,\text{GeV}) \to qW$	$0.83 \pm 0.09^{+0.16}_{-0.13}$	$2.43 \pm 0.16^{+0.43}_{-0.36}$	$1.44 \pm 0.12^{+0.29}_{-0.25}$
$b'(750\,\text{GeV}) \to qW$	$0.43 \pm 0.05^{+0.09}_{-0.08}$	$1.37 \pm 0.09^{+0.25}_{-0.20}$	$0.90 \pm 0.07^{+0.18}_{-0.15}$
$b'(800\,\text{GeV}) \to qW$	$0.38 \pm 0.04^{+0.07}_{-0.06}$	$0.95 \pm 0.06^{+0.18}_{-0.15}$	$0.57 \pm 0.05^{+0.11}_{-0.09}$
$b'(850\,\text{GeV}) \to qW$	$0.21 \pm 0.02^{+0.04}_{-0.03}$	$0.57 \pm 0.04^{+0.11}_{-0.09}$	$0.34 \pm 0.03^{+0.07}_{-0.06}$
$b'(900\,\text{GeV}) \to qW$	$0.12 \pm 0.01^{+0.02}_{-0.02}$	$0.38 \pm 0.02^{+0.08}_{-0.06}$	$0.24 \pm 0.02^{+0.05}_{-0.04}$
$b'(950\,\text{GeV}) \to qW$	$0.09 \pm 0.01^{+0.02}_{-0.01}$	$0.25 \pm 0.02^{+0.05}_{-0.04}$	$0.15 \pm 0.01^{+0.03}_{-0.03}$
$b'(1000\,\text{GeV}) \to qW$	$0.048 \pm 0.005^{+0.011}_{-0.008}$	$0.146 \pm 0.009^{+0.034}_{-0.025}$	$0.092 \pm 0.007^{+0.022}_{-0.017}$

Table 6.29: Expected number of signal events for the $b' \to qW$ ($q = u, c, t$ with equal branching fractions of 1/3) samples after the final event selection. For each event yield, the statistical (first) and total upward and downward systematic uncertainties (second) are presented. A detailed summary of the estimated systematics is given in Section 6.8.4.

Process	ee	$e\mu$	$\mu\mu$
$b'(400\,\text{GeV}) \to tW$	$0.0011^{+0.0001}_{-0.0001}$	$0.0039^{+0.0002}_{-0.0002}$	$0.0025^{+0.0002}_{-0.0001}$
$b'(450\,\text{GeV}) \to tW$	$0.0018^{+0.0001}_{-0.0001}$	$0.0054^{+0.0002}_{-0.0002}$	$0.0033^{+0.0002}_{-0.0002}$
$b'(500\,\text{GeV}) \to tW$	$0.0024^{+0.0001}_{-0.0001}$	$0.0075^{+0.0003}_{-0.0002}$	$0.0039^{+0.0002}_{-0.0002}$
$b'(550\,\text{GeV}) \to tW$	$0.0026^{+0.0002}_{-0.0001}$	$0.0084^{+0.0003}_{-0.0003}$	$0.0050^{+0.0002}_{-0.0002}$
$b'(600\,\text{GeV}) \to tW$	$0.0030^{+0.0002}_{-0.0002}$	$0.0082^{+0.0003}_{-0.0003}$	$0.0053^{+0.0002}_{-0.0002}$
$b'(650\,\text{GeV}) \to tW$	$0.0035^{+0.0002}_{-0.0002}$	$0.0099^{+0.0003}_{-0.0003}$	$0.0059^{+0.0002}_{-0.0002}$
$b'(700\,\text{GeV}) \to tW$	$0.0034^{+0.0002}_{-0.0002}$	$0.0102^{+0.0003}_{-0.0003}$	$0.0058^{+0.0002}_{-0.0002}$
$b'(750\,\text{GeV}) \to tW$	$0.0041^{+0.0002}_{-0.0002}$	$0.0106^{+0.0003}_{-0.0003}$	$0.0067^{+0.0002}_{-0.0002}$
$b'(800\,\text{GeV}) \to tW$	$0.0037^{+0.0002}_{-0.0002}$	$0.0103^{+0.0003}_{-0.0003}$	$0.0064^{+0.0002}_{-0.0002}$
$b'(850\,\text{GeV}) \to tW$	$0.0037^{+0.0002}_{-0.0002}$	$0.0103^{+0.0003}_{-0.0003}$	$0.0065^{+0.0002}_{-0.0002}$
$b'(900\,\text{GeV}) \to tW$	$0.0043^{+0.0002}_{-0.0002}$	$0.0107^{+0.0003}_{-0.0003}$	$0.0064^{+0.0002}_{-0.0002}$
$b'(950\,\text{GeV}) \to tW$	$0.0036^{+0.0002}_{-0.0002}$	$0.0106^{+0.0003}_{-0.0003}$	$0.0066^{+0.0002}_{-0.0002}$
$b'(1000\,\text{GeV}) \to tW$	$0.0035^{+0.0002}_{-0.0002}$	$0.0111^{+0.0003}_{-0.0003}$	$0.0063^{+0.0002}_{-0.0002}$

Table 6.30: Total selection efficiencies for the $b' \to tW$ samples when applying the final event selection. The limits on these efficiencies have been determined with the method described in Section 6.4.1.

6.8.1.1 Validation of the signal samples with fast detector simulation

As already mentioned, the signal samples ($b' \to tW$ and $b' \to qW$) have been produced with the fast detector simulation `ATLFAST-II`. Although there have been already validation studies for the fast detector simulation in general, as presented in Section 4.2.2, I will compare the b' samples used in the analysis with samples generated using the full detector simulation.

In order to save computing resources, the b' samples with masses in the range $m_{b'} \in [400, 1000]$ GeV have been all generated with the fast detector simulation. However, for the mass points $m_{b'} = 500\,\text{GeV}$ and $m_{b'} = 800\,\text{GeV}$ the samples have been additionally produced with the full detector simulation, while using the same generator output. The comparison of the distributions of H_T and N_{Jets} in case of the $b' \to tW$ sample with $m_{b'} = 800\,\text{GeV}$ after applying the final event selection is shown in Figure 6.28 separately for the ee, $e\mu$ and $\mu\mu$ channel. Distributions for additional kinematic variables, as well as the plots for the $b' \to tW$ samples with $m_{b'} = 500\,\text{GeV}$, can be looked up in Appendix C.2.
Overall, the shapes show a reasonable agreement between `ATLFAST-II` and full detector simulation. In addition, also the ratio of the two distributions is presented. One should note that the presented statistical uncertainties on the ratios have been calculated with a simple error propagation for the division. This is of course not correct as the two samples are highly correlated, but a correct treatment was not performed here, because

Process	ee	$e\mu$	$\mu\mu$
$b'(400\,\text{GeV}) \to qW$	$\left(23.8^{+4.3}_{-3.7}\right) \cdot 10^{-5}$	$\left(82.5^{+7.5}_{-6.9}\right) \cdot 10^{-5}$	$\left(60.4^{+6.5}_{-5.9}\right) \cdot 10^{-5}$
$b'(450\,\text{GeV}) \to qW$	$\left(29.7^{+4.8}_{-4.2}\right) \cdot 10^{-5}$	$\left(137.7^{+9.6}_{-9.0}\right) \cdot 10^{-5}$	$\left(82.2^{+7.6}_{-7.0}\right) \cdot 10^{-5}$
$b'(500\,\text{GeV}) \to qW$	$\left(50.3^{+6.3}_{-5.7}\right) \cdot 10^{-5}$	$0.0018^{+0.0001}_{-0.0001}$	$\left(124.2^{+9.6}_{-8.9}\right) \cdot 10^{-5}$
$b'(550\,\text{GeV}) \to qW$	$\left(69.8^{+7.2}_{-6.6}\right) \cdot 10^{-5}$	$0.0023^{+0.0001}_{-0.0001}$	$\left(136.4^{+9.8}_{-9.2}\right) \cdot 10^{-5}$
$b'(600\,\text{GeV}) \to qW$	$\left(92.4^{+8.3}_{-7.6}\right) \cdot 10^{-5}$	$0.0025^{+0.0001}_{-0.0001}$	$0.0014^{+0.0001}_{-0.0001}$
$b'(650\,\text{GeV}) \to qW$	$\left(86.8^{+8.1}_{-7.4}\right) \cdot 10^{-5}$	$0.0026^{+0.0001}_{-0.0001}$	$0.0017^{+0.0001}_{-0.0001}$
$b'(700\,\text{GeV}) \to qW$	$\left(101.3^{+8.8e}_{-8.1}\right) \cdot 10^{-5}$	$0.0030^{+0.0002}_{-0.0001}$	$0.0018^{+0.0001}_{-0.0001}$
$b'(750\,\text{GeV}) \to qW$	$\left(88.4^{+8.2}_{-7.6}\right) \cdot 10^{-5}$	$0.0028^{+0.0001}_{-0.0001}$	$0.0019^{+0.0001}_{-0.0001}$
$b'(800\,\text{GeV}) \to qW$	$\left(125.9^{+9.7}_{-9.1}\right) \cdot 10^{-5}$	$0.0032^{+0.0002}_{-0.0001}$	$0.0019^{+0.0001}_{-0.0001}$
$b'(850\,\text{GeV}) \to qW$	$\left(112.7^{+9.3}_{-8.6}\right) \cdot 10^{-5}$	$0.0031^{+0.0002}_{-0.0001}$	$0.0018^{+0.0001}_{-0.0001}$
$b'(900\,\text{GeV}) \to qW$	$\left(102.0^{+8.9}_{-8.2}\right) \cdot 10^{-5}$	$0.0033^{+0.0002}_{-0.0002}$	$0.0021^{+0.0001}_{-0.0001}$
$b'(950\,\text{GeV}) \to qW$	$\left(118.1^{+9.5e}_{-8.9}\right) \cdot 10^{-5}$	$0.0034^{+0.0002}_{-0.0002}$	$0.0020^{+0.0001}_{-0.0001}$
$b'(1000\,\text{GeV}) \to qW$	$\left(102.1^{+9.0}_{-8.3}\right) \cdot 10^{-5}$	$0.0032^{+0.0002}_{-0.0002}$	$0.0020^{+0.0001}_{-0.0001}$

Table 6.31: Total selection efficiencies for the $b' \to qW$ ($q = u, c, t$ with equal branching fractions of 1/3) samples when applying the final event selection. The limits on these efficiencies have been determined with the method described in Section 6.4.1.

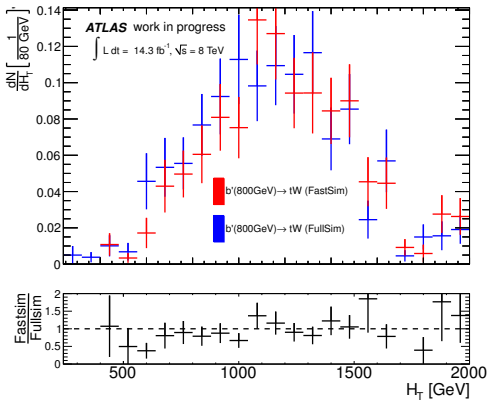

(a) ee: H_T

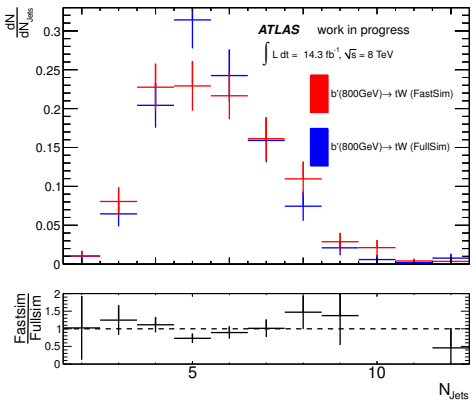

(b) ee: N_{Jets}

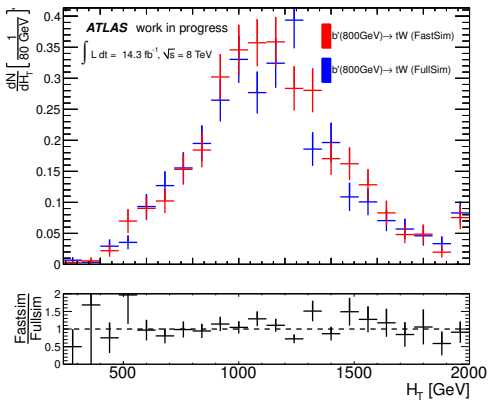

(c) $e\mu$: H_T

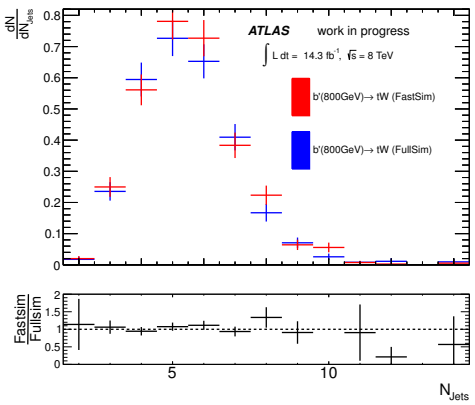

(d) $e\mu$: N_{Jets}

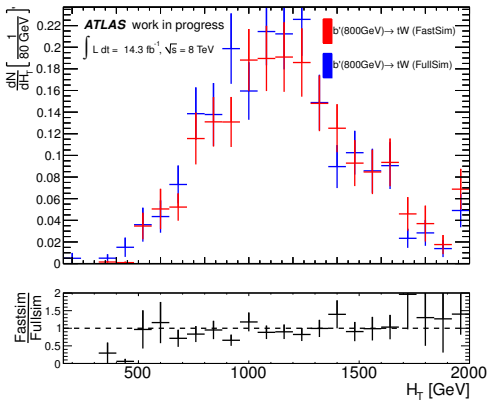

(e) $\mu\mu$: H_T

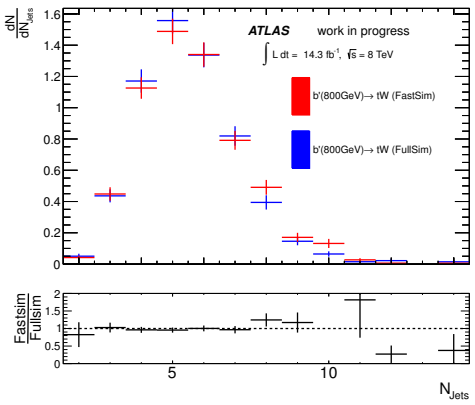

(f) $\mu\mu$: N_{Jets}

Figure 6.28: Comparison of H_T and N_{Jets} distributions in the ee, $e\mu$ and $\mu\mu$ channel after applying the final event selection (Table 6.24) obtained for the $b' \to tW$ ($m_{b'} = 800\,\mathrm{GeV}$) signal samples generated with the fast and full detector simulation. In each plot the cut on the corresponding variable has been removed. Only statistical uncertainties are shown.

this was beyond the scope of this study.

In order to quantify the differences between the fast and full simulated samples, the amount of selected events for the final selection was compared, as reported in Table 6.32. Together with the yields for the fast and full simulated $b' \to tW$ samples with masses

Process	ee	$e\mu$	$\mu\mu$
$b'(800\,\text{GeV}) \to tW$ (FastSim)	1.09 ± 0.07	3.08 ± 0.12	1.89 ± 0.09
$b'(800\,\text{GeV}) \to tW$ (FullSim)	1.11 ± 0.07	2.93 ± 0.12	1.99 ± 0.10
δ	-0.012	$+0.049$	-0.052
$b'(500\,\text{GeV}) \to$ tW (FastSim)	19.49 ± 1.56	61.09 ± 2.80	32.07 ± 2.03
$b'(500\,\text{GeV}) \to$ tW (FullSim)	18.11 ± 1.45	57.08 ± 2.60	30.88 ± 1.92
δ	$+0.071$	$+0.066$	$+0.037$

Table 6.32: Comparison of the yields in the ee, $e\mu$ and $\mu\mu$ channel after the final event selection (Table 6.24) obtained for the $b' \to tW$ signal samples generated with `ATLFAST-II` and full detector simulation. The numbers are presented with the statistical uncertainties for the two mass points (500 GeV and 800 GeV) for which the samples with full simulation were available. In addition the relative difference of the yields is shown.

$m_{b'} = 500\,\text{GeV}$ and $m_{b'} = 800\,\text{GeV}$ in the three channels ee, $e\mu$ and $\mu\mu$, there are also the relative differences shown. At maximum these yield to deviations of 7%, which is small compared to the other systematic uncertainties on the signal MC samples (see also Section 6.8.4). Therefore, this effect was considered as negligible in the analysis of reference [250]. However, in principle one could have considered this effect by including it as systematic uncertainty to the analysis.

6.8.2 Background estimates and observed data

In this section, I will present the observed data and expected background estimates for the final event selection (Section 6.8.2.2). Beforehand, I will present a validation of the background estimation (Section 6.8.2.1). Furthermore, I will show various kinematic distributions for the final signal region selection, in order to get an idea which parameter space is populated by the observed events (Section 6.8.3). Finally, I summarise the systematic uncertainties determined for the final event selection (Section 6.8.4), which will then be considered in the limit calculations.

6.8.2.1 Background validation

In the following, I will present several kinematic distributions for three different control region event selections, which are orthogonal to the final event selection. Before looking into distributions and observed events for the final signal region selection, the data were first compared with the background expectations in these control regions, in order to validate the background estimate. If there is a reasonable agreement in these control

regions, it is expected that the background is also correctly estimated for the signal region selection. Therefore, the definitions of the control region selections have to be as close as possible to the signal region selection, while being orthogonal to it and having only a small contamination of the considered signal process.

The first control region, which was investigated, is called 'low-H_T' control region and the selection criteria are presented in Table 6.33. In comparison to the final event selec-

Selection	Criterion
Basic	Table 6.15
N_{Jets}	≥ 2
N_{bJets}	≥ 1
E_T^{miss}	no cut
H_T	$\in [100, 400]$ GeV

Table 6.33: Summary of the selection criteria of the low-H_T control region.

tion,the cut on the E_T^{miss} is removed and the H_T variable is restricted to the range $[100, 400]$ GeV. Several kinematic distributions are shown for this selection in Figures 6.29, 6.30 and 6.31 for the ee, $e\mu$ and $\mu\mu$ channels, respectively. The presented distributions are namely the total transverse energy sum H_T, the missing transverse energy E_T^{miss}, the number of jets N_{Jets}, the number of b-tagged jets N_{bJets}, the transverse momentum of the leading lepton $p_T^{\text{LeadingLepton}}$ (the lepton with highest p_T in the event) and the transverse momentum of the leading jet $p_T^{\text{LeadingJet}}$. In addition to the background expectations, the contamination of the $b' \to tW$ sample with $m_{b'} = 800\,\text{GeV}$ is plotted. This control region is dominated by the lepton fakes and charge mis-id backgrounds. Overall, all distributions show a reasonable agreement between data and background expectation, the significances of the deviations being below 2σ in all cases. In Table 6.34, the counted event yields for this low-H_T control region selection for the various backgrounds and the observed data are presented. Furthermore the signal contamination is shown. In all three channels, the observed data events are slightly below the total background expectation. However, the expected and observed event yields agree within the uncertainties, reflecting the reasonable agreement in the distributions shown before. As required there is only a negligible signal contamination to this control region selection.

The second control region is called 'low-E_T^{miss}' control region and the selection criteria are summarised in Table 6.35. The cut on E_T^{miss} is inverted compared to the final event selection, which allows to completely remove the requirement on the variable H_T. The corresponding distributions for this selection are reported in Figures 6.32, 6.33 and 6.34.

As for the low-H_T selection, the most dominant backgrounds are the lepton fakes and charge mis-id, and the distributions reveal a similar agreement between data and expectation.

This is also reflected in the counted event yields for data and background expectation, shown in Table 6.36, which agree within the uncertainties. As for the low-H_T control region, the total background yields are slightly above the observed data yields.

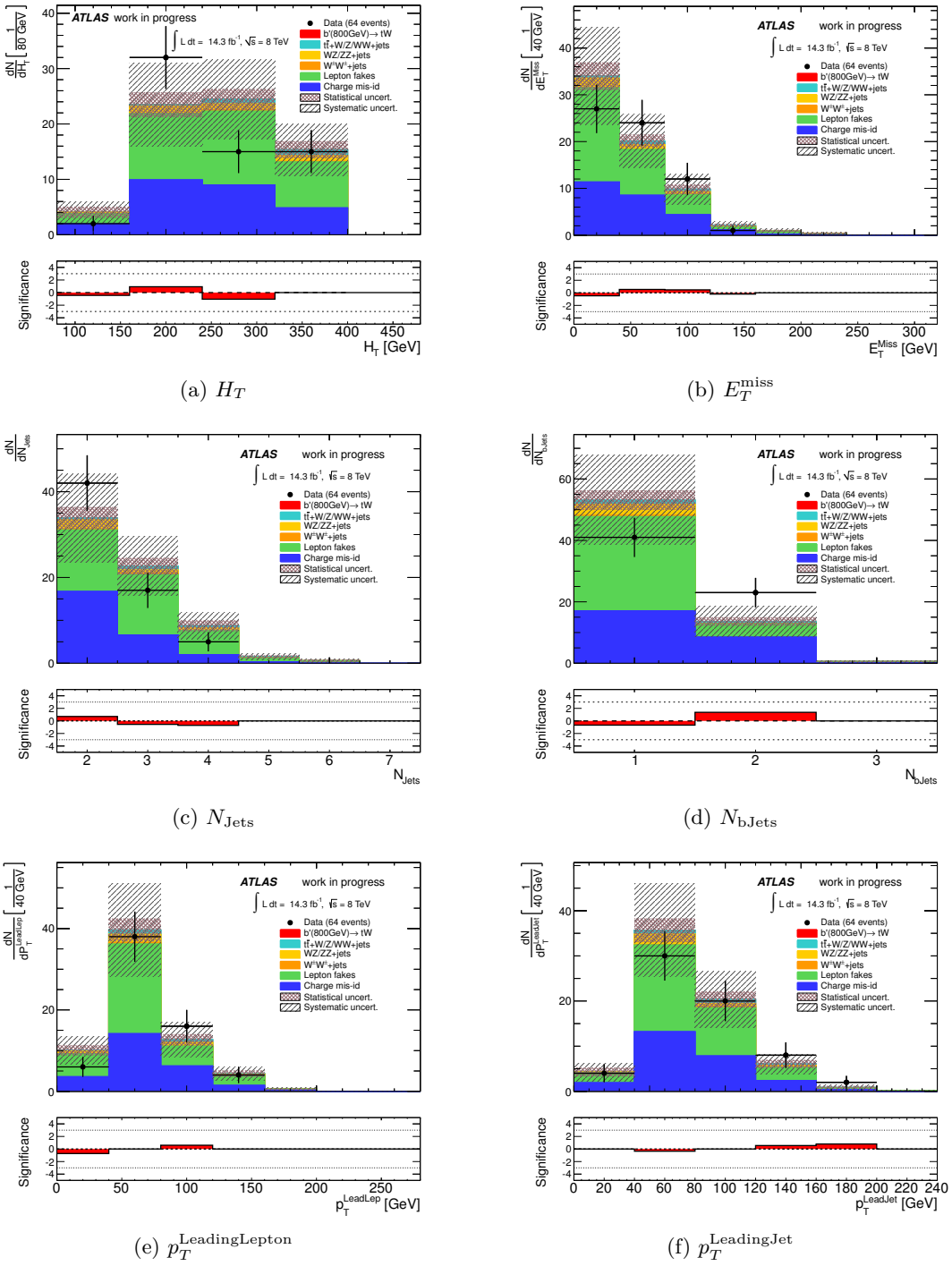

(a) H_T (b) E_T^{miss}

(c) N_{Jets} (d) N_{bJets}

(e) $p_T^{\text{LeadingLepton}}$ (f) $p_T^{\text{LeadingJet}}$

Figure 6.29: Distributions of kinematic variables for the ee channel after the low-H_T (Table 6.33) control region selection for the various backgrounds and the $b' \to tW$ ($m_{b'} = 800\,\text{GeV}$) signal sample. The statistical and systematic uncertainties are represented by the shaded areas and the lower plots depict the significance of the deviations between data and expectation, which has been calculated with the method described in Section 6.4.2.

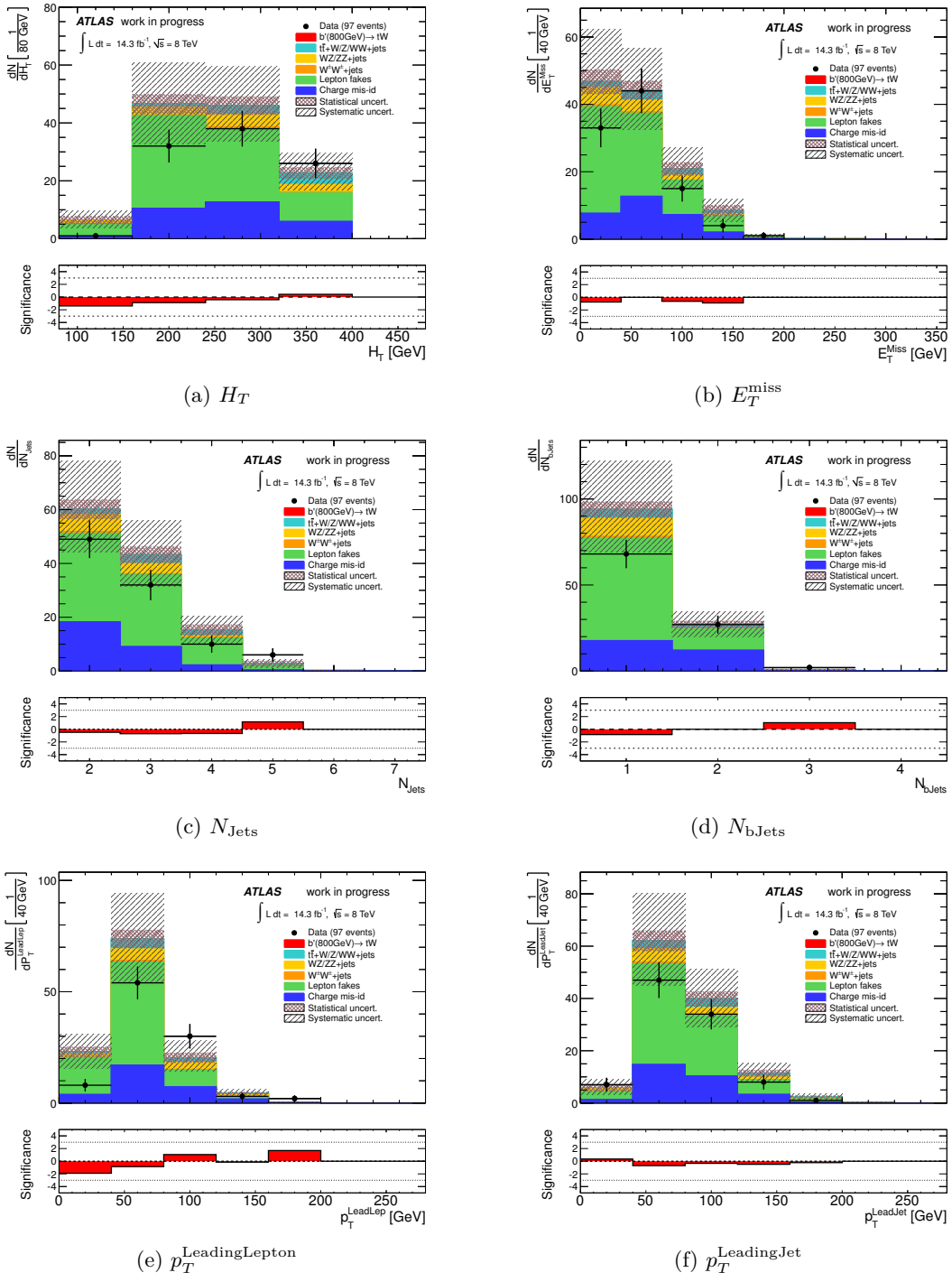

(a) H_T (b) E_T^{miss}

(c) N_{Jets} (d) N_{bJets}

(e) $p_T^{\text{LeadingLepton}}$ (f) $p_T^{\text{LeadingJet}}$

Figure 6.30: Distributions of kinematic variables for the $e\mu$ channel after the low-H_T (Table 6.33) control region selection for the various backgrounds and the $b' \to tW$ ($m_{b'} = 800\,\text{GeV}$) signal sample. The statistical and systematic uncertainties are represented by the shaded areas and the lower plots depict the significance of the deviations between data and expectation, which has been calculated with the method described in Section 6.4.2.

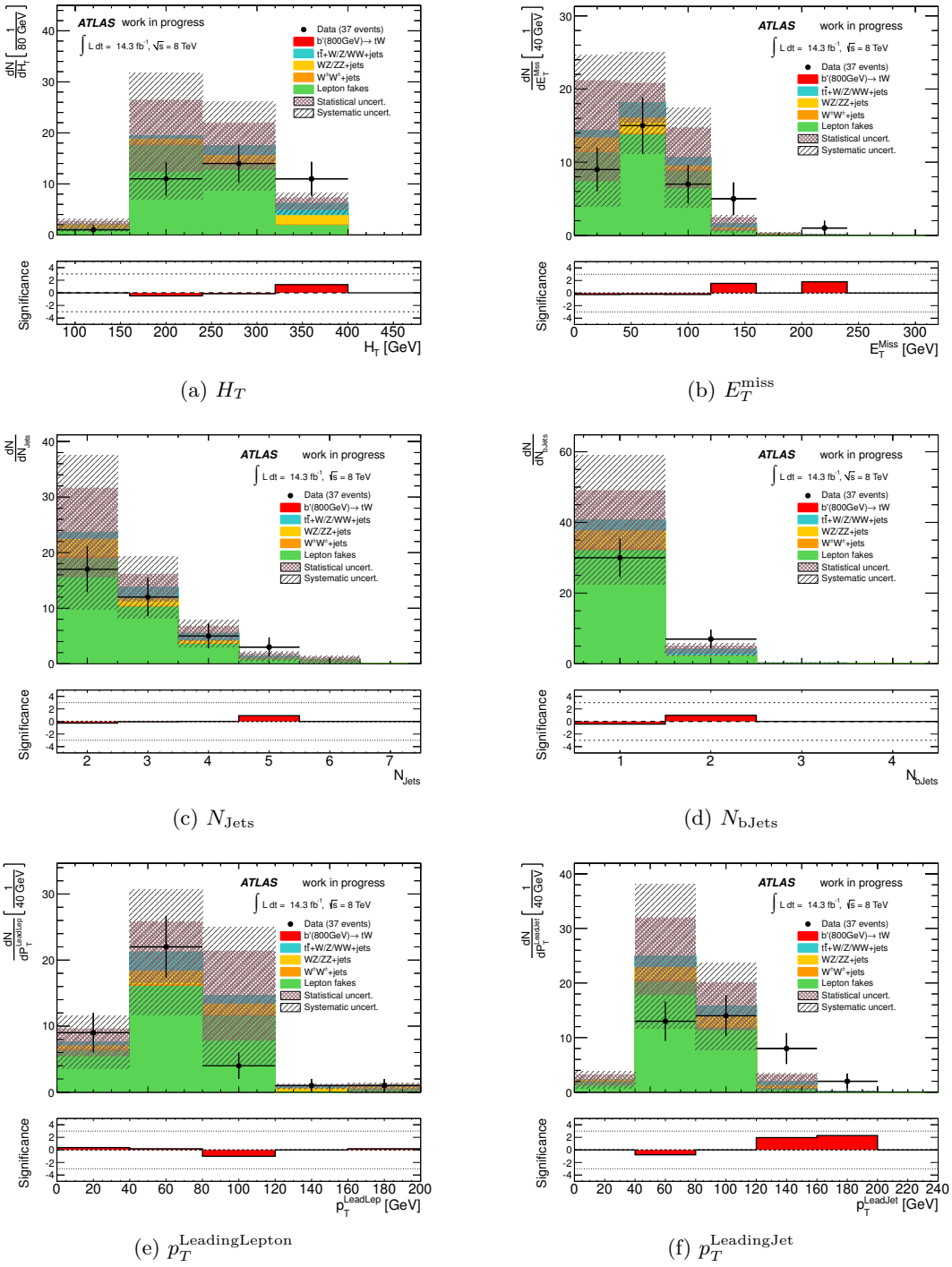

(a) H_T (b) E_T^{miss}

(c) N_{Jets} (d) N_{bJets}

(e) $p_T^{\text{LeadingLepton}}$ (f) $p_T^{\text{LeadingJet}}$

Figure 6.31: Distributions of kinematic variables for the $\mu\mu$ channel after the low-H_T (Table 6.33) control region selection for the various backgrounds and the $b' \to tW$ ($m_{b'} = 800\,\text{GeV}$) signal sample. The statistical and systematic uncertainties are represented by the shaded areas and the lower plots depict the significance of the deviations between data and expectation, which has been calculated with the method described in Section 6.4.2.

Process	ee	$e\mu$	$\mu\mu$
$t\bar{t}+W$+jets	$1.65 \pm 0.10^{+0.56}_{-0.54}$	$6.57 \pm 0.21^{+2.10}_{-2.13}$	$4.30 \pm 0.17^{+1.42}_{-1.42}$
$t\bar{t}+Z$+jets	$0.48 \pm 0.05^{+0.15}_{-0.18}$	$1.50 \pm 0.09^{+0.49}_{-0.50}$	$0.78 \pm 0.06^{+0.27}_{-0.27}$
$t\bar{t}+WW$	$0.011 \pm 0.002^{+0.005}_{-0.003}$	$0.050 \pm 0.004^{+0.019}_{-0.014}$	$0.030 \pm 0.003^{+0.012}_{-0.009}$
WZ/ZZ+jets	$3.72 \pm 0.66^{+1.40}_{-1.35}$	$10.83 \pm 1.21^{+13.72}_{-5.81}$	$5.04 \pm 0.81^{+1.84}_{-1.84}$
$W^{\pm}W^{\pm}$+jets	$0.44 \pm 0.16^{+0.12}_{-0.12}$	$1.18 \pm 0.26^{+0.48}_{-0.39}$	$0.66 \pm 0.17^{+0.22}_{-0.22}$
Lepton fakes	$35.35 \pm 3.34^{+10.60}_{-10.60}$	$71.60 \pm 5.07^{+21.48}_{-21.48}$	$34.06 \pm 8.51^{+10.22}_{-10.22}$
Charge mis-id	$25.66 \pm 0.68^{+9.95}_{-9.74}$	$29.92 \pm 0.64^{+10.54}_{-10.40}$	—
Total background	$67.30 \pm 3.48^{+14.62}_{-14.48}$	$121.6 \pm 5.3^{+27.7}_{-24.7}$	$44.86 \pm 8.63^{+10.48}_{-10.49}$
$b'(800\,\text{GeV}) \to tW$	< 0.003	$0.009 \pm 0.006^{+0.002}_{-0.001}$	$0.002 \pm 0.001^{+0.0003}_{-0.0002}$
Observed	64	97	37

Table 6.34: Expected number of background events and observed number of events for the low-H_T control region selection (Table 6.33). For each event yield, the statistical (first) and total upper and lower systematic uncertainties (second) are presented. Furthermore, the contamination of the $b' \to tW$ ($m_{b'} = 800\,\text{GeV}$) sample is shown.

Selection	Criterion
Basic	Table 6.15
N_{Jets}	≥ 2
N_{bJets}	≥ 1
E_T^{miss}	$E_T^{\text{miss}} < 40\,\text{GeV}$
H_T	no cut

Table 6.35: Summary of the selection criteria of the low-E_T^{miss} control region.

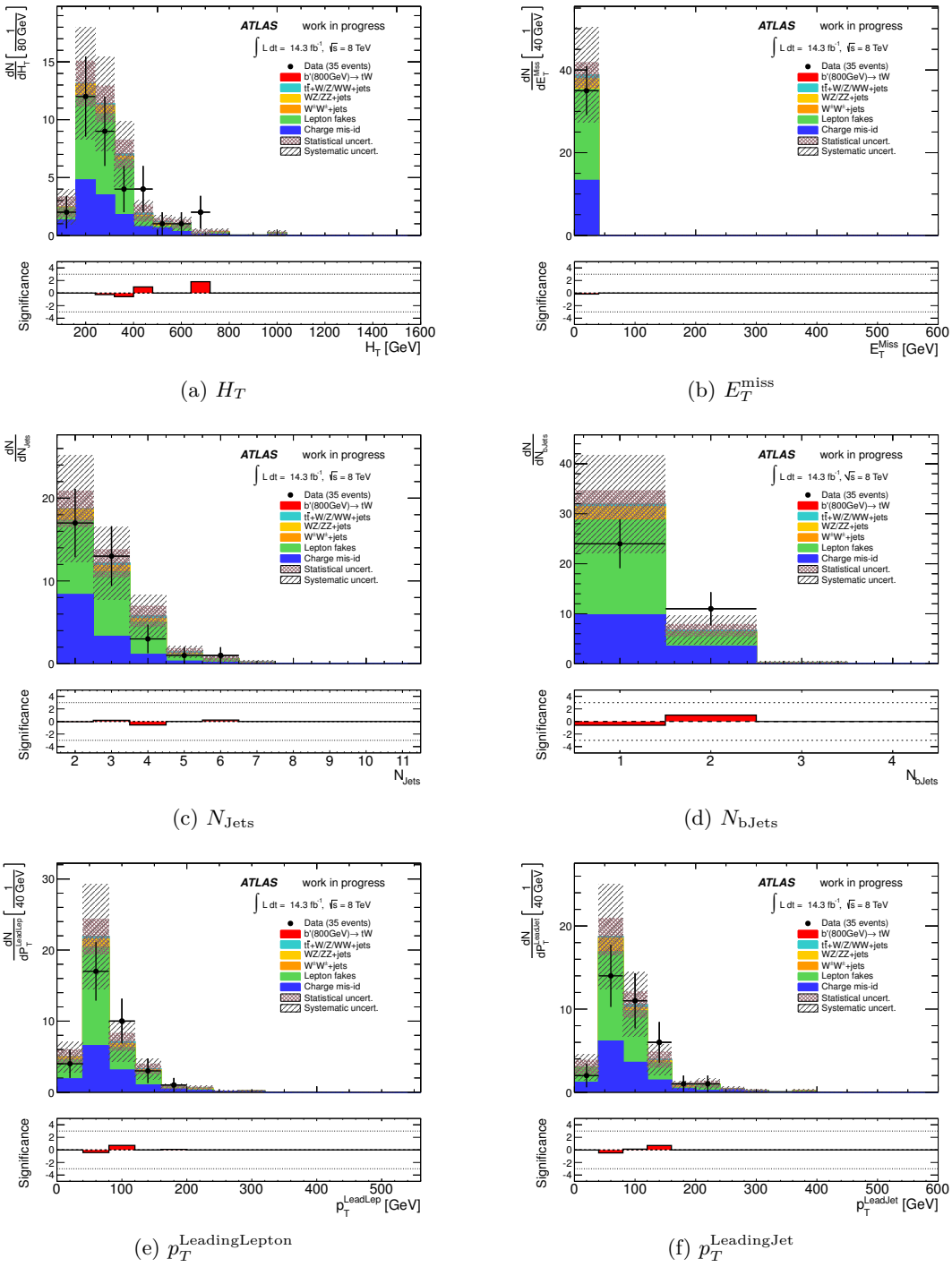

(a) H_T (b) E_T^{miss}

(c) N_{Jets} (d) N_{bJets}

(e) $p_T^{\text{LeadingLepton}}$ (f) $p_T^{\text{LeadingJet}}$

Figure 6.32: Distributions of kinematic variables for the ee channel after the low-E_T^{miss} (Table 6.35) control region selection for the various backgrounds and the $b' \to tW$ ($m_{b'} = 800\,\text{GeV}$) signal sample. The statistical and systematic uncertainties are represented by the shaded areas and the lower plots depict the significance of the deviations between data and expectation, which has been calculated with the method described in Section 6.4.2.

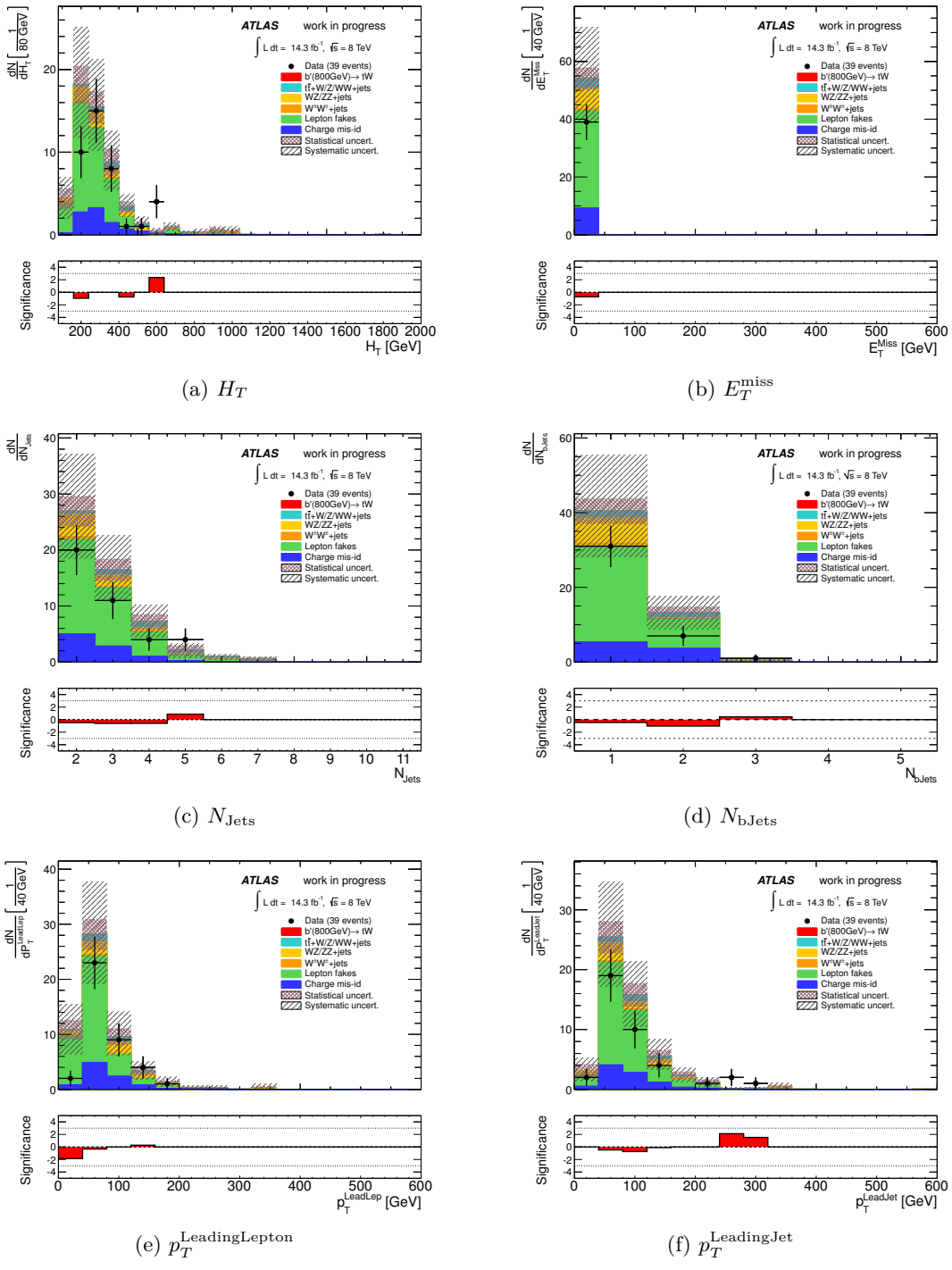

(a) H_T (b) E_T^{miss}

(c) N_{Jets} (d) N_{bJets}

(e) $p_T^{\text{LeadingLepton}}$ (f) $p_T^{\text{LeadingJet}}$

Figure 6.33: Distributions of kinematic variables for the $e\mu$ channel after the low-E_T^{miss} (Table 6.35) control region selection for the various backgrounds and the $b' \to tW$ ($m_{b'} = 800\,\text{GeV}$) signal sample. The statistical and systematic uncertainties are represented by the shaded areas and the lower plots depict the significance of the deviations between data and expectation, which has been calculated with the method described in Section 6.4.2.

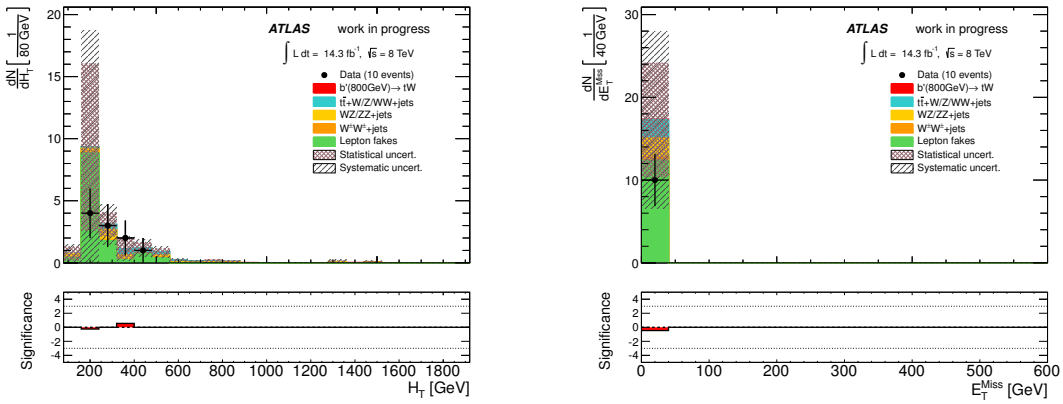

(a) H_T

(b) E_T^{miss}

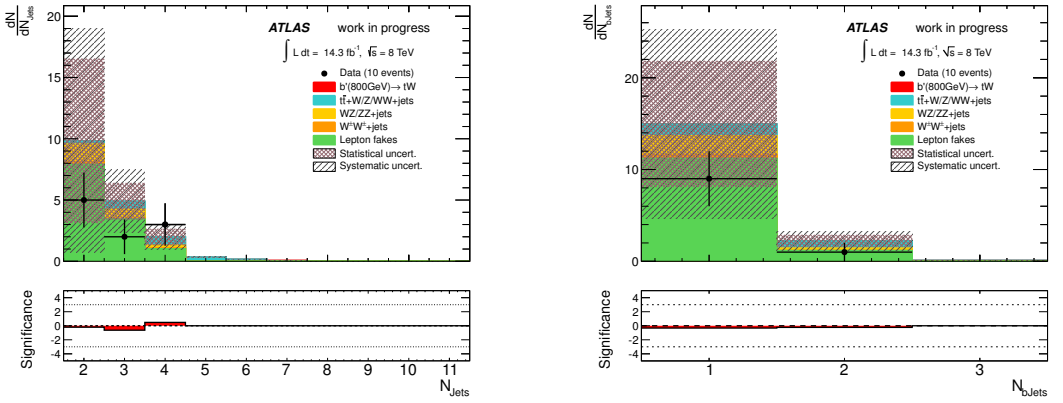

(c) N_{Jets}

(d) N_{bJets}

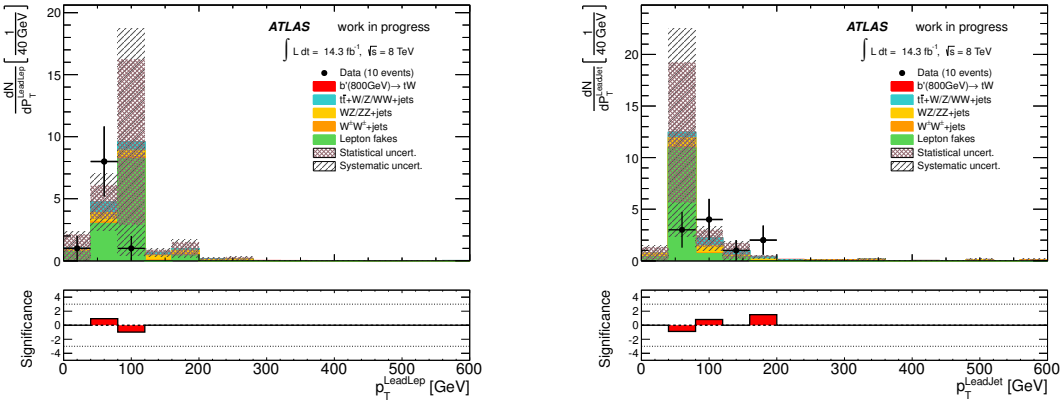

(e) $p_T^{\text{LeadingLepton}}$

(f) $p_T^{\text{LeadingJet}}$

Figure 6.34: Distributions of kinematic variables for the $\mu\mu$ channel after the low-E_T^{miss} (Table 6.35) control region selection for the various backgrounds and the $b' \to tW$ ($m_{b'} = 800\,\text{GeV}$) signal sample. The statistical and systematic uncertainties are represented by the shaded areas and the lower plots depict the significance of the deviations between data and expectation, which has been calculated with the method described in Section 6.4.2.

Process	ee	$e\mu$	$\mu\mu$
$t\bar{t}+W$+jets	$0.61 \pm 0.06^{+0.21}_{-0.20}$	$2.50 \pm 0.12^{+0.80}_{-0.81}$	$1.61 \pm 0.10^{+0.53}_{-0.53}$
$t\bar{t}+Z$+jets	$0.37 \pm 0.04^{+0.12}_{-0.14}$	$0.96 \pm 0.06^{+0.31}_{-0.32}$	$0.54 \pm 0.05^{+0.18}_{-0.19}$
$t\bar{t}+WW$	$0.007 \pm 0.001^{+0.003}_{-0.002}$	$0.034 \pm 0.003^{+0.013}_{-0.010}$	$0.021 \pm 0.003^{+0.008}_{-0.006}$
WZ/ZZ+jets	$2.49 \pm 0.54^{+0.93}_{-0.90}$	$7.04 \pm 0.96^{+8.92}_{-3.78}$	$2.35 \pm 0.58^{+0.86}_{-0.86}$
$W^{\pm}W^{\pm}$+jets	$0.09 \pm 0.07^{+0.03}_{-0.03}$	$0.70 \pm 0.20^{+0.29}_{-0.23}$	$0.38 \pm 0.14^{+0.13}_{-0.13}$
Lepton fakes	$21.97 \pm 3.02^{+6.59}_{-6.59}$	$33.68 \pm 3.65^{+10.10}_{-10.10}$	$12.37 \pm 6.89^{+3.71}_{-3.71}$
Charge mis-id	$13.27 \pm 0.52^{+5.15}_{-5.04}$	$9.15 \pm 0.37^{+3.22}_{-3.18}$	—
Total background	$38.80 \pm 3.11^{+8.42}_{-8.35}$	$54.07 \pm 3.79^{+13.89}_{-11.28}$	$17.27 \pm 7.01^{+3.85}_{-3.85}$
$b'(800\,\text{GeV}) \to tW$	$0.029 \pm 0.010^{+0.005}_{-0.004}$	$0.13 \pm 0.02^{+0.02}_{-0.02}$	$0.09 \pm 0.02^{+0.02}_{-0.01}$
Observed	35	39	10

Table 6.36: Expected number of background events and observed number of events for the low-E_T^{miss} control region selection (Table 6.35). For each event yield, the statistical (first) and total upper and lower systematic uncertainties (second) are presented. Furthermore, the contamination of the $b' \to tW$ ($m_{b'} = 800\,\text{GeV}$) sample is shown.

The last control region that was considered is called 'Zero b-tag' and is summarised in Table 6.37. The b-tag requirement of the final selection is inverted to requiring that there

Selection	Criterion
Basic	Table 6.15
N_{Jets}	≥ 2
N_{bJets}	$= 0$
E_T^{miss}	no cut
H_T	no cut

Table 6.37: Summary of the selection criteria of the Zero b-tag control region.

is no b-tagged jet in the events. Furthermore, the cuts on E_T^{miss} and H_T are removed. The distributions of this selection are depicted in Figures 6.35, 6.36 and 6.37. Compared to the two former control regions, the contribution from the diboson backgrounds is larger. This comes from the fact that there are no b-jets expected from such processes (when neglecting diboson production with additional heavy flavor partons) and hence due to the control region selection this background is enhanced. Furthermore, this control region has improved statistics compared to the two former ones. In all three channels there is a reasonable agreement between data and expectation.
This can be also seen in the counted event yields for this selection reported in Table 6.38, where the deviation is at maximum of the order of 1.5 σ.

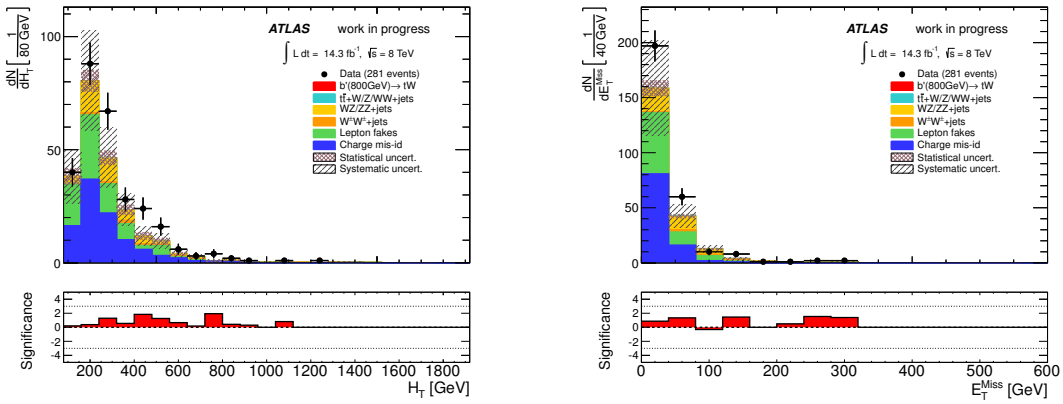

(a) H_T (b) E_T^{miss}

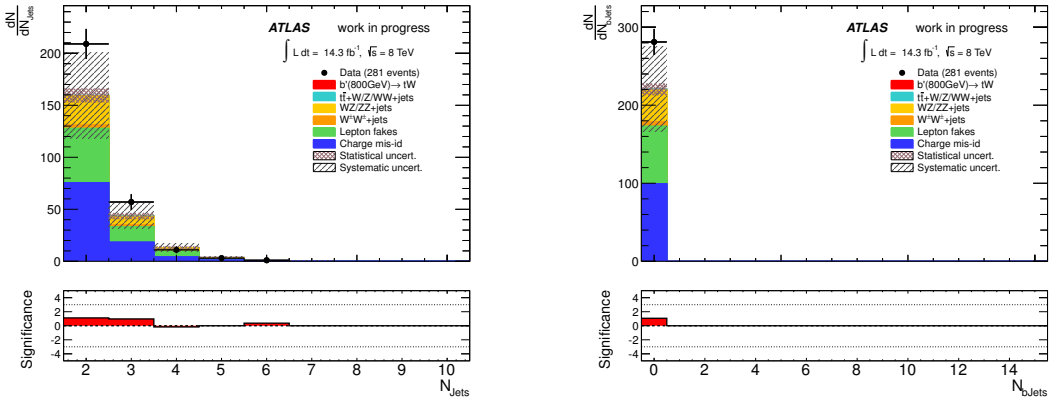

(c) N_{Jets} (d) N_{bJets}

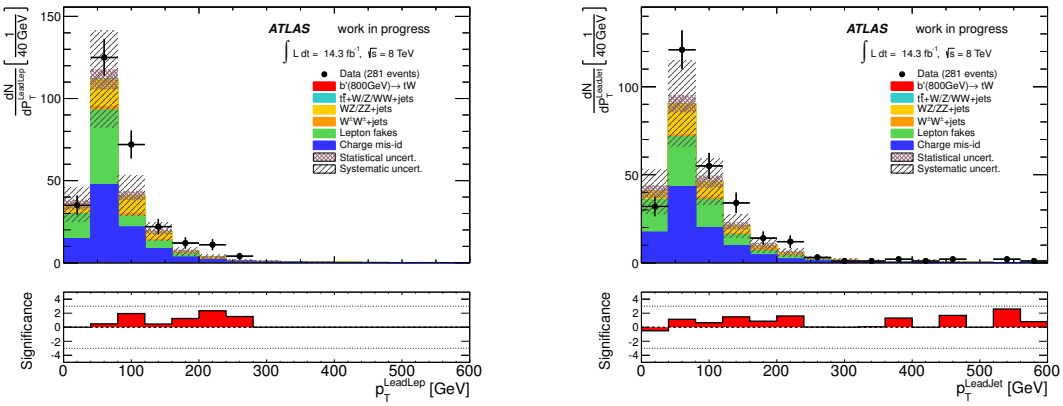

(e) $p_T^{\text{LeadingLepton}}$ (f) $p_T^{\text{LeadingJet}}$

Figure 6.35: Distributions of kinematic variables for the ee channel after the Zero b-tag (Table 6.37) control region selection for the various backgrounds and the $b' \to tW$ ($m_{b'} = 800\,\text{GeV}$) signal sample. The statistical and systematic uncertainties are represented by the shaded areas and the lower plots depict the significance of the deviations between data and expectation, which has been calculated with the method described in Section 6.4.2.

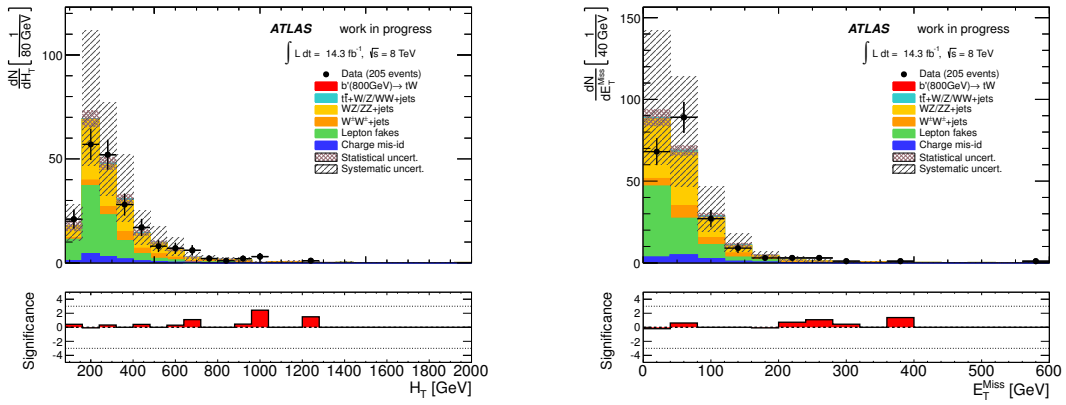

(a) H_T (b) E_T^{miss}

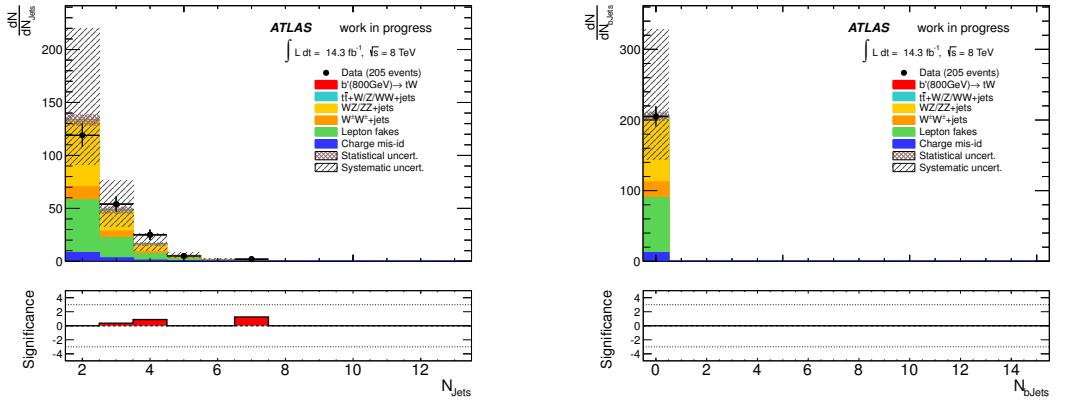

(c) N_{Jets} (d) N_{bJets}

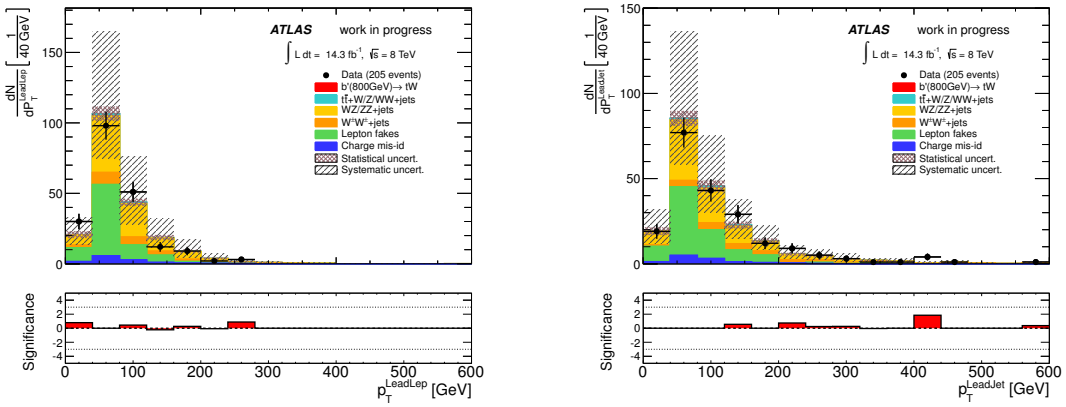

(e) $p_T^{\text{LeadingLepton}}$ (f) $p_T^{\text{LeadingJet}}$

Figure 6.36: Distributions of kinematic variables for the $e\mu$ channel after the Zero b-tag (Table 6.37) control region selection for the various backgrounds and the $b' \to tW$ ($m_{b'} = 800\,\text{GeV}$) signal sample. The statistical and systematic uncertainties are represented by the shaded areas and the lower plots depict the significance of the deviations between data and expectation, which has been calculated with the method described in Section 6.4.2.

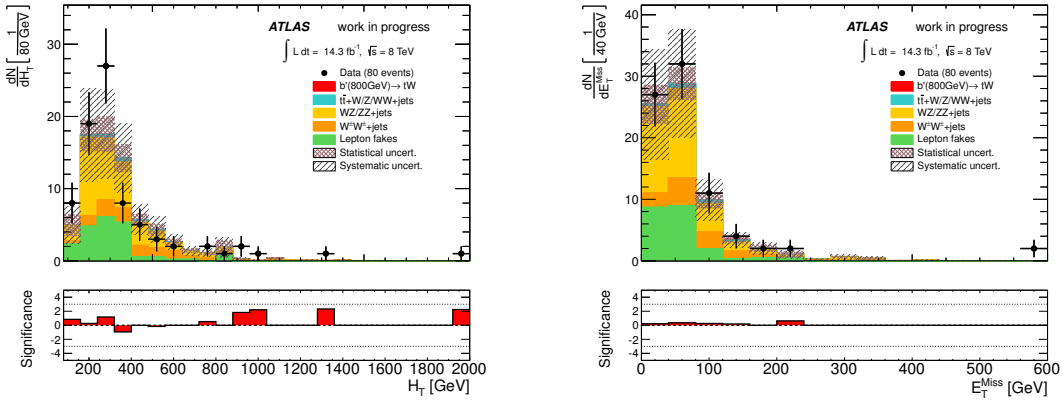

(a) H_T (b) E_T^{miss}

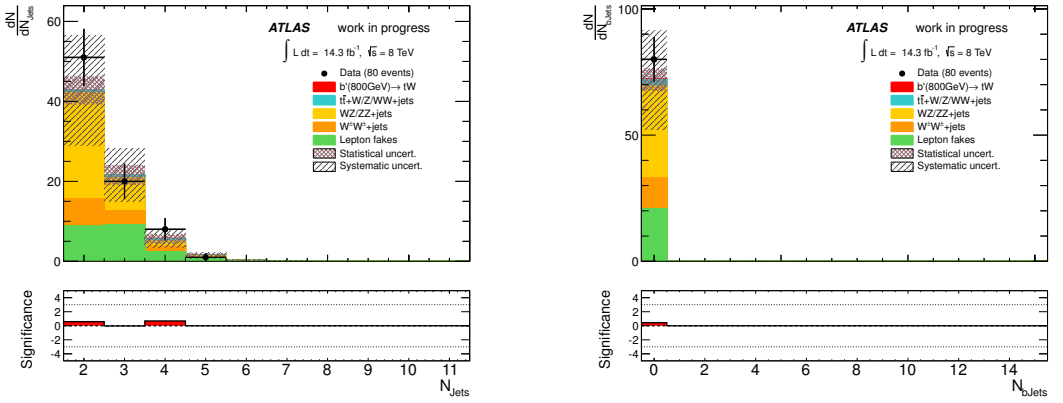

(c) N_{Jets} (d) N_{bJets}

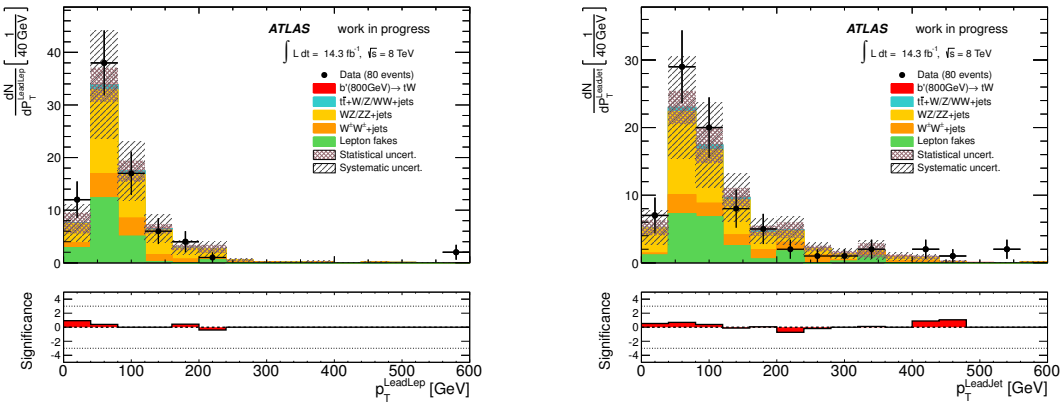

(e) $p_T^{\text{LeadingLepton}}$ (f) $p_T^{\text{LeadingJet}}$

Figure 6.37: Distributions of kinematic variables for the $\mu\mu$ channel after the Zero b-tag (Table 6.37) control region selection for the various backgrounds and the $b' \to tW$ ($m_{b'} = 800\,\text{GeV}$) signal sample. The statistical and systematic uncertainties are represented by the shaded areas and the lower plots depict the significance of the deviations between data and expectation, which has been calculated with the method described in Section 6.4.2.

Process	ee	$e\mu$	$\mu\mu$
$t\bar{t}+W$+jets	$0.87 \pm 0.08^{+0.30}_{-0.29}$	$2.84 \pm 0.14^{+0.91}_{-0.92}$	$2.02 \pm 0.12^{+0.67}_{-0.67}$
$t\bar{t}+Z$+jets	$0.29 \pm 0.04^{+0.09}_{-0.11}$	$0.99 \pm 0.07^{+0.32}_{-0.33}$	$0.50 \pm 0.05^{+0.17}_{-0.17}$
$t\bar{t}+WW$	$0.021 \pm 0.003^{+0.008}_{-0.006}$	$0.052 \pm 0.004^{+0.020}_{-0.015}$	$0.039 \pm 0.004^{+0.016}_{-0.011}$
WZ/ZZ+jets	$40.27 \pm 2.04^{+15.11}_{-14.58}$	$89.79 \pm 3.03^{+113.78}_{-48.13}$	$36.41 \pm 1.96^{+13.27}_{-13.29}$
$W^{\pm}W^{\pm}$+jets	$6.03 \pm 0.54^{+1.71}_{-1.72}$	$21.83 \pm 1.04^{+8.89}_{-7.27}$	$12.11 \pm 0.76^{+4.08}_{-4.10}$
Lepton fakes	$73.73 \pm 7.12^{+22.12}_{-22.12}$	$78.03 \pm 5.70^{+23.41}_{-23.41}$	$20.84 \pm 3.94^{+6.25}_{-6.25}$
Charge mis-id	$99.07 \pm 1.55^{+38.43}_{-37.62}$	$11.84 \pm 0.43^{+4.17}_{-4.11}$	—
Total background	$220.27 \pm 7.59^{+46.88}_{-46.05}$	$205.36 \pm 6.55^{+116.59}_{-54.18}$	$71.91 \pm 4.61^{+15.24}_{-15.27}$
$b'(800\,\text{GeV}) \to tW$	$0.25 \pm 0.04^{+0.05}_{-0.04}$	$0.53 \pm 0.06^{+0.10}_{-0.09}$	$0.49 \pm 0.05^{+0.10}_{-0.08}$
Observed	281	205	80

Table 6.38: Expected number of background events and observed number of events for the Zero b-tag control region selection (Table 6.37). For each event yield, the statistical (first) and total upper and lower systematic uncertainties (second) are presented. Furthermore, the contamination of the $b' \to tW$ ($m_{b'} = 800\,\text{GeV}$) sample is shown.

6.8.2.2 Background estimates and observed data for the final selection

After applying the final event selection to data, a total of 15 events was selected. This compares to a total of 9.3±1.7 expected background events, as it is reported in Table 6.39, where the details of the observed number of events, as well as the total expected number of background events are shown separately for the three channels ee, $e\mu$ and $\mu\mu$. The largest contributions to the signal region come from the data-driven lepton fakes and charge mis-id backgrounds, as well as from the $t\bar{t}+W$+jets background. The diboson and $t\bar{t}+Z$+jets backgrounds have smaller contributions and the $t\bar{t}+WW$ background is negligible.
The largest expected and observed yield was found in the $e\mu$ channel, which is due to the combinatorics of the electron and the muon. Furthermore, there is a slight excess in this channel, where 10 events were observed, while expecting 4.36 background events. Using the method described in Section 6.4.2, the p-value and z-value for this deviation were computed when considering the statistical and systematic uncertainties as reported in the Table. These yield in values of

$$p\text{-value} = 0.0335 \tag{6.54}$$
$$z\text{-value} = 1.8311, \tag{6.55}$$
$$\tag{6.56}$$

which means that the significance of this excess is below 2σ.
For the ee and the $\mu\mu$ channel the observed events are comparable with the expectation

Backgrounds	Channel		
Samples	ee	$e\mu$	$\mu\mu$
Charge mis-id	$0.61 \pm 0.12^{+0.24}_{-0.23}$	$0.90 \pm 0.12^{+0.32}_{-0.31}$	—
Lepton fakes	$0.84 \pm 0.39^{+0.25}_{-0.25}$	$0.21 \pm 0.38^{+0.064}_{-0.064}$	< 1.14
Diboson			
• WZ/ZZ+jets	$0.29 \pm 0.20^{+0.10}_{-0.10}$	$0.34 \pm 0.18^{+0.44}_{-0.18}$	$0.39 \pm 0.20^{+0.14}_{-0.14}$
• $W^{\pm}W^{\pm}$+jets	$0.17 \pm 0.088^{+0.048}_{-0.048}$	$0.31 \pm 0.15^{+0.13}_{-0.10}$	$0.23 \pm 0.11^{+0.078}_{-0.078}$
$t\bar{t} + W/Z$			
• $t\bar{t} + W$+jets	$0.55 \pm 0.048^{+0.19}_{-0.18}$	$1.87 \pm 0.093^{+0.60}_{-0.60}$	$1.27 \pm 0.077^{+0.42}_{-0.42}$
• $t\bar{t} + Z$+jets	$0.18 \pm 0.028^{+0.057}_{-0.066}$	$0.66 \pm 0.052^{+0.21}_{-0.22}$	$0.31 \pm 0.037^{+0.10}_{-0.10}$
• $t\bar{t} + WW$	$0.024 \pm 0.0027^{+0.0095}_{-0.0070}$	$0.072 \pm 0.0045^{+0.028}_{-0.020}$	$0.055 \pm 0.0042^{+0.022}_{-0.016}$
Total	$2.66 \pm 0.47^{+0.41}_{-0.41}$	$4.36 \pm 0.47^{+0.85}_{-0.74}$	$2.25 \pm 1.16^{+0.46}_{-0.46}$
Observed	3	10	2

Table 6.39: Expected number of background events and observed number of events for the final selection, as it is also reported in reference [250]. For each event yield, the statistical (first) and total upper and lower systematic uncertainties (second) are presented. A detailed summary of the estimated systematics is given in Section 6.8.4.

within the uncertainties.

Since there is no significant excess observed over the background expectation, I have set limits on the considered signal processes $b' \to tW$ and $b' \to qW$. These results will be shown in Section 6.9.

6.8.3 Signal region distributions

In summary, the previously presented control region distributions revealed a reasonable agreement between data and background expectation. Hence, the background estimate for the signal region selection is expected to be trustable and some distributions after applying the final event selection are presented in this section.

As there is very low statistics after applying the final event selection, it is not really possible to check for the agreement between data and background expectation in particular distributions. However, the distributions shown in Figures 6.38, 6.39 and 6.40 are supposed to present the parameter space for the observed data events. Depicted are the distributions of H_T, E_T^{miss}, N_{Jets} and N_{bJets} for the ee, $e\mu$ and $\mu\mu$ channel, respectively. The three observed events in the ee channel are populated at H_T values below 1000 GeV and contain 2, 5 and 6 jets, respectively. Overall, the observed events agree with the background expectation. The same applies for the $\mu\mu$ channel.

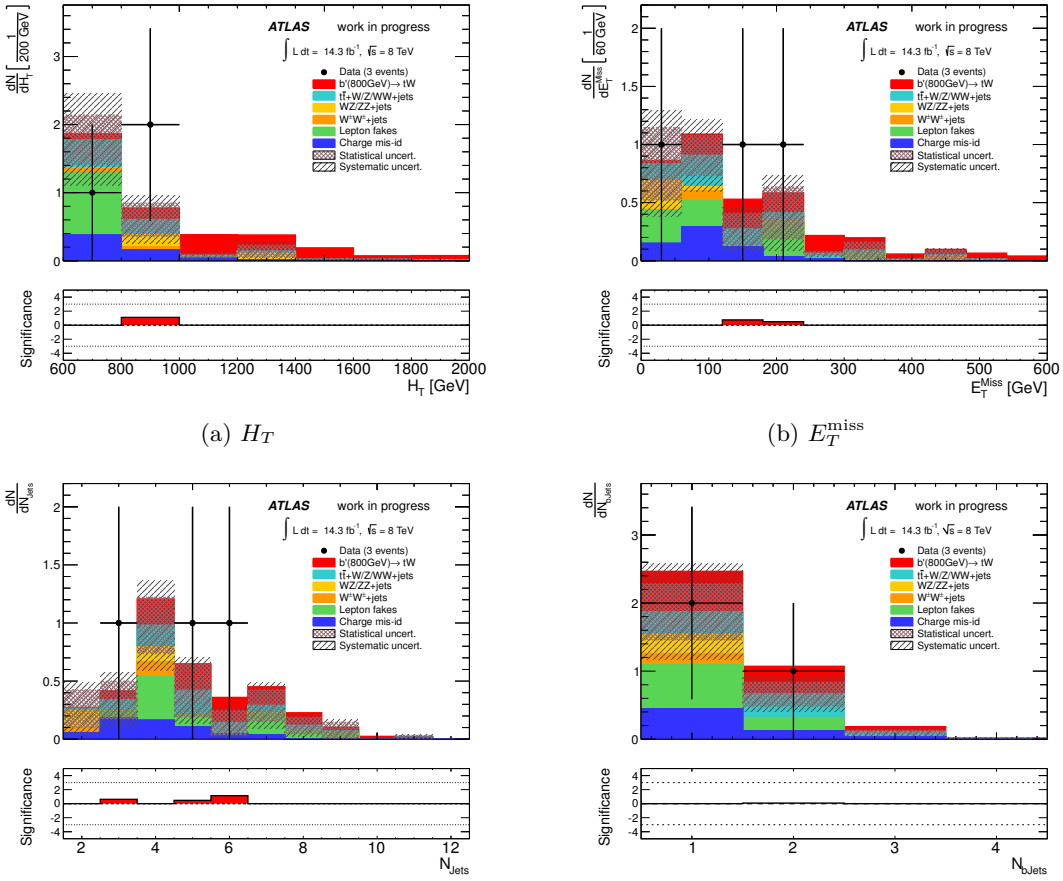

(a) H_T (b) E_T^{miss}

(c) N_{Jets} (d) N_{bJets}

Figure 6.38: Distributions of kinematic variables for the ee channel after the final signal region selection (Table 6.24) for the various backgrounds and the $b' \to tW$ ($m_{b'} = 800\,\text{GeV}$) signal sample. The statistical and systematic uncertainties are represented by the shaded areas and The lower plots depict the significance of the deviations between data and expectation, which has been calculated with the method described in Section 6.4.2.

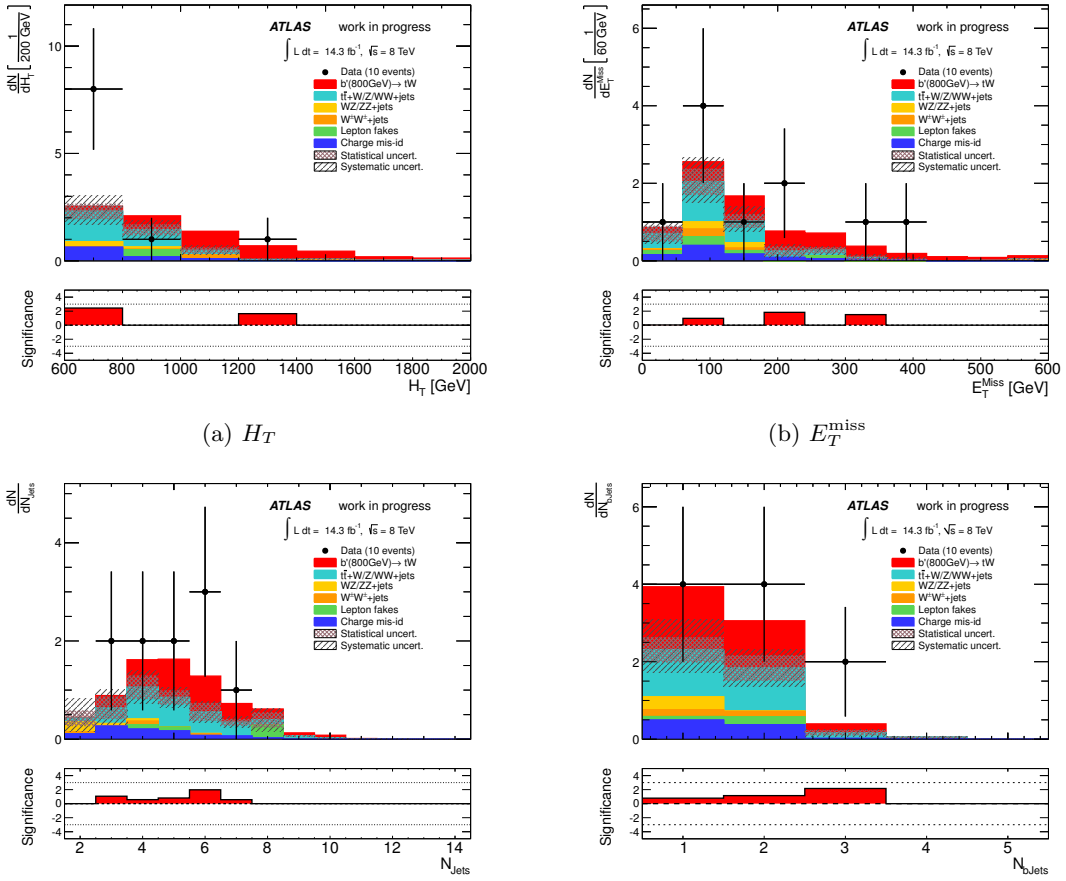

(a) H_T (b) E_T^{miss}

(c) N_{Jets} (d) N_{bJets}

Figure 6.39: Distributions of kinematic variables for the $e\mu$ channel after the final signal region selection (Table 6.24) for the various backgrounds and the $b' \to tW$ ($m_{b'} = 800\,\text{GeV}$) signal sample. The statistical and systematic uncertainties are represented by the shaded areas and the lower plots depict The lower plots depict the significance of the deviations between data and expectation, which has been calculated with the method described in Section 6.4.2.

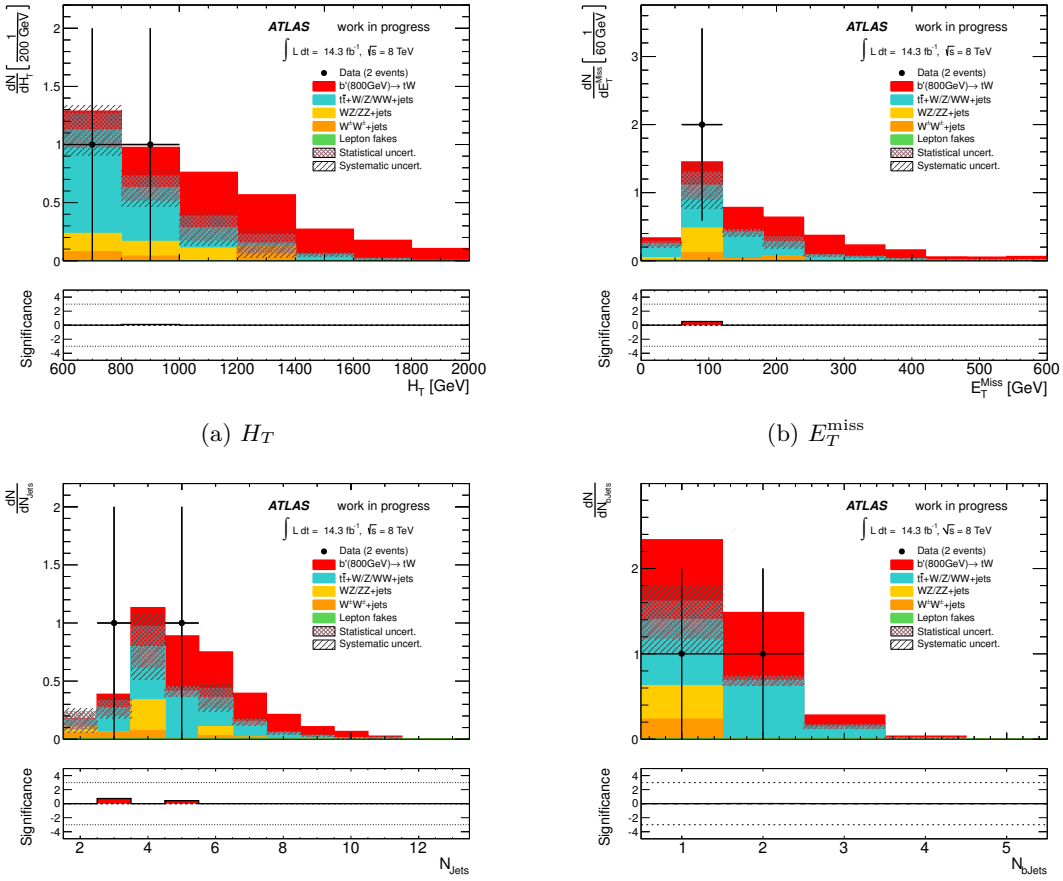

(a) H_T (b) E_T^{miss}

(c) N_{Jets} (d) N_{bJets}

Figure 6.40: Distributions of kinematic variables for the $\mu\mu$ channel after the final signal region selection (Table 6.24) for the various backgrounds and the $b' \to tW$ ($m_{b'} = 800\,\text{GeV}$) signal sample. The statistical and systematic uncertainties are represented by the shaded areas and The lower plots depict the significance of the deviations between data and expectation, which has been calculated with the method described in Section 6.4.2.

In the $e\mu$ channel, a slight excess of about 5 events was observed. In the variables N_{Jets}, N_{bJets} and E_T^{miss}, these events tend to be signal-like. However, in H_T these events appear in the range $[600, 800]$ GeV, where the contribution from the signal with $m_{b'} = 800\,\text{GeV}$ is small. Notably lower masses would have higher contributions in this H_T region, but are already excluded from direct searches. Furthermore, the expected excess at higher H_T values would be higher than the one observed.

6.8.4 Estimated systematic uncertainties for signal and backgrounds

In the following, I will summarise the systematic uncertainties considered in the limit determination, that will be presented in Section 6.9.
Thereby, I will focus on the estimated systematic uncertainties on the object energy scales, resolutions and efficiency scale factors (object systematics) after applying the final event selection. The systematic uncertainties due to the luminosity measurement, cross sections and data-driven techniques have been discussed in Section 6.6 and do not depend on the event selection. Therefore, these uncertainties that were already summarised in Tables 6.9, 6.10, 6.13 and 6.14, will not be repeated here.

The different object systematics have been derived for electrons, muons, jets and the E_T^{miss}, using the procedures presented in Sections 6.6.1, 6.6.2, 6.6.3 and 6.6.4, respectively.
In general, these are determined by performing the analysis on the various MC background and signal samples several times, while varying the different scale and resolution parameters and the efficiency scale factors and counting the amount of selected events. The obtained systematic uncertainties, which will be shown in the following, were then derived by calculating the relative differences to the selected event yields from the nominal analysis.
This procedure was performed separately for the channels ee, $e\mu$ and $\mu\mu$, in order to take into account differences of the particular systematics among these channels.

In Tables 6.40, 6.41 and 6.42, the estimated object systematics for the various MC background samples are reported. The largest uncertainties arise from the jet energy scale and the jet energy resolution, followed by the different scale factors for the b-tagging and jet vertex fraction efficiencies. There are also small contributions from the scale factors for the electron and muon identification and reconstruction efficiencies, whereas the trigger scale factors and electron/muon scale and resolution uncertainties can be neglected. The same applies to the systematic of the E_T^{miss}.

The same behaviour can be also seen for the object systematics determined for the $b' \to tW$ signal samples, as reported in Tables 6.43, 6.44 and 6.45 for the three channels.

Systematic	$t\bar{t}+W$+jets	$t\bar{t}+WW$	$t\bar{t}+Z$+jets	WZ/ZZ+jets	$W^{\pm}W^{\pm}$+jets
JES	$13.5/-9.4$	$4.4/-10.8$	$7.8/-21.0$	$3.7/-2.8$	$0.2/-0.4$
JER	$3.7/-3.7$	$1.0/-1.0$	$0.9/-0.9$	$0.8/-0.8$	$0.1/-0.1$
JRE	$0.0/-0.0$	$0.0/-0.0$	$0.0/-0.0$	$0.0/-0.0$	$0.0/-0.0$
JVFSF	$1.9/-2.0$	$2.8/-2.3$	$2.5/-2.2$	$5.0/-2.9$	$1.3/-1.6$
ESFRecId	$5.0/-4.9$	$5.4/-5.2$	$5.0/-4.9$	$5.0/-4.9$	$5.3/-5.2$
ESFTrig	$1.4/-0.0$	$0.7/-0.0$	$3.5/-0.0$	$0.0/-8.3$	$0.0/-0.5$
EER	$0.0/-0.5$	$0.0/-0.0$	$0.0/-0.8$	$0.0/-0.0$	$0.0/-0.0$
EES	$2.0/-4.4$	$0.0/-1.8$	$0.0/-0.6$	$12.8/-0.0$	$0.2/-0.0$
MuSFRecId	$0.1/-0.1$	$0.1/-0.1$	$0.0/-0.0$	$0.0/-0.0$	$0.0/-0.0$
MuSFTrig	$0.0/-0.0$	$0.0/-0.0$	$0.0/-0.0$	$0.0/-0.0$	$0.0/-0.0$
MES	$0.0/-0.0$	$0.0/-0.0$	$0.0/-0.0$	$0.0/-0.0$	$0.0/-0.0$
MER	$0.0/-0.0$	$0.0/-0.0$	$0.0/-0.0$	$0.0/-0.0$	$0.0/-0.0$
MET	$1.2/-0.0$	$0.0/-0.0$	$0.0/-0.8$	$0.0/-0.0$	$0.0/-0.0$
BTagSFb	$4.1/-5.1$	$2.8/-3.9$	$3.1/-4.4$	$3.3/-5.5$	$4.3/-4.3$
BTagSFc	$1.1/-1.2$	$1.6/-1.7$	$1.5/-1.2$	$0.6/-0.6$	$0.0/-0.0$
BTagSFmistag	$0.4/-0.3$	$0.3/-0.3$	$0.1/-0.1$	$0.4/-0.4$	$10.9/-11.1$
Total	$+16.2/-13.7$	$+9.2/-13.5$	$+11.4/-22.5$	$+15.8/-12.4$	$+13.5/-13.7$

Table 6.40: Estimated systematic uncertainties in percent (%) on object scale, resolution and efficiency scale factors for the various backgrounds in the ee channel. These systematics have been determined with the procedures described in Section 6.6.

Systematic	$t\bar{t}+W$+jets	$t\bar{t}+WW$	$t\bar{t}+Z$+jets	WZ/ZZ+jets	$W^{\pm}W^{\pm}$+jets
JES	$7.0/-8.2$	$2.9/-7.9$	$8.3/-10.7$	$117.6/-28.3$	$26.8/-12.7$
JER	$0.0/-0.0$	$0.8/-0.8$	$2.3/-2.3$	$27.7/-27.7$	$2.9/-2.9$
JRE	$0.0/-0.0$	$0.0/-0.0$	$0.0/-0.0$	$0.0/-0.0$	$0.0/-0.0$
JVFSF	$2.1/-2.0$	$2.5/-2.3$	$2.8/-2.4$	$1.0/-1.2$	$1.6/-1.7$
ESFRecId	$2.5/-2.5$	$2.6/-2.6$	$2.5/-2.5$	$2.5/-2.5$	$2.6/-2.6$
ESFTrig	$0.4/-0.1$	$0.0/-1.1$	$0.1/-0.1$	$0.0/-1.1$	$0.3/-0.1$
EER	$0.2/-0.3$	$0.9/-0.4$	$0.7/-0.0$	$0.0/-0.0$	$0.0/-0.0$
EES	$0.9/-1.1$	$0.4/-0.9$	$0.9/-0.6$	$8.8/-0.0$	$0.0/-0.0$
MuSFRecId	$4.1/-4.1$	$4.1/-4.1$	$4.3/-4.2$	$4.0/-4.0$	$4.0/-4.0$
MuSFTrig	$0.0/-0.0$	$0.0/-0.0$	$0.0/-0.0$	$0.0/-0.0$	$0.0/-0.0$
MES	$0.0/-0.0$	$0.0/-0.0$	$0.1/-0.1$	$0.0/-0.0$	$0.0/-0.0$
MER	$0.0/-0.0$	$0.2/-0.2$	$0.1/-0.1$	$0.0/-0.0$	$0.0/-0.0$
MET	$0.3/-0.2$	$0.4/-0.3$	$3.2/-0.0$	$8.8/-0.0$	$0.0/-0.0$
BTagSFb	$5.5/-6.6$	$2.8/-3.6$	$4.8/-5.8$	$2.4/-2.4$	$1.5/-1.5$
BTagSFc	$0.8/-0.9$	$1.5/-1.6$	$0.7/-0.7$	$1.7/-2.2$	$13.0/-13.1$
BTagSFmistag	$0.4/-0.4$	$0.4/-0.4$	$0.6/-0.5$	$10.1/-10.1$	$9.9/-10.0$
Total	$10.4/-11.8$	$7.1/-10.5$	$11.9/-13.6$	$122.0/-41.3$	$32.0/-21.7$

Table 6.41: Estimated systematic uncertainties in percent (%) on object scale, resolution and efficiency scale factors for the various backgrounds in the $e\mu$ channel. These systematics have been determined with the procedures described in Section 6.6.

Systematic	$t\bar{t}+W$+jets	$t\bar{t}+WW$	$t\bar{t}+Z$+jets	WZ/ZZ+jets	$W^{\pm}W^{\pm}$+jets
JES	$8.7/-8.2$	$8.1/-8.4$	$10.5/-11.3$	$0.2/-0.3$	$0.1/-3.0$
JER	$1.8/-1.8$	$0.8/-0.8$	$2.5/-2.5$	$5.5/-5.5$	$6.3/-6.3$
JRE	$0.0/-0.0$	$0.0/-0.0$	$0.0/-0.0$	$0.0/-0.0$	$0.0/-0.0$
JVFSF	$2.3/-2.1$	$2.5/-2.2$	$3.1/-2.5$	$1.4/-1.6$	$1.5/-1.8$
ESFRecId	$0.0/-0.0$	$0.0/-0.0$	$0.0/-0.0$	$0.0/-0.0$	$0.0/-0.0$
ESFTrig	$0.0/-0.0$	$0.0/-0.0$	$0.0/-0.0$	$0.0/-0.0$	$0.0/-0.0$
EER	$0.0/-0.1$	$0.0/-0.0$	$0.0/-0.0$	$0.0/-0.0$	$0.0/-0.0$
EES	$0.0/-0.1$	$0.0/-0.0$	$0.0/-0.0$	$0.0/-0.0$	$0.0/-0.0$
MuSFRecId	$8.2/-7.9$	$8.2/-7.9$	$8.9/-8.5$	$8.2/-7.9$	$8.2/-7.9$
MuSFTrig	$0.4/-0.4$	$0.4/-0.3$	$0.3/-0.2$	$0.8/-0.7$	$0.2/-0.2$
MES	$0.0/-0.0$	$0.0/-0.0$	$0.0/-0.0$	$0.0/-0.0$	$0.0/-0.0$
MER	$0.3/-0.3$	$0.0/-0.0$	$0.0/-0.0$	$0.0/-0.0$	$0.0/-0.0$
MET	$0.1/-1.8$	$1.0/-0.4$	$1.2/-1.0$	$0.0/-0.0$	$0.0/-0.0$
BTagSFb	$4.7/-5.9$	$2.7/-3.3$	$5.9/-6.4$	$7.1/-7.6$	$2.4/-2.3$
BTagSFc	$0.8/-0.8$	$0.3/-0.4$	$0.1/-0.1$	$3.0/-3.4$	$0.3/-0.3$
BTagSFmistag	$0.5/-0.5$	$0.8/-0.8$	$0.2/-0.2$	$0.5/-0.5$	$19.6/-19.7$
Total	$13.2/-13.3$	$12.2/-12.3$	$15.5/-16.0$	$12.6/-12.9$	$22.3/-22.5$

Table 6.42: Estimated systematic uncertainties in percent (%) on object scale, resolution and efficiency scale factors for the various backgrounds in the $\mu\mu$ channel. These systematics have been determined with the procedures described in Section 6.6.

Systematic	$b'(400GeV) \to tW$	$b'(450GeV) \to tW$	$b'(500GeV) \to tW$	$b'(550GeV) \to tW$	$b'(600GeV) \to tW$	$b'(650GeV) \to tW$	$b'(700GeV) \to tW$
JES	5.8/ − 10.1	9.8/ − 10.2	6.1/ − 7.5	7.3/ − 3.5	2.7/ − 1.4	5.0/ − 4.1	2.4/ − 1.3
JER	1.4/ − 1.4	2.5/ − 2.5	0.5/ − 0.5	0.6/ − 0.6	0.3/ − 0.3	0.8/ − 0.8	0.7/ − 0.7
JRE	0.0/ − 0.0	0.0/ − 0.0	0.0/ − 0.0	0.0/ − 0.0	0.0/ − 0.0	0.0/ − 0.0	0.0/ − 0.0
JVFSF	2.7/ − 2.4	2.6/ − 2.3	3.2/ − 2.9	2.5/ − 2.3	2.8/ − 2.6	2.5/ − 2.5	2.9/ − 2.7
ESFRecId	5.3/ − 5.2	5.4/ − 5.2	5.3/ − 5.2	5.3/ − 5.2	5.3/ − 5.2	5.4/ − 5.2	5.4/ − 5.2
ESFTrig	2.3/ − 0.0	1.3/ − 0.0	1.4/ − 0.0	1.5/ − 0.0	2.0/ − 0.0	1.9/ − 0.0	2.6/ − 0.0
EER	0.0/ − 1.1	0.4/ − 1.7	0.0/ − 1.1	0.0/ − 0.6	0.3/ − 0.0	0.2/ − 0.0	0.6/ − 0.0
EES	4.6/ − 0.6	0.0/ − 1.0	0.0/ − 1.3	2.5/ − 3.0	1.0/ − 0.4	0.8/ − 0.0	1.0/ − 0.6
MuSFRecId	0.1/ − 0.1	0.1/ − 0.1	0.1/ − 0.1	0.1/ − 0.1	0.1/ − 0.1	0.1/ − 0.1	0.2/ − 0.2
MuSFTrig	0.0/ − 0.0	0.0/ − 0.0	0.0/ − 0.0	0.0/ − 0.0	0.0/ − 0.0	0.0/ − 0.0	0.0/ − 0.0
MES	0.0/ − 0.0	0.0/ − 0.0	0.0/ − 0.0	0.0/ − 0.0	0.0/ − 0.0	0.0/ − 0.0	0.0/ − 0.0
MER	0.0/ − 0.0	0.0/ − 0.0	0.0/ − 0.0	0.0/ − 0.0	0.0/ − 0.0	0.0/ − 0.0	0.0/ − 0.0
MET	0.0/ − 1.0	1.4/ − 0.3	0.7/ − 1.2	0.6/ − 0.6	0.0/ − 0.3	0.7/ − 0.0	0.0/ − 0.0
BTagSFb	2.3/ − 3.2	0.7/ − 1.9	1.5/ − 2.8	4.1/ − 5.2	0.6/ − 2.4	4.1/ − 5.1	0.6/ − 1.8
BTagSFc	0.3/ − 0.4	0.5/ − 0.5	0.2/ − 0.1	0.3/ − 0.3	1.3/ − 1.4	0.3/ − 0.3	0.3/ − 0.2
BTagSFmistag	0.5/ − 0.5	0.3/ − 0.3	0.5/ − 0.5	0.2/ − 0.2	0.1/ − 0.1	0.0/ − 0.0	0.5/ − 0.5
Total	10.2/ − 12.2	12.0/ − 12.3	9.0/ − 10.2	10.7/ − 9.0	7.1/ − 6.6	9.1/ − 8.8	7.3/ − 6.4

Systematic	$b'(750GeV) \to tW$	$b'(800GeV) \to tW$	$b'(850GeV) \to tW$	$b'(900GeV) \to tW$	$b'(950GeV) \to tW$	$b'(1000GeV) \to tW$
JES	0.8/ − 2.3	0.8/ − 1.5	2.1/ − 0.5	0.3/ − 0.1	1.3/ − 1.5	1.7/ − 0.0
JER	0.2/ − 0.2	0.4/ − 0.4	0.1/ − 0.1	0.6/ − 0.6	0.3/ − 0.3	0.4/ − 0.4
JRE	0.0/ − 0.0	0.0/ − 0.0	0.0/ − 0.0	0.0/ − 0.0	0.0/ − 0.0	0.0/ − 0.0
JVFSF	2.8/ − 2.8	3.0/ − 3.0	2.9/ − 3.0	3.1/ − 3.1	2.6/ − 2.7	3.1/ − 3.1
ESFRecId	5.3/ − 5.2	5.4/ − 5.2	5.4/ − 5.2	5.4/ − 5.2	5.4/ − 5.2	5.4/ − 5.2
ESFTrig	2.5/ − 0.0	1.7/ − 0.0	2.3/ − 0.0	1.9/ − 0.0	2.7/ − 0.0	2.7/ − 0.0
EER	0.0/ − 0.1	0.0/ − 0.0	0.0/ − 0.7	0.0/ − 0.8	0.2/ − 1.0	0.2/ − 0.7
EES	0.6/ − 0.1	0.7/ − 0.5	0.0/ − 0.4	0.2/ − 0.4	0.0/ − 1.3	0.6/ − 0.2
MuSFRecId	0.1/ − 0.1	0.0/ − 0.0	0.1/ − 0.1	0.1/ − 0.1	0.3/ − 0.3	0.2/ − 0.2
MuSFTrig	0.0/ − 0.0	0.0/ − 0.0	0.0/ − 0.0	0.0/ − 0.0	0.0/ − 0.0	0.0/ − 0.0
MES	0.0/ − 0.0	0.0/ − 0.0	0.0/ − 0.0	0.0/ − 0.0	0.0/ − 0.0	0.0/ − 0.0
MER	0.0/ − 0.0	0.0/ − 0.0	0.0/ − 0.0	0.0/ − 0.0	0.0/ − 0.0	0.0/ − 0.0
MET	0.0/ − 0.2	0.0/ − 0.0	0.5/ − 0.7	0.2/ − 0.5	0.4/ − 0.1	0.6/ − 0.0
BTagSFb	2.6/ − 3.8	1.2/ − 2.1	3.6/ − 4.2	0.0/ − 1.4	0.7/ − 1.7	1.4/ − 2.6
BTagSFc	0.6/ − 0.5	1.3/ − 1.3	0.3/ − 0.4	0.7/ − 0.7	0.6/ − 0.5	0.7/ − 0.7
BTagSFmistag	0.1/ − 0.1	0.6/ − 0.6	1.0/ − 1.0	0.3/ − 0.3	0.7/ − 0.7	0.6/ − 0.6
Total	7.1/ − 7.4	6.8/ − 6.7	7.8/ − 7.5	6.6/ − 6.4	6.8/ − 6.6	7.3/ − 6.7

Table 6.43: Estimated systematic uncertainties in percent (%) on object scale, resolution and efficiency scale factors for the $b' \to tW$ samples in the *ee* channel.

Systematic	$b'(400GeV) \to tW$	$b'(450GeV) \to tW$	$b'(500GeV) \to tW$	$b'(550GeV) \to tW$	$b'(600GeV) \to tW$	$b'(650GeV) \to tW$	$b'(700GeV) \to tW$
JES	6.6/ − 7.4	7.5/ − 6.0	3.4/ − 7.2	3.6/ − 4.4	3.5/ − 3.1	2.2/ − 2.8	1.1/ − 2.6
JER	2.2/ − 2.2	2.1/ − 2.1	1.4/ − 1.4	0.2/ − 0.2	0.1/ − 0.1	0.9/ − 0.9	0.7/ − 0.7
JRE	0.0/ − 0.0	0.0/ − 0.0	0.0/ − 0.0	0.0/ − 0.0	0.0/ − 0.0	0.0/ − 0.0	0.0/ − 0.0
JVFSF	2.9/ − 2.4	2.7/ − 2.5	2.5/ − 2.4	2.6/ − 2.4	2.6/ − 2.5	2.9/ − 2.8	2.9/ − 2.8
ESFRecId	2.6/ − 2.6	2.6/ − 2.6	2.6/ − 2.6	2.6/ − 2.6	2.6/ − 2.6	2.6/ − 2.6	2.6/ − 2.6
ESFTrig	0.1/ − 0.1	0.5/ − 0.2	0.0/ − 0.3	0.0/ − 0.2	0.0/ − 0.2	0.2/ − 0.2	0.0/ − 0.4
EER	0.0/ − 0.5	0.4/ − 0.1	0.2/ − 0.0	0.2/ − 0.5	0.3/ − 0.0	0.2/ − 0.1	0.0/ − 0.2
EES	0.4/ − 0.4	0.4/ − 0.7	0.3/ − 0.0	0.1/ − 0.2	0.3/ − 0.0	0.3/ − 0.4	0.0/ − 0.4
MuSFRecId	4.1/ − 4.1	4.1/ − 4.1	4.1/ − 4.1	4.1/ − 4.1	4.1/ − 4.1	4.1/ − 4.1	4.1/ − 4.1
MuSFTrig	0.0/ − 0.0	0.0/ − 0.0	0.0/ − 0.0	0.0/ − 0.0	0.0/ − 0.0	0.0/ − 0.0	0.0/ − 0.0
MES	0.0/ − 0.0	0.0/ − 0.0	0.0/ − 0.0	0.1/ − 0.1	0.0/ − 0.0	0.0/ − 0.0	0.0/ − 0.0
MER	0.0/ − 0.0	0.1/ − 0.1	0.0/ − 0.0	0.2/ − 0.2	0.0/ − 0.0	0.1/ − 0.1	0.0/ − 0.0
MET	0.4/ − 0.0	0.7/ − 0.5	0.5/ − 0.0	0.2/ − 0.2	0.3/ − 0.0	0.2/ − 0.0	0.0/ − 0.2
BTagSFb	4.2/ − 5.0	1.5/ − 2.2	2.8/ − 3.7	2.6/ − 3.9	1.0/ − 2.0	2.4/ − 3.7	2.0/ − 3.2
BTagSFc	0.7/ − 0.6	1.3/ − 1.4	1.1/ − 1.0	1.2/ − 1.3	0.4/ − 0.4	0.4/ − 0.4	0.1/ − 0.1
BTagSFmistag	0.1/ − 0.1	0.4/ − 0.3	0.6/ − 0.6	0.4/ − 0.4	0.6/ − 0.6	0.1/ − 0.1	0.4/ − 0.4
Total	9.9/ − 10.7	9.8/ − 8.8	7.3/ − 9.9	7.2/ − 8.1	6.7/ − 6.6	6.6/ − 7.4	6.2/ − 7.0

Systematic	$b'(750GeV) \to tW$	$b'(800GeV) \to tW$	$b'(850GeV) \to tW$	$b'(900GeV) \to tW$	$b'(950GeV) \to tW$	$b'(1000GeV) \to tW$
JES	0.2/ − 1.4	0.8/ − 0.9	1.3/ − 0.5	0.8/ − 0.3	0.8/ − 0.0	0.1/ − 0.2
JER	0.7/ − 0.7	0.2/ − 0.2	0.3/ − 0.3	0.4/ − 0.4	0.2/ − 0.2	0.1/ − 0.1
JRE	0.0/ − 0.0	0.0/ − 0.0	0.0/ − 0.0	0.0/ − 0.0	0.0/ − 0.0	0.0/ − 0.0
JVFSF	2.8/ − 2.8	2.9/ − 2.9	3.2/ − 3.1	3.1/ − 3.1	3.0/ − 3.0	3.3/ − 3.4
ESFRecId	2.6/ − 2.6	2.6/ − 2.6	2.6/ − 2.6	2.6/ − 2.6	2.6/ − 2.6	2.6/ − 2.6
ESFTrig	0.0/ − 0.4	0.0/ − 0.6	0.0/ − 0.8	0.0/ − 0.4	0.0/ − 0.7	0.0/ − 0.7
EER	0.0/ − 0.2	0.2/ − 0.0	0.1/ − 0.1	0.1/ − 0.1	0.1/ − 0.1	0.0/ − 0.0
EES	0.0/ − 0.5	0.2/ − 0.0	0.3/ − 0.4	0.1/ − 0.0	0.2/ − 0.0	0.1/ − 0.0
MuSFRecId	4.1/ − 4.1	4.1/ − 4.1	4.1/ − 4.1	4.2/ − 4.1	4.2/ − 4.2	4.2/ − 4.2
MuSFTrig	0.0/ − 0.0	0.0/ − 0.0	0.0/ − 0.0	0.0/ − 0.0	0.0/ − 0.0	0.0/ − 0.0
MES	0.0/ − 0.0	0.0/ − 0.0	0.0/ − 0.0	0.0/ − 0.0	0.0/ − 0.0	0.0/ − 0.0
MER	0.0/ − 0.0	0.0/ − 0.0	0.0/ − 0.0	0.0/ − 0.0	0.0/ − 0.0	0.0/ − 0.0
MET	0.2/ − 0.0	0.3/ − 0.0	0.2/ − 0.0	0.2/ − 0.0	0.2/ − 0.4	0.1/ − 0.2
BTagSFb	2.2/ − 3.3	1.1/ − 2.1	1.6/ − 3.1	2.4/ − 3.9	2.6/ − 3.8	0.3/ − 2.1
BTagSFc	0.3/ − 0.3	0.8/ − 0.8	0.3/ − 0.3	0.2/ − 0.2	0.5/ − 0.4	0.5/ − 0.5
BTagSFmistag	0.6/ − 0.6	0.2/ − 0.2	0.0/ − 0.0	0.2/ − 0.2	0.2/ − 0.1	0.3/ − 0.3
Total	6.1/ − 6.8	5.9/ − 6.2	6.2/ − 6.6	6.4/ − 7.0	6.4/ − 7.0	6.0/ − 6.4

Table 6.44: Estimated systematic uncertainties in percent (%) on object scale, resolution and efficiency scale factors for the $b' \to tW$ samples in the $e\mu$ channel.

Systematic	$b'(400GeV) \to tW$	$b'(450GeV) \to tW$	$b'(500GeV) \to tW$	$b'(550GeV) \to tW$	$b'(600GeV) \to tW$	$b'(650GeV) \to tW$	$b'(700GeV) \to tW$
JES	5.0/ − 10.3	5.6/ − 7.6	5.4/ − 6.5	3.9/ − 1.9	2.2/ − 1.0	0.4/ − 0.0	0.7/ − 0.0
JER	1.4/ − 1.4	1.6/ − 1.6	0.2/ − 0.2	1.4/ − 1.4	0.5/ − 0.5	0.3/ − 0.3	0.4/ − 0.4
JRE	0.0/ − 0.0	0.0/ − 0.0	0.0/ − 0.0	0.0/ − 0.0	0.0/ − 0.0	0.0/ − 0.0	0.0/ − 0.0
JVFSF	2.9/ − 2.4	2.8/ − 2.3	3.2/ − 2.8	2.7/ − 2.4	2.7/ − 2.6	2.6/ − 2.5	3.2/ − 3.0
ESFRecId	0.0/ − 0.0	0.0/ − 0.0	0.0/ − 0.0	0.0/ − 0.0	0.0/ − 0.0	0.0/ − 0.0	0.0/ − 0.0
ESFTrig	0.0/ − 0.0	0.0/ − 0.0	0.0/ − 0.0	0.0/ − 0.0	0.0/ − 0.0	0.0/ − 0.0	0.0/ − 0.0
EER	0.0/ − 0.0	0.0/ − 0.3	0.0/ − 0.0	0.0/ − 0.0	0.0/ − 0.0	0.0/ − 0.0	0.0/ − 0.0
EES	0.0/ − 0.0	0.0/ − 0.3	0.0/ − 0.0	0.3/ − 0.0	0.0/ − 0.0	0.0/ − 0.0	0.2/ − 0.0
MuSFRecId	8.3/ − 7.9	8.2/ − 7.9	8.3/ − 7.9	8.3/ − 7.9	8.2/ − 7.9	8.3/ − 8.0	8.3/ − 7.9
MuSFTrig	0.5/ − 0.4	0.5/ − 0.4	0.4/ − 0.4	0.4/ − 0.4	0.5/ − 0.4	0.4/ − 0.4	0.4/ − 0.4
MES	0.0/ − 0.0	0.0/ − 0.0	0.2/ − 0.2	0.0/ − 0.0	0.0/ − 0.0	0.0/ − 0.0	0.0/ − 0.0
MER	0.5/ − 0.5	0.1/ − 0.1	0.5/ − 0.5	0.0/ − 0.0	0.0/ − 0.0	0.0/ − 0.0	0.0/ − 0.0
MET	0.9/ − 0.1	0.5/ − 0.3	0.7/ − 0.0	0.6/ − 0.4	0.7/ − 0.0	0.3/ − 0.0	0.3/ − 0.0
BTagSFb	3.9/ − 5.0	5.3/ − 6.1	1.5/ − 2.8	1.3/ − 2.2	2.6/ − 3.6	2.4/ − 3.5	1.1/ − 2.9
BTagSFc	0.9/ − 0.9	0.1/ − 0.2	0.3/ − 0.3	0.2/ − 0.2	0.5/ − 0.5	0.2/ − 0.2	0.5/ − 0.5
BTagSFmistag	0.4/ − 0.3	0.0/ − 0.0	0.1/ − 0.1	0.4/ − 0.4	0.0/ − 0.0	0.4/ − 0.5	0.3/ − 0.3
Total	11.0/ − 14.2	11.7/ − 12.9	10.6/ − 11.0	9.8/ − 8.9	9.3/ − 9.2	9.1/ − 9.1	9.0/ − 9.0

Systematic	$b'(750GeV) \to tW$	$b'(800GeV) \to tW$	$b'(850GeV) \to tW$	$b'(900GeV) \to tW$	$b'(950GeV) \to tW$	$b'(1000GeV) \to tW$
JES	0.0/ − 0.7	0.5/ − 0.9	1.5/ − 1.5	1.1/ − 1.5	1.9/ − 1.7	0.0/ − 1.4
JER	0.3/ − 0.3	0.6/ − 0.6	1.0/ − 1.0	0.7/ − 0.7	0.1/ − 0.1	0.2/ − 0.2
JRE	0.0/ − 0.0	0.0/ − 0.0	0.0/ − 0.0	0.0/ − 0.0	0.0/ − 0.0	0.0/ − 0.0
JVFSF	2.9/ − 2.8	3.8/ − 3.5	3.2/ − 3.1	3.2/ − 3.1	3.5/ − 3.3	4.0/ − 3.8
ESFRecId	0.0/ − 0.0	0.0/ − 0.0	0.0/ − 0.0	0.0/ − 0.0	0.0/ − 0.0	0.0/ − 0.0
ESFTrig	0.0/ − 0.0	0.0/ − 0.0	0.0/ − 0.0	0.0/ − 0.0	0.0/ − 0.0	0.0/ − 0.0
EER	0.0/ − 0.0	0.0/ − 0.0	0.0/ − 0.0	0.2/ − 0.0	0.0/ − 0.0	0.0/ − 0.0
EES	0.0/ − 0.0	0.0/ − 0.0	0.0/ − 0.0	0.0/ − 0.0	0.0/ − 0.0	0.0/ − 0.0
MuSFRecId	8.3/ − 7.9	8.3/ − 7.9	8.3/ − 7.9	8.3/ − 8.0	8.4/ − 8.0	8.4/ − 8.0
MuSFTrig	0.5/ − 0.4	0.5/ − 0.4	0.4/ − 0.4	0.5/ − 0.4	0.4/ − 0.4	0.4/ − 0.4
MES	0.1/ − 0.1	0.0/ − 0.0	0.1/ − 0.1	0.0/ − 0.0	0.0/ − 0.0	0.0/ − 0.0
MER	0.0/ − 0.0	0.1/ − 0.1	0.1/ − 0.1	0.0/ − 0.0	0.1/ − 0.1	0.0/ − 0.0
MET	0.0/ − 0.3	0.5/ − 0.2	0.0/ − 0.4	0.1/ − 0.3	0.4/ − 0.0	0.0/ − 0.3
BTagSFb	3.1/ − 4.2	0.2/ − 1.3	3.7/ − 4.7	2.4/ − 3.6	1.4/ − 2.7	1.3/ − 2.9
BTagSFc	0.2/ − 0.3	0.5/ − 0.4	0.6/ − 0.7	1.0/ − 1.0	0.1/ − 0.1	0.1/ − 0.1
BTagSFmistag	0.1/ − 0.1	0.3/ − 0.4	0.2/ − 0.2	0.0/ − 0.0	0.4/ − 0.4	0.1/ − 0.1
Total	9.3/ − 9.4	9.2/ − 8.8	9.8/ − 9.9	9.4/ − 9.5	9.4/ − 9.2	9.4/ − 9.4

Table 6.45: Estimated systematic uncertainties in percent (%) on object scale, resolution and efficiency scale factors for the $b' \to tW$ samples in the $\mu\mu$ channel.

The object systematic uncertainties have been also determined for the $b' \to qW$ samples and the results are presented in Appendix B.3.1.

6.9 Final limit determination

The observed data events for the final signal region selection were compatible with the background expectation, as previously reported in Section 6.8.2.2. Therefore, I have set limits within the two scenarios of $b' \to tW$ and $b' \to qW$. In the following, I will present the limit results, which were obtained using the method described in Section 6.4.3.

In case of the $b' \to tW$ scenario with 100% branching fraction, I have set upper limits on the production cross-sections, which are translated into a lower mass limit on the b' quark for this particular scenario.

In case of the $b' \to qW$ scenario, I derived exclusion ranges on the branching fractions for the decays into tW, cW and uW as a function of $m_{b'}$.

6.9.1 $b' \to tW$

For setting limits on the b' pair production with exclusive $b' \to tW$ decays, the expected signal yields summarised in Table 6.28 were used. Together with the amount of observed data and expected background events for the three dilepton channels ee, $e\mu$ and $\mu\mu$, these were used as input for the limit setting procedure. This was performed in the same way as for the event selection optimisation discussed in Section 6.7.1, but additionally calculating the observed limits. All the previously mentioned systematic uncertainties were considered in the limit calculations.

For each b' mass point, the expected and observed signal scale factors were obtained, which are summarised in Table 6.46. Multiplying these by the theoretical cross-section predictions, yields in the upper cross-section limits with 95% confidence level (CL), reported in the same table.

These upper cross-section limits are plotted in Figure 6.41 as a function of the b' mass. In addition to the median expected upper cross-section limits (derived from the median signal scale factors), there are also the $\pm 1\sigma$ and $\pm 2\sigma$ intervals shown, together with the theoretical NNLO cross-section prediction. One can see that the observed limit lies very close to the $+1\sigma$ expectation, which is due to the fact that the number of observed events is slightly above the background expectation. The intersection of the expected median and observed cross-section limit curves with the theoretical prediction yields in the lower expected and observed b' mass limits as follows:

$$m_{b'}^{\text{expected}} \geq 0.767\,\text{TeV}$$
$$m_{b'}^{\text{observed}} \geq 0.724\,\text{TeV}\ .$$

The limit calculation involved the generation of pseudo-experiments, in order to derive the probability density distributions of the LLR (Log-Likelihood ratio) values, as described in Section 6.4.3. The distributions of these obtained LLR values, under the 'background-only' and the 'signal+background' hypotheses, are presented in Figure 6.42

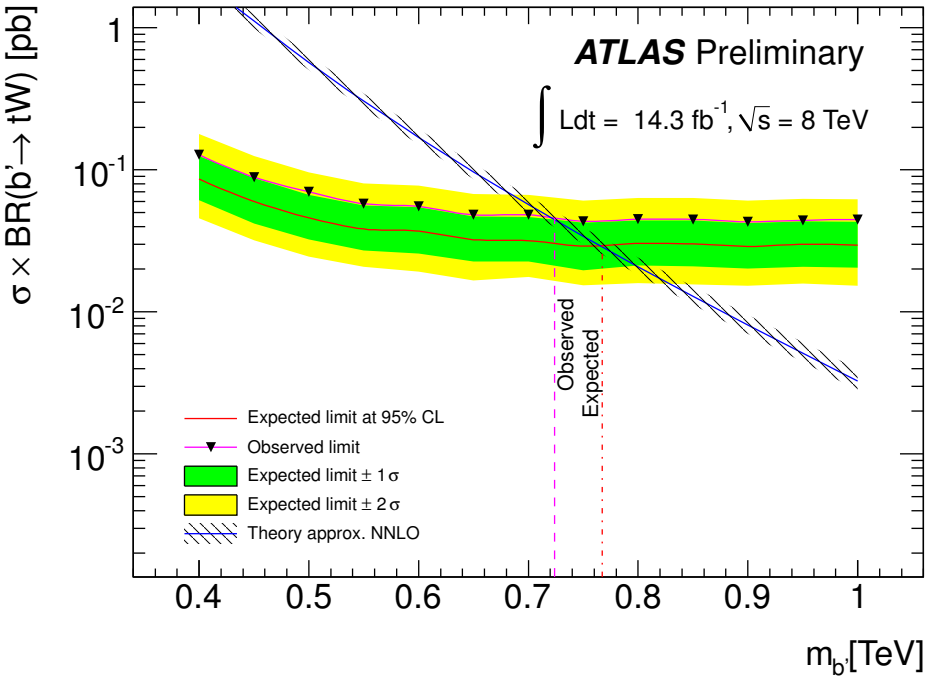

Figure 6.41: Expected and observed upper limits on the b' pair production cross-section (assuming $b' \to tW$ with 100% branching fraction) as a function of their mass [250]. The median expected limit is presented together with the $\pm 1\sigma$ and $\pm 2\sigma$ variations. The intersection with the theoretical NNLO cross-section prediction reveals an expected lower mass limit of $m_{b'} \geq 0.767\,\text{TeV}$ and an observed limit of $m_{b'} \geq 0.724\,\text{TeV}$.

	Expected limits		Observed limits	
$m_{b'}$ [GeV]	Scale factor	σ_{limit} [pb]	Scale factor	σ_{limit} [pb]
400	0.0376	0.0862	0.0557	0.1280
450	0.0540	0.0601	0.0798	0.0888
500	0.0807	0.0460	0.1228	0.0700
550	0.1256	0.0384	0.1893	0.0578
600	0.2188	0.0371	0.3261	0.0553
650	0.3327	0.0323	0.4966	0.0482
700	0.5581	0.0318	0.8481	0.0483
750	0.8531	0.0291	1.2737	0.0434
800	1.4589	0.0303	2.1628	0.0450
850	2.3387	0.0301	3.4842	0.0448
900	3.5784	0.0289	5.3500	0.0432
950	5.8588	0.0300	8.6454	0.0442
1000	9.0020	0.0294	13.6899	0.0448

Table 6.46: Presented are the expected and observed signal scale factors, which yield in the upper cross-section limits σ_{limit} with 95% confidence. The obtained results set limits on the b' pair production cross-section (assuming $b' \to tW$ with 100% BF) for different b' masses.

for a few selected b' masses. In addition, the observed LLR value is given. The distributions for all b' mass points can be looked up in Appendix D.1.1. One notices that for masses below 700 GeV the distributions are well separated. The signal yield is high enough to provide a good sensitivity for the signal. For higher masses the sensitivity decreases and the two distributions come closer. In the case of $m_{b'} = 900\,\text{GeV}$ (Figure 6.42f), the two distributions have a large overlap and hence one can not distinguish between the two hypotheses anymore.

The obtained expected and observed lower mass limits differ by about 40 GeV, which results from the 1σ deviation between the expected and observed limit curves. This is due to the slight excess in the $e\mu$ channel. In order to verify this argumentation, the limits were determined separately for each channel ee, $e\mu$ and $\mu\mu$. This means that only the event yields of the particular dilepton channel were used for the limit calculation. The obtained upper cross-section limits as a function of the b' mass, as well as the derived lower mass limits are presented in Figure 6.43. In the ee channel the observed event yield was comparable with the background expectation and hence the observed cross-section limits agree with the background-only hypothesis expectation. Therefore, the derived expected and observed mass limits are equal.
In the $\mu\mu$ channel, slightly less events were observed compared to the background expectation. Therefore, the observed upper cross-section limit curve is slightly below the expected one. This results in the observed b' mass limit being slightly above the expected limit.
The $e\mu$ channel showed a small excess of the observed yield with about 2σ significance

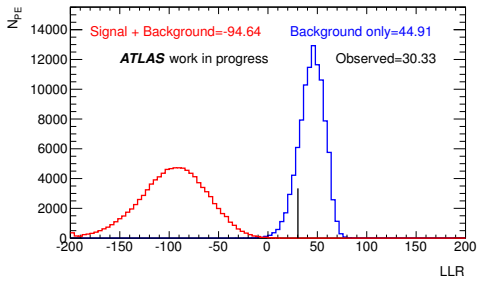

(a) $m_{b'} = 600\,\text{GeV}$

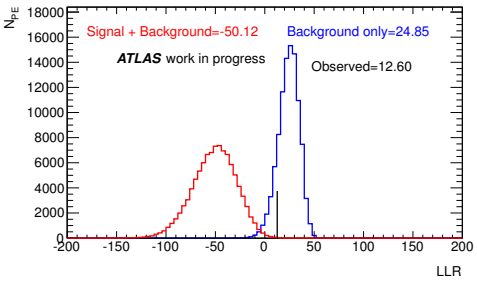

(b) $m_{b'} = 650\,\text{GeV}$

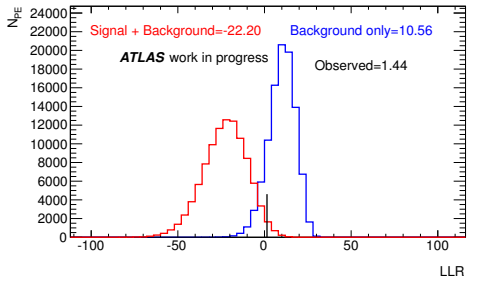

(c) $m_{b'} = 700\,\text{GeV}$

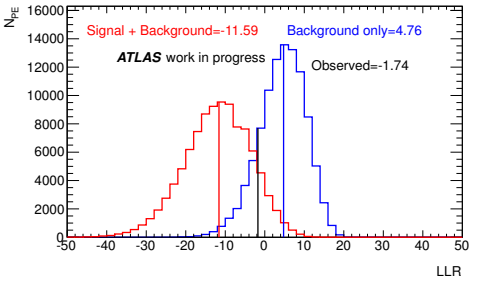

(d) $m_{b'} = 750\,\text{GeV}$

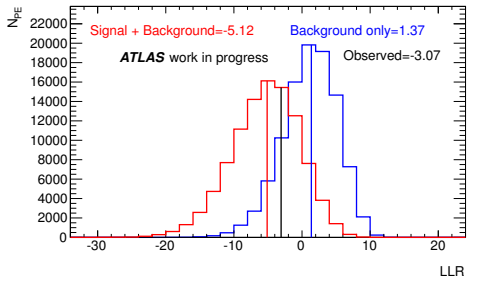

(e) $m_{b'} = 800\,\text{GeV}$

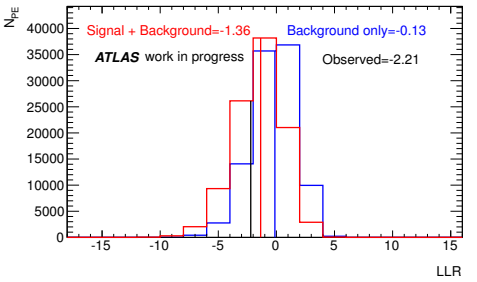

(f) $m_{b'} = 900\,\text{GeV}$

Figure 6.42: Distributions of the LLR (Log-Likelihood ratio) values from the generated pseudo-experiments. The distributions are presented for different selected b' mass points. Each plot depicts the distributions for the generated pseudo-experiments assuming the 'background-only' and the 'signal+background' hypotheses. In addition, the mean values of the two distributions are shown, as well as the observed LLR value.

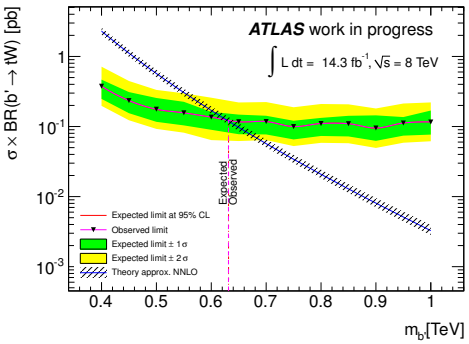

(a) ee

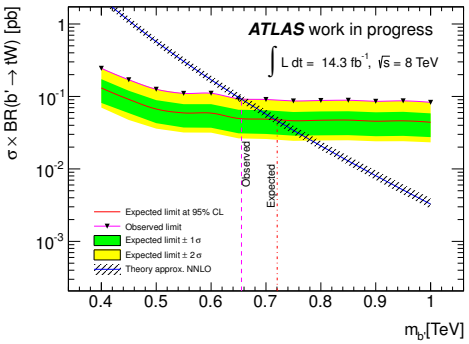

(b) $e\mu$

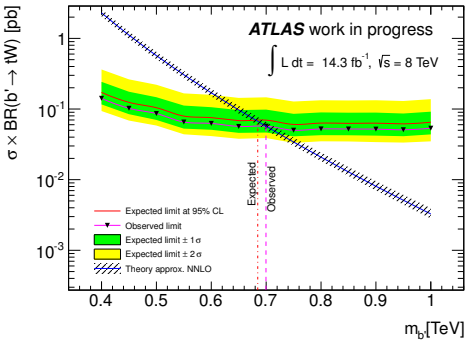

(c) $\mu\mu$

Channel	Expected mass limit	Observed mass limit
ee	0.631	0.631
$e\mu$	0.720	0.655
$\mu\mu$	0.685	0.700

(d) Mass limits in TeV

Figure 6.43: Expected and observed upper limits on the b' pair production cross-section (assuming $b' \to tW$ with 100% branching fraction) as a function of their mass, which have been computed separately for the ee, $e\mu$ and $\mu\mu$ channel. The median expected limit is presented together with the $\pm 1\sigma$ and $\pm 2\sigma$ variations. The intersection with the theoretical NNLO cross-section prediction reveals the expected and observed lower mass limits (in TeV) summarised in (d).

above the background expectation. This explains that the observed upper cross-section limit curve follows the $+2\sigma$ expectation curve and yields in the large difference between expected and observed mass limit.

Finally, the impact of the systematic uncertainties on the limit was studied. This was performed by computing the limits when considering only the statistical uncertainties. Hence, the generated pseudo-events in the limit calculation procedure are taken from Poisson distributions only. The resulting upper cross-section limits as a function of the b' mass are presented in Figure 6.44. The expected mass limit increases to 0.774 TeV, whilst

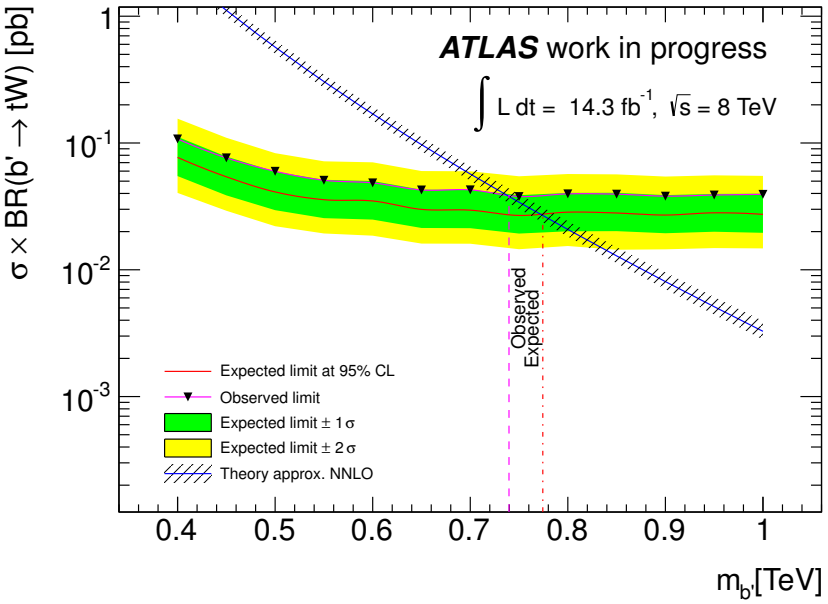

Figure 6.44: Expected and observed upper limits on the b' pair production cross-section (assuming $b' \to tW$ with 100% branching fraction) as a function of their mass when considering only the statistical uncertainties. This means that all systematic uncertainties have been not considered in the limit computation. The median expected limit is presented together with the $\pm 1\sigma$ and $\pm 2\sigma$ variations. The intersection with the theoretical NNLO cross-section prediction reveals an expected lower mass limit of $m_{b'} \geq 0.774$ TeV and an observed limit of $m_{b'} \geq 0.740$ TeV.

the observed limit is determined to be 0.740 TeV. Hence, the impact of the systematic uncertainties on the obtained b' mass limits is only of the order of 10 GeV. In conclusion, this analysis is mostly limited by the statistics rather than by the various systematics.

6.9.2 $b' \to qW$

In addition to set a limit on the scenario of exclusive $b' \to tW$ decays, I investigated also the scenario of a lower branching fraction of the $b' \to tW$ decay. The main idea is to

draw exclusion ranges depending on the b' mass and the branching fractions for the b' decays into tW, cW and uW.

In order to test the signal hypothesis under the assumption of particular branching fractions $BF(b' \to tW)$, $BF(b' \to cW)$ and $BF(b' \to uW)$, one needs to obtain the expected signal yields after the final event selection for this particular scenario. For this, the $b' \to qW$ samples can be used, that have been generated assuming branching fractions of

$$BF(b' \to tW) = 1/3,\ BF(b' \to cW) = 1/3,\ BF(b' \to uW) = 1/3\ . \tag{6.57}$$

For convenience, the three different branching fractions will be denoted as follows:

$$x = BF(b' \to tW),\ y = BF(b' \to cW),\ z = BF(b' \to uW)\ . \tag{6.58}$$

Although equal branching fractions have been assumed in the sample generation for the three different decay modes, the actual branching fractions in the samples can be slightly different. The MC samples do not have unlimited statistics and hence the different branching fractions will be only approximately around 1/3. Therefore, the exact branching fractions for each decay mode were determined by separately counting the number of b' decays into tW, cW and uW and dividing these numbers by twice the total amount of generated events (the information of the b' decays is accessible in the 'truth' content of the MC samples). The factor of two is due to the fact that each generated event contains the pair production of b' quarks. These exact branching fractions in the samples will be denoted as x_{org}, y_{org} and z_{org}.
In order to calculate the signal yields depending on the branching fractions, one needs to categorise the events in the $b' \to qW$ samples into the six possible decay scenarios of the b' pair: $tWtW$, $tWcW$, $tWuW$, $cWcW$, $cWuW$ and $uWuW$. Then, the number of events after applying the final event selection were counted for each of the six decay scenarios, which gives the event yields $n(tWtW)$, $n(tWcW)$, $n(tWuW)$, $n(cWcW)$, $n(cWuW)$ and $n(uWuW)$. In order to obtain then the expected signal event yield for particular desired branching fractions x_{new}, y_{new} and z_{new}, the event yields need to be rescaled by scaling factors defined as follows:

$$x_{SF} = \frac{x_{\text{new}}}{x_{\text{org}}},\ y_{SF} = \frac{y_{\text{new}}}{y_{\text{org}}},\ z_{SF} = \frac{z_{\text{new}}}{z_{\text{org}}}\ . \tag{6.59}$$

When setting particular branching fractions for x_{new} and y_{new}, the z_{new} branching fraction is automatically given by $z_{\text{new}} = 1 - x_{\text{new}} - y_{\text{new}}$. Hence, the total expected signal yield for a given set of branching fractions x_{new}, y_{new} and z_{new} is given by

$$\begin{aligned} n_{\text{tot}}(x,y,z) =& x_{SF}^2 \cdot n(tWtW) + x_{SF} \cdot y_{SF} \cdot n(tWcW) + x_{SF} \cdot z_{SF} \cdot n(tWuW) + \\ & y_{SF}^2 \cdot n(cWcW) + y_{SF} \cdot z_{SF} \cdot n(cWuW) + z_{SF}^2 \cdot n(uWuW)\ . \end{aligned} \tag{6.60}$$

This procedure was performed separately for each of the three dilepton channels ee, $e\mu$ and $\mu\mu$, and the obtained event yields are supposed to enter as signal expectation in the

limit calculation. The branching fractions for $b' \to tW$ and $b' \to cW$ were varied in the range $[0, 1]$ in steps of 0.05. The distribution of the expected event yields for different b' masses $m_{b'} \in [400, 750]$ GeV as a function of the branching fractions of $b' \to tW$ and $b' \to cW$ is depicted in Figure 6.45 for the combination of the three channels ee, $e\mu$ and $\mu\mu$. Separate distributions for each dilepton channel, as well as the distributions for the higher mass points, can be looked up in Appendix D.2.1.
One notices that the highest event yields are populated at $BF(b' \to tW)$ close to one. This comes from the fact that at least one of the two b' quarks in each event needs to decay into tW in order to achieve a same-sign dilepton signature in the final state. Moreover, one notices that the signal yield for a fixed value of $BF(b' \to tW)$ is nearly independent of $BF(b' \to cW)$, which indicates that the decays into cW and uW are not really distinguishable and the outcoming events are selected with the same rates.

After the determination of the expected signal yields for each dilepton channel, b' mass and combination of branching fractions, these event yields were used as input for the limit calculation procedure described in Section 6.4.3. The procedure is similar to what has been done to derive the limits on the exclusive $b' \to tW$ scenario reported in the previous Section 6.9.1. The same background expectations and observed events have been used, as well as the determined systematic uncertainties on the background estimates. In case of the object scale, resolution and efficiency scale factor systematics for the signal, the relative uncertainties derived for the $b' \to qW$ samples with equal branching fractions of 1/3 were used. In principle, one would need to derive these uncertainties separately for each combination of branching fractions, but this would have been technically too expensive. As already shown in the previous section, the analysis is mostly limited by the statistical uncertainties, and hence small variations in the systematic uncertainties are expected to have no significant effect on the limit calculation.

The limit determination was performed for each point in the $[BF(b' \to tW), BF(b' \to cW)]$ space, using the event yields separately for the dilepton channels ee, $e\mu$ and $\mu\mu$. Hence, these are provided as three histogram bins, as it was also performed for the limit calculation in the exclusive $b' \to tW$ scenario. Instead of obtaining the signal scale factors and setting limits on the b' pair production cross-sections, the expected and observed CL_s values were retrieved, in order to exclude certain points in the $[BF(b' \to tW), BF(b' \to cW)]$ space if $CL_s < 0.05$. This means that the particular point in the phase space is then excluded with 95% confidence. The outcome for b' masses $m_{b'} \in [400, 700]$ GeV is reported in Figure 6.46, where the expected and observed exclusion areas (which had $CL_s < 0.05$) are drawn in the $[BF(b' \to tW), BF(b' \to cW)]$ space. For increasing b' masses the exclusion areas become smaller due to the decreasing sensitivity for the signal. In case of $m_{b'} \geq 750$ GeV no exclusion statement can be made based on the observed data. This is due to the fact that the observed lower mass limit in the exclusive $b' \to tW$ scenario is below 750 GeV. This scenario is supposed to give the highest possible signal yields compared to scenarios with lower branching fractions and hence has the highest sensitivity. On the other hand, the expected lower mass limit in the $b' \to tW$ scenario with 100% branching fraction is slightly above 750 GeV and hence a small expected exclusion area is visible in Figure 6.46h for $BF(b' \to tW)$ close to one. In addition to these Figures, the same distributions for the higher mass points are

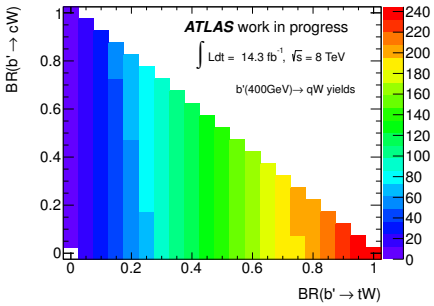

(a) $m_{b'} = 400\,\text{GeV}$

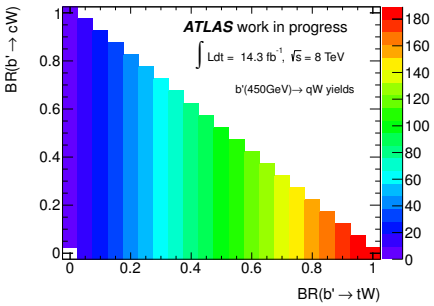

(b) $m_{b'} = 450\,\text{GeV}$

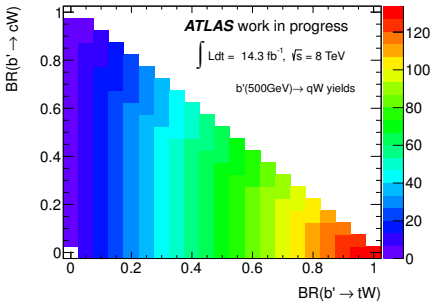

(c) $m_{b'} = 500\,\text{GeV}$

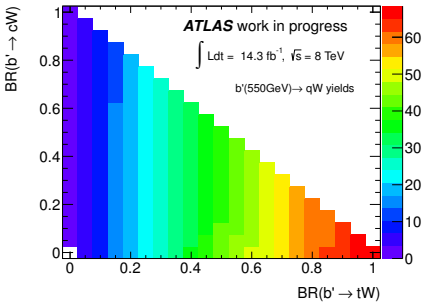

(d) $m_{b'} = 550\,\text{GeV}$

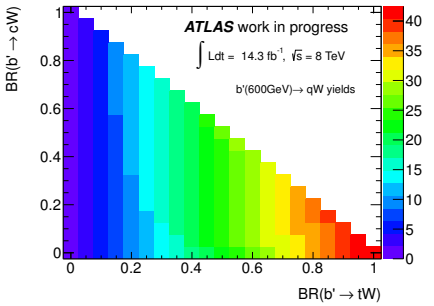

(e) $m_{b'} = 600\,\text{GeV}$

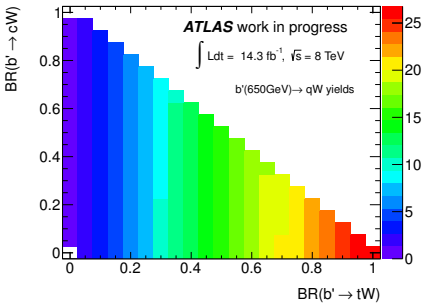

(f) $m_{b'} = 650\,\text{GeV}$

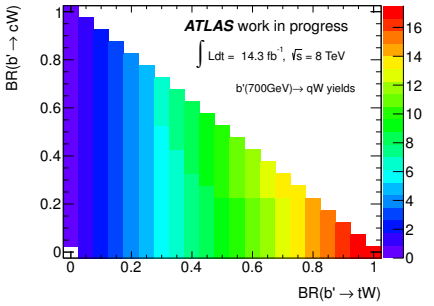

(g) $m_{b'} = 700\,\text{GeV}$

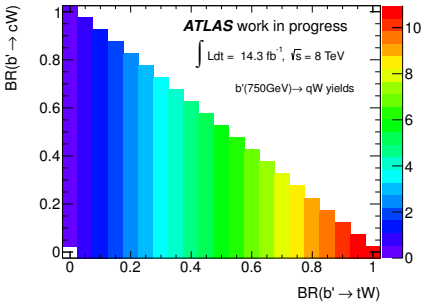

(h) $m_{b'} = 750\,\text{GeV}$

Figure 6.45: Expected signal yields depending on the branching fractions for $b' \to cW$ and $b' \to tW$ and for different b' masses. The yields are presented for the combination of the ee, $e\mu$ and $\mu\mu$ channel.

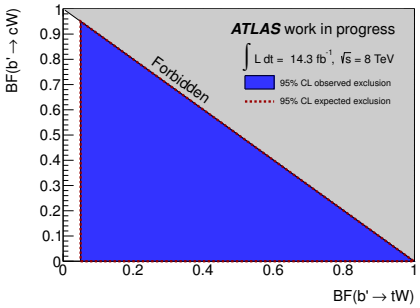

(a) $m_{b'} = 400\,\text{GeV}$

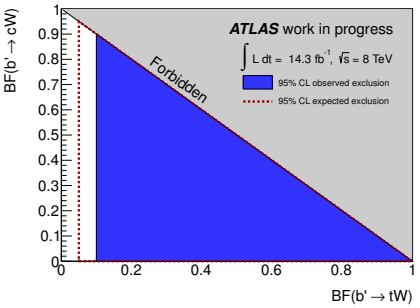

(b) $m_{b'} = 450\,\text{GeV}$

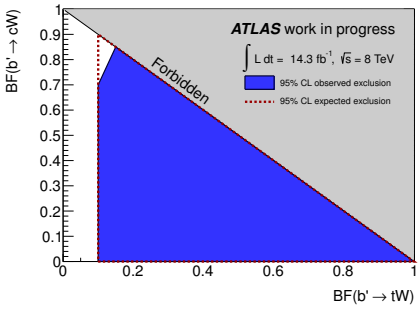

(c) $m_{b'} = 500\,\text{GeV}$

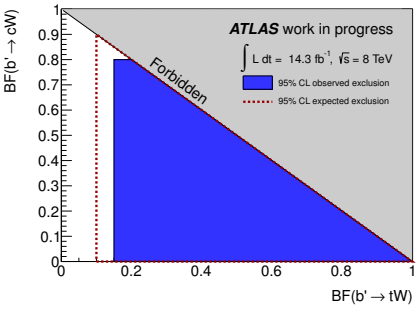

(d) $m_{b'} = 550\,\text{GeV}$

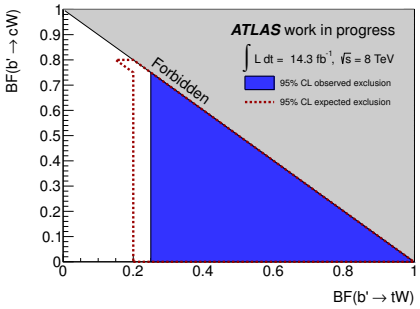

(e) $m_{b'} = 600\,\text{GeV}$

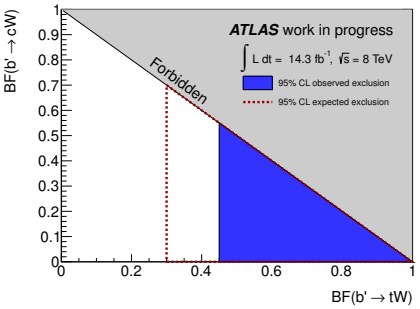

(f) $m_{b'} = 650\,\text{GeV}$

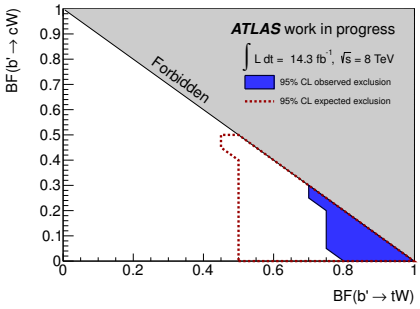

(g) $m_{b'} = 700\,\text{GeV}$

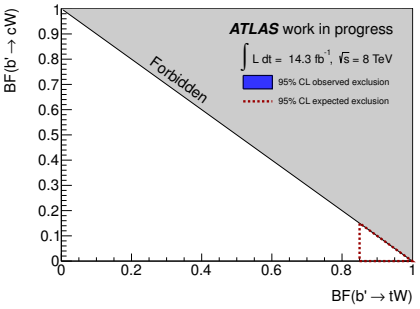

(h) $m_{b'} = 750\,\text{GeV}$

Figure 6.46: Expected and observed 95% CL exclusion ranges in the branching fraction plane for $b' \to cW$ and $b' \to tW$ and for different b' masses.

presented in Appendix D.2.2, showing that there are no exclusion areas visible. Furthermore, the obtained CL_s values in the $[BF(b' \to tW), BF(b' \to cW)]$ space are presented in the same Appendix.

In the exclusion areas of Figure 6.46, one also notices that these areas are nearly independent of the branching fraction for $b' \to cW$. This is expected due to the distribution of the signal yields previously presented in Figure 6.45. Therefore, it is justified to combine the obtained results for each b' mass point and present the exclusion areas in the $[BF(b' \to tW), m_{b'}]$ space, which is depicted in Figure 6.47. Here, a point for a

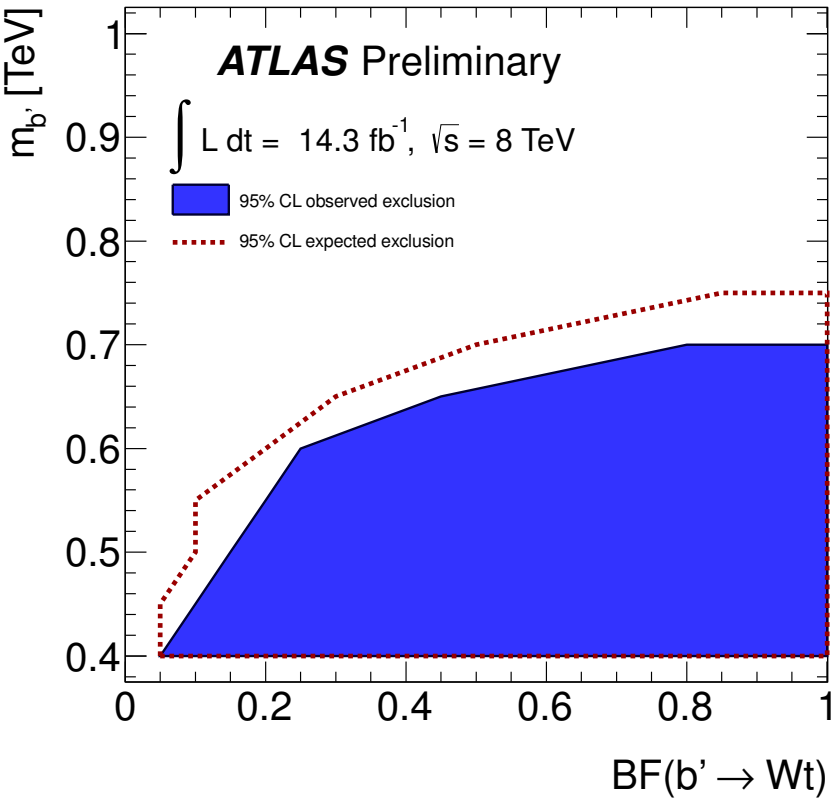

Figure 6.47: Expected and observed 95% CL exclusion ranges depending on the b' mass and the branching fraction for $b' \to tW$ [250]. A point is considered as excluded if it is also excluded over the whole branching fraction range for $b' \to cW$ and $b' \to uW$.

particular $b' \to tW$ branching fraction is considered as excluded, if it was excluded over the whole range of branching fractions for $b' \to cW$ and $b' \to uW$.
In the case of a zero branching fraction for $b' \to tW$, there can be no mass points excluded for any $BF(b' \to cW)$ and $BF(b' \to uW)$. This is explained by the fact that at least one b' quark is required to decay into tW in order to achieve a same-sign dilepton signature. In this case, no signal events are expected, which can be also seen in the

yields of Figure 6.45.
At $BF(b' \to tW) = 0.05$, only a mass of 400 GeV can be excluded. With increasing branching fractions for $b' \to tW$, the observed b' mass exclusion range becomes larger and reaches a maximum value of 750 GeV for branching fractions above 80%. While there is a sharp increase for branching fractions $BF(b' \to tW)$ between 0.05 and 0.25, the growth is smaller for branching fractions above 0.25.
One notices that for $BF(b' \to tW) = 100\%$, the exclusion range is slightly weaker than in the result obtained in Section 6.9.1 for the exclusive $b' \to tW$ sample. This is due to the fact, that both MC samples, $b' \to tW$ and $b' \to qW$, were generated with the same number of events. In the $b' \to qW$ sample, only about 1/3 of the b' quarks decay into tW and therefore, when assuming $BF(b' \to tW) = 100\%$, only a subset of the events is available compared to the $b' \to tW$ sample. This results in larger statistical uncertainties and hence weaker expected and observed limits. In order to obtain compatible results, one would have needed to generate the $b' \to qW$ samples with more statistics, or to combine the samples for $b' \to tW$ and $b' \to qW$.

7 Summary and outlook

In this thesis, I presented an analysis searching for $b'\bar{b}'$ production of the fourth generation b' quark. In this analysis, the fourth generation is considered as simple extension of the SM. This extension consists of the addition of two new quarks, the up-type t' and the down-type b', as well as two new leptons, the neutrino ν' and the charged lepton ℓ'. These particles were not discovered so far and hence lower mass constraints were derived in previous analyses as discussed in Section 2.2.3.
In Section 2.2.4, I discussed the implications of the recent Higgs results at the LHC for the model of the fourth generation. If the observed boson at a mass of 125 GeV is indeed the SM Higgs boson, then a fourth generation is ruled out with a significance of more than 5σ. However, additional studies have showed that a fourth generation might be still in accordance with the observations, if one extends the Higgs sector. For instance, the two Higgs doublet model (2HDM) would be a possible candidate model.

For the search for $b'\bar{b}'$ production, I analysed the data taken from the ATLAS detector in the time period between April and October 2012, which corresponds to an integrated luminosity of $\mathcal{L} = 14.3\,\text{fb}^{-1}$. The search was performed by selecting events with same-sign charged dileptons (ee, $e\mu$ or $\mu\mu$ events), which is a rare SM signature and hence well suited for searches for physics processes beyond the SM. In the analysis, I considered two different scenarios for the decay topology of the two b' quarks, which have been discussed in Sections 2.2.6 and 6.1:

- In the first scenario, I assumed that each b' quark decays exclusively into a t quark and a W boson. This represents the case that the mixing between the fourth and third fermion generation is significantly larger compared to the mixings with the second and first generation. Such a scenario is also preferred by the results from the studies on the electroweak precision observables (EWPOs), as it was discussed in Section 2.2.2. The resulting decay chain is as follows:

  $$b'\bar{b}' \to tW^+tW^- \to bW^+W^-bW^+W^-$$

  The last decays $t \to bW$ appear nearly exclusively due to the large size of the CKM matrix element $|V_{tb}|$. When two of the same-sign charged W bosons decay leptonically, this results in the final state of two same-sign charged dileptons.

- In the second scenario, I considered sizeable branching fractions for the decays $b' \to tW$, $b' \to cW$ and $b' \to uW$. This allowed for a more model independent study (in the sense of the size of the CKM matrix elements). When requiring two same-sign charged dileptons in the final state, at least one of the b' quarks needs

to decay into tW. This results in the following decay chain for this scenario:

$$b'\bar{b}' \rightarrow tW^+u/cW^- \rightarrow bW^+W^-u/cW^-$$

The case that both b' decay into tW is equal to the first considered scenario. Although a large mixing between the fourth and third generation (compared to the mixings with the first and second generation) is favoured by the EWPOs, mixings with the lighter second and first generation are not excluded. Therefore, I was able to draw conclusions depending on the branching fractions for $b' \rightarrow tW$, $b' \rightarrow cW$ and $b' \rightarrow uW$.

The processes for both scenarios were modelled by MC samples using the techniques described in Chapter 4.

For the final state of two same-sign charged leptons I needed to consider several background processes. On the one hand, there were irreducible backgrounds. These are SM processes that have same-sign dileptons in the final state and have been modelled by MC samples. In particular these were $t\bar{t}$ production in association with additional vector bosons, $W^{\pm}Z$ and ZZ diboson processes, and same-sign $W^{\pm}W^{\pm}$ production. On the other hand, a same-sign dilepton signature can arise from lepton mis-reconstruction and charge mis-identification in processes, that do not contain real same-sign dileptons in the final state.

The lepton mis-reconstruction background, also called 'lepton fakes', can arise from jets mis-identified as leptons, as well as reconstructed leptons coming from hadron decays. This background is estimated on data using the so-called 'matrix method', as described in Section 6.2.4. Additional precautions needed to be taken, in order to deal with the bias introduced by the isolated single muon trigger, which was used in the analysis. This required to select the real and fake muon efficiencies according to the muons trigger matches.

The charge mis-identification background, also called 'charge mis-id', can arise from true opposite-sign charged dilepton events, where the charge of one lepton is mis-identified. There are two main sources, which can yield in this effect. One source can come from hard bremsstrahlung of electrons, producing trident electrons in the events. Another source are mis-reconstructed track curvatures for electron candidates with high transverse momenta. The charge mis-id background is negligible for muons, therefore it was only considered for electrons in same-sign ee and $e\mu$ events. The overlap of the events used for the charge mis-id estimate, which were also captured by the matrix method for the lepton fakes, was taken into account.

The background modelling was validated in several control regions, which revealed a reasonable agreement between the observed data and the various background expectations (Section 6.8.2.1). The final event selection was optimised by assuming that no signal contribution above the background expectation would be observed. For this, I derived lower limits on the b' mass using the statistical method described in Section 6.4.3 after applying different event selection criteria. The combination of event selection criteria yielding in the highest mass limit, while retaining sufficient statistics, was taken as final event selection, as described in Section 6.7.1. This optimisation was performed for

the exclusive $b' \to tW$ scenario and revealed optimal cuts of at least two jets, at least one b-tagged jet, missing transverse energy of $E_T^{\text{miss}} \geq 40\,\text{GeV}$ and a total sum of the transverse momenta of electrons, muons and jets of $H_T \geq 650\,\text{GeV}$. These cuts were applied in addition to the basic event selection summarised in Table 6.15.

When applying the final event selection criteria on data, a total of 15 events were observed, while 9.3 ± 1.7 events were expected from the background estimate. The analysis was performed separately for the three dilepton channels ee, $e\mu$ and $\mu\mu$. In the $e\mu$ channel, a slight excess was observed, but with a significance below 2σ. Therefore, limits have been set within the two mentioned scenarios using the CL_s method described in Section 6.4.3. In the limit setting procedure, the various systematic uncertainties coming from the objects (electrons, muons and jets) energy scales, resolutions and efficiency scale factors have been considered. Furthermore, I included the systematic uncertainties on the luminosity measurement and the cross-sections assumed for the various processes modelled by MC. Finally, systematic uncertainties on the data-driven background estimates, lepton fakes and charge mis-id, were derived, which are considered in the limit setting as well.

In case of the exclusive $b' \to tW$ scenario, I derived upper cross-section limits for different b' masses, which were presented in Figure 6.41. Using the calculated approximate NNLO pair production cross-sections as a function of the b' mass, the cross-section limits were translated into a lower mass limit of the b'. In the scenario of exclusive $b' \to tW$ decays with 100% branching fraction, I have set a lower b' mass limit of $m_{b'} \geq 0.724\,\text{TeV}$, whereas I expected $m_{b'} \geq 0.767\,\text{TeV}$. The difference of about 40 GeV is due to the slight excess in the $e\mu$ channel. It should be noted, that this is the most stringent b' mass limit under this decay assumption, that has been set until now.

In case of the second scenario with mixed $b' \to qW$ ($q = u, c, t$) decays, I derived exclusion areas in the space of the branching fractions for $b' \to tW$, $b' \to cW$ and $b' \to uW$. This was performed separately for b' masses in the range $m_{b'} \in [400, 1000]$ GeV. The results revealed a strong dependence on the $b' \to tW$ branching fractions, which was expected due to the fact that at least one of the two b' quarks needs to decay into tW for achieving a same-sign dilepton signature. Therefore, I presented the exclusion area as a function of the b' mass and the branching fraction for $b' \to tW$ in Figure 6.47. The results showed that the observed mass limit is between 600 GeV and 700 GeV for branching fractions $BF(b' \to tW)$ between 0.25 and 1. For branching fractions below 0.25, the observed mass limit sharply decreases down to 400 GeV for $BF(b' \to tW) = 0.05$. No exclusion statement can be made for branching fractions $BF(b' \to tW)$ below 0.05. This was the first analysis that derived limits on the b' mass depending on the branching fractions for $b' \to tW$, $b' \to cW$ and $b' \to uW$. Hence, it is the most model independent b' search so far.

The presented limit results are the most stringent up to now, but there is still space for improvements. For instance, when lowering the systematic uncertainties, the derived limits would become more stringent.
This could be achieved by an improved estimation of the uncertainties on the cross sections for the processes modelled with MC. Another possibility would be to improve the data-driven techniques used for deriving the charge mis-id and lepton fakes backgrounds,

and lower their uncertainties.
However, in Section 6.9.1, I derived the lower b' mass limit when only considering the statistical uncertainties. The increase of the mass limit was only about 10 GeV and hence lowering the systematic uncertainties will have only a low impact.

A better sensitivity for higher b' masses could be achieved by increasing the data statistics. This analysis was performed using a reduced dataset corresponding to $\mathcal{L} = 14.3\,\text{fb}^{-1}$. When moving to the full dataset taken in 2012, which corresponds to $\mathcal{L} = 20.3\,\text{fb}^{-1}$, higher b' masses would be accessible. An even larger increase in the sensitivity is expected for the larger dataset expected for the data taking period starting in 2014 with a centre-of-mass energy of at least 13 TeV.

The final state of two same-sign charged leptons has a high sensitivity for the scenario, where both b' decay as $b' \to tW$. In case of the $b' \to u/c + W$ decays, the analysis has no sensitivity. This was visible from the results in Section 6.9.2, where the limit results were mostly independent on the branching fractions for the decays $b' \to cW$ and $b' \to uW$. Hence, the analysis could be improved for such decays, by selecting a different final state with higher sensitivity (for instance single leptons or opposite-sign dileptons, as it is done in top-like searches). This would allow to obtain complementary results for the decay topologies $b' \to tW$ and $b' \to u/c + W$.

The presented results were all derived under the assumption that the fourth generation quarks have short lifetimes. As I already mentioned in Section 2.2.3, the assumption of longer lifetimes would require different search strategies, and hence could result in different mass limits.

A Samples used in the analysis

This appendix gives a summary of the samples used in the analysis.
Each MC sample is given with the ATLAS dataset identification number (DSID) and the D3PD sample name. Number of events, cross-section and corresponding integrated luminosity are summarised in Tables 6.2 and 6.3.
For the data samples only the D3PD names are given.

A.1 Data samples

Run number	D3PD name
00200804	data12_8TeV.00200804.physics_Egamma.merge.NTUP_TOPEL.f437_m1126_p1269_p1270/
00200842	data12_8TeV.00200842.physics_Egamma.merge.NTUP_TOPEL.f437_m1126_p1269_p1270/
00200863	data12_8TeV.00200863.physics_Egamma.merge.NTUP_TOPEL.f437_m1126_p1269_p1270/
00200913	data12_8TeV.00200913.physics_Egamma.merge.NTUP_TOPEL.f437_m1126_p1269_p1270/
00200926	data12_8TeV.00200926.physics_Egamma.merge.NTUP_TOPEL.f437_m1126_p1269_p1270/
00200965	data12_8TeV.00200965.physics_Egamma.merge.NTUP_TOPEL.f437_m1126_p1269_p1270/
00200967	data12_8TeV.00200967.physics_Egamma.merge.NTUP_TOPEL.f437_m1126_p1269_p1270/
00200982	data12_8TeV.00200982.physics_Egamma.merge.NTUP_TOPEL.f437_m1126_p1269_p1270/
00200987	data12_8TeV.00200987.physics_Egamma.merge.NTUP_TOPEL.f437_m1126_p1269_p1270/
00201006	data12_8TeV.00201006.physics_Egamma.merge.NTUP_TOPEL.f437_m1126_p1269_p1270/
00201052	data12_8TeV.00201052.physics_Egamma.merge.NTUP_TOPEL.f437_m1126_p1269_p1270/
00201113	data12_8TeV.00201113.physics_Egamma.merge.NTUP_TOPEL.f437_m1126_p1269_p1270/
00201120	data12_8TeV.00201120.physics_Egamma.merge.NTUP_TOPEL.f437_m1126_p1269_p1270/
00201138	data12_8TeV.00201138.physics_Egamma.merge.NTUP_TOPEL.f437_m1126_p1269_p1270/
00201190	data12_8TeV.00201190.physics_Egamma.merge.NTUP_TOPEL.f437_m1126_p1269_p1270/
00201191	data12_8TeV.00201191.physics_Egamma.merge.NTUP_TOPEL.f437_m1126_p1269_p1270/
00201257	data12_8TeV.00201257.physics_Egamma.merge.NTUP_TOPEL.f437_m1126_p1269_p1270/
00201269	data12_8TeV.00201269.physics_Egamma.merge.NTUP_TOPEL.f437_m1126_p1269_p1270/
00201280	data12_8TeV.00201280.physics_Egamma.merge.NTUP_TOPEL.f437_m1126_p1269_p1270/
00201289	data12_8TeV.00201289.physics_Egamma.merge.NTUP_TOPEL.f437_m1126_p1269_p1270/
00201351	data12_8TeV.00201351.physics_Egamma.merge.NTUP_TOPEL.f437_m1126_p1269_p1270/
00201383	data12_8TeV.00201383.physics_Egamma.merge.NTUP_TOPEL.f437_m1126_p1269_p1270/
00201489	data12_8TeV.00201489.physics_Egamma.merge.NTUP_TOPEL.f437_m1126_p1269_p1270/
00201494	data12_8TeV.00201494.physics_Egamma.merge.NTUP_TOPEL.f437_m1126_p1269_p1270/
00201555	data12_8TeV.00201555.physics_Egamma.merge.NTUP_TOPEL.f437_m1126_p1269_p1270/
00201556	data12_8TeV.00201556.physics_Egamma.merge.NTUP_TOPEL.f437_m1126_p1269_p1270/
00202660	data12_8TeV.00202660.physics_Egamma.merge.NTUP_TOPEL.f442_m1136_p1269_p1270/
00202668	data12_8TeV.00202668.physics_Egamma.merge.NTUP_TOPEL.f443_m1136_p1269_p1270/
00202712	data12_8TeV.00202712.physics_Egamma.merge.NTUP_TOPEL.f443_m1136_p1269_p1270/
00202740	data12_8TeV.00202740.physics_Egamma.merge.NTUP_TOPEL.f443_m1136_p1269_p1270/
00202798	data12_8TeV.00202798.physics_Egamma.merge.NTUP_TOPEL.f443_m1136_p1269_p1270/
00202965	data12_8TeV.00202965.physics_Egamma.merge.NTUP_TOPEL.f443_m1136_p1269_p1270/
00202987	data12_8TeV.00202987.physics_Egamma.merge.NTUP_TOPEL.f443_m1136_p1269_p1270/
00202991	data12_8TeV.00202991.physics_Egamma.merge.NTUP_TOPEL.f443_m1136_p1269_p1270/
00203027	data12_8TeV.00203027.physics_Egamma.merge.NTUP_TOPEL.f443_m1143_p1269_p1270/
00203169	data12_8TeV.00203169.physics_Egamma.merge.NTUP_TOPEL.f444_m1143_p1269_p1270/
00203191	data12_8TeV.00203191.physics_Egamma.merge.NTUP_TOPEL.f444_m1143_p1269_p1270/
00203195	data12_8TeV.00203195.physics_Egamma.merge.NTUP_TOPEL.f444_m1143_p1269_p1270/
00203228	data12_8TeV.00203228.physics_Egamma.merge.NTUP_TOPEL.f444_m1143_p1269_p1270/
00203256	data12_8TeV.00203256.physics_Egamma.merge.NTUP_TOPEL.f444_m1143_p1269_p1270/
00203258	data12_8TeV.00203258.physics_Egamma.merge.NTUP_TOPEL.f444_m1143_p1269_p1270/
00203277	data12_8TeV.00203277.physics_Egamma.merge.NTUP_TOPEL.f444_m1148_p1269_p1270/
00203335	data12_8TeV.00203335.physics_Egamma.merge.NTUP_TOPEL.f446_m1148_p1269_p1270/
00203336	data12_8TeV.00203336.physics_Egamma.merge.NTUP_TOPEL.f446_m1148_p1269_p1270/
00203353	data12_8TeV.00203353.physics_Egamma.merge.NTUP_TOPEL.f446_m1148_p1269_p1270/
00203432	data12_8TeV.00203432.physics_Egamma.merge.NTUP_TOPEL.f446_m1148_p1269_p1270/
00203454	data12_8TeV.00203454.physics_Egamma.merge.NTUP_TOPEL.f446_m1148_p1269_p1270/
00203456	data12_8TeV.00203456.physics_Egamma.merge.NTUP_TOPEL.f446_m1148_p1269_p1270/
00203523	data12_8TeV.00203523.physics_Egamma.merge.NTUP_TOPEL.f446_m1148_p1269_p1270/
00203524	data12_8TeV.00203524.physics_Egamma.merge.NTUP_TOPEL.f446_m1148_p1269_p1270/
00203602	data12_8TeV.00203602.physics_Egamma.merge.NTUP_TOPEL.f446_m1148_p1269_p1270/
00203605	data12_8TeV.00203605.physics_Egamma.merge.NTUP_TOPEL.f446_m1148_p1269_p1270/
00203636	data12_8TeV.00203636.physics_Egamma.merge.NTUP_TOPEL.f446_m1148_p1269_p1270/

00203680	data12_8TeV.00203680.physics_Egamma.merge.NTUP_TOPEL.f446_m1148_p1269_p1270/
00203719	data12_8TeV.00203719.physics_Egamma.merge.NTUP_TOPEL.f446_m1148_p1269_p1270/
00203739	data12_8TeV.00203739.physics_Egamma.merge.NTUP_TOPEL.f446_m1148_p1269_p1270/
00203745	data12_8TeV.00203745.physics_Egamma.merge.NTUP_TOPEL.f446_m1148_p1269_p1270/
00203760	data12_8TeV.00203760.physics_Egamma.merge.NTUP_TOPEL.f446_m1148_p1269_p1270/
00203779	data12_8TeV.00203779.physics_Egamma.merge.NTUP_TOPEL.f446_m1153_p1269_p1270/
00203792	data12_8TeV.00203792.physics_Egamma.merge.NTUP_TOPEL.f446_m1153_p1269_p1270/
00203875	data12_8TeV.00203875.physics_Egamma.merge.NTUP_TOPEL.f446_m1153_p1269_p1270/
00203876	data12_8TeV.00203876.physics_Egamma.merge.NTUP_TOPEL.f447_m1153_p1269_p1270/
00203934	data12_8TeV.00203934.physics_Egamma.merge.NTUP_TOPEL.f447_m1153_p1269_p1270/
00204025	data12_8TeV.00204025.physics_Egamma.merge.NTUP_TOPEL.f447_m1153_p1269_p1270/
00204026	data12_8TeV.00204026.physics_Egamma.merge.NTUP_TOPEL.f447_m1153_p1269_p1270/
00204071	data12_8TeV.00204071.physics_Egamma.merge.NTUP_TOPEL.f447_m1153_p1269_p1270/
00204073	data12_8TeV.00204073.physics_Egamma.merge.NTUP_TOPEL.f447_m1153_p1269_p1270/
00204134	data12_8TeV.00204134.physics_Egamma.merge.NTUP_TOPEL.f447_m1153_p1269_p1270/
00204153	data12_8TeV.00204153.physics_Egamma.merge.NTUP_TOPEL.f447_m1153_p1269_p1270/
00204158	data12_8TeV.00204158.physics_Egamma.merge.NTUP_TOPEL.f447_m1153_p1269_p1270/
00204240	data12_8TeV.00204240.physics_Egamma.merge.NTUP_TOPEL.f447_m1153_p1269_p1270/
00204265	data12_8TeV.00204265.physics_Egamma.merge.NTUP_TOPEL.f447_m1158_p1269_p1270/
00204416	data12_8TeV.00204416.physics_Egamma.merge.NTUP_TOPEL.f448_m1158_p1269_p1270/
00204442	data12_8TeV.00204442.physics_Egamma.merge.NTUP_TOPEL.f448_m1158_p1269_p1270/
00204474	data12_8TeV.00204474.physics_Egamma.merge.NTUP_TOPEL.f448_m1158_p1269_p1270/
00204564	data12_8TeV.00204564.physics_Egamma.merge.NTUP_TOPEL.f448_m1158_p1269_p1270/
00204633	data12_8TeV.00204633.physics_Egamma.merge.NTUP_TOPEL.f448_m1158_p1269_p1270/
00204668	data12_8TeV.00204668.physics_Egamma.merge.NTUP_TOPEL.f448_m1158_p1269_p1270/
00204707	data12_8TeV.00204707.physics_Egamma.merge.NTUP_TOPEL.f448_m1163_p1269_p1270/
00204726	data12_8TeV.00204726.physics_Egamma.merge.NTUP_TOPEL.f448_m1163_p1269_p1270/
00204763	data12_8TeV.00204763.physics_Egamma.merge.NTUP_TOPEL.f448_m1163_p1269_p1270/
00204769	data12_8TeV.00204769.physics_Egamma.merge.NTUP_TOPEL.f448_m1163_p1269_p1270/
00204772	data12_8TeV.00204772.physics_Egamma.merge.NTUP_TOPEL.f449_m1163_p1269_p1270/
00204796	data12_8TeV.00204796.physics_Egamma.merge.NTUP_TOPEL.f449_m1163_p1269_p1270/
00204853	data12_8TeV.00204853.physics_Egamma.merge.NTUP_TOPEL.f449_m1163_p1269_p1270/
00204857	data12_8TeV.00204857.physics_Egamma.merge.NTUP_TOPEL.f449_m1163_p1269_p1270/
00204910	data12_8TeV.00204910.physics_Egamma.merge.NTUP_TOPEL.f449_m1163_p1269_p1270/
00204932	data12_8TeV.00204932.physics_Egamma.merge.NTUP_TOPEL.f449_m1163_p1269_p1270/
00204954	data12_8TeV.00204954.physics_Egamma.merge.NTUP_TOPEL.f449_m1163_p1269_p1270/
00204955	data12_8TeV.00204955.physics_Egamma.merge.NTUP_TOPEL.f449_m1163_p1269_p1270/
00204976	data12_8TeV.00204976.physics_Egamma.merge.NTUP_TOPEL.f449_m1163_p1269_p1270/
00205010	data12_8TeV.00205010.physics_Egamma.merge.NTUP_TOPEL.f449_m1163_p1269_p1270/
00205016	data12_8TeV.00205016.physics_Egamma.merge.NTUP_TOPEL.f449_m1163_p1269_p1270/
00205017	data12_8TeV.00205017.physics_Egamma.merge.NTUP_TOPEL.f449_m1163_p1269_p1270/
00205055	data12_8TeV.00205055.physics_Egamma.merge.NTUP_TOPEL.f449_m1163_p1269_p1270/
00205071	data12_8TeV.00205071.physics_Egamma.merge.NTUP_TOPEL.f449_m1163_p1269_p1270/
00205112	data12_8TeV.00205112.physics_Egamma.merge.NTUP_TOPEL.f449_m1163_p1269_p1270/
00205113	data12_8TeV.00205113.physics_Egamma.merge.NTUP_TOPEL.f449_m1163_p1269_p1270/
00206248	data12_8TeV.00206248.physics_Egamma.merge.NTUP_TOPEL.f452_m1170_p1269_p1270/
00206253	data12_8TeV.00206253.physics_Egamma.merge.NTUP_TOPEL.f452_m1170_p1269_p1270/
00206299	data12_8TeV.00206299.physics_Egamma.merge.NTUP_TOPEL.f450_m1170_p1269_p1270/
00206367	data12_8TeV.00206367.physics_Egamma.merge.NTUP_TOPEL.f450_m1170_p1269_p1270/
00206368	data12_8TeV.00206368.physics_Egamma.merge.NTUP_TOPEL.f450_m1170_p1269_p1270/
00206369	data12_8TeV.00206369.physics_Egamma.merge.NTUP_TOPEL.f450_m1175_p1269_p1270/
00206409	data12_8TeV.00206409.physics_Egamma.merge.NTUP_TOPEL.f450_m1175_p1269_p1270/
00206497	data12_8TeV.00206497.physics_Egamma.merge.NTUP_TOPEL.f453_m1175_p1269_p1270/
00206564	data12_8TeV.00206564.physics_Egamma.merge.NTUP_TOPEL.f457_m1180_p1269_p1270/
00206573	data12_8TeV.00206573.physics_Egamma.merge.NTUP_TOPEL.f458_m1180_p1269_p1270/
00206614	data12_8TeV.00206614.physics_Egamma.merge.NTUP_TOPEL.f456_m1180_p1269_p1270/
00206955	data12_8TeV.00206955.physics_Egamma.merge.NTUP_TOPEL.f456_m1180_p1269_p1270/
00206962	data12_8TeV.00206962.physics_Egamma.merge.NTUP_TOPEL.f456_m1186_p1269_p1270/
00206971	data12_8TeV.00206971.physics_Egamma.merge.NTUP_TOPEL.f456_m1186_p1269_p1270/
00207044	data12_8TeV.00207044.physics_Egamma.merge.NTUP_TOPEL.f462_m1186_p1269_p1270/
00207046	data12_8TeV.00207046.physics_Egamma.merge.NTUP_TOPEL.f462_m1186_p1269_p1270/
00207113	data12_8TeV.00207113.physics_Egamma.merge.NTUP_TOPEL.f464_m1186_p1269_p1270/
00207221	data12_8TeV.00207221.physics_Egamma.merge.NTUP_TOPEL.f464_m1186_p1269_p1270/
00207262	data12_8TeV.00207262.physics_Egamma.merge.NTUP_TOPEL.f464_m1186_p1269_p1270/
00207304	data12_8TeV.00207304.physics_Egamma.merge.NTUP_TOPEL.f464_m1186_p1269_p1270/
00207306	data12_8TeV.00207306.physics_Egamma.merge.NTUP_TOPEL.f464_m1186_p1269_p1270/
00207332	data12_8TeV.00207332.physics_Egamma.merge.NTUP_TOPEL.f464_m1191_p1269_p1270/
00207397	data12_8TeV.00207397.physics_Egamma.merge.NTUP_TOPEL.f464_m1191_p1269_p1270/
00207447	data12_8TeV.00207447.physics_Egamma.merge.NTUP_TOPEL.f466_m1191_p1269_p1270/
00207490	data12_8TeV.00207490.physics_Egamma.merge.NTUP_TOPEL.f466_m1191_p1269_p1270/
00207528	data12_8TeV.00207528.physics_Egamma.merge.NTUP_TOPEL.f467_m1191_p1269_p1270/
00207531	data12_8TeV.00207531.physics_Egamma.merge.NTUP_TOPEL.f467_m1191_p1269_p1270/
00207532	data12_8TeV.00207532.physics_Egamma.merge.NTUP_TOPEL.f467_m1191_p1269_p1270/
00207582	data12_8TeV.00207582.physics_Egamma.merge.NTUP_TOPEL.f467_m1191_p1269_p1270/
00207589	data12_8TeV.00207589.physics_Egamma.merge.NTUP_TOPEL.f467_m1191_p1269_p1270/
00207620	data12_8TeV.00207620.physics_Egamma.merge.NTUP_TOPEL.f467_m1197_p1269_p1270/
00207664	data12_8TeV.00207664.physics_Egamma.merge.NTUP_TOPEL.f468_m1202_p1269_p1270/
00207696	data12_8TeV.00207696.physics_Egamma.merge.NTUP_TOPEL.f468_m1202_p1269_p1270/
00207749	data12_8TeV.00207749.physics_Egamma.merge.NTUP_TOPEL.f469_m1202_p1269_p1270/
00207772	data12_8TeV.00207772.physics_Egamma.merge.NTUP_TOPEL.f469_m1202_p1269_p1270/
00207800	data12_8TeV.00207800.physics_Egamma.merge.NTUP_TOPEL.f470_m1202_p1269_p1270/
00207809	data12_8TeV.00207809.physics_Egamma.merge.NTUP_TOPEL.f470_m1202_p1269_p1270/
00207845	data12_8TeV.00207845.physics_Egamma.merge.NTUP_TOPEL.f470_m1202_p1269_p1270/
00207864	data12_8TeV.00207864.physics_Egamma.merge.NTUP_TOPEL.f470_m1202_p1269_p1270/

00207865	data12_8TeV.00207865.physics_Egamma.merge.NTUP_TOPEL.f470_m1202_p1269_p1270/
00207929	data12_8TeV.00207929.physics_Egamma.merge.NTUP_TOPEL.f470_m1202_p1269_p1270/
00207931	data12_8TeV.00207931.physics_Egamma.merge.NTUP_TOPEL.f470_m1202_p1269_p1270/
00207934	data12_8TeV.00207934.physics_Egamma.merge.NTUP_TOPEL.f470_m1202_p1269_p1270/
00207975	data12_8TeV.00207975.physics_Egamma.merge.NTUP_TOPEL.f470_m1202_p1269_p1270/
00207982	data12_8TeV.00207982.physics_Egamma.merge.NTUP_TOPEL.f470_m1202_p1269_p1270/
00208123	data12_8TeV.00208123.physics_Egamma.merge.NTUP_TOPEL.f470_m1202_p1269_p1270/
00208126	data12_8TeV.00208126.physics_Egamma.merge.NTUP_TOPEL.f470_m1202_p1269_p1270/
00208179	data12_8TeV.00208179.physics_Egamma.merge.NTUP_TOPEL.f470_m1202_p1269_p1270/
00208184	data12_8TeV.00208184.physics_Egamma.merge.NTUP_TOPEL.f470_m1202_p1269_p1270/
00208189	data12_8TeV.00208189.physics_Egamma.merge.NTUP_TOPEL.f470_m1208_p1269_p1270/
00208258	data12_8TeV.00208258.physics_Egamma.merge.NTUP_TOPEL.f470_m1208_p1269_p1270/
00208261	data12_8TeV.00208261.physics_Egamma.merge.NTUP_TOPEL.f472_m1208_p1269_p1270/
00208354	data12_8TeV.00208354.physics_Egamma.merge.NTUP_TOPEL.f472_m1208_p1269_p1270/
00208484	data12_8TeV.00208484.physics_Egamma.merge.NTUP_TOPEL.f472_m1208_p1269_p1270/
00208485	data12_8TeV.00208485.physics_Egamma.merge.NTUP_TOPEL.f472_m1208_p1269_p1270/
00208631	data12_8TeV.00208631.physics_Egamma.merge.NTUP_TOPEL.f472_m1208_p1269_p1270/
00208642	data12_8TeV.00208642.physics_Egamma.merge.NTUP_TOPEL.f472_m1208_p1269_p1270/
00208662	data12_8TeV.00208662.physics_Egamma.merge.NTUP_TOPEL.f472_m1208_p1269_p1270/
00208705	data12_8TeV.00208705.physics_Egamma.merge.NTUP_TOPEL.f472_m1208_p1269_p1270/
00208717	data12_8TeV.00208717.physics_Egamma.merge.NTUP_TOPEL.f472_m1208_p1269_p1270/
00208720	data12_8TeV.00208720.physics_Egamma.merge.NTUP_TOPEL.f472_m1208_p1269_p1270/
00208780	data12_8TeV.00208780.physics_Egamma.merge.NTUP_TOPEL.f472_m1208_p1269_p1270/
00208781	data12_8TeV.00208781.physics_Egamma.merge.NTUP_TOPEL.f472_m1208_p1269_p1270/
00208811	data12_8TeV.00208811.physics_Egamma.merge.NTUP_TOPEL.f472_m1208_p1269_p1270/
00208870	data12_8TeV.00208870.physics_Egamma.merge.NTUP_TOPEL.f472_m1208_p1269_p1270/
00208930	data12_8TeV.00208930.physics_Egamma.merge.NTUP_TOPEL.f472_m1208_p1269_p1270/
00208931	data12_8TeV.00208931.physics_Egamma.merge.NTUP_TOPEL.f472_m1208_p1269_p1270/
00208970	data12_8TeV.00208970.physics_Egamma.merge.NTUP_TOPEL.f472_m1208_p1269_p1270/
00208982	data12_8TeV.00208982.physics_Egamma.merge.NTUP_TOPEL.f472_m1213_p1269_p1270/
00209025	data12_8TeV.00209025.physics_Egamma.merge.NTUP_TOPEL.f473_m1213_p1269_p1270/
00209074	data12_8TeV.00209074.physics_Egamma.merge.NTUP_TOPEL.f473_m1213_p1269_p1270/
00209084	data12_8TeV.00209084.physics_Egamma.merge.NTUP_TOPEL.f473_m1213_p1269_p1270/
00209109	data12_8TeV.00209109.physics_Egamma.merge.NTUP_TOPEL.f473_m1213_p1269_p1270/
00209161	data12_8TeV.00209161.physics_Egamma.merge.NTUP_TOPEL.f473_m1213_p1269_p1270/
00209183	data12_8TeV.00209183.physics_Egamma.merge.NTUP_TOPEL.f473_m1213_p1269_p1270/
00209214	data12_8TeV.00209214.physics_Egamma.merge.NTUP_TOPEL.f473_m1213_p1269_p1270/
00209254	data12_8TeV.00209254.physics_Egamma.merge.NTUP_TOPEL.f473_m1213_p1269_p1270/
00209265	data12_8TeV.00209265.physics_Egamma.merge.NTUP_TOPEL.f473_m1213_p1269_p1270/
00209269	data12_8TeV.00209269.physics_Egamma.merge.NTUP_TOPEL.f473_m1218_p1269_p1270/
00209353	data12_8TeV.00209353.physics_Egamma.merge.NTUP_TOPEL.f473_m1218_p1269_p1270/
00209381	data12_8TeV.00209381.physics_Egamma.merge.NTUP_TOPEL.f473_m1218_p1269_p1270/
00209550	data12_8TeV.00209550.physics_Egamma.merge.NTUP_TOPEL.f475_m1218_p1269_p1270/
00209580	data12_8TeV.00209580.physics_Egamma.merge.NTUP_TOPEL.f475_m1218_p1269_p1270/
00209608	data12_8TeV.00209608.physics_Egamma.merge.NTUP_TOPEL.f475_m1218_p1269_p1270/
00209628	data12_8TeV.00209628.physics_Egamma.merge.NTUP_TOPEL.f475_m1218_p1269_p1270/
00209629	data12_8TeV.00209629.physics_Egamma.merge.NTUP_TOPEL.f475_m1218_p1269_p1270/
00209736	data12_8TeV.00209736.physics_Egamma.merge.NTUP_TOPEL.f475_m1218_p1269_p1270/
00209776	data12_8TeV.00209776.physics_Egamma.merge.NTUP_TOPEL.f475_m1218_p1269_p1270/
00209787	data12_8TeV.00209787.physics_Egamma.merge.NTUP_TOPEL.f475_m1218_p1269_p1270/
00209812	data12_8TeV.00209812.physics_Egamma.merge.NTUP_TOPEL.f475_m1218_p1269_p1270/
00209864	data12_8TeV.00209864.physics_Egamma.merge.NTUP_TOPEL.f475_m1218_p1269_p1270/
00209866	data12_8TeV.00209866.physics_Egamma.merge.NTUP_TOPEL.f475_m1223_p1269_p1270/
00209899	data12_8TeV.00209899.physics_Egamma.merge.NTUP_TOPEL.f475_m1223_p1269_p1270/
00209909	data12_8TeV.00209909.physics_Egamma.merge.NTUP_TOPEL.f475_m1223_p1269_p1270/
00209980	data12_8TeV.00209980.physics_Egamma.merge.NTUP_TOPEL.f476_m1223_p1269_p1270/
00209994	data12_8TeV.00209994.physics_Egamma.merge.NTUP_TOPEL.f476_m1223_p1269_p1270/
00209995	data12_8TeV.00209995.physics_Egamma.merge.NTUP_TOPEL.f476_m1223_p1269_p1270/
00210302	data12_8TeV.00210302.physics_Egamma.merge.NTUP_TOPEL.f476_m1223_p1269_p1270/
00210308	data12_8TeV.00210308.physics_Egamma.merge.NTUP_TOPEL.f476_m1223_p1269_p1270/
00211522	data12_8TeV.00211522.physics_Egamma.merge.NTUP_TOPEL.f479_m1228_p1269_p1270/
00211620	data12_8TeV.00211620.physics_Egamma.merge.NTUP_TOPEL.f479_m1228_p1269_p1270/
00211670	data12_8TeV.00211670.physics_Egamma.merge.NTUP_TOPEL.f479_m1228_p1269_p1270/
00211697	data12_8TeV.00211697.physics_Egamma.merge.NTUP_TOPEL.f479_m1228_p1269_p1270/
00211772	data12_8TeV.00211772.physics_Egamma.merge.NTUP_TOPEL.f479_m1228_p1269_p1270/
00211787	data12_8TeV.00211787.physics_Egamma.merge.NTUP_TOPEL.f479_m1228_p1269_p1270/
00211867	data12_8TeV.00211867.physics_Egamma.merge.NTUP_TOPEL.f479_m1228_p1269_p1270/
00211902	data12_8TeV.00211902.physics_Egamma.merge.NTUP_TOPEL.f479_m1228_p1269_p1270/
00211937	data12_8TeV.00211937.physics_Egamma.merge.NTUP_TOPEL.f479_m1228_p1269_p1270/
00212000	data12_8TeV.00212000.physics_Egamma.merge.NTUP_TOPEL.f479_m1228_p1269_p1270/
00212034	data12_8TeV.00212034.physics_Egamma.merge.NTUP_TOPEL.f479_m1228_p1269_p1270/
00212103	data12_8TeV.00212103.physics_Egamma.merge.NTUP_TOPEL.f479_m1228_p1269_p1270/
00212142	data12_8TeV.00212142.physics_Egamma.merge.NTUP_TOPEL.f479_m1228_p1269_p1270/
00212144	data12_8TeV.00212144.physics_Egamma.merge.NTUP_TOPEL.f479_m1228_p1269_p1270/
00212172	data12_8TeV.00212172.physics_Egamma.merge.NTUP_TOPEL.f479_m1228_p1269_p1270/
00212199	data12_8TeV.00212199.physics_Egamma.merge.NTUP_TOPEL.f479_m1228_p1269_p1270/
00212272	data12_8TeV.00212272.physics_Egamma.merge.NTUP_TOPEL.f479_m1228_p1269_p1270/

Table A.1: Data samples from the `Egamma` stream used in the analysis. Each sample corresponds to one run number. All listed runs represent the collected data in the periods A-G.

Run number	D3PD name
00200804	data12_8TeV.00200804.physics_Muons.merge.NTUP_TOPMU.f437_m1126_p1269_p1270/
00200842	data12_8TeV.00200842.physics_Muons.merge.NTUP_TOPMU.f437_m1126_p1269_p1270/
00200863	data12_8TeV.00200863.physics_Muons.merge.NTUP_TOPMU.f437_m1126_p1269_p1270/
00200913	data12_8TeV.00200913.physics_Muons.merge.NTUP_TOPMU.f437_m1126_p1269_p1270/
00200926	data12_8TeV.00200926.physics_Muons.merge.NTUP_TOPMU.f437_m1126_p1269_p1270/
00200965	data12_8TeV.00200965.physics_Muons.merge.NTUP_TOPMU.f437_m1126_p1269_p1270/
00200967	data12_8TeV.00200967.physics_Muons.merge.NTUP_TOPMU.f437_m1126_p1269_p1270/
00200982	data12_8TeV.00200982.physics_Muons.merge.NTUP_TOPMU.f437_m1126_p1269_p1270/
00200987	data12_8TeV.00200987.physics_Muons.merge.NTUP_TOPMU.f437_m1126_p1269_p1270/
00201006	data12_8TeV.00201006.physics_Muons.merge.NTUP_TOPMU.f437_m1126_p1269_p1270/
00201052	data12_8TeV.00201052.physics_Muons.merge.NTUP_TOPMU.f437_m1126_p1269_p1270/
00201113	data12_8TeV.00201113.physics_Muons.merge.NTUP_TOPMU.f437_m1126_p1269_p1270/
00201120	data12_8TeV.00201120.physics_Muons.merge.NTUP_TOPMU.f437_m1126_p1269_p1270/
00201138	data12_8TeV.00201138.physics_Muons.merge.NTUP_TOPMU.f437_m1126_p1269_p1270/
00201190	data12_8TeV.00201190.physics_Muons.merge.NTUP_TOPMU.f437_m1126_p1269_p1270/
00201191	data12_8TeV.00201191.physics_Muons.merge.NTUP_TOPMU.f437_m1126_p1269_p1270/
00201257	data12_8TeV.00201257.physics_Muons.merge.NTUP_TOPMU.f437_m1126_p1269_p1270/
00201269	data12_8TeV.00201269.physics_Muons.merge.NTUP_TOPMU.f437_m1126_p1269_p1270/
00201280	data12_8TeV.00201280.physics_Muons.merge.NTUP_TOPMU.f437_m1126_p1269_p1270/
00201289	data12_8TeV.00201289.physics_Muons.merge.NTUP_TOPMU.f437_m1126_p1269_p1270/
00201351	data12_8TeV.00201351.physics_Muons.merge.NTUP_TOPMU.f437_m1126_p1269_p1270/
00201383	data12_8TeV.00201383.physics_Muons.merge.NTUP_TOPMU.f437_m1126_p1269_p1270/
00201489	data12_8TeV.00201489.physics_Muons.merge.NTUP_TOPMU.f437_m1126_p1269_p1270/
00201494	data12_8TeV.00201494.physics_Muons.merge.NTUP_TOPMU.f437_m1126_p1269_p1270/
00201555	data12_8TeV.00201555.physics_Muons.merge.NTUP_TOPMU.f437_m1126_p1269_p1270/
00201556	data12_8TeV.00201556.physics_Muons.merge.NTUP_TOPMU.f437_m1126_p1269_p1270/
00202660	data12_8TeV.00202660.physics_Muons.merge.NTUP_TOPMU.f442_m1136_p1269_p1270/
00202668	data12_8TeV.00202668.physics_Muons.merge.NTUP_TOPMU.f443_m1136_p1269_p1270/
00202712	data12_8TeV.00202712.physics_Muons.merge.NTUP_TOPMU.f443_m1136_p1269_p1270/
00202740	data12_8TeV.00202740.physics_Muons.merge.NTUP_TOPMU.f443_m1136_p1269_p1270/
00202798	data12_8TeV.00202798.physics_Muons.merge.NTUP_TOPMU.f443_m1136_p1269_p1270/
00202965	data12_8TeV.00202965.physics_Muons.merge.NTUP_TOPMU.f443_m1136_p1269_p1270/
00202987	data12_8TeV.00202987.physics_Muons.merge.NTUP_TOPMU.f443_m1136_p1269_p1270/
00202991	data12_8TeV.00202991.physics_Muons.merge.NTUP_TOPMU.f443_m1143_p1269_p1270/
00203027	data12_8TeV.00203027.physics_Muons.merge.NTUP_TOPMU.f443_m1143_p1269_p1270/
00203169	data12_8TeV.00203169.physics_Muons.merge.NTUP_TOPMU.f444_m1143_p1269_p1270/
00203191	data12_8TeV.00203191.physics_Muons.merge.NTUP_TOPMU.f444_m1143_p1269_p1270/
00203195	data12_8TeV.00203195.physics_Muons.merge.NTUP_TOPMU.f444_m1143_p1269_p1270/
00203228	data12_8TeV.00203228.physics_Muons.merge.NTUP_TOPMU.f444_m1143_p1269_p1270/
00203256	data12_8TeV.00203256.physics_Muons.merge.NTUP_TOPMU.f444_m1143_p1269_p1270/
00203258	data12_8TeV.00203258.physics_Muons.merge.NTUP_TOPMU.f444_m1148_p1269_p1270/
00203277	data12_8TeV.00203277.physics_Muons.merge.NTUP_TOPMU.f444_m1148_p1269_p1270/
00203335	data12_8TeV.00203335.physics_Muons.merge.NTUP_TOPMU.f446_m1148_p1269_p1270/
00203336	data12_8TeV.00203336.physics_Muons.merge.NTUP_TOPMU.f446_m1148_p1269_p1270/
00203353	data12_8TeV.00203353.physics_Muons.merge.NTUP_TOPMU.f446_m1148_p1269_p1270/
00203432	data12_8TeV.00203432.physics_Muons.merge.NTUP_TOPMU.f446_m1148_p1269_p1270/
00203454	data12_8TeV.00203454.physics_Muons.merge.NTUP_TOPMU.f446_m1148_p1269_p1270/
00203456	data12_8TeV.00203456.physics_Muons.merge.NTUP_TOPMU.f446_m1148_p1269_p1270/
00203523	data12_8TeV.00203523.physics_Muons.merge.NTUP_TOPMU.f446_m1148_p1269_p1270/
00203524	data12_8TeV.00203524.physics_Muons.merge.NTUP_TOPMU.f446_m1148_p1269_p1270/
00203602	data12_8TeV.00203602.physics_Muons.merge.NTUP_TOPMU.f446_m1148_p1269_p1270/
00203605	data12_8TeV.00203605.physics_Muons.merge.NTUP_TOPMU.f446_m1148_p1269_p1270/
00203636	data12_8TeV.00203636.physics_Muons.merge.NTUP_TOPMU.f446_m1148_p1269_p1270/
00203680	data12_8TeV.00203680.physics_Muons.merge.NTUP_TOPMU.f446_m1148_p1269_p1270/
00203719	data12_8TeV.00203719.physics_Muons.merge.NTUP_TOPMU.f446_m1148_p1269_p1270/
00203739	data12_8TeV.00203739.physics_Muons.merge.NTUP_TOPMU.f446_m1153_p1269_p1270/
00203745	data12_8TeV.00203745.physics_Muons.merge.NTUP_TOPMU.f446_m1148_p1269_p1270/
00203760	data12_8TeV.00203760.physics_Muons.merge.NTUP_TOPMU.f446_m1153_p1269_p1270/
00203779	data12_8TeV.00203779.physics_Muons.merge.NTUP_TOPMU.f446_m1153_p1269_p1270/
00203792	data12_8TeV.00203792.physics_Muons.merge.NTUP_TOPMU.f446_m1153_p1269_p1270/
00203875	data12_8TeV.00203875.physics_Muons.merge.NTUP_TOPMU.f446_m1153_p1269_p1270/
00203876	data12_8TeV.00203876.physics_Muons.merge.NTUP_TOPMU.f447_m1153_p1269_p1270/
00203934	data12_8TeV.00203934.physics_Muons.merge.NTUP_TOPMU.f447_m1153_p1269_p1270/
00204025	data12_8TeV.00204025.physics_Muons.merge.NTUP_TOPMU.f447_m1153_p1269_p1270/
00204026	data12_8TeV.00204026.physics_Muons.merge.NTUP_TOPMU.f447_m1153_p1269_p1270/
00204071	data12_8TeV.00204071.physics_Muons.merge.NTUP_TOPMU.f447_m1153_p1269_p1270/
00204073	data12_8TeV.00204073.physics_Muons.merge.NTUP_TOPMU.f447_m1153_p1269_p1270/
00204134	data12_8TeV.00204134.physics_Muons.merge.NTUP_TOPMU.f447_m1153_p1269_p1270/
00204153	data12_8TeV.00204153.physics_Muons.merge.NTUP_TOPMU.f447_m1153_p1269_p1270/
00204158	data12_8TeV.00204158.physics_Muons.merge.NTUP_TOPMU.f447_m1153_p1269_p1270/
00204240	data12_8TeV.00204240.physics_Muons.merge.NTUP_TOPMU.f447_m1158_p1269_p1270/
00204265	data12_8TeV.00204265.physics_Muons.merge.NTUP_TOPMU.f447_m1158_p1269_p1270/
00204416	data12_8TeV.00204416.physics_Muons.merge.NTUP_TOPMU.f448_m1158_p1269_p1270/
00204442	data12_8TeV.00204442.physics_Muons.merge.NTUP_TOPMU.f448_m1158_p1269_p1270/
00204474	data12_8TeV.00204474.physics_Muons.merge.NTUP_TOPMU.f448_m1158_p1269_p1270/
00204564	data12_8TeV.00204564.physics_Muons.merge.NTUP_TOPMU.f448_m1158_p1269_p1270/
00204633	data12_8TeV.00204633.physics_Muons.merge.NTUP_TOPMU.f448_m1158_p1269_p1270/
00204668	data12_8TeV.00204668.physics_Muons.merge.NTUP_TOPMU.f448_m1158_p1269_p1270/
00204707	data12_8TeV.00204707.physics_Muons.merge.NTUP_TOPMU.f448_m1163_p1269_p1270/
00204726	data12_8TeV.00204726.physics_Muons.merge.NTUP_TOPMU.f448_m1163_p1269_p1270/
00204763	data12_8TeV.00204763.physics_Muons.merge.NTUP_TOPMU.f448_m1163_p1269_p1270/
00204769	data12_8TeV.00204769.physics_Muons.merge.NTUP_TOPMU.f448_m1163_p1269_p1270/
00204772	data12_8TeV.00204772.physics_Muons.merge.NTUP_TOPMU.f449_m1163_p1269_p1270/

00204796 data12_8TeV.00204796.physics_Muons.merge.NTUP_TOPMU.f449_m1163_p1269_p1270/
00204853 data12_8TeV.00204853.physics_Muons.merge.NTUP_TOPMU.f449_m1163_p1269_p1270/
00204857 data12_8TeV.00204857.physics_Muons.merge.NTUP_TOPMU.f449_m1163_p1269_p1270/
00204910 data12_8TeV.00204910.physics_Muons.merge.NTUP_TOPMU.f449_m1163_p1269_p1270/
00204932 data12_8TeV.00204932.physics_Muons.merge.NTUP_TOPMU.f449_m1163_p1269_p1270/
00204954 data12_8TeV.00204954.physics_Muons.merge.NTUP_TOPMU.f449_m1163_p1269_p1270/
00204955 data12_8TeV.00204955.physics_Muons.merge.NTUP_TOPMU.f449_m1163_p1269_p1270/
00204976 data12_8TeV.00204976.physics_Muons.merge.NTUP_TOPMU.f449_m1163_p1269_p1270/
00205010 data12_8TeV.00205010.physics_Muons.merge.NTUP_TOPMU.f449_m1163_p1269_p1270/
00205016 data12_8TeV.00205016.physics_Muons.merge.NTUP_TOPMU.f449_m1163_p1269_p1270/
00205017 data12_8TeV.00205017.physics_Muons.merge.NTUP_TOPMU.f449_m1163_p1269_p1270/
00205055 data12_8TeV.00205055.physics_Muons.merge.NTUP_TOPMU.f449_m1163_p1269_p1270/
00205071 data12_8TeV.00205071.physics_Muons.merge.NTUP_TOPMU.f449_m1163_p1269_p1270/
00205112 data12_8TeV.00205112.physics_Muons.merge.NTUP_TOPMU.f449_m1163_p1269_p1270/
00205113 data12_8TeV.00205113.physics_Muons.merge.NTUP_TOPMU.f449_m1163_p1269_p1270/
00206248 data12_8TeV.00206248.physics_Muons.merge.NTUP_TOPMU.f452_m1170_p1269_p1270/
00206253 data12_8TeV.00206253.physics_Muons.merge.NTUP_TOPMU.f452_m1175_p1269_p1270/
00206299 data12_8TeV.00206299.physics_Muons.merge.NTUP_TOPMU.f450_m1170_p1269_p1270/
00206367 data12_8TeV.00206367.physics_Muons.merge.NTUP_TOPMU.f450_m1175_p1269_p1270/
00206368 data12_8TeV.00206368.physics_Muons.merge.NTUP_TOPMU.f450_m1175_p1269_p1270/
00206369 data12_8TeV.00206369.physics_Muons.merge.NTUP_TOPMU.f450_m1175_p1269_p1270/
00206409 data12_8TeV.00206409.physics_Muons.merge.NTUP_TOPMU.f450_m1175_p1269_p1270/
00206497 data12_8TeV.00206497.physics_Muons.merge.NTUP_TOPMU.f453_m1175_p1269_p1270/
00206564 data12_8TeV.00206564.physics_Muons.merge.NTUP_TOPMU.f457_m1180_p1269_p1270/
00206573 data12_8TeV.00206573.physics_Muons.merge.NTUP_TOPMU.f458_m1180_p1269_p1270/
00206614 data12_8TeV.00206614.physics_Muons.merge.NTUP_TOPMU.f456_m1180_p1269_p1270/
00206717 data12_8TeV.00206717.physics_Muons.merge.NTUP_TOPMU.f456_m1180_p1269_p1270/
00206724 data12_8TeV.00206724.physics_Muons.merge.NTUP_TOPMU.f456_m1180_p1269_p1270/
00206725 data12_8TeV.00206725.physics_Muons.merge.NTUP_TOPMU.f456_m1180_p1269_p1270/
00206955 data12_8TeV.00206955.physics_Muons.merge.NTUP_TOPMU.f456_m1180_p1269_p1270/
00206962 data12_8TeV.00206962.physics_Muons.merge.NTUP_TOPMU.f456_m1186_p1269_p1270/
00206971 data12_8TeV.00206971.physics_Muons.merge.NTUP_TOPMU.f456_m1186_p1269_p1270/
00207044 data12_8TeV.00207044.physics_Muons.merge.NTUP_TOPMU.f462_m1186_p1269_p1270/
00207046 data12_8TeV.00207046.physics_Muons.merge.NTUP_TOPMU.f462_m1186_p1269_p1270/
00207113 data12_8TeV.00207113.physics_Muons.merge.NTUP_TOPMU.f464_m1186_p1269_p1270/
00207221 data12_8TeV.00207221.physics_Muons.merge.NTUP_TOPMU.f464_m1186_p1269_p1270/
00207262 data12_8TeV.00207262.physics_Muons.merge.NTUP_TOPMU.f464_m1186_p1269_p1270/
00207304 data12_8TeV.00207304.physics_Muons.merge.NTUP_TOPMU.f464_m1186_p1269_p1270/
00207306 data12_8TeV.00207306.physics_Muons.merge.NTUP_TOPMU.f464_m1191_p1269_p1270/
00207332 data12_8TeV.00207332.physics_Muons.merge.NTUP_TOPMU.f464_m1191_p1269_p1270/
00207397 data12_8TeV.00207397.physics_Muons.merge.NTUP_TOPMU.f464_m1191_p1269_p1270/
00207447 data12_8TeV.00207447.physics_Muons.merge.NTUP_TOPMU.f466_m1191_p1269_p1270/
00207490 data12_8TeV.00207490.physics_Muons.merge.NTUP_TOPMU.f466_m1191_p1269_p1270/
00207528 data12_8TeV.00207528.physics_Muons.merge.NTUP_TOPMU.f467_m1191_p1269_p1270/
00207531 data12_8TeV.00207531.physics_Muons.merge.NTUP_TOPMU.f467_m1191_p1269_p1270/
00207532 data12_8TeV.00207532.physics_Muons.merge.NTUP_TOPMU.f467_m1191_p1269_p1270/
00207582 data12_8TeV.00207582.physics_Muons.merge.NTUP_TOPMU.f467_m1191_p1269_p1270/
00207589 data12_8TeV.00207589.physics_Muons.merge.NTUP_TOPMU.f467_m1191_p1269_p1270/
00207620 data12_8TeV.00207620.physics_Muons.merge.NTUP_TOPMU.f467_m1197_p1269_p1270/
00207664 data12_8TeV.00207664.physics_Muons.merge.NTUP_TOPMU.f468_m1202_p1269_p1270/
00207696 data12_8TeV.00207696.physics_Muons.merge.NTUP_TOPMU.f468_m1202_p1269_p1270/
00207749 data12_8TeV.00207749.physics_Muons.merge.NTUP_TOPMU.f469_m1202_p1269_p1270/
00207772 data12_8TeV.00207772.physics_Muons.merge.NTUP_TOPMU.f469_m1202_p1269_p1270/
00207800 data12_8TeV.00207800.physics_Muons.merge.NTUP_TOPMU.f470_m1202_p1269_p1270/
00207809 data12_8TeV.00207809.physics_Muons.merge.NTUP_TOPMU.f470_m1202_p1269_p1270/
00207845 data12_8TeV.00207845.physics_Muons.merge.NTUP_TOPMU.f470_m1202_p1269_p1270/
00207864 data12_8TeV.00207864.physics_Muons.merge.NTUP_TOPMU.f470_m1202_p1269_p1270/
00207865 data12_8TeV.00207865.physics_Muons.merge.NTUP_TOPMU.f470_m1202_p1269_p1270/
00207929 data12_8TeV.00207929.physics_Muons.merge.NTUP_TOPMU.f470_m1202_p1269_p1270/
00207931 data12_8TeV.00207931.physics_Muons.merge.NTUP_TOPMU.f470_m1202_p1269_p1270/
00207934 data12_8TeV.00207934.physics_Muons.merge.NTUP_TOPMU.f470_m1202_p1269_p1270/
00207975 data12_8TeV.00207975.physics_Muons.merge.NTUP_TOPMU.f470_m1202_p1269_p1270/
00207982 data12_8TeV.00207982.physics_Muons.merge.NTUP_TOPMU.f470_m1202_p1269_p1270/
00208123 data12_8TeV.00208123.physics_Muons.merge.NTUP_TOPMU.f470_m1202_p1269_p1270/
00208126 data12_8TeV.00208126.physics_Muons.merge.NTUP_TOPMU.f470_m1202_p1269_p1270/
00208179 data12_8TeV.00208179.physics_Muons.merge.NTUP_TOPMU.f470_m1202_p1269_p1270/
00208184 data12_8TeV.00208184.physics_Muons.merge.NTUP_TOPMU.f470_m1208_p1269_p1270/
00208189 data12_8TeV.00208189.physics_Muons.merge.NTUP_TOPMU.f470_m1208_p1269_p1270/
00208258 data12_8TeV.00208258.physics_Muons.merge.NTUP_TOPMU.f470_m1208_p1269_p1270/
00208261 data12_8TeV.00208261.physics_Muons.merge.NTUP_TOPMU.f472_m1208_p1269_p1270/
00208354 data12_8TeV.00208354.physics_Muons.merge.NTUP_TOPMU.f472_m1208_p1269_p1270/
00208484 data12_8TeV.00208484.physics_Muons.merge.NTUP_TOPMU.f472_m1208_p1269_p1270/
00208485 data12_8TeV.00208485.physics_Muons.merge.NTUP_TOPMU.f472_m1208_p1269_p1270/
00208631 data12_8TeV.00208631.physics_Muons.merge.NTUP_TOPMU.f472_m1208_p1269_p1270/
00208642 data12_8TeV.00208642.physics_Muons.merge.NTUP_TOPMU.f472_m1208_p1269_p1270/
00208662 data12_8TeV.00208662.physics_Muons.merge.NTUP_TOPMU.f472_m1208_p1269_p1270/
00208705 data12_8TeV.00208705.physics_Muons.merge.NTUP_TOPMU.f472_m1208_p1269_p1270/
00208717 data12_8TeV.00208717.physics_Muons.merge.NTUP_TOPMU.f472_m1208_p1269_p1270/
00208720 data12_8TeV.00208720.physics_Muons.merge.NTUP_TOPMU.f472_m1208_p1269_p1270/
00208780 data12_8TeV.00208780.physics_Muons.merge.NTUP_TOPMU.f472_m1208_p1269_p1270/
00208781 data12_8TeV.00208781.physics_Muons.merge.NTUP_TOPMU.f472_m1208_p1269_p1270/
00208811 data12_8TeV.00208811.physics_Muons.merge.NTUP_TOPMU.f472_m1208_p1269_p1270/
00208870 data12_8TeV.00208870.physics_Muons.merge.NTUP_TOPMU.f472_m1208_p1269_p1270/
00208930 data12_8TeV.00208930.physics_Muons.merge.NTUP_TOPMU.f472_m1208_p1269_p1270/

00208931	data12_8TeV.00208931.physics_Muons.merge.NTUP_TOPMU.f472_m1208_p1269_p1270/
00208970	data12_8TeV.00208970.physics_Muons.merge.NTUP_TOPMU.f472_m1213_p1269_p1270/
00208982	data12_8TeV.00208982.physics_Muons.merge.NTUP_TOPMU.f472_m1213_p1269_p1270/
00209024	data12_8TeV.00209024.physics_Muons.merge.NTUP_TOPMU.f473_m1213_p1269_p1270/
00209025	data12_8TeV.00209025.physics_Muons.merge.NTUP_TOPMU.f473_m1213_p1269_p1270/
00209074	data12_8TeV.00209074.physics_Muons.merge.NTUP_TOPMU.f473_m1213_p1269_p1270/
00209084	data12_8TeV.00209084.physics_Muons.merge.NTUP_TOPMU.f473_m1213_p1269_p1270/
00209109	data12_8TeV.00209109.physics_Muons.merge.NTUP_TOPMU.f473_m1213_p1269_p1270/
00209161	data12_8TeV.00209161.physics_Muons.merge.NTUP_TOPMU.f473_m1213_p1269_p1270/
00209183	data12_8TeV.00209183.physics_Muons.merge.NTUP_TOPMU.f473_m1213_p1269_p1270/
00209214	data12_8TeV.00209214.physics_Muons.merge.NTUP_TOPMU.f473_m1213_p1269_p1270/
00209254	data12_8TeV.00209254.physics_Muons.merge.NTUP_TOPMU.f473_m1213_p1269_p1270/
00209265	data12_8TeV.00209265.physics_Muons.merge.NTUP_TOPMU.f473_m1213_p1269_p1270/
00209269	data12_8TeV.00209269.physics_Muons.merge.NTUP_TOPMU.f473_m1218_p1269_p1270/
00209353	data12_8TeV.00209353.physics_Muons.merge.NTUP_TOPMU.f473_m1218_p1269_p1270/
00209381	data12_8TeV.00209381.physics_Muons.merge.NTUP_TOPMU.f473_m1218_p1269_p1270/
00209550	data12_8TeV.00209550.physics_Muons.merge.NTUP_TOPMU.f475_m1218_p1269_p1270/
00209580	data12_8TeV.00209580.physics_Muons.merge.NTUP_TOPMU.f475_m1218_p1269_p1270/
00209608	data12_8TeV.00209608.physics_Muons.merge.NTUP_TOPMU.f475_m1218_p1269_p1270/
00209628	data12_8TeV.00209628.physics_Muons.merge.NTUP_TOPMU.f475_m1218_p1269_p1270/
00209629	data12_8TeV.00209629.physics_Muons.merge.NTUP_TOPMU.f475_m1218_p1269_p1270/
00209736	data12_8TeV.00209736.physics_Muons.merge.NTUP_TOPMU.f475_m1218_p1269_p1270/
00209776	data12_8TeV.00209776.physics_Muons.merge.NTUP_TOPMU.f475_m1218_p1269_p1270/
00209787	data12_8TeV.00209787.physics_Muons.merge.NTUP_TOPMU.f475_m1218_p1269_p1270/
00209812	data12_8TeV.00209812.physics_Muons.merge.NTUP_TOPMU.f475_m1218_p1269_p1270/
00209864	data12_8TeV.00209864.physics_Muons.merge.NTUP_TOPMU.f475_m1223_p1269_p1270/
00209866	data12_8TeV.00209866.physics_Muons.merge.NTUP_TOPMU.f475_m1223_p1269_p1270/
00209899	data12_8TeV.00209899.physics_Muons.merge.NTUP_TOPMU.f475_m1223_p1269_p1270/
00209909	data12_8TeV.00209909.physics_Muons.merge.NTUP_TOPMU.f475_m1223_p1269_p1270/
00209980	data12_8TeV.00209980.physics_Muons.merge.NTUP_TOPMU.f476_m1223_p1269_p1270/
00209994	data12_8TeV.00209994.physics_Muons.merge.NTUP_TOPMU.f476_m1223_p1269_p1270/
00209995	data12_8TeV.00209995.physics_Muons.merge.NTUP_TOPMU.f476_m1223_p1269_p1270/
00210302	data12_8TeV.00210302.physics_Muons.merge.NTUP_TOPMU.f476_m1223_p1269_p1270/
00210308	data12_8TeV.00210308.physics_Muons.merge.NTUP_TOPMU.f476_m1223_p1269_p1270/
00211522	data12_8TeV.00211522.physics_Muons.merge.NTUP_TOPMU.f479_m1228_p1269_p1270/
00211620	data12_8TeV.00211620.physics_Muons.merge.NTUP_TOPMU.f479_m1228_p1269_p1270/
00211670	data12_8TeV.00211670.physics_Muons.merge.NTUP_TOPMU.f479_m1228_p1269_p1270/
00211697	data12_8TeV.00211697.physics_Muons.merge.NTUP_TOPMU.f479_m1228_p1269_p1270/
00211772	data12_8TeV.00211772.physics_Muons.merge.NTUP_TOPMU.f479_m1228_p1269_p1270/
00211787	data12_8TeV.00211787.physics_Muons.merge.NTUP_TOPMU.f479_m1228_p1269_p1270/
00211867	data12_8TeV.00211867.physics_Muons.merge.NTUP_TOPMU.f479_m1228_p1269_p1270/
00211902	data12_8TeV.00211902.physics_Muons.merge.NTUP_TOPMU.f479_m1228_p1269_p1270/
00211937	data12_8TeV.00211937.physics_Muons.merge.NTUP_TOPMU.f479_m1228_p1269_p1270/
00212000	data12_8TeV.00212000.physics_Muons.merge.NTUP_TOPMU.f479_m1228_p1269_p1270/
00212034	data12_8TeV.00212034.physics_Muons.merge.NTUP_TOPMU.f479_m1228_p1269_p1270/
00212103	data12_8TeV.00212103.physics_Muons.merge.NTUP_TOPMU.f479_m1228_p1269_p1270/
00212142	data12_8TeV.00212142.physics_Muons.merge.NTUP_TOPMU.f479_m1228_p1269_p1270/
00212144	data12_8TeV.00212144.physics_Muons.merge.NTUP_TOPMU.f479_m1228_p1269_p1270/
00212172	data12_8TeV.00212172.physics_Muons.merge.NTUP_TOPMU.f479_m1228_p1269_p1270/
00212199	data12_8TeV.00212199.physics_Muons.merge.NTUP_TOPMU.f479_m1228_p1269_p1270/
00212272	data12_8TeV.00212272.physics_Muons.merge.NTUP_TOPMU.f479_m1228_p1269_p1270/

Table A.2: Data samples from the `Muons` stream used in the analysis. Each sample corresponds to one run number. All listed runs represent the collected data in the periods A-G.

A.2 Signal samples

Process	DSID	D3PD name
$b'(400\,\text{GeV}) \to tW$	158102	mc12_8TeV.158102.Pythia8_AU2MSTW2008LO_d4PairToWtWtbar_400_1LepIncl.merge.NTUP_TOP.e1320_a159_a171_r3549_p1269/
$b'(450\,\text{GeV}) \to tW$	158103	mc12_8TeV.158103.Pythia8_AU2MSTW2008LO_d4PairToWtWtbar_450_1LepIncl.merge.NTUP_TOP.e1320_a159_a171_r3549_p1269/
$b'(500\,\text{GeV}) \to tW$	158104	mc12_8TeV.158104.Pythia8_AU2MSTW2008LO_d4PairToWtWtbar_500_1LepIncl.merge.NTUP_TOP.e1320_a159_a171_r3549_p1269/
$b'(500\,\text{GeV}) \to tW$ (G4)	158104	mc12_8TeV.158104.Pythia8_AU2MSTW2008LO_d4PairToWtWtbar_500_1LepIncl.merge.NTUP_TOP.e1320_s1499_s1504_r3542_r3549_p1269/
$b'(550\,\text{GeV}) \to tW$	158105	mc12_8TeV.158105.Pythia8_AU2MSTW2008LO_d4PairToWtWtbar_550_1LepIncl.merge.NTUP_TOP.e1320_a159_a171_r3549_p1269/
$b'(600\,\text{GeV}) \to tW$	158106	mc12_8TeV.158106.Pythia8_AU2MSTW2008LO_d4PairToWtWtbar_600_1LepIncl.merge.NTUP_TOP.e1320_a159_a165_r3549_p1269/
$b'(650\,\text{GeV}) \to tW$	158107	mc12_8TeV.158107.Pythia8_AU2MSTW2008LO_d4PairToWtWtbar_650_1LepIncl.merge.NTUP_TOP.e1320_a159_a165_r3549_p1269/
$b'(700\,\text{GeV}) \to tW$	158108	mc12_8TeV.158108.Pythia8_AU2MSTW2008LO_d4PairToWtWtbar_700_1LepIncl.merge.NTUP_TOP.e1320_a159_a171_r3549_p1269/
$b'(750\,\text{GeV}) \to tW$	158109	mc12_8TeV.158109.Pythia8_AU2MSTW2008LO_d4PairToWtWtbar_750_1LepIncl.merge.NTUP_TOP.e1320_a159_a171_r3549_p1269/
$b'(800\,\text{GeV}) \to tW$	158110	mc12_8TeV.158110.Pythia8_AU2MSTW2008LO_d4PairToWtWtbar_800_1LepIncl.merge.NTUP_TOP.e1320_a159_a171_r3549_p1269/
$b'(800\,\text{GeV}) \to tW$ (G4)	158110	mc12_8TeV.158110.Pythia8_AU2MSTW2008LO_d4PairToWtWtbar_800_1LepIncl.merge.NTUP_TOP.e1320_s1499_s1504_r3752_r3549_p1269/
$b'(850\,\text{GeV}) \to tW$	158111	mc12_8TeV.158111.Pythia8_AU2MSTW2008LO_d4PairToWtWtbar_850_1LepIncl.merge.NTUP_TOP.e1320_a159_a171_r3549_p1269/
$b'(900\,\text{GeV}) \to tW$	158112	mc12_8TeV.158112.Pythia8_AU2MSTW2008LO_d4PairToWtWtbar_900_1LepIncl.merge.NTUP_TOP.e1320_a159_a171_r3549_p1269/
$b'(950\,\text{GeV}) \to tW$	158113	mc12_8TeV.158113.Pythia8_AU2MSTW2008LO_d4PairToWtWtbar_950_1LepIncl.merge.NTUP_TOP.e1320_a159_a165_r3549_p1269/
$b'(1000\,\text{GeV}) \to tW$	158114	mc12_8TeV.158114.Pythia8_AU2MSTW2008LO_d4PairToWtWtbar_1000_1LepIncl.merge.NTUP_TOP.e1320_a159_a171_r3549_p1269/
$b'(400\,\text{GeV}) \to qW$	158115	mc12_8TeV.158115.Pythia8_AU2MSTW2008LO_d4d4_400_q.merge.NTUP_TOP.e1320_a159_a165_r3549_p1269/
$b'(450\,\text{GeV}) \to qW$	158116	mc12_8TeV.158116.Pythia8_AU2MSTW2008LO_d4d4_450_q.merge.NTUP_TOP.e1320_a159_a171_r3549_p1269/
$b'(500\,\text{GeV}) \to qW$	158117	mc12_8TeV.158117.Pythia8_AU2MSTW2008LO_d4d4_500_q.merge.NTUP_TOP.e1320_a159_a165_r3549_p1269/
$b'(500\,\text{GeV}) \to qW$ (G4)	158117	mc12_8TeV.158117.Pythia8_AU2MSTW2008LO_d4d4_500_q.merge.NTUP_TOP.e1320_s1499_s1504_r3542_r3549_p1269/
$b'(550\,\text{GeV}) \to qW$	158118	mc12_8TeV.158118.Pythia8_AU2MSTW2008LO_d4d4_550_q.merge.NTUP_TOP.e1320_a159_a171_r3549_p1269/
$b'(600\,\text{GeV}) \to qW$	158119	mc12_8TeV.158119.Pythia8_AU2MSTW2008LO_d4d4_600_q.merge.NTUP_TOP.e1320_a159_a165_r3549_p1269/
$b'(650\,\text{GeV}) \to qW$	158120	mc12_8TeV.158120.Pythia8_AU2MSTW2008LO_d4d4_650_q.merge.NTUP_TOP.e1320_a159_a165_r3549_p1269/
$b'(700\,\text{GeV}) \to qW$	158121	mc12_8TeV.158121.Pythia8_AU2MSTW2008LO_d4d4_700_q.merge.NTUP_TOP.e1320_a159_a165_r3549_p1269/
$b'(750\,\text{GeV}) \to qW$	158122	mc12_8TeV.158122.Pythia8_AU2MSTW2008LO_d4d4_750_q.merge.NTUP_TOP.e1320_a159_a165_r3549_p1269/
$b'(800\,\text{GeV}) \to qW$	158123	mc12_8TeV.158123.Pythia8_AU2MSTW2008LO_d4d4_800_q.merge.NTUP_TOP.e1320_a159_a171_r3549_p1269/
$b'(800\,\text{GeV}) \to qW$ (G4)	158123	mc12_8TeV.158123.Pythia8_AU2MSTW2008LO_d4d4_800_q.merge.NTUP_TOP.e1320_s1499_s1504_r3542_r3549_p1269/
$b'(850\,\text{GeV}) \to qW$	158124	mc12_8TeV.158124.Pythia8_AU2MSTW2008LO_d4d4_850_q.merge.NTUP_TOP.e1320_a159_a165_r3549_p1269/
$b'(900\,\text{GeV}) \to qW$	158125	mc12_8TeV.158125.Pythia8_AU2MSTW2008LO_d4d4_900_q.merge.NTUP_TOP.e1320_a159_a165_r3549_p1269/
$b'(950\,\text{GeV}) \to qW$	158126	mc12_8TeV.158126.Pythia8_AU2MSTW2008LO_d4d4_950_q.merge.NTUP_TOP.e1320_a159_a171_r3549_p1269/
$b'(1000\,\text{GeV}) \to qW$	158127	mc12_8TeV.158127.Pythia8_AU2MSTW2008LO_d4d4_1000_q.merge.NTUP_TOP.e1320_a159_a165_r3549_p1269/

Table A.3: MC signal samples used in the analysis. For each process/sample, the dataset identification number (DSID) and the D3PD sample name are given. The corresponding cross-sections, generated number of events and luminosities can be looked up in Table 6.2. G4 denotes samples that have been generated using the full detector simulation `GEANT4`, whereas the fast detector simulation `ATLFAST-II` was used in all other samples.

A.3 Background samples

Process	DSID	D3PD name
$t\bar{t}+Z$	119355	mc12_8TeV.119355.MadGraphPythia_AUET2BCTEQ6L1_ttbarZ.merge.NTUP_TOP.e1352_s1499_s1504_r3658_r3549_p1269/
$t\bar{t}+Z$+j	174832	mc12_8TeV.174832.MadGraphPythia_AUET2BCTEQ6L1_ttbarZjExcl.merge.NTUP_TOP.e1672_s1499_s1504_r3658_r3549_p1269/
$t\bar{t}+Z$+jj	174833	mc12_8TeV.174833.MadGraphPythia_AUET2BCTEQ6L1_ttbarZjjIncl.merge.NTUP_TOP.e1672_s1499_s1504_r3658_r3549_p1269/
$t\bar{t}+W$	119353	mc12_8TeV.119353.MadGraphPythia_AUET2BCTEQ6L1_ttbarW.merge.NTUP_TOP.e1352_s1499_s1504_r3658_r3549_p1269/
$t\bar{t}+W$+j	174830	mc12_8TeV.174830.MadGraphPythia_AUET2BCTEQ6L1_ttbarWjExcl.merge.NTUP_TOP.e1672_s1499_s1504_r3658_r3549_p1269/
$t\bar{t}+W$+jj	174831	mc12_8TeV.174831.MadGraphPythia_AUET2BCTEQ6L1_ttbarWjjIncl.merge.NTUP_TOP.e1672_s1499_s1504_r3658_r3549_p1269/
$W^{\pm}W^{\pm}$+jj (AF2)	158819	mc12_8TeV.158819.MadgraphPythia8_AU2_MSTW2008LO_SSWWjj.merge.NTUP_TOP.e1632_a159_a171_r3549_p1269/
$t\bar{t}+WW$ (AF2)	158814	mc12_8TeV.158814.MadgraphPythia8_AU2_MSTW2008LO_ttbarWW.merge.NTUP_TOP.e1632_a159_a171_r3549_p1269/
$WZ \to \ell\ell\ell\nu$	126893	mc12_8TeV.126893.Sherpa_CT10_lllnu_WZ.merge.NTUP_TOP.e1434_s1499_s1504_r3658_r3549_p1269/
$ZZ \to \ell\ell\ell\ell$	126894	mc12_8TeV.126894.Sherpa_CT10_llll_ZZ.merge.NTUP_TOP.e1434_s1499_s1504_r3658_r3549_p1269/

Table A.4: MC background samples used in the analysis. For each process/sample, the dataset identification number (DSID) and the D3PD sample name are given. The corresponding cross-sections, generated number of events and luminosities can be looked up in Table 6.3. AF2 denotes samples that have been generated using the fast detector simulation `ATLFAST-II`, whereas the full detector simulation `GEANT4` was used in all other samples.

B Event selection

This appendix provides additional material regarding the event selection and its optimisation.

B.1 Basic selection

B.1.1 Discriminant variables

Figures B.1, B.2 and B.3 present distributions of the discriminant variables in the ee, $e\mu$ and $\mu\mu$ channel after applying the basic event selection summarised in Table 6.15.

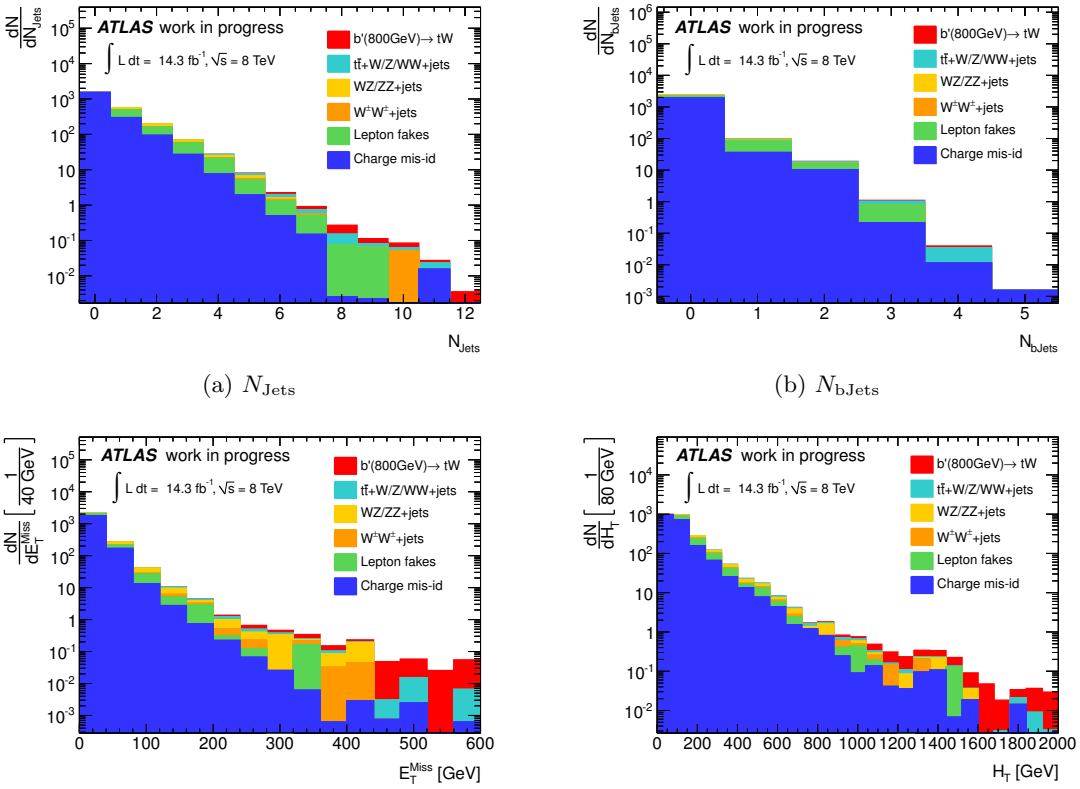

(a) N_{Jets} (b) N_{bJets}

(c) E_T^{miss} (d) H_T

Figure B.1: Presented are the distributions of the discriminant variables N_{Jets} (a), N_{bJets} (b), E_T^{miss} (c) and H_T (d) after the basic event selection (Table 6.15) for the *ee* channel.

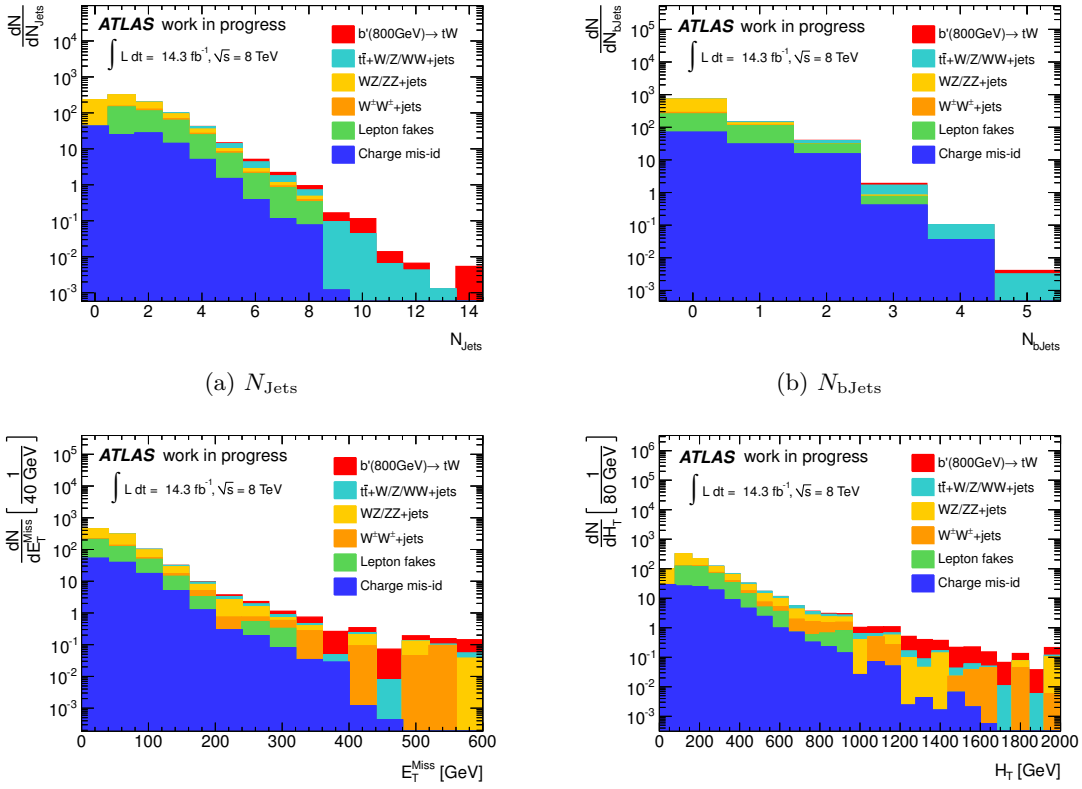

(a) N_{Jets} (b) N_{bJets}

(c) E_T^{miss} (d) H_T

Figure B.2: Presented are the distributions of the discriminant variables N_{Jets} (a), N_{bJets} (b), E_T^{miss} (c) and H_T (d) after the basic event selection (Table 6.15) for the $e\mu$ channel.

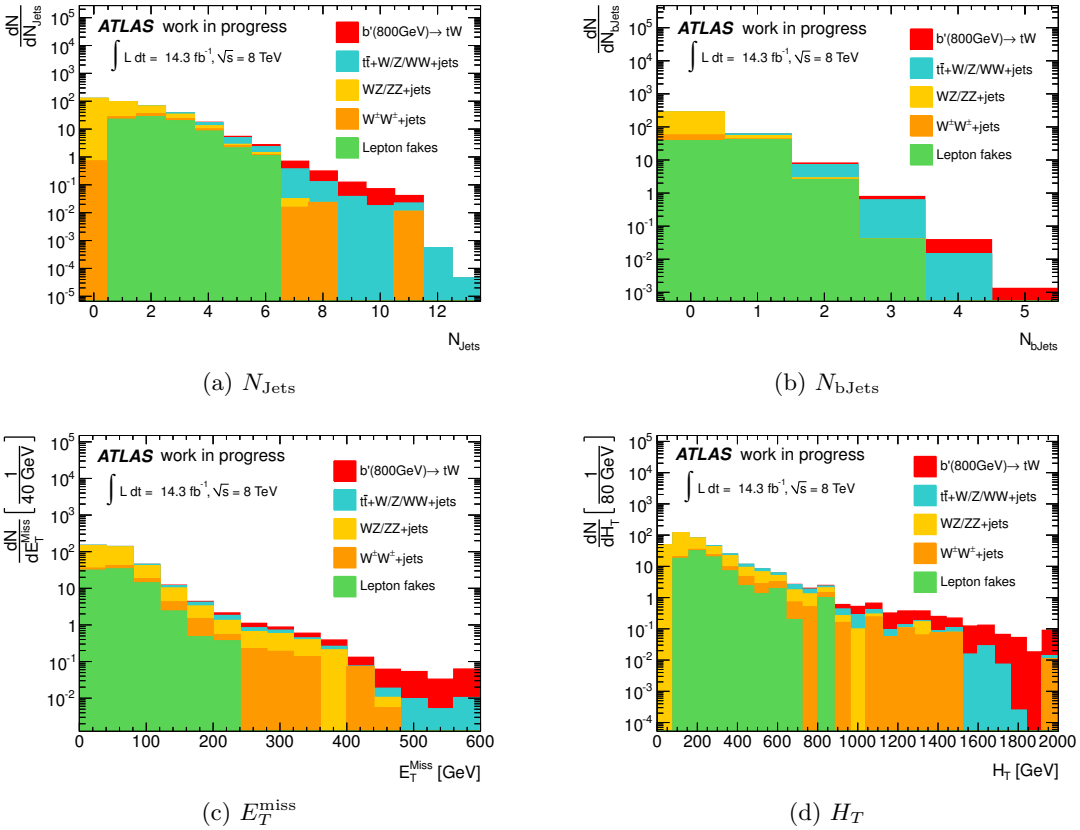

(a) N_{Jets} (b) N_{bJets}

(c) E_T^{miss} (d) H_T

Figure B.3: Presented are the distributions of the discriminant variables N_{Jets} (a), N_{bJets} (b), E_T^{miss} (c) and H_T (d) after the basic event selection (Table 6.15) for the $\mu\mu$ channel.

B.1.2 Discriminant variables after default selection

Figures B.4, B.5 and B.6 present the distributions of discriminant variables in the ee, $e\mu$ and $\mu\mu$ channel after applying the default event selection summarised in Table 6.19. In each plot, the cut on the corresponding variable has been removed.

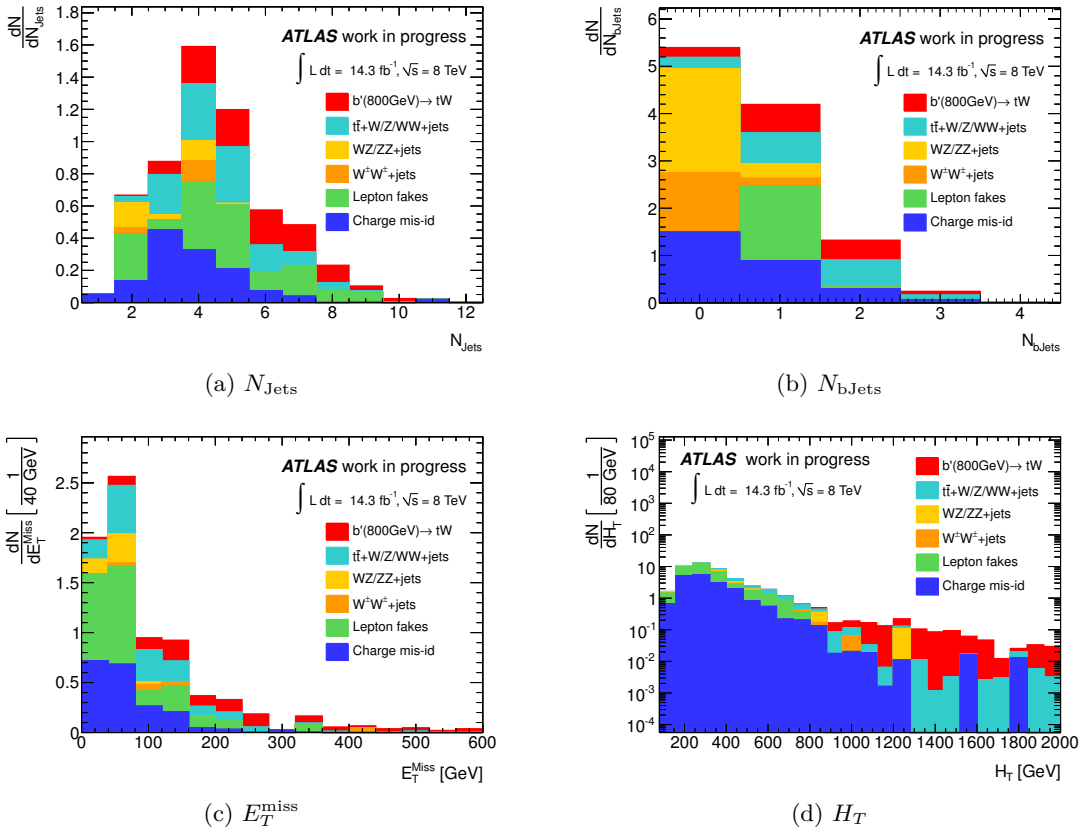

(a) N_{Jets} (b) N_{bJets}

(c) E_T^{miss} (d) H_T

Figure B.4: Presented are the distributions of the discriminant variables N_{Jets} (a), N_{bJets} (b), E_T^{miss} (c) and H_T (d) after the default event selection (Table 6.19) for the ee channel. In each plot, the cut on the corresponding variable has been removed.

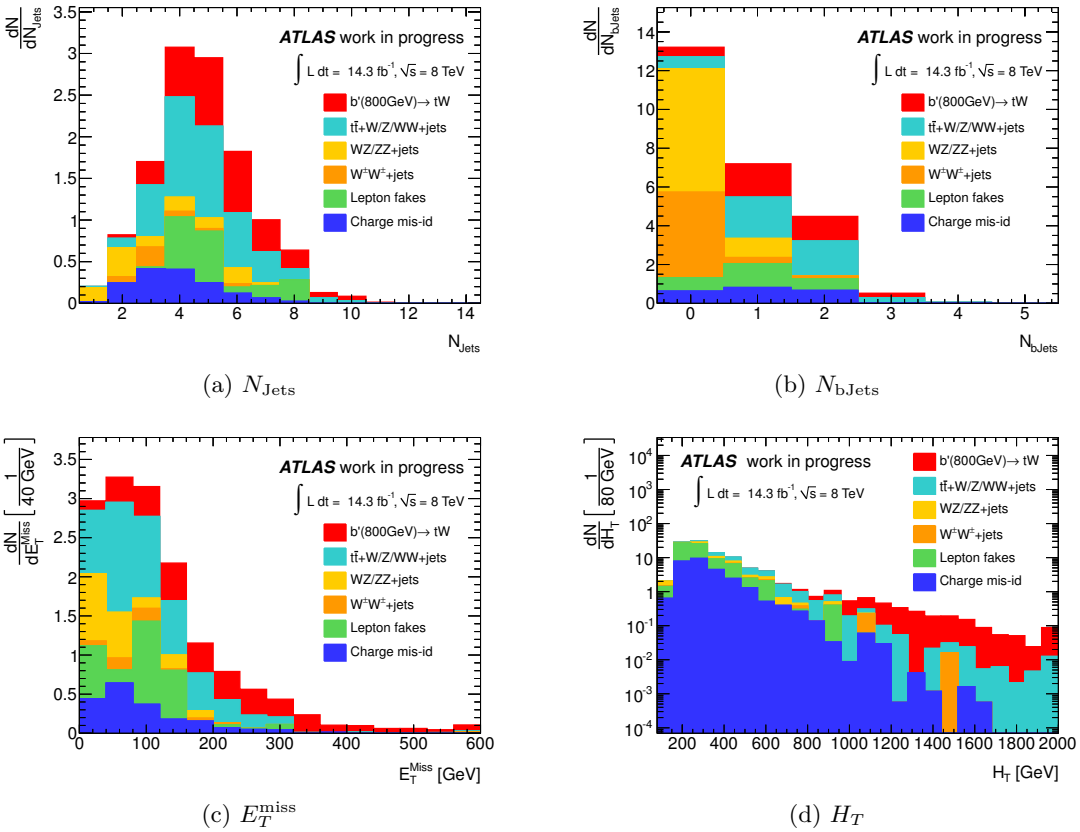

(a) N_{Jets} (b) N_{bJets}

(c) E_T^{miss} (d) H_T

Figure B.5: Presented are the distributions of the discriminant variables N_{Jets} (a), N_{bJets} (b), E_T^{miss} (c) and H_T (d) after the default event selection (Table 6.19) for the $e\mu$ channel. In each plot, the cut on the corresponding variable has been removed.

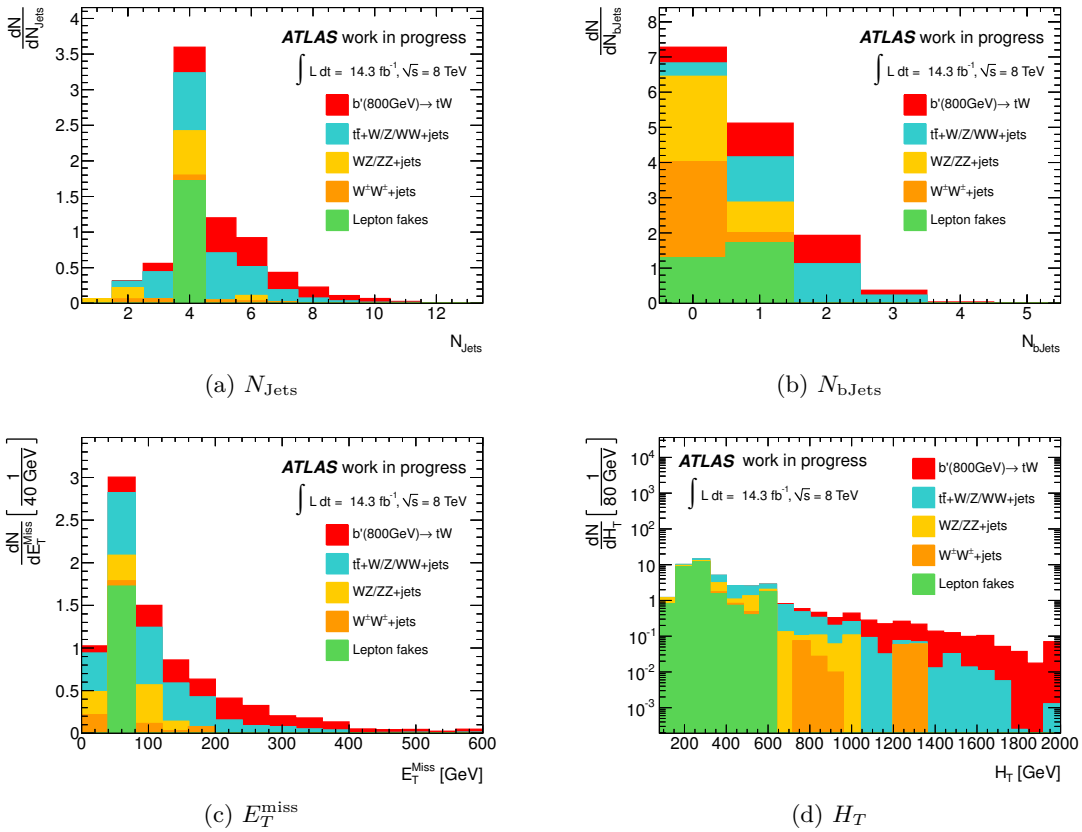

(a) N_{Jets} (b) N_{bJets}

(c) E_T^{miss} (d) H_T

Figure B.6: Presented are the distributions of the discriminant variables N_{Jets} (a), N_{bJets} (b), E_T^{miss} (c) and H_T (d) after the default event selection (Table 6.19) for the $\mu\mu$ channel. In each plot, the cut on the corresponding variable has been removed.

B.2 Event selection optimisation

B.2.1 Systematic uncertainties

This section summarises the derived systematic uncertainties, which have been used in the limit setting procedure for the event selection optimisation. These uncertainties have been derived for the default event selection summarised in Table 6.19. The systematics on the data-driven backgrounds (charge mis-id and lepton fakes) are summarised in Table B.1. Tables B.2, B.3 and B.4 present the systematic uncertainties on the energy scale, resolution and efficiency scale factors for the MC background samples in the ee, $e\mu$ and $\mu\mu$ channel, respectively. The same uncertainties on the $b' \to tW$ signal samples are summarised in Tables B.5, B.6 and B.7.

Background	ee	$e\mu$	$\mu\mu$
Lepton fakes	$+30.0/-30.0$	$+30.0/-30.0$	$+30.0/-30.0$
Charge mis-id	$+37.2/-36.5$	$+33.4/-33.0$	—

Table B.1: Relative systematic uncertainties in percent (%) on the data-driven backgrounds for the default selection in the ee, $e\mu$ and $\mu\mu$ channel.

Systematic	$t\bar{t}+W$+jets	$t\bar{t}+WW$	$t\bar{t}+Z$+jets	WZ/ZZ+jets	$W^{\pm}W^{\pm}$+jets
JES	$12.6/-6.1$	$10.3/-7.4$	$14.9/-7.0$	$0.1/-7.3$	$22.6/-0.4$
JER	$2.6/-2.6$	$0.6/-0.6$	$3.4/-3.4$	$6.2/-6.2$	$11.3/-11.3$
JRE	$0.0/-0.0$	$0.0/-0.0$	$0.0/-0.0$	$0.0/-0.0$	$0.0/-0.0$
JVFSF	$1.8/-1.7$	$2.8/-2.3$	$2.4/-2.0$	$4.9/-2.9$	$1.3/-1.6$
ESFRecId	$5.0/-4.9$	$5.4/-5.2$	$5.0/-4.9$	$5.0/-4.9$	$5.3/-5.2$
ESFTrig	$1.5/-0.0$	$0.8/-0.0$	$2.4/-0.0$	$0.0/-7.5$	$0.0/-0.5$
EER	$0.1/-0.3$	$0.0/-0.0$	$2.3/-0.1$	$0.0/-0.0$	$0.0/-0.0$
EES	$1.0/-2.2$	$0.0/-1.3$	$2.5/-2.3$	$11.4/-0.1$	$0.2/-0.0$
MuSFRecId	$0.0/-0.0$	$0.0/-0.0$	$0.0/-0.0$	$0.0/-0.0$	$0.0/-0.0$
MuSFTrig	$0.0/-0.0$	$0.0/-0.0$	$0.0/-0.0$	$0.0/-0.0$	$0.0/-0.0$
MES	$0.0/-0.0$	$0.0/-0.0$	$0.0/-0.0$	$0.0/-0.0$	$0.0/-0.0$
MER	$0.0/-0.0$	$0.0/-0.0$	$0.0/-0.0$	$0.0/-0.0$	$0.0/-0.0$
MET	$0.9/-0.0$	$1.1/-0.0$	$1.2/-0.0$	$0.0/-0.0$	$0.0/-0.0$
BTagSFb	$5.7/-6.4$	$2.3/-3.4$	$4.4/-5.5$	$1.7/-3.7$	$4.3/-4.3$
BTagSFc	$0.5/-0.6$	$1.7/-1.8$	$0.3/-0.2$	$0.3/-0.3$	$0.0/-0.0$
BTagSFmistag	$0.2/-0.2$	$0.4/-0.4$	$0.1/-0.1$	$0.3/-0.3$	$10.9/-11.1$
Total	$15.2/-10.8$	$12.4/-10.2$	$17.4/-11.1$	$14.8/-13.9$	$28.4/-17.3$

Table B.2: Systematic object scale, resolution and efficiency scale factor relative uncertainties in percent (%) of the MC backgrounds for the default selection in the ee channel.

Systematic	$t\bar{t}+W$+jets	$t\bar{t}+WW$	$t\bar{t}+Z$+jets	WZ/ZZ+jets	$W^{\pm}W^{\pm}$+jets
JES	$6.3/-9.7$	$4.2/-6.2$	$10.0/-8.4$	$22.1/-0.0$	$4.8/-0.0$
JER	$0.1/-0.1$	$0.8/-0.8$	$1.8/-1.8$	$13.4/-13.4$	$8.8/-8.8$
JRE	$0.0/-0.0$	$0.0/-0.0$	$0.0/-0.0$	$0.0/-0.0$	$0.0/-0.0$
JVFSF	$2.1/-1.9$	$2.4/-2.1$	$2.6/-2.1$	$1.2/-1.1$	$1.4/-1.6$
ESFRecId	$2.5/-2.5$	$2.6/-2.6$	$2.5/-2.5$	$2.5/-2.5$	$2.6/-2.6$
ESFTrig	$0.2/-0.1$	$0.0/-0.5$	$0.1/-0.1$	$2.1/-0.1$	$0.0/-0.3$
EER	$0.2/-1.2$	$0.6/-0.2$	$0.6/-0.3$	$0.0/-0.0$	$0.0/-0.0$
EES	$1.0/-1.7$	$0.1/-0.3$	$1.6/-0.0$	$3.1/-0.0$	$0.0/-0.0$
MuSFRecId	$4.1/-4.1$	$4.1/-4.1$	$4.3/-4.2$	$4.8/-4.7$	$4.0/-4.0$
MuSFTrig	$0.0/-0.0$	$0.0/-0.0$	$0.0/-0.0$	$0.0/-0.0$	$0.0/-0.0$
MES	$0.0/-0.0$	$0.0/-0.0$	$0.1/-0.1$	$0.0/-0.0$	$0.0/-0.0$
MER	$0.0/-0.0$	$0.0/-0.0$	$0.1/-0.1$	$0.0/-0.0$	$0.0/-0.0$
MET	$0.0/-0.3$	$0.1/-1.0$	$2.2/-0.0$	$3.1/-0.0$	$0.0/-0.0$
BTagSFb	$5.6/-6.6$	$3.3/-4.0$	$4.2/-5.3$	$2.9/-2.9$	$1.0/-1.0$
BTagSFc	$0.7/-0.7$	$1.2/-1.2$	$0.7/-0.7$	$3.3/-3.8$	$10.1/-10.1$
BTagSFmistag	$0.3/-0.3$	$0.2/-0.2$	$0.2/-0.2$	$5.4/-5.4$	$12.3/-12.5$
Total	$10.0/-13.0$	$7.8/-9.3$	$12.7/-11.4$	$27.8/-16.2$	$19.5/-19.0$

Table B.3: Systematic object scale, resolution and efficiency scale factor relative uncertainties in percent (%) of the MC backgrounds for the default selection in the $e\mu$ channel.

Systematic	$t\bar{t}+W$+jets	$t\bar{t}+WW$	$t\bar{t}+Z$+jets	WZ/ZZ+jets	$W^{\pm}W^{\pm}$+jets
JES	$6.6/-8.1$	$4.3/-3.4$	$10.9/-7.7$	$16.0/-25.6$	$0.1/-2.5$
JER	$1.3/-1.3$	$1.5/-1.5$	$1.9/-1.9$	$9.0/-9.0$	$5.2/-5.2$
JRE	$0.0/-0.0$	$0.0/-0.0$	$0.0/-0.0$	$0.0/-0.0$	$0.0/-0.0$
JVFSF	$2.2/-1.9$	$2.5/-2.1$	$2.9/-2.2$	$1.1/-1.4$	$1.5/-1.8$
ESFRecId	$0.0/-0.0$	$0.0/-0.0$	$0.0/-0.0$	$0.0/-0.0$	$0.0/-0.0$
ESFTrig	$0.0/-0.0$	$0.0/-0.0$	$0.0/-0.0$	$0.0/-0.0$	$0.0/-0.0$
EER	$0.0/-0.1$	$0.0/-0.0$	$0.0/-0.0$	$0.0/-0.0$	$0.0/-0.0$
EES	$0.0/-0.1$	$0.0/-0.0$	$0.0/-0.0$	$0.0/-0.0$	$0.0/-0.0$
MuSFRecId	$8.2/-7.9$	$8.2/-7.9$	$9.0/-8.5$	$8.2/-7.9$	$8.2/-7.9$
MuSFTrig	$0.4/-0.4$	$0.4/-0.3$	$0.3/-0.3$	$0.5/-0.5$	$0.2/-0.2$
MES	$0.0/-0.0$	$0.0/-0.0$	$0.0/-0.0$	$0.0/-0.0$	$0.0/-0.0$
MER	$0.2/-0.2$	$0.2/-0.2$	$0.0/-0.0$	$0.0/-0.0$	$0.0/-0.0$
MET	$0.0/-0.9$	$0.7/-0.5$	$0.8/-0.4$	$0.0/-0.0$	$0.0/-0.0$
BTagSFb	$4.5/-5.6$	$4.3/-4.9$	$6.0/-6.7$	$1.5/-1.7$	$0.4/-0.3$
BTagSFc	$1.0/-1.0$	$0.1/-0.2$	$0.1/-0.1$	$4.4/-5.1$	$0.9/-0.9$
BTagSFmistag	$0.2/-0.2$	$0.8/-0.8$	$0.0/-0.0$	$3.9/-4.0$	$16.0/-16.1$
Total	$11.8/-12.9$	$10.7/-10.3$	$15.8/-13.6$	$21.0/-29.1$	$18.8/-18.9$

Table B.4: Systematic object scale, resolution and efficiency scale factor relative uncertainties in percent (%) of the MC backgrounds for the default selection in the $\mu\mu$ channel.

Systematic	$b'(400GeV) \to tW$	$b'(450GeV) \to tW$	$b'(500GeV) \to tW$	$b'(550GeV) \to tW$	$b'(600GeV) \to tW$	$b'(650GeV) \to tW$	$b'(700GeV) \to tW$
JES	4.4/ − 8.9	6.9/ − 4.2	3.9/ − 7.4	3.9/ − 1.3	1.0/ − 0.4	3.3/ − 1.7	1.7/ − 0.7
JER	0.3/ − 0.3	0.9/ − 0.9	0.5/ − 0.5	0.4/ − 0.4	0.3/ − 0.3	0.1/ − 0.1	1.0/ − 1.0
JRE	0.0/ − 0.0	0.0/ − 0.0	0.0/ − 0.0	0.0/ − 0.0	0.0/ − 0.0	0.0/ − 0.0	0.0/ − 0.0
JVFSF	2.6/ − 2.2	2.3/ − 2.1	3.0/ − 2.6	2.4/ − 2.3	2.8/ − 2.5	2.6/ − 2.5	3.1/ − 2.8
ESFRecId	5.3/ − 5.2	5.4/ − 5.2	5.3/ − 5.2	5.3/ − 5.2	5.3/ − 5.2	5.4/ − 5.2	5.4/ − 5.2
ESFTrig	1.9/ − 0.0	1.2/ − 0.0	1.3/ − 0.0	1.4/ − 0.0	1.9/ − 0.0	1.8/ − 0.0	2.5/ − 0.0
EER	0.0/ − 1.2	0.3/ − 1.3	0.0/ − 0.9	0.0/ − 0.6	0.3/ − 0.0	0.2/ − 0.0	0.6/ − 0.0
EES	2.2/ − 0.8	0.0/ − 1.4	0.0/ − 0.9	3.2/ − 2.4	0.9/ − 0.3	1.3/ − 0.0	1.6/ − 0.1
MuSFRecId	0.0/ − 0.0	0.1/ − 0.1	0.0/ − 0.0	0.1/ − 0.1	0.1/ − 0.1	0.1/ − 0.1	0.2/ − 0.2
MuSFTrig	0.0/ − 0.0	0.0/ − 0.0	0.0/ − 0.0	0.0/ − 0.0	0.0/ − 0.0	0.0/ − 0.0	0.0/ − 0.0
MES	0.0/ − 0.0	0.0/ − 0.0	0.0/ − 0.0	0.0/ − 0.0	0.0/ − 0.0	0.0/ − 0.0	0.0/ − 0.0
MER	0.0/ − 0.0	0.0/ − 0.0	0.0/ − 0.0	0.0/ − 0.0	0.0/ − 0.0	0.0/ − 0.0	0.0/ − 0.0
MET	0.0/ − 0.8	1.1/ − 0.0	0.9/ − 0.9	0.6/ − 0.6	0.0/ − 0.2	0.6/ − 0.0	0.0/ − 0.0
BTagSFb	3.2/ − 4.0	1.4/ − 2.5	2.6/ − 3.8	3.4/ − 4.6	0.5/ − 2.3	4.1/ − 5.1	1.0/ − 2.1
BTagSFc	0.4/ − 0.5	0.2/ − 0.2	1.0/ − 0.8	0.2/ − 0.2	1.1/ − 1.2	0.0/ − 0.0	0.3/ − 0.3
BTagSFmistag	0.5/ − 0.5	0.3/ − 0.3	0.3/ − 0.3	0.1/ − 0.1	0.1/ − 0.1	0.0/ − 0.0	0.4/ − 0.5
Total	8.6/ − 11.4	9.4/ − 7.7	7.9/ − 10.3	8.6/ − 7.9	6.6/ − 6.4	8.3/ − 7.9	7.3/ − 6.4

Systematic	$b'(750GeV) \to tW$	$b'(800GeV) \to tW$	$b'(850GeV) \to tW$	$b'(900GeV) \to tW$	$b'(950GeV) \to tW$	$b'(1000GeV) \to tW$
JES	0.6/ − 2.6	1.1/ − 1.2	1.2/ − 0.6	0.0/ − 0.1	1.2/ − 2.0	1.0/ − 0.0
JER	0.3/ − 0.3	0.3/ − 0.3	0.1/ − 0.1	0.5/ − 0.5	0.0/ − 0.0	0.3/ − 0.3
JRE	0.0/ − 0.0	0.0/ − 0.0	0.0/ − 0.0	0.0/ − 0.0	0.0/ − 0.0	0.0/ − 0.0
JVFSF	2.8/ − 2.7	3.0/ − 3.0	3.2/ − 3.2	3.1/ − 3.1	2.7/ − 2.7	3.1/ − 3.1
ESFRecId	5.3/ − 5.2	5.4/ − 5.2	5.4/ − 5.2	5.4/ − 5.2	5.4/ − 5.2	5.3/ − 5.2
ESFTrig	2.4/ − 0.0	1.7/ − 0.0	2.3/ − 0.0	1.9/ − 0.0	2.6/ − 0.0	2.7/ − 0.0
EER	0.0/ − 0.1	0.0/ − 0.0	0.0/ − 0.2	0.0/ − 0.8	0.2/ − 1.0	0.2/ − 0.7
EES	0.4/ − 0.3	0.7/ − 0.6	0.0/ − 0.3	0.2/ − 0.4	0.0/ − 1.2	0.5/ − 0.2
MuSFRecId	0.1/ − 0.1	0.0/ − 0.0	0.1/ − 0.1	0.1/ − 0.1	0.3/ − 0.3	0.2/ − 0.2
MuSFTrig	0.0/ − 0.0	0.0/ − 0.0	0.0/ − 0.0	0.0/ − 0.0	0.0/ − 0.0	0.0/ − 0.0
MES	0.0/ − 0.0	0.0/ − 0.0	0.0/ − 0.0	0.0/ − 0.0	0.0/ − 0.0	0.0/ − 0.0
MER	0.0/ − 0.0	0.0/ − 0.0	0.0/ − 0.0	0.0/ − 0.0	0.0/ − 0.0	0.0/ − 0.0
MET	0.0/ − 0.2	0.0/ − 0.0	0.5/ − 0.6	0.2/ − 0.5	0.4/ − 0.1	0.6/ − 0.0
BTagSFb	2.8/ − 4.0	1.2/ − 2.1	3.6/ − 4.2	0.0/ − 1.6	1.0/ − 2.0	1.4/ − 2.6
BTagSFc	0.7/ − 0.7	1.2/ − 1.2	0.2/ − 0.2	0.7/ − 0.7	0.6/ − 0.5	0.6/ − 0.6
BTagSFmistag	0.1/ − 0.1	0.6/ − 0.6	1.0/ − 1.0	0.3/ − 0.3	0.6/ − 0.6	0.6/ − 0.6
Total	7.1/ − 7.6	6.8/ − 6.6	7.8/ − 7.5	6.6/ − 6.4	6.8/ − 6.7	7.0/ − 6.7

Table B.5: Systematic object scale, resolution and efficiency scale factor relative uncertainties in percent (%) of the MC signals ($b' \to tW$) for the default selection in the ee channel.

Systematic	$b'(400GeV) \to tW$	$b'(450GeV) \to tW$	$b'(500GeV) \to tW$	$b'(550GeV) \to tW$	$b'(600GeV) \to tW$	$b'(650GeV) \to tW$	$b'(700GeV) \to tW$
JES	4.9/ − 6.2	3.7/ − 3.1	1.7/ − 3.5	1.8/ − 1.7	2.1/ − 2.0	0.9/ − 1.9	1.2/ − 1.8
JER	1.5/ − 1.5	1.4/ − 1.4	1.0/ − 1.0	0.3/ − 0.3	0.2/ − 0.2	0.8/ − 0.8	0.4/ − 0.4
JRE	0.0/ − 0.0	0.0/ − 0.0	0.0/ − 0.0	0.0/ − 0.0	0.0/ − 0.0	0.0/ − 0.0	0.0/ − 0.0
JVFSF	2.7/ − 2.2	2.6/ − 2.3	2.5/ − 2.3	2.6/ − 2.4	2.6/ − 2.5	2.8/ − 2.7	3.0/ − 2.8
ESFRecId	2.6/ − 2.6	2.6/ − 2.6	2.6/ − 2.6	2.6/ − 2.6	2.6/ − 2.6	2.6/ − 2.6	2.6/ − 2.6
ESFTrig	0.0/ − 0.1	0.2/ − 0.1	0.0/ − 0.5	0.2/ − 0.1	0.0/ − 0.2	0.2/ − 0.2	0.0/ − 0.4
EER	0.0/ − 0.0	0.3/ − 0.0	0.1/ − 0.0	0.1/ − 0.1	0.1/ − 0.0	0.2/ − 0.0	0.0/ − 0.2
EES	0.4/ − 0.6	0.3/ − 0.1	0.0/ − 0.0	0.3/ − 0.0	0.5/ − 0.0	0.3/ − 0.0	0.0/ − 0.3
MuSFRecId	4.1/ − 4.1	4.1/ − 4.1	4.1/ − 4.1	4.1/ − 4.1	4.1/ − 4.1	4.1/ − 4.1	4.1/ − 4.1
MuSFTrig	0.0/ − 0.0	0.0/ − 0.0	0.0/ − 0.0	0.0/ − 0.0	0.0/ − 0.0	0.0/ − 0.0	0.0/ − 0.0
MES	0.0/ − 0.0	0.0/ − 0.0	0.1/ − 0.1	0.1/ − 0.1	0.0/ − 0.0	0.0/ − 0.0	0.0/ − 0.0
MER	0.0/ − 0.0	0.1/ − 0.1	0.1/ − 0.1	0.0/ − 0.0	0.0/ − 0.0	0.1/ − 0.1	0.0/ − 0.0
MET	0.6/ − 0.0	0.5/ − 0.3	0.4/ − 0.0	0.2/ − 0.2	0.2/ − 0.1	0.2/ − 0.0	0.0/ − 0.2
BTagSFb	4.2/ − 4.9	2.0/ − 2.7	3.1/ − 4.0	2.6/ − 3.9	1.5/ − 2.4	2.4/ − 3.7	2.3/ − 3.5
BTagSFc	0.1/ − 0.1	0.9/ − 1.0	1.2/ − 1.1	1.2/ − 1.2	0.4/ − 0.4	0.3/ − 0.4	0.1/ − 0.1
BTagSFmistag	0.0/ − 0.1	0.3/ − 0.3	0.5/ − 0.4	0.4/ − 0.4	0.6/ − 0.6	0.1/ − 0.1	0.4/ − 0.4
Total	8.7/ − 9.7	7.2/ − 7.0	6.7/ − 7.7	6.5/ − 7.0	6.2/ − 6.3	6.2/ − 7.0	6.3/ − 6.9

Systematic	$b'(750GeV) \to tW$	$b'(800GeV) \to tW$	$b'(850GeV) \to tW$	$b'(900GeV) \to tW$	$b'(950GeV) \to tW$	$b'(1000GeV) \to tW$
JES	0.0/ − 0.4	0.1/ − 1.4	1.1/ − 0.5	0.8/ − 0.3	1.2/ − 0.0	0.0/ − 0.5
JER	0.3/ − 0.3	0.8/ − 0.8	0.4/ − 0.4	0.3/ − 0.3	0.2/ − 0.2	0.0/ − 0.0
JRE	0.0/ − 0.0	0.0/ − 0.0	0.0/ − 0.0	0.0/ − 0.0	0.0/ − 0.0	0.0/ − 0.0
JVFSF	2.8/ − 2.8	2.9/ − 2.9	3.4/ − 3.2	3.2/ − 3.1	3.0/ − 3.0	3.3/ − 3.4
ESFRecId	2.6/ − 2.6	2.6/ − 2.6	2.6/ − 2.6	2.6/ − 2.6	2.6/ − 2.6	2.6/ − 2.6
ESFTrig	0.0/ − 0.3	0.0/ − 0.4	0.0/ − 0.8	0.0/ − 0.4	0.0/ − 0.7	0.0/ − 0.7
EER	0.1/ − 0.3	0.2/ − 0.0	0.1/ − 0.2	0.1/ − 0.1	0.1/ − 0.1	0.0/ − 0.2
EES	0.0/ − 0.5	0.1/ − 0.2	0.3/ − 0.4	0.1/ − 0.0	0.4/ − 0.0	0.1/ − 0.2
MuSFRecId	4.1/ − 4.1	4.1/ − 4.1	4.1/ − 4.1	4.2/ − 4.1	4.2/ − 4.2	4.2/ − 4.2
MuSFTrig	0.0/ − 0.0	0.0/ − 0.0	0.0/ − 0.0	0.0/ − 0.0	0.0/ − 0.0	0.0/ − 0.0
MES	0.0/ − 0.0	0.0/ − 0.0	0.0/ − 0.0	0.0/ − 0.0	0.0/ − 0.0	0.0/ − 0.0
MER	0.0/ − 0.0	0.0/ − 0.0	0.0/ − 0.0	0.0/ − 0.0	0.0/ − 0.0	0.0/ − 0.0
MET	0.2/ − 0.0	0.4/ − 0.0	0.2/ − 0.0	0.2/ − 0.0	0.2/ − 0.4	0.1/ − 0.2
BTagSFb	2.3/ − 3.4	1.3/ − 2.3	1.8/ − 3.2	2.5/ − 3.9	2.6/ − 3.9	0.5/ − 2.3
BTagSFc	0.2/ − 0.2	0.7/ − 0.8	0.3/ − 0.4	0.1/ − 0.1	0.5/ − 0.4	0.5/ − 0.4
BTagSFmistag	0.6/ − 0.6	0.3/ − 0.3	0.0/ − 0.0	0.2/ − 0.2	0.2/ − 0.1	0.3/ − 0.3
Total	6.1/ − 6.6	5.9/ − 6.4	6.3/ − 6.7	6.5/ − 7.0	6.5/ − 7.0	6.0/ − 6.5

Table B.6: Systematic object scale, resolution and efficiency scale factor relative uncertainties in percent (%) of the MC signals ($b' \to tW$) for the default selection in the $e\mu$ channel.

Systematic	$b'(400GeV) \to tW$	$b'(450GeV) \to tW$	$b'(500GeV) \to tW$	$b'(550GeV) \to tW$	$b'(600GeV) \to tW$	$b'(650GeV) \to tW$	$b'(700GeV) \to tW$
JES	4.8/ − 4.6	4.2/ − 6.3	3.1/ − 3.1	1.9/ − 0.0	0.0/ − 1.4	0.4/ − 1.0	1.7/ − 0.3
JER	0.1/ − 0.1	0.8/ − 0.8	0.2/ − 0.2	0.5/ − 0.5	0.5/ − 0.5	1.1/ − 1.1	0.7/ − 0.7
JRE	0.0/ − 0.0	0.0/ − 0.0	0.0/ − 0.0	0.0/ − 0.0	0.0/ − 0.0	0.0/ − 0.0	0.0/ − 0.0
JVFSF	2.7/ − 2.2	2.6/ − 2.2	2.9/ − 2.6	2.6/ − 2.3	2.6/ − 2.5	2.8/ − 2.6	3.2/ − 2.9
ESFRecId	0.0/ − 0.0	0.0/ − 0.0	0.0/ − 0.0	0.0/ − 0.0	0.0/ − 0.0	0.0/ − 0.0	0.0/ − 0.0
ESFTrig	0.0/ − 0.0	0.0/ − 0.0	0.0/ − 0.0	0.0/ − 0.0	0.0/ − 0.0	0.0/ − 0.0	0.0/ − 0.0
EER	0.0/ − 0.0	0.0/ − 0.2	0.0/ − 0.0	0.0/ − 0.0	0.0/ − 0.0	0.0/ − 0.0	0.0/ − 0.0
EES	0.0/ − 0.0	0.0/ − 0.2	0.0/ − 0.0	0.3/ − 0.0	0.0/ − 0.0	0.0/ − 0.0	0.2/ − 0.0
MuSFRecId	8.3/ − 7.9	8.2/ − 7.9	8.3/ − 7.9	8.3/ − 7.9	8.2/ − 7.9	8.4/ − 8.0	8.3/ − 7.9
MuSFTrig	0.5/ − 0.4	0.4/ − 0.4	0.4/ − 0.4	0.4/ − 0.4	0.4/ − 0.4	0.4/ − 0.4	0.4/ − 0.4
MES	0.0/ − 0.0	0.0/ − 0.0	0.1/ − 0.1	0.0/ − 0.0	0.0/ − 0.0	0.0/ − 0.0	0.0/ − 0.0
MER	0.3/ − 0.3	0.1/ − 0.1	0.0/ − 0.0	0.0/ − 0.0	0.0/ − 0.0	0.0/ − 0.0	0.0/ − 0.0
MET	0.6/ − 0.2	0.4/ − 0.3	1.0/ − 0.0	0.5/ − 0.3	0.6/ − 0.0	0.2/ − 0.0	0.3/ − 0.0
BTagSFb	3.8/ − 4.7	4.3/ − 5.2	1.6/ − 2.8	1.6/ − 2.4	2.8/ − 3.8	2.3/ − 3.4	1.1/ − 2.9
BTagSFc	0.4/ − 0.4	0.4/ − 0.4	0.3/ − 0.3	0.2/ − 0.2	1.0/ − 0.9	0.2/ − 0.2	0.4/ − 0.4
BTagSFmistag	0.3/ − 0.3	0.1/ − 0.1	0.1/ − 0.1	0.3/ − 0.3	0.0/ − 0.0	0.4/ − 0.4	0.2/ − 0.2
Total	10.7/ − 10.5	10.5/ − 11.6	9.5/ − 9.3	9.1/ − 8.6	9.1/ − 9.3	9.2/ − 9.2	9.2/ − 9.0

Systematic	$b'(750GeV) \to tW$	$b'(800GeV) \to tW$	$b'(850GeV) \to tW$	$b'(900GeV) \to tW$	$b'(950GeV) \to tW$	$b'(1000GeV) \to tW$
JES	0.0/ − 0.8	1.4/ − 0.9	1.2/ − 1.5	1.3/ − 1.7	2.2/ − 1.6	0.1/ − 0.6
JER	0.2/ − 0.2	0.5/ − 0.5	1.2/ − 1.2	0.9/ − 0.9	0.0/ − 0.0	0.0/ − 0.0
JRE	0.0/ − 0.0	0.0/ − 0.0	0.0/ − 0.0	0.0/ − 0.0	0.0/ − 0.0	0.0/ − 0.0
JVFSF	2.9/ − 2.8	3.8/ − 3.5	3.1/ − 3.1	3.2/ − 3.1	3.5/ − 3.3	4.1/ − 3.8
ESFRecId	0.0/ − 0.0	0.0/ − 0.0	0.0/ − 0.0	0.0/ − 0.0	0.0/ − 0.0	0.0/ − 0.0
ESFTrig	0.0/ − 0.0	0.0/ − 0.0	0.0/ − 0.0	0.0/ − 0.0	0.0/ − 0.0	0.0/ − 0.0
EER	0.0/ − 0.0	0.0/ − 0.0	0.0/ − 0.0	0.2/ − 0.0	0.0/ − 0.0	0.0/ − 0.0
EES	0.0/ − 0.0	0.0/ − 0.0	0.0/ − 0.0	0.0/ − 0.0	0.0/ − 0.0	0.0/ − 0.0
MuSFRecId	8.3/ − 7.9	8.3/ − 7.9	8.3/ − 7.9	8.3/ − 8.0	8.4/ − 8.0	8.4/ − 8.0
MuSFTrig	0.5/ − 0.4	0.5/ − 0.4	0.4/ − 0.4	0.5/ − 0.4	0.4/ − 0.4	0.4/ − 0.4
MES	0.1/ − 0.1	0.0/ − 0.0	0.1/ − 0.1	0.0/ − 0.0	0.0/ − 0.0	0.0/ − 0.0
MER	0.0/ − 0.0	0.1/ − 0.1	0.1/ − 0.1	0.0/ − 0.0	0.1/ − 0.1	0.0/ − 0.0
MET	0.0/ − 0.3	0.5/ − 0.2	0.0/ − 0.5	0.1/ − 0.3	0.4/ − 0.0	0.0/ − 0.3
BTagSFb	3.3/ − 4.4	0.5/ − 1.5	4.1/ − 5.0	2.4/ − 3.6	1.6/ − 2.9	1.5/ − 3.1
BTagSFc	0.2/ − 0.3	0.4/ − 0.3	0.6/ − 0.7	1.0/ − 1.0	0.1/ − 0.1	0.1/ − 0.1
BTagSFmistag	0.1/ − 0.1	0.3/ − 0.3	0.3/ − 0.3	0.0/ − 0.0	0.4/ − 0.4	0.1/ − 0.1
Total	9.4/ − 9.5	9.3/ − 8.9	9.9/ − 10.1	9.4/ − 9.6	9.5/ − 9.3	9.5/ − 9.4

Table B.7: Systematic object scale, resolution and efficiency scale factor relative uncertainties in percent (%) of the MC signals ($b' \to tW$) for the default selection in the $\mu\mu$ channel.

B.2.2 Additional variations of cuts

The event selection optimisation was performed by varying the cuts on the variables H_T and N_{Jets}. In addition, I also tried to vary the cuts on the variables N_{bJets} and E_T^{miss}.

The obtained mass limits when requiring $N_{\text{bJets}} \geq 2$, fixing $E_T^{\text{miss}} \geq 40\,\text{GeV}$ and varying H_T and N_{Jets} are presented in Table B.8. As can be seen, no cut combination

H_T [GeV] \ N_{Jets}	≥ 2	≥ 3	≥ 4
≥ 550	0.582	0.707	0.711
≥ 600	0.717	—	—

Table B.8: Expected lower b' mass limits in TeV assuming $b' \to tW$ with 100% branching fraction for several combinations of cuts on N_{Jets} and H_T. Besides the basic selection summarised in Table 6.15, the cuts on E_T^{miss} and N_{bJets} were fixed to $E_T^{\text{miss}} \geq 40\,\text{GeV}$ and $N_{\text{bJets}} \geq 2$.

gives a higher mass limit than the one obtained before.
Finally, I also tried to vary the cut value on E_T^{miss}, where the results are shown in Table B.9. Here, only at least one b-tagged jet was required. Also these variations

H_T/E_T^{miss} [GeV] \ N_{Jets}	≥ 2	≥ 3	≥ 4
$\geq 500/\geq 60$	0.737	—	—
$\geq 500/\geq 80$	0.744	—	—
$\geq 550/\geq 60$	0.747	0.750	0.753
$\geq 550/\geq 80$	0.753	—	—
$\geq 600/\geq 60$	0.762	—	—
$\geq 600/\geq 80$	0.764	—	—

Table B.9: Expected lower b' mass limits in TeV assuming $b' \to tW$ with 100% branching fraction for several combinations of cuts on E_T^{miss}, N_{Jets} and H_T. Besides the basic selection summarised in Table 6.15, the cut on N_{bJets} was fixed to $N_{\text{bJets}} \geq 1$.

revealed no improvement in the expected mass limit.

B.2.3 Expected limits for several event selections

For the event selection optimisation, upper limits on the b' pair production cross-sections for several sets of cuts on the discriminant variables were derived. These cross-section limits were translated into lower b' mass limits. The distributions for the upper cross-section limits as a function of the b' mass for all considered sets of cuts are presented in Figures B.7, B.8, B.9, B.10, B.11, B.12 and B.13. In very few cases the calculation of the $\pm 2\sigma$ band failed for particular mass points, which results in misleading points in

some plots. This is due to the fact, that a smaller number of pseudo experiments was generated compared to the final limit calculation, in order to save computing time. In these cases, a larger number of pseudo experiments would fix this problem. However, this is not problematic for the cut optimisation, because the expected mass limits are derived from the intersection of the theoretical cross-section prediction and the median expected cross-section limit.

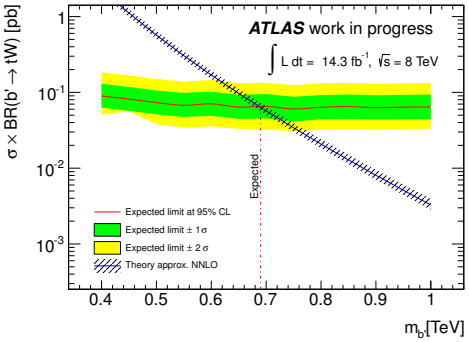

(a) $N_{\text{Jets}} \geq 2$, $N_{\text{bJets}} \geq 1$, $E_T^{\text{miss}} \geq 40\,\text{GeV}$, $H_T \geq 400\,\text{GeV}$

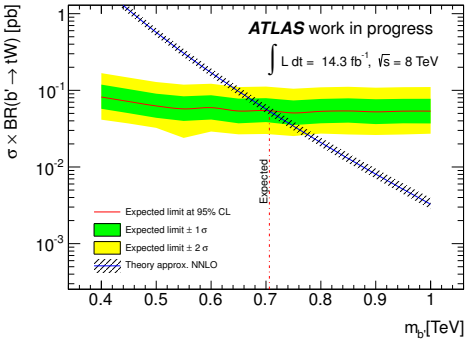

(b) $N_{\text{Jets}} \geq 2$, $N_{\text{bJets}} \geq 1$, $E_T^{\text{miss}} \geq 40\,\text{GeV}$, $H_T \geq 450\,\text{GeV}$

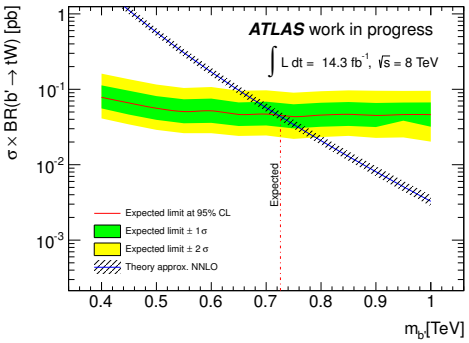

(c) $N_{\text{Jets}} \geq 2$, $N_{\text{bJets}} \geq 1$, $E_T^{\text{miss}} \geq 40\,\text{GeV}$, $H_T \geq 500\,\text{GeV}$

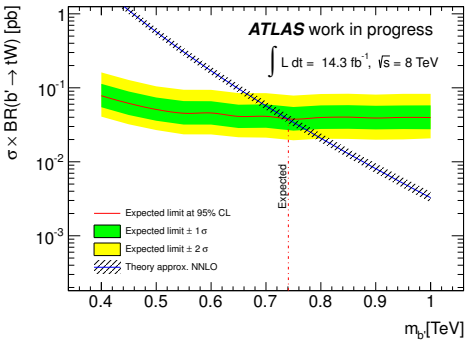

(d) $N_{\text{Jets}} \geq 2$, $N_{\text{bJets}} \geq 1$, $E_T^{\text{miss}} \geq 40\,\text{GeV}$, $H_T \geq 550\,\text{GeV}$

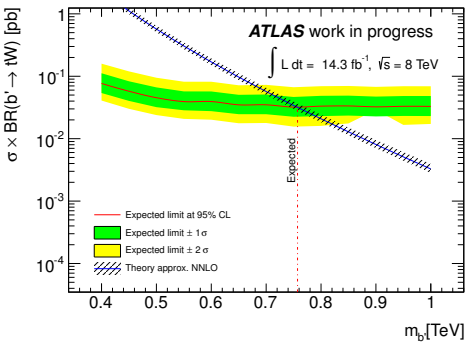

(e) $N_{\text{Jets}} \geq 2$, $N_{\text{bJets}} \geq 1$, $E_T^{\text{miss}} \geq 40\,\text{GeV}$, $H_T \geq 600\,\text{GeV}$

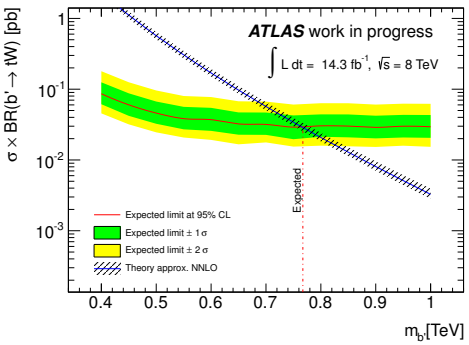

(f) $N_{\text{Jets}} \geq 2$, $N_{\text{bJets}} \geq 1$, $E_T^{\text{miss}} \geq 40\,\text{GeV}$, $H_T \geq 650\,\text{GeV}$

Figure B.7: Expected cross-section limits as a function of the b' mass (assuming $b' \to tW$ with 100% BF) for several event selections. In all cases the basic selection was applied (Table 6.15).

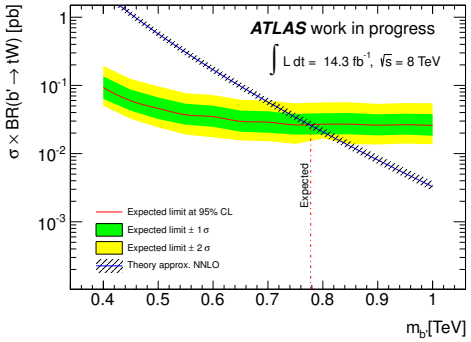

(a) $N_{\text{Jets}} \geq 2$, $N_{\text{bJets}} \geq 1$, $E_T^{\text{miss}} \geq 40\,\text{GeV}$, $H_T \geq 700\,\text{GeV}$

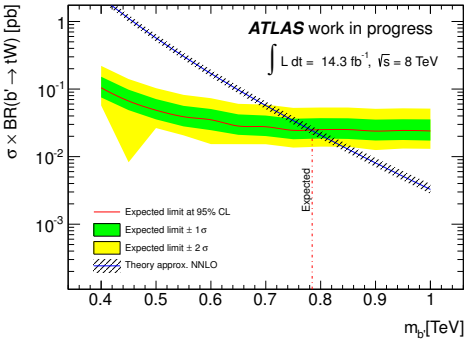

(b) $N_{\text{Jets}} \geq 2$, $N_{\text{bJets}} \geq 1$, $E_T^{\text{miss}} \geq 40\,\text{GeV}$, $H_T \geq 750\,\text{GeV}$

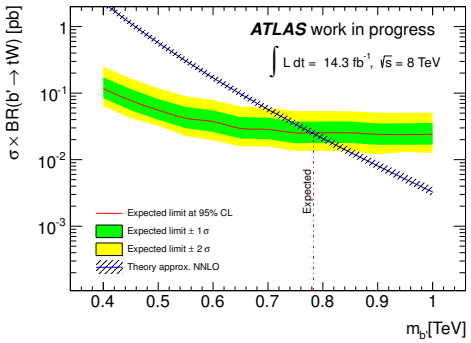

(c) $N_{\text{Jets}} \geq 2$, $N_{\text{bJets}} \geq 1$, $E_T^{\text{miss}} \geq 40\,\text{GeV}$, $H_T \geq 800\,\text{GeV}$

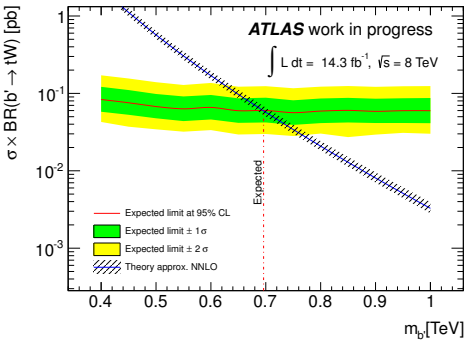

(d) $N_{\text{Jets}} \geq 3$, $N_{\text{bJets}} \geq 1$, $E_T^{\text{miss}} \geq 40\,\text{GeV}$, $H_T \geq 400\,\text{GeV}$

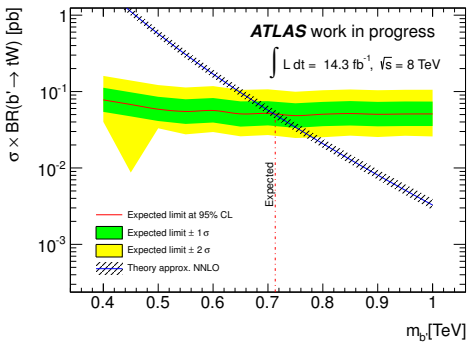

(e) $N_{\text{Jets}} \geq 3$, $N_{\text{bJets}} \geq 1$, $E_T^{\text{miss}} \geq 40\,\text{GeV}$, $H_T \geq 450\,\text{GeV}$

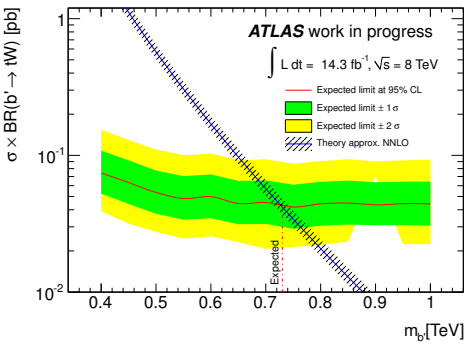

(f) $N_{\text{Jets}} \geq 3$, $N_{\text{bJets}} \geq 1$, $E_T^{\text{miss}} \geq 40\,\text{GeV}$, $H_T \geq 500\,\text{GeV}$

Figure B.8: Expected cross-section limits as a function of the b' mass (assuming $b' \to tW$ with 100% BF) for several event selections. In all cases the basic selection was applied (Table 6.15).

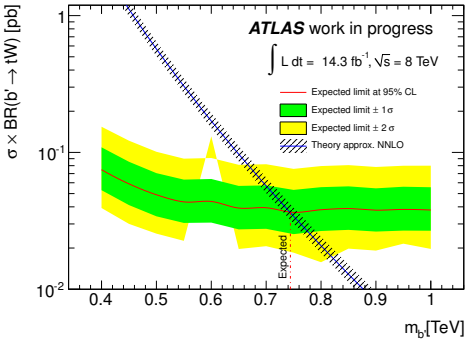

(a) $N_{\text{Jets}} \geq 3$, $N_{\text{bJets}} \geq 1$, $E_T^{\text{miss}} \geq 40\,\text{GeV}$, $H_T \geq 550\,\text{GeV}$

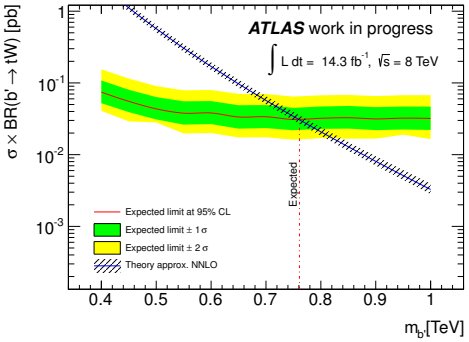

(b) $N_{\text{Jets}} \geq 3$, $N_{\text{bJets}} \geq 1$, $E_T^{\text{miss}} \geq 40\,\text{GeV}$, $H_T \geq 600\,\text{GeV}$

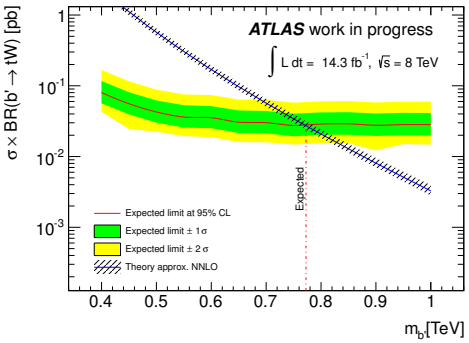

(c) $N_{\text{Jets}} \geq 3$, $N_{\text{bJets}} \geq 1$, $E_T^{\text{miss}} \geq 40\,\text{GeV}$, $H_T \geq 650\,\text{GeV}$

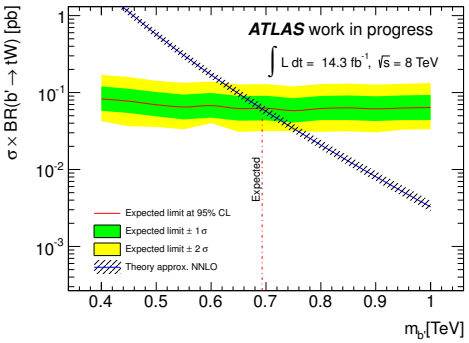

(d) $N_{\text{Jets}} \geq 4$, $N_{\text{bJets}} \geq 1$, $E_T^{\text{miss}} \geq 40\,\text{GeV}$, $H_T \geq 350\,\text{GeV}$

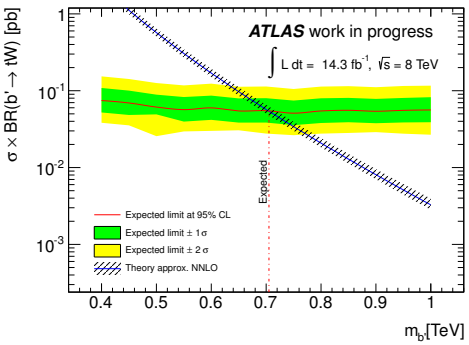

(e) $N_{\text{Jets}} \geq 4$, $N_{\text{bJets}} \geq 1$, $E_T^{\text{miss}} \geq 40\,\text{GeV}$, $H_T \geq 400\,\text{GeV}$

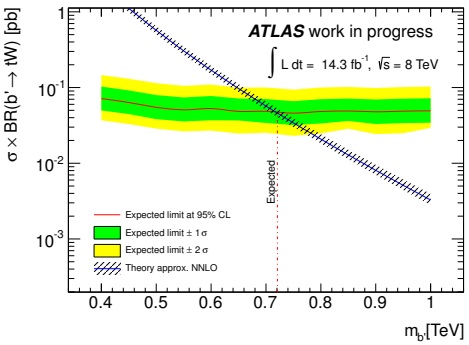

(f) $N_{\text{Jets}} \geq 4$, $N_{\text{bJets}} \geq 1$, $E_T^{\text{miss}} \geq 40\,\text{GeV}$, $H_T \geq 450\,\text{GeV}$

Figure B.9: Expected cross-section limits as a function of the b' mass (assuming $b' \to tW$ with 100% BF) for several event selections. In all cases the basic selection was applied (Table 6.15).

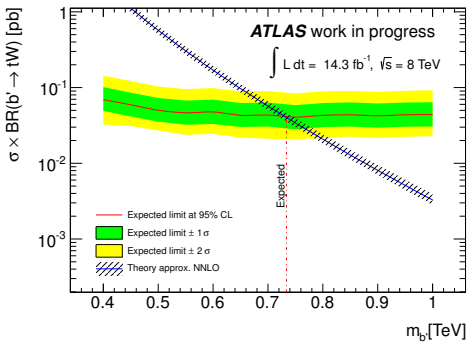

(a) $N_{\text{Jets}} \geq 4$, $N_{\text{bJets}} \geq 1$, $E_T^{\text{miss}} \geq 40\,\text{GeV}$, $H_T \geq 500\,\text{GeV}$

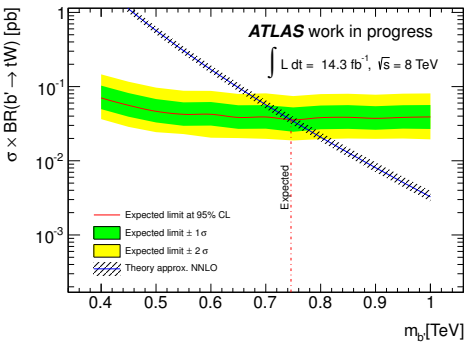

(b) $N_{\text{Jets}} \geq 4$, $N_{\text{bJets}} \geq 1$, $E_T^{\text{miss}} \geq 40\,\text{GeV}$, $H_T \geq 550\,\text{GeV}$

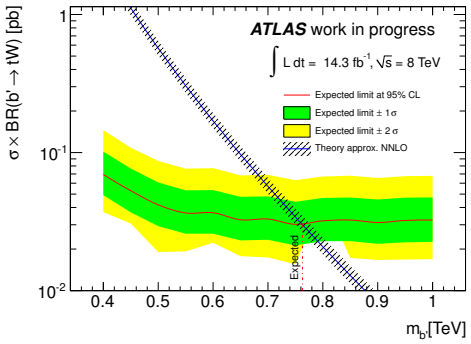

(c) $N_{\text{Jets}} \geq 4$, $N_{\text{bJets}} \geq 1$, $E_T^{\text{miss}} \geq 40\,\text{GeV}$, $H_T \geq 600\,\text{GeV}$

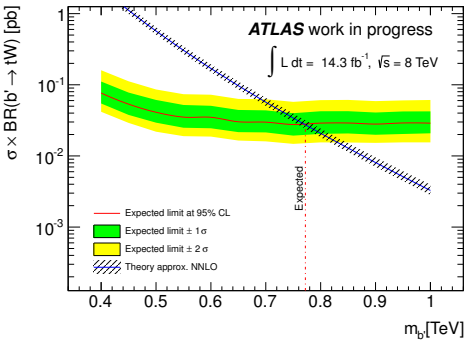

(d) $N_{\text{Jets}} \geq 4$, $N_{\text{bJets}} \geq 1$, $E_T^{\text{miss}} \geq 40\,\text{GeV}$, $H_T \geq 650\,\text{GeV}$

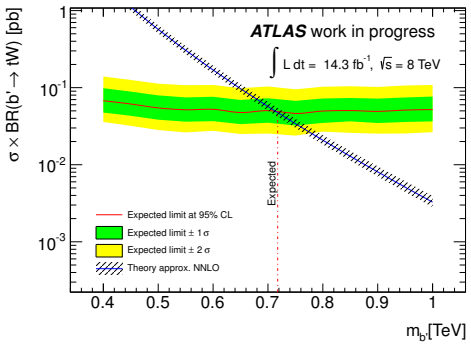

(e) $N_{\text{Jets}} \geq 5$, $N_{\text{bJets}} \geq 1$, $E_T^{\text{miss}} \geq 40\,\text{GeV}$, $H_T \geq 350\,\text{GeV}$

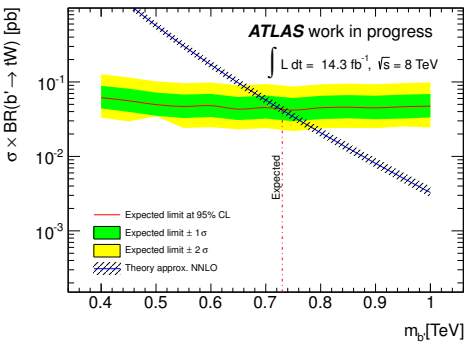

(f) $N_{\text{Jets}} \geq 5$, $N_{\text{bJets}} \geq 1$, $E_T^{\text{miss}} \geq 40\,\text{GeV}$, $H_T \geq 400\,\text{GeV}$

Figure B.10: Expected cross-section limits as a function of the b' mass (assuming $b' \to tW$ with 100% BF) for several event selections. In all cases the basic selection was applied (Table 6.15).

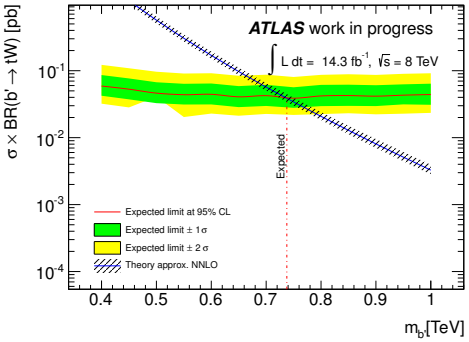

(a) $N_{\text{Jets}} \geq 5$, $N_{\text{bJets}} \geq 1$, $E_T^{\text{miss}} \geq 40\,\text{GeV}$, $H_T \geq 450\,\text{GeV}$

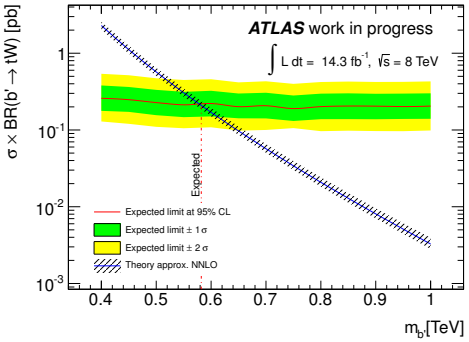

(b) $N_{\text{Jets}} \geq 2$, $N_{\text{bJets}} \geq 2$, $E_T^{\text{miss}} \geq 40\,\text{GeV}$, $H_T \geq 550\,\text{GeV}$

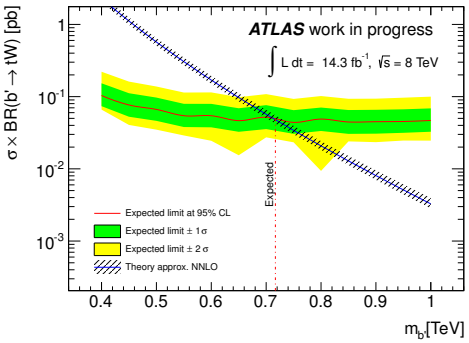

(c) $N_{\text{Jets}} \geq 2$, $N_{\text{bJets}} \geq 2$, $E_T^{\text{miss}} \geq 40\,\text{GeV}$, $H_T \geq 600\,\text{GeV}$

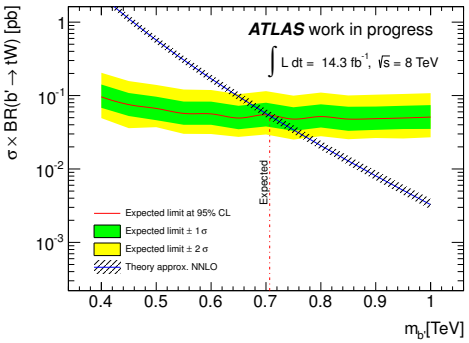

(d) $N_{\text{Jets}} \geq 3$, $N_{\text{bJets}} \geq 2$, $E_T^{\text{miss}} \geq 40\,\text{GeV}$, $H_T \geq 550\,\text{GeV}$

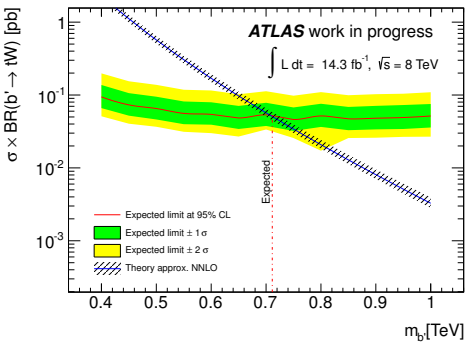

(e) $N_{\text{Jets}} \geq 4$, $N_{\text{bJets}} \geq 2$, $E_T^{\text{miss}} \geq 40\,\text{GeV}$, $H_T \geq 550\,\text{GeV}$

Figure B.11: Expected cross-section limits as a function of the b' mass (assuming $b' \to tW$ with 100% BF) for several event selections. In all cases the basic selection was applied (Table 6.15).

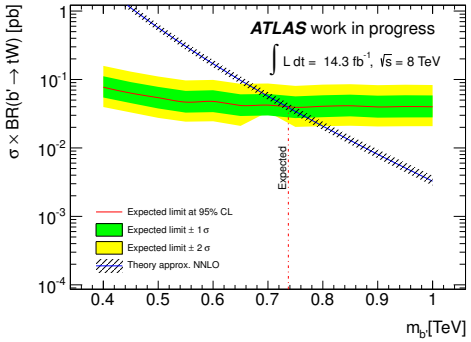

(a) $N_{\text{Jets}} \geq 2$, $N_{\text{bJets}} \geq 1$, $E_T^{\text{miss}} \geq 60\,\text{GeV}$, $H_T \geq 500\,\text{GeV}$

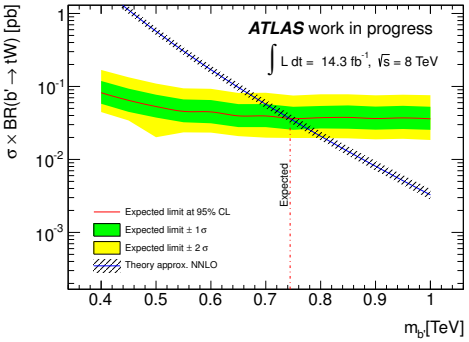

(b) $N_{\text{Jets}} \geq 2$, $N_{\text{bJets}} \geq 1$, $E_T^{\text{miss}} \geq 80\,\text{GeV}$, $H_T \geq 500\,\text{GeV}$

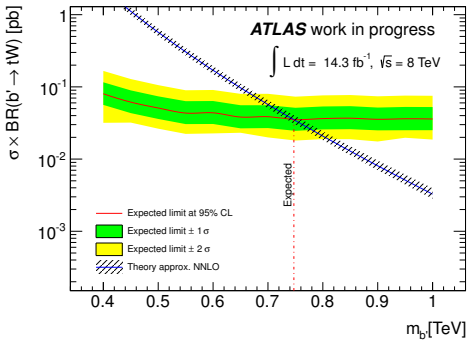

(c) $N_{\text{Jets}} \geq 2$, $N_{\text{bJets}} \geq 1$, $E_T^{\text{miss}} \geq 60\,\text{GeV}$, $H_T \geq 550\,\text{GeV}$

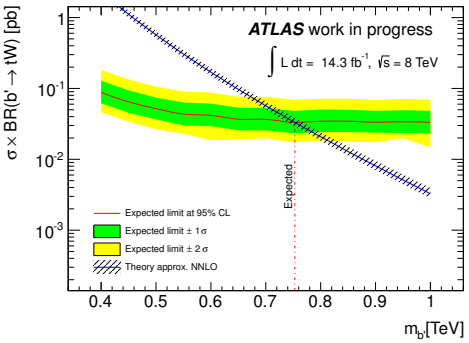

(d) $N_{\text{Jets}} \geq 2$, $N_{\text{bJets}} \geq 1$, $E_T^{\text{miss}} \geq 80\,\text{GeV}$, $H_T \geq 550\,\text{GeV}$

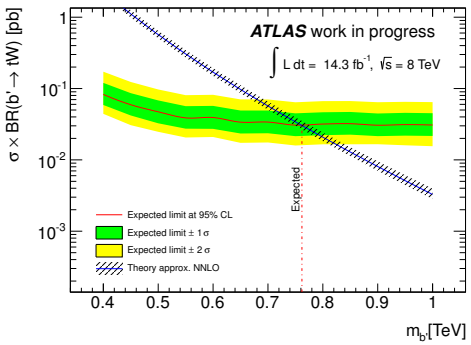

(e) $N_{\text{Jets}} \geq 2$, $N_{\text{bJets}} \geq 1$, $E_T^{\text{miss}} \geq 60\,\text{GeV}$, $H_T \geq 600\,\text{GeV}$

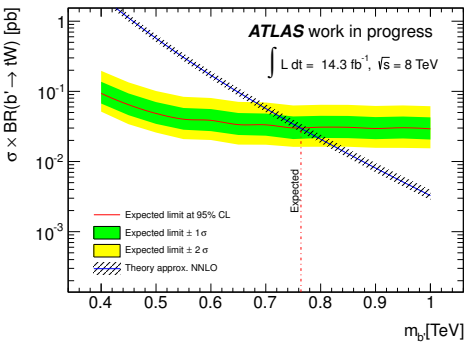

(f) $N_{\text{Jets}} \geq 2$, $N_{\text{bJets}} \geq 1$, $E_T^{\text{miss}} \geq 80\,\text{GeV}$, $H_T \geq 600\,\text{GeV}$

Figure B.12: Expected cross-section limits as a function of the b' mass (assuming $b' \to tW$ with 100% BF) for several event selections. In all cases the basic selection was applied (Table 6.15).

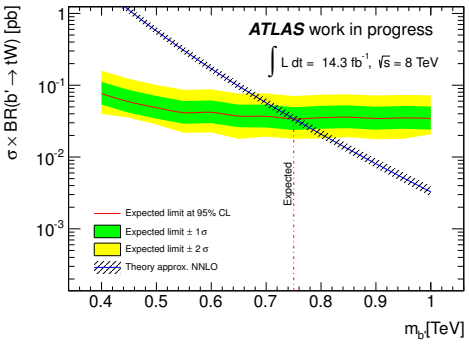

(a) $N_{\text{Jets}} \geq 3$, $N_{\text{bJets}} \geq 1$, $E_T^{\text{miss}} \geq 60\,\text{GeV}$, $H_T \geq 550\,\text{GeV}$

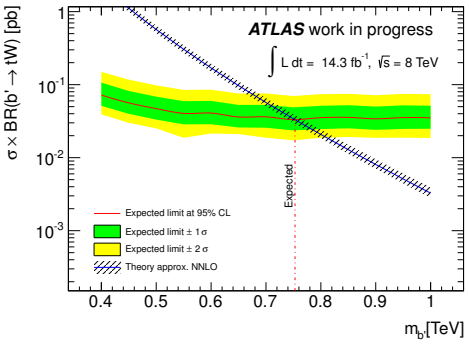

(b) $N_{\text{Jets}} \geq 4$, $N_{\text{bJets}} \geq 1$, $E_T^{\text{miss}} \geq 60\,\text{GeV}$, $H_T \geq 550\,\text{GeV}$

Figure B.13: Expected cross-section limits as a function of the b' mass (assuming $b' \to tW$ with 100% BF) for several event selections. In all cases the basic selection was applied (Table 6.15).

B.3 Final event selection

B.3.1 Systematic uncertainties on $b' \to qW$ samples

The systematic uncertainties on energy scale, resolution and efficiency scale factors have been derived for the $b' \to qW$ samples, which were used to derive the exclusion areas as a function of the b' mass and the decay branching fractions for $b' \to tW$, $b' \to cW$ and $b' \to uW$. These systematics have been derived after applying the final event selection, which is summarised in Table 6.24, and are presented in Tables B.10, B.11 and B.12 for the ee, $e\mu$ and $\mu\mu$ channel, respectively.

Systematic	$b'(400GeV) \to qW$	$b'(450GeV) \to qW$	$b'(500GeV) \to qW$	$b'(550GeV) \to qW$	$b'(600GeV) \to qW$	$b'(650GeV) \to qW$	$b'(700GeV) \to qW$
JES	5.3/ − 3.7	9.9/ − 3.3	19.7/ − 8.0	2.9/ − 4.8	3.9/ − 1.9	2.9/ − 6.4	1.1/ − 0.0
JER	2.4/ − 2.4	3.4/ − 3.4	1.5/ − 1.5	0.5/ − 0.5	0.8/ − 0.8	2.8/ − 2.8	0.3/ − 0.3
JRE	0.0/ − 0.0	0.0/ − 0.0	0.0/ − 0.0	0.0/ − 0.0	0.0/ − 0.0	0.0/ − 0.0	0.0/ − 0.0
JVFSF	2.6/ − 2.2	1.7/ − 1.9	2.4/ − 2.5	2.3/ − 2.1	2.2/ − 2.3	2.2/ − 2.2	2.7/ − 2.5
ESFRecId	5.3/ − 5.2	5.3/ − 5.2	5.3/ − 5.2	5.4/ − 5.2	5.3/ − 5.2	5.4/ − 5.2	5.4/ − 5.2
ESFTrig	1.8/ − 0.0	1.6/ − 0.0	2.0/ − 0.0	1.7/ − 0.0	2.1/ − 0.0	2.0/ − 0.0	2.5/ − 0.0
EER	0.0/ − 0.0	0.0/ − 0.0	0.0/ − 3.5	0.0/ − 0.0	0.0/ − 0.0	0.0/ − 1.9	0.0/ − 0.0
EES	4.9/ − 1.9	4.8/ − 4.2	2.0/ − 2.3	1.6/ − 0.0	2.0/ − 0.0	0.0/ − 1.9	0.0/ − 0.4
MuSFRecId	0.0/ − 0.0	0.1/ − 0.1	0.0/ − 0.0	0.0/ − 0.0	0.1/ − 0.1	0.1/ − 0.1	0.1/ − 0.1
MuSFTrig	0.0/ − 0.0	0.0/ − 0.0	0.0/ − 0.0	0.0/ − 0.0	0.0/ − 0.0	0.0/ − 0.0	0.0/ − 0.0
MES	0.0/ − 0.0	0.0/ − 0.0	0.0/ − 0.0	0.0/ − 0.0	0.0/ − 0.0	0.0/ − 0.0	0.0/ − 0.0
MER	0.0/ − 0.0	0.0/ − 0.0	0.0/ − 0.0	0.0/ − 0.0	0.0/ − 0.0	0.0/ − 0.0	0.0/ − 0.0
MET	0.0/ − 0.0	1.3/ − 0.0	2.5/ − 1.7	0.0/ − 0.0	0.0/ − 0.0	0.0/ − 1.3	1.0/ − 0.0
BTagSFb	6.9/ − 6.8	7.6/ − 7.6	10.2/ − 10.2	5.8/ − 6.1	6.0/ − 6.1	4.9/ − 5.1	7.8/ − 8.1
BTagSFc	0.3/ − 0.4	0.5/ − 0.8	0.0/ − 0.0	0.8/ − 0.8	0.2/ − 0.2	1.0/ − 1.1	0.8/ − 0.9
BTagSFmistag	0.7/ − 0.7	0.5/ − 0.5	0.3/ − 0.3	0.9/ − 0.9	2.0/ − 2.0	0.1/ − 0.1	0.8/ − 0.8
Total	12.0/ − 10.1	15.0/ − 11.4	23.3/ − 15.0	9.1/ − 9.7	9.9/ − 8.8	8.9/ − 10.8	10.4/ − 10.0

Systematic	$b'(750GeV) \to qW$	$b'(800GeV) \to qW$	$b'(850GeV) \to qW$	$b'(900GeV) \to qW$	$b'(950GeV) \to qW$	$b'(1000GeV) \to qW$
JES	2.0/ − 0.0	0.1/ − 0.9	4.1/ − 2.5	1.1/ − 2.3	0.4/ − 0.1	3.7/ − 0.0
JER	3.2/ − 3.2	0.6/ − 0.6	0.3/ − 0.3	1.3/ − 1.3	1.7/ − 1.7	1.0/ − 1.0
JRE	0.0/ − 0.0	0.0/ − 0.0	0.0/ − 0.0	0.0/ − 0.0	0.0/ − 0.0	0.0/ − 0.0
JVFSF	2.8/ − 2.7	2.7/ − 2.7	2.7/ − 2.8	3.3/ − 3.3	3.5/ − 3.7	4.0/ − 4.0
ESFRecId	5.3/ − 5.2	5.4/ − 5.2	5.3/ − 5.2	5.4/ − 5.2	5.4/ − 5.2	5.4/ − 5.2
ESFTrig	2.5/ − 0.0	2.3/ − 0.0	2.4/ − 0.0	2.3/ − 0.0	3.0/ − 0.0	2.5/ − 0.0
EER	0.0/ − 1.1	0.0/ − 0.0	1.4/ − 0.0	0.5/ − 0.0	0.0/ − 0.0	1.7/ − 0.0
EES	1.1/ − 0.0	0.0/ − 0.6	0.0/ − 0.2	1.3/ − 0.0	1.1/ − 0.0	1.1/ − 0.0
MuSFRecId	0.0/ − 0.0	0.1/ − 0.1	0.1/ − 0.1	0.3/ − 0.3	0.0/ − 0.0	0.0/ − 0.0
MuSFTrig	0.0/ − 0.0	0.0/ − 0.0	0.0/ − 0.0	0.0/ − 0.0	0.0/ − 0.0	0.0/ − 0.0
MES	0.0/ − 0.0	0.0/ − 0.0	0.0/ − 0.0	0.0/ − 0.0	0.0/ − 0.0	0.0/ − 0.0
MER	0.0/ − 0.0	0.0/ − 0.0	0.0/ − 0.0	0.0/ − 0.0	0.0/ − 0.0	0.0/ − 0.0
MET	1.4/ − 0.0	0.0/ − 0.0	0.0/ − 0.0	0.0/ − 0.0	0.0/ − 0.0	0.0/ − 0.0
BTagSFb	10.6/ − 10.3	5.8/ − 6.0	5.0/ − 4.8	1.2/ − 1.4	4.5/ − 4.5	5.6/ − 6.0
BTagSFc	0.1/ − 0.1	2.4/ − 2.3	0.5/ − 0.4	0.0/ − 0.1	1.1/ − 1.1	1.4/ − 1.2
BTagSFmistag	1.8/ − 1.8	0.0/ − 0.0	0.2/ − 0.2	0.0/ − 0.1	0.1/ − 0.1	0.1/ − 0.1
Total	13.2/ − 12.5	9.0/ − 8.8	9.2/ − 8.0	7.2/ − 6.9	8.7/ − 8.1	10.2/ − 9.0

Table B.10: Estimated systematic uncertainties in percent (%) on object scale, resolution and efficiency scale factors for the $b' \to qW$ samples in the *ee* channel.

Systematic	$b'(400GeV) \to qW$	$b'(450GeV) \to qW$	$b'(500GeV) \to qW$	$b'(550GeV) \to qW$	$b'(600GeV) \to qW$	$b'(650GeV) \to qW$	$b'(700GeV) \to qW$
JES	15.1/ − 2.0	3.0/ − 3.3	6.7/ − 6.8	3.0/ − 6.5	3.3/ − 3.3	0.1/ − 4.7	0.0/ − 1.7
JER	3.7/ − 3.7	0.3/ − 0.3	1.7/ − 1.7	0.7/ − 0.7	0.4/ − 0.4	0.7/ − 0.7	0.3/ − 0.3
JRE	0.0/ − 0.0	0.0/ − 0.0	0.0/ − 0.0	0.0/ − 0.0	0.0/ − 0.0	0.0/ − 0.0	0.0/ − 0.0
JVFSF	2.0/ − 1.9	2.7/ − 2.3	2.5/ − 2.2	2.1/ − 2.2	2.3/ − 2.3	2.6/ − 2.5	2.6/ − 2.7
ESFRecId	2.6/ − 2.6	2.6/ − 2.6	2.6/ − 2.6	2.6/ − 2.6	2.6/ − 2.6	2.6/ − 2.6	2.7/ − 2.7
ESFTrig	0.9/ − 0.2	0.3/ − 0.2	0.0/ − 0.3	0.1/ − 0.1	0.0/ − 0.2	0.0/ − 1.1	0.4/ − 0.2
EER	0.0/ − 0.0	0.0/ − 0.0	0.0/ − 0.0	0.0/ − 0.4	0.8/ − 0.0	0.3/ − 0.0	0.0/ − 0.9
EES	1.7/ − 0.4	0.3/ − 0.4	0.0/ − 1.6	0.0/ − 0.4	0.8/ − 0.0	0.0/ − 0.5	0.0/ − 1.0
MuSFRecId	4.0/ − 4.0	4.0/ − 4.0	4.1/ − 4.1	4.0/ − 4.0	4.0/ − 4.0	4.0/ − 4.0	4.2/ − 4.1
MuSFTrig	0.0/ − 0.0	0.0/ − 0.0	0.0/ − 0.0	0.0/ − 0.0	0.0/ − 0.0	0.0/ − 0.0	0.0/ − 0.0
MES	0.0/ − 0.0	0.0/ − 0.0	0.0/ − 0.0	0.0/ − 0.0	0.2/ − 0.2	0.0/ − 0.0	0.0/ − 0.0
MER	0.0/ − 0.0	0.2/ − 0.2	0.0/ − 0.0	0.0/ − 0.0	0.2/ − 0.2	0.0/ − 0.0	0.0/ − 0.0
MET	2.2/ − 0.0	0.5/ − 0.0	0.0/ − 2.5	0.0/ − 0.6	0.6/ − 0.3	0.0/ − 0.5	0.0/ − 0.9
BTagSFb	5.4/ − 5.8	2.0/ − 2.3	5.9/ − 6.2	6.2/ − 6.0	2.4/ − 2.7	5.8/ − 6.1	4.3/ − 4.7
BTagSFc	2.3/ − 2.5	4.6/ − 4.8	1.0/ − 1.0	0.2/ − 0.3	3.0/ − 3.1	0.0/ − 0.1	1.5/ − 1.7
BTagSFmistag	0.1/ − 0.0	1.4/ − 1.3	1.2/ − 1.3	1.3/ − 1.3	0.1/ − 0.1	0.7/ − 0.7	1.0/ − 1.0
Total	17.6/ − 9.2	8.2/ − 8.3	10.7/ − 11.3	8.8/ − 10.4	7.5/ − 7.5	8.0/ − 9.5	7.3/ − 7.9

Systematic	$b'(750GeV) \to qW$	$b'(800GeV) \to qW$	$b'(850GeV) \to qW$	$b'(900GeV) \to qW$	$b'(950GeV) \to qW$	$b'(1000GeV) \to qW$
JES	3.0/ − 1.1	0.0/ − 0.7	1.8/ − 1.2	0.0/ − 1.4	0.0/ − 1.4	1.2/ − 0.9
JER	0.2/ − 0.2	0.4/ − 0.4	1.0/ − 1.0	0.3/ − 0.3	1.1/ − 1.1	0.3/ − 0.3
JRE	0.0/ − 0.0	0.0/ − 0.0	0.0/ − 0.0	0.0/ − 0.0	0.0/ − 0.0	0.0/ − 0.0
JVFSF	2.7/ − 2.6	2.7/ − 2.8	2.6/ − 2.9	3.0/ − 2.9	2.7/ − 2.8	4.0/ − 4.1
ESFRecId	2.6/ − 2.6	2.6/ − 2.6	2.6/ − 2.6	2.6/ − 2.6	2.6/ − 2.6	2.6/ − 2.6
ESFTrig	0.3/ − 0.2	0.0/ − 0.6	0.1/ − 0.2	0.0/ − 0.4	0.0/ − 0.7	0.1/ − 0.2
EER	0.0/ − 0.5	0.3/ − 0.0	0.0/ − 0.3	0.1/ − 0.4	0.0/ − 0.2	0.3/ − 0.2
EES	0.7/ − 0.7	0.5/ − 0.0	0.4/ − 0.4	0.0/ − 0.1	0.0/ − 0.2	0.1/ − 0.6
MuSFRecId	4.1/ − 4.1	4.1/ − 4.1	4.1/ − 4.1	4.1/ − 4.0	4.1/ − 4.1	4.0/ − 4.0
MuSFTrig	0.0/ − 0.0	0.0/ − 0.0	0.0/ − 0.0	0.0/ − 0.0	0.0/ − 0.0	0.0/ − 0.0
MES	0.0/ − 0.0	0.3/ − 0.3	0.0/ − 0.0	0.0/ − 0.0	0.0/ − 0.0	0.0/ − 0.0
MER	0.0/ − 0.0	0.1/ − 0.1	0.0/ − 0.0	0.0/ − 0.0	0.0/ − 0.0	0.0/ − 0.0
MET	0.2/ − 0.5	0.4/ − 0.0	0.0/ − 0.6	0.0/ − 0.4	0.4/ − 0.0	0.6/ − 0.6
BTagSFb	3.8/ − 4.2	5.7/ − 6.0	5.8/ − 6.2	4.5/ − 5.0	5.6/ − 5.9	3.2/ − 3.3
BTagSFc	0.2/ − 0.3	0.7/ − 0.6	0.6/ − 0.8	1.5/ − 1.6	1.3/ − 1.4	0.2/ − 0.3
BTagSFmistag	0.3/ − 0.3	1.1/ − 1.1	0.4/ − 0.3	0.1/ − 0.1	0.3/ − 0.3	1.0/ − 1.0
Total	7.4/ − 7.1	8.1/ − 8.4	8.3/ − 8.6	7.4/ − 7.8	8.1/ − 8.5	7.2/ − 7.3

Table B.11: Estimated systematic uncertainties in percent (%) on object scale, resolution and efficiency scale factors for the $b' \to qW$ samples in the $e\mu$ channel.

Systematic	$b'(400GeV) \to qW$	$b'(450GeV) \to qW$	$b'(500GeV) \to qW$	$b'(550GeV) \to qW$	$b'(600GeV) \to qW$	$b'(650GeV) \to qW$	$b'(700GeV) \to qW$
JES	5.5/ − 1.7	5.4/ − 1.5	2.4/ − 3.3	1.2/ − 0.4	1.8/ − 4.8	1.0/ − 4.1	0.0/ − 2.1
JER	3.8/ − 3.8	1.9/ − 1.9	1.3/ − 1.3	1.2/ − 1.2	2.2/ − 2.2	1.4/ − 1.4	0.4/ − 0.4
JRE	0.0/ − 0.0	0.0/ − 0.0	0.0/ − 0.0	0.0/ − 0.0	0.0/ − 0.0	0.0/ − 0.0	0.0/ − 0.0
JVFSF	3.6/ − 3.2	2.5/ − 2.4	2.5/ − 2.4	2.7/ − 2.4	3.0/ − 2.6	2.3/ − 2.3	2.6/ − 2.7
ESFRecId	0.0/ − 0.0	0.0/ − 0.0	0.0/ − 0.0	0.0/ − 0.0	0.0/ − 0.0	0.0/ − 0.0	0.0/ − 0.0
ESFTrig	0.0/ − 0.0	0.0/ − 0.0	0.0/ − 0.0	0.0/ − 0.0	0.0/ − 0.0	0.0/ − 0.0	0.0/ − 0.0
EER	0.0/ − 0.0	0.0/ − 0.0	0.0/ − 0.0	0.0/ − 0.0	0.0/ − 0.0	0.0/ − 0.0	0.0/ − 0.0
EES	0.0/ − 0.0	0.0/ − 0.0	0.0/ − 0.0	0.0/ − 0.0	0.0/ − 0.0	0.5/ − 0.0	0.0/ − 0.0
MuSFRecId	8.2/ − 7.9	8.2/ − 7.9	8.2/ − 7.9	8.4/ − 8.0	8.3/ − 7.9	8.2/ − 7.9	8.3/ − 8.0
MuSFTrig	0.4/ − 0.3	0.3/ − 0.3	0.4/ − 0.4	0.5/ − 0.4	0.5/ − 0.4	0.4/ − 0.4	0.4/ − 0.4
MES	0.0/ − 0.0	0.0/ − 0.0	0.0/ − 0.0	0.0/ − 0.0	0.3/ − 0.3	0.0/ − 0.0	0.0/ − 0.0
MER	0.0/ − 0.0	0.3/ − 0.3	0.0/ − 0.0	0.0/ − 0.0	0.3/ − 0.3	0.5/ − 0.5	0.0/ − 0.0
MET	0.0/ − 0.0	0.0/ − 0.0	0.0/ − 1.8	0.0/ − 0.2	0.8/ − 0.6	0.0/ − 0.6	0.0/ − 0.0
BTagSFb	0.9/ − 1.2	9.3/ − 9.3	5.6/ − 5.7	7.2/ − 7.3	6.2/ − 6.9	7.8/ − 8.3	8.1/ − 8.2
BTagSFc	3.5/ − 3.2	1.2/ − 1.2	1.9/ − 2.1	1.1/ − 1.1	0.3/ − 0.3	0.3/ − 0.2	2.3/ − 2.1
BTagSFmistag	0.7/ − 0.7	0.1/ − 0.1	0.1/ − 0.1	0.0/ − 0.0	0.2/ − 0.2	0.5/ − 0.6	0.3/ − 0.3
Total	11.8/ − 10.1	13.9/ − 12.7	10.8/ − 11.0	11.6/ − 11.2	11.2/ − 12.1	11.7/ − 12.5	12.1/ − 12.2

Systematic	$b'(750GeV) \to qW$	$b'(800GeV) \to qW$	$b'(850GeV) \to qW$	$b'(900GeV) \to qW$	$b'(950GeV) \to qW$	$b'(1000GeV) \to qW$
JES	1.6/ − 0.9	0.0/ − 1.4	1.2/ − 0.2	0.0/ − 1.6	0.2/ − 1.0	0.0/ − 0.8
JER	0.8/ − 0.8	3.1/ − 3.1	1.6/ − 1.6	0.6/ − 0.6	1.3/ − 1.3	1.8/ − 1.8
JRE	0.0/ − 0.0	0.0/ − 0.0	0.0/ − 0.0	0.0/ − 0.0	0.0/ − 0.0	0.0/ − 0.0
JVFSF	2.7/ − 2.7	2.8/ − 2.8	2.8/ − 2.8	4.2/ − 3.9	2.7/ − 2.8	3.1/ − 3.2
ESFRecId	0.0/ − 0.0	0.0/ − 0.0	0.0/ − 0.0	0.0/ − 0.0	0.0/ − 0.0	0.0/ − 0.0
ESFTrig	0.0/ − 0.0	0.0/ − 0.0	0.0/ − 0.0	0.0/ − 0.0	0.0/ − 0.0	0.0/ − 0.0
EER	0.0/ − 0.0	0.0/ − 0.0	0.0/ − 0.0	0.0/ − 0.0	0.0/ − 0.0	0.0/ − 0.0
EES	0.0/ − 0.0	0.0/ − 0.0	0.0/ − 0.0	0.0/ − 0.0	0.0/ − 0.0	0.0/ − 0.0
MuSFRecId	8.2/ − 7.9	8.3/ − 8.0	8.2/ − 7.9	8.3/ − 7.9	8.2/ − 7.9	8.2/ − 7.9
MuSFTrig	0.4/ − 0.4	0.5/ − 0.4	0.4/ − 0.4	0.6/ − 0.5	0.4/ − 0.4	0.4/ − 0.4
MES	0.0/ − 0.0	0.1/ − 0.1	0.0/ − 0.0	0.0/ − 0.0	0.0/ − 0.0	0.0/ − 0.0
MER	0.0/ − 0.0	0.1/ − 0.1	0.0/ − 0.0	0.0/ − 0.0	0.0/ − 0.0	0.0/ − 0.0
MET	0.0/ − 0.8	0.0/ − 0.3	0.6/ − 0.0	0.6/ − 0.0	0.0/ − 0.0	0.0/ − 0.0
BTagSFb	5.8/ − 6.4	2.4/ − 2.5	4.7/ − 5.3	7.3/ − 7.6	5.2/ − 5.7	5.8/ − 6.3
BTagSFc	0.4/ − 0.6	0.4/ − 0.4	1.1/ − 1.0	0.3/ − 0.3	0.9/ − 0.8	0.5/ − 0.6
BTagSFmistag	0.4/ − 0.4	0.2/ − 0.2	0.5/ − 0.5	1.0/ − 1.0	0.2/ − 0.2	0.1/ − 0.1
Total	10.6/ − 10.7	9.6/ − 9.5	10.2/ − 10.1	11.9/ − 11.8	10.2/ − 10.3	10.7/ − 10.8

Table B.12: Estimated systematic uncertainties in percent (%) on object scale, resolution and efficiency scale factors for the $b' \to qW$ samples in the $\mu\mu$ channel.

C Signal and background validation

This appendix provides additional material for the validation of the signal and background estimates.

C.1 Fakes over-estimate

In Section 6.2.4, I presented that we observed a significant over-estimate of the lepton fakes background, when simply selecting the muon real and fake efficiencies according to the muon p_T. Figures C.1 and C.2 depict additional distributions for the $e\mu$ and $\mu\mu$ channel, respectively.

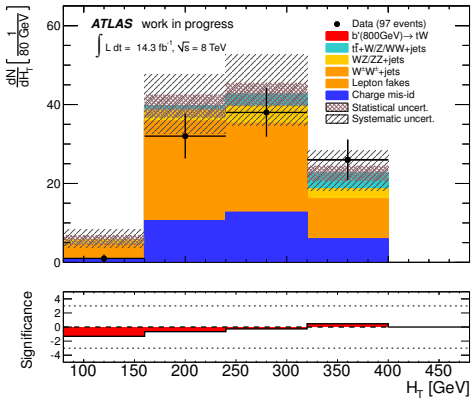

(a) H_T

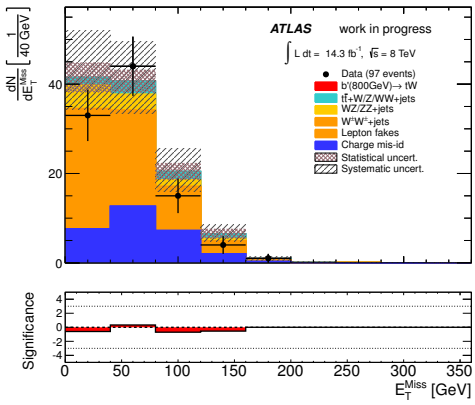

(b) E_T^{miss}

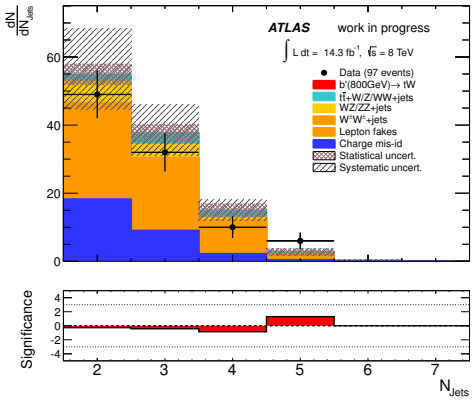

(c) N_{Jets}

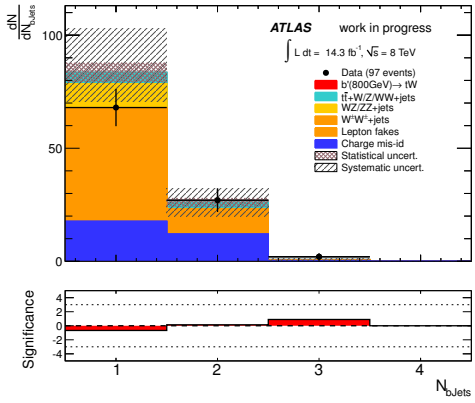

(d) N_{bJets}

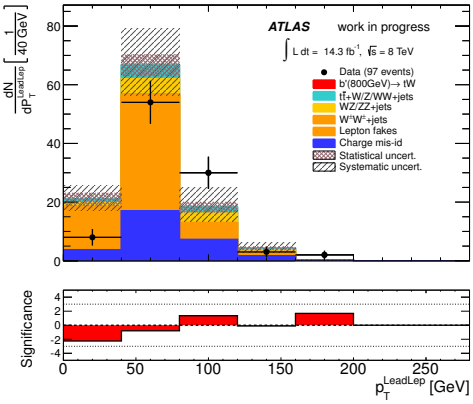

(e) $p_T^{\text{LeadingLepton}}$

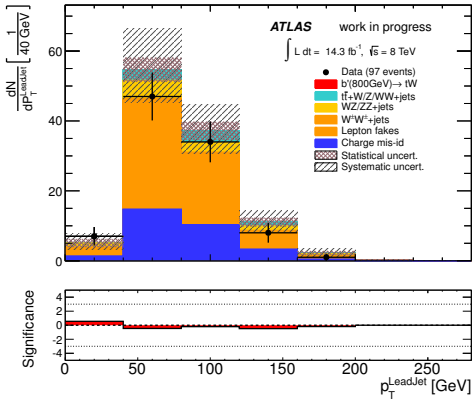

(f) $p_T^{LeadingJet}$

Figure C.1: Shown are the distributions for several kinematic variables in the same-sign $e\mu$ channel in one of our control regions. This control region is defined as $100\,\text{GeV} < H_T < 400\,\text{GeV}$, no E_T^{miss} cut and the other cuts as for the signal region selection described in Section 6.7. The muon real and fake efficiencies have been simply selected according to the muon p_T.

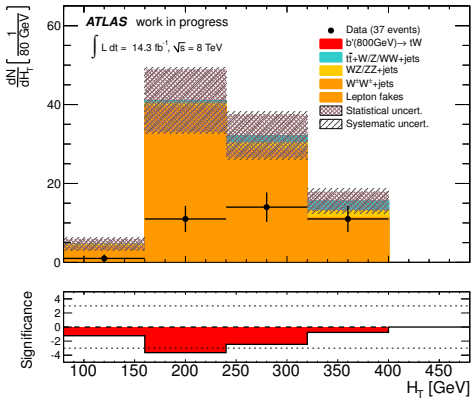

(a) H_T

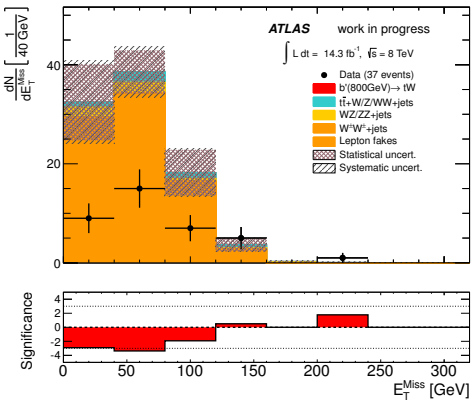

(b) E_T^{miss}

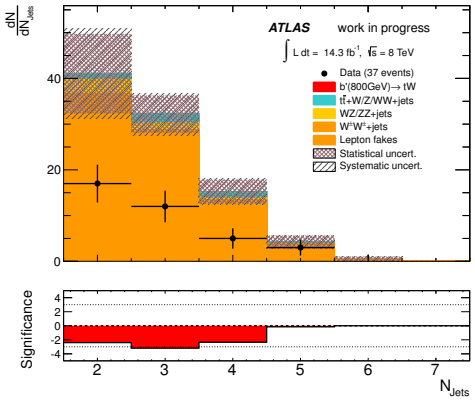

(c) N_{Jets}

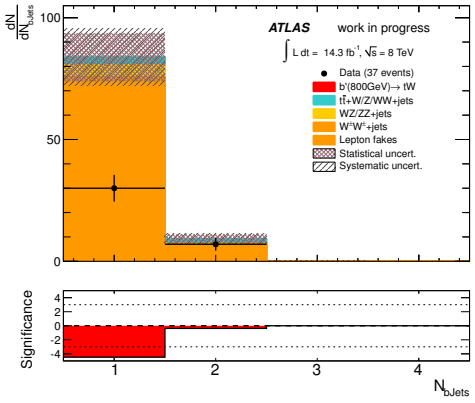

(d) N_{bJets}

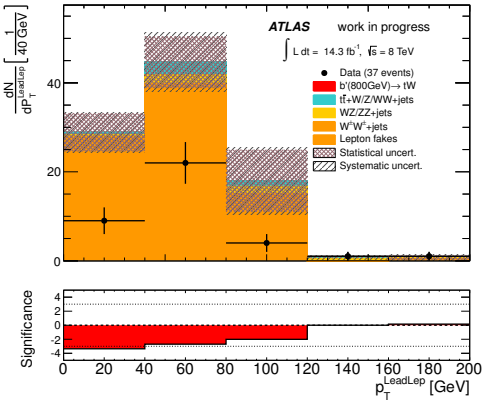

(e) $p_T^{\text{LeadingLepton}}$

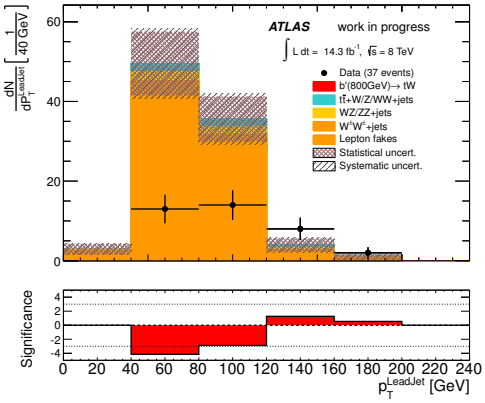

(f) $p_T^{LeadingJet}$

Figure C.2: Shown are the distributions for several kinematic variables in the same-sign $\mu\mu$ channel in one of our control regions. This control region is defined as $100\,\text{GeV} < H_T < 400\,\text{GeV}$, no E_T^{miss} cut and the other cuts as for the signal region selection described in Section 6.7. The muon real and fake efficiencies have been simply selected according to the muon p_T.

C.2 Signal validation

The signal samples used in the analysis have been produced using the fast detector simulation. The distributions in Section 6.8.1.1, which show a comparison of the $b' \to tW$ ($m_{b'} = 800\,\text{GeV}$) samples generated with the full and fast detector simulation, revealed a reasonable agreement. Figures C.3, C.4 and C.5 present additional distributions for the ee, $e\mu$ and $\mu\mu$ channel, respectively. The same distributions for the $b' \to tW$ sample with $m_{b'} = 500\,\text{GeV}$ are depicted in Figures C.6, C.7, C.8 and C.9.

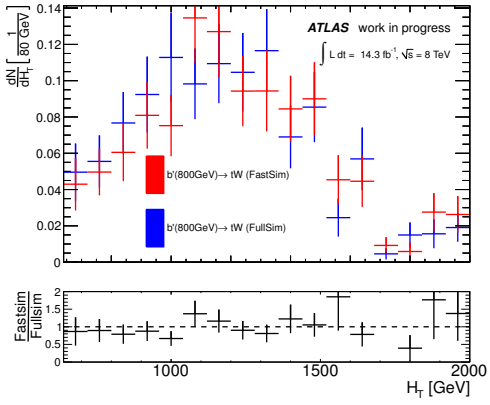

(a) H_T

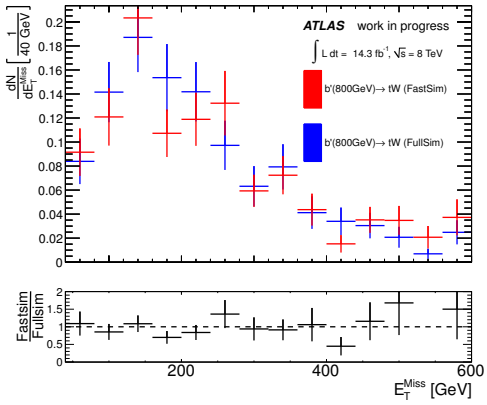

(b) E_T^{miss}

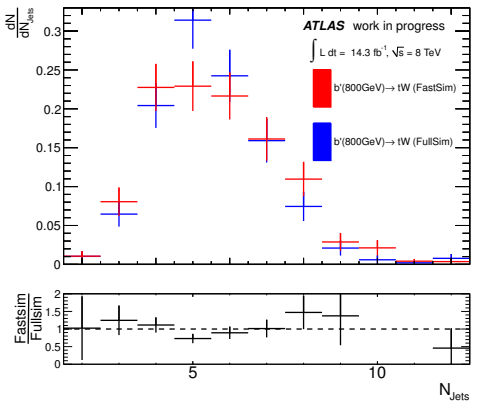

(c) N_{Jets}

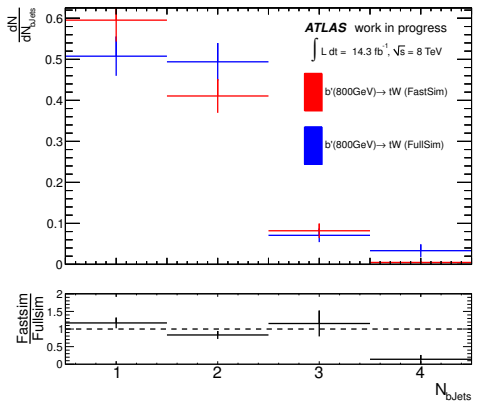

(d) N_{bJets}

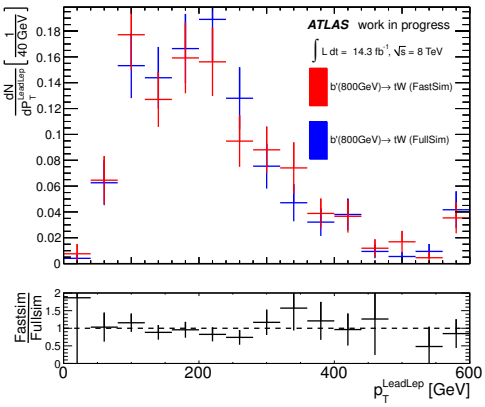

(e) $p_T^{\text{LeadingLepton}}$

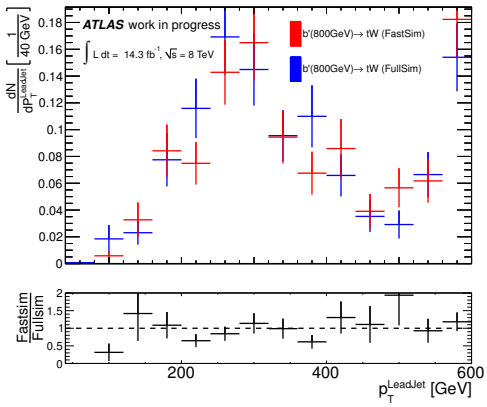

(f) $p_T^{\text{LeadingJet}}$

Figure C.3: Comparison of distributions in the *ee* channel after applying the final event selection (Table 6.24) obtained for the $b' \to tW$ ($m_{b'} = 800\,\text{GeV}$) signal samples generated with the fast and full detector simulation. The shown distributions are the H_T, E_T^{miss}, N_{Jets}, N_{bJets}, the p_T of the leading lepton $p_T^{\text{LeadingLepton}}$ and the p_T of the leading jet $p_T^{\text{LeadingJet}}$.

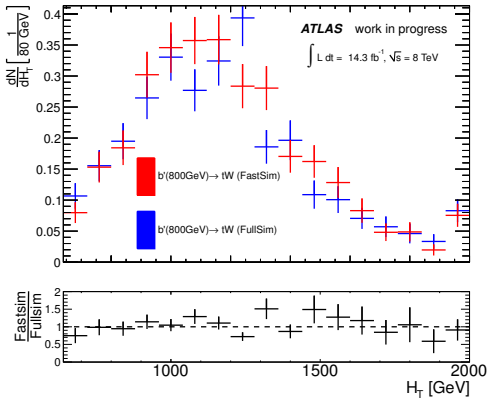

(a) H_T

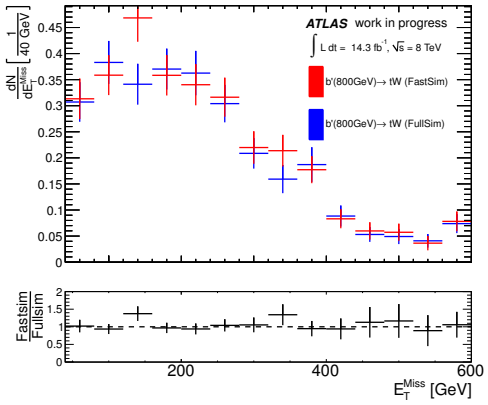

(b) E_T^{miss}

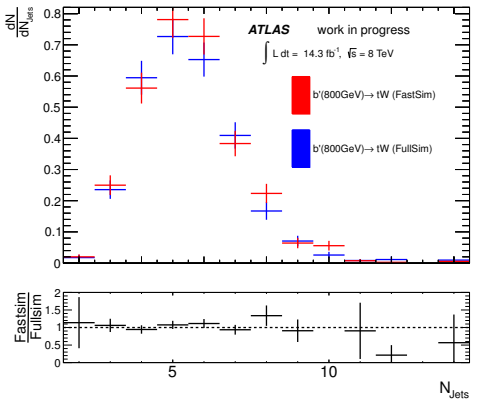

(c) N_{Jets}

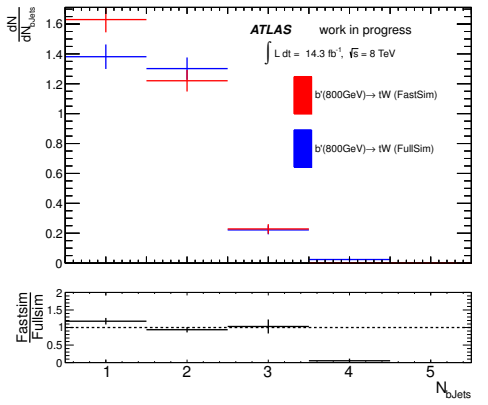

(d) N_{bJets}

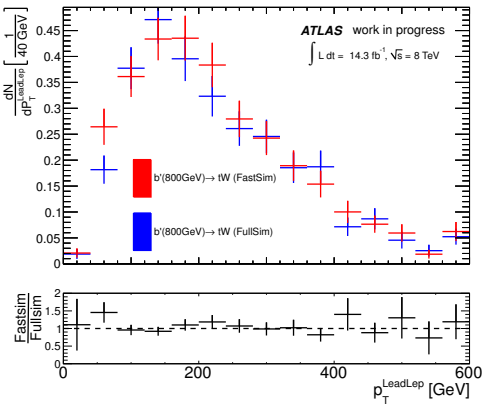

(e) $p_T^{\text{LeadingLepton}}$

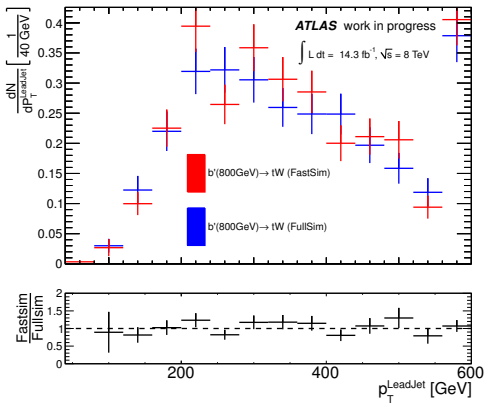

(f) $p_T^{\text{LeadingJet}}$

Figure C.4: Comparison of distributions in the $e\mu$ channel after applying the final event selection (Table 6.24) obtained for the $b' \to tW$ ($m_{b'} = 800\,\text{GeV}$) signal samples generated with the fast and full detector simulation. The shown distributions are the H_T, E_T^{miss}, N_{Jets}, N_{bJets}, the p_T of the leading lepton $p_T^{\text{LeadingLepton}}$ and the p_T of the leading jet $p_T^{\text{LeadingJet}}$.

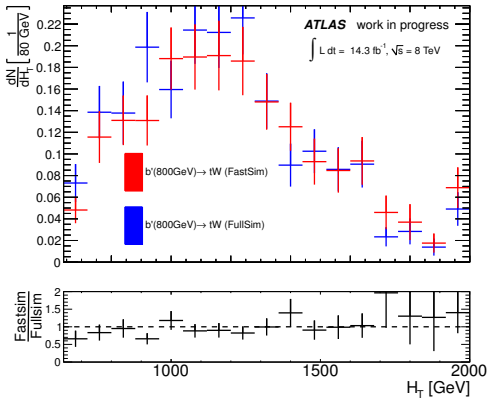

(a) H_T

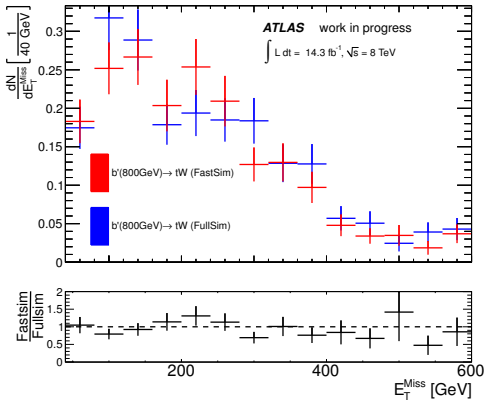

(b) E_T^{miss}

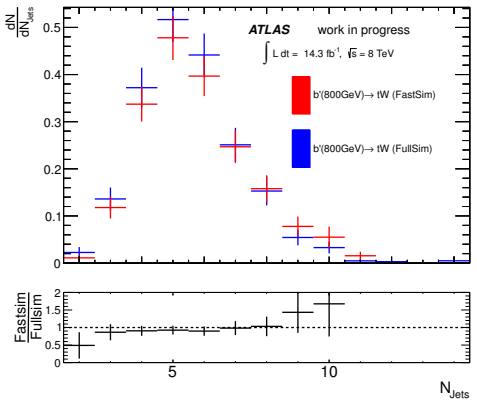

(c) N_{Jets}

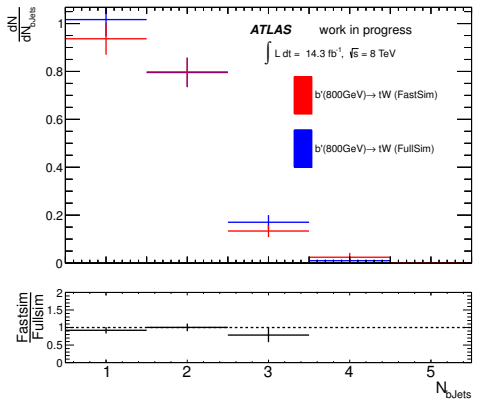

(d) N_{bJets}

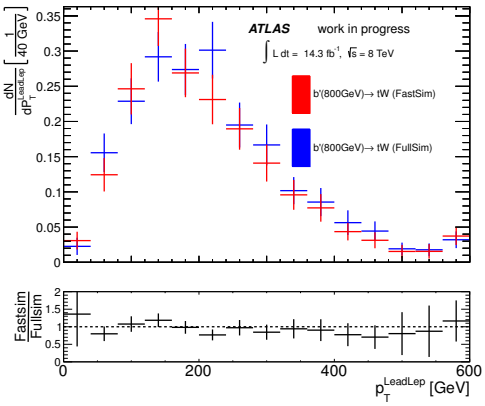

(e) $p_T^{\text{LeadingLepton}}$

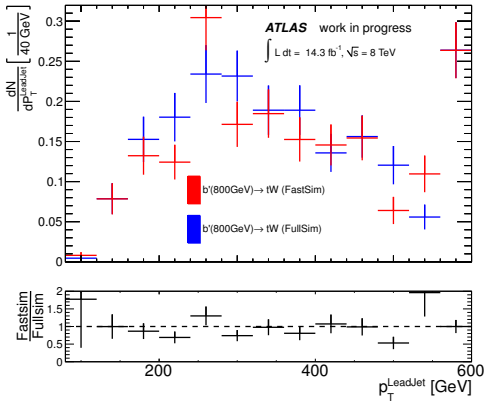

(f) $p_T^{\text{LeadingJet}}$

Figure C.5: Comparison of distributions in the $\mu\mu$ channel after applying the final event selection (Table 6.24) obtained for the $b' \to tW$ ($m_{b'} = 800\,\text{GeV}$) signal samples generated with the fast and full detector simulation. The shown distributions are the H_T, E_T^{miss}, N_{Jets}, N_{bJets}, the p_T of the leading lepton $p_T^{\text{LeadingLepton}}$ and the p_T of the leading jet $p_T^{\text{LeadingJet}}$.

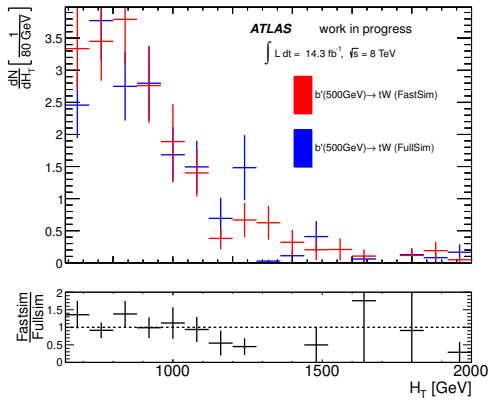

(a) H_T

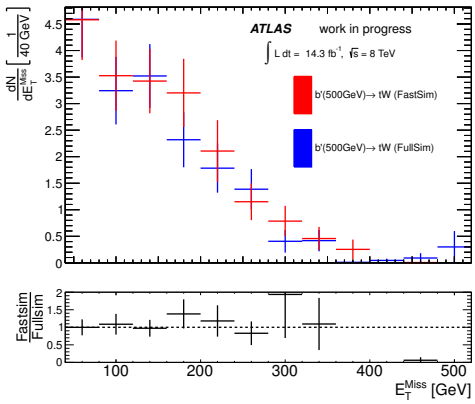

(b) E_T^{miss}

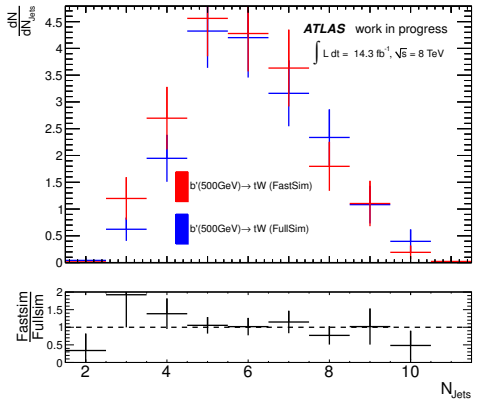

(c) N_{Jets}

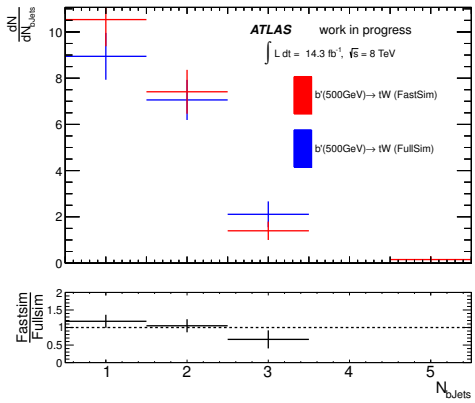

(d) N_{bJets}

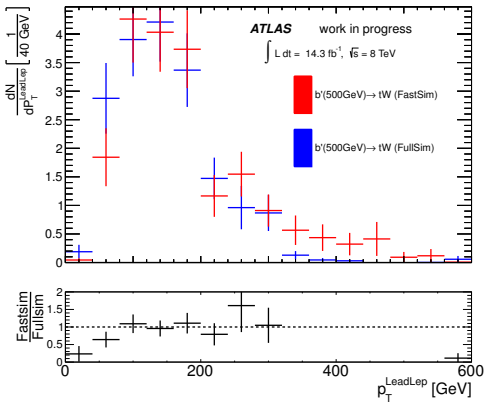

(e) $p_T^{\text{LeadingLepton}}$

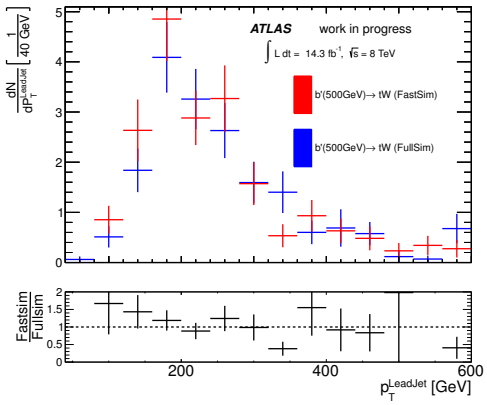

(f) $p_T^{\text{LeadingJet}}$

Figure C.6: Comparison of distributions in the *ee* channel after applying the final event selection (Table 6.24) obtained for the $b' \to tW$ ($m_{b'} = 500\,\text{GeV}$) signal samples generated with the fast and full detector simulation. The shown distributions are the H_T, E_T^{miss}, N_{Jets}, N_{bJets}, the p_T of the leading lepton $p_T^{\text{LeadingLepton}}$ and the p_T of the leading jet $p_T^{\text{LeadingJet}}$.

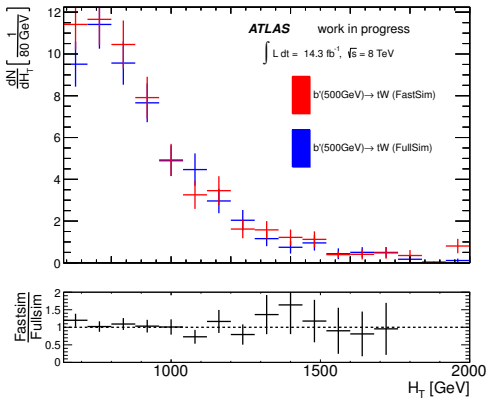

(a) H_T

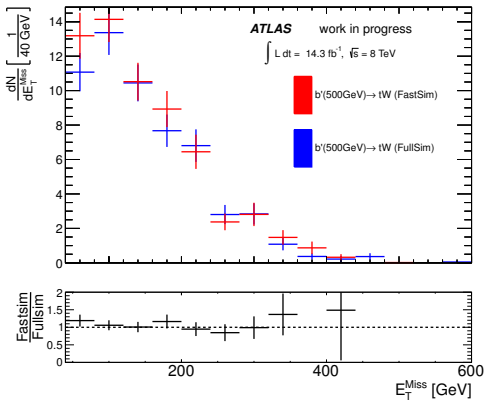

(b) E_T^{miss}

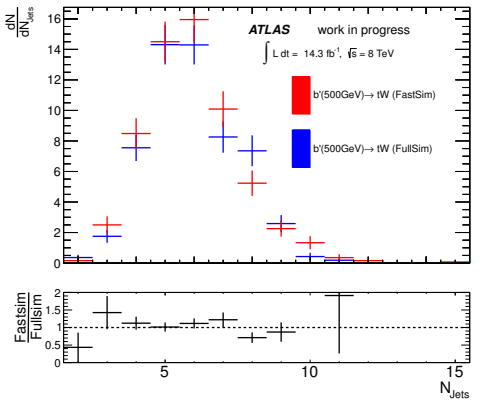

(c) N_{Jets}

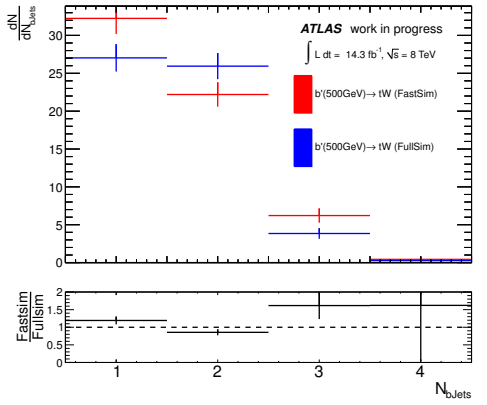

(d) N_{bJets}

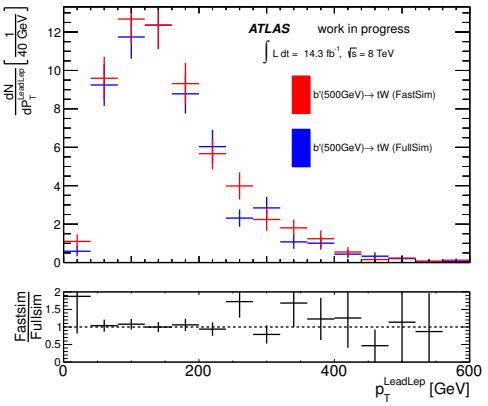

(e) $p_T^{\text{LeadingLepton}}$

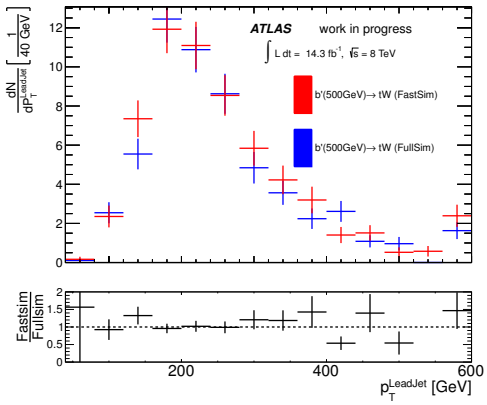

(f) $p_T^{\text{LeadingJet}}$

Figure C.7: Comparison of distributions in the $e\mu$ channel after applying the final event selection (Table 6.24) obtained for the $b' \to tW$ ($m_{b'} = 500\,\text{GeV}$) signal samples generated with the fast and full detector simulation. The shown distributions are the H_T, E_T^{miss}, N_{Jets}, N_{bJets}, the p_T of the leading lepton $p_T^{\text{LeadingLepton}}$ and the p_T of the leading jet $p_T^{\text{LeadingJet}}$.

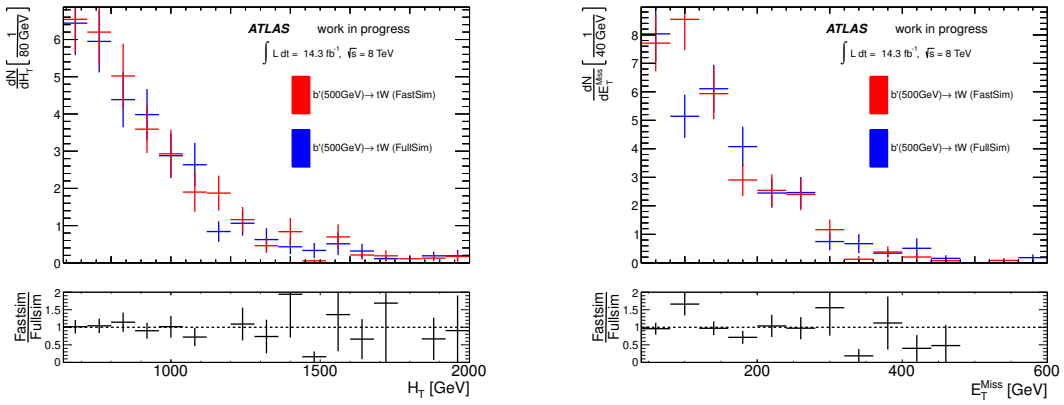

(a) H_T (b) E_T^{miss}

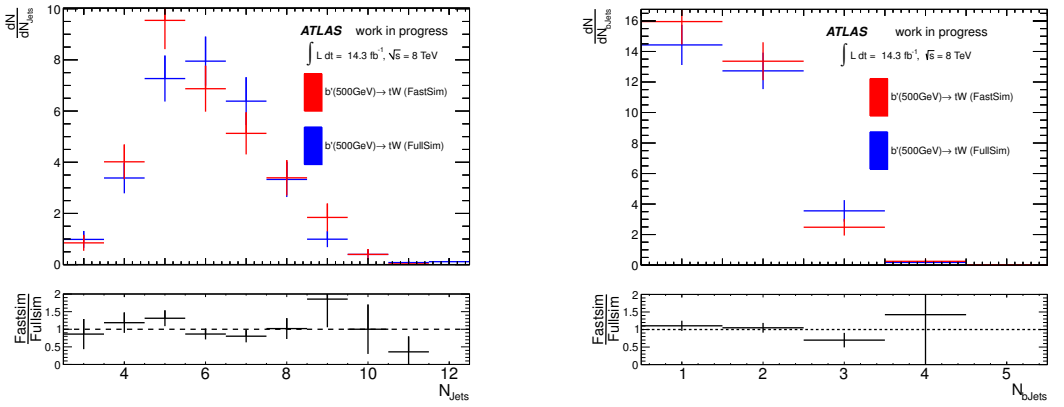

(c) N_{Jets} (d) N_{bJets}

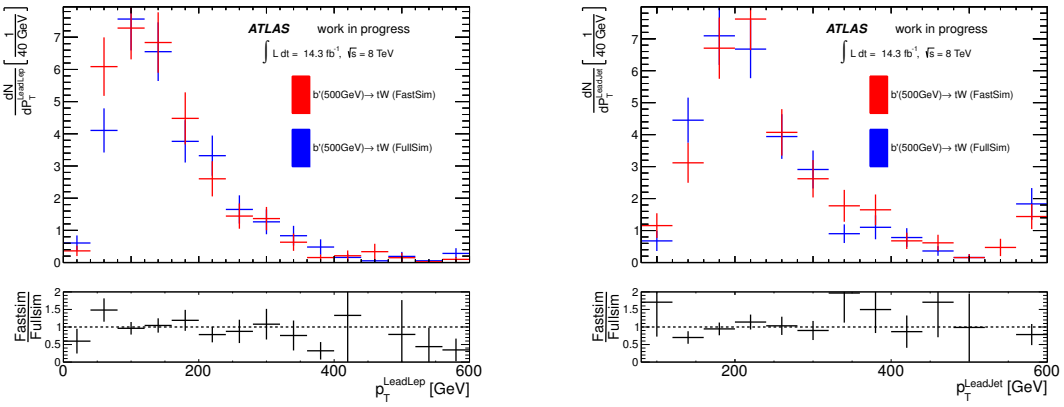

(e) $p_T^{\text{LeadingLepton}}$ (f) $p_T^{\text{LeadingJet}}$

Figure C.8: Comparison of distributions in the $\mu\mu$ channel after applying the final event selection (Table 6.24) obtained for the $b' \to tW$ ($m_{b'} = 500\,\text{GeV}$) signal samples generated with the fast and full detector simulation. The shown distributions are the H_T, E_T^{miss}, N_{Jets}, N_{bJets}, the p_T of the leading lepton $p_T^{\text{LeadingLepton}}$ and the p_T of the leading jet $p_T^{\text{LeadingJet}}$.

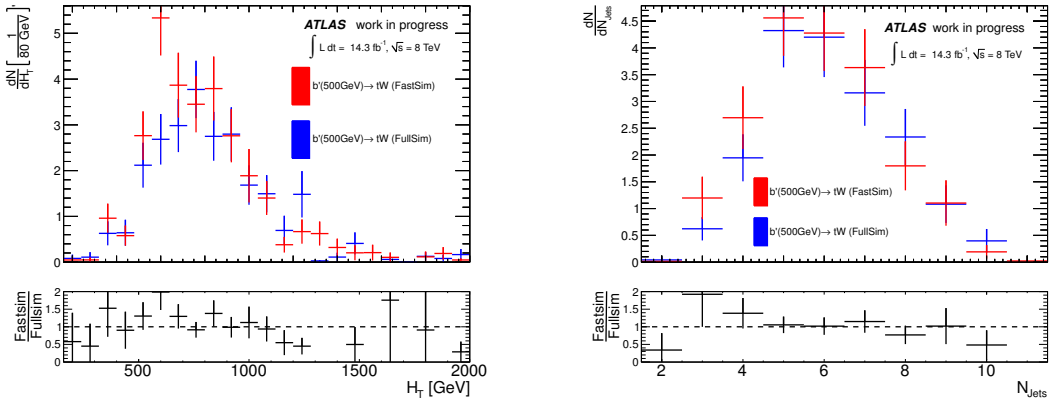

(a) ee: H_T

(b) ee: N_{Jets}

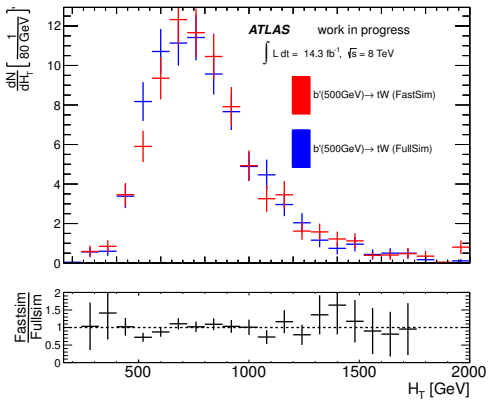

(c) $e\mu$: H_T

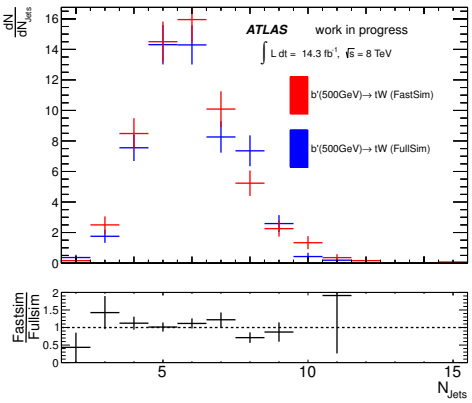

(d) $e\mu$: N_{Jets}

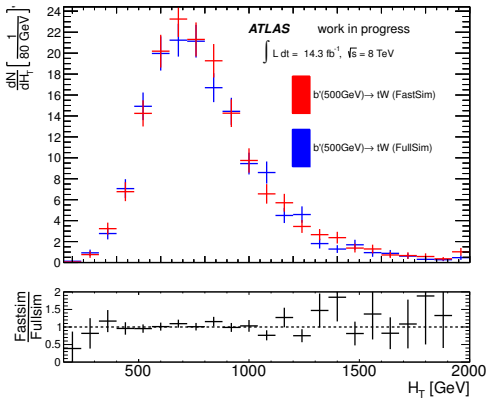

(e) $\mu\mu$: H_T

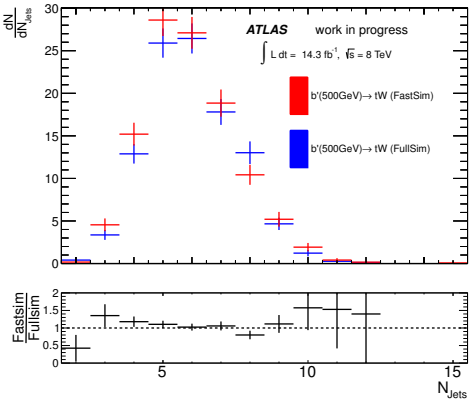

(f) $\mu\mu$: N_{Jets}

Figure C.9: Comparison of H_T and N_{Jets} distributions in the ee, $e\mu$ and $\mu\mu$ channel after applying the final event selection (Table 6.24) obtained for the $b' \to tW$ ($m_{b'} = 500\,\text{GeV}$) signal samples generated with the fast and full detector simulation. In each plot the cut on the corresponding variable has been removed.

C.3 Background validation

The background validation was performed by comparing several distributions for data and the background expectation after applying particular control region selections. Additional distributions are presented in the following, namely the η of the (second) leading lepton and jet, and the p_T of the second leading lepton and jet. The distributions for the 'low-H_T' selection (Table 6.33) are presented in Figures C.10, C.11 and C.12 for the ee, $e\mu$ and $\mu\mu$ channel, respectively. The additional distributions for the 'low-E_T^{miss}' control region (Table 6.35) are depicted in Figures C.13, C.14 and C.15. Finally, Figures C.16, C.17 and C.18 show the additional distributions for the 'Zero b-tag' control region (Table 6.37).

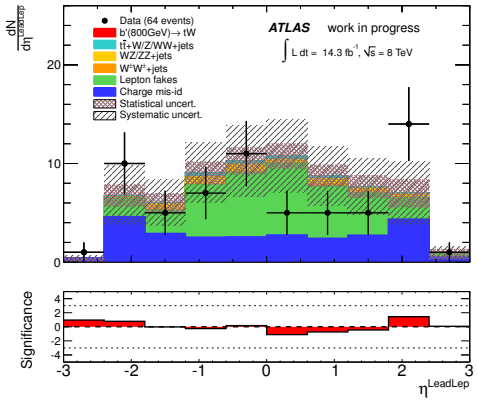

(a) $\eta^{\text{LeadingLepton}}$

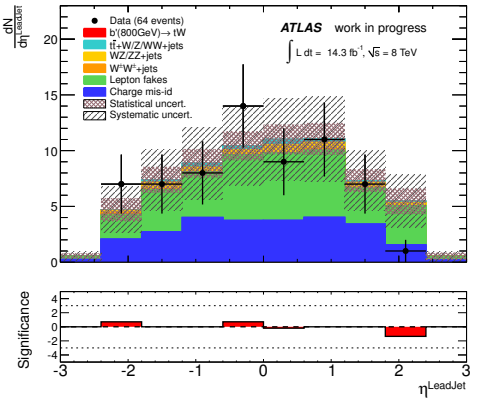

(b) $\eta^{\text{LeadingJet}}$

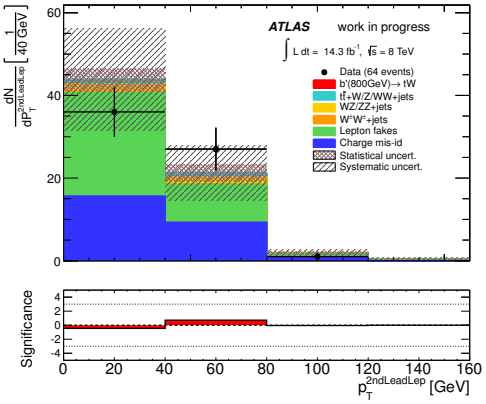

(c) $p_T^{\text{2ndLeadingLepton}}$

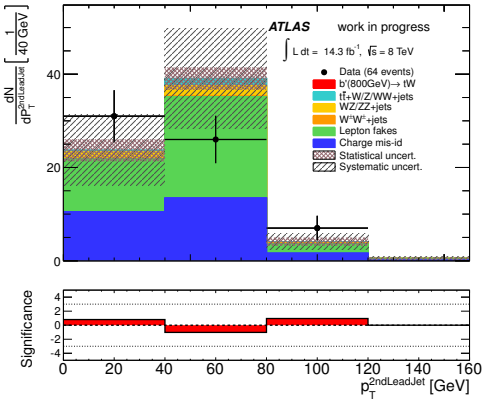

(d) $p_T^{\text{2ndLeadingJet}}$

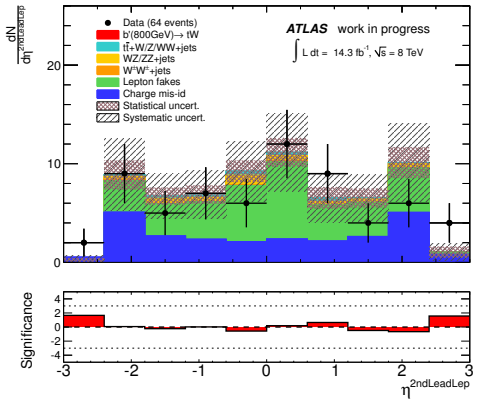

(e) $\eta^{\text{2ndLeadingLepton}}$

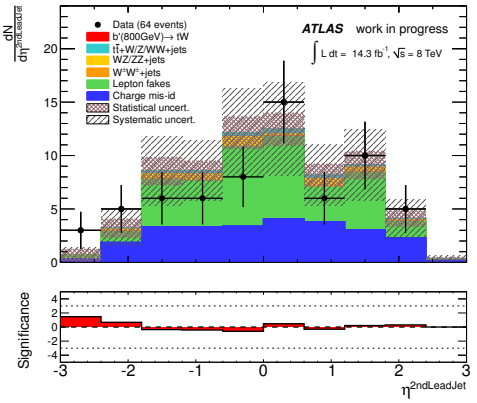

(f) $\eta^{\text{2ndLeadingJet}}$

Figure C.10: Distributions of kinematic variables for the *ee* channel after the low-H_T (Table 6.33) control region selection for the various backgrounds and the $b' \to tW$ ($m_{b'} = 800\,\text{GeV}$) signal sample. The statistical and systematic uncertainties are represented by the shaded areas and the lower plots depict the significance of the deviations between data and expectation, which has been calculated with the method described in Section 6.4.2.

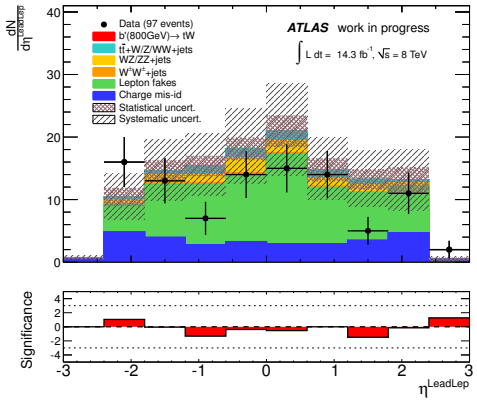

(a) $\eta^{\text{LeadingLepton}}$

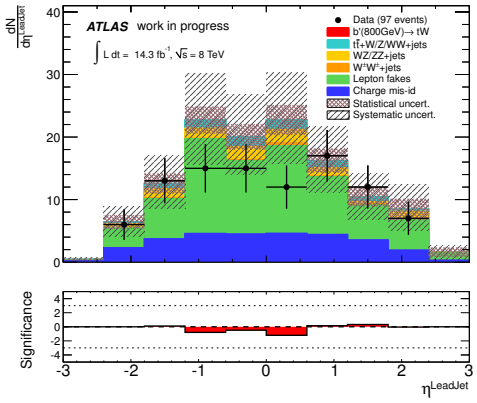

(b) $\eta^{\text{LeadingJet}}$

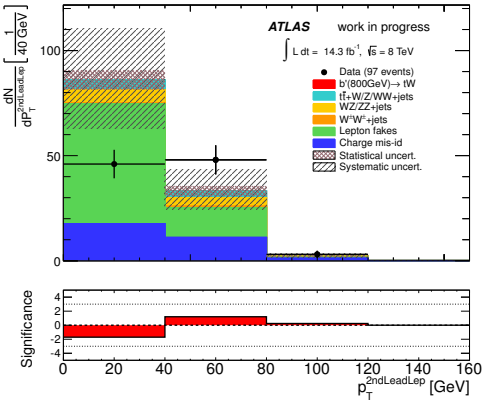

(c) $p_T^{\text{2ndLeadingLepton}}$

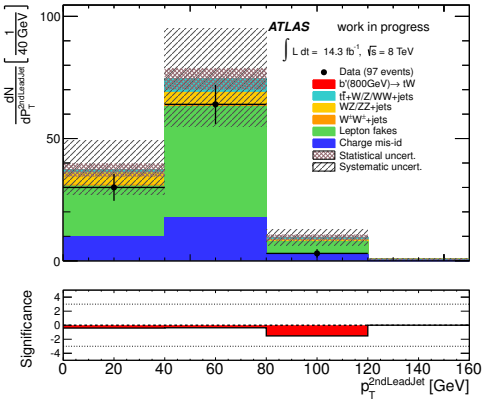

(d) $p_T^{\text{2ndLeadingJet}}$

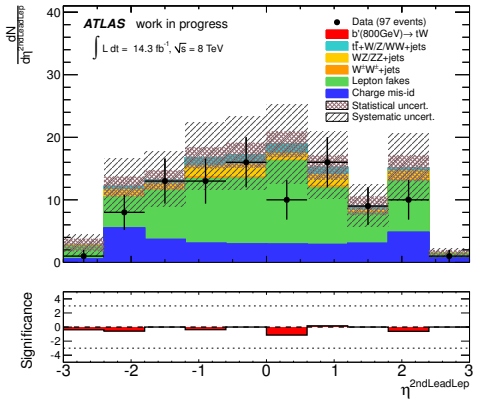

(e) $\eta^{\text{2ndLeadingLepton}}$

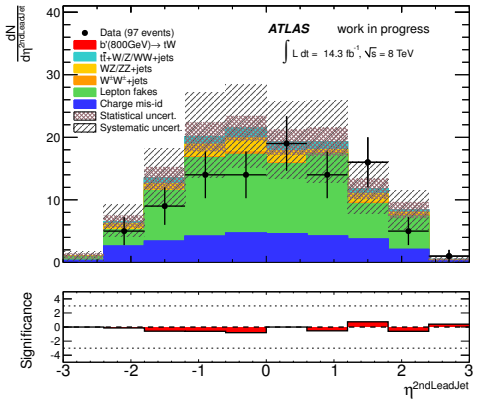

(f) $\eta^{\text{2ndLeadingJet}}$

Figure C.11: Distributions of kinematic variables for the $e\mu$ channel after the low-H_T (Table 6.33) control region selection for the various backgrounds and the $b' \to tW$ ($m_{b'} = 800\,\text{GeV}$) signal sample. The statistical and systematic uncertainties are represented by the shaded areas and the lower plots depict the significance of the deviations between data and expectation, which has been calculated with the method described in Section 6.4.2.

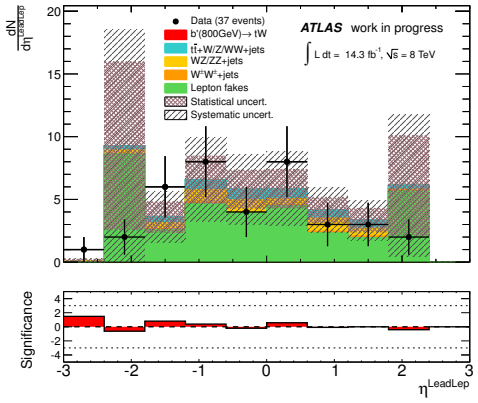

(a) $\eta^{\text{LeadingLepton}}$

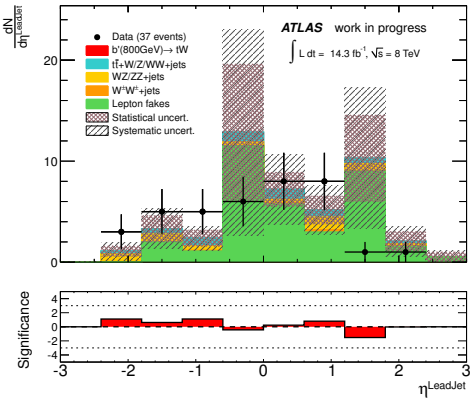

(b) $\eta^{\text{LeadingJet}}$

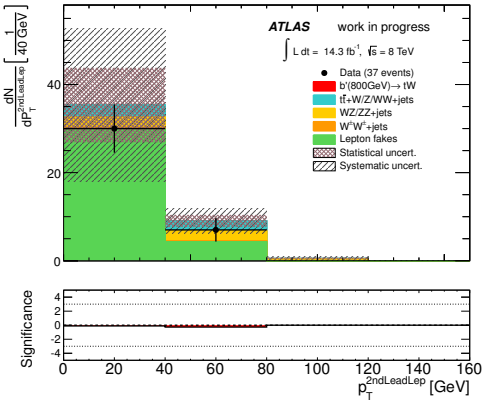

(c) $p_T^{\text{2ndLeadingLepton}}$

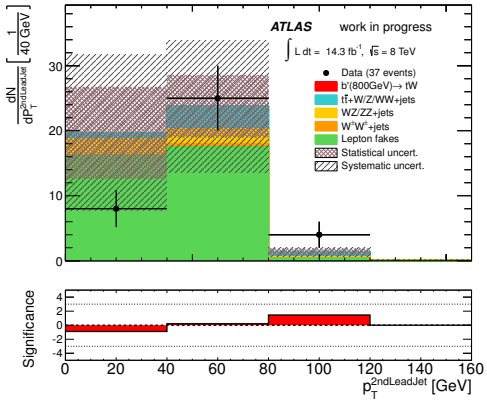

(d) $p_T^{\text{2ndLeadingJet}}$

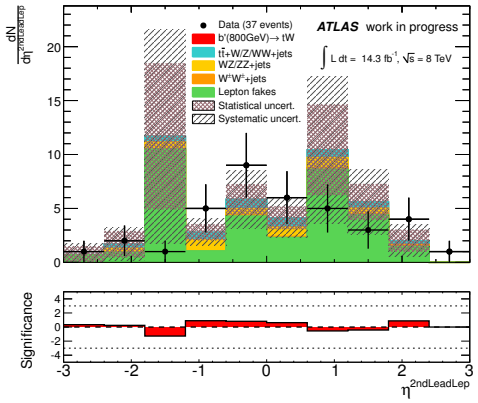

(e) $\eta^{\text{2ndLeadingLepton}}$

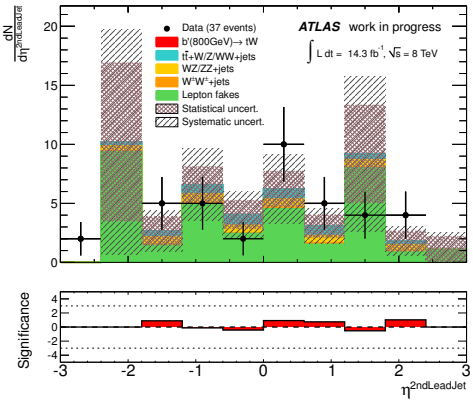

(f) $\eta^{\text{2ndLeadingJet}}$

Figure C.12: Distributions of kinematic variables for the $\mu\mu$ channel after the low-H_T (Table 6.33) control region selection for the various backgrounds and the $b' \to tW$ ($m_{b'} = 800\,\text{GeV}$) signal sample. The statistical and systematic uncertainties are represented by the shaded areas and the lower plots depict the significance of the deviations between data and expectation, which has been calculated with the method described in Section 6.4.2.

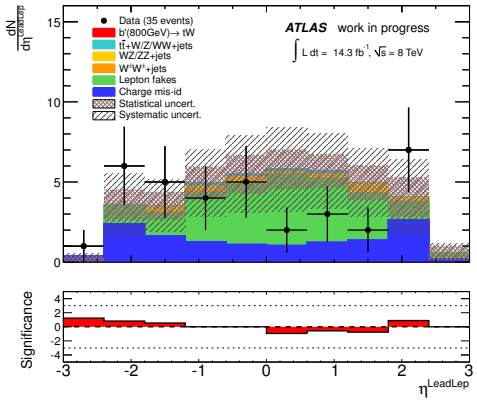

(a) $\eta^{\text{LeadingLepton}}$

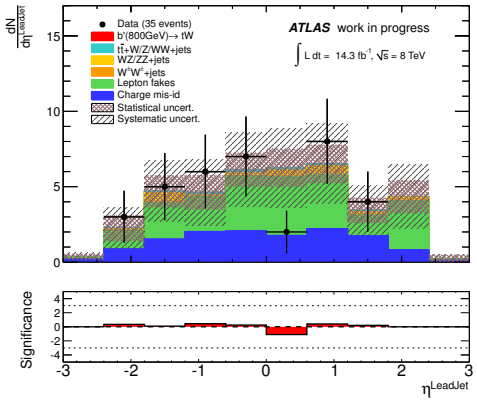

(b) $\eta^{\text{LeadingJet}}$

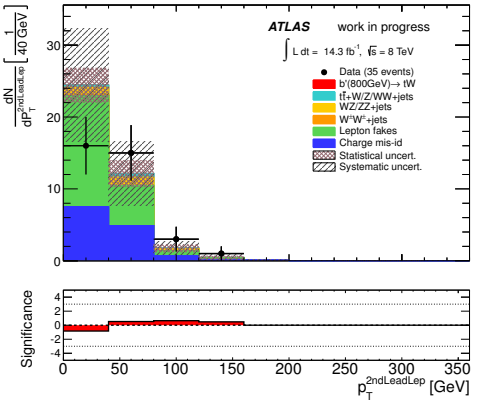

(c) $p_T^{\text{2ndLeadingLepton}}$

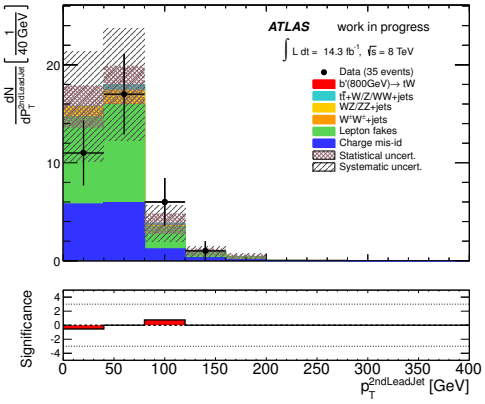

(d) $p_T^{\text{2ndLeadingJet}}$

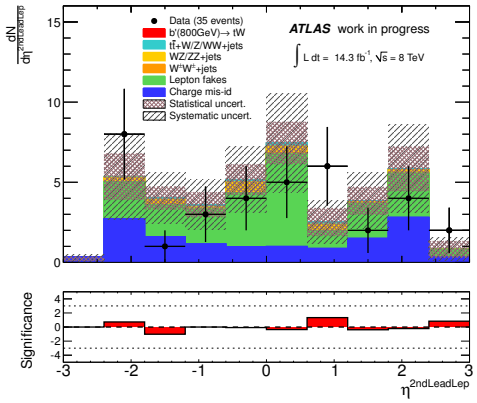

(e) $\eta^{\text{2ndLeadingLepton}}$

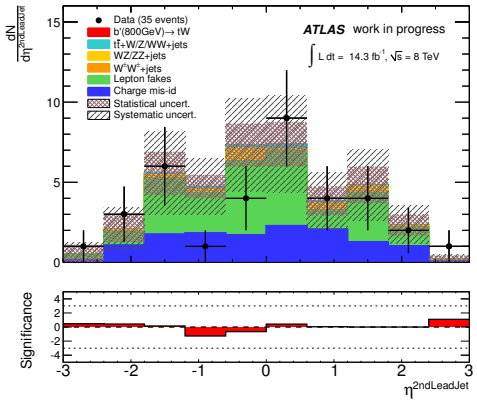

(f) $\eta^{\text{2ndLeadingJet}}$

Figure C.13: Distributions of kinematic variables for the *ee* channel after the low-E_T^{miss} (Table 6.35) control region selection for the various backgrounds and the $b' \to tW$ ($m_{b'} = 800\,\text{GeV}$) signal sample. The statistical and systematic uncertainties are represented by the shaded areas and the lower plots depict the significance of the deviations between data and expectation, which has been calculated with the method described in Section 6.4.2.

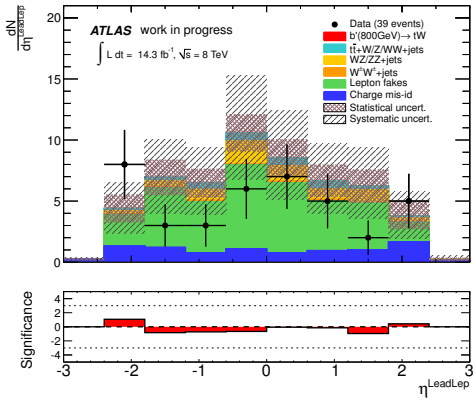

(a) $\eta^{\text{LeadingLepton}}$

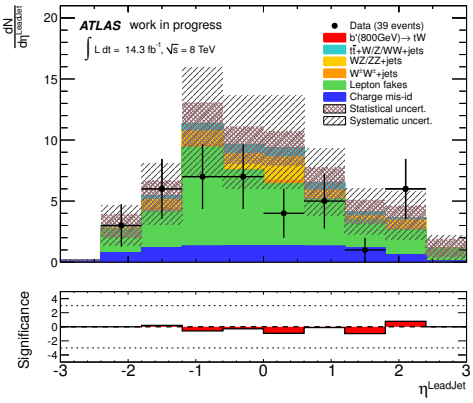

(b) $\eta^{\text{LeadingJet}}$

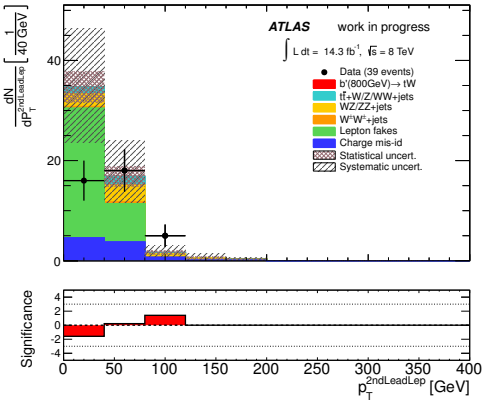

(c) $p_T^{\text{2ndLeadingLepton}}$

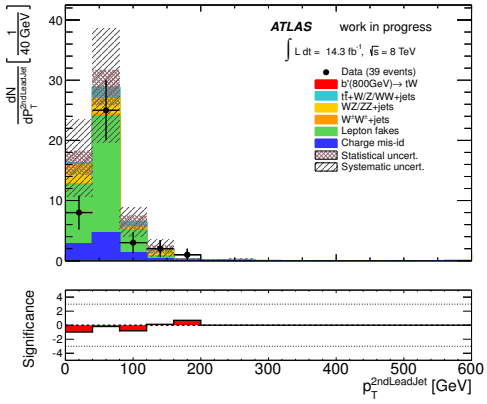

(d) $p_T^{\text{2ndLeadingJet}}$

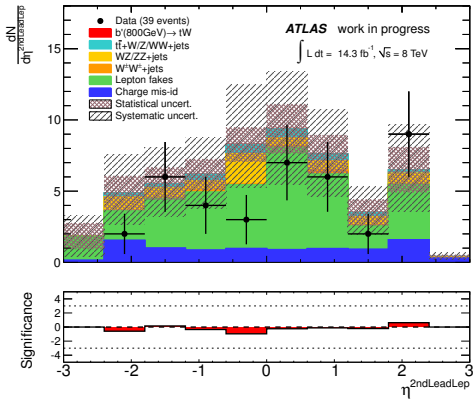

(e) $\eta^{\text{2ndLeadingLepton}}$

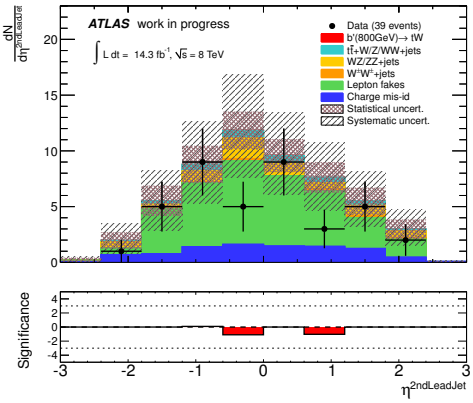

(f) $\eta^{\text{2ndLeadingJet}}$

Figure C.14: Distributions of kinematic variables for the $e\mu$ channel after the low-E_T^{miss} (Table 6.35) control region selection for the various backgrounds and the $b' \to tW$ ($m_{b'} = 800\,\text{GeV}$) signal sample. The statistical and systematic uncertainties are represented by the shaded areas and the lower plots depict the significance of the deviations between data and expectation, which has been calculated with the method described in Section 6.4.2.

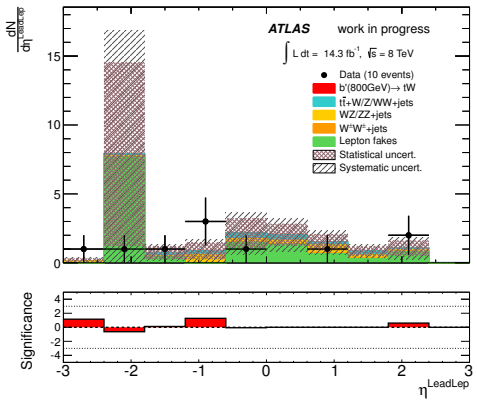

(a) $\eta^{\text{LeadingLepton}}$

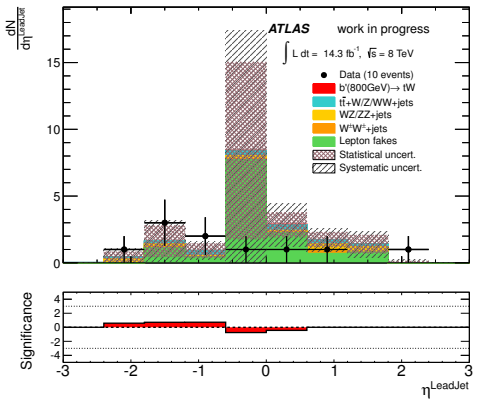

(b) $\eta^{\text{LeadingJet}}$

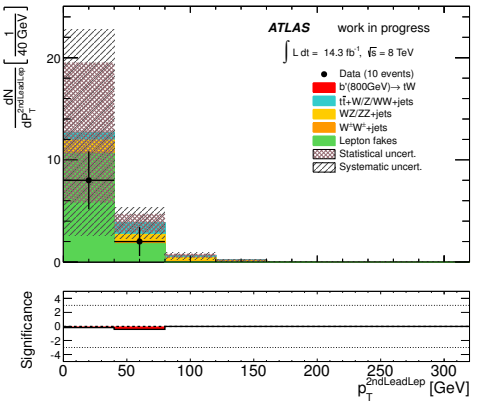

(c) $p_T^{\text{2ndLeadingLepton}}$

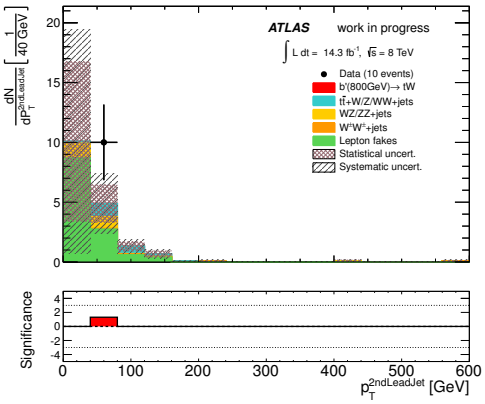

(d) $p_T^{\text{2ndLeadingJet}}$

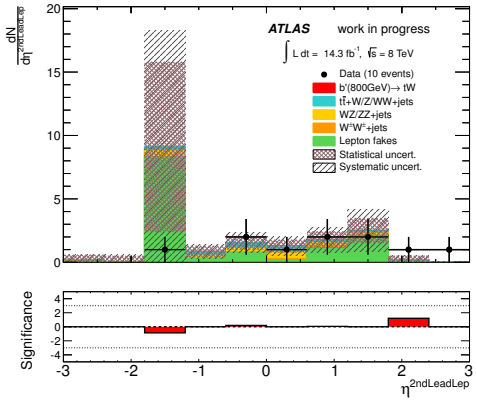

(e) $\eta^{\text{2ndLeadingLepton}}$

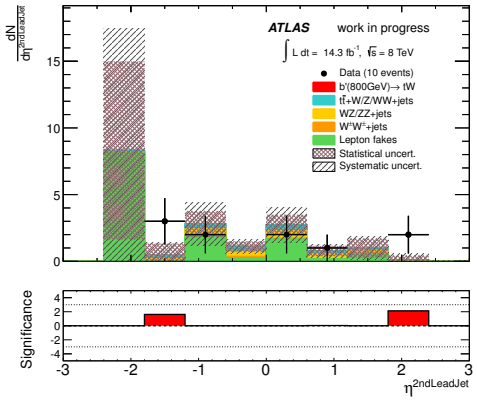

(f) $\eta^{\text{2ndLeadingJet}}$

Figure C.15: Distributions of kinematic variables for the $\mu\mu$ channel after the low-E_T^{miss} (Table 6.35) control region selection for the various backgrounds and the $b' \to tW$ ($m_{b'} = 800\,\text{GeV}$) signal sample. The statistical and systematic uncertainties are represented by the shaded areas and the lower plots depict the significance of the deviations between data and expectation, which has been calculated with the method described in Section 6.4.2.

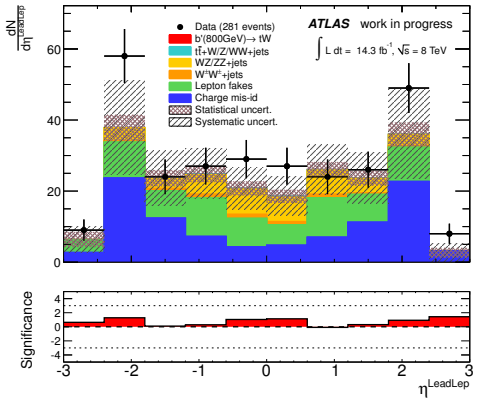

(a) $\eta^{\text{LeadingLepton}}$

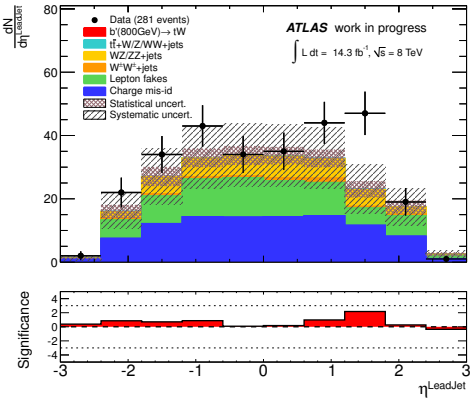

(b) $\eta^{\text{LeadingJet}}$

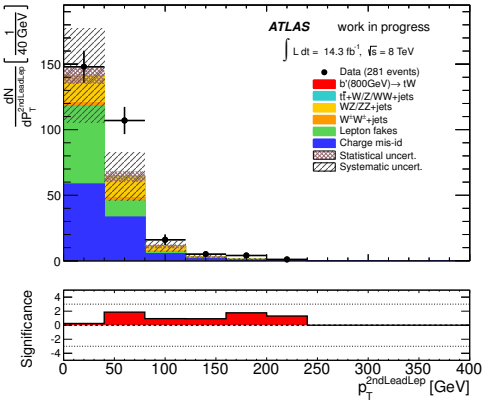

(c) $p_T^{\text{2ndLeadingLepton}}$

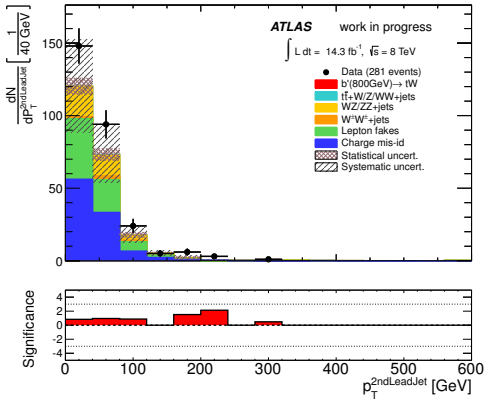

(d) $p_T^{\text{2ndLeadingJet}}$

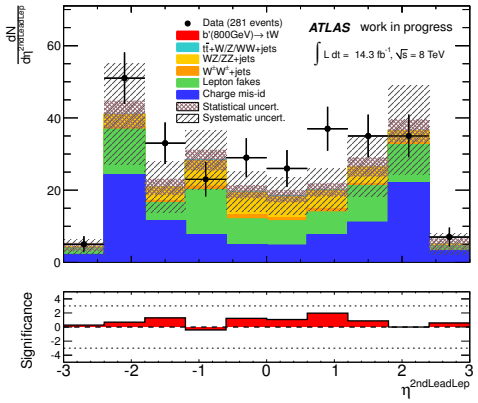

(e) $\eta^{\text{2ndLeadingLepton}}$

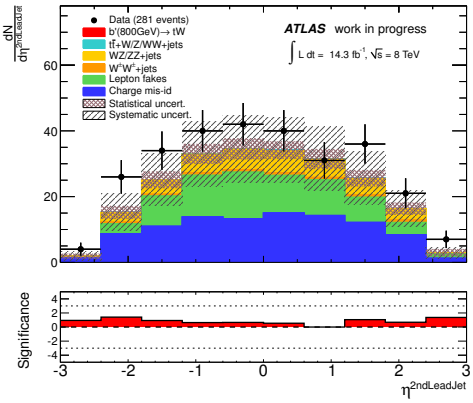

(f) $\eta^{\text{2ndLeadingJet}}$

Figure C.16: Distributions of kinematic variables for the *ee* channel after the Zero *b*-tag (Table 6.37) control region selection for the various backgrounds and the $b' \to tW$ ($m_{b'} = 800\,\text{GeV}$) signal sample. The statistical and systematic uncertainties are represented by the shaded areas and the lower plots depict the significance of the deviations between data and expectation, which has been calculated with the method described in Section 6.4.2.

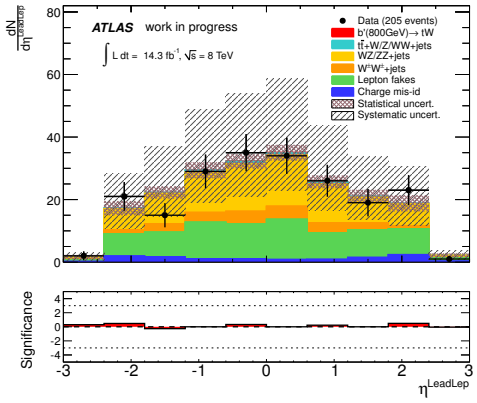

(a) $\eta^{\text{LeadingLepton}}$

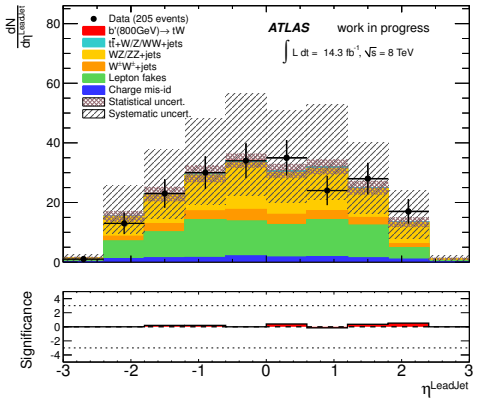

(b) $\eta^{\text{LeadingJet}}$

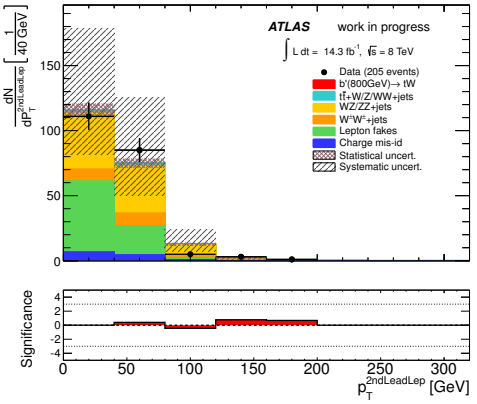

(c) $p_T^{\text{2ndLeadingLepton}}$

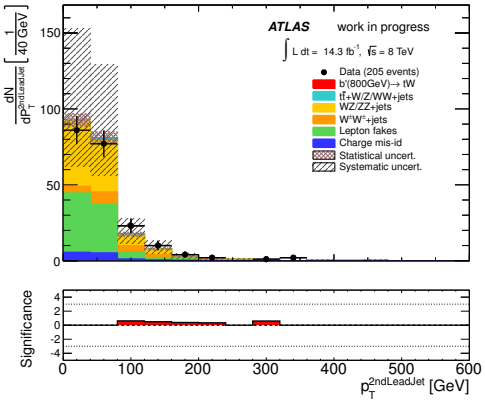

(d) $p_T^{\text{2ndLeadingJet}}$

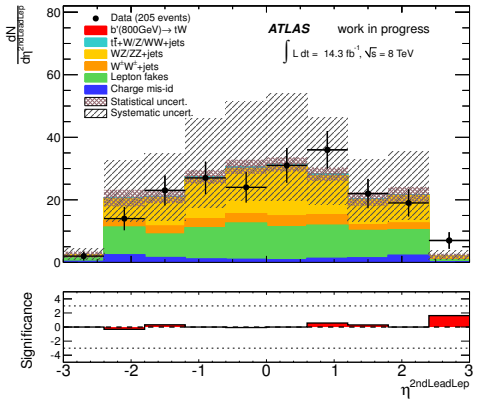

(e) $\eta^{\text{2ndLeadingLepton}}$

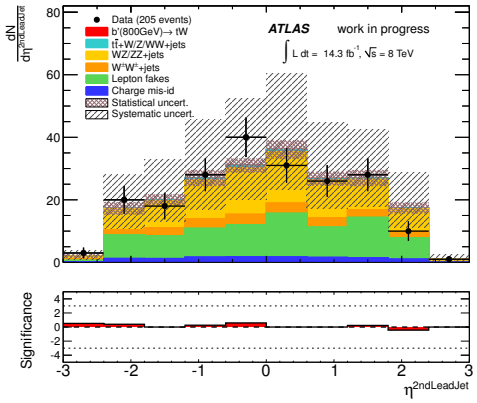

(f) $\eta^{\text{2ndLeadingJet}}$

Figure C.17: Distributions of kinematic variables for the $e\mu$ channel after the Zero b-tag (Table 6.37) control region selection for the various backgrounds and the $b' \to tW$ ($m_{b'} = 800\,\text{GeV}$) signal sample. The statistical and systematic uncertainties are represented by the shaded areas and the lower plots depict the significance of the deviations between data and expectation, which has been calculated with the method described in Section 6.4.2.

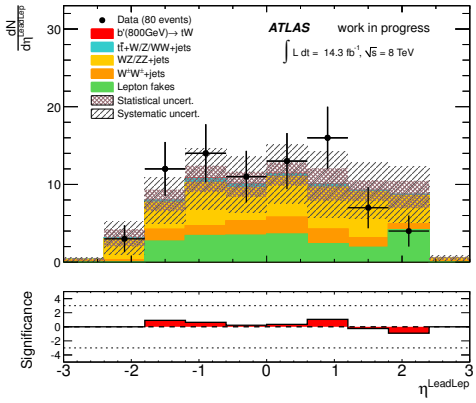

(a) $\eta^{\text{LeadingLepton}}$

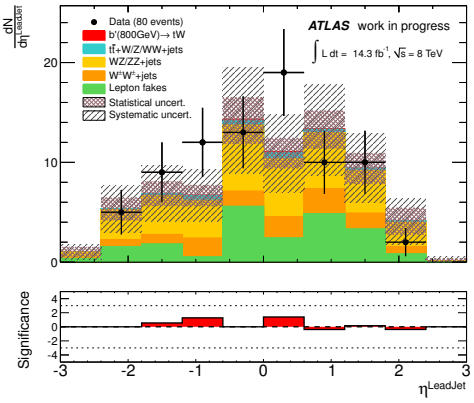

(b) $\eta^{\text{LeadingJet}}$

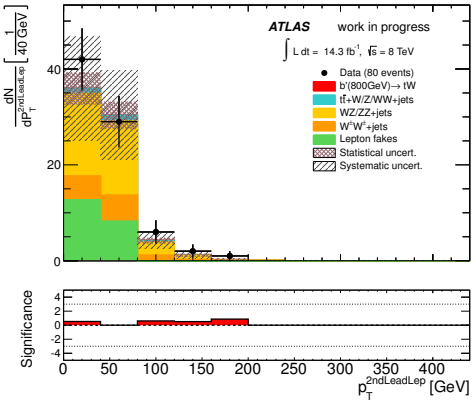

(c) $p_T^{\text{2ndLeadingLepton}}$

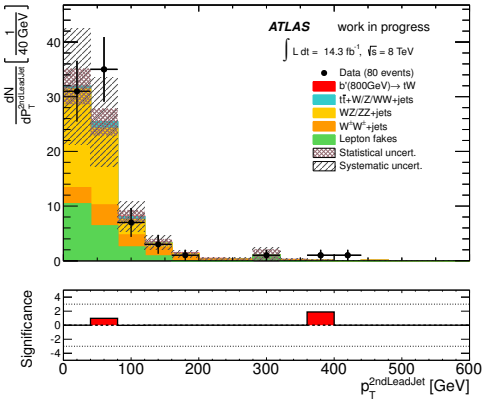

(d) $p_T^{\text{2ndLeadingJet}}$

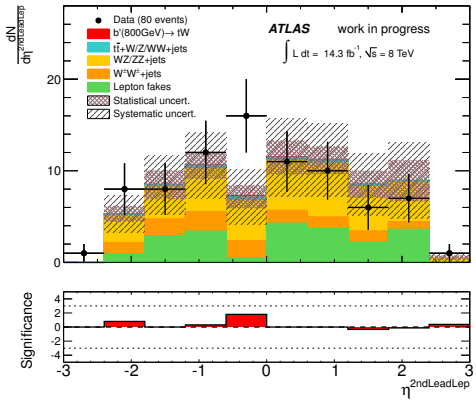

(e) $\eta^{\text{2ndLeadingLepton}}$

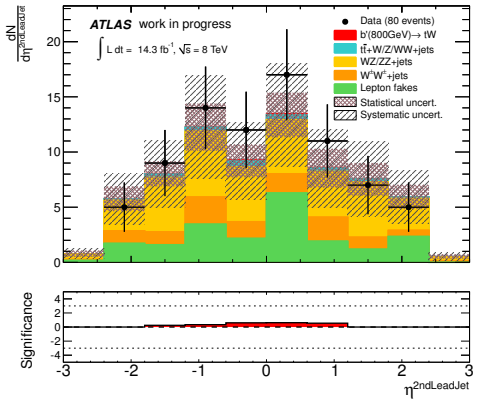

(f) $\eta^{\text{2ndLeadingJet}}$

Figure C.18: Distributions of kinematic variables for the $\mu\mu$ channel after the Zero b-tag (Table 6.37) control region selection for the various backgrounds and the $b' \to tW$ ($m_{b'} = 800\,\text{GeV}$) signal sample. The statistical and systematic uncertainties are represented by the shaded areas and the lower plots depict the significance of the deviations between data and expectation, which has been calculated with the method described in Section 6.4.2.

D Final limit results

This appendix provides additional material for the derived limits in Sections 6.9.1 and 6.9.2.

D.1 Limit determination for $b' \to tW$

D.1.1 LLR distributions

Several pseudo-experiments have been generated for the 'signal+background' and 'background-only' hypotheses, in order to derive the LLR probability density distributions. These distributions are presented in Figures D.1 and D.2 for the $b' \to tW$ samples with different b' masses.

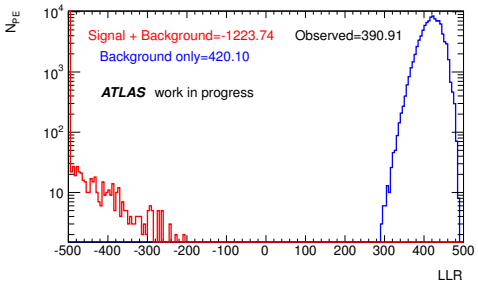

(a) $m_{b'} = 400\,\text{GeV}$

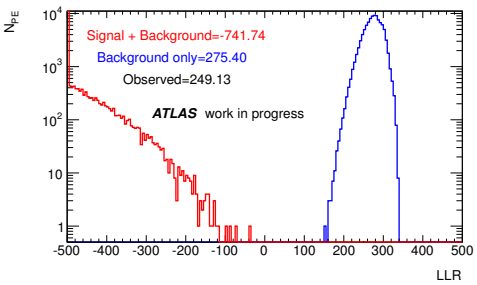

(b) $m_{b'} = 450\,\text{GeV}$

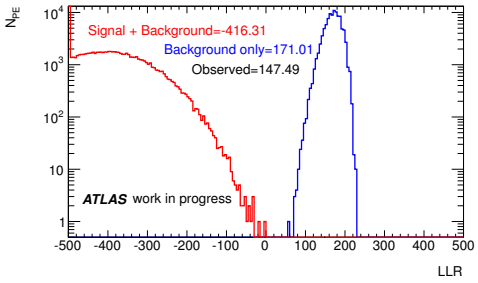

(c) $m_{b'} = 500\,\text{GeV}$

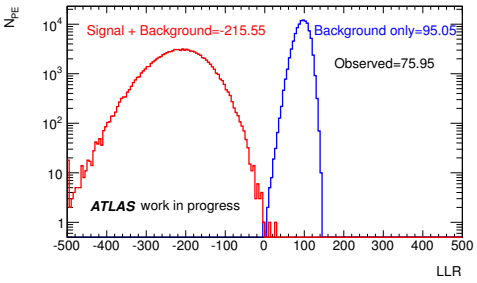

(d) $m_{b'} = 550\,\text{GeV}$

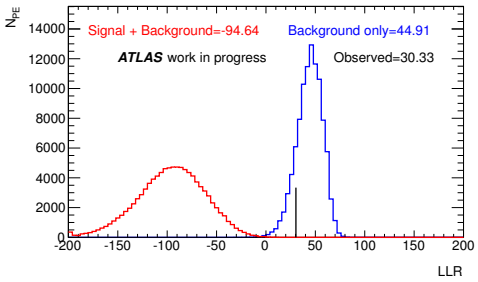

(e) $m_{b'} = 600\,\text{GeV}$

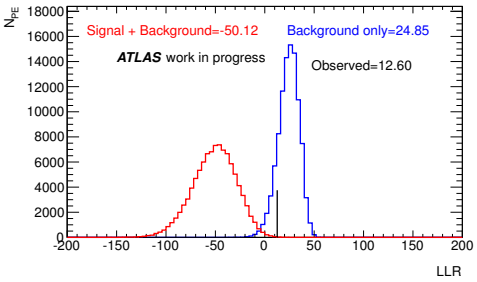

(f) $m_{b'} = 650\,\text{GeV}$

Figure D.1: Distributions of the LLR (Log-Likelihood ratio) values from the generated pseudo-experiments. The distributions are presented for different b' mass points ($m_{b'} \in [400, 650]$ GeV). Each plot depicts the distributions for the generated pseudo-experiments assuming the 'background-only' and the 'signal+background' hypotheses. In addition, the mean values of the two distributions are shown, as well as the observed LLR value.

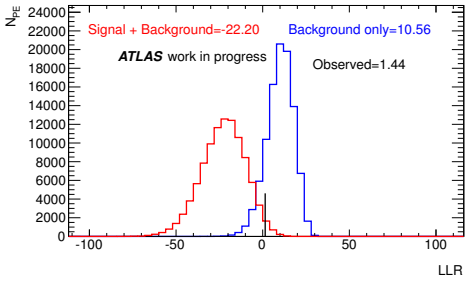

(a) $m_{b'} = 700\,\text{GeV}$

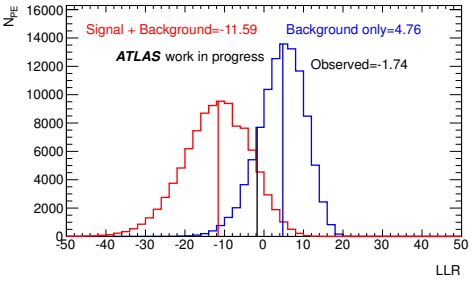

(b) $m_{b'} = 750\,\text{GeV}$

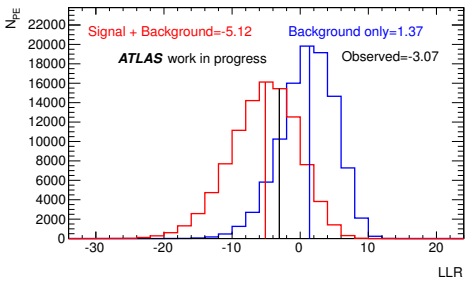

(c) $m_{b'} = 800\,\text{GeV}$

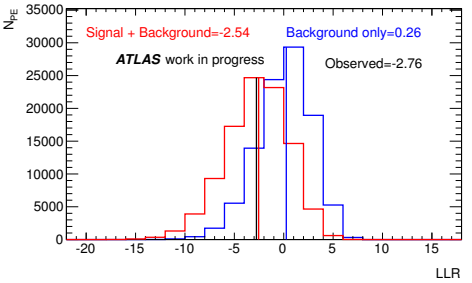

(d) $m_{b'} = 850\,\text{GeV}$

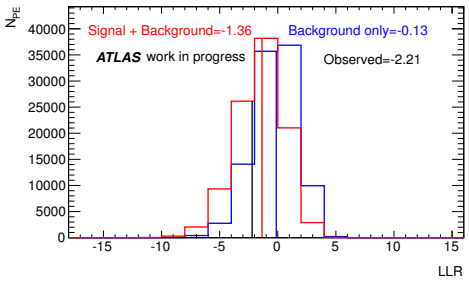

(e) $m_{b'} = 900\,\text{GeV}$

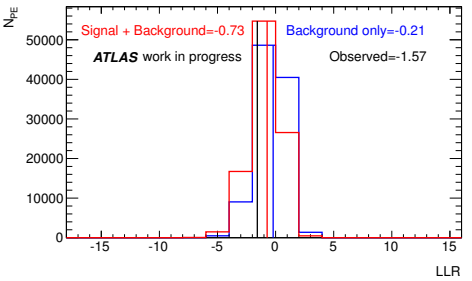

(f) $m_{b'} = 950\,\text{GeV}$

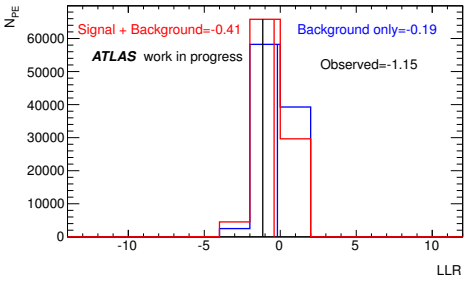

(g) $m_{b'} = 1000\,\text{GeV}$

Figure D.2: Distributions of the LLR (Log-Likelihood ratio) values from the generated pseudo-experiments. The distributions are presented for different b' mass points ($m_{b'} \in [700, 1000]$ GeV). Each plot depicts the distributions for the generated pseudo-experiments assuming the 'background-only' and the 'signal+background' hypotheses. In addition, the mean values of the two distributions are shown, as well as the observed LLR value.

D.2 Limit determination for $b' \to qW$

D.2.1 Expected signal yields

In order to draw the exclusion areas as a function of the b' mass and its branching fractions for the decays into tW, cW and uW, the expected event yields have been determined as a function of these branching fractions. Figure D.3 depicts these event yields for the combination of the ee, $e\mu$ and $\mu\mu$ channels for b' masses, that have not been presented in Section 6.9.2.
The b' signal yields, derived separately for each dilepton channel, are presented in Figures D.4 and D.5 (ee), D.6 and D.7 ($e\mu$), and D.8 and D.9 ($\mu\mu$).

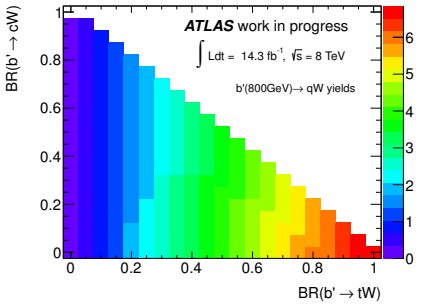

(a) $m_{b'} = 800\,\text{GeV}$

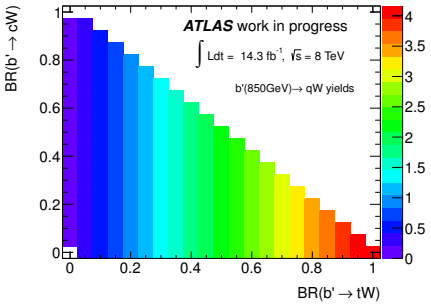

(b) $m_{b'} = 850\,\text{GeV}$

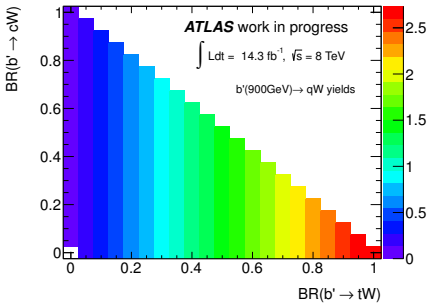

(c) $m_{b'} = 900\,\text{GeV}$

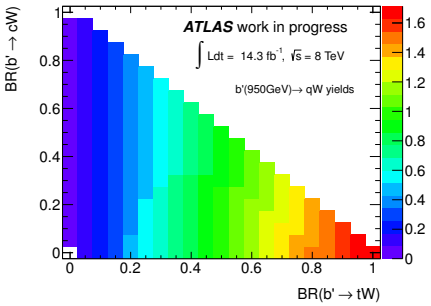

(d) $m_{b'} = 950\,\text{GeV}$

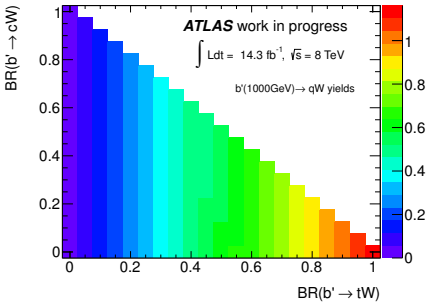

(e) $m_{b'} = 1000\,\text{GeV}$

Figure D.3: Expected signal yields depending on the branching fractions for $b' \to cW$ and $b' \to tW$ and for different b' masses ($m_{b'} \in [800, 1000]$ GeV). The yields are presented for the combination of the ee, $e\mu$ and $\mu\mu$ channel.

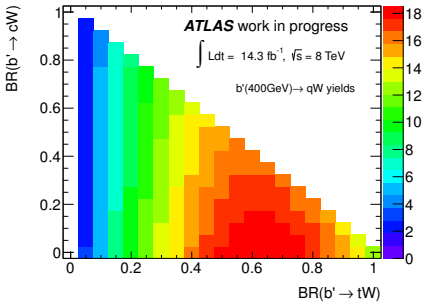

(a) $m_{b'} = 400\,\text{GeV}$

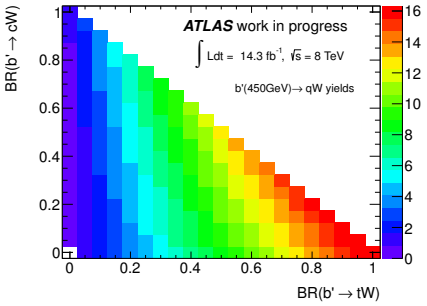

(b) $m_{b'} = 450\,\text{GeV}$

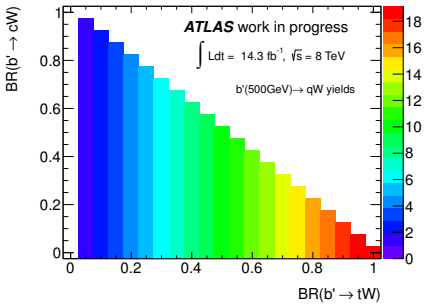

(c) $m_{b'} = 500\,\text{GeV}$

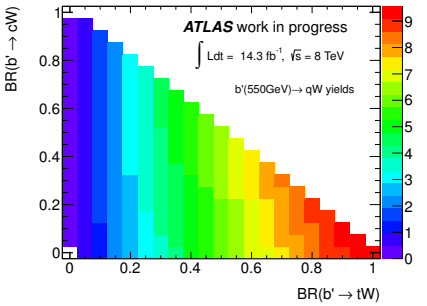

(d) $m_{b'} = 550\,\text{GeV}$

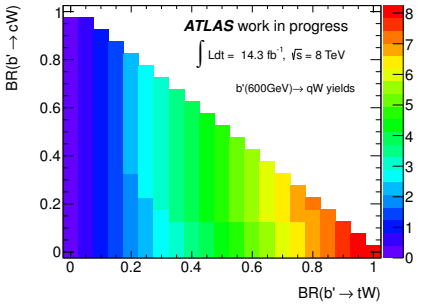

(e) $m_{b'} = 600\,\text{GeV}$

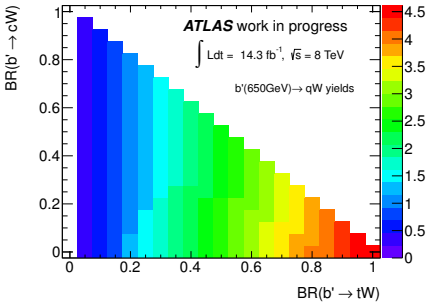

(f) $m_{b'} = 650\,\text{GeV}$

Figure D.4: Expected signal yields depending on the branching fractions for $b' \to cW$ and $b' \to tW$ and for different b' masses ($m_{b'} \in [400, 650]$ GeV). The yields are presented for the ee channel.

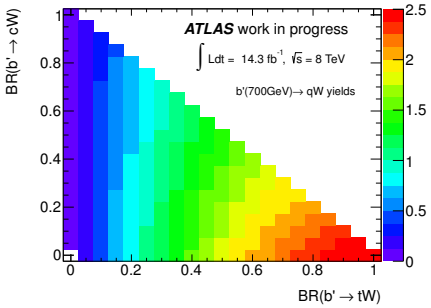

(a) $m_{b'} = 700\,\text{GeV}$

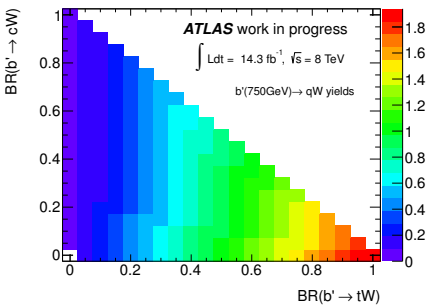

(b) $m_{b'} = 750\,\text{GeV}$

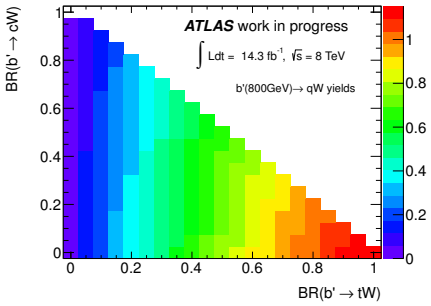

(c) $m_{b'} = 800\,\text{GeV}$

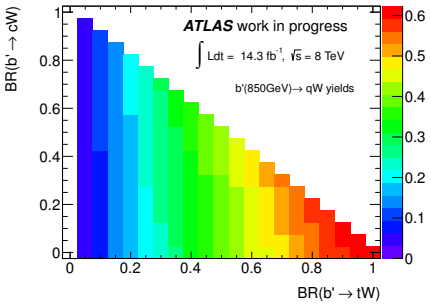

(d) $m_{b'} = 850\,\text{GeV}$

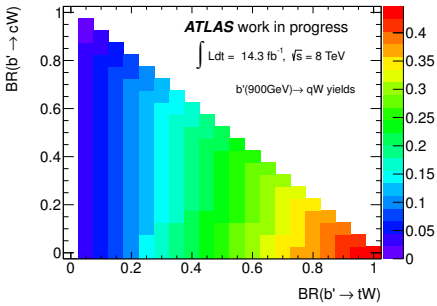

(e) $m_{b'} = 900\,\text{GeV}$

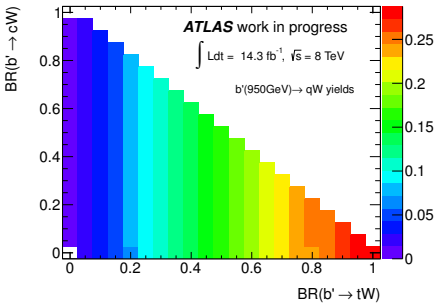

(f) $m_{b'} = 950\,\text{GeV}$

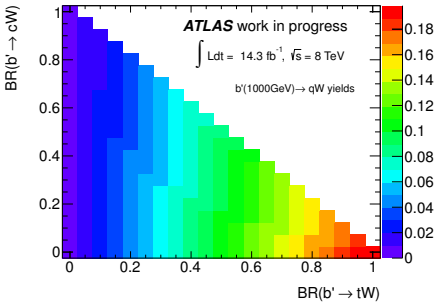

(g) $m_{b'} = 1000\,\text{GeV}$

Figure D.5: Expected signal yields depending on the branching fractions for $b' \to cW$ and $b' \to tW$ and for different b' masses ($m_{b'} \in [700, 1000]$ GeV). The yields are presented for the ee channel.

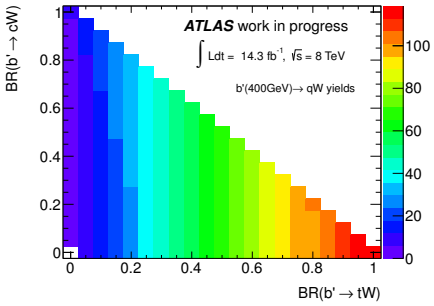

(a) $m_{b'} = 400\,\text{GeV}$

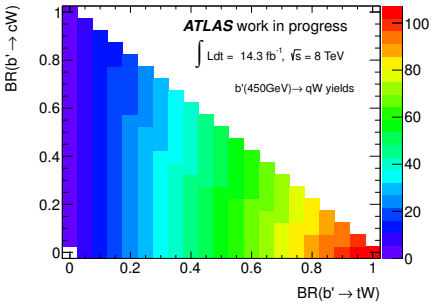

(b) $m_{b'} = 450\,\text{GeV}$

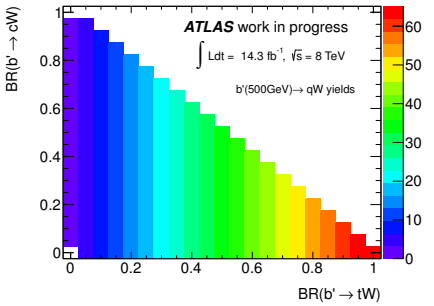

(c) $m_{b'} = 500\,\text{GeV}$

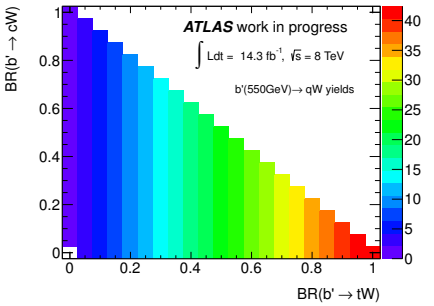

(d) $m_{b'} = 550\,\text{GeV}$

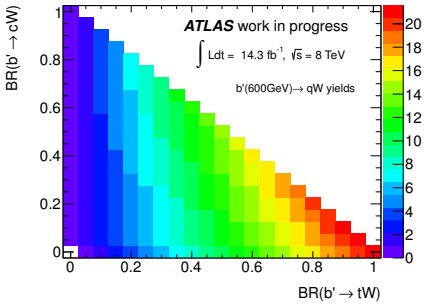

(e) $m_{b'} = 600\,\text{GeV}$

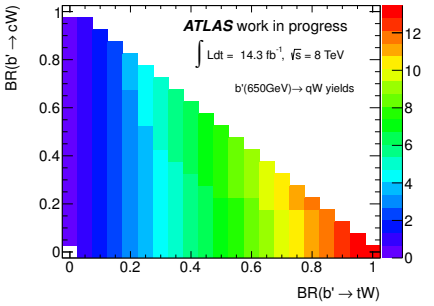

(f) $m_{b'} = 650\,\text{GeV}$

Figure D.6: Expected signal yields depending on the branching fractions for $b' \to cW$ and $b' \to tW$ and for different b' masses ($m_{b'} \in [400, 650]$ GeV). The yields are presented for the $e\mu$ channel.

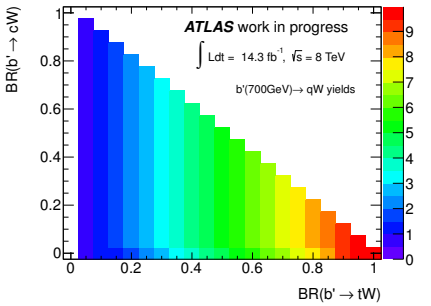

(a) $m_{b'} = 700\,\text{GeV}$

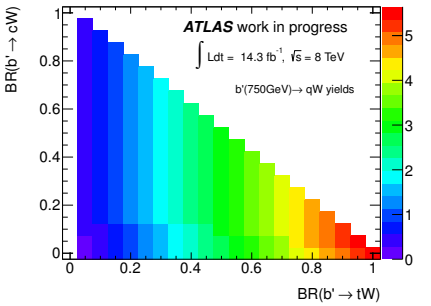

(b) $m_{b'} = 750\,\text{GeV}$

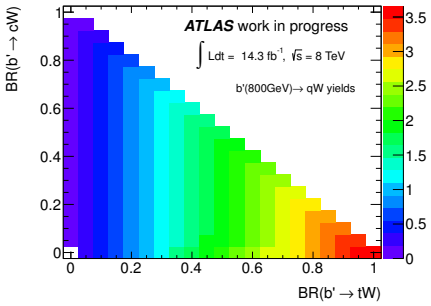

(c) $m_{b'} = 800\,\text{GeV}$

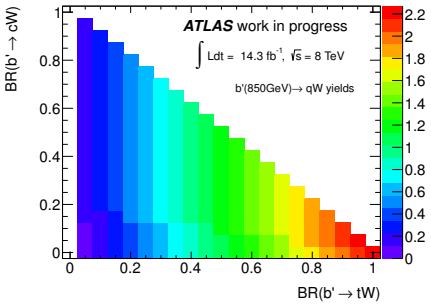

(d) $m_{b'} = 850\,\text{GeV}$

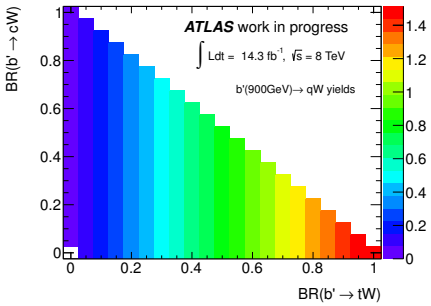

(e) $m_{b'} = 900\,\text{GeV}$

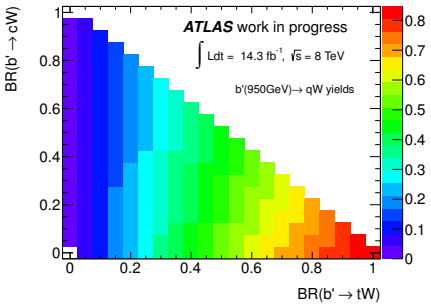

(f) $m_{b'} = 950\,\text{GeV}$

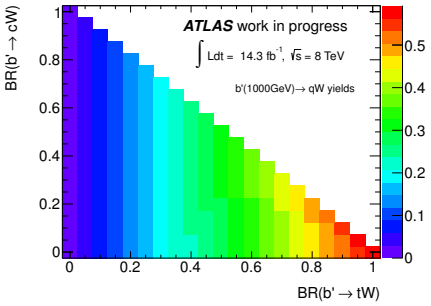

(g) $m_{b'} = 1000\,\text{GeV}$

Figure D.7: Expected signal yields depending on the branching fractions for $b' \to cW$ and $b' \to tW$ and for different b' masses ($m_{b'} \in [700, 1000]$ GeV). The yields are presented for the $e\mu$ channel.

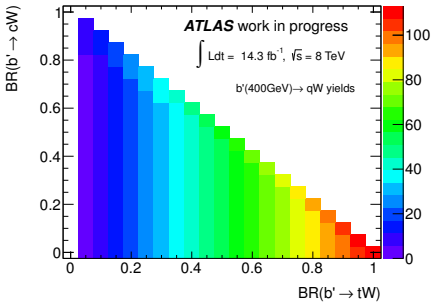

(a) $m_{b'} = 400\,\text{GeV}$

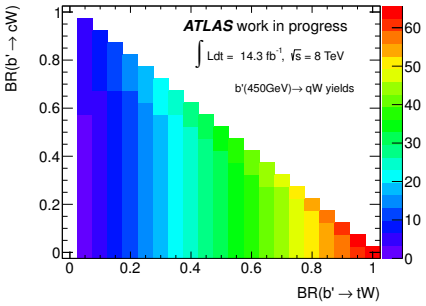

(b) $m_{b'} = 450\,\text{GeV}$

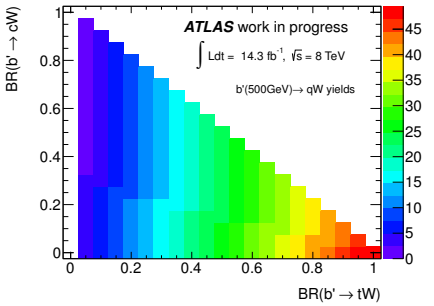

(c) $m_{b'} = 500\,\text{GeV}$

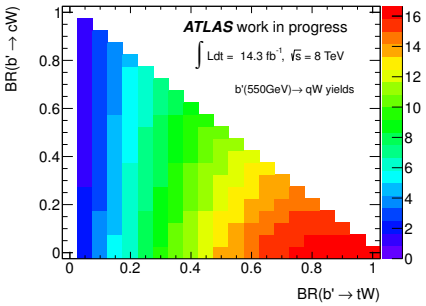

(d) $m_{b'} = 550\,\text{GeV}$

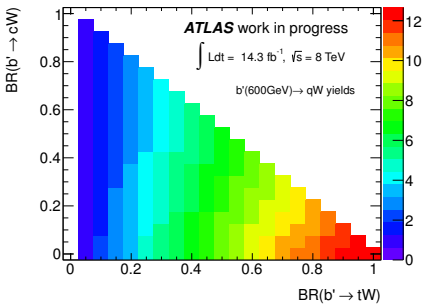

(e) $m_{b'} = 600\,\text{GeV}$

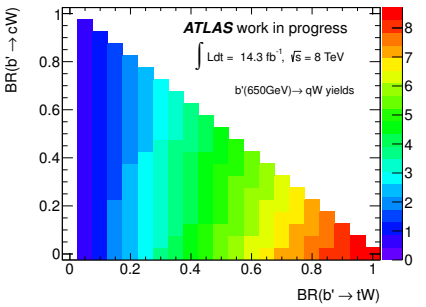

(f) $m_{b'} = 650\,\text{GeV}$

Figure D.8: Expected signal yields depending on the branching fractions for $b' \to cW$ and $b' \to tW$ and for different b' masses ($m_{b'} \in [400, 650]$ GeV). The yields are presented for the $\mu\mu$ channel.

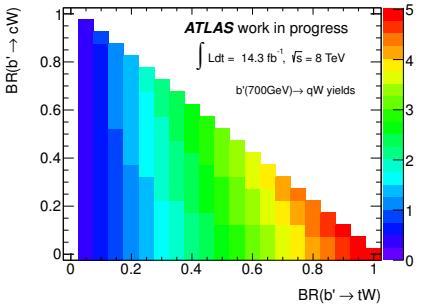

(a) $m_{b'} = 700\,\text{GeV}$

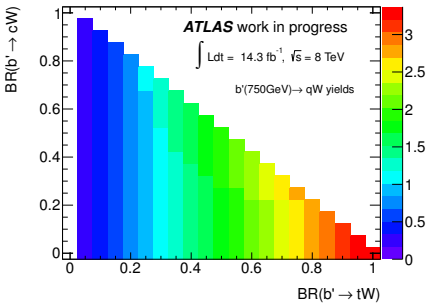

(b) $m_{b'} = 750\,\text{GeV}$

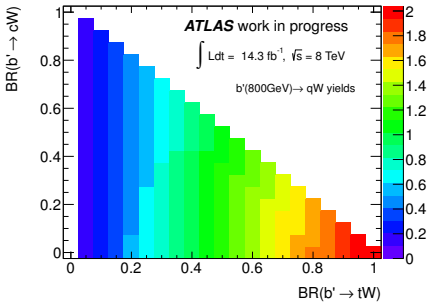

(c) $m_{b'} = 800\,\text{GeV}$

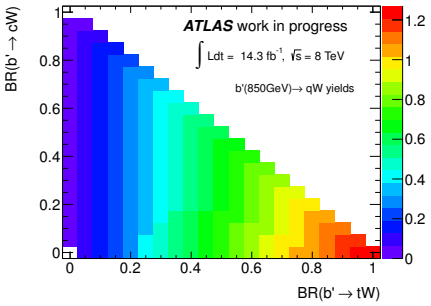

(d) $m_{b'} = 850\,\text{GeV}$

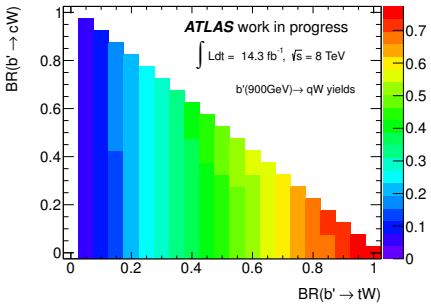

(e) $m_{b'} = 900\,\text{GeV}$

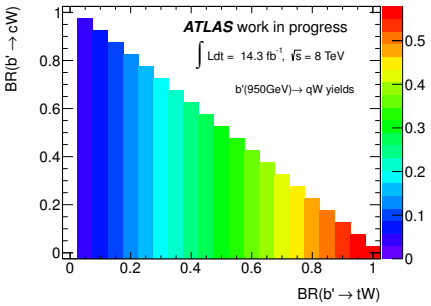

(f) $m_{b'} = 950\,\text{GeV}$

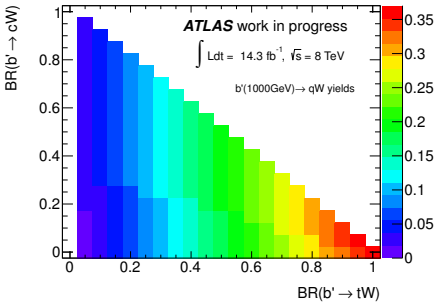

(g) $m_{b'} = 1000\,\text{GeV}$

Figure D.9: Expected signal yields depending on the branching fractions for $b' \to cW$ and $b' \to tW$ and for different b' masses ($m_{b'} \in [700, 1000]$ GeV). The yields are presented for the $\mu\mu$ channel.

D.2.2 Expected and observed limits

The exclusion areas presented in Section 6.9.2 have been only shown for b' masses, where it was possible to make an exclusion statement. As can be seen in Figure D.10, b' masses above 800 GeV can not be excluded for any branching fractions.
A point in the branching fraction plane was considered as excluded, if the obtained CL_s value was below 0.05. The expected and observed CL_s values in the branching fraction plane for the different b' masses are depicted in Figures D.11, D.12, D.13, D.14 and D.15.

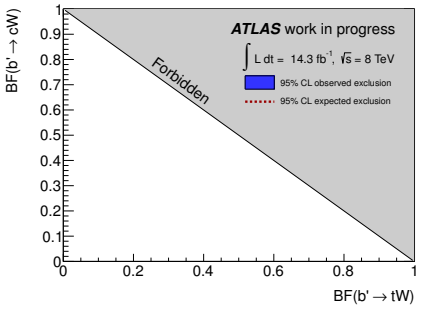

(a) $m_{b'} = 800\,\text{GeV}$

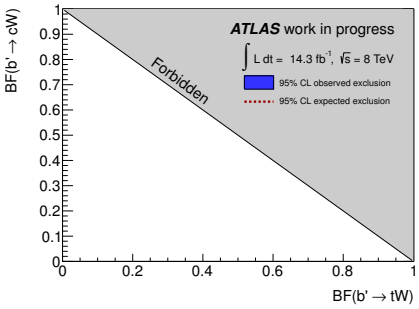

(b) $m_{b'} = 850\,\text{GeV}$

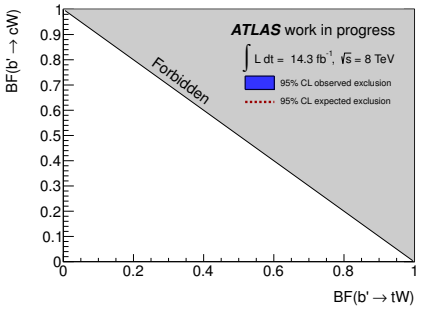

(c) $m_{b'} = 900\,\text{GeV}$

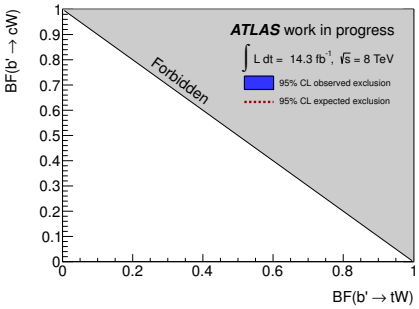

(d) $m_{b'} = 950\,\text{GeV}$

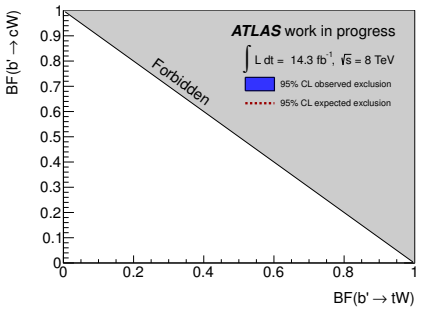

(e) $m_{b'} = 1000\,\text{GeV}$

Figure D.10: Expected and observed 95% CL exclusion ranges in the branching fraction plane for $b' \to cW$ and $b' \to tW$ and for different b' masses ($m_{b'} \in [800, 1000]$ GeV).

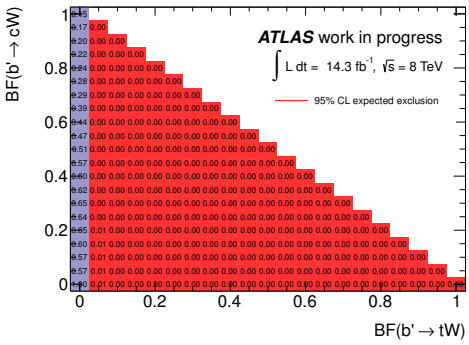

(a) Expected: $m_{b'} = 400\,\text{GeV}$

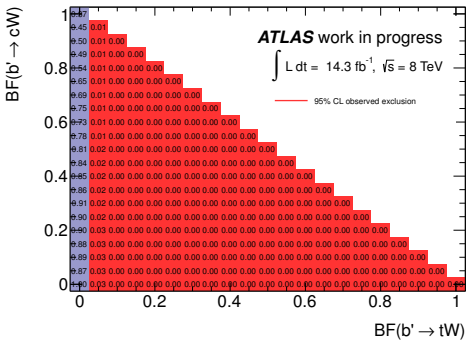

(b) Observed: $m_{b'} = 400\,\text{GeV}$

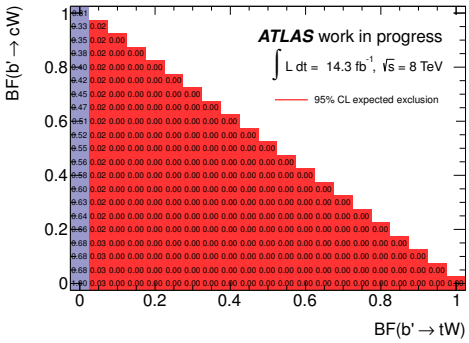

(c) Expected: $m_{b'} = 450\,\text{GeV}$

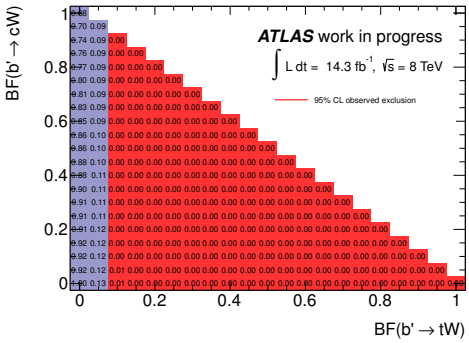

(d) Observed: $m_{b'} = 450\,\text{GeV}$

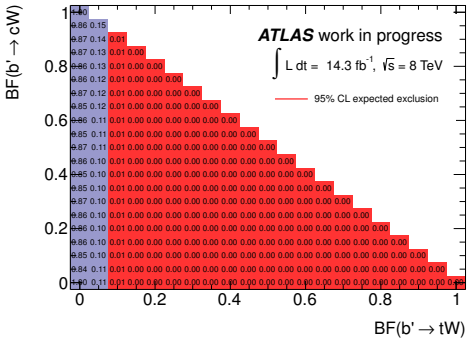

(e) Expected: $m_{b'} = 500\,\text{GeV}$

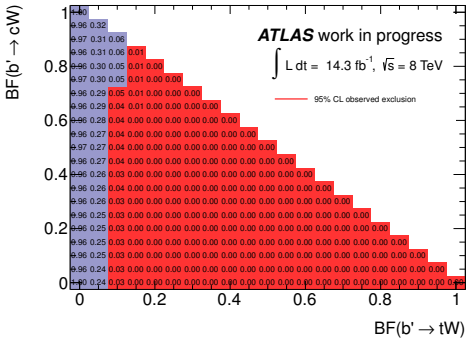

(f) Observed: $m_{b'} = 500\,\text{GeV}$

Figure D.11: Expected and observed CL_s values in the branching fraction plane for $b' \to cW$ and $b' \to tW$ and for different b' masses ($m_{b'} \in [400, 500]$ GeV). A point is considered to be excluded with 95% CL (red), if $CL_s < 0.05$.

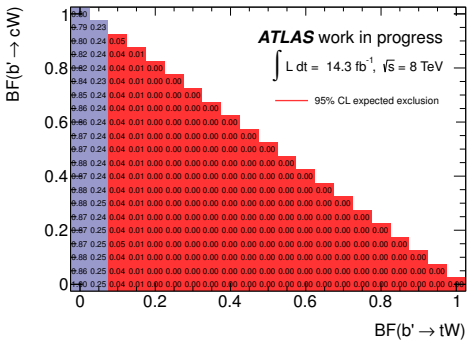

(a) Expected: $m_{b'} = 550\,\text{GeV}$

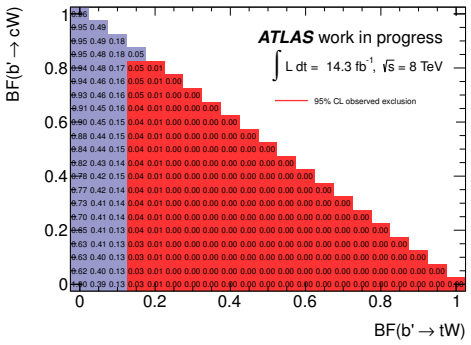

(b) Observed: $m_{b'} = 550\,\text{GeV}$

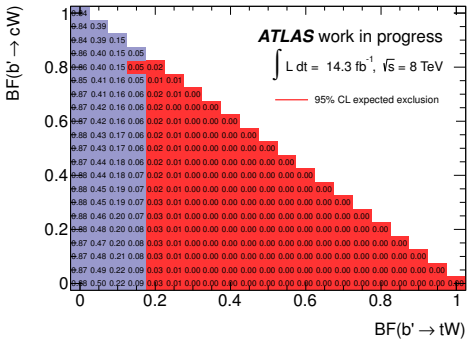

(c) Expected: $m_{b'} = 600\,\text{GeV}$

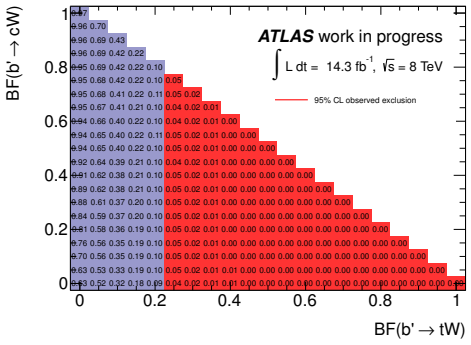

(d) Observed: $m_{b'} = 600\,\text{GeV}$

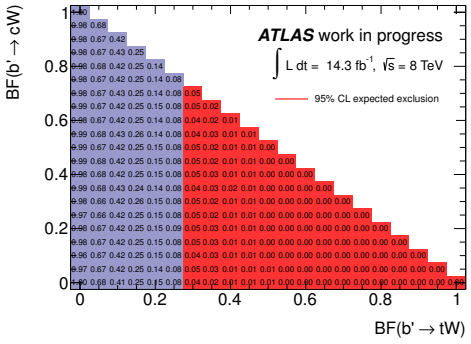

(e) Expected: $m_{b'} = 650\,\text{GeV}$

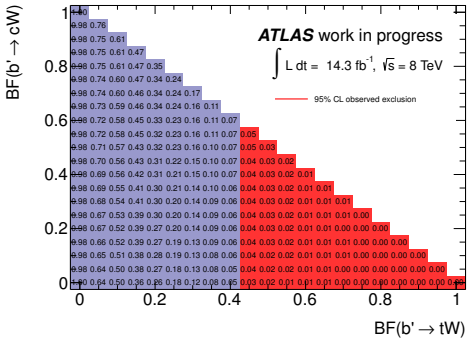

(f) Observed: $m_{b'} = 650\,\text{GeV}$

Figure D.12: Expected and observed CL_s values in the branching fraction plane for $b' \to cW$ and $b' \to tW$ and for different b' masses ($m_{b'} \in [550, 650]$ GeV). A point is considered to be excluded with 95% CL (red), if $CL_s < 0.05$.

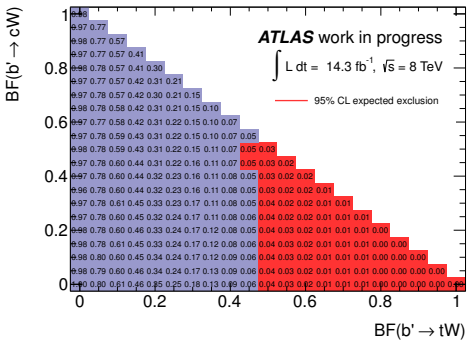

(a) Expected: $m_{b'} = 700\,\text{GeV}$

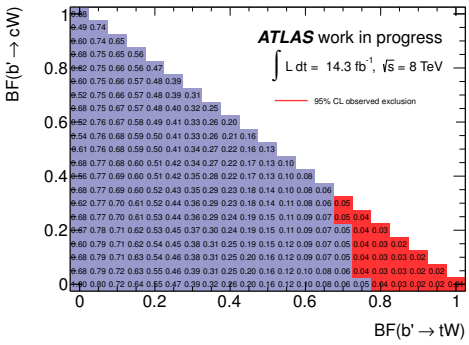

(b) Observed: $m_{b'} = 700\,\text{GeV}$

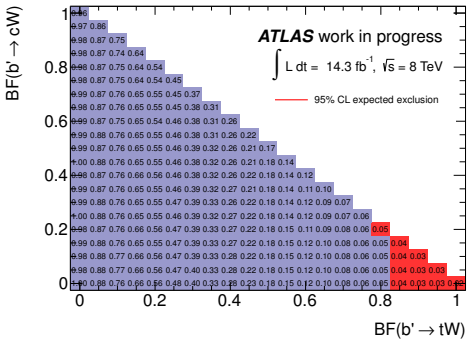

(c) Expected: $m_{b'} = 750\,\text{GeV}$

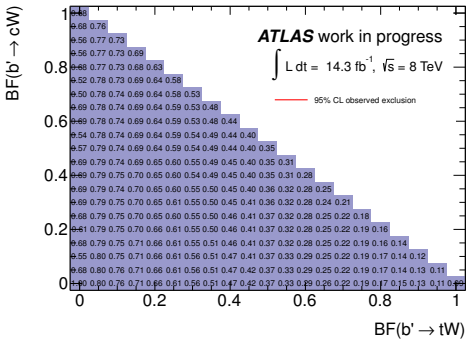

(d) Observed: $m_{b'} = 750\,\text{GeV}$

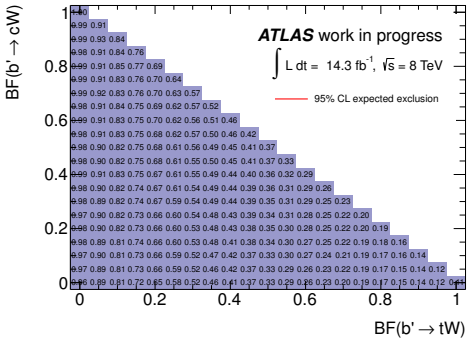

(e) Expected: $m_{b'} = 800\,\text{GeV}$

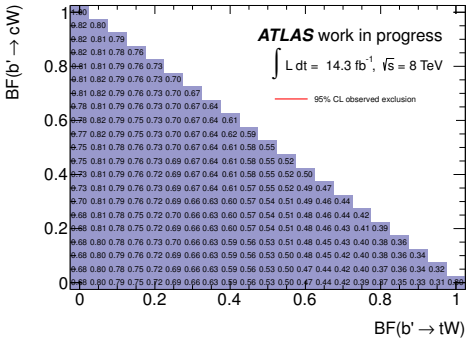

(f) Observed: $m_{b'} = 800\,\text{GeV}$

Figure D.13: Expected and observed CL_s values in the branching fraction plane for $b' \to cW$ and $b' \to tW$ and for different b' masses ($m_{b'} \in [700, 800]$ GeV). A point is considered to be excluded with 95% CL (red), if $CL_s < 0.05$.

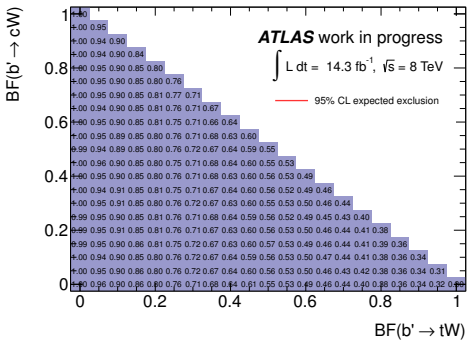

(a) Expected: $m_{b'} = 850\,\text{GeV}$

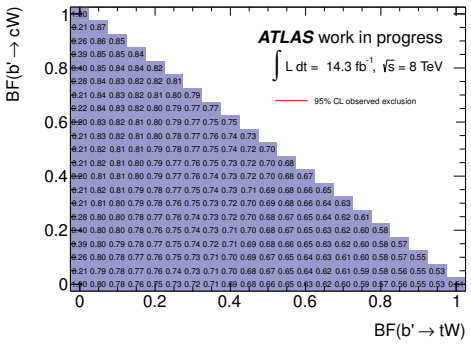

(b) Observed: $m_{b'} = 850\,\text{GeV}$

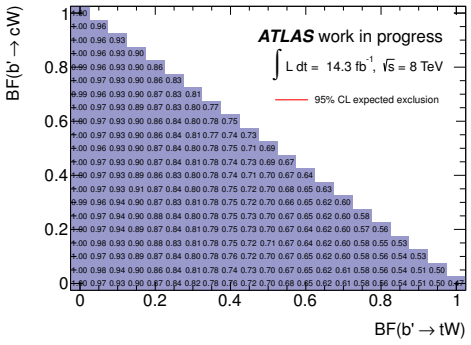

(c) Expected: $m_{b'} = 900\,\text{GeV}$

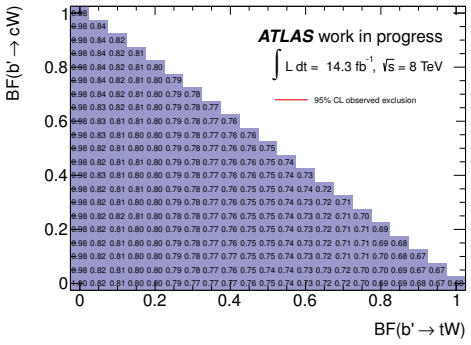

(d) Observed: $m_{b'} = 900\,\text{GeV}$

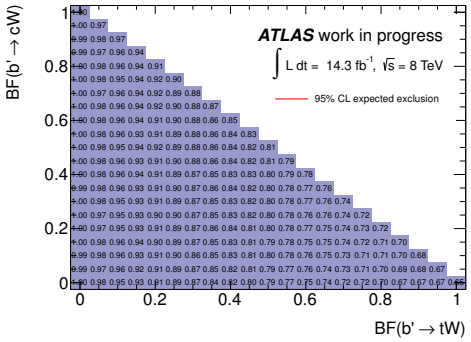

(e) Expected: $m_{b'} = 950\,\text{GeV}$

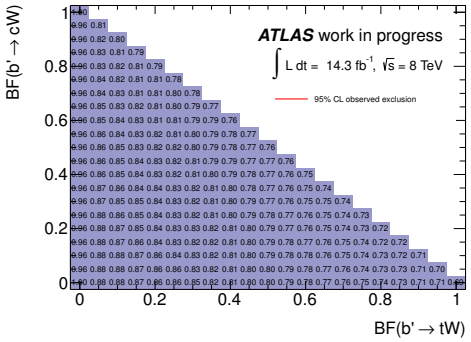

(f) Observed: $m_{b'} = 950\,\text{GeV}$

Figure D.14: Expected and observed CL_s values in the branching fraction plane for $b' \to cW$ and $b' \to tW$ and for different b' masses ($m_{b'} \in [850, 950]$ GeV). A point is considered to be excluded with 95% CL (red), if $CL_s < 0.05$.

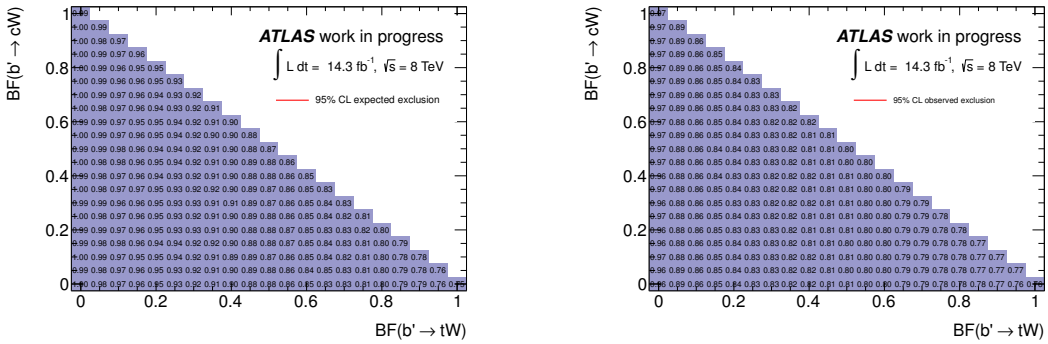

(a) Expected: $m_{b'} = 1000\,\text{GeV}$ (b) Observed: $m_{b'} = 1000\,\text{GeV}$

Figure D.15: Expected and observed CL_s values in the branching fraction plane for $b' \to cW$ and $b' \to tW$ and for different b' masses ($m_{b'} = 1000\,\text{GeV}$). A point is considered to be excluded with 95% CL (red), if $CL_s < 0.05$.

Bibliography

[1] O. S. Bruning, P. Collier, P. Lebrun, S. Myers, R. Ostojic, J. Poole, and P. Proudlock. *LHC Design Report*. CERN, Geneva, 2004.

[2] L. Evans and P. Bryant. LHC Machine. *Journal of Instrumentation*, 3(08):S08001, 2008. URL `http://stacks.iop.org/1748-0221/3/i=08/a=S08001`.

[3] R. R. Wilson. The Tevatron. *Phys.Today*, 30N10:23–30, 1977.

[4] A. Salam. *in Elementary Particle Theory, p. 367*. Almqvist and Wiksell, Stockholm, 1968.

[5] G.'t Hooft. Renormalizable Lagrangians for massive Yang-Mills fields. *Nuclear Physics B*, 35(1):167 – 188, 1971. ISSN 0550-3213. doi: 10.1016/0550-3213(71)90139-8. URL `http://www.sciencedirect.com/science/article/pii/0550321371901398`.

[6] G.'t Hooft and M. Veltman. Regularization and renormalization of gauge fields. *Nuclear Physics B*, 44(1):189 – 213, 1972. ISSN 0550-3213. doi: 10.1016/0550-3213(72)90279-9. URL `http://www.sciencedirect.com/science/article/pii/0550321372902799`.

[7] S. Weinberg. Non-Abelian Gauge Theories of the Strong Interactions. *Phys. Rev. Lett.*, 31:494–497, Aug 1973. doi: 10.1103/PhysRevLett.31.494. URL `http://link.aps.org/doi/10.1103/PhysRevLett.31.494`.

[8] D. J. Gross and F. Wilczek. Ultraviolet Behavior of Non-Abelian Gauge Theories. *Phys. Rev. Lett.*, 30:1343–1346, Jun 1973. doi: 10.1103/PhysRevLett.30.1343. URL `http://link.aps.org/doi/10.1103/PhysRevLett.30.1343`.

[9] H. Fritzsch, M. Gell-Mann, and H. Leutwyler. Advantages of the Color Octet Gluon Picture. *Phys.Lett.*, B47:365–368, 1973. doi: 10.1016/0370-2693(73)90625-4.

[10] F. Englert and R. Brout. Broken Symmetry and the Mass of Gauge Vector Mesons. *Phys.Rev.Lett.*, 13:321–323, 1964. doi: 10.1103/PhysRevLett.13.321.

[11] G. S. Guralnik, C. R. Hagen, and T. W. B. Kibble. Global Conservation Laws and Massless Particles. *Phys.Rev.Lett.*, 13:585–587, 1964. doi: 10.1103/PhysRevLett.13.585.

[12] P. W. Higgs. Broken symmetries, massless particles and gauge fields. *Phys. Lett.*, 12:132–133, 1964. doi: 10.1016/0031-9163(64)91136-9.

[13] P. W. Higgs. Broken Symmetries And The Masses Of Gauge Bosons. *Phys. Rev. Lett.*, 13:508–509, 1964. doi: 10.1103/PhysRevLett.13.508.

[14] F. Englert and R. Brout. Broken Symmetry and the Mass of Gauge Vector Mesons. *Phys. Rev. Lett.*, 13:321–323, Aug 1964. doi: 10.1103/PhysRevLett.13.321. URL `http://link.aps.org/doi/10.1103/PhysRevLett.13.321`.

[15] P. W. Higgs. Spontaneous Symmetry Breakdown Without Massless Bosons. *Phys. Rev.*, 145:1156–1163, 1966. doi: 10.1103/PhysRev.145.1156.

[16] The ATLAS Collaboration, G. Aad, et al. The ATLAS Experiment at the CERN Large Hadron Collider. *Journal of Instrumentation*, 3(08):S08003, 2008. URL `http://stacks.iop.org/1748-0221/3/i=08/a=S08003`.

[17] The CMS Collaboration, S. Chatrchyan, et al. The CMS experiment at the CERN LHC. *Journal of Instrumentation*, 3(08):S08004, 2008. URL `http://stacks.iop.org/1748-0221/3/i=08/a=S08004`.

[18] G. Aad et al. Observation of a new particle in the search for the Standard Model Higgs boson with the ATLAS detector at the LHC. *Phys.Lett.*, B716:1–29, 2012. doi: 10.1016/j.physletb.2012.08.020.

[19] S. Chatrchyan et al. Observation of a new boson at a mass of 125 GeV with the CMS experiment at the LHC. *Phys.Lett.*, B716:30–61, 2012. doi: 10.1016/j.physletb.2012.08.021.

[20] A. D. Sakharov. Violation of CP Invariance, C Asymmetry, and Baryon Asymmetry of the Universe. *Pisma Zh.Eksp.Teor.Fiz.*, 5:32–35, 1967. doi: 10.1070/PU1991v034n05ABEH002497.

[21] C. T. Hill and E. H. Simmons. Strong dynamics and electroweak symmetry breaking. *Phys.Rept.*, 381:235–402, 2003. doi: 10.1016/S0370-1573(03)00140-6.

[22] K. Lane. Search for low-scale technicolor at the Tevatron. *hep-ph/0605119*, 2006.

[23] D. E. Knuth. *The TeXbook: a complete user's guide to computer typesetting with TEX*. Addison-Wesley, 1984. ISBN 0-201-13447-0.

[24] T. Ohl. Drawing Feynman Diagrams with Latex and METAFONT, December 1996. URL `http://www.ctan.org/pkg/feynmf`.

[25] F. Rademakers, P. Canal, B. Bellenot, O. Couet, A. Naumann, G. Ganis, M. Tadel, L. Moneta, V. Vasilev, A. Gheata, P. Russo, and R. Brun. ROOT, 2013. URL `http://root.cern.ch`.

[26] G. v. Rossum. Python v2.6.2 documentation, April 2009. URL `http://docs.python.org/release/2.6.2/index.html`.

[27] W. Lavrijsen. PyROOT, December 2012. URL `http://wlav.web.cern.ch/wlav/pyroot/`.

[28] D. Griffiths. *Introduction to Elementary Particles*. John Wiley & Sons, New York, USA, 1987.

[29] F. Halzen and A. D. Martin. *Quarks and Leptons*. 1985.

[30] R. K. Ellis, W. J. Stirling, and B. R. Webber. *QCD and Collider Physics*, volume 8. Cambridge University Press, 1996.

[31] C. Kiefer. Quantum gravity: general introduction and recent developments. *Annalen der Physik*, 518:129–148, January 2006. doi: 10.1002/andp.200510175.

[32] S. Carlip. Quantum gravity: A Progress report. *Rept.Prog.Phys.*, 64:885, 2001. doi: 10.1088/0034-4885/64/8/301.

[33] Wikimedia Commons. Standard Model of Elementary Particles, June 2006. URL `http://en.wikipedia.org/wiki/File:Standard_Model_of_Elementary_Particles.svg`.

[34] M. C. Gonzalez-Garcia and Y. Nir. Neutrino masses and mixing: Evidence and implications. *Rev.Mod.Phys.*, 75:345–402, 2003. doi: 10.1103/RevModPhys.75.345.

[35] G. L. Fogli, E. Lisi, A. Marrone, D. Montanino, A. Palazzo, et al. Global analysis of neutrino masses, mixings and phases: entering the era of leptonic CP violation searches. *Phys.Rev.*, D86:013012, 2012. doi: 10.1103/PhysRevD.86.013012.

[36] S. L. Glashow. Partial Symmetries of Weak Interactions. *Nucl. Phys.*, 22:579–588, 1961. doi: 10.1016/0029-5582(61)90469-2.

[37] S. Weinberg. A Model of Leptons. *Phys.Rev.Lett.*, 19:1264–1266, 1967. doi: 10.1103/PhysRevLett.19.1264.

[38] A. Salam. Gauge Unification of Fundamental Forces. *Rev. Mod. Phys.*, 52:525–538, 1980. doi: 10.1103/RevModPhys.52.525.

[39] J. Beringer et al. The Review of Particle Physics. *Physical Review D*, 86(010001), 2012.

[40] H. Yukawa. On the interaction of elementary particles. *Proc. Phys. Math. Soc. Jap.*, 17:48–57, 1935.

[41] The CKMfitter Group: J. Charles et al. CP violation and the CKM matrix: Assessing the impact of the asymmetric B factories. *Eur. Phys. J.*, C41:1–131, 2005. doi: 10.1140/epjc/s2005-02169-1.

[42] A. Höcker, H. Lacker, S. Laplace, and F. Le Diberder. A new approach to a global fit of the CKM matrix. *Eur.Phys.J.*, C21:225–259, 2001. doi: 10.1007/s100520100729. 66 pages, added figures, corrected typos, no quantitative changes Report-no: LAL 01-06.

[43] M. Kobayashi and T. Maskawa. CP Violation in the Renormalizable Theory of Weak Interaction. *Prog. Theor. Phys.*, 49:652–657, 1973. doi: 10.1143/PTP.49.652.

[44] B. Pontecorvo. Superweak interactions and double beta decay. *Phys.Lett.*, B26: 630–632, 1968. doi: 10.1016/0370-2693(68)90437-1.

[45] Z. Maki, M. Nakagawa, and S. Sakata. Remarks on the unified model of elementary particles. *Prog.Theor.Phys.*, 28:870–880, 1962. doi: 10.1143/PTP.28.870.

[46] M. Kobayashi and T. Maskawa. CP violation in the Renormalizable Theory of Weak Interaction. *Progr. Theor. Phys.*, 49(2):6, Feb 1973.

[47] J. Charles, A. Höcker, H. Lacker, S. Laplace, F. R. Le Diberder, J. Malcles, J. Ocariz, M. Pivk, and L. Roos. CP violation and the CKM matrix: assessing the impact of the asymmetric B factories. *The European Physical Journal C - Particles and Fields*, 41:1–131, 2005. ISSN 1434-6044. URL `http://dx.doi.org/10.1140/epjc/s2005-02169-1`. 10.1140/epjc/s2005-02169-1.

[48] L. Wolfenstein. Parametrization of the Kobayashi-Maskawa Matrix. *Phys. Rev. Lett.*, 51:1945–1947, Nov 1983. doi: 10.1103/PhysRevLett.51.1945. URL `http://link.aps.org/doi/10.1103/PhysRevLett.51.1945`.

[49] P. H. Frampton, P.Q. Hung, and M. Sher. Quarks and leptons beyond the third generation. *Phys.Rept.*, 330:263, 2000. doi: 10.1016/S0370-1573(99)00095-2.

[50] B. Holdom. The discovery of the fourth family at the LHC: what if? *Journal of High Energy Physics*, 2006(08):076, 2006. URL `http://stacks.iop.org/1126-6708/2006/i=08/a=076`.

[51] Y. Nambu and G. Jona-Lasinio. Dynamical Model of Elementary Particles Based on an Analogy with Superconductivity. I. *Physical Review*, 122:345–358, April 1961. doi: 10.1103/PhysRev.122.345.

[52] Y. Nambu and G. Jona-Lasinio. Dynamical Model of Elementary Particles Based on an Analogy with Superconductivity. II. *Physical Review*, 124:246–254, October 1961. doi: 10.1103/PhysRev.124.246.

[53] H. Pagels and S. Stokar. Pion decay constant, electromagnetic form factor, and quark electromagnetic self-energy in quantum chromodynamics. *Phys. Rev. D*, 20: 2947–2952, Dec 1979. doi: 10.1103/PhysRevD.20.2947. URL `http://link.aps.org/doi/10.1103/PhysRevD.20.2947`.

[54] H. Georgi and S. L. Glashow. Unity of All Elementary-Particle Forces. *Phys. Rev. Lett.*, 32:438–441, Feb 1974. doi: 10.1103/PhysRevLett.32.438. URL `http://link.aps.org/doi/10.1103/PhysRevLett.32.438`.

[55] P. Q. Hung. Minimal $SU(5)$ resuscitated by longlived quarks and leptons. *Phys.Rev.Lett.*, 80:3000–3003, 1998. doi: 10.1103/PhysRevLett.80.3000.

[56] W. E. Caswell. Asymptotic Behavior of Non-Abelian Gauge Theories to Two-Loop Order. *Phys. Rev. Lett.*, 33:244–246, Jul 1974. doi: 10.1103/PhysRevLett.33.244. URL `http://link.aps.org/doi/10.1103/PhysRevLett.33.244`.

[57] P. Q. Hung and C. Xiong. Implication of a Quasi Fixed Point with a Heavy Fourth Generation: The emergence of a TeV-scale physical cutoff. *Phys.Lett.*, B694:430–434, 2011. doi: 10.1016/j.physletb.2010.10.004.

[58] D. N. Spergel et al. First year Wilkinson Microwave Anisotropy Probe (WMAP) observations: Determination of cosmological parameters. *Astrophys.J.Suppl.*, 148: 175–194, 2003. doi: 10.1086/377226.

[59] J. M. Cline. Baryogenesis. *hep-ph/0609145*, 2006.

[60] C. Jarlskog. Commutator of the Quark Mass Matrices in the Standard Electroweak Model and a Measure of Maximal CP Nonconservation. *Phys. Rev. Lett.*, 55:1039–1042, Sep 1985. doi: 10.1103/PhysRevLett.55.1039. URL `http://link.aps.org/doi/10.1103/PhysRevLett.55.1039`.

[61] V. A. Kuzmin, V. A. Rubakov, and M. E. Shaposhnikov. On anomalous electroweak baryon-number non-conservation in the early universe. *Physics Letters B*, 155:36–42, May 1985. doi: 10.1016/0370-2693(85)91028-7.

[62] G. W-S. Hou. Source of CP Violation for the Baryon Asymmetry of the Universe. *Int.J.Mod.Phys.*, D20:1521–1532, 2011. doi: 10.1142/S0218271811019694.

[63] G. W-S. Hou. Source of CP Violation for the Baryon Asymmetry of the Universe. *Chin.J.Phys.*, 47:134, 2009.

[64] H-S. Lee, Z. Liu, and A. Soni. Neutrino dark matter candidate in fourth generation scenarios. *Phys.Lett.*, B704:30–35, 2011. doi: 10.1016/j.physletb.2011.08.051.

[65] Y-F. Zhou. Probing the fourth generation Majorana neutrino dark matter. *Phys.Rev.*, D85:053005, 2012. doi: 10.1103/PhysRevD.85.053005.

[66] P. Schwaller. Long Lived 4th generation, Higgs physics, and cosmology, 2011. URL `https://indico.desy.de/materialDisplay.py?contribId=10&materialId=slides&confId=3531`. Slides of a talk given at 2nd workshop on single top quark production and fourth generations at DESY Hamburg, Germany.

[67] A. J. Buras, R. Fleischer, S. Recksiegel, and F. Schwab. Anatomy of prominent B and K decays and signatures of CP violating new physics in the electroweak penguin sector. *Nucl.Phys.*, B697:133–206, 2004. doi: 10.1016/j.nuclphysb.2004.07.009.

[68] M. S. Chanowitz. Electroweak Constraints on the Fourth Generation at Two Loop Order. *hep-ph/1212.3209*, 2012.

[69] T. Yanir. Phenomenological constraints on extended quark sectors. *JHEP*, 0206: 044, 2002.

[70] G. W-S. Hou, M. Nagashima, and A. Soddu. Difference in B^+ and B^0 direct CP asymmetry as effect of a fourth generation. *Phys.Rev.Lett.*, 95:141601, 2005. doi: 10.1103/PhysRevLett.95.141601.

[71] M. Bobrowski, A. Lenz, J. Riedl, and J. Rohrwild. How much space is left for a new family of fermions? *Phys.Rev.*, D79:113006, 2009. doi: 10.1103/PhysRevD.79.113006.

[72] A. J. Buras, B. Duling, T. Feldmann, T. Heidsieck, C. Promberger, et al. Patterns of Flavour Violation in the Presence of a Fourth Generation of Quarks and Leptons. *JHEP*, 1009:106, 2010. doi: 10.1007/JHEP09(2010)106.

[73] A. J. Buras, B. Duling, T. Feldmann, T. Heidsieck, C. Promberger, et al. The Impact of a 4th Generation on Mixing and CP Violation in the Charm System. *JHEP*, 1007:094, 2010. doi: 10.1007/JHEP07(2010)094.

[74] A. N. Rozanov and M. I. Vysotsky. $(\Delta A_{CP})_{LHCb}$ and the fourth generation. *hep-ph/1111.6949*, 2011.

[75] The LHCb Collaboration, A. A. Alves Jr, et al. The LHCb Detector at the LHC. *Journal of Instrumentation*, 3(08):S08005, 2008. URL `http://stacks.iop.org/1748-0221/3/i=08/a=S08005`.

[76] R. Aaij et al. Evidence for CP violation in time-integrated $D^0 \to h^-h^+$ decay rates. *Phys.Rev.Lett.*, 108:111602, 2012. doi: 10.1103/PhysRevLett.108.129903, 10.1103/PhysRevLett.108.111602.

[77] S. Schael et al. Precision electroweak measurements on the Z resonance. *Phys.Rept.*, 427:257–454, 2006. doi: 10.1016/j.physrep.2005.12.006.

[78] S. Myers. *The LEP Collider, from Design to Approval and Commissioning: CAS Cern Accelerator School; 6th John Adams Memorial Lecture; Delivered at CERN on 26 November 1990*. CERN, 1991. URL `http://books.google.de/books?id=Ny7EtgAACAAJ`.

[79] M. E. Peskin and T. Takeuchi. New constraint on a strongly interacting Higgs sector. *Phys. Rev. Lett.*, 65:964–967, Aug 1990. doi: 10.1103/PhysRevLett.65.964. URL `http://link.aps.org/doi/10.1103/PhysRevLett.65.964`.

[80] M. E. Peskin and T. Takeuchi. Estimation of oblique electroweak corrections. *Phys. Rev. D*, 46:381–409, Jul 1992. doi: 10.1103/PhysRevD.46.381. URL `http://link.aps.org/doi/10.1103/PhysRevD.46.381`.

[81] H-J. He, N. Polonsky, and S-F. Su. Extra families, Higgs spectrum and oblique corrections. *Phys.Rev.*, D64:053004, 2001. doi: 10.1103/PhysRevD.64.053004.

[82] G. D. Kribs, T. Plehn, M. Spannowsky, and T. M. P. Tait. Four generations and Higgs physics. *Phys.Rev.*, D76:075016, 2007. doi: 10.1103/PhysRevD.76.075016.

[83] J. Alcaraz et al. A Combination of preliminary electroweak measurements and constraints on the standard model. 2006.

[84] M. S. Chanowitz. Bounding CKM Mixing with a Fourth Family. *Phys.Rev.*, D79: 113008, 2009. doi: 10.1103/PhysRevD.79.113008.

[85] M. S. Chanowitz. Higgs Mass Constraints on a Fourth Family: Upper and Lower Limits on CKM Mixing. *Phys.Rev.*, D:035018, 2010. doi: 10.1103/PhysRevD.82.035018.

[86] J. Erler and P. Langacker. Precision Constraints on Extra Fermion Generations. *Phys.Rev.Lett.*, 105:031801, 2010. doi: 10.1103/PhysRevLett.105.031801.

[87] O. Eberhardt, A. Lenz, and J. Rohrwild. Less space for a new family of fermions. *Phys.Rev.*, D82:095006, 2010. doi: 10.1103/PhysRevD.82.095006.

[88] O. Eberhardt. CKM fits of the fourth family parameters, 2011. Slides of a talk given at the SuperB physics meeting in Frascati, Italy, 12th December 2011. The values were obtained via private communication.

[89] B. W. Lee, C. Quigg, and H. B. Thacker. Weak interactions at very high energies: The role of the Higgs-boson mass. *Phys. Rev. D*, 16:1519–1531, Sep 1977. doi: 10.1103/PhysRevD.16.1519. URL `http://link.aps.org/doi/10.1103/PhysRevD.16.1519`.

[90] M. S. Chanowitz, M. A. Furman, and I. Hinchliffe. Weak interactions of ultra heavy fermions (II). *Nuclear Physics B*, 153:402–430, 1979. doi: 10.1016/0550-3213(79)90606-0.

[91] W. Marciano, G. Valencia, and S. Willenbrock. Renormalization-group-improved unitarity bounds on the Higgs-boson and top-quark masses. *Phys. Rev. D*, 40: 1725–1729, Sep 1989. doi: 10.1103/PhysRevD.40.1725. URL `http://link.aps.org/doi/10.1103/PhysRevD.40.1725`.

[92] P. Gerhold, K. Jansen, and J. Kallarackal. Higgs boson mass bounds in the presence of a very heavy fourth quark generation. *JHEP*, 1101:143, 2011. doi: 10.1007/JHEP01(2011)143.

[93] G. Aad et al. Search for pair-produced heavy quarks decaying to Wq in the two-lepton channel at $\sqrt{s} = 7\,\text{TeV}$ with the ATLAS detector. *Phys.Rev.*, D86:012007, 2012. doi: 10.1103/PhysRevD.86.012007.

[94] G. Aad et al. Search for pair production of a heavy up-type quark decaying to a W boson and a b quark in the lepton+jets channel with the ATLAS detector. *Phys.Rev.Lett.*, 108:261802, 2012. doi: 10.1103/PhysRevLett.108.261802.

[95] CMS Collaboration. Search for heavy, top-like quark pair production in the dilepton final state in pp collisions at $\sqrt{s} = 7\,\text{TeV}$. *Phys.Lett.*, B716:103–121, 2012. doi: 10.1016/j.physletb.2012.07.059.

[96] G. Aad et al. Search for down-type fourth generation quarks with the ATLAS detector in events with one lepton and hadronically decaying W bosons. *Phys.Rev.Lett.*, 109:032001, 2012. doi: 10.1103/PhysRevLett.109.032001.

[97] S. Chatrchyan et al. Search for heavy bottom-like quarks in 4.9 inverse femtobarns of pp collisions at $\sqrt{s} = 7\,\text{TeV}$. *JHEP*, 1205:123, 2012. doi: 10.1007/JHEP05(2012)123.

[98] G. Aad et al. Search for exotic same-sign dilepton signatures (b' quark, $T_{5/3}$ and four top quarks production) in $4.7/fb$ of pp collisions at $\sqrt{s} = 7\,\text{TeV}$ with the ATLAS detector. Technical Report ATLAS-CONF-2012-130, CERN, Geneva, Sep 2012.

[99] CMS Collaboration. Inclusive search for a sequential fourth generation of quarks. Technical Report CMS-PAS-EXO-11-098, CERN, Geneva, 2012.

[100] P. Q. Hung and M. Sher. Experimental constraints on fourth generation quark masses. *Phys.Rev.*, D77:037302, 2008. doi: 10.1103/PhysRevD.77.037302.

[101] B. Adeva et al. The construction of the L3 experiment. *Nuclear Instruments and Methods in Physics Research Section A: Accelerators, Spectrometers, Detectors and Associated Equipment*, 289(1-2):35–102, 1990. ISSN 0168-9002. doi: 10.1016/0168-9002(90)90250-A. URL `http://www.sciencedirect.com/science/article/pii/016890029090250A`.

[102] P. Achard et al. Search for heavy neutral and charged leptons in e^+e^- annihilation at LEP. *Phys.Lett.*, B517:75–85, 2001. doi: 10.1016/S0370-2693(01)01005-X.

[103] L. M. Carpenter and A. Rajaraman. Revisiting Constraints on Fourth Generation Neutrino Masses. *Phys.Rev.*, D82:114019, 2010. doi: 10.1103/PhysRevD.82.114019.

[104] LHC Higgs Cross Section Working Group, S. Dittmaier, C. Mariotti, G. Passarino, and R. Tanaka (Eds.). Handbook of LHC Higgs Cross Sections: 2. Differential Distributions. *CERN-2012-002*, CERN, Geneva, 2012.

[105] J. F. Gunion, D. W. McKay, and H. Pois. Gauge coupling unification and the minimal SUSY model: a Fourth generation below the top? *Phys.Lett.*, B334: 339–347, 1994. doi: 10.1016/0370-2693(94)90698-X.

[106] J. F. Gunion, D. W. McKay, and H. Pois. A Minimal four family supergravity model. *Phys.Rev.*, D53:1616–1647, 1996. doi: 10.1103/PhysRevD.53.1616.

[107] X. Ruan and Z. Zhang. Impact on the Higgs Production Cross Section and Decay Branching Fractions of Heavy Quarks and Leptons in a Fourth Generation Model. 2011.

[108] A. Djouadi and A. Lenz. Sealing the fate of a fourth generation of fermions. *Phys.Lett.*, B715:310–314, 2012. doi: 10.1016/j.physletb.2012.07.060.

[109] A. Djouadi, J. Kalinowski, and M. Spira. HDECAY: A Program for Higgs boson decays in the standard model and its supersymmetric extension. *Comput.Phys.Commun.*, 108:56–74, 1998. doi: 10.1016/S0010-4655(97)00123-9.

[110] M. Spira. HIGLU: A program for the calculation of the total Higgs production cross-section at hadron colliders via gluon fusion including QCD corrections. 1995.

[111] A. Djouadi, P. Gambino, and B. A. Kniehl. Two loop electroweak heavy fermion corrections to Higgs boson production and decay. *Nucl.Phys.*, B523:17–39, 1998. doi: 10.1016/S0550-3213(98)00147-3.

[112] O. Eberhardt, G. Herbert, H. Lacker, A. Lenz, A. Menzel, U. Nierste, and M. Wiebusch. Joint analysis of Higgs boson decays and electroweak precision observables in the standard model with a sequential fourth generation. *Phys. Rev. D*, 86:013011, Jul 2012. doi: 10.1103/PhysRevD.86.013011. URL `http://link.aps.org/doi/10.1103/PhysRevD.86.013011`.

[113] O. Eberhardt, A. Lenz, A. Menzel, U. Nierste, and M. Wiebusch. Status of the fourth fermion generation before ICHEP2012: Higgs data and electroweak precision observables. *Phys. Rev. D*, 86:074014, Oct 2012. doi: 10.1103/PhysRevD.86.074014. URL `http://link.aps.org/doi/10.1103/PhysRevD.86.074014`.

[114] O. Eberhardt, G. Herbert, H. Lacker, A. Lenz, A. Menzel, et al. Impact of a Higgs boson at a mass of 126 GeV on the standard model with three and four fermion generations. *Phys.Rev.Lett.*, 109:241802, 2012. doi: 10.1103/PhysRevLett.109.241802.

[115] CDF Group, D0 Collaborations, the Tevatron New Physics, and Higgs Working. Updated Combination of CDF and D0 Searches for Standard Model Higgs Boson Production with up to 10.0 fb^{-1} of Data. 2012.

[116] M. Wiebusch. Numerical Computation of p-values with myFitter. 2012.

[117] S. Bar-Shalom, M. Geller, S. Nandi, and A. Soni. Two Higgs doublets, a 4th generation and a 125 GeV Higgs. 2012.

[118] HERA Collaboration. HERA - A Proposal for a Large Electron Proton Colliding Beam Facility at DESY. 1981.

[119] A. D. Martin, W. J. Stirling, R. S. Thorne, and G. Watt. Parton distributions for the LHC. *Eur.Phys.J.*, C63:189–285, 2009. doi: 10.1140/epjc/s10052-009-1072-5.

[120] J. Pumplin, D. R. Stump, J. Huston, H. L. Lai, Pavel M. Nadolsky, et al. New generation of parton distributions with uncertainties from global QCD analysis. *JHEP*, 0207:012, 2002.

[121] H-L. Lai, M. Guzzi, J. Huston, Z. Li, P. M. Nadolsky, et al. New parton distributions for collider physics. *Phys.Rev.*, D82:074024, 2010. doi: 10.1103/PhysRevD.82.074024.

[122] M. Aliev, H. Lacker, U. Langenfeld, S. Moch, P. Uwer, et al. HATHOR: HAdronic Top and Heavy quarks crOss section calculatoR. *Comput.Phys.Commun.*, 182: 1034–1046, 2011. doi: 10.1016/j.cpc.2010.12.040.

[123] M. R. Whalley, D. Bourilkov, and R. C. Group. The Les Houches accord PDFs (LHAPDF) and LHAGLUE. 2005.

[124] A. D. Martin, W. J. Stirling, R. S. Thorne, and G. Watt. Uncertainties on α_s in global PDF analyses and implications for predicted hadronic cross sections. *Eur.Phys.J.*, C64:653–680, 2009. doi: 10.1140/epjc/s10052-009-1164-2.

[125] S. Chatrchyan et al. Measurement of the single-top-quark t-channel cross section in pp collisions at $\sqrt{s} = 7\,\text{TeV}$. *J. High Energy Phys.*, 12(arXiv:1209.4533. CMS-TOP-11-021. CERN-PH-EP-2012-274):41, Sep 2012.

[126] S. Chatrchyan et al. Measurement of the single-top t-channel cross section in pp collisions at centre-of-mass energy of 8 TeV. Technical Report CMS-PAS-TOP-12-011, CERN, Geneva, 2012.

[127] The ATLAS Collaboration, G. Aad, et al. Measurement of t-Channel Single Top-Quark Production in pp Collisions at $\sqrt{s} = 8\,\text{TeV}$ with the ATLAS detector. Technical Report ATLAS-CONF-2012-132, CERN, Geneva, Sep 2012.

[128] H. Lacker, A. Menzel, F. Spettel, D. Hirschbuhl, J. Luck, et al. Model-independent extraction of $|V_{tq}|$ matrix elements from top-quark measurements at hadron colliders. *Eur.Phys.J.*, C72:2048, 2012. doi: 10.1140/epjc/s10052-012-2048-4.

[129] C. Lefevre. The CERN accelerator complex. Complexe des accelerateurs du CERN. Dec 2008. URL `http://cds.cern.ch/record/1260465`.

[130] I. G. Brown. *The physics and technology of ion sources*. Wiley-VCH, Weinheim, 2004. ISBN 3-527-40410-4, 978-3-527-40410-0.

[131] L. Rossi. Superconductivity: its role, its success and its setbacks in the Large Hadron Collider of CERN. *Superconductor Science and Technology*, 23(3):034001, 2010. URL `http://stacks.iop.org/0953-2048/23/i=3/a=034001`.

[132] The ALICE Collaboration, K. Aamodt, et al. The ALICE experiment at the CERN LHC. *Journal of Instrumentation*, 3(08):S08002, 2008. URL `http://stacks.iop.org/1748-0221/3/i=08/a=S08002`.

[133] Wikimedia Commons. A graphic showing the relationship between angle and pseudorapidity, May 2007. URL `http://en.wikipedia.org/wiki/File:Pseudorapidity2.png`.

[134] D. V. Schroeder. *An Introduction to Thermal Physics*. Addison Wesley Longman, 2000.

[135] The ATLAS Collaboration. ATLAS: Detector and physics performance technical design report. Volume 1. Technical Report CERN-LHCC-99-14, CERN, 1999.

[136] I. Gorelov, G. Gorfine, M. Hoeferkamp, S. C. Seidel, A. Ciocio, et al. A measurement of Lorentz angle and spatial resolution of radiation hard silicon pixel sensors. *Nucl.Instrum.Meth.*, A481:204–221, 2002. doi: 10.1016/S0168-9002(01)01413-9.

[137] ATLAS Collaboration. ATLAS liquid argon calorimeter: Technical design report. 1996.

[138] ATLAS Collaboration. ATLAS tile calorimeter: Technical design report. 1996.

[139] H. Bethe. Zur Theorie des Durchgangs schneller Korpuskularstrahlen durch Materie. *Annalen der Physik*, 397:325–400, 1930. doi: 10.1002/andp.19303970303.

[140] G. Aad et al. Commissioning of the ATLAS Muon Spectrometer with Cosmic Rays. *Eur.Phys.J.*, C70:875–916, 2010. doi: 10.1140/epjc/s10052-010-1415-2.

[141] J. Haller, A. Dos Anjos, N. Ellis, M. Landon, R. Spiwoks, T. Wengler, W. Wiedenmann, and H. Zobernig. Configuration of the ATLAS trigger. Technical Report ATL-DAQ-CONF-2005-024. ATL-COM-DAQ-2005-030. CERN-ATL-COM-DAQ-2005-030, CERN, Geneva, 2005.

[142] ATLAS Collaboration. Luminosity Determination in pp Collisions at $\sqrt{s} = 7\,\text{TeV}$ using the ATLAS Detector in 2011. Technical Report ATLAS-CONF-2011-116, CERN, Geneva, Aug 2011.

[143] S. van der Meer. Calibration of the effective beam height in the ISR. Technical Report CERN-ISR-PO-68-31. ISR-PO-68-31, CERN, Geneva, 1968.

[144] M. Bruschi. The ATLAS luminosity monitor. *Nucl.Instrum.Meth.*, A623:371–373, 2010. doi: 10.1016/j.nima.2010.02.252.

[145] V. Cindro et al. The ATLAS Beam Conditions Monitor. *Journal of Instrumentation*, 3(02):P02004, 2008. URL `http://stacks.iop.org/1748-0221/3/i=02/a=P02004`.

[146] P. Jenni, M. Nordberg, M. Nessi, and K. Jon-And. *ATLAS Forward Detectors for Measurement of Elastic Scattering and Luminosity*. Technical Design Report. CERN, Geneva, 2008.

[147] R. G. Newton. Optical theorem and beyond. *American Journal of Physics*, 44: 639–642, July 1976. doi: 10.1119/1.10324.

[148] ATLAS collaboration. Peak Luminosity versus time, 2013. URL `https://atlas.web.cern.ch/Atlas/GROUPS/DATAPREPARATION/PublicPlots/2012/DataSummary/figs/lumivstime.eps`.

[149] ATLAS collaboration. Delivered Luminosity versus time for 2010, 2011, 2012 (p-p data only), 2013. URL `https://atlas.web.cern.ch/Atlas/GROUPS/DATAPREPARATION/PublicPlots/2012/DataSummary/figs/intlumivsyear.eps`.

[150] M. A. Dobbs, S. Frixione, E. Laenen, K. Tollefson, H. Baer, et al. Les Houches guidebook to Monte Carlo generators for hadron collider physics. pages 411–459, 2004.

[151] K. Harada, T. Kaneko, and N. Sakai. Parton primordial transverse momentum in perturbative QCD. *Lettere Al Nuovo Cimento Series 2*, 24:279–283, 1979. ISSN 0375-930X. doi: 10.1007/BF02725423. URL `http://dx.doi.org/10.1007/BF02725423`.

[152] G. Aad, B. Abbott, J. Abdallah, A. A. Abdelalim, A. Abdesselam, O. Abdinov, B. Abi, M. Abolins, H. Abramowicz, H. Abreu, et al. The ATLAS Simulation Infrastructure. *European Physical Journal C*, 70:823–874, December 2010. doi: 10.1140/epjc/s10052-010-1429-9.

[153] T. Gleisberg, S. Hoeche, F. Krauss, M. Schonherr, S. Schumann, et al. Event generation with SHERPA 1.1. *JHEP*, 0902:007, 2009. doi: 10.1088/1126-6708/2009/02/007.

[154] A. Buckley, J. Butterworth, S. Gieseke, D. Grellscheid, S. Höche, et al. General-purpose event generators for LHC physics. *Phys.Rept.*, 504:145–233, 2011. doi: 10.1016/j.physrep.2011.03.005.

[155] M. L. Mangano, F. Piccinini, A. D. Polosa, M. Moretti, and R. Pittau. ALPGEN, a generator for hard multiparton processes in hadronic collisions. *Journal of High Energy Physics*, 2003(07):001, 2003. URL `http://stacks.iop.org/1126-6708/2003/i=07/a=001`.

[156] F. Krauss, R. Kuhn, and G. Soff. AMEGIC++ 1.0: A Matrix element generator in C++. *JHEP*, 0202:044, 2002.

[157] T. Gleisberg and S. Höche. Comix, a new matrix element generator. *JHEP*, 0812: 039, 2008. doi: 10.1088/1126-6708/2008/12/039.

[158] J. Alwall, P. Demin, S. de Visscher, R. Frederix, M. Herquet, et al. MadGraph/MadEvent v4: The New Web Generation. *JHEP*, 0709:028, 2007. doi: 10.1088/1126-6708/2007/09/028.

[159] S. Frixione and B. R. Webber. Matching NLO QCD computations and parton shower simulations. *JHEP*, 0206:029, 2002.

[160] S. Alioli, P. Nason, C. Oleari, and E. Re. A general framework for implementing NLO calculations in shower Monte Carlo programs: the POWHEG BOX. *JHEP*, 1006:043, 2010. doi: 10.1007/JHEP06(2010)043.

[161] P. Nason. A New method for combining NLO QCD with shower Monte Carlo algorithms. *JHEP*, 0411:040, 2004. doi: 10.1088/1126-6708/2004/11/040.

[162] A. Markov. Extension of the Limit Theorems of Probability Theory to a Sum of Variables Connected in a Chain. In R. Howard, editor, *Dynamic Probabilistic Systems (Volume I: Markov Models)*, chapter Appendix B, pages 552–577. John Wiley & Sons, Inc., New York City, 1971.

[163] V. V. Sudakov. Vertex parts at very high-energies in quantum electrodynamics. *Sov.Phys.JETP*, 3:65–71, 1956.

[164] T. Sjöstrand and M. van Zijl. A Multiple Interaction Model for the Event Structure in Hadron Collisions. *Phys.Rev.*, D36:2019, 1987. doi: 10.1103/PhysRevD.36.2019.

[165] T. Sjöstrand, S. Mrenna, and P. Skands. PYTHIA 6.4 physics and manual. *Journal of High Energy Physics*, 2006(05):026, 2006. URL `http://stacks.iop.org/1126-6708/2006/i=05/a=026`.

[166] G. Corcella, I. G. Knowles, G. Marchesini, S. Moretti, K. Odagiri, P. Richardson, M. H. Seymour, and B. R. Webber. HERWIG 6: an event generator for hadron emission reactions with interfering gluons (including supersymmetric processes). *Journal of High Energy Physics*, 2001(01):010, 2001. URL `http://stacks.iop.org/1126-6708/2001/i=01/a=010`.

[167] D. Amati and G. Veneziano. Preconfinement as a property of perturbative QCD. *Physics Letters B*, 83(1):87 – 92, 1979. ISSN 0370-2693. doi: 10.1016/0370-2693(79)90896-7. URL `http://www.sciencedirect.com/science/article/pii/0370269379908967`.

[168] T. Sjöstrand, S. Mrenna, and P. Z. Skands. A Brief Introduction to PYTHIA 8.1. *Comput.Phys.Commun.*, 178:852–867, 2008. doi: 10.1016/j.cpc.2008.01.036.

[169] B. Andersson, G. Gustafson, G. Ingelman, and T. Sjöstrand. Parton fragmentation and string dynamics. *Physics Reports*, 97(2-3):31 – 145, 1983. ISSN 0370-1573. doi:

10.1016/0370-1573(83)90080-7. URL http://www.sciencedirect.com/science/article/pii/0370157383900807.

[170] T. Sjöstrand. Jet fragmentation of multiparton configurations in a string framework. *Nuclear Physics B*, 248(2):469 – 502, 1984. ISSN 0550-3213. doi: 10.1016/0550-3213(84)90607-2. URL http://www.sciencedirect.com/science/article/pii/0550321384906072.

[171] F. A. Berends and W. T. Giele. Recursive Calculations for Processes with n Gluons. *Nucl.Phys.*, B306:759, 1988. doi: 10.1016/0550-3213(88)90442-7.

[172] S. Catani and M. H. Seymour. A General algorithm for calculating jet cross-sections in NLO QCD. *Nucl.Phys.*, B485:291–419, 1997. doi: 10.1016/S0550-3213(96)00589-5.

[173] S. Catani, S. Dittmaier, M. H. Seymour, and Z. Trocsanyi. The Dipole formalism for next-to-leading order QCD calculations with massive partons. *Nucl.Phys.*, B627:189–265, 2002. doi: 10.1016/S0550-3213(02)00098-6.

[174] J-C. Winter, F. Krauss, and G. Soff. A Modified cluster hadronization model. *Eur.Phys.J.*, C36:381–395, 2004. doi: 10.1140/epjc/s2004-01960-8.

[175] J. Alwall, M. Herquet, F. Maltoni, O. Mattelaer, and T. Stelzer. MadGraph 5 : Going Beyond. *JHEP*, 1106:128, 2011. doi: 10.1007/JHEP06(2011)128.

[176] H. Murayama, I. Watanabe, and K. Hagiwara. HELAS: HELicity amplitude subroutines for Feynman diagram evaluations. 1992.

[177] ATLAS collaboration. Summary of ATLAS Pythia 8 tunes. Technical Report ATL-PHYS-PUB-2012-003, CERN, Geneva, Aug 2012.

[178] G. Duckeck et al. ATLAS computing: Technical design report. 2005.

[179] S. Agostinelli et al. Geant4 - a simulation toolkit. *Nuclear Instruments and Methods in Physics Research Section A: Accelerators, Spectrometers, Detectors and Associated Equipment*, 506(3):250 – 303, 2003. ISSN 0168-9002. doi: 10.1016/S0168-9002(03)01368-8. URL http://www.sciencedirect.com/science/article/pii/S0168900203013688.

[180] J. Boudreau and V. Tsulaia. The GeoModel toolkit for detector description. pages 353–356, 2005.

[181] E. Barberio, J. Boudreau, B. Butler, S. L. Cheung, A. Della Acqua, et al. The Geant4-Based ATLAS Fast Electromagnetic Shower Simulation. 2007.

[182] D. Cavalli, D. Costanzo, S. Dean, M. Dührssen, S. Hassani, M. Heldmann, K. Jakobs, A. Nairz, A. Phillips, S. Resconi, E. Richter-Was, P. Sherwood, L. Vacavant, I. Vivarelli, J. B. De Vivie de Regie, and I. Wingerter-Seez. Performance of

the ATLAS fast simulation ATLFAST. Technical Report ATL-PHYS-INT-2007-005. ATL-COM-PHYS-2007-012, CERN, Geneva, Jan 2007.

[183] E. Torro Pastor, D. Cote, and X. Portell Bueso. Validation of the ATLFAST-II package for the simulation of supersymmetry events. Technical Report ATL-COM-PHYS-2011-1181, CERN, Geneva, Sep 2011.

[184] M Dührssen. The fast calorimeter simulation FastCaloSim. Technical Report ATL-PHYS-INT-2008-043. ATL-COM-PHYS-2008-093, CERN, Geneva, Jul 2008.

[185] K. Edmonds, S. Fleischmann, T. Lenz, C. Magass, J. Mechnich, and A. Salzburger. The Fast ATLAS Track Simulation (FATRAS). Technical Report ATL-SOFT-PUB-2008-001. ATL-COM-SOFT-2008-002, CERN, Geneva, Mar 2008.

[186] H. Bethe and W. Heitler. On the Stopping of Fast Particles and on the Creation of Positive Electrons. *Royal Society of London Proceedings Series A*, 146:83–112, August 1934. doi: 10.1098/rspa.1934.0140.

[187] D. Cavalli, W. Davey, S. Dean, M. Dührssen, S. Elles, M. Hohlfeld, K. Jakobs, E. Schmidt, I. Vivarelli, and S. Yamamoto. Validation of the fast calorimeter simulation FastCaloSim against the Athena release 10 and 13.0.40 full simulation. Technical Report ATL-PHYS-INT-2009-073, CERN, Geneva, Aug 2009.

[188] D. Adams, S. Asai, D. Cavalli, M. Dührssen, K. Edmonds, S. Elles, M. Fehling, U. Felzmann, L. Gladilin, L. Helary, M. Hohlfeld, S. Horvat, K. Jakobs, M. Kaneda, G. Kirsch, S. Kuehn, J. F. Marchand, C. Pizio, X. Portell, D. Rebuzzi, E. Schmidt, A. Shibata, I. Vivarelli, S. Winkelmann, and S. Yamamoto. The ATLFAST-II performance in release 14 -particle signatures and selected benchmark processes-. Technical Report ATL-PHYS-INT-2009-110, CERN, Geneva, Dec 2009.

[189] Collaboration ATLAS, M. Beckingham, M. Duehrssen, E. Schmidt, M. Shapiro, M. Venturi, J. Virzi, I. Vivarelli, M. Werner, S. Yamamoto, and T. Yamanaka. The simulation principle and performance of the ATLAS fast calorimeter simulation FastCaloSim. Technical Report ATL-PHYS-PUB-2010-013, CERN, Geneva, Oct 2010.

[190] ATLAS collaboration. Number of Interactions per Crossing, 2013. URL `https://atlas.web.cern.ch/Atlas/GROUPS/DATAPREPARATION/InteractionsperCrossing/muplot/2012/mu_2011_2012-nov.eps`.

[191] G Aad et al. *Expected performance of the ATLAS experiment: detector, trigger and physics*. CERN, Geneva, 2009.

[192] G. Aad et al. Electron performance measurements with the ATLAS detector using the 2010 LHC proton-proton collision data. *The European Physical Journal C*, 72:1–46, 2012. ISSN 1434-6044. doi: 10.1140/epjc/s10052-012-1909-1. URL `http://dx.doi.org/10.1140/epjc/s10052-012-1909-1`.

[193] ATLAS collaboration. Improved electron reconstruction in ATLAS using the Gaussian Sum Filter-based model for bremsstrahlung. Technical Report ATLAS-CONF-2012-047, CERN, Geneva, May 2012.

[194] R. Fruhwirth. Application of Kalman filtering to track and vertex fitting. *Nucl.Instrum.Meth.*, A262:444–450, 1987. doi: 10.1016/0168-9002(87)90887-4.

[195] T. M. Atkinson. *Electron reconstruction with the ATLAS Inner Detector*. PhD thesis, University of Melbourne, Australia, 2006.

[196] ATLAS collaboration. Electron reconstruction and identification efficiencies, 2012. URL `https://atlas.web.cern.ch/Atlas/GROUPS/PHYSICS/EGAMMA/PublicPlots/20120611/ElectronEfficiency2012/ATL-COM-PHYS-2011-783/ATL-COM-PHYS-2011-783.pdf`.

[197] ATLAS collaboration. Expected electron performance in the ATLAS experiment. Technical Report ATL-PHYS-PUB-2011-006, CERN, Geneva, Apr 2011.

[198] D. Banfi, L. Carminati, and L. Mandelli. Calibration of the ATLAS electromagnetic calorimeter using calibration hits. Technical Report ATL-LARG-PUB-2007-012. ATL-COM-LARG-2007-007, CERN, Geneva, Jul 2007.

[199] G. Unal and D. Froidevaux. Higgs mass measurements and uncertainties in 2011 and 2012 data. Technical Report ATL-COM-PHYS-2012-1774, CERN, Geneva, Dec 2012. Internal ATLAS support note.

[200] T. Skwarnicki. A study of the radiative CASCADE transitions between the Upsilon-Prime and Upsilon resonances. 1986.

[201] M. Cacciari and G. P. Salam. Pileup subtraction using jet areas. *Phys.Lett.*, B659: 119–126, 2008. doi: 10.1016/j.physletb.2007.09.077.

[202] M. Cacciari, G. P. Salam, and S. Sapeta. On the characterisation of the underlying event. *JHEP*, 1004:065, 2010. doi: 10.1007/JHEP04(2010)065.

[203] B. Acharya, J. Adelman, S. Adomeit, M. Aoki, B. Alvarez, F. Balli, W. Bell, K. Becker, K. Behr, D. Benjamin, E. Bergeaas Kuutmann, C. Bernard, K. Black, S. Calvet, R. Camacho, Y. Coadou, G. Cortiana, N. Cooper-Smith, T. Cornelissen, M. Cristinziani, V. Dao, U. De Sanctis, C. Doglioni, F. Derue, K. Finelli, K. J. Grahn, J. Groth-Jensen, S. Head, A. Henrichs, D. Hirschbuehl, V. Kaushik, O. M. Kind, A. Krasznahorkay, T. Kuhl, E. Le Menedeu, HC. Lee, A. Lister, K. F. Loureiro, L. Miljovic, J. D. Morris, R. Moles Valls, O. Nackenhorst, D. Pelikan, M. Owen, M. Pinamonti, K. Rao, K. Rosbach, M. Rudolph, G. Salamanna, J. Schwindling, J. Searcy, E. Shabalina, K. Shaw, J. Sjolin, R. Soualah, S. Stamm, D. B. Ta, T. Theveneaux-Pelzer, E. Thompson, K. Uchida, L. Valery, M. Vreeswijk, C. Wasicki, I. J. Watson, K. Yau, J. Zhong, H. Zhu, and M. zur Nedden. Object selection and calibration, background estimations and MC samples for the Winter

2013 Top Quark analyses with 2012 data. Technical Report ATL-COM-PHYS-2013-088, CERN, Geneva, Jan 2013. Internal ATLAS support note.

[204] ATLAS collaboration. ATLAS muon spectrometer: Technical design report. 1997.

[205] P. Bagnaia, T. Baroncelli, O. Biebel, C. Bini, S. Borroni, P. Celio, M. Cirilli, M. Curti, A. De Salvo, M. Deile, S. Di Luise, A. Di Mattia, E. Diehl, G. Dimitrov, J. Dubbert, G. Duckeck, S. Falciano, S. Gadomski, P. Gauzzi, M. Groh, R. Hertenberger, N. Hessey, S. Horvat, M. Iodice, S. Kaiser, O. Kortner, H. Kroha, S. Kolos, D. Levin, L. Luminari, B. Martin, S. McKee, D. Merkl, D. Orestano, E. Pasqualucci, F. Petrucci, L. Pontecorvo, I. Potrap, F. Rauscher, S. Rosati, E. S. Camillocci, L. Spogli, R. Ströhmer, F. T. A. Viegas, M. Verducci, E. Vilucchi, N. Van Eldik, Z. van Kesteren, J. von Loeben, M. Woudstra, and B. Zhou. Calibration model for the MDT chambers of the ATLAS Muon Spectrometer. Technical Report ATL-MUON-PUB-2008-004. ATL-COM-MUON-2008-006, CERN, Geneva, Feb 2008. backup paper for Atlas Detector paper.

[206] R. O. Duda and P. E. Hart. Use of the Hough transformation to detect lines and curves in pictures. *Commun. ACM*, 15(1):11–15, January 1972. ISSN 0001-0782. doi: 10.1145/361237.361242. URL `http://doi.acm.org/10.1145/361237.361242`.

[207] T. Lagouri, D. Adams, K. Assamagan, M. Biglietti, G. Carlino, G. Cataldi, F. Conventi, A. Farilla, Y. Fisyak, S. Goldafarb, E. Gorini, K. Mair, L. Merola, A. Nairz, A. Poppleton, M. Primavera, S. Rosati, J. Shank, S. Spagnolo, L. Spogli, G. Stavropoulos, M. Verducci, and T. Wenaus. A muon identification and combined reconstruction procedure for the ATLAS detector at the LHC at CERN. In *Nuclear Science Symposium Conference Record, 2003 IEEE*, volume 3, pages 1545–1548 Vol.3, Oct 2003. doi: 10.1109/NSSMIC.2003.1352171.

[208] ATLAS collaboration. Muons in the Calorimeters: Energy Loss Corrections and Muon Tagging. Technical Report ATL-PHYS-PUB-2009-009. ATL-COM-PHYS-2009-153, CERN, Geneva, Mar 2009.

[209] M. Schott, N. Benekos, J. F. Laporte, and L. Chevalier. Impacts of misalignment effects on the Muon Spectrometer Performance. Technical Report ATL-MUON-PUB-2007-006. ATL-COM-MUON-2007-007, CERN, Geneva, Jun 2007.

[210] ATLAS collaboration. Plots of Muon Performance in 2012 Data. Technical Report ATL-COM-PHYS-2012-716, CERN, Geneva, Jun 2012.

[211] ATLAS collaboration. Muon Momentum Resolution in First Pass Reconstruction of pp Collision Data Recorded by ATLAS in 2010. Technical Report ATLAS-CONF-2011-046, CERN, Geneva, Mar 2011.

[212] A. Salvucci, M. Corradi, J. Catmore, and O. Kortner. Dimuon mass reconstruction in 2012 data. Dec 2012. Figures released by the MCP group as a support of the

CONF note on Higgs→ 4*l* (ATLAS-COM-CONF-2012-204). More details in the internal note (ATLAS-COM-PHYS-2012-1774).

[213] K. Rehermann and B. Tweedie. Efficient Identification of Boosted Semileptonic Top Quarks at the LHC. *JHEP*, 1103:059, 2011. doi: 10.1007/JHEP03(2011)059.

[214] M. Aharrouche, G. Artoni, J. Barreiro Guimaraes da Costa, M. Bellomo, A. Belloni, E. F. Berglund, C. Bini, S. Borroni, R. Di Nardo, F. Ellinghaus, J. Ferrando, D. Froidevaux, C. Gatti, S. Giagu, M. Giunta, A. Glazov, F. Guescini, J. Hartert, V. Ippolito, F. Lo Sterzo, P. Mastrandrea, P. Onyisi, A. Kapliy, M. Karnevskiy, M. Klein, U. Klein, J. Kretzschmar, R. Poettgen, S. Prasad, M. Rescigno, E. Richter-Was, S. Rosati, A. Salvucci, A. Sapronov, M. Schott, M. Shochet, and E. Solfaroli Camillocci. Total and differential $W \to \ell\nu$ and $Z \to \ell\ell$ cross-sections measurements in proton-proton collisions at $\sqrt{s} = 7\,\text{TeV}$ with the ATLAS Detector. Technical Report ATL-COM-PHYS-2011-751, CERN, Geneva, Jun 2011.

[215] ATLAS collaboration. Efficiency of single isolated muon trigger as a function of muon p_T (barrel), 2012. URL `https://twiki.cern.ch/twiki/pub/AtlasPublic/MuonTriggerPublicResults/ICHEP12_mu24i_tight_barrel_Efficiency_pt.eps`.

[216] S. Catani, Y. L. Dokshitzer, and B. R. Webber. The K^- perpendicular clustering algorithm for jets in deep inelastic scattering and hadron collisions. *Phys.Lett.*, B285:291–299, 1992. doi: 10.1016/0370-2693(92)91467-N.

[217] Y. L. Dokshitzer, G. D. Leder, S. Moretti, and B. R. Webber. Better jet clustering algorithms. *JHEP*, 9708:001, 1997.

[218] M. Cacciari, G. P. Salam, and G. Soyez. The Anti-k_T jet clustering algorithm. *JHEP*, 0804:063, 2008. doi: 10.1088/1126-6708/2008/04/063.

[219] M. Cacciari, G. P. Salam, and G. Soyez. FastJet User Manual. *Eur.Phys.J.*, C72: 1896, 2012. doi: 10.1140/epjc/s10052-012-1896-2.

[220] ATLAS collaboration. Jet energy resolution and selection efficiency relative to track jets from in-situ techniques with the ATLAS Detector using proton-proton collisions at a Center of Mass Energy $\sqrt{s} = 7\,\text{TeV}$. Technical Report ATLAS-CONF-2010-054, CERN, Geneva, Jul 2010.

[221] R. Wigmans. High resolution hadron calorimetry. *Nuclear Instruments and Methods in Physics Research Section A: Accelerators, Spectrometers, Detectors and Associated Equipment*, 265(1-2):273–290, 1988. ISSN 0168-9002. doi: 10.1016/0168-9002(88)91081-9. URL `http://www.sciencedirect.com/science/article/pii/0168900288910819`.

[222] R. Wigmans. Effects of Calorimeter Peculiarities on the Jet Energy Scale. *Journal of Physics: Conference Series*, 323(1):012001, 2011. URL `http://stacks.iop.org/1742-6596/323/i=1/a=012001`.

[223] G. Aad et al. Jet energy resolution in proton-proton collisions at $\sqrt{s} = 7\,\text{TeV}$ recorded in 2010 with the ATLAS detector. *Eur.Phys.J.*, C73:2306, 2013. doi: 10.1140/epjc/s10052-013-2306-0.

[224] G. Aad et al. Jet energy measurement with the ATLAS detector in proton-proton collisions at $\sqrt{s} = 7\,\text{TeV}$. 2011.

[225] Yu. A. Kulchitskii, P. V. Tsiareshka, Yu. A. Budagov, J. I. Khubua, N. A. Rusakovitch, V. B. Vinogradov, A. Henriques, T. Davidek, S. Tokar, A. Solodkov, and I. Vichou. Electromagnetic Cell Level Calibration for ATLAS Tile Calorimeter Modules. Technical Report ATL-TILECAL-PUB-2007-001. ATL-COM-TILECAL-2006-013. CERN-ATL-TILECAL-PUB-2007-001, CERN, Geneva, Dec 2006.

[226] W. Lampl, S. Laplace, D. Lelas, P. Loch, H. Ma, S. Menke, S. Rajagopalan, D. Rousseau, S. Snyder, and G. Unal. Calorimeter Clustering Algorithms: Description and Performance. Technical Report ATL-LARG-PUB-2008-002. ATL-COM-LARG-2008-003, CERN, Geneva, Apr 2008.

[227] ATLAS collaboration. Jet energy scale and its systematic uncertainty in proton-proton collisions at $\sqrt{s} = 7\,\text{TeV}$ with ATLAS 2011 data. Technical Report ATLAS-CONF-2013-004, CERN, Geneva, Jan 2013.

[228] ATLAS collaboration. Close-by Jet Effects on Jet Energy Scale Calibration in pp Collisions at $\sqrt{s} = 7\,\text{TeV}$ with the ATLAS Detector. Technical Report ATLAS-CONF-2011-062, CERN, Geneva, Apr 2011.

[229] ATLAS collaboration. Light-quark and Gluon Jets in ATLAS. Technical Report ATLAS-CONF-2011-053, CERN, Geneva, Apr 2011.

[230] ATLAS collaboration. JetEtmissApproved2013JESUncertainty, 2012. URL `https://twiki.cern.ch/twiki/bin/view/AtlasPublic/JetEtmissApproved2013JESUncertainty`.

[231] ATLAS collaboration. JetEtmissApproved2011JetResolution, 2011. URL `https://twiki.cern.ch/twiki/bin/view/AtlasPublic/JetEtmissApproved2011JetResolution`.

[232] ATLAS collaboration. Data-Quality Requirements and Event Cleaning for Jets and Missing Transverse Energy Reconstruction with the ATLAS Detector in Proton-Proton Collisions at a Center-of-Mass Energy of $\sqrt{s} = 7\,\text{TeV}$. Technical Report ATLAS-CONF-2010-038, CERN, Geneva, Jul 2010.

[233] A. Coccaro. Track Reconstruction and b-Jet Identification for the ATLAS Trigger System. *J.Phys.Conf.Ser.*, 368:012034, 2012. doi: 10.1088/1742-6596/368/1/012034.

[234] ATLAS collaboration. Commissioning of the ATLAS high-performance b-tagging algorithms in the 7 TeV collision data. Technical Report ATLAS-CONF-2011-102, CERN, Geneva, Jul 2011.

[235] ATLAS collaboration. Calibrating the b-Tag and Mistag Efficiencies of the SV0 b-Tagging Algorithm in $3\,\mathrm{pb}^{-1}$ of Data with the ATLAS Detector. Technical Report ATLAS-CONF-2010-099, CERN, Geneva, Dec 2010.

[236] ATLAS collaboration. Performance of the ATLAS Secondary Vertex b-tagging Algorithm in 7 TeV Collision Data. Technical Report ATLAS-CONF-2010-042, CERN, Geneva, Jul 2010.

[237] G. Piacquadio and C. Weiser. A new inclusive secondary vertex algorithm for b-jet tagging in ATLAS. *Journal of Physics: Conference Series*, 119(3):032032, 2008. URL `http://stacks.iop.org/1742-6596/119/i=3/a=032032`.

[238] ATLAS collaboration. Measuring the b-tag efficiency in a top-pair sample with $4.7\,\mathrm{fb}^{-1}$ of data from the ATLAS detector. Technical Report ATLAS-CONF-2012-097, CERN, Geneva, Jul 2012.

[239] ATLAS collaboration. Measurement of the b-tag Efficiency in a Sample of Jets Containing Muons with $5\,\mathrm{fb}^{-1}$ of Data from the ATLAS Detector. Technical Report ATLAS-CONF-2012-043, CERN, Geneva, Mar 2012.

[240] R. K. Bock and J. Allison. *Formulae and Methods In Experimental Data Evaluation : with Emphasis On High Energy Physics*. European Physical Society Computational Physics Group, Switzerland, 1984.

[241] L. Lyons. Statistics for Nuclear and Particle Physicists, 1986.

[242] J. D'Hondt, S. Lowette, O. L. Buchmüller, S. Cucciarelli, F-P. Schilling, M. Spiropulu, S. Paktinat-Mehdiabadi, D. Benedetti, and L. Pape. Fitting of Event Topologies with External Kinematic Constraints in CMS. Technical Report CMS-NOTE-2006-023, CERN, Geneva, Jan 2006.

[243] ATLAS collaboration. Measurement of the Mistag Rate with $5\,\mathrm{fb}^{-1}$ of Data Collected by the ATLAS Detector. Technical Report ATLAS-CONF-2012-040, CERN, Geneva, Mar 2012.

[244] ATLAS collaboration. b-jet tagging calibration on c-jets containing D^{*+} mesons. Technical Report ATLAS-CONF-2012-039, CERN, Geneva, Mar 2012.

[245] ATLAS collaboration. Performance of Missing Transverse Momentum Reconstruction in ATLAS with 2011 Proton-Proton Collisions at $\sqrt{s} = 7\,\mathrm{TeV}$. Technical Report ATLAS-CONF-2012-101, CERN, Geneva, Jul 2012.

[246] ATLAS collaboration. Etmiss performance under high pile conditions in 2012 data, 2012. URL `https://twiki.cern.ch/twiki/bin/view/AtlasPublic/JetEtmissApproved2012EtmissWithPileup#Etmiss_performance_under_high_pi`.

[247] ATLAS collaboration. Performance of the ATLAS Inner Detector Track and Vertex Reconstruction in the High Pile-Up LHC Environment. Technical Report ATLAS-CONF-2012-042, CERN, Geneva, Mar 2012.

[248] ATLAS collaboration. Performance of primary vertex reconstruction in proton-proton collisions at $\sqrt{s} = 7\,\text{TeV}$ in the ATLAS experiment. Technical Report ATLAS-CONF-2010-069, CERN, Geneva, Jul 2010.

[249] ATLAS collaboration. Number of Interactions per Crossing, 2012. URL `https://atlas.web.cern.ch/Atlas/GROUPS/DATAPREPARATION/InteractionsperCrossing/muplot/2012/mu_2012-september2012.eps`.

[250] ATLAS Collaboration. Search for anomalous production of events with same-sign dileptons and b jets in $14.3\,\text{fb}^{-1}$ of pp collisions at $\sqrt{s} = 8\,\text{TeV}$ with the ATLAS detector. Technical Report ATLAS-CONF-2013-051, CERN, Geneva, May 2013. URL `http://atlas.web.cern.ch/Atlas/GROUPS/PHYSICS/CONFNOTES/ATLAS-CONF-2013-051/`.

[251] Humboldt University of Berlin. Physics department, 2013. URL `http://www.physik.hu-berlin.de/home/`. Web-page of the physics department of the Humboldt University of Berlin.

[252] University of Arizona. Department of Physics, 2013. URL `http://www.physics.arizona.edu/physics/`. Web-page of the physics department of the University of Arizona.

[253] University of Clermon-Ferrand. Laboratory for Particle Physics, 2013. URL `http://clrwww.in2p3.fr/`. Web-page of the laboratory for particle physics of the University of Clermont-Ferrand.

[254] J. M. Campbell and R. K. Ellis. $t\bar{t}W^{\pm}$ production and decay at NLO. *JHEP*, 1207:052, 2012. doi: 10.1007/JHEP07(2012)052.

[255] J. M. Campbell and R. K. Ellis. MCFM for the Tevatron and the LHC. *Nucl.Phys.Proc.Suppl.*, 205-206:10–15, 2010. doi: 10.1016/j.nuclphysbps.2010.08.011. URL `http://mcfm.fnal.gov/`.

[256] M. V. Garzelli, A. Kardos, C. G. Papadopoulos, and Z. Trocsanyi. $t\bar{t}\,W^{\pm}$ and $t\bar{t}\,Z$ Hadroproduction at NLO accuracy in QCD with Parton Shower and Hadronization effects. *JHEP*, 1211:056, 2012. doi: 10.1007/JHEP11(2012)056.

[257] Search for direct production of charginos and neutralinos in events with three leptons and missing transverse momentum in $13\,\text{fb}^{-1}$ of pp collisions at $\sqrt{s} = 8\,\text{TeV}$

with the ATLAS detector. Technical Report ATLAS-CONF-2012-154, CERN, Geneva, Nov 2012.

[258] D. Boumediene, E. Busato, D. Calvet, S. Calvet, E. Dubreuil, S. Grancagnolo, C. Helsens, V. Kaushik, H. Lacker, X. Lei, R. Nayyar, F. O'Grady, D. Paredes, D. Simon, D. Sperlich, L. Valery, E. Varnes, and D. Wendland. Search for exotic same-sign dilepton signatures in $14.3\,\mathrm{fb}^{-1}$ of pp collisions at $\sqrt{s} = 8\,\mathrm{TeV}$ with the ATLAS detector. Technical Report ATL-COM-PHYS-2013-086, CERN, Geneva, Jan 2013. Internal ATLAS support document.

[259] F. James and M. Roos. Minuit: A System for Function Minimization and Analysis of the Parameter Errors and Correlations. *Comput.Phys.Commun.*, 10:343–367, 1975. doi: 10.1016/0010-4655(75)90039-9.

[260] J. W. Chinneck. MINOS(IIS): Infeasibility analysis using MINOS. *Computers & Operations Research*, 21(1):1 – 9, 1994. ISSN 0305-0548. doi: 10.1016/0305-0548(94)90057-4.

[261] DESY ATLAS group. DESY ATLAS Framework, 2013. URL `https://wiki-zeuthen.desy.de/ATLAS/Projects/TopPhysicsInternal/AnalysisFramework`.

[262] DESY ATLAS. DESY ATLAS group, 2013. URL `http://www-atlas.desy.de/`.

[263] D. Berge, J. Haller, and A. Krasznahorkay. SFrame - A ROOT data analysis framework, 2012. URL `http://sourceforge.net/projects/sframe/`.

[264] G. Choudalakis and D. Casadei. Plotting the differences between data and expectation. *European Physical Journal Plus*, 127:25, February 2012. doi: 10.1140/epjp/i2012-12025-y.

[265] T. Junk. Confidence level computation for combining searches with small statistics. *Nucl.Instrum.Meth.*, A434:435–443, 1999. doi: 10.1016/S0168-9002(99)00498-2.

[266] A. L. Read. Modified frequentist analysis of search results (the CL_s method). (CERN-OPEN-2000-205), 2000.

[267] P. K. Sinervo. Signal significance in particle physics. pages 64–76, 2002.

[268] A. L. Read. Presentation of search results: the CL_s technique. *Journal of Physics G: Nuclear and Particle Physics*, 28(10):2693, 2002. URL `http://stacks.iop.org/0954-3899/28/i=10/a=313`.

[269] T. Junk. Sensitivity, Exclusion and Discovery with Small Signals, Large Backgrounds, and Large Systematic Uncertainties. (CDF/DOC/STATISTICS/PUBLIC/8128), 2007.

[270] J. Neyman and E. S. Pearson. On the Problem of the Most Efficient Tests of Statistical Hypotheses. *Philosophical Transactions of the Royal Society of London. Series A, Containing Papers of a Mathematical or Physical Character*, 231:pp. 289–337, 1933. ISSN 02643952. URL `http://www.jstor.org/stable/91247`.

[271] C. Helsens. mclimitCode, 2013. URL `svn+ssh://svn.cern.ch/reps/atlasphys/Physics/Exotic/Analysis/HeavyQuarks/LimitsCode/mclimitCode/tags/mclimitCode-01-02-01`.

[272] G. Aad et al. Measurement of the top quark-pair production cross section with ATLAS in pp collisions at $\sqrt{s} = 7\,\text{TeV}$. *Eur.Phys.J.*, C71:1577, 2011. doi: 10.1140/epjc/s10052-011-1577-6.

[273] J. Alwall, S. Höche, F. Krauss, N. Lavesson, L. Lonnblad, et al. Comparative study of various algorithms for the merging of parton showers and matrix elements in hadronic collisions. *Eur.Phys.J.*, C53:473–500, 2008. doi: 10.1140/epjc/s10052-007-0490-5.

[274] D. Bourilkov, R. C. Group, and M. R. Whalley. LHAPDF: PDF use from the Tevatron to the LHC. *hep-ph/0605240*, 2006.

[275] A. Sherstnev and R .S. Thorne. Parton Distributions for LO Generators. *Eur.Phys.J.*, C55:553–575, 2008. doi: 10.1140/epjc/s10052-008-0610-x.

[276] A. Sherstnev and R. S. Thorne. Different PDF approximations useful for LO Monte Carlo generators. page 149, 2008. doi: 10.3360/dis.2008.149.

[277] H-L. Lai, J. Huston, S. Mrenna, P. Nadolsky, D. Stump, et al. Parton Distributions for Event Generators. *JHEP*, 1004:035, 2010. doi: 10.1007/JHEP04(2010)035.

[278] K. Joshi, M. Owen, and A. D." Pilkington. Measurement of top-antitop production with a veto on additional central jet activity in pp collisions at $\sqrt{s} = 7\,\text{TeV}$ using the ATLAS detector. Technical Report ATL-COM-PHYS-2011-1740, CERN, Geneva, Dec 2011.

[279] I. Dumanoglu. Introduction to Calorimeters, 2006. URL `http://thm.ankara.edu.tr/tac/YAZOKULU/yazokulu2/dersnotlari/bodrum_isa.pdf`. Slides of a talk given at Bodrum Accelerator School 2006 in Bodrum, Turkey.

[280] S. Stefanidis. Performance studies on the EM calorimeter, July 2006. URL `http://www.hep.ucl.ac.uk/~sstef/EMCalo/LArSamplingCalorimeter.png`. Personal web-page of Stathis Stefanidis at the University College London, UK.

[281] M. E. Reinhard. Determination of the Muon Reconstruction and Identification Efficiencies in the CMS Experiment. Master's thesis, ETH Institute for Particle Physics, Switzerland, 2008.

List of Figures

List of Tables